The Origin and Evolution of the Siletz Terrane in Oregon, Washington and Vancouver Island

Bethan Alys Phillips

School of Earth and Ocean Sciences

Cardiff University

Submitted in partial fulfilment of the requirements for the
degree of
Doctor of Philosophy

April 2017

ABSTRACT

The Siletz terrane, a predominantly mafic accreted oceanic terrane, is located in the Cascadia Forearc region of Oregon, Washington and Vancouver Island. The terrane represents a late Palaeocene – Eocene large igneous province that consists of pillow lavas, massive flows and intrusive sheets. Previously it has been proposed that the Siletz terrane represents either an accreted oceanic plateau, hotspot island chain, back -arc basin, island arc, or a sequence of slab window volcanics. A province-wide geochemical reassessment of the terrane, including new high precision Sr-Pb-Nd-Hf isotope, has been used to evaluate the validity of the proposed tectonomagmatic models for the Siletz terrane along with the subsequent evolution of the magmas.

Fractional crystallisation of the primary magmas of the terrane appears to have occurred at relatively low pressures. The estimated initial mantle potential temperatures of the Siletz terrane range from 1400 - 1500 °C while the amount of partial melting undergone generally varies between ~ 25 – 33 %. The rocks of the terrane are geochemically similar, both in trace element (generally flat to Light Rare Earth Element (REE) enriched REE patterns) and radiogenic isotope composition to several well-characterised oceanic plateaus. The data produced in this study are consistent with a mantle source for the Siletz terrane that appears to have been heterogeneous and slightly enriched. The enriched signature has characteristics of both EM2 and HIMU components and this, combined with a calculated mantle potential temperature significant above that of ambient mantle, indicates derivation of the Siletz magmatism from a source influenced by a mantle plume, possibly the Yellowstone Hotspot. Overall, the terranes' geochemistry suggests interaction between the Farallon – Kula/ Resurrection ridge and a hotter enriched mantle source region. It is therefore concluded that the Siletz terrane represents an accreted oceanic plateau and so is the youngest oceanic plateau thus far characterised.

Declaration

This work has not been submitted in substance for any other degree or award at this or any other university or place of learning, nor is being submitted concurrently in candidature for any degree or other award.

Signed …………………………………………………………………. (candidate)

Date ……………………

Statement 1

This thesis is being submitted in partial fulfilment of the requirements for the degree of PhD.

Signed …………………………………………………………………. (candidate)

Date ……………………

Statement 2

This thesis is the result of my own independent work/investigation, except where otherwise stated, and the thesis has not been edited by a third party beyond what is permitted by Cardiff University's policy on the Use of Third Party Editors by Research Degree Students. Other sources are acknowledged by explicit references. The views expressed are my own.

Signed …………………………………………………………………. (candidate)

Date ……………………

Statement 3

I hereby give consent for my thesis, if accepted, to be available online in the University's Open Access repository and for inter-library loan, and for the title and summary to be made available to outside organisations.

Signed …………………………………………………………………. (candidate)

Date ……………………

Statement 4

I hereby give consent of my thesis, if accepted, to be available online in the University's Open Access repository and for inter-library loans after expiry of a bar on access previously approved by the Academic Standards & Quality Committee.

Signed …………………………………………………………………. (candidate)

Date ……………………

ACKNOWLEDGMENTS

Finally I would like to thank my Mam, Dad and sister Nia, their support and patience has known no bounds over the last three and half years. I'm not sure if words can convey the magnitude of my gratitude, but I do know that the completion of this thesis would have been impossible without them. It is to them that I dedicate this work, diolch am bopeth.

TABLE OF CONTENTS

1. INTRODUCTION

1.1 Rationale

The Siletz terrane represents a Late Palaeocene - Early Eocene accreted mafic oceanic Large Igneous Province, situated in the present day Cascadia forearc in Oregon, Washington and Vancouver Island (Figure 1.1). The terrane represents a large scale magmatic event and its formation is concurrent with a major shift in the plate tectonic configuration of the region (Atwater, 1989; Seton et al., 2012). In addition, it has been suggested that this Large Igneous Province was erupted and emplaced as a result of the arrival of the Yellowstone hotspot in the region (e.g., Duncan, 1982; Babcock et al., 1992; Pyle et al., 2009; Wells et al., 2014). At present however, there is little consensus on the tectonic setting in which the Siletz terrane magmas were generated and therefore understanding the geochemistry of the Siletz terrane is key to unravelling its origin and evolution.

Prior to this investigation, no comprehensive large scale geochemical investigation into the Siletz terrane had been undertaken. This study therefore presents a province-wide geochemical reassessment of the terrane, including new high precision Sr-Pb-Nd-Hf isotope data on 20 basaltic and gabbroic samples. The primary goals of this investigation are to use these new geochemical data to assess the nature of the mantle source region and the validity of the proposed tectonomagmatic models for the Siletz terrane.

1.2 Objectives

The main aims of this study are to utilise the major, trace, radiogenic isotope and petrological data to:

- Produce a coherent and comprehensive geochemical data set for each of the igneous suites thought to be part of the Siletz terrane
- Determine the extent and effect of magma chamber processes, such as fractional crystallisation, on the evolution of the Siletz terrane magmas.

- Investigate whether the primary magmas are the product of melting of source region which is hotter than ambient due to the presence of a mantle plume.
- Assess the composition of the mantle source regions from which the Siletz terrane primary magmas originated.
- Produce a synthesis of the tectonic environment in which the Siletz terrane formed and how this impacts the overall evolution of the region.
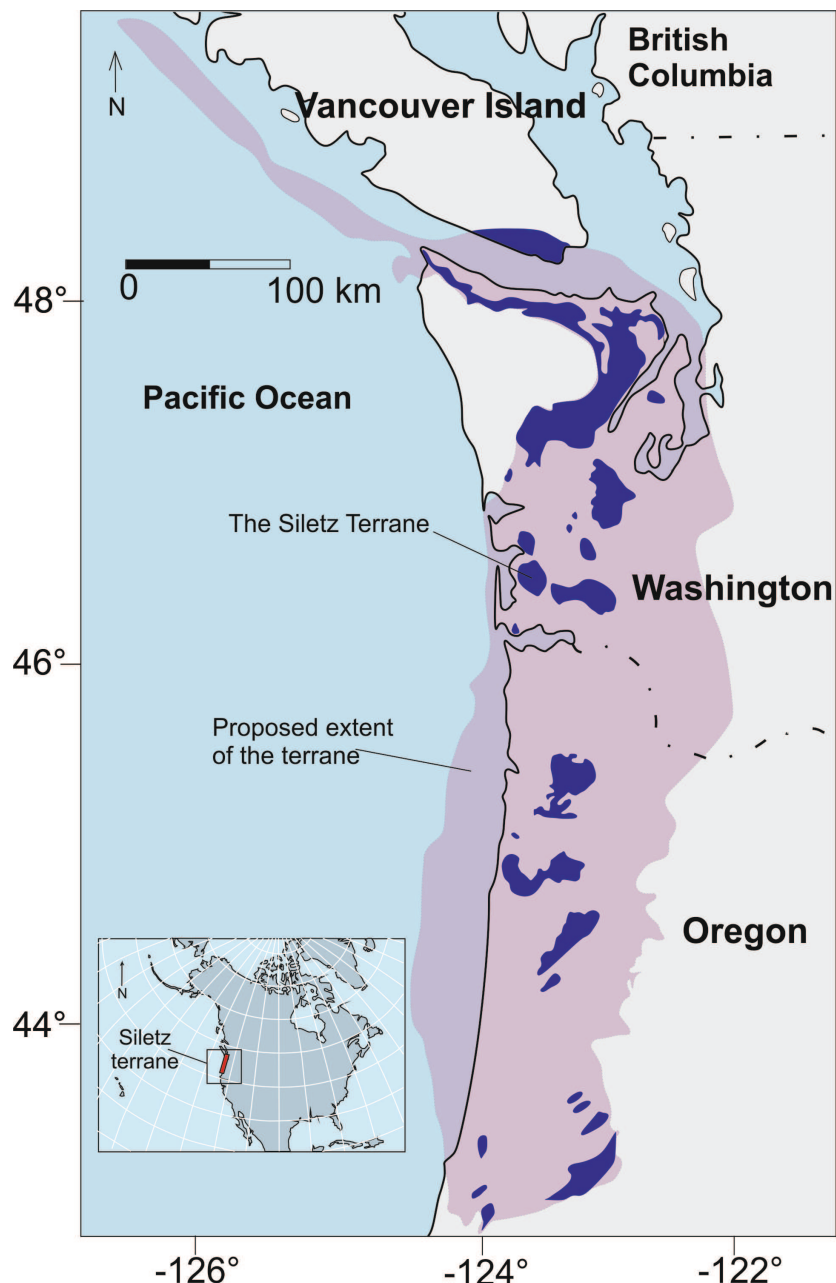
Figure 1.1 Map highlighting the location of the Siletz terrane (Dark purple) and the proposed extent of the terrane (light purple) in the present day Cascadia forearc. Adapted from McCrory and Wilson (2013).

1.3 Thesis Structure

This thesis contains seven chapters. Following this introduction, Chapter 2 consists of a geological overview and background of the Siletz terrane and surrounding region, along with a synthesis of previous work and models for the

origin of the terrane. Chapter 3 describes the geology of each area of the terrane and the details of sample collection. Chapter 4 primarily focuses on the petrography and alteration of the rocks analysed in this study along with their mineral compositions, obtained via quantitative mineral analyses. The next chapter (Chapter 5) is the main results chapter and presents the major and trace element, radiogenic isotope and geochronological results analysed during this study. Chapter 6 discusses the geochemical data and investigates the evolution of the suites of the terrane using petrogenetic models, their melting history and the nature of the mantle source before to constraining the tectonomagamtic environment in which the terrane formed. Finally, Chapter 7 presents a brief summary of the project, highlighting key conclusions. Any additional sample information, methods and geochemical data are presented in the electronic appendices.

2. GEOLOGICAL OVERVIEW

2.1 Accreted Oceanic Terranes

Accreted oceanic mafic terranes are an ubiquitous feature of destructive plate margins across the globe, including the northern Andes, i.e., western Ecuador and western Colombia (Kerr et al., 1997; Kerr et al., 2002a); the Wrangellia terrane and other coastal ranges of western Canada and Alaska (Greene et al., 2009a;b); and the Sorachi Plateau, Japan (Kimura et al., 1994; Ichiyama et al., 2014). Accreted oceanic terranes are also prominent in several continental collision zones such as that represented by the closure of the Tethyan Ocean, e.g., the Mirdita Ophiolite, Turkey (Whattam and Stern, 2011), Dur'ngoi ophiolite, Tibet (Chen et al., 2001) and the Dehshir ophiolite central Iran (Moghadam et al., 2010). Such mafic accreted terranes are common throughout most of Earths' history (e.g., Kerr 2014) and are thought to have contributed significantly to the growth of continental crust (Condie, 1998; Stern and Scholl, 2010). Accreted oceanic mafic rocks are generally taken to represent areas of over-thickened (> 6-7 km) oceanic crust (e.g., seamounts, ocean islands, aseismic ridges or oceanic plateaus) that was too buoyant to subduct (e.g., Cloos, 1993; Tetreault and Buiter, 2014). This uplifted and accreted oceanic crust affords an excellent opportunity to study the structure, composition and origin of a part of the ocean floor that would otherwise be relatively inaccessible.

2.2 Large Igneous Provinces

Large Igneous Provinces (LIPs) are defined as areas of rapidly erupted high Fe-Mg magmatism in a setting, which is not associated with 'normal' plate margin processes, such as spreading and subduction (Coffin and Eldholm, 1991). Included in this original definition are flood basalts, dyke swarms, submarine ridges, seamount chains, oceanic plateaus and volcanic rifted margins (Coffin and Eldholm, 1992; 1994). Sheth (2007) has subsequently suggested expanding the definition to include any igneous province with an aerial extent of > 50,000 km^2.

While Bryan and Ernst (2008) proposed a more constrained definition of what constitutes as a LIP, stipulating an aerial extent of $> 0.1M$ km^2, volumes of $> 0.1M$ km^3, active ages of ≤ 50 Myr, intraplate geochemical signatures and a defining pulse of igneous activity of around 1-5 Myr, by the end of which most of the igneous province has been erupted. In any case LIPs preserve exceptional eruption events of significant, if episodic, periods of magmatism and crustal growth (Bryan and Ferrari, 2013). While the mechanism of their formation has been the subject of considerable debate (Foulger and Jurdy, 2007), most authors agree that a mantle plume model is the most applicable (e.g. Campbell and Griffiths, 1990; Coffin and Eldholm, 1994; Ernst and Bleeker, 2010; Timm et al., 2011).

The exploration and examination of LIPs has been used to constrain large scale mantle geodynamics and the evolution and characteristics of the deep mantle. LIP eruptions are thought to have a significant effect on the biosphere, hydrosphere and atmosphere, and several of these eruption events are thought to be linked to mass extinction events (Bond and Wignall, 2014). Additionally LIPs have proved to be an important source of major PGE, precious metal and hydrocarbon deposits (Bryan and Ferrari, 2013).

2.2.1 Oceanic Plateaus

The term oceanic plateau was first used by Kroenke (1974) as a description of the Ontong Java Plateau, an area of predominantly mafic thickened oceanic crust in the southwest Pacific Ocean. Oceanic plateaus have therefore only been recognised for ~40 years and despite a significant increase in our knowledge and understanding since their discovery in the early 1970s they still remain the least well-understood type of magmatic province (Kerr, 2003). However, during the subsequent decades many more oceanic plateaus have been recognised and described, both in situ and as accreted terranes (Figure 2.1) (Kerr, 2014).
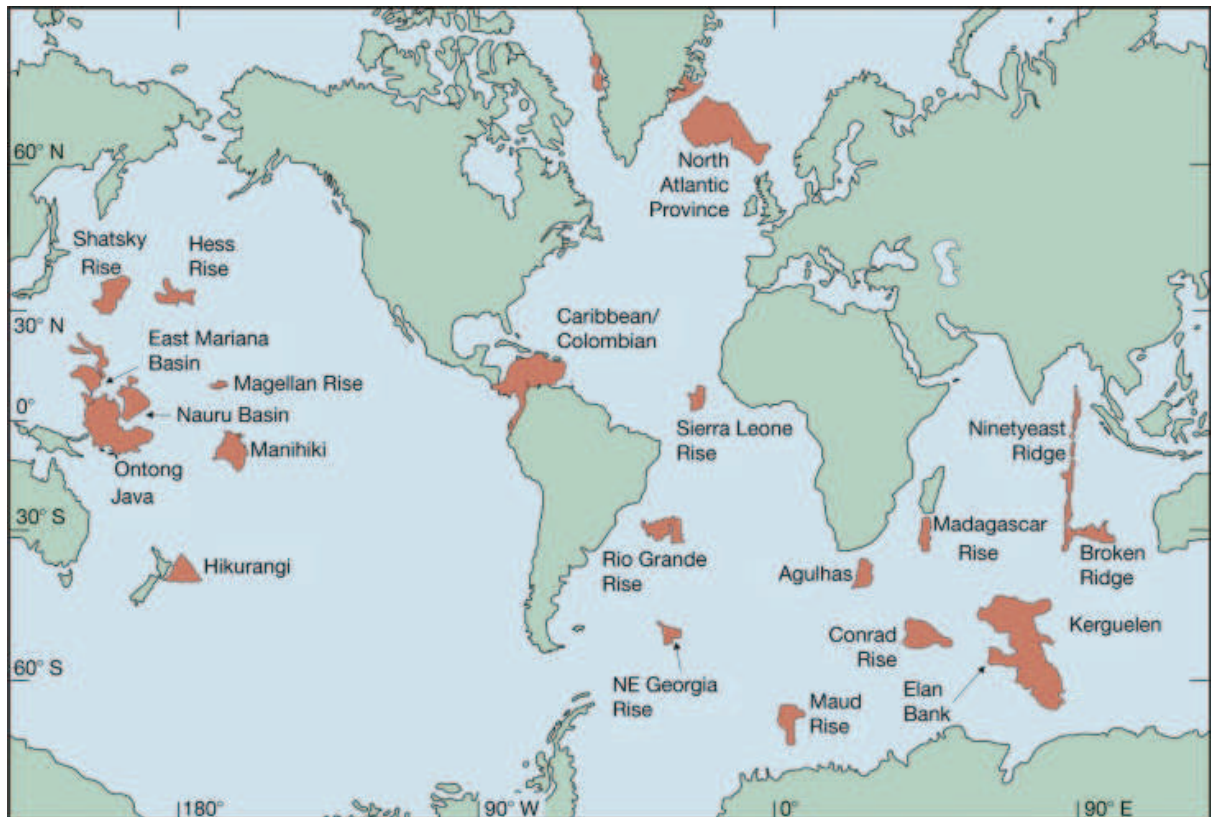
Figure 2.1. Map highlighting the major oceanic plateaus recognised from the last 150 Ma (Kerr, 2014).

Oceanic plateaus represent an ideal setting in which to further our understanding of the source and petrogenesis of LIPs, as they generally reflect the composition of their mantle source regions to a greater extent than their continental flood basalt counterparts. This preservation of mantle signatures is a result of eruption through thin (~ 6 -7 km) mafic and ultramafic oceanic crust, whereby oceanic plateaus generally avoid contamination by continental crustal melts. In addition to this, oceanic plateaus have elevated topography and greater crustal thickness in comparison with 'normal' oceanic crust, which leads to an increase in buoyancy. Therefore, notably for plateaus that collide with subduction zones shortly after formation (< 5 Ma) (Cloos, 1993), the probability of partial accretion to the adjacent upper continental plate margin and so preservation within the geologic record is greatly increased (Cloos, 1993; Abbott and Mooney, 1995; Tetreault and Buiter, 2014). This uplifted and accreted oceanic crust affords an excellent opportunity to study the structure, composition and origin of a part of the ocean floor that would otherwise be relatively inaccessible. In contrast,

continental flood basalts undergo a larger degree of subaerial erosion, both during and after their eruption, decreasing their preservation potential in comparison with accreted fragments of oceanic plateaus (Kerr and Mahoney, 2007).

2.2.2 Oceanic Plateau Characteristics

Along with seismic surveys conducted on extant oceanic plateaus (Farnetani et al., 1996; Miura et al., 2004), field investigations of accreted fragments have determined the structure and stratigraphy of oceanic plateaus (Kerr et al., 1997a; b; 1998; Petterson et al., 1997; Petterson, 2004). Olivine cumulates are thought to form the basal layer of most oceanic plateaus, which are then overlain by isotropic gabbros. The earliest lavas in the sequence are geochemically heterogeneous picrites and komatiites (with MgO contents of > 12 wt. %). These primitive lavas display a wide range of isotopic ratios and incompatible trace element concentrations and ratios (Kerr and Mahoney, 2007). Overlying the picrites and komatiites are thick sequences of homogeneous basaltic lavas and dolerite sheets that show little variation in major element, trace element and radiogenic isotope compositions (Kerr and Mahoney, 2007). These basalts and dolerites generally have Rare Earth Element (REE) patterns that are flat to slightly Light REE enriched, along with other trace element signatures similar to Mid Ocean Ridge Basalts (MORB) and Ocean Island Basalt type (OIB)-like isotopic ratios (Nd, Pb, Hf and Sr) (Mahoney, 1987; Kerr and Mahoney, 2007).

However, while the largest oceanic plateau, the Cretaceous Ontong Java Plateau, is significantly homogeneous in composition (Fitton and Godard, 2004), other well characterised oceanic plateaus such as the Cretaceous Caribbean plateau (Kerr and Mahoney, 2007) and the Late Triassic (*c.* 225-231 Ma) Karmusten flood basalts of Vancouver Island and Alaska (Greene et al., 2009) display more heterogeneous trace element compositions.

While sheeted dykes are usually absent in oceanic plateaus, the sequences are commonly intruded by sills and sheets (Kerr et al., 1996; Kerr et al., 1997a; Petterson et al., 1997). It has been suggested that the lack of sheeted dykes is a

result of extension being unable to accommodate the emplacement of vast volumes of magma into the plateau, leading instead to lateral intrusion as sills and sheets (Kerr et al., 1997b; Hansen et al., 2004).

2.2.3 Oceanic Plateau (LIP) Formation and Accretion

As discussed above, as a result of geochemical, physical and computational modelling, the most widely accepted mechanism of formation for oceanic plateaus is partial adiabatic decompression melting of a mantle plume head as it impinges with the base of the lithosphere (e.g. Campbell and Griffiths, 1990; Farnetani and Richards, 1995 Fitton and Godard, 2004; Campbell, 2007). In this model the rising plume has an above ambient mantle temperature (average mantle temperature below oceanic ridges at a given time (Herzberg et al., 2007), a heterogeneous composition and, usually, a lower mantle origin. However, the viability of mantle plumes have been questioned by several authors (Anderson and Natland, 2007; Falloon et al., 2007; Anderson, 2013) and thus other processes have been proposed for oceanic plateau formation, including back arc basin settings (Rivers and Corrigon 2000), leaky transform faults (Hilde et al., 1976), unusually active mid oceanic ridges (Winterer et al., 1974; Winterer, 1976), plate reorganisations involving triple junctions and plume interactions (Sager et al., 1999) and meteorite impact (Rogers, 1982; Ingle and Coffin, 2004).

Most recognised oceanic plateaus are thought to have undergone the majority of their eruption and emplacement during one main and initial volcanic episode (Kerr et al., 2014). A large percentage of the Ontong Java Plateau was erupted over a few million years between ~ 122 Ma and 120 Ma (e.g. Chambers et al., 2004; Mahoney et al., 1993a; b; Tejada et al., 1996; 2002), the majority of the Caribbean Plateau between 93 – 89 Ma (Kerr et al., 2003) and most of the southern Kerguelen plateau between 119 – 118 Ma (Coffin et al., 2002; Duncan, 2002). To be able to generate such quantities of magma over such relatively short periods of geological time, the source region is required to be fundamentally different to the ambient mantle, i.e. it must be either, hotter, more fertile or more volatile rich. It has been determined that decompression partial melting of a

dominantly peridotite mantle source with a higher than ambient T_p (potential temperature, that is the temperature mantle material would have were it adiabatically decompressed to the surface of the earth) can produce the volumes of magma observed in oceanic plateaus over the time scales described above (Fitton and Godard, 2004; Herzberg, 2004; Herzberg et al., 2007; Putirka et al., 2008).

However, conventional mantle plume theory cannot explain all features of all oceanic plateaus. In particular several of the anomalous features of the Ontong Java Plateau are difficult to reconcile with a mantle plume model. For example the majority of volcanism was submarine in nature, while the domal uplift expected to have occurred (due to the plateau's substantial thickness) predicts significant subaerial volcanism (Mahoney et al., 2001). Additionally although the majority of the magmatism occurred over a few million years, the overall magmatism of the Ontong Java Plateau was long lived (Ito and Clift, 1998) and there is a lack of an expected hotspot track (Fitton and Godard, 2004). However, the lack of succeeding hotspot track may indicate that the nature of upwelling mantle plumes is variable (Kerr and Mahoney, 2007). Several thermochemical plume types may be generated through the interaction of lateral heterogeneities in both composition and density ~100 – 200 km above the Core Mantle Boundary (Davaille et al., 2002; Davaille et al., 2005; Farnetani and Samuel, 2005; Lin and van Keken, 2006a; 2006b). Plumes with a high proportion of a stabilizing chemical density anomaly are thought to be anchored, producing a long lived hotspot (Davaille et al., 2002). While plumes with a greater thermal anomaly are domed with little or no plume tail (Davaille et al., 2005; Kerr and Mahoney, 2007). Additionally, it has been suggested that some plumes produce what has been termed double flood basalts which occur as two eruptive events separated by between 20 and 90 million years (Bercovici and Mahoney 1994).

Oceanic plateaus have greater crustal thicknesses than 'normal' oceanic crust, which formed at mid ocean ridges, thus resulting in increased buoyancy in the plateaus. Therefore, the upper layers of oceanic plateaus in particular are more likely to undergo accretion to island arcs and continental margins as they are 'scraped off' during subduction (Ben-Avraham et al., 1981; Cloos, 1993; Kimura

and Ludden, 1995). Additionally a plateau which collides with a subduction zone shortly after formation (< 5Ma) is more likely to undergo at least partial accretion than older plateaus that are colder and denser (Cloos, 1993), and complete subduction of oceanic plateaus is more likely when they are older than 40 Ma (Vogt and Gerya, 2014). Oceanic plateaus therefore have a greater probability of preservation in the geological record than normal oceanic crust (Kerr et al., 2014). Accretion of an oceanic plateau to an island arc may result in subduction polarity reversal, while accretion onto a continental margin is thought to lead to subduction back-stepping behind the accreted terrane, and thus continental growth (Kerr and Mahoney, 2007). However, despite accreted oceanic plateaus and other thickened areas of oceanic crust playing a significant role in continental growth relatively little is known about the mechanisms responsible for this accretion (e.g., Vogt and Gerya, 2014).

2.2.4 Environmental Impact of Oceanic Plateaus

The addition of large volumes of magma that occur during oceanic plateau eruption have been shown to have a significant effect on the climate and biota and indeed many second order extinction events have been shown to correlate with their formation (Sepkoski, 1996; Kerr, 1998). Global oceanic anoxia, black shale deposition and mass extinction events which took place during the Cretaceous have been found to coincide with oceanic plateau eruption, specifically around the Cenomanian – Turonian boundary (CTB) (93.5 Ma) and the Aptian (124-112 Ma) (Vogt, 1989; Sinton and Duncan, 1997; Kerr, 1998; Kuroda et al., 2007; Tejada et al., 2009). Along with higher average surface and ocean temperatures and a major sea level transgression, the extinction of 26 % of all known genera is thought to have occurred at the CTB (Sepkoski, 1996).

The numerous potential physical and chemical effects of oceanic plateau volcanism on the global environment are summarized in Figure 2.2 (Kerr, 2005; 2014). One potential consequence is the displacement of seawater caused by the impinging plume and emplacement of massive amounts of material along with thermal expansion of water, results in a rise in the surrounding sea level

(Campbell, 2007; Courtney and White, 1986). Additionally, ocean circulation patterns can be affected by the emplacement of an oceanic plateau (Kerr, 1998). Increased volcanic activity leads to increased emissions of volatiles (e.g., CO_2, SO_2, Cl, F and H_2S) into the atmosphere, affecting both long and short term climate patterns and ocean acidity (Kerr 1998; 2005). Positive $\delta^{13}C$ anomalies noted in the CTB are a reflection of increased upwellings of hydrothermal plumes from eruption sites containing deep-water nutrients (Sinton et al., 1997), along with an increase in CO_2 results in higher organic productivity (Arthur et al., 1987; Barclay et al., 2010). The net result of this is a reduction of dissolved O_2 and black shale formation and ocean anoxia (Kerr, 2005).
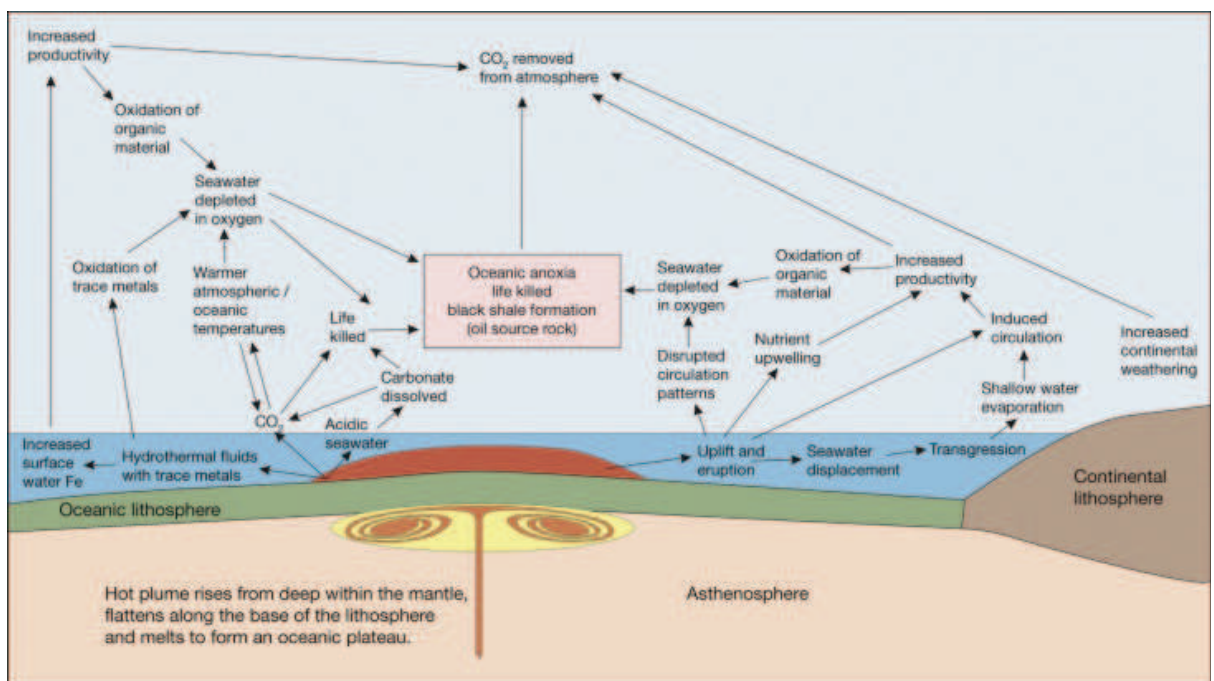
Figure 2.2. Summary of the potential physical and chemical environmental effects and consequences of oceanic plateau eruption and emplacement (Kerr, 2005; Kerr, 2014).

2.3 Regional Geology

2.3.1 Cordilleran Geology Overview

It has been proposed that at the time of formation of the Siletz terrane (Late Palaeocene - Early Eocene) there were 4 (or 5) plates in the North East Pacific; the Farallon, Kula, Pacific, North American (and Resurrection) plates

(Figure 2.3) (Haeussler et al., 2003; Seton et al., 2012). During this time a major change in the plate configuration took place, which resulted in an adjustment in spreading direction between the Pacific and Farallon plates from WSW-ENE to E-W (Atwater, 1989). The Pacific- Kula ridge also underwent a change in spreading direction from N–S to NW–SE (Seton et al. 2012) before an eventual cessation of spreading (Engebretson, 1985). Most early Eocene plate reconstruction models agree that the Farallon – Kula ridge was striking NE–SW at the time of formation of the Siletz terrane, intersecting the North American plate to the east, forming a triple junction with the Pacific plate in the west and a slab window at the adjacent margin of the North American continent (Engebretson, 1985; Atwater, 1989; Breitsprecher et al., 2003; Madsen et al., 2006; Seton et al., 2012).

The existence of an additional Resurrection plate between the Kula plate and the North American plate, to the north of the Farallon plate has been proposed to account for the migration of magmatism along the southern margin of Alaska during the late Palaeocene to early Eocene (Haeussler et al., 2003). The Kula-Resurrection ridge has been modelled to have been subducted by 50 Ma (Breitsprecher et al., 2003; Haeussler et al., 2003; Wells et al., 2014) and the Siletz terrane is suggested to have formed on, or adjacent to, the mid ocean ridge located between the Resurrection plate and the Farallon plate (McCrory and Wilson, 2013). It has also been argued that at this time (and at least since 60 Ma) the Yellowstone hotspot was located offshore of the North American continent; however, its location remains unclear (McCrory and Wilson, 2013). O'Neill et al. (2005) proposed that at 55 Ma the Yellowstone hotspot was located on the Kula – Farallon or Farallon – Resurrection ridge. Alternatively, Doubrovine et al. (2012) suggested that the hotspot was located off-axis on the Farallon plate whereas Müller et al. (1993) argued that it was adjacent to the North American continent and had moved underneath it by 50 Ma. A series of accreted terranes are presently found along this margin and these terranes form the basement to the Cascade magmatic arc, which now dominates the region. This arc has been active since 40 Ma and is a result the Juan de Fuca plate subducting beneath the North American plate (Hildreth, 2007).
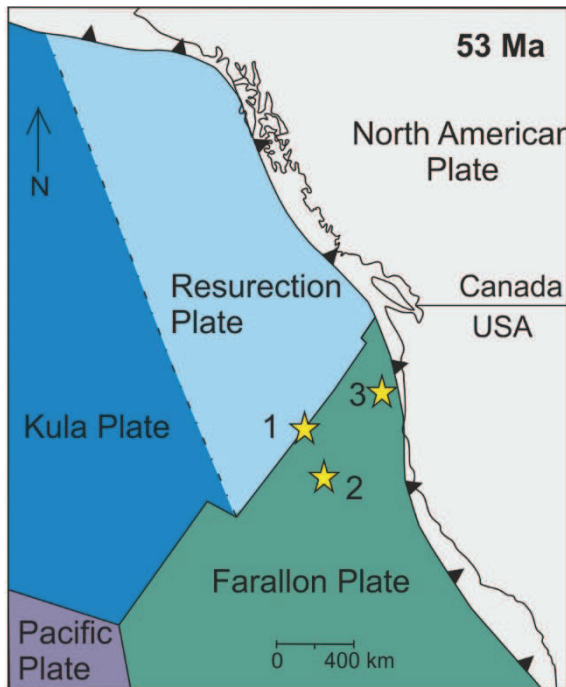
Figure 2.3. Diagram displaying a suggested plate configuration at in the region at ~ 53Ma. Adapted from Seton et al., (2012) and Wells et al., (2014), where the stars represent the proposed positions of the Yellowstone hotspot; 1 (O'Neill et al. (2005), 2 (Doubrovine et al., 2012) 3 (Müller et al., 1993).

2.3.2 Yellowstone Hotspot

Most models for the Yellowstone hotspot place the rising plume reaching the base of the lithosphere at around 20 Ma (Pierce and Morgan, 2009). It has been suggested that the hotspot intersected the subducting Juan de Fuca slab, causing the tearing of the slab at 400 km (Geist and Richards, 1993; Pierce et al., 2000; Xue and Allen, 2007) or alternatively that the plume rose through a slab window (Roth et al., 2008). In either case, volcanism recorded between 16.7 – 14 Ma has been proposed to represent the initial plume head melting phase (Pierce and Morgan, 2009). Large basaltic dyke swarms in north and central Nevada, flood basalt volcanism in Washington and the Columbia River Flood Basalts (CRFB) and rhyolitic flows at the Nevada – Oregon – Idaho border erupted during this time period (16.7 – 14 Ma) are all used as evidence in support of a mantle

plume melting event (Pierce and Morgan, 2009). Additionally 15.4 Ma basalts in north western California (Wagner et al., 2000; Garrison et al., 2008), 16.5 – 15.5 Ma rhyolitic lavas in north western Nevada and the 16.1 Ma McDermitt volcanic field on the Nevada – Oregon border (Pierce et al., 2000; Coble and Mahood, 2008) are also thought to be related to this initial melting event (Pierce and Morgan, 2009).

It has been suggested by some authors by some authors that the Yellowstone hotspot is significantly older than the CRFB and associated volcanism that occurred at ~17 Ma (Duncan, 1982; Johnston et al., 1996). Plate reconstructions have proposed that the Yellowstone hotspot initially resided beneath, or proximal to, the Kula – Farallon ridge until around 53 Ma before moving eastward beneath the North American plate by around 50 Ma (Murphey et al., 2003; Seton et al., 2012). Geist and Richards (1993) proposed that the plume tail then incubated beneath the subducting Farallon plate before rising through the slab. Deflection of the plume northwards may have been a result of the rollback of the Farallon slab and delamination of the lithosphere from the base of the North American plate near Oregon, which in turn was triggered by the presence of the Yellowstone plume (Humphreys, 2015). Subsequently, by 35 Ma, the plume was thought to be beneath central Oregon (Wells et al., 2014). It has been suggested that the Crooked River Caldera (32-28 Ma) is also related to the Yellowstone hotspot, which removes the 30 million year amagmatic gap between the waning of magmatism in the Siletz terrane (~49 Ma) and the beginning of the eruption of the Columbia River Flood Basalts at ~ 17 Ma (Seligman et al., 2014; Wells et al., 2014) (Figure 2.4). Following this, melting then produced the Grande Ronde, Steens and Imnaha flood basalts at the Oregon – Washington – Idaho border (Figure 2.4) (Geist and Richards, 1993).

It has been suggested that a deep mantle plume, such as the Yellowstone hotspot, would not be able to persist in the long-lived subduction system setting of the NE Pacific (Fouch, 2012). However, several mechanisms have been suggested to explain how the hotspot may be sustained in such a system and subsequently successfully cross the subduction zone. These mechanisms include: migration through the Farallon slab gap (Seligman et al., 2014), movement around the

subducting slab, melting through a zone of weakness in the slab (e.g. Obrebski et al., 2010) or ponding underneath the slab and then melting through it (Geist and Richards, 1993).

Alternatively, models without a plume origin include flow of mantle material around a sub-horizontal slab remnant of the Juan de Fuca Plate (Fouch, 2012). This would produce upwelling of deep mantle beneath the whole of the Yellowstone province (James et al., 2011) and can explain the prevalence of lower mantle related melts with high ^{3}He/^{4}He ratios and generate the recorded geothermal gradient and geoid high (Moniche et al., 2009). This model is supported by the observation that the current Yellowstone plume has been geophysically determined to only extend to mantle depths of around 500 km (Waite et al., 2005; Schutt et al., 2008). However, the proposed size of the plume head may indicate a deeper source for the plume, 800 km into the lower mantle (Parsons et al., 1994). Christiansen et al., (2002) argues for an upper mantle origin for the Yellowstone hotspot due to; the continual eruptions of basaltic material along across the hotspot track, the suggested timing of formation during a plate reorganization in the middle Miocene, development of the hotspot track along older lithospheric structures, migration of coeval magmatism to the northwest of the region along a major tectonic boundary and finally the suggested shallow depth of origin.
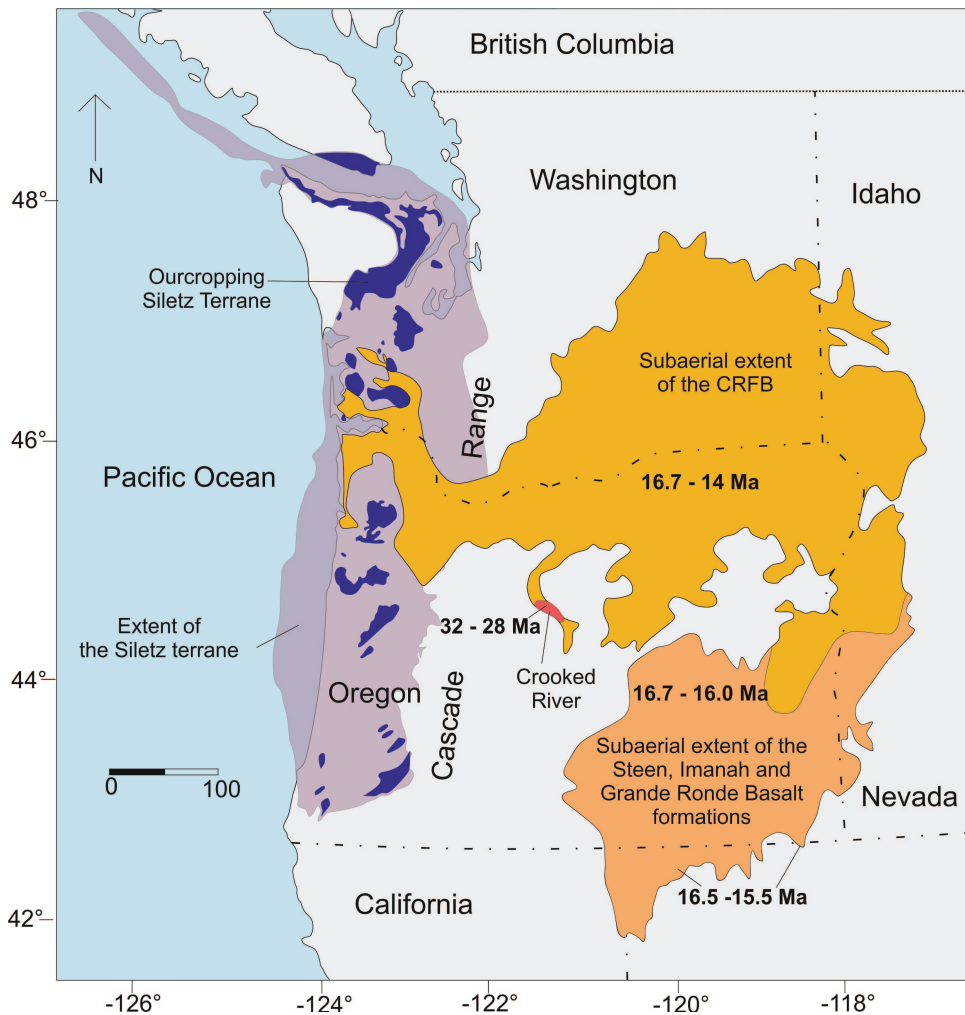
Figure 2.4. Map outlining the geographical extent of the CRFB in comparison to that of the Siletz terrane.

2.2.3.1 Columbia River Flood Basalts

The CRFB, which as discussed above, are thought to be linked to the Yellowstone Hotspot, represent one of the youngest and smallest continental flood basalt provinces. The province is located predominantly in eastern Oregon and western Idaho, but also extends into Washington, Nevada and California (Figure 2.4), and is dominated by tholeiitic basalts (Swanson et al., 1989). Camp and Ross (2004) calculated that 95 % of the Columbia River and Steens flood basalts were erupted within 1.5 million years. The plume tail phase is thought to have begun at around 10 Ma following a transitional period that occurred at the cessation of the of the main head phase (14 – 10 Ma) (e.g. Pierce and Morgan, 2009). The oldest

lavas of the CRFB are found in south central Oregon, subsequently the magmatism appears to have migrated northwards with the largest eruptions located around 300 km to the north of the calculated Yellowstone hotspot track (Pierce and Morgan 1992; Pierce and Morgan, 2009; Humphreys, 2015).

While most authors agree that there is a link between the Yellowstone plume and the CRFB, whether or not the Yellowstone plume is the source of the flood basalt province is controversial (Hooper, 1997). The debate centres on the fact that at ~16 Ma, during eruption, the CRFB did not lie on the calculated Yellowstone hotspot track (Hooper, 1997). However, in many models the CRFB are attributed to the starting plume head of the Yellowstone hotspot, which it is proposed was then (17Ma) centred near the Oregon –Idaho border (e.g. Pierce and Morgan 1992). As the plume flattened at the base of the lithosphere 1,750,000 km^3 of flood basalt and minor rhyolite erupted (Pierce and Morgan 1992). Alternate models propose that CRFB province was not generated by a Miocene starting plume head, but rather by sub – crustal accumulation and subsequent breakthrough of basalt generated above a long lived steady state hotspot, which can therefore account for an older Yellowstone hotspot (Johnston and Thorkelson, 2000). It has also been suggested that the CRFB was produced via lithospheric delamination related to the arrival of the Yellowstone plume (Humphreys, 2015). In this model the plume is thought to have triggered delamination of the Farallon lithosphere resulting in the detachment of a Cretaceous dense lithospheric mantle root, which in turn allowed uplift and increased mantle flow in the region (Humphreys, 2015). It has also been suggested that a 33 Ma amagmatic interval occurred after the arrival of the Yellowstone hotspot at around 56 Ma before northward deflection of the plume occurred due to subduction of the Farallon plate resulting in the Snake River plain volcanic rocks and then eruption of the CRFB (Johnston and Thorkelson, 2000). Other suggested models of origin for the CRFB include magmatism related to the detachment and downwelling of a compositionally dense plutonic root below the province (Hales et al., 2005), back-arc rifting related volcanism (Carlson and Hart, 1987), the induced plume model (Dickinson, 1997), deflection of the Yellowstone plume (Geist and Richards, 1993) and deformation of the Yellowstone plume head (Camp, 1995).

2.4 Overview of the Siletz terrane

This study focuses on the Siletz terrane, a mostly Eocene Large Igneous Province (LIP) located in the present Cascadia forearc region of Oregon, Washington and Vancouver Island (Figure 2.5). The terrane consists of a series of accreted basaltic pillow lavas, massive flows and intrusive sheets (Snavely et al., 1968; Wells et al., 2014) and is composed of both subaerial and sub-marine rocks, with an estimated magmatic volume of 2.6 x 10^6 km^3 (Trehu et al., 1994). Rapid eruption and intrusion of the Siletz terrane magmas is thought to have taken place from ~56-49 Ma (Duncan, 1982; Massey, 1986; Haeussler et al., 2000; Hirsch and Babcock, 2009; Wells et al., 2014) during a time of major plate reorganisation in the Pacific (Engebretson, 1985; Atwater, 1989; Seton et al., 2012). The terrane was rotated during accretion, shortly after formation within 300 km of the North American Pacific continental margin (McCrory and Wilson, 2013). The province has been variously known as: Siletzia (Irving, 1979), the Coast Range Volcanic Province (Babcock et al., 1992), the Siletz – Crescent terrane (McCrory and Wilson, 2013) and the Siletz terrane (Snavely et al., 1968; Fleming and Trehu, 1999) (used in this thesis).

Three formations contribute to this expansive ~ 650 km-long terrane; the Siletz River Volcanics in Oregon, the Crescent Formation in southern Washington and the Olympic Peninsula and the Metchosin Igneous Complex in south eastern Vancouver Island (Figure 2.5; Figure 2.6). Although exposure is generally poor across most of the Siletz terrane, it is clear that the lower part of the terrane sequence comprises mostly submarine pillow basalts, pillow breccia, gabbros and occasional sheeted dyke units (Figure 2.7)(Snavely et al., 1968; Duncan, 1982; Massey; 1986; Haeussler and Clark, 2000; Wells et al., 2000). The upper part of the sequence contains both submarine pillow basalts and subaerial massive flows with oxidised flow tops along with rare felsic flows (Snavely et al., 1968; Duncan, 1982; Massey; 1986; Haeussler and Clark, 2000; Wells et al., 2000). These subaerial units are interbedded with brecciated lapilli tuffs, laminated tuffs and volcaniclastic sediments (Figure 2.7). The thickest part of the terrane occurs in central Oregon, where the accreted units reach 27± 5 km (Trehu et al., 1994).

Beneath northwestern Oregon and southwestern Washington, the terrane is approximately 20 km thick (Parsons et al., 1999), thinning to 10 km in northwestern Washington and southwestern Vancouver Island and down to 6 km offshore Vancouver Island (Hyndman et al., 1990).
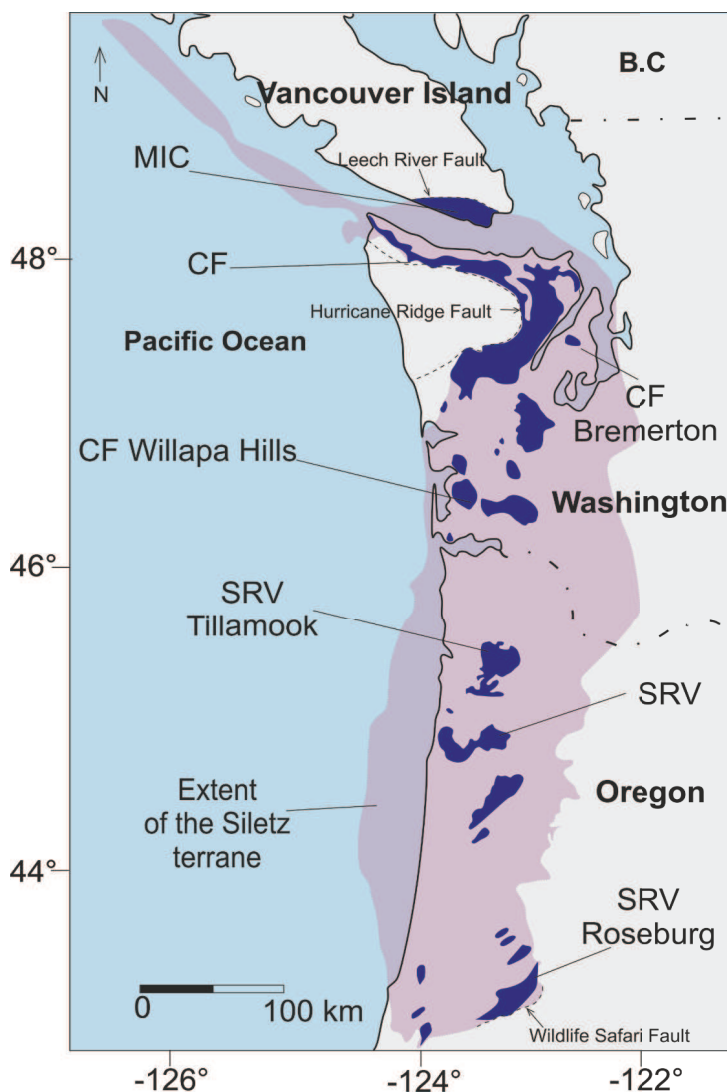
Figure 2.5. Map highlighting the subaerial and exposed extent of the Siletz terrane, adapted from McCrory and Wilson (2013). Where MIC – Metchosin Igneous Complex, CF – Crescent Formation and SRV – Siletz River Volcanics Formation.

The western boundary of the terrane is exposed at the Hurricane Ridge fault (Figure 2.5) on the Olympic Peninsula, Washington, but is generally poorly exposed (Cady, 1975; Hirsch and Babcock, 2009). Using magnetic anomalies this

boundary has been traced southwards (offshore Oregon) and northwards (off the coast of Vancouver Island) (Figure 2.5) (Snavely et al., 1980; Fleming and Tréhu, 1999). In the north, the Leech River Fault, a thrust contact, on Vancouver Island represents the eastern boundary of the terrane (Massey, 1986) while another thrust contact (Wildlife Safari fault) near Roseburg, Oregon defines the eastern boundary in the south of the terrane (Wells et al., 2000) (Figure 2.5). The southern margin of the Yakutat terrane in Alaska (Davis and Plafker, 1986) and the Wheatfield Fork Terrane of the Franciscan Complex in Northern California (McLaughlin, 2009) have also been proposed to be remnants of the Siletz terrane.

The age of the Siletz terrane has generally been constrained using ^{40}Ar-^{39}Ar whole rock dating techniques, placing the maximum age range of the terrane between 56-49 Ma, with the majority of the terrane having erupted between 54 and 50 Ma (Brandon, 2014; Duncan, 1982; Pyle et al., 2009). Nanoplankton ages from interbedded sediments have also been correlated by Wells et al. (2014) with other ages from across the terrane. In addition to this, limited U-Pb ages have also been determined. Haeussler et al. (2000) reported a U-Pb zircon age of 50.5 Ma for the Bremerton Igneous Complex in the Crescent Formation and U-Pb zircon ages of 52 and 54 Ma have been determined for the volcanics of the Metchosin Igneous Complex by Yorath et al. (1999). Several areas of the terrane have not been dated, resulting in some uncertainties in the relative timing of magmatism across the terrane. In addition, correlating the stratigraphy of different units across the terrane has proven difficult due to the lack of exposure.

Figure 2.6 Schematic time – rock diagram for the Siletz terrane and associated rocks which is roughly parallel to the subduction margin, from Wells et al., (2014).
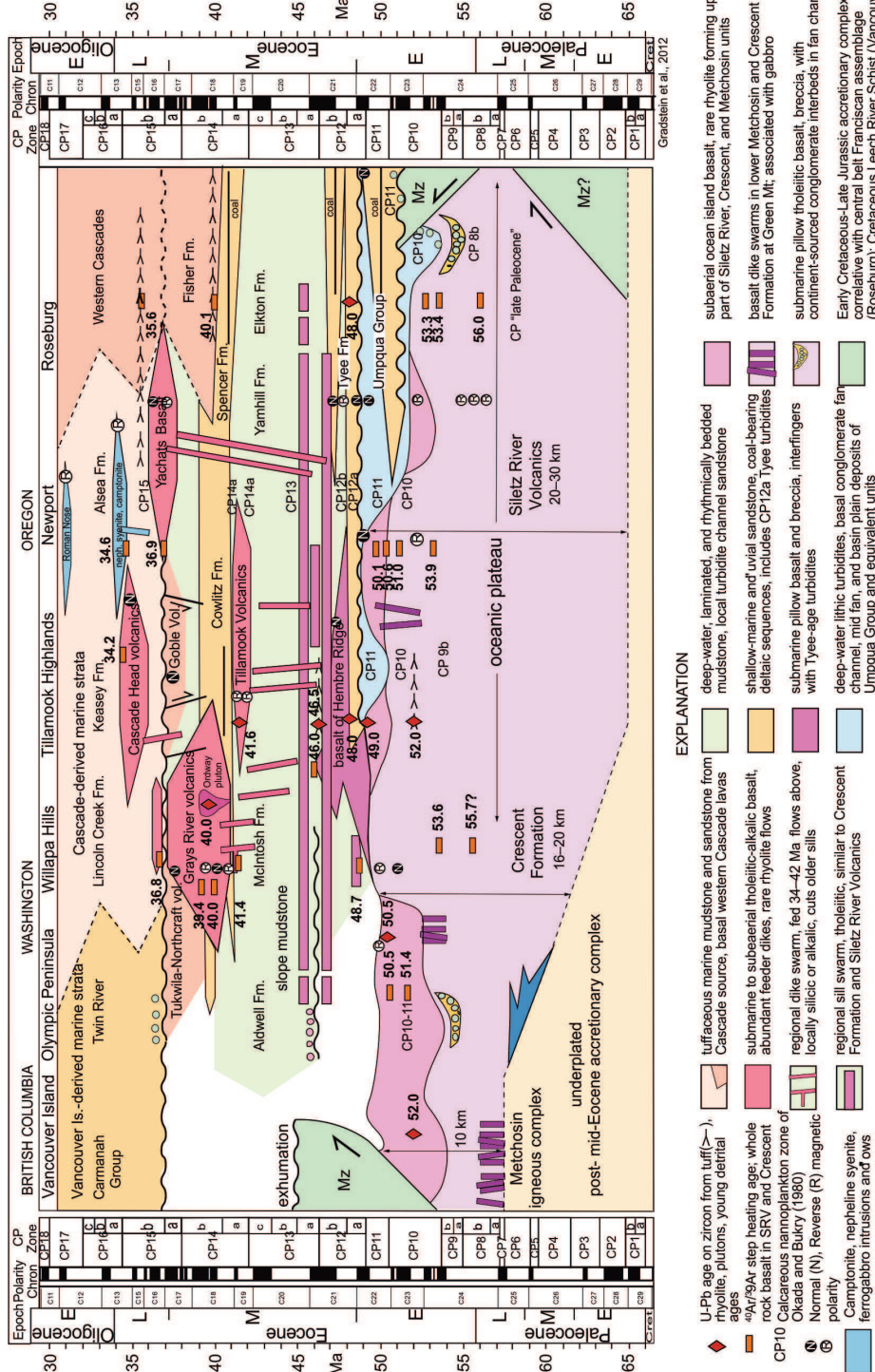
Accretion is thought to have occurred rapidly after, and probably even during, the eruption of the terrane, first in the south between 51 and 49 Ma (Wells et al., 2014) and subsequently in the north from 48 Ma to 45 Ma (McCrory and

Wilson 2013; Wells et al., 2014). Accretion of the Siletz terrane may have triggered the break- up of the subducting Farallon slab and back-stepping of the subduction zone to the west of the accreted Siletz terrane (e.g., Gao et al., 2011).
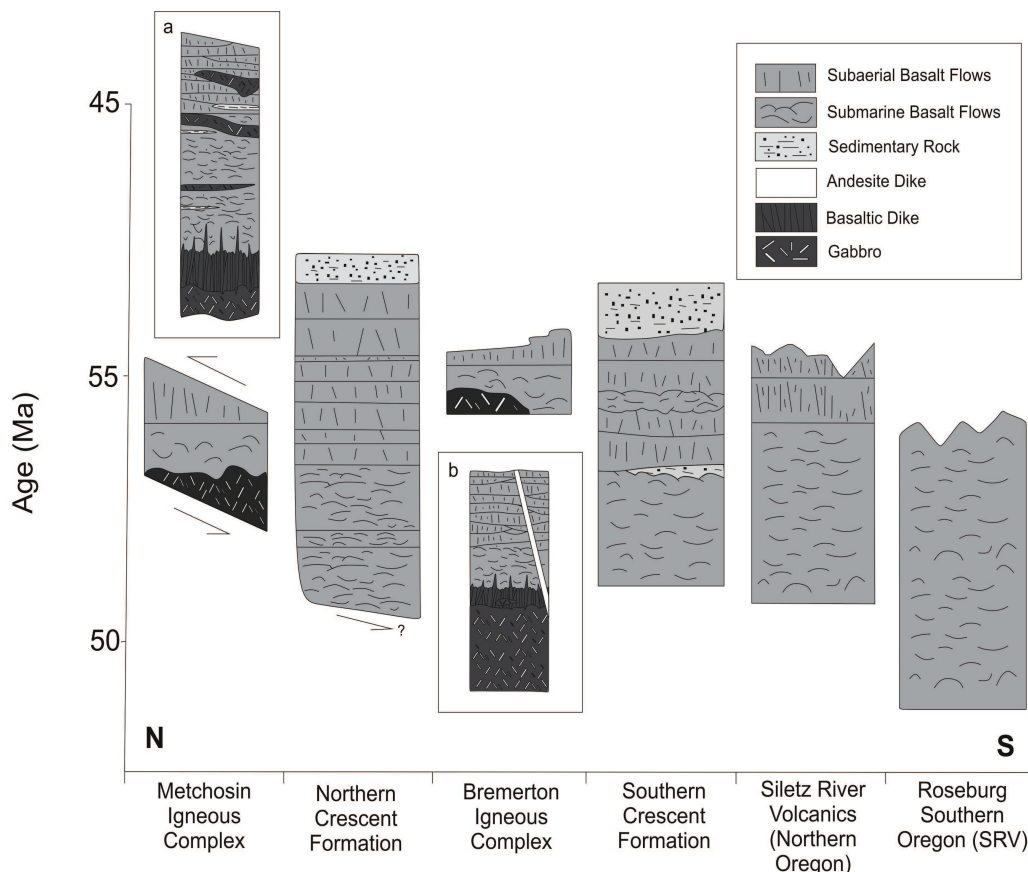
Figure 2.7 Chronostratigraphic chart showing the main geological units and their stratigraphic relations between the studied areas in the Siletz terrane, adapted from Eddy et al., (2017). Where inset a) is a detailed lithostratographic column of the Metchosin Igneous Complex, and inset b) is a detailed lithostratographic column of the Bremerton Igneous Complex.

2.4.1 Mantle plume models for the Siletz terrane

Simpson and Cox (1977) first suggested that the Siletz terrane represents an accreted mid oceanic ridge. Duncan (1982) then proposed that the systematic age progression that was thought to occur across the terrane was best represented by the accretion of rocks formed by hotspot volcanism (thought to be the Yellowstone hotspot) that was centred beneath the early Eocene Kula-Farallon spreading ridge. In this model volcanism was short lived at each centre, moving from the northern and southern ends toward the centre of the province, creating a

v-shaped pattern between 64 - 47 Ma (Duncan, 1982). Haeussler et al. (2003) further developed this model and proposed that the terrane comprises several composite terranes, which represent two Yellowstone hotspot traces formed at the Resurrection-Farallon ridge and the Kula – Farallon ridge. McCrory and Wilson (2013) further developed this model proposing that the Siletz terrane is in fact, two composite terranes, which formed as a pair of Yellowstone hotspot traces generated at the Resurrection-Farallon ridge (Haeussler et al., 2003) and the Kula – Farallon ridge. Comparable modern analogues include Iceland and the Galapagos (McCrory and Wilson, 2013). The Siletz ridge segment accreted at ~ 53 Ma before subsequent accretion of the Crescent block to the north at ~48 Ma. Recent age ranges of 55-49 Ma for the terrane (Haeussler and Kenneth, 2000; Hirsch and Babcock 2009; Wells et al., 2014) indicate faster spreading rates than Duncan's (1982) range of 64-47 Ma (McCrory and Wilson, 2013).

A more recent model has proposed that the Siletz terrane formed on the Farallon plate and a sister terrane, the Yakutat terrane, erupted on the Kula (or Resurrection) plate as the Yellowstone hotspot interacted with the corresponding ridges (Wells et al., 2014). The tectonic plate configuration of the region in this model proposes a near-shore source for the Siletz terrane between 56-49 Ma (Wells et al., 2014). In the reconstruction of Seton et al (2012) the north Kula – Farallon ridge intersects the Yellowstone hotspot and remains relatively stable, while travelling from 40°- 50°N along the coast between 60-50Ma. While the Yakutut terrane moves rapidly northward shortly after formation (Wells et al., 2014). Following accretion of the Siletz terrane the North American plate overrode the Yellowstone hotspot at 42 Ma, resulting in Tillmook volcanics (Seton et al., 2012; Wells et al., 2014). Pyle et al. (2009) suggested that the melting of the Yellowstone mantle plume head phase was the dominant mechanism of formation for the Siletz terrane. This model was supported by the homogenous compositions and apparently restricted isotopic range of the Crescent Formation and Metchosin Igneous Complex that are comparable to the (~17Ma) Columbia River Basalts. This isotopic evidence indicates that despite a 41 - 22 Ma year age gap, the two provinces have a similar mantle source (Pyle et al., 2009; 2015).

2.4.2 Alternative models for the Siletz terrane

Marginal basin related models propose that the Siletz terrane was created primarily by oblique rifting of the continental margin between the Kula-North American plates, combined in some models with coeval Yellowstone hotspot volcanism (e.g. Wells et al., 1984; Clowes et al., 1987; Snavely 1987; Babcock et al. 1992; Brandon, 2014). Wells et al. (1984) argued that the rate of the motion suggested by Duncan's (1982) ages were slower than the plate motions of both the Kula and Farallon plates with respect to the hotspot reference frame. They therefore suggested the accretion of the oceanic island chains on coherent plate fragments could not explain the apparent age progression (Wells et al., 1984). In addition to this, early Eocene (56-52Ma) continentally-derived conglomerates are interbedded with the Siletz basalts, requiring the oldest part of the terrane to have formed near the Klamath margin and these contrast with the predicted rapid northward movement of plates (Wells et al., 2000). However the proposed existence of an additional plate (the Resurrection plate) between the Kula and Farallon plates during the Palaeogene (Haeussler et al., 2003) may have resulted in slower spreading rates on the Farallon – Resurrection boundary near Oregon than for the spreading rate of the Kula- Resurrection boundary (McCrory and Wilson, 2013), and so become more comparable with rates required for the model proposed by Duncan (1982).

The model suggested by Wells et al. (1984) proposed that Yellowstone plume related volcanism took place on transform faults as multiple Kula – Farallon ridge reorganisations occurred between 61 – 48Ma. The arrival of the Yellowstone hotspot triggered rifting of the continental margin resulting in thick accumulations of basaltic lava in the back-arc basins (Wells et al., 1984). Brandon (2014), also suggested a back arc basin setting for the Siletz terrane and interpreted the terrane as an accreted ophiolite and argued that the terrane is underlain by continental sedimentary rocks to the west (the Blue Mountain unit) and peridotite to the east (determined via geophysical data). The Blue Mountain unit has been dated with young peaks of 50.0 and 54.7 Ma, ages which overlap

with those suggested for the overlying basalts (Babcock et al., 1992). In the marginal basin model, accretion of the terrane is thought to follow the migration of the Kula – Farallon triple junction northward along with the Yakutut terrane leading to a shift in the plate motions to subduction of the Farallon plate (Wells et al., 1984; Davies and Plafker, 1986; Wells et al., 2000).

Thorkelson, (1995) suggested that the south westward movement of magmatism along the western margin of North America during the Eocene is related to the north eastward steepening of the southern margin of the Kula-Farallon slab window. Babcock et al. (1992) therefore further developed the model of Wells et al. (1984) and proposed that the Siletz terrane formed as a result of slab-window development related to the subduction of a mid ocean ridge. Subduction of a mid ocean ridge can be lead to a slab free region beneath the overriding plate termed a slab window (Dickinson and Synder, 1979; Forsythe and Nelson, 1985; Thorkelson and Taylor, 1989; Thorkelson, 1996). Any magma generated in this region of asthenosphere will subsequently rise through the trailing slab edges preserving the slab window or gap (Thorkelson, 1996). Slab window regions have high heat flow (Gill, 1981; Best, 1982; Bucher and Frey, 1994), anomalous magmatism, deformation and high temperature metamorphism (Dickinson and Synder, 1979; Hibbard and Karig, 1990; Barker et al., 1992; Sisson and Pavlis, 1993; Pavlis and Sisson, 1995; Kusky et al., 1997; Thorkelson, 1996; Lytwyn et al., 1997; Breitsprecher et al., 2003; Groome et al., 2003). The magmas produced are therefore more tholeiitic to alkaline in composition, than the characteristic calc alkaline magmas of island arcs (e.g., Forsythe and Prior, 1992; Cole and Basu, 1995). Decompression melting is also facilitated by the narrow region through which the magmas rise, resulting in further geochemical changes (Presnall et al., 1979). Therefore more tholeiitic magmas are produced proximal to the trench (Bradley et al., 1995) and alkalic magmas are more common in the forearc region (Hole and Larter, 1993). Formation of a slab window may have triggered rifting in the forearc region of the existing subducting system (Babcock et al., 1992). It has been suggested that ridge subduction and so slab window related magmatism may have played an important role in particular in the northern portion of the terrane, where the crust thins to 10 km and sheeted

dykes are found (Babcock et al., 1992). Conversely, the thickest areas of volcanic rock appear to correspond to the calculated position of triple junction at the time of extrusion (Babcock et al., 1992). Breitsprecher et al., (2003) also suggest a slab window model for the origin of the Siletz terrane where by the subduction of the Kula-Farallon mid ocean ridge (from around 83 – 41 Ma) is the trigger for the creation of a slab window beneath North America during this time. Evidence supporting a slab window origin includes adakites of a similar age to the Siletz terrane found in the region along with felsic and tonalite intrusions and lavas (the Walker Creek intrusions, 50.7-50.9 Ma) on Vancouver Island thought to be related to ridge subduction (Breitsprecher et al., 2003).

Mid ocean ridge related volcanism at a spreading centre located near the continental margin between the now subducted Farallon Plate and the hypothesised Resurrection Plate, has also been suggested as a model of formation for the Siletz terrane (Haeussler et al., 2003; Madsen et al., 2006). The Resurrection plate is proposed to have been located east of the Kula plate and north of the Farallon plate (Haeussler et al., 2003). A portion of the later magmatism is explained by subduction of this spreading centre and the subsequent occurrence of slab window magmatism at around 50 Ma (Haeussler et al. 2003). The suggested lack of clear age progression across the Siletz terrane is thought to indicate little movement of the triple junction discussed above (Haeussler et al., 2003; Madsen et al., 2006).

Another suggested model of formation for the Siletz terrane proposes subduction initiation along a transform fault, which can explain both the linear geometry of the terrane and its suggested volume (Stern, 2004). In this model a transform fault parallel to the North American margin between the Farallon and the partially subducted Kula/Resurrection plate represents a zone of weakness along which subduction can propagate (e.g., Babcock et al., 1992; Wells et al., 1998; Haeussler et al., 2003; Stern, 2004; Denny, 2012).

2.4.3 Accretion of the Siletz terrane

The general consensus is that the Siletz terrane was rotated into its present position during collision with the North American plate shortly after its initial formation, less than 300 km offshore (Duncan, 1982; Beck, 1984; McCrory and Wilson, 2013). Accretion onto the margin of the North American plate is thought to have occurred during the last phase of eruption. This is supported by the presence of undeformed sediments overlying the youngest basalts, which suggests that accretion occurred less than 5 Ma years after formation (Snavely et al., 1968; Duncan, 1982). The paleocontinental margin of North America was orientated around N30°W in Oregon and about N60°W in Washington during the Early Eocene (Wells et al., 2000). Palaeomagnetic results from early Eocene to Miocene volcanic and sedimentary rocks of the Oregon coastal region imply around 75° clockwise rotation of the Siletz terrane in the area with respect to the stable North American plate (Simpson and Cox, 1977; England and Wells, 1991). Accretion occurred in the south of the terrane between 50.5 – 49 Ma and as late as 45 Ma in the north (as recorded by the Leech River fault, Vancouver Island) (Wells et al., 2014). Heller and Ryberg (1983) have suggested that the Tyee basin fill records the transition from subduction to forearc basin following the collision of the seamount terrane and the resulting westward stepping of the subduction zone.

Evidence for the temporal and spatial characteristics of the accretion of the Siletz terrane is recorded in adjacent sedimentary basins (Eddy et al., 2016), in which a reversal in the paleoflow direction and an increase in sediment accumulation largely composed of conglomerates (in the Swauk basin, Washington) indicates its position as a foreland basin between 51.3 and 49.9 Ma (Eddy et al., 2016). Contemporary basin deformation exhibited by westward trending fold and thrust belts on Vancouver Island (Johnston and Acton, 2003) and in Oregon (Wells et al., 2014) are also thought to be related to the accretion of the Siletz terrane (Eddy et al., 2016).

The accretion of the Siletz terrane is proposed to have resulted in the break-up of the subducting Farallon slab, westward jump of the subduction zone to the west of the accreted terrane and cessation of movement of the almost horizontal Farallon slab beneath Oregon to until the present day (Gao et al., 2011; Darold and Humphreys, 2013; Seligman et al., 2014).

2.5 Palaeocene Eocene Thermal Maximum

As discussed in section 2.2.4, the formation of oceanic plateaus has been shown to have significant impacts on the atmosphere, biosphere and hydrosphere and have been correlated to many second order extinction events (e.g., Kerr, 2005). The Palaeocene-Eocene Thermal Maximum (PETM) represents an abrupt climate warming of 5-8 °C at around 55.5 Ma (McInerney and Wing, 2011; Westerhold et al., 2012). It is thought to be the result of a catastrophic release of several thousands of petagrams of carbon into the ocean atmosphere system (Dickens et al., 1997), however the source of the carbon and the number of pulses of release are controversial (e.g. Bowen et al., 2015). The Palaeocene – Eocene boundary marks the start of magmatism in the Siletz terrane and so the formation of the terrane may in fact be linked to this rapid climate change.

The PETM itself is thought to have been a relatively short lived event that lasted around 200 ka (McInerney and Wing, 2011), with the carbon release spanning less than 20 ka (but it may have occurred in less than a year according to some estimates (Higgins and Schrag, 2006; Bowen et al., 2015). With the exception of benthic foraminifera relatively few groups suffered major extinctions despite most terrestrial and marine organisms experiencing large shifts in geographic distribution, rapid evolution and changes in trophic ecology (McInerney and Wing, 2011).

The age of onset of the PETM has been estimated at around 56 Ma using radiometric dates of marine ash layers and orbital timing of marine sediments (Westerhold et al., 2009), while the upper boundary of the negative carbon isotopic excursion (calculated from zircons in the upper part of the sequence) is thought to be 56.09 ± 0.03 Ma, (Jaramillo et al., 2010). Therefore the timing of the PETM may coincide with the eruption of the Siletz terrane. As discussed above, the environmental effects of oceanic plateau eruption may indicate a link between the two events.

The PETM is marked by a global temperature rise inferred from a >1 ‰ negative excursion in $\delta^{18}O$ of benthic foraminifera, indicating around a 5 °C

increase in the temperature of deep waters (Zachos et al., 2001). The massive release of carbon, which occurred at the PETM is inferred from the large global negative carbon isotopic excursion and the extensive dissolution of deep-ocean carbonates (McInerney and Wing, 2011). However, as discussed there are still several unanswered questions regarding the PETM, significantly how much carbon was released and from which sources. Methane hydrate reservoirs or clathrates were initially widely accepted as the source of the carbon (Dickens et al., 1997), but the highly depleted carbon isotope composition (δ^{13}C of ~ - 60 ‰) (Kvenvolden, 1993) is difficult to reconcile with the requirements of carbonate dissolution, warming and the carbon isotopic excursion (Pagani et al., 2006). It has therefore been suggested that carbon released from Antarctic permafrost and peat (δ^{13}C of ~ - 30 ‰) can explain these features as well as the magnitude and evolution of the PETM (DeConto et al., 2012).

Other potential sources of carbon include wildfires from the extensive burning of peat and coal (Kurtz et al., 2003), however, there is a lack of evidence in the geological record for this (Moore and Kurtz, 2008). Another possible mechanism involves thermogenic methane, which results from the injection of magma into organic rich sediments of Cretaceous - Palaeocene mudstones in North America (Westerhold et al., 2009). Finally the drying of epicontinental seas could lead to rapid (<20 ka) desiccation and oxidation of organic matter (Higgins and Schrag, 2006) however, although shallow seaways were common at this time in Asia none are known to have dried up (Garvrilov et al., 2003). Bowen et al., (2015) have suggested that the PETM is related to the release of carbon from reservoirs, which are capable of producing one or more major pulses.

The effects of the PETM on the marine ecosystem are only documented via microfossils due to a lack of macrovertebrate fossils in the sedimentary record (Ivany and Sessa, 2010). The group of organisms most affected were the benthic foraminifera that show a 30-50 % drop in diversity (Thomas, 2007). This began at the onset of the carbon isotopic excursion, and took place mostly in deep waters where corrosion increased, oxygen levels dropped and temperatures rose (Thomas, 2003; 2007). Despite this marked extinction in benthic foraminifera, other groups of benthic and planktonic microfossils show little or no extinction at

the PETM. Ostracods are the only other group of deep benthic organisms with detailed records across the PETM and they show a varied response (Morsi et al., 2011).

Geographic distributions of both marine and terrestrial organisms were radically altered due to the temperature increase (McInerney and Wing, 2011). Rapid morphological change also occurred in both marine and terrestrial organisms, which suggests that they adapted to climate change through evolution. In addition to this dispersal and local extirpation also occurred indicating that the changes in morphology and location appear to be linked to nutrient and/ or food limitations (McInerney and Wing, 2011).

2.6 Summary

This chapter reviews the formation and geological features expected of Large Igneous Provinces and oceanic plateaus, which primarily include the rapid eruption of large volumes of magma. The overall geology and key events of the Cordilleran region during the late Palaeocene and Eocene are linked to a major shift in the tectonic plate configuration which was most likely linked to the eruption of the Siletz terrane. The previous work which has contributed to our understanding of the Siletz terrane largely agree that the Siletz terrane is a $56 - 49$ Ma predominantly mafic terrane which may represent an oceanic plateau. Previously proposed models also conclude that shortly after formation, the Siletz terrane was accreted to the North American margin in a series of faulted blocks whose volume is thought to reach $2.6 \times 10^6 \, km^3$. While several authors agree that large scale melting of a mantle plume head (which may be the Yellowstone hotspot) has contributed to the formation of the Siletz terrane, others argue for a plume-free model based solely in the upper mantle and lithosphere. Although several small scale geochemical investigations of the terrane have been conducted, the majority of studies of the terrane as a whole are predominantly structural in nature. Finally the PETM is thought to have occurred during the onset of magmatism and may therefore represent a consequence of the eruption of the Siletz terrane.

3. GEOLOGY OF THE SILETZ TERRANE AND ASSOCIATED ROCKS

3.1 Introduction

The rocks of the Siletz Terrane are largely comprised of basaltic flows, basaltic breccias together with interbedded volcaniclastic sediments and marine and continentally-derived sediments. The geological features of each of the areas of the terrane are described below along with the tectonic interpretation of individual complexes, relationships with associated rocks and the age ranges for each area. The samples utilised in this study were collected in 2014, and in 2004 and 2005 by Derek Laidlaw. Broad sample locations are reviewed below with more detailed locations given in Appendix E1.

3.2 Siletz River Volcanics, Oregon

3.2.1 Roseburg

3.2.1.1 Geology

In the Roseburg area (Figures 3.1, 3.2) the Siletz terrane is largely comprised of both alkalic and tholeiitic pillow lavas interbedded with submarine basaltic breccias (Wells et al., 2000). Sedimentary interbeds are also common in the Roseburg areas, with many turbidite sandstones, mudstones and conglomerates forming these units. Finally, overlying the submarine sequences are subaerial basaltic flows with oxidised flow tops.
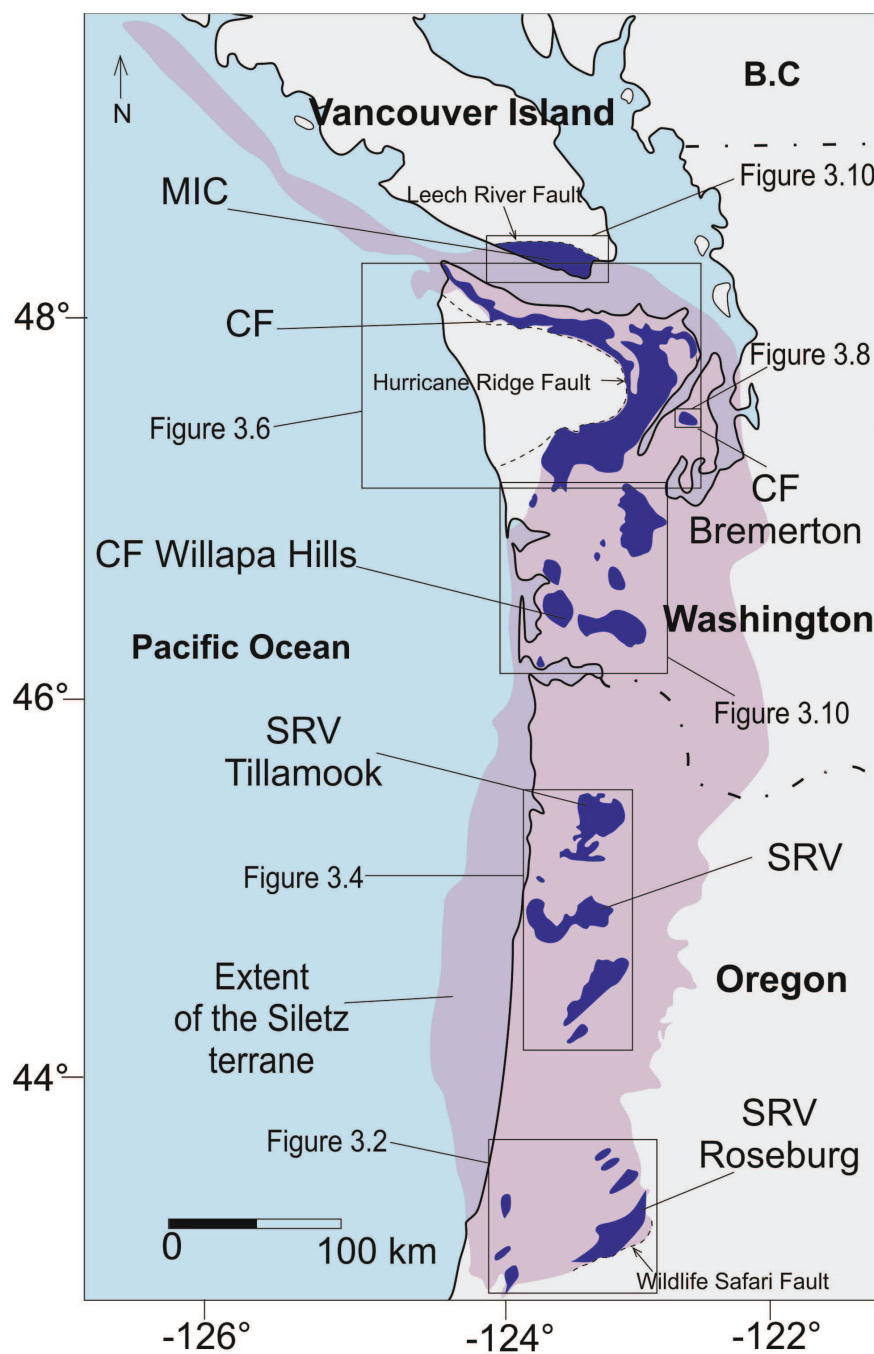
Figure 3.1 Map highlighting the regions of the Siletz terrane described within this section, adapted from McCrory and Wilson (2013). Where MIC – Metchosin Igneous Complex, CF – Crescent Formation and SRV – Siletz River Volcanics Formation.

The rocks of the Siletz Terrane in this region predominantly outcrop in uplifted anticlinal folds north of Roseburg itself, with other exposures to the west

in the Coos area (Figure 3.2). The submarine rocks are mostly comprised of aphyric pillow basalts, however there are also several instances of pillow breccias, lapilli and laminated tuffs. Exposure of the lower submarine section of the volcanic pile predominantly occurs in the Roseburg area (Figure 3.2) and the Sugar Loaf Mountain outcrops to the southwest (Figure 3.2). In the Roseburg exposures, both thick massive flows, flows with columnar jointing and pillow basalt flows can be found (Figure 3.3a, c, d, e). The pillow basalts often grade into angular pillow breccia, and occur at the margins of the massive flows (Figure 3.3a; e) (Pyle, 1988). Interbedded in the basalts are basaltic sandstone and conglomerate deposits. Exposures of the conglomerates occur locally (Figure 3.2) while turbidities (the Roseburg Member, Figure 3.3b) are found throughout the sequence but are more common within the pillow basalts (Wells et al., 2000). The thick conglomerate units comprise clasts ranging from boulder to pebble size, with a variety of lithologies recorded, including; chert, limestone, greenstone, greywacke and plutonic igneous rocks. It is thought that the sedimentary interbeds are derived from the Klamath Mountains (the Dothan Formation and the Klamath terranes) due to shared characteristics with other Umpqua Group rocks (Wells et al., 2000) and the Roseburg Member in particular correlates with the older rocks of the Umpqua Group (Bukry and Snavely, 1988; Ryu et al., 1992).

The Sugar Loaf Mountain exposures (Figure 3.2) are mostly composed of pillow basalt flows along with thin manganese crust layers which are thought to represent altered glass and so the occurrence of hydrothermal circulation in the seafloor (Pyle, 1988). Additionally the rocks in this area exhibit more pervasive alteration than those in the Roseburg area and exposures are often oxidised and friable (Figure 3.3f). As a result of the described features, it has been suggested that the Roseburg area represents the centre of the volcanic pile and Sugar Loaf the margins (Pyle, 1988).

The Red Hill Anticline and the Coquille exposures (Figure 3.2) outcrop to the north of the Roseburg and Sugar Loaf exposures respectively. The NE – SW structural trend of the rocks in the area implies that the two groups of volcanics are of equivalent stratigraphic position despite the lack of exposure of any direct geological evidence due to the overlying Tyee Formation marine turbidite

sandstones (Figure 3.2) (Pyle, 1988). Both pillow and massive flow types are observed and the sequence shifts from submarine to subaerial in both sets of exposures, evidenced by the presence of pahoehoe lavas exhibiting oxidised flow tops (Pyle, 1988). Although sedimentary interbeds are present in the Coquille exposures they are absent in the Red Hill Anticline, while amygdule rich basalts and pervasive alteration are more common in the Coquille basalts (Pyle, 1988). These observations also suggest that the west of this area represents the periphery of the volcanic pile (Pyle, 1988).

Subaerial basalts are most abundant in the northern-most outcrops of the area and are found overlying the submarine basalts in the Drain, Jack Creek, Blue Mountain, Coos and Kentucky Slough areas (Figure 3.2) (Snavely et al., 1968; Wells et al., 2000 Hoover, 1963; Pyle, 1988, Ryu et al., 1992). The Drain and Jack Creek exposures to the east contain aphyric alkali basalt flows, which are thinly-bedded with oxidised flow tops. Interbedded with these flows are vitric and lapilli tuffs (Pyle, 1988). The western exposures (Blue Mountain, Coos and Kentucky Slough) comprise both aphyric and plagioclase porphyritic basalts and
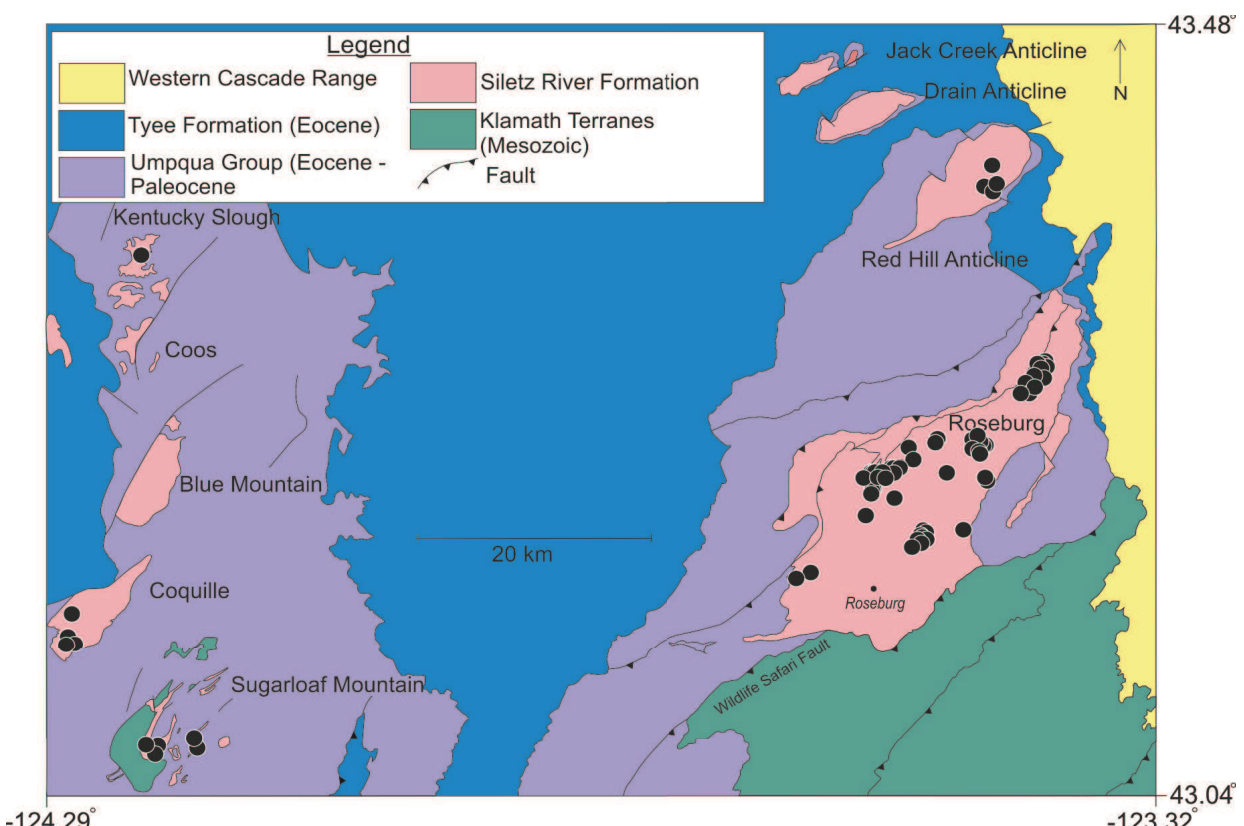
Figure 3.2 Map showing the sample locations of the Roseburg rocks used in this study. Map compiled after Pyle, (1988) and Wells et al., (2014).

these are associated with weathered pyroclastic tuffs. Some submarine rocks also occur, most commonly pillow basalts displaying bread crust textures, which indicate that the volcanic pile is emerging into shallower water depths (Kokleaar, 1986). Picrites have also been observed in the Blue Mountains (Pyle, 1988). Zeolite and calcite alteration is abundant and within the lower more coarsely crystalline rocks of the Kentucky Slough exposure, the alteration is pervasive though the rock. The subaerial basalts are in turn overlain by basaltic sandstones, which are locally fossiliferous, containing for example echinoderms (Wells et al., 2000).

The Mesozoic rocks of the Jurassic Rogue volcanic arc complex and the Dothan Formation (a Jurassic and Early Cretaceous accretionary complex) have been folded and thrust over the Siletz terrane sequences (Ramp, 1972, Baldwin, 1974, Champ, 1969, Ryberg, 1984). The contact with the Dothan Formation is exposed at the Wildlife Safari Fault near Roseburg (Figure 3.1; Figure 3.2), which is thought to represent an Eocene subduction zone (Heller and Ryberg, 1983). The sediments in the early Eocene Umpqua basin formed coevally with this thrusting event and subsequently the Siletz River Volcanics where thrusted over the sediments of the basin, resulting in the Umpqua fold and thrust belt (Wells et al., 2000). The (Middle Eocene aged) Tyee Formation was then deposited unconformably on the described sequences in this area (Baldwin, 1974; Wells et al., 2000).

It has been suggested that the Roseburg volcanics and adjacent areas formed proximal to the continent, and this is supported by the interbedded terrestrial sediments and conglomerates (Wells et al., 2000). The volcanic pile has been proposed to correspond to the gradual emergence of an oceanic island, progressing from submarine to subaerial and from tholeiitic to alkalic (Pyle, 1988). Pyle (1988) has suggested that the Roseburg rocks are an analogue of the Hawaiian model of an oceanic island and that the southern tholeiitic pillow lavas in the Sugar Loaf and Roseburg areas are characteristic of the shield building phase, while the Red Hill Anticline and Coquille exposures are evidence of emergent transitional volcanic activity and the northern most exposures are the renewed volcanism which occurs post erosion. Finally, the subsidence of the

volcanic edifice is reflected by the later Eocene Tyee Formation marine sandstone and siltstones (Pyle, 1988).

Figure 3.3 Photographs of exposures of rocks in the Roseburg areas. a) Pillow basalts in the main Roseburg area (sample 018); b) Interbedded marine sediments (same location as sample 024); c and d) Quarry exposures of columnar jointed basalts (site of sample 026); e) Pillow basalts and interbedded marine mudstones (sample 039); f) weathered roadside basalt exposure (sample 089 – 3).

3.2.1.2 Age

This sequence has an age range of 56–52 Ma (Wells et al., 2000). Late Palaeocene (57-56 Ma) calcareous nanoplankton have been observed along the main axis of the Roseburg anticlinorium in sedimentary interbeds within the basaltic sequences (Bukry and Snavely, 1988; Wells et al., 2000). While nanoplankton from Sugar Loaf Mountain and Coquille have an age of 56-55 Ma (Wells et al., 2000). Coccoliths described in sedimentary interbeds in basalt flows, which interfinger with the Umpqua Group at the edges of anticlinorium are early Eocene in age (53.5-50.5 Ma) (Bukry and Snavely, 1988; Wells et al., 2000).

Duncan (1982) determined $^{40}Ar/^{39}Ar$ radiometric ages of 56.0 ± 0.8 Ma from the Roseburg and Drain areas while Pyle et al., (2009) reported an $^{40}Ar/^{39}Ar$ age of 53 Ma from a related uplift, which is consistent with the reported nanoplankton age ranges (Wells et al., 2000). Paleomagnetic results from basalts in Roseburg, Turkey Hill and the Coquille River show reversed polarity, which is also consistent with the suggested ages (Wells et al., 2000).

3.2.1.3 Sample Collection

Derek Laidlaw collected 115 samples from the Roseburg area during the summer and autumn of 2004, predominantly from the main Roseburg area (Figure 3.2). Samples were collected from the massive flows and pillow lavas and a selection of mostly fine grained to coarse sedimentary rocks were obtained from interbedded units. The majority of samples were from quarries and road cuttings. Six samples were collected from the contemporaneous Sugarloaf area to the West (Figure 3.2). In the Sugarloaf area samples were collected from the fresher interior of pervasively altered pillow basalt flows (with average pillow diameters of ~ 1m), which in the field are orange-brown in colour. The Coquille and Red Hill samples were obtained from both pillowed and massive basaltic flows (Figure 3.23). Finally the sample collected from the Kentucky Slough area, (Figure 3.2), was from an aphyric basalt flow around 5 m thick.

3.2.2 Siletz River

3.2.2.1 Geology

The Siletz River region represents the 'type area' of the Siletz River Volcanics Formation and is located, between Newport and Corvallis, Oregon (Figure 3.1). In addition to the type area, exposures in this region also occur to the south in Corvallis and to the north in the Tillamook highlands (Figure 3.4). The lower tholeiitic flows, comprising submarine pillow lavas and pillow breccias, are exposed in a NE trending anticlorium in the Corvallis area and in the most of the Siletz River area (Figure 3.5) (Snavely et al., 1968). Dark green-to-grey finely crystalline amygdaloidal pillow basalt dominates this unit (Figure 3.5b; e; f). The pillows are usually around 1 m in diameter and display radial cooling joints. Additionally, angular poorly bedded basaltic breccias (Figure 3.5c) interbedded with massive and columnar jointed basaltic flows (Figure 3.5a) (up to 15 m thick) are also found (Snavely et al., 1968). Thin beds of deep-water mudstones are locally observed interbedded with the flows (Figure 3.5d) (Wells et al., 2014).

The upper unit is exposed near Ball Mountain in the type area of the Siletz River Volcanics formation (Snavely et al., 1968). Carapaces of pillow lavas overlying large feeder tubes constitute the majority of this unit along with local occurrences of pillow breccias (Snavely et al., 1968). These pillow breccias are characteristic of the submarine part of the upper flows throughout the Siletz terrane (Wells et al., 2014). The pillow lavas are predominately clinopyroxene phryic, although picrite basalt flows, massive feldspar phyric basalt flows and tholeiitic olivine basalts with breccias are also present (Snavely et al., 1968; Wells et al., 2000). In terms of the intrusive rocks, thin (0.2 – 1.5 m wide) mafic alkalic dykes are observed while thicker tholeiitic sills (2 – 30 m thick) have been noted intruding interbedded marine tuffaceous silts and associated tuffs (Snavely et al., 1968). Tuffaceous flows are common, as are interbedded debris flows consisting of basaltic breccia and lapilli tuffs (Snavely et al., 1968). Red oxidised flow tops are observed capping some of the massive basaltic flows along with shallow water sandstones and conglomerates indicating an emergent setting, which is shifting to subaerial eruption.
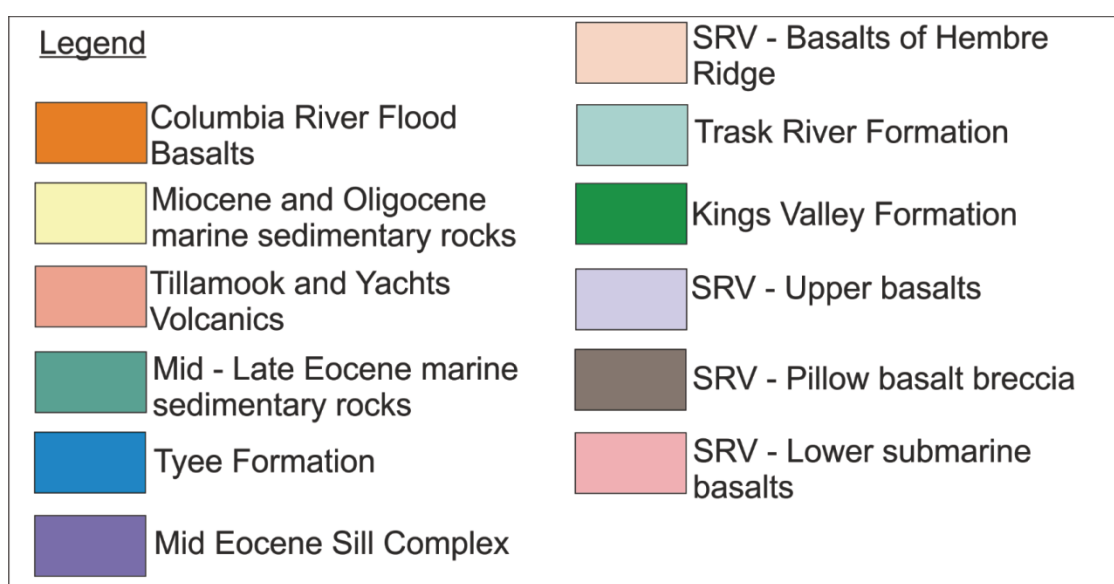
Figure 3.4 Map and legend showing the location and geology of the samples collected from the Corvallis, Siletz River type area and the Tillamook area of the Siletz River Volcanic Formation in Northern Oregon. Map compiled from Snavely et al., (1969), Wells et al., (2014) and http://www.oregongeology.org/geologicmap/ [Accessed November 2016].
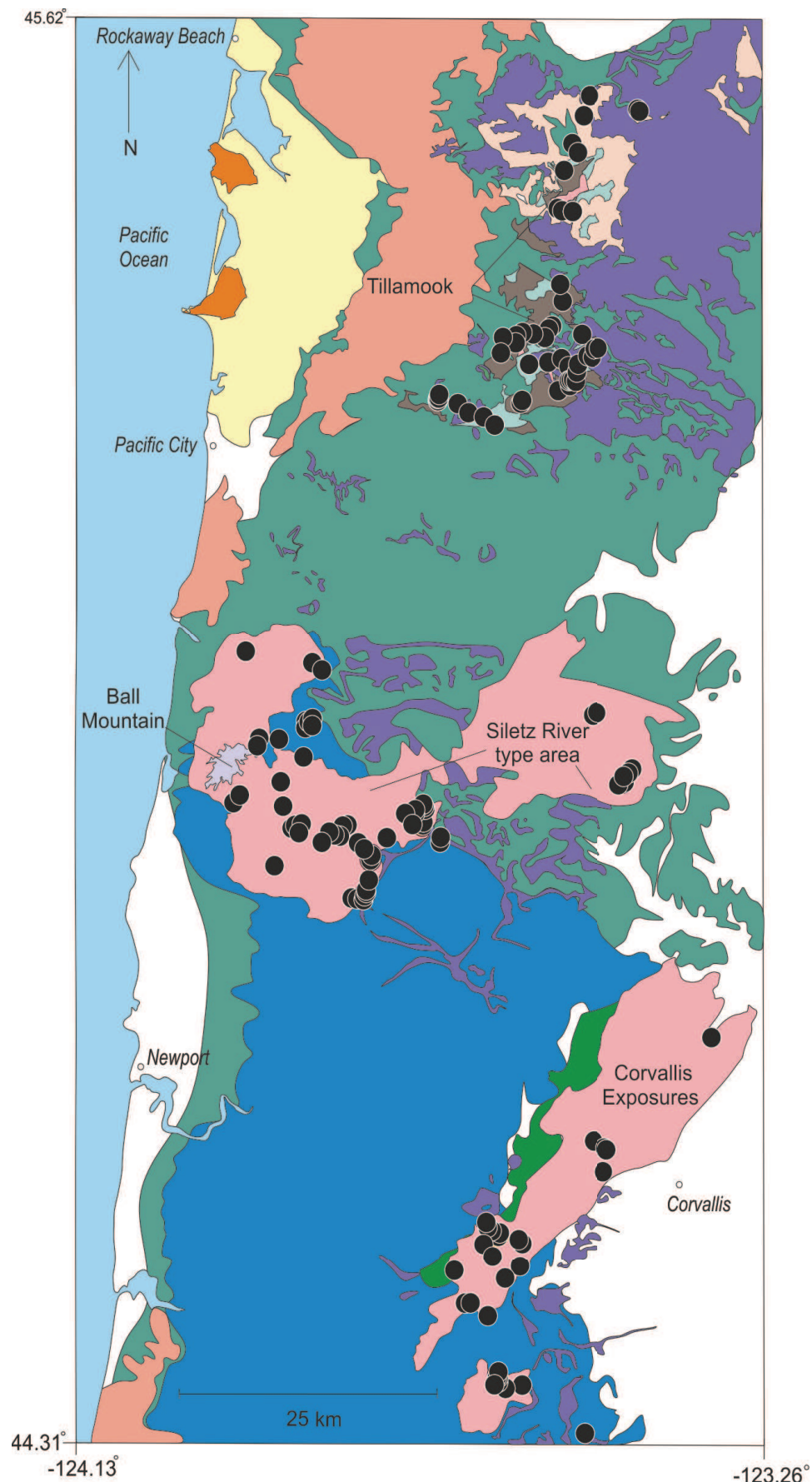
In the Tillamook area of the Siletz River Volcanics Formation the Siletz terrane consists of tholeiitic and alkalic pillow basalt and pillow breccias. (Wells et al., 2014). Overlying these rocks are plagioclase and clinopyroxene phyric basalt flows and fossiliferous basaltic sandstones, thought to have a shallow water origin (Wells et al., 2014). In the north of the area the uppermost flows are represented by the basalts of Hembre Ridge which are composed of tholeiitic lava tubes and associated carapaces of pillow lavas, similar to those observed elsewhere in the upper units of the Siletz terrane (Wells et al., 2014).

Basalt flows in the upper part of the sequence in the Siletz River area are observed interfingering with the overlying Kings Valley siltstone member (Wells et al., 2014). The Kings Valley member has been dated between 53.5 – 49 Ma, with nanoplankton falling in the CP10 – CP11 categories (Wells et al., 2014). Unconformably overlying both the Siletz terrane volcanics and the Kings Valley member is the Tyee Formation, a Middle Eocene (49 – 46.5 Ma) turbidite sandstone deposit (Wells et al., 2014) that is also observed to the south in the Roseburg area (Pyle et al., 1988).

In the Tillamook area beds of the Trask River basaltic turbidites overlie and interfinger the Siletz terrane flows (Wells et al., 2014). The turbidites have been dated to 53.5 – 49 Ma (CP10 – 11) using calcareous nanoplankton (Burkly and Snavely, 1988; Wells et al., 1995; Wells et al., 2014). This age range, along with their stratigraphical position in relation to the Siletz basalts suggests that they can be correlated with the Kings Valley member discussed above (Wells et al., 2014). In addition to this, it has been proposed that both the Trask River and Kings Valley members can be correlated with the Umpqua group, which overlies the Siletz terrane in the Roseburg area (Pyle et al., 1988; Wells et al., 2000; Wells et al., 2014). The basalts of Hembre Ridge found in the north of the Tillamook area are observed interfingering and underlying a turbidite sandstone member containing 49 – 46.5 Ma (CP zones 12a and b) nanoplankton (Wells et al., 2014). These basalts are therefore slightly younger than the other rocks described in the northern Oregon region of the Siletz terrane. The turbidite sandstone which overlies these rocks is mica rich and this lithology along with its age, are similar

to the Tyee Formation, the base of which has produced U-Pb zircon ages of 48 Ma (Wells et al., 2014).

The rocks in the Siletz River type area and those in the Corvallis area to the south, are thought to represent an emergent volcanic setting, which moves from predominantly deep-water pillow lavas to subaerial massive basalts with oxidised flow tops (Snavely et al., 1968). While the basalt flows and breccias that outcrop in the Tillamook area have been interpreted as upper part of an ocean island (Wells et al., 2014). It has been proposed that the younger basalts of Hembre Ridge may represent a late seamount, which formed concurrently with accretion during the last stages of eruption of the terrane (Wells et al., 2014). In this model the contemporaneous base of the Tyee Formation is then interpreted as a foreland basin, which formed proximal to the volcanism (Wells et al., 2014).

3.2.2.2 Age

In the Corvallis and Siletz River areas both normal and reversed paleomagnetic polarities are observed (Wells et al., 2014). Ages of 53.5 – 49 Ma have been determined for nanoplankton (CP zones 10 and 11) found in interbedded marine mudstones. While the Tillamook region was originally dated between 67 and 50 Ma using K-Ar and $^{40}Ar/^{39}Ar$ methods (Duncan, 1982) nanoplankton from interbedded sediments give an age range of 54.5 – 49 Ma (CP9b, 10 and 11). A sample from a pillow basalt flow in the south of the Tillamook area has yielded a $^{40}Ar/^{39}Ar$ step-heating age of 50.6 ± 0.8 Ma, which is consistent with the nanoplankton ages (Pyle et al., 2009). The overlying Trask River turbidites contain nanoplankton, which correspond to coccolith zones CP10-11 (53.5 – 49 Ma) (Wells et al., 1995). In addition to this a U-Pb zircon age of 52 ± 1 Ma has been derived from a tuff bed at the base of the turbidites (Wells et al., 2014). The youngest basalts in the area have been dated at around 49 – 47 Ma using nanoplankton from the turbidite sandstone, which interfingers with, and overlies, it (Wells et al., 2014).

3.2.2.3 Sample Collection

The samples collected from the Corvallis region (Figure3.4) were taken largely from pillow basalt flows exposed in road cuttings and quarries. The samples were collected during the summer of 2014 (14 samples) along with additional samples collected by Derek Laidlaw in 2004 (18 samples). The outcrops exhibited extensive brown/orange weathering. Samples were also collected from columnar jointed and massive finely crystalline basalt flows.

Fifty Samples from the Siletz River area, shown in Figure 3.4 were collected by Derek Laidlaw during 2004, while a further 11 samples were collected in 2014. The samples were collected from highly weathered pillow basalts, massive flows and from finely interbedded tuffs. While samples from the upper flows, which outcrop near Ball Mountain, were collected from basaltic hyaloclastite breccias, pillow basalts and massive flows.

Derek Laidlaw collected 29 samples during 2004 from the Tillamook area, while an additional 10 samples were collected in 2014 (Figure 3.4. The samples were taken from pillow basalt flows, hyaloclastite pillow breccias and purple-grey massive flows.

Figure 3.5 Pictures of outcrops in the Siletz River, Corvallis and Tillamook areas. a) Columnar jointed basalt (sample 148); b) Amygdaloidal basalt outcrop (sample 117); c) Basaltic breccia (sample 199); d) interbedded sediments and ash layers (sample 180); e) Quarry with pillow basalt outcrops (sample 099); f) heavily zeolitised basalt (sample 130).

3.3 Crescent Formation, Washington

3.3.1 North Crescent (Olympic Mountains) and Bremerton

3.3.1.1 Geology

The main sequence of the Crescent Formation outcrops in the Olympic Mountains in a horseshoe-shaped pattern (Figure 3.6). The Crescent Formation in this region is divided into a lower submarine basalt dominated unit and an upper subaerial unit, which is not present in the north of the outcropping area (Glassley, 1974; Cady, 1975; Babcock et al., 1992). In the east of the area, where the stratigraphy is most complete and well exposed, a thickness of as much as 16.5 km has been determined (Glassley, 1974; Cady, 1975; Babcock et al., 1992; Hirsch and Babcock, 2009; Blakely et al., 2009). The lower unit is dominated by pillow basalts (Figure 3.7a; c; d; f), but also contains submarine massive flows and basaltic breccias (Figure 3.7b; c) (Babcock et al., 1992). Rare microgabbro sills and localised interbedded sediments comprising basaltic sandstone, siltstone and conglomerate also occur (Babcock et al., 1992; Babcock and Hirsch, 2009). The upper unit is mostly subaerial in nature, containing columnar jointed to massive basaltic flows with oxidised flow contacts in addition to basaltic sills (Babcock et al., 1992). Sedimentary interbeds are also locally observed in the upper unit and comprise basaltic breccia, sandstone, siltstone and foraminiferal limestone (Babcock et al., 1992; Babcock and Hirsch, 2009). Exposure in this region is however, restricted by dense forestation (Figure 3.7e).

The base of the lower basalts are observed overlying and interfingering with the Blue Mountain unit comprising lithic turbidite sandstones and mudstones (Tabor and Cady, 1978; Babcock et al., 1992). The Blue Mountain unit is thought to represent a continentally derived submarine fan, with which the lower Crescent basalts are generally conformable (Emarson, 1987; Tabor and Cady, 1978). The uppermost flows of the Crescent Formation in the Olympic Mountains are observed interfingering with the sandstones, shale and conglomerate dominated Aldwell Formation (Babcock et al., 1992; Babcock and Hirsch, 2009). In this region the Crescent Formation has been underthrust by a series of younger marine sedimentary units (the Olympic Core) (Figure 3.6), which are proposed to

represent part of an accretionary wedge (Tabor and Cady, 1978) or a subduction complex (Babcock and Hirsch, 2009). The Crescent Formation and Olympic Core sediments are largely separated by faulted contacts, the most predominant of which is the Hurricane Ridge fault (Tabour and Cady, 1978). Glacial deposits
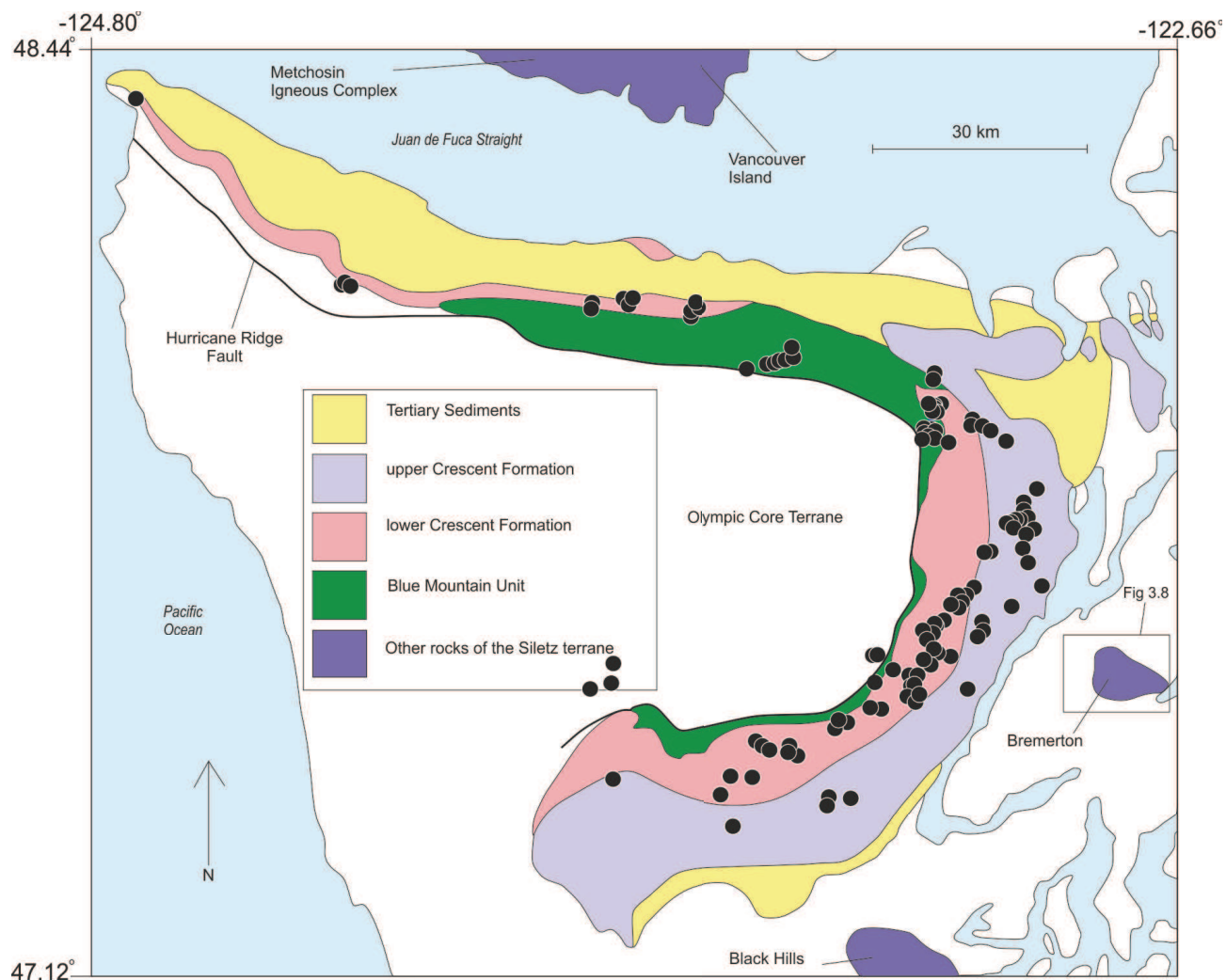
Figure 3.6 Map showing the location and general geology of the samples from the Crescent area in the Olympic Mountains, of the Crescent Formation. Map adapted from Babcock and Hirsh (2009).

cover the contact with the rocks to the east of the Crescent Formation (Babcock and Hirsch, 2009).

This region of the Crescent Formation has been suggested to have formed in an extensional basin at the Kula – Farallon – North American triple junction, between the Olympic Core terrane and the North American continent (Babcock et al., 1992; Brown and Dragovich, 2003). Other interpretations for the origin of the rocks of the Crescent Formation include oceanic plateau/oceanic islands (Wells et

Figure 3.7 Pictures of exposures in the Crescent Formation in the Olympic Mountains. a) Pillow basalt pile outcrop; b) Massive basalt flows and dykes; c) Volcanic pile exposure; d) Pillow basalt flow; e) Heavily forested view seen across much of the area; f) Pillow basalt.

al., 2014) and an accreted ophiolite (Glassley, 1974).

The section of the Crescent Formation exposed in the uplifted Bremerton area at the Gold and Green Mountains consists of a series of rocks ranging from a basal gabbro up to subaerial basalt flows (Figure 3.8) (Clark, 1989). Weaver (1937) originally connected the rocks exposed here to those of the Metchosin Igneous Complex (on Vancouver Island) and later mapping of the area was conducted by Clark (1989). The sequence, at the Green and Gold Mountains is as follows: 60 m of basal leucogabbros and gabbros (Figure 3.9d), sheeted dykes (150 m thick) (Figure 3.9c) and sub marine basalts, which are overlain by a subaerial basalt unit (with an overall thickness of over 180 m) (Figure 3.9a) and volcaniclastics (Figure 3.8; 3.9) (Clark, 1989; Haussler et al., 2000). Clark (1989) reported that the majority of the dykes in the Bremerton area strike N-NE, but can vary from E-SE to W-NW. Washington Quaternary glacial deposits then overlie much of section (Tabor et al., 2011), which is, addition, densely forested (Figure 3.9b). The dolerite and basaltic sheeted dykes intruding and cross cutting the complex are thought to have a thickness of 150 m and only occur at Green Mountain within the Crescent Formation (Clark, 1989; Haussler et al., 2000). The submarine volcanics are comprised of basaltic flows, interbedded with basaltic sandstone, siltstone, tuffs and basaltic breccia (Clark, 1989; Haussler et al., 2000). The average subaerial flow is approximately 9 m thick, which is far thinner than the average observed elsewhere in the Crescent Formation (30 – 50 m) (Clark, 1989; Babcock et al., 1992). Additionally vesicles measured in the basalt flows at Bremerton are larger (around 7 mm) in comparison to vesicles measured in other outcrops of the Crescent Formation (<4 mm) (Clark, 1989).

The Bremerton exposures are cross cut by hornblende dolerite (adakite) dykes with $^{40}Ar/^{39}Ar$ ages of 47.8 ± 1.4 Ma to 46.6 ± 1.4 Ma (Clark, 1989). However, the dykes are not thought to be related to the igneous complex and have been proposed to be associated with the subduction system that developed after the accretion of the Siletz terrane (Clark, 1989; Tabor, 2011). To the north of Green Mountain (Figure 3.8) the Seattle Fault and Seattle Basin, and are thought to have developed either during the Late Eocene (Johnson et al., 1994) or in the Mid – Miocene (Brink et al., 2002).

While the Green and Gold Mountains section shares some similarities to a classic ophiolite sequence, there is no ultramafic unit exposed and the total thickness of sheeted dyke's is low in comparison to other ophiolites (Clark, 1989; Haussler et al., 2000). Additionally, the sequence is capped by subaerial basalts in contrast to deep marine sediments observed in most ophiolites (Clark, 1989). Despite this, however, geophysical studies have revealed that there are highly magnetic and dense rocks below the area, which may represent unexposed ultramafic rocks (Haussler et al., 2000). The presence of the sheeted dyke complex has led some authors to suggest that the rocks exposed in the Bremerton area developed in an extensional setting (Tabor et al., 2011), which may have been a rifted continental margin (Babcock et al., 1992).
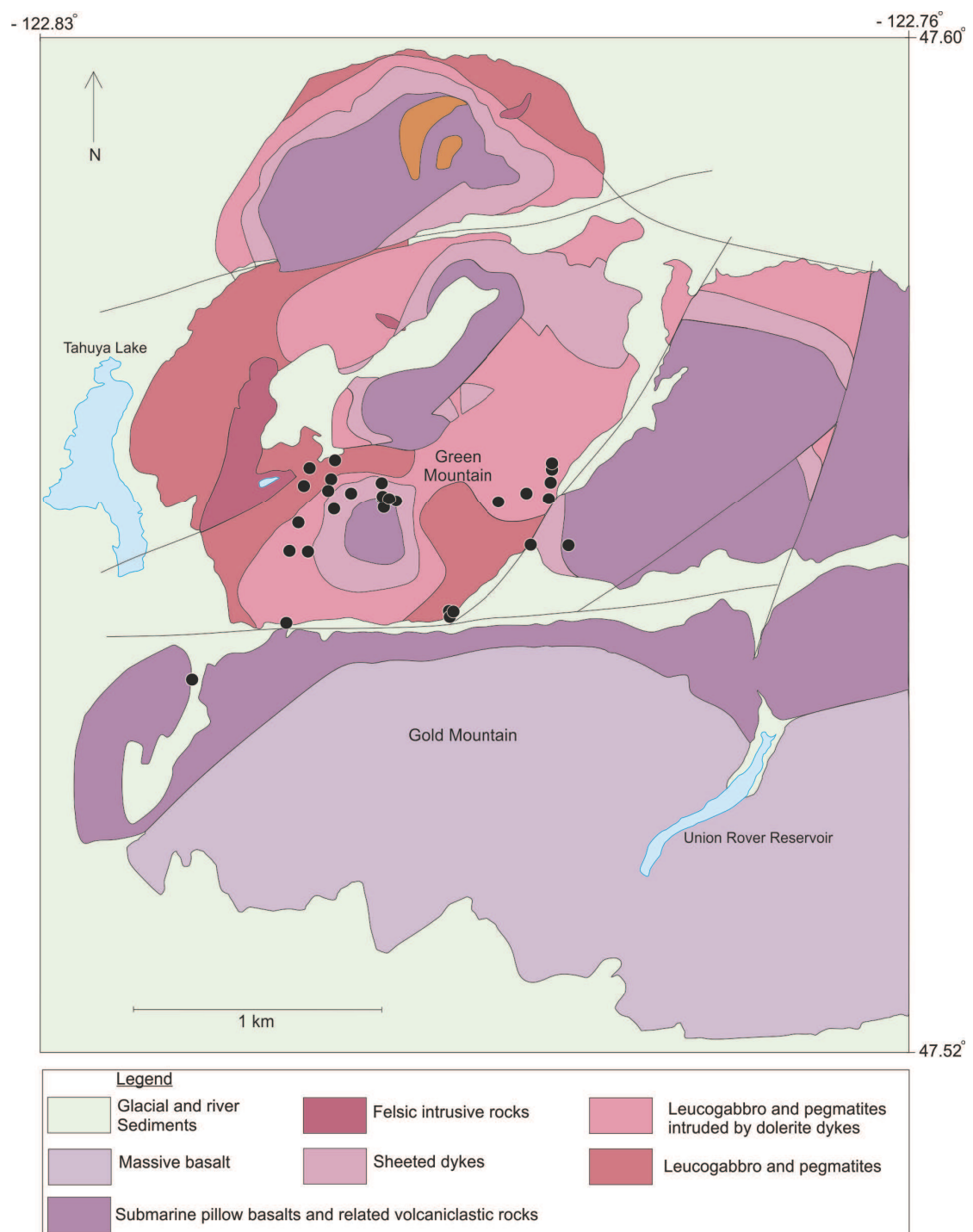
Figure 3.8 Map of the geology and sample locations at the Bremerton exposures. Adapted from Tabor et al., (2011).

3.3.1.2 Age

In the Olympic Mountains the age of the upper unit of the Crescent Formation has been constrained using ^{40}Ar/^{39}Ar isochron and whole rock fusion methods, and ranges between 51.0 ± 4.7 Ma at the base, to 50.5 ± 1.6 Ma at the top (Babcock and Hirsch, 2006). In the lower unit a sample from a massive flow has been dated at 56.0 ± 1 Ma using ^{40}Ar/^{39}Ar whole rock fusion, however, the sample is thought to have undergone argon retention (Babcock and Hirsch, 2006). While samples from the base of the lower unit in the north of the outcropping area have produced ^{40}Ar/^{39}Ar ages of 52.9 ± 4.6 Ma and 45.4 ± 0.6 Ma (Babcock and Hirsch, 2009). Wells et al., (2014) report that while detrital zircons derived from the sediments of the Blue Mountain unit (which interfingers with the basal pillow basalts) are generally Cretaceous in age, 4 grains have a young ^{40}Ar/^{39}Ar peak at around 49 Ma. Brandon (2014) also determined that samples from the Blue Mountain unit had a young peak of 50.0 Ma and 54.7 Ma respectively. Duncan (1982) reported an ^{40}Ar/^{39}Ar age of 57.8 ± 0.8 Ma for the Crescent Formation in the Olympic Mountains. While an age range of $53.5 – 49$ Ma using calcareous nanoplankton has been proposed for mudstone interbeds in basaltic flows from the top of the Crescent Formation (Squires et al., 1992).

In terms of the Bremerton complex ages, whole rock K-Ar dating for samples from 3 basalt flows to the southeast of Bremerton produced ages between 43.3 and 49.2 Ma (Duncan, 1982). Duncan (1982) also reanalysed two of these samples using ^{40}Ar/^{39}Ar that yielded whole rock total fusion ages of 51.7 ± 2.4 and 55.3 ± 3.1 Ma, and a step-heating age of 55.4 ± 3.2 Ma. However, Haussler et al. (2000) reported a ^{206}Pb/^{238}U age of 50.5 ± 0.6 Ma from a leucogabbro sample from the base of the sequence. This younger age, along with Clark's (1989) ^{40}Ar/^{39}Ar total fusion ages of 50.4 ± 0.6 Ma and 49.2 ± 0.8 Ma for another leucogabbro sample, indicates that the ages from the basalts may be erroneously too old (Haussler et al., 2000). Additionally, there are contemporaneous submarine basalt flows from other nearby Crescent Formation exposures, which are overlain by sediments containing foraminifera with ages of around $51 – 48$ Ma (Spencer, 1984). Therefore, the ^{40}Ar/^{39}Ar ages for the basalt flows have most likely acquired excess argon or undergone recoil (Haussler et al., 2000). The age

range for the basaltic units in the North Crescent therefore appears to vary from 53 – 50 Ma.

Figure 3.9 Pictures of outcropping rocks at Bremerton. a) Oxidised massive basalt flow; b) View over Gold Mountain and surrounding area; c) Dolerite dyke from sheeted dyke complex; d) Gabbro outcrop.

3.3.1.3 Sample Collection

Derek Laidlaw collected the majority of the 130 samples from the North Crescent area in 2005. The samples were from both the predominately pillow basalt lower unit and the massive basalt flow dominated upper unit and were largely collected from logging-road cuttings, although quarries and river cuttings were utilised where possible. Exposure in this area is relatively poor due to the dense forestation that occurs across the region (Figures 3.8e; 3.9b).

Thirty samples were collected from transects across the exposures at Green Mountain, Bremerton, in the summer of 2014 (Figure 3.8). The samples included massive basalt flows, pillow basalt flows, leucogabbro outcrops, sheeted dykes and gabbro exposures. Unfortunately, access to the southern parts of the area (including Gold Mountain) was restricted as the mountain lies on private land containing the City of Bremerton watershed.

3.3.2 South Crescent (Willapa Hills)

3.3.2.1 Geology

The Crescent Formation occurs as basement highs in southern Washington, and is exposed in the Black, Doty and Willapa Hills (Figure 3.10) (Wells, 1981; Duncan, 1982). The dominant structural features in this region are the broad faulted anticlinorium. The Siletz terrane, where exposed in these structures dominantly comprises massive basalt flows and pillow basalts (Figure 3.11b; c) (Wells, 1981; Wells and Swalon, 2014). In addition, columnar jointed basalt flows, doleritic dykes and gabbros are also observed overlying and intruding the pillow basalts (Figure 3.11a; d) (Wells, 1981; Wells and Swalon, 2014). Locally hyaloclastite pillow breccias and basaltic sandstones overly the pillow and massive basalt flows, which also contain thin interbeds of siltstone and mudstone (Moothart, 1993).

The pillow basalts are finely crystalline and occasionally contain amygdules and small clinopyroxene and plagioclase phenocrysts (Wells, 1981; Moothart, 1993). The pillows range in diameter from 0.25 – 1.25 m and often display radial cooling joints and glassy rims (Moothart, 1993). Pillow lava carapaces are often observed overlying aphanatic massive basalt flows (Figure 3.11c), which is comparable to what is observed elsewhere in the upper parts of the Siletz terrane (Wells et al., 2014). Columnar jointed subaerial basaltic flows, which are clinopyroxene and plagioclase phyric, locally overly the pillow lavas (Figure3.11b) (Wells and Swalon, 2014). These subaerial basaltic flows have been suggested to be related to the later intrusive rocks, which are observed across the

region (Wells et al., 2014). The intrusive rocks comprise fine- to medium-crystalline plagioclase and clinopyroxene phyric basalts, dolerites and gabbros (Moothart, 1993). The basaltic tuff breccias observed consist of angular basalt and basaltic glass fragments which are cemented by zeolite (Moothart, 1993).The breccias are frequently capped by basaltic sandstones and are observed near the top of the Crescent Formation in this region (Wells, 1981).

Sedimentary interbeds in the basalt flows are thin (1 -2 m thick) deposits of siltstone and mudstone (Moothart, 1993). Locally sandstone deposits are observed overlying the finer grained sediments, and in some sections contain rounded quartz and chert clasts and elsewhere subrounded coarse basaltic clasts (Moothart, 1993).

The basal contact of the Siletz terrane is not exposed in the southern Crescent Formation outcrops. The Middle – Late Eocene Fork Creek member (of the McIntosh Formation) represents a series of bedded fine- to medium- grained, micaceous, arkose sandstone and carbonate rich siltstones (along with local basaltic sandstones) which conformably overlies and interfingers with the upper pillow basalts of the Crescent Formation in some areas of this region (Moothart, 1993). Elsewhere, there are faulted contacts observed between the Fork Creek member and Crescent Formation (Moothart, 1993). Gabbroic and doleritic sills are noted intruding both the Crescent Formation and the Fork Creek member near the contact between the two (Wells, 1981) (Figure 3.10). Unconformably overlying the Eocene rocks in the southern Crescent is the Oligocene Lincoln Creek Formation (Wells, 1981).

The volcanic rocks in the South Crescent are thought to represent the upper/ later stages of volcanism in an ocean island environment (Wells and Swalon, 2014). The basaltic hyaloclastite breccia deposits have been suggested to have formed by phreatic eruption of glassy material during the subaqueous formation of pillow lavas (Williams and McBriney, 1979; Moothart, 1993). The interbedding of the breccia and basaltic sandstone units with the McIntosh Formation suggests that the volcanic vents were still active during the deposition

of the continentally derived sediments of the McIntosh Formation (Moothart, 1993).

The intrusive rocks observed have been proposed to have formed either during late stage magmatic events in the Crescent Formation or alternatively may represent a section of the feeder system of the Middle to Late Eocene Grays River Volcanics (Figure 3.10) (Wells, 1981; Rau, 1986; Phillips et al., 1989). Contemporaneous sills are observed in the basalts of Hembre Ridge and are suggested to have formed subsequent and during accretion of the terrane as a result of changes in the forearc stresses and later subduction zone development (Wells et al., 2014; Gurnis et al., 2012).
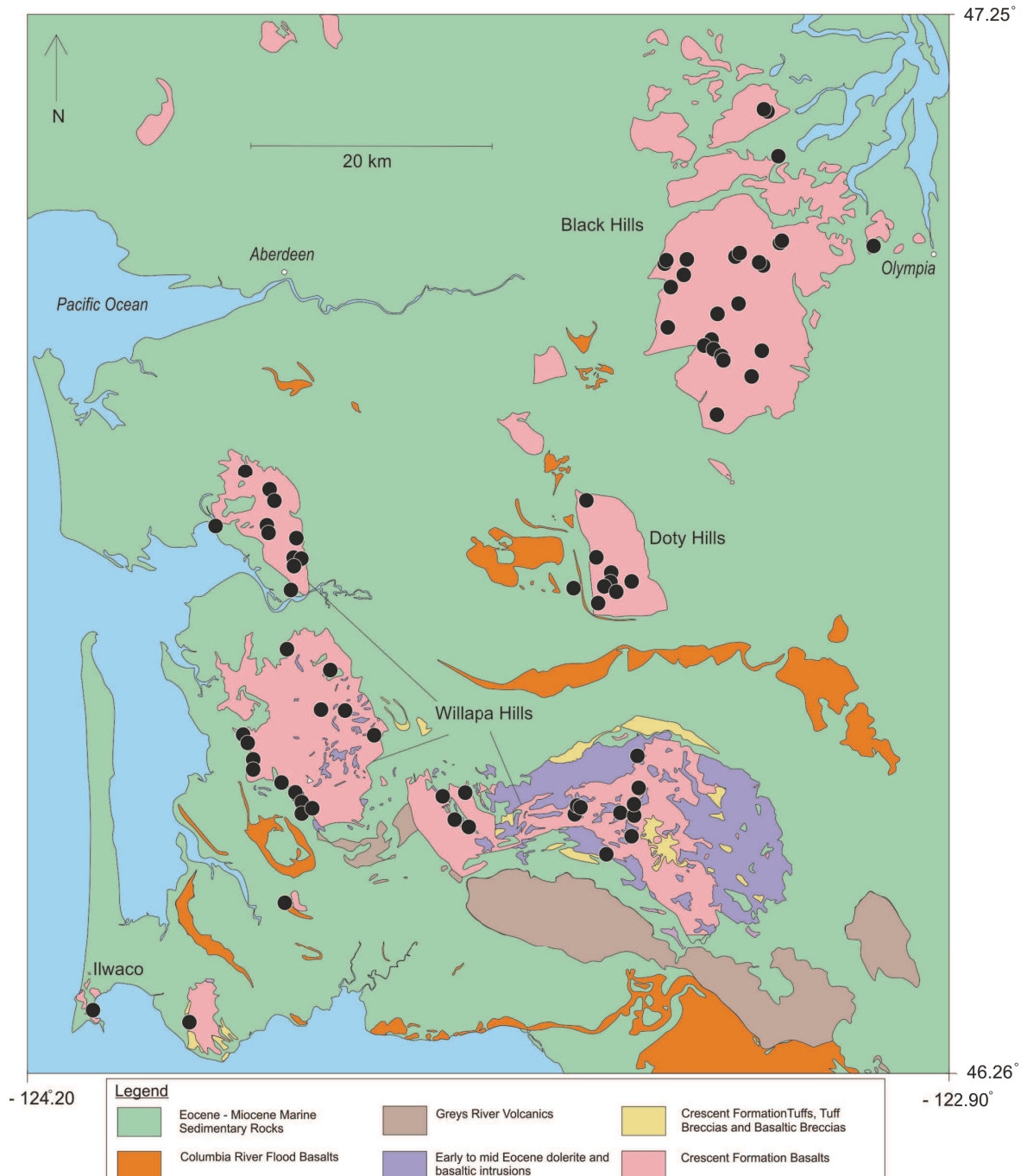
Figure 3.10 Map showing the locations and geology of the Southern Crescent Formation samples. Map compiled from Moothhart, (1993); Wells et al., (2014) and https://fortress.wa.gov/dnr/protectiongis/geology/?Theme=wigm [Accessed November 2016].

3.3.2.2 Age

Duncan (1982) reported K-Ar ages of 56 – 51 Ma for basalt flows from the Black Hills region. Pillow basalts from the Willapa Hills section have yielded $^{40}Ar/^{39}Ar$ step heating ages of 55.7 ± 1 Ma and 53.6 ± 2 Ma, however, the reported ages may have been affected by inheritance of argon (Moothart, 1993). Additionally, a sill belonging to the Crescent Formation found intruding the Fork Creek member has a reported $^{40}Ar/^{39}Ar$ step heating age of 48.7 Ma (Moothart, 1993). No nanoplankton have been dated from the outcrops in southern Washington, nor are there any U-Pb ages.

3.3.2.3 Sample Collection

All except 3 samples (collected in 2014) were collected by Derek Laidlaw in 2004 and 2005 and their location is shown in Figure 3.10. The samples were mostly taken from the pillowed and massive basalt flows, with a selection of samples also collected from the overlying columnar jointed basalts and hyaloclastite breccias. Most samples from this area were collected from quarries, as exposures are rare.
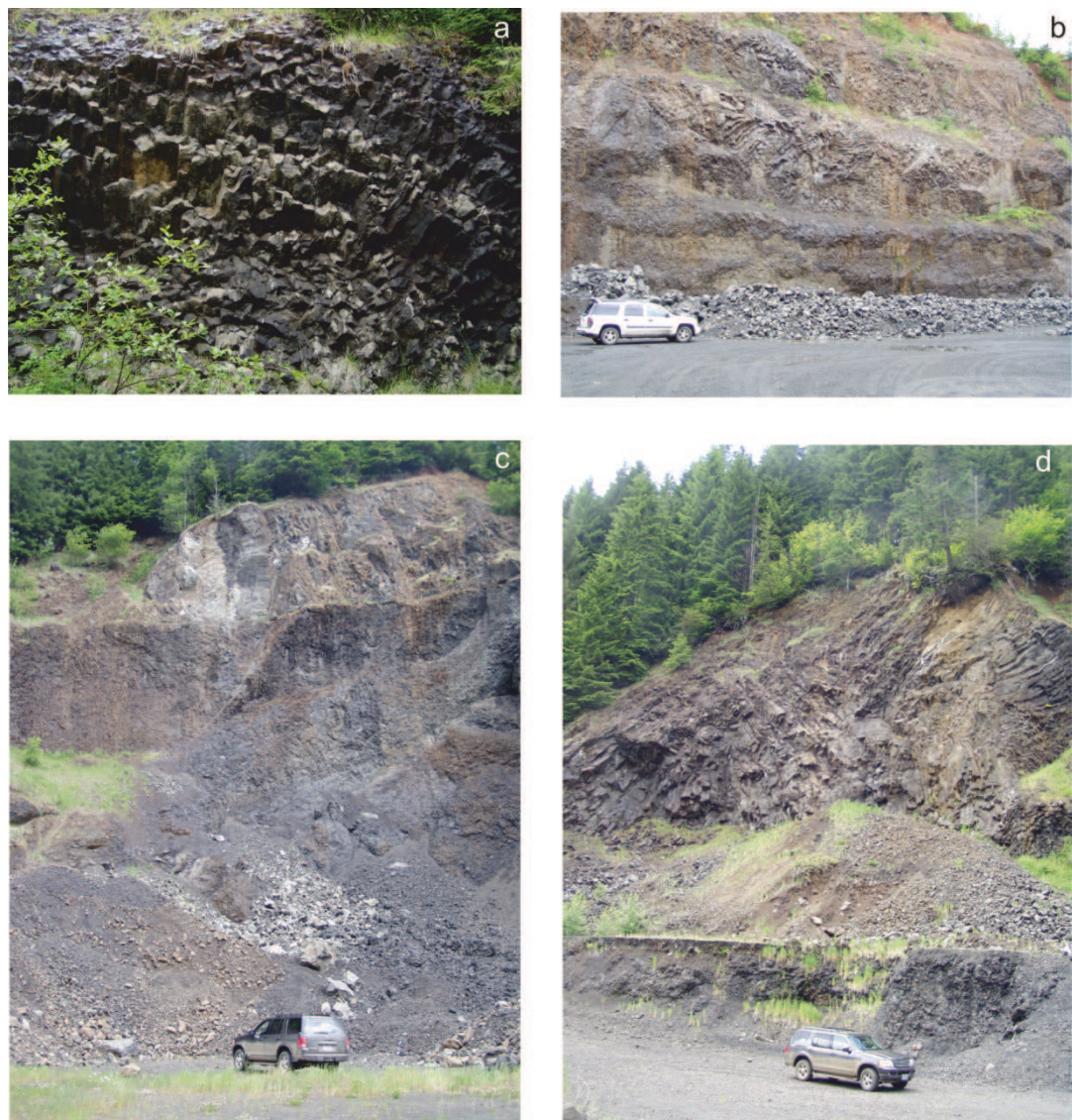
Figure 3.11 Pictures of exposures in the southern Crescent Formation. a) Columnar jointed basalts; b) Quarry exposure of columnar jointed basalts and pillow basalts; c) Pillow basalts and massive flows exposed in quarry; d) Columnar basalts in quarry.

3.4 Metchosin Igneous Complex, Vancouver Island

3.4.1 Geology

The Metchosin Igneous Complex consists of a series of gabbros, sheeted dykes, basalts and localised tuff breccias and volcaniclastic deposits (Figure 3.12) The gabbros are exposed in the south of the complex at the base of the sequence and comprise both layered and isotropic gabbros in addition to a limited amount of leucogabbros (Massey, 1986). The gabbro sequence is relatively thin, however, higher level gabbro and tonalite sills are observed intruding the volcanic rocks and are subsequently intruded by cross-cutting dolerite dykes (Massey, 1986; Timpa, 2000). Stratigraphically above the gabbro stocks is a well exposed 500 – 1500 m thick sheeted dyke complex (Massey, 1986; Timpa, 2000). The dykes primarily comprise medium grained dolerites, although microgabbro, feldspar rich dolerites and basalts are also observed (Massey, 1986). The dykes are generally 1-3 m wide, but can be as wide as 8-10 m (Massey, 1986). Late trondhjemite sills are also observed cross-cutting the sheeted dykes (Massey, 1986). The volcanic rocks overlie the sheeted dykes and are are predominantly comprised of basalts (Massey, 1986). The lower basalts are submarine and consist of 1500 m of pillow basalts and massive flows. Interbedded with the basalts are tuff breccias, volcaniclastic sediments and local chert beds (Massey, 1986; Timpa, 2000). At the top of the lower unit well -bedded tuffs, breccias and massive flows dominate. The overlying upper unit comprises 1000 m of subaerial massive sheet basalt flows with abundant amygdales (Massey, 1986). The upper unit also contains
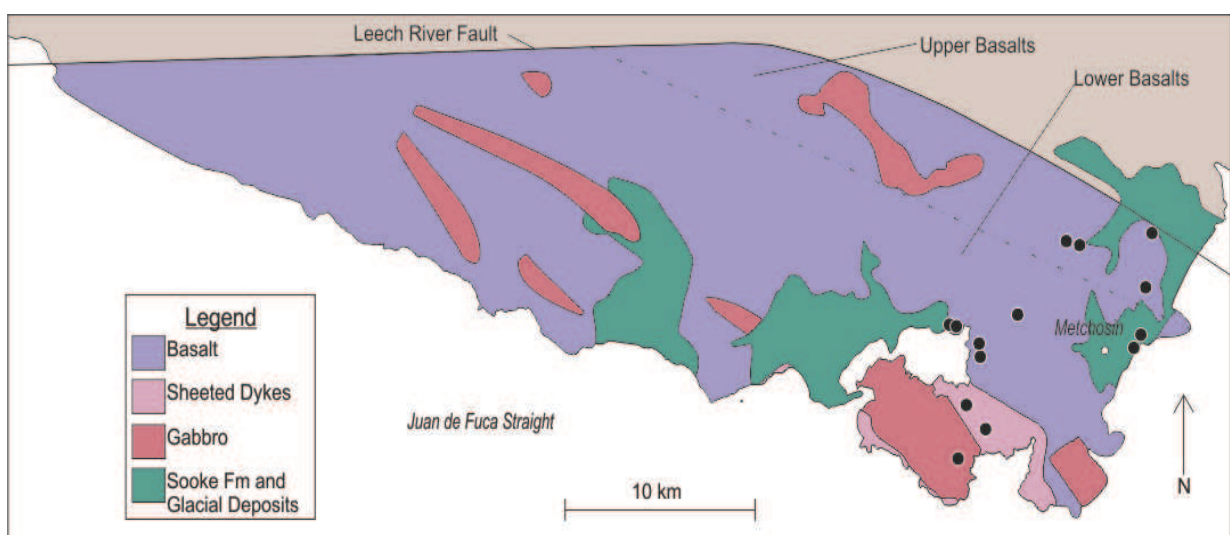
Figure 3.12 Map highlighting the sample locations and geology of the Metchosin Igneous Complex and associated rocks. Adapted from Massey, (1986).

local tuff and basaltic breccias towards the top of the unit proximal to the Leech River Fault (Massey, 1986). Alteration of the samples is seen to increase upwards through the sequence towards the Leech River Fault in the north.

It has been suggested that the upwardly emergent sequence of the Metchosin Igneous Complex represents the development of an oceanic island, which formed in an extensional setting (Massey, 1986). This extensional regime is proposed to explain the presence of the sheeted dyke complex, which is not normally observed in intraplate environments and may indicate a mid-oceanic ridge or a transform marginal basin (Massey, 1986).

The complex on Vancouver Island is bounded to the north and west by the Leech River Fault (Figure 3.12). The fault separates the complex from the Pacific Rim and Wrangellia terranes under which the complex was thrust at around 42 Ma (Yorath et al., 1999). In places the Oligocene Sooke Formation, which comprises clastic sedimentary rocks, overlies the complex, as do Pleistocene glacial sediments (Figure 3.12) (Muller, 1980). The complex has been determined to be continuous with the Crescent Formation beneath the Juan de Fuca Straight (Yorath et al., 1999).

3.4.2 Age

Yorath et al., (1999) reported U-Pb zircon ages of 52 and 54 Ma for the volcanic rocks while an age of 52 Ma has also been determined for a dolerite dyke using U-Pb zircon methods (Massey, 1986). Duncan (1982) produced an age range of 58 – 42 Ma, however these ages were calculated using K-Ar and $^{40}Ar/^{39}Ar$ methods, which are prone to uncertainties in altered rocks (Maluski et al., 1995).

3.4.3 Sample Collection

Derek Laidlaw collected 14 samples in a generally SW – NE transect through the eastern part of the Metchosin Igneous Complex where the most

complete stratigraphy is observed (Figure 3.11). Samples were collected from the isotropic gabbro exposure, sheeted dykes and both lower (pillow) and upper (massive) basalt flows. The basalts are locally interbedded with tuff breccias and volcaniclastic sediments, however these were not sampled.

3.5 Associated Terranes

3.5.1 Yakutat Terrane, South Eastern Alaska

The Yakutat terrane, which is currently located in the north of the Gulf of Alaska (Figure 3.13), has been proposed to share a similar source to the Siletz terrane, and the two have been described as sister terranes (Plafker, 1987; Wells et al., 2014). At present the Yakutat terrane is largely offshore the coast of south Alaska and is undergoing subduction beneath the accretionary complex terranes of the Alaskan margin (Worthington et al., 2010; Gulich et al., 2013). Rare outcrops of the Yakutat terrane are exposed on land (Plafker, 1987). The exposed rocks include 55 – 50 Ma pillow basalts and breccias which are overlain by Eocene mudstones (Plafker et al., 1994). The sequence has been proposed (using seismic data) to reach a thickness of 15 km onshore and where it extends offshore the terrane may reach a crustal thickness of up to 24 – 27 km (Christenson et al., 2012; Worthington et al., 2010).

The terrane, where exposed onshore, is overthrust by Cretaceous accretionary rocks (Plafker et al., 1994). The Transition Fault constrains the western boundary of the terrane offshore (Figure 3.13) (Christenson et al., 2012; Worthington et al., 2010). It has been proposed that the terrane formed in a similar region to the Siletz terrane, before it rifted northwards to its present location, although, the exact location, is uncertain (Plafker et al., 1994; Perry et al., 2009).
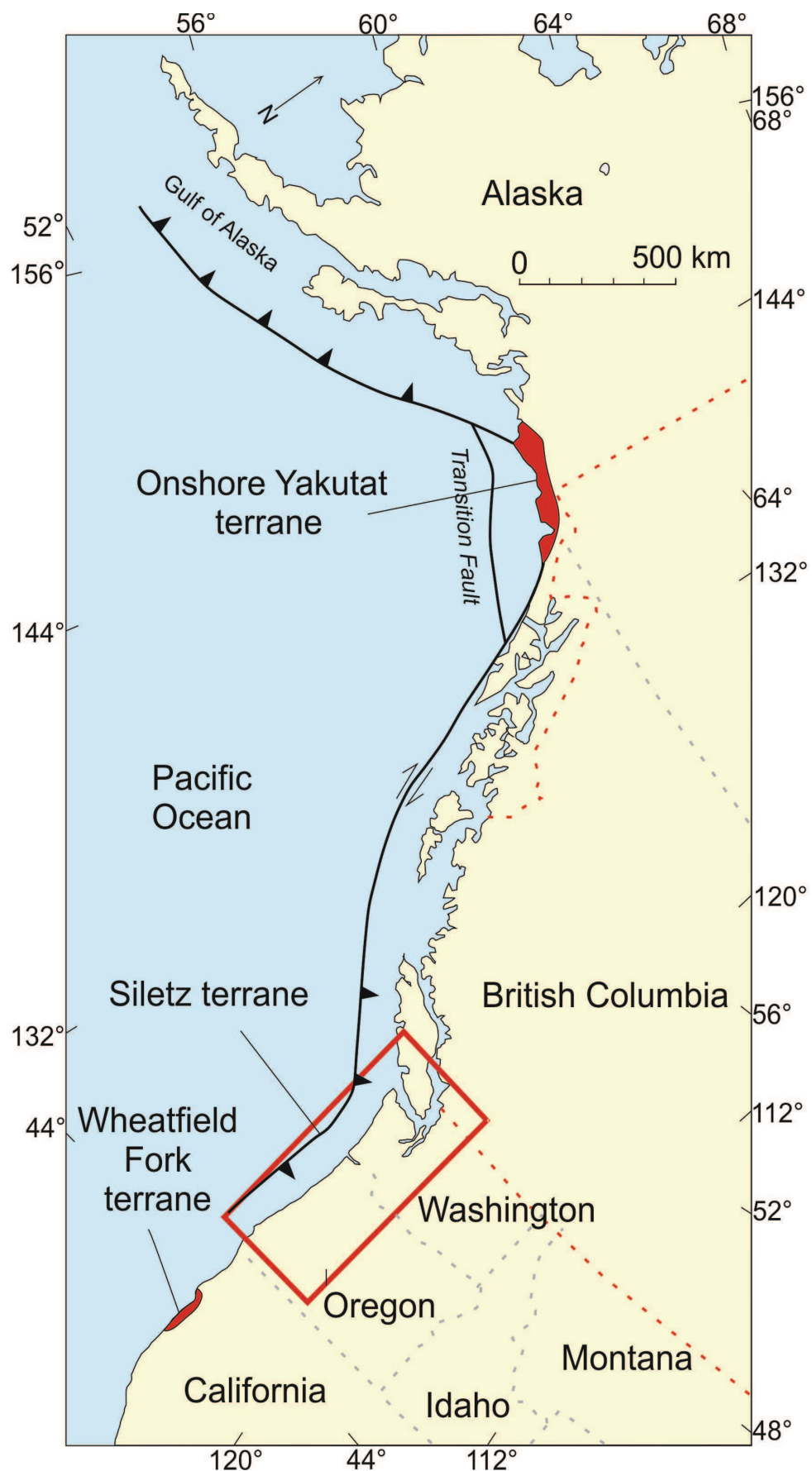
Figure 3.13 Map highlighting the location of the Yakutat and Wheatfield Fork terranes in comparison to the Siletz terrane.

3.5.2 Wheatfield Fork Terrane

The Wheatfield Fork Terrane is also thought to represent a fragment of the Siletz terrane (McLaughlin, 2009). A 13 km sliver of the Wheatfield Fork Terrane is exposed in the Franciscan Complex in the coastal belt of Northern California (Figure 3.13) (McLaughlin, 2009). The terrane contains basalt flows and basaltic breccias along with interbedded pelagic limestone, while the remainder of the Franciscan Complex is not oceanic in nature (McLaughlin, 2009). Foraminifera derived from the limestones have been recognised as belonging to the late early to middle Eocene (~ 51 – 46 Ma) (McLaughlin, 2009). The Wheatfield Fork Terrane therefore has a similar depositional setting and timing of magmatism to the Siletz terrane and so has been proposed to correlate with it. McLaughlin, (2009) suggested that the Wheatfield Fork Terrane formed on the south-eastern part of the Kula (or Resurrection) plate and had accreted onto the North American continent by the early Miocene. This model however, requires that a significant offset in Kula – Farallon mid oceanic ridge system has occurred which is not consistent with current plate models (McLaughlin, 2009; Seton et al., 2012).

3.6 Summary

The Siletz terrane is dominated by submarine pillow lavas and massive flows, which are frequently associated with basaltic breccias, tuff breccias, submarine and continentally derived sediments. Subaerial massive and columnar jointed basalts are often observed overlying the submarine rocks, and also contain tuff and basaltic breccias in addition to interbedded sediments. Gabbros, cross cutting dykes and sills also occur frequently in the terrane while leucogabbros and sheeted dyke complexes are locally observed. Several of the upper contacts between the Siletz terrane and younger rocks are conformable and interfingered, suggesting the magmatism continued during accretion of the terrane. Generally, the various exposures and formations of the terrane have been interpreted to represent oceanic islands, although other tectonic settings have been frequently proposed, such as formation in a marginal basin environment.

Overall, the age of the terrane has been constrained between 56 – 49 Ma, however some of the proposed dates fall outside of this range (Figure 3.14). The majority of magmatism appears to have taken place between 54 – 50 Ma (Figure 3.14). The dominant method of dating the terrane is ^{40}Ar/ ^{39}Ar, however, as discussed in this section, there are caveats to its use and therefore more U-Pb zircon/ baddeleyite ages may add to the robustness of the data set. Sample collection took place across the terrane, however, time, money access and most significantly, exposure, limited the amount of coverage in some areas.
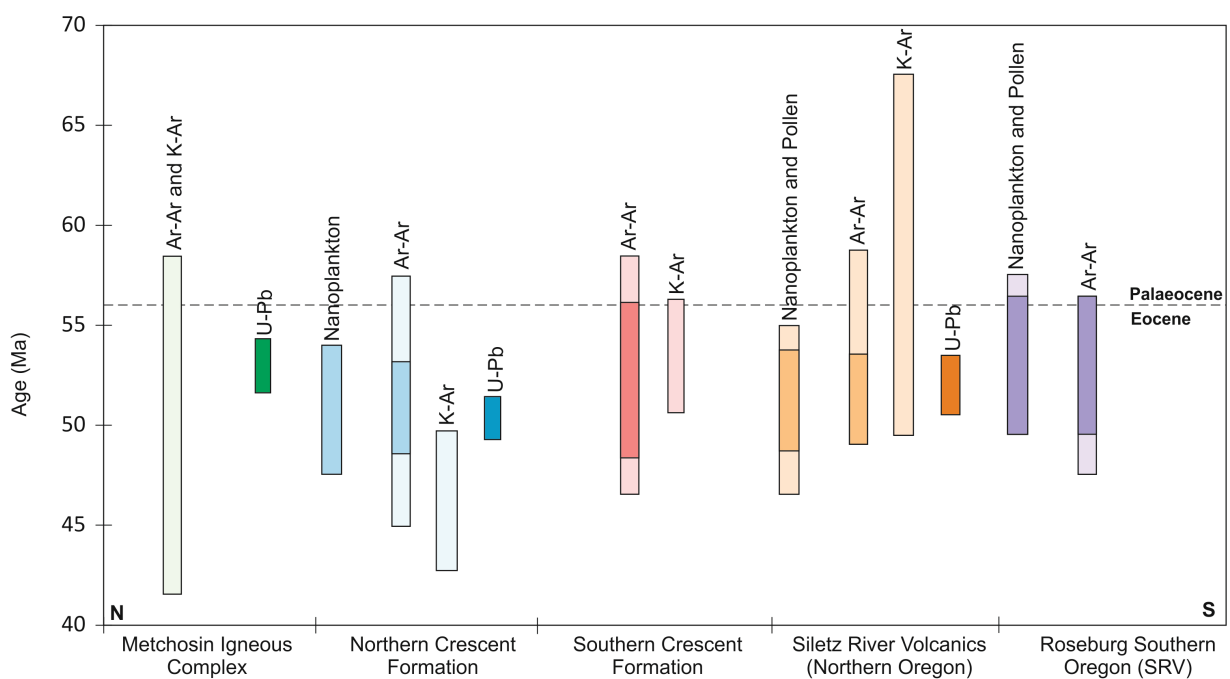
Figure 3.14 Summary of the ages and dating methods of the Siletz terrane, where the weight of the colour of each bar corresponds to the certainty of a given age range. See text for data sources and section 5.7 for the geochronological data collected in this study.

4. PETROGRAPHY AND MINERAL CHEMISTRY

4.1 Introduction

This section discusses the petrography, alteration and mineral compositions of the samples in this study. The majority of the samples comprise vesicular basalts, dolerites, and gabbros, with occasional rhyolites and leucogabbros. The mafic rocks are generally composed of plagioclase, clinopyroxene and Fe-Ti oxide. Sub-ophitic textures in the plagioclase and clinopyroxene are common across the entire terrane, and zeolite-filled amygdales are abundant. Several samples collected from the Siletz River Volcanics also contain olivine in addition to the minerals noted above. Opaque minerals comprise between 10 % and 20 % of most samples and are particularly abundant in the Siletz River Volcanics (in the Roseburg region).

The rocks of the Siletz terrane exhibit variable degrees and grades of alteration. The Metchosin Igneous Complex and some Crescent Formation samples display greenschist-facies alteration with chlorite, albite and epidote. Other Crescent Formation samples, and the Siletz River Volcanics to the south, have undergone zeolite to prehnite – pumpellyite facies alteration and contain zeolite, calcite, pumpellyite and prehnite. Palagonite is also a common alteration phase throughout the Siletz terrane samples and is interpreted to represent altered volcanic glass.

The composition of minerals in a magma can provide significant insight into the conditions under which it crystallised, including the temperature, pressure and chemistry of the melt (Pearce, 1994; Ginibre et al., 2007). Therefore, quantitative microanalyses of the mineral composition of representative samples were obtained using an Oxford Instruments EDS analyser, which was attached to the Scanning Electron Microscope at Cardiff University. The operating conditions were set at 20kV, the specimen calibration current at ~2 nA at a fixed working distance of 8.5 mm. Analytical drift checks were carried out at 30 minute intervals using the Co reference standard while clinopyroxene and plagioclase standards from MircoAnalysis Consultants limited were used to calibrate the EDS analyser.

The clinopyroxene and plagioclase crystal targets were identified for spot analysis during petrographic evaluation. Full standards and results data can be found in Appendix E2. However, there are some analytical limitations to using the EDS SEM and the resulting data. Limitations can for example include, misidentification of major constituent peak and so element identification and large systematic errors which are a result of EDS large volume of acceptance meaning that spectra which are not in fact credible are accepted (Newbery and Ritchie, 2012). In addition in this study the elemental values for Ti analysed in the feldspars are too close to the detection limits of the instrument and so cannot be clearly discernable. These analyses are therefore omitted.

The Mg# of the clinopyroxenes were calculated using the equations of Derr et al (2013). In this method the wt.% of the oxides is used to derive their molecular proportion, then their atomic proportion which is subsequently used to calculate the ionic proportion of the elements. These ionic proportions were then used in the equations that calculate the Mg# of the pyroxenes and end member proportions of the analysed pyroxenes and feldspars (Equations 4.1, 2, 3 and 4, where all elements are ionic proportions).

Equation 4.1 $Mg\# = Mg / Mg + Fe \times 100$

Equation 4.2 $En = Mg / (Mg + Fe + Ca) \times 100$

Equation 4.3 $Fs = Fe / (Mg + Fe + Ca) \times 100$

Equation 4.4 $Di = Ca / (Mg + Fe + Ca) \times 100$

While the end member compositions of the analysed feldspars were determined using the following equations.

Equation 4.5 $An = Ca / (Ca + Na + K) \times 100$

Equation 4.6 $Ab = Na / (Ca + Na + K) \times 100$

Equation 4.7 $Or = K / (Ca + Na + K) \times 100$

4.2 Siletz River Volcanics, Oregon

4.2.1 Roseburg

4.2.1.1 Petrography

Aphyric basalt flows predominate in the southernmost outcrops of terrane, they generally comprise 45 vol. % plagioclase, 45 vol. % clinopyroxene and 10 vol.%[1] ilmenite, although, some samples contain greater abundances of opaque oxide minerals (Figure 4.1A). Plagioclase crystals are needle shaped, while clinopyroxene crystals are generally subhedral in appearance. The texture is largely intergranular, however, subophitic textures also occur in several of the samples (Figure 4.1B), and overall, the basalts tend to vary from hypocrystalline (Figure 4.1C) to holocrystalline. Basalts with predominantly clinopyroxene and plagioclase rich glomerocrysts are also observed. Additionally, phyric basalts occur, with minor lath shaped plagioclase phenocrysts (0.2-0.5 mm) and minor subhedral clinopyroxene phenocrysts of a similar size (Figure 4.1D). Pervasive fracturing and fragmenting of plagioclase and clinopyroxene, along with zeolite and clay alteration, is noted in the groundmass of these samples. Variolitic textures are also occasionally observed (Figure 4.1E) along with abundant pervasive alteration in the plagioclase crystals. Minor amounts of olivine are present in basalts from the Red Hill and Coquille exposures, where they occur as small sub-rounded crystals or as pseudomorphs. Olivine phyric basalts, along with smaller clinopyroxene and plagioclase phenocrysts, are observed in the Kentucky Slough area, while the groundmass is predominately plagioclase and opaque rich (Pyle, 1988). Basaltic sandstones are observed (Figure 4.1F) (interbedded in places with the Roseburg area basalts), with small rounded fragmented crystals of clinopyroxene and olivines along with minor feldspars.

Abundant zeolite and clay alteration occurs in the Roseburg groups, along with additional palagonite and calcite alteration (Figure 4.1G). Plagioclase phenocrysts are often fractured and exhibit sericitisation or are present only as pseudomorphs. The groundmass of the samples is often completely altered to brown/ orange zeolites and clays. Cross-cutting veins of zeolite alteration occur

---

[1] All mineral proportions are in vol. % for the remainder of this chapter.

frequently as do quartz and calcite veins. Palagonite filled amygdales are less common in the Roseburg groups. The basaltic sandstone samples display abundant pervasive alteration, with patches of zeolite and calcite also apparent (Figure 4.1F).
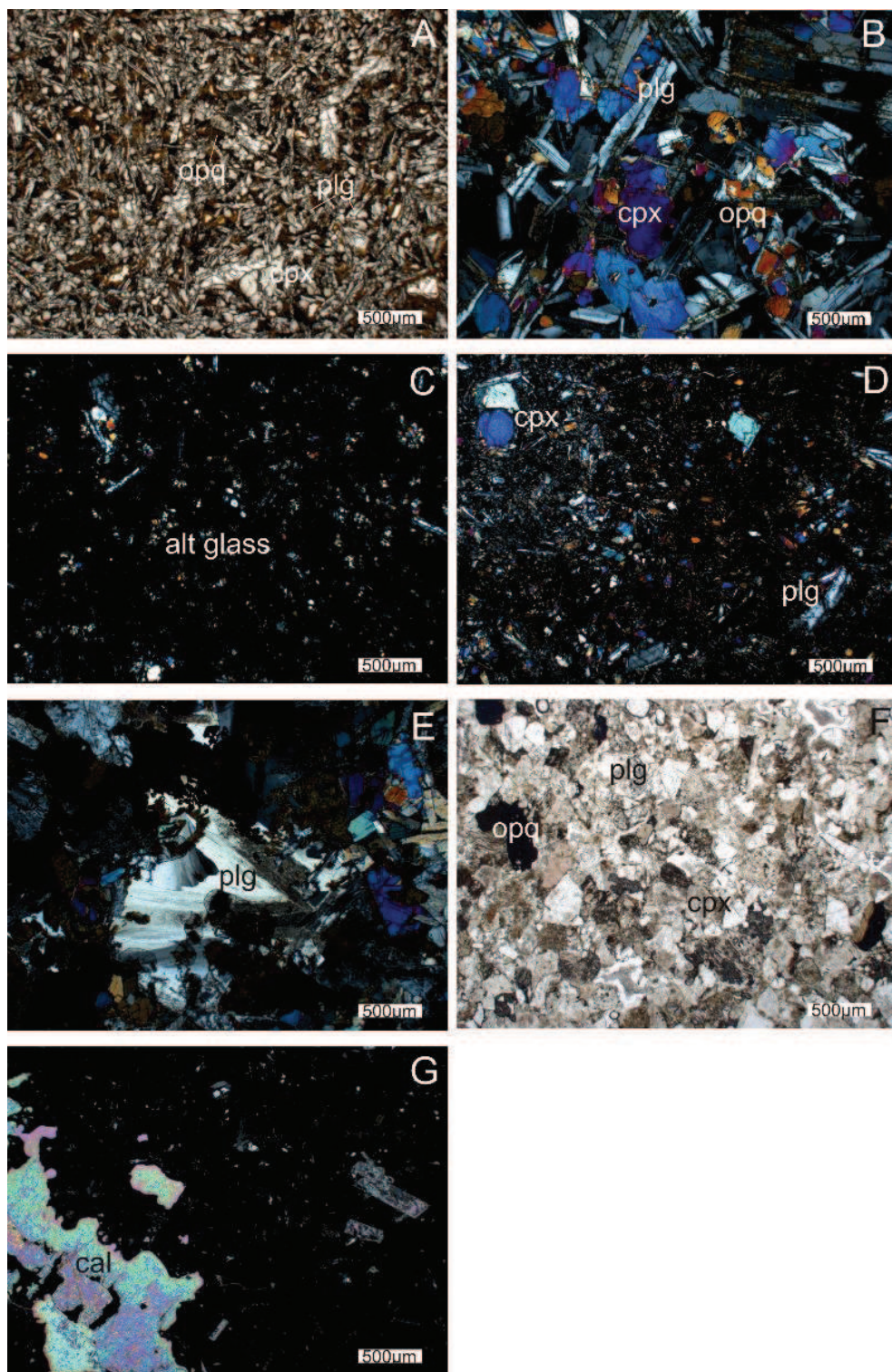
Figure 4.1 Photomicrographs of the Roseburg area samples. **A)** PPL view of the typical texture and composition of the basalts from this area (sample 009RO). **B)** XPL view of both the intergranular and subophitic texture observed in dolerites (sample 057RO). **C)** XPL view of a hypocrystalline sample now composed predominantly of altered glass (sample 061RO). **D)** XPL view of clinopyroxene and plagioclase phenocrysts (sample 053RO). **E)** XPL view of variolitic texture in plagioclase crystals (sample 076RO). **F)** PPL view of basaltic sandstone (sample 002RO). **G)** XPL view of calcite alteration in a basaltic sample (sample 041RO).

4.2.1.1 Mineral Compositions

The majority of clinopyroxenes analysed have Mg# compositions that vary between 74 – 84 Mg#, however, there is also a secondary array of analyses that extend down to a Mg# of 49, which are most likely a result of alteration (Figure 4.2). The CaO wt.% of the Roseburg Group samples varies between 16.2 – 21.2 wt.%, displaying a positive correlation trend at lower Mg#, however most data points cluster at a high Mg# (Figure 4.2). When the scattered low Mg# points are omitted, the Al_2O_3 content of the clinopyroxenes generally decreases with increasing Mg#. The Al_2O_3 abundance has a relatively narrow range of abundances varying from 2.1 – 5.1 wt.%. The lowest TiO_2 wt.% values are found at the highest Mg# content, with more scatter observed at lower Mg# (Figure 4.2). Between 1.0 and 2.5 Al_2O_3 wt.% the CaO abundances increases from 16 to 19 wt.% before becoming scattered at higher CaO concentrations. The TiO_2 content shows a small peak at around 1.5 Al_2O_3 wt.% before decreasing again at higher Al_2O_3 concentrations (Figure 4.2). Samples with high Mg# numbers (in this instance > 77) display the highest C_2O_3 wt. %.
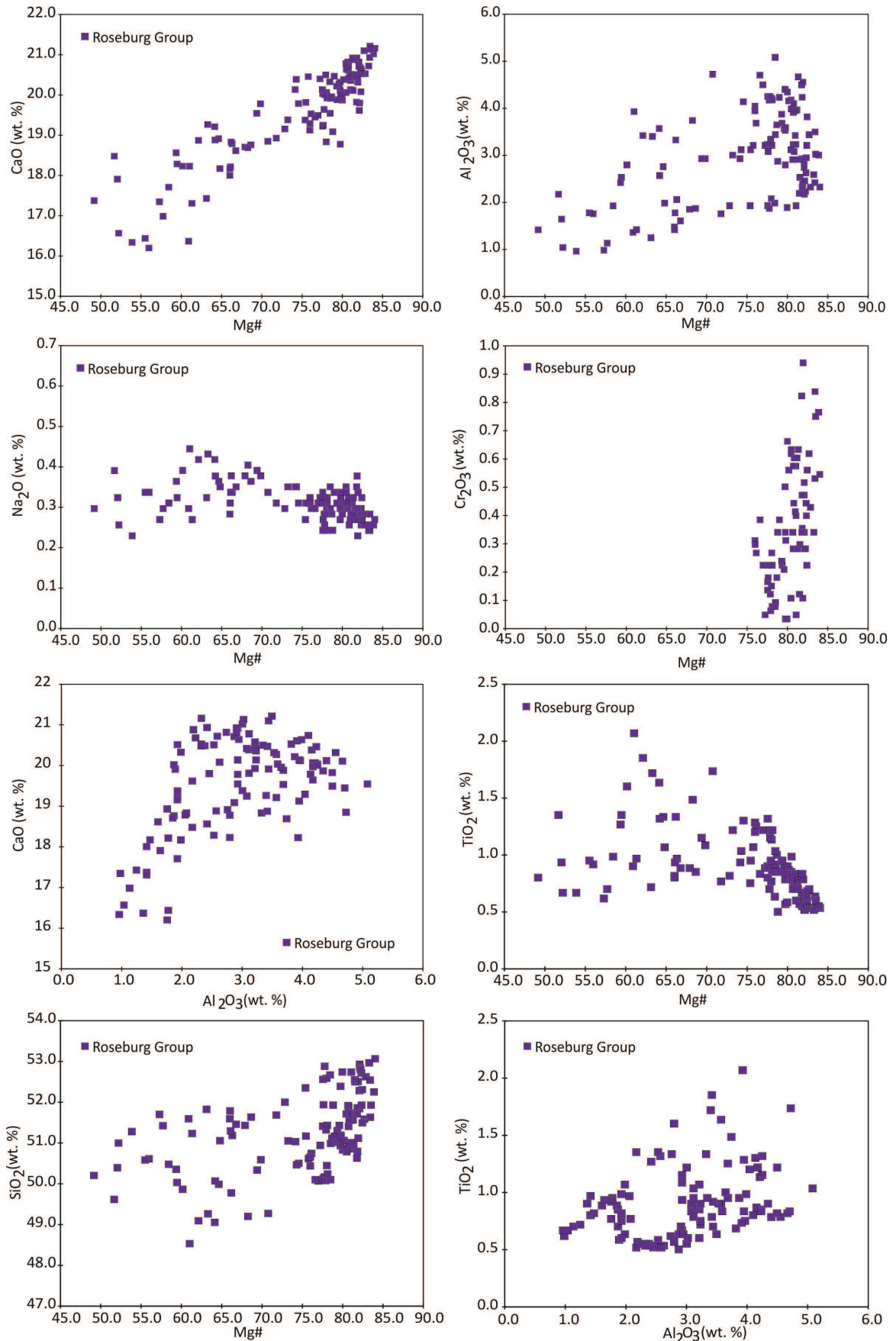
Figure 4.2 Bivariate diagrams of the major element compositions of clinopyroxenes from the Roseburg Group.

In Figure 4.3 the plagioclase crystals K_2O and Na_2O abundances show a positive correlation with SiO_2, which ranges from 47.9 – 63.0 wt. %. The Al_2O_3 content of the feldspars decreases with increasing SiO_2 wt. % (Figure 4.3).
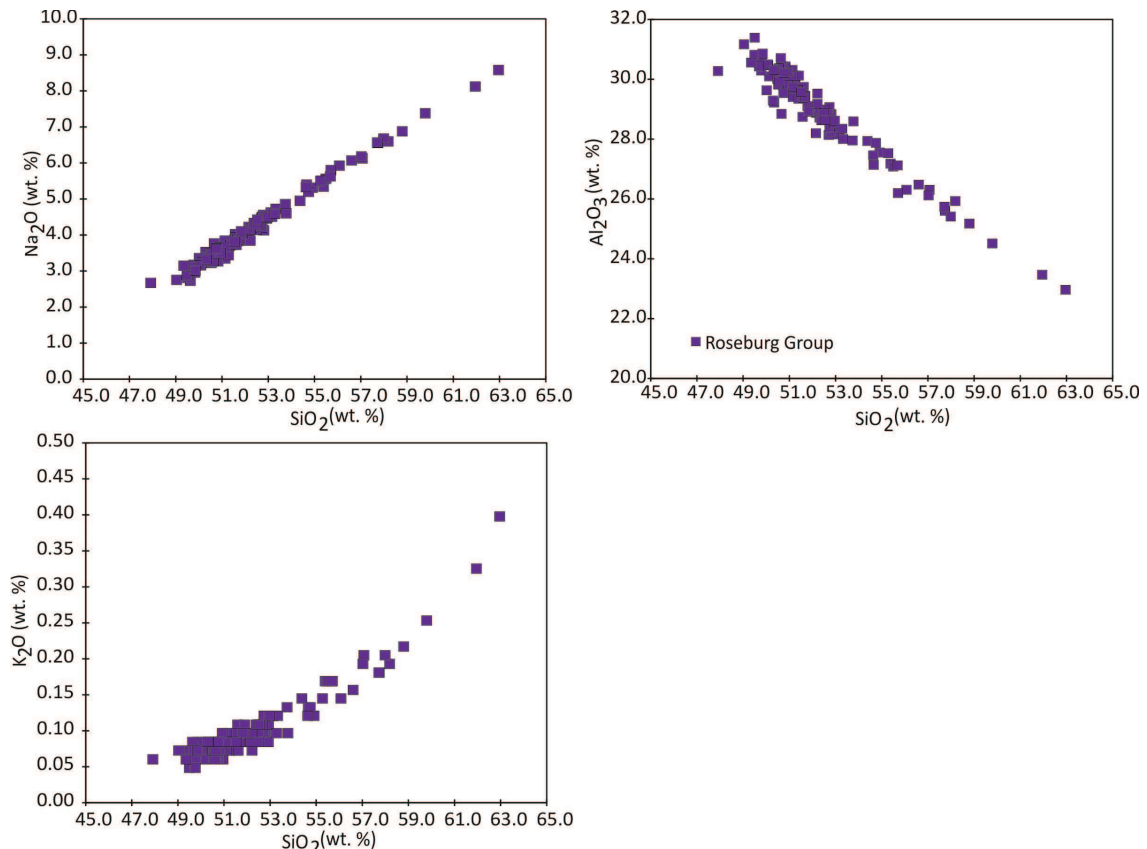
Figure 4.3 Bivariate diagrams of the major element compositions of feldspars from the Roseburg Group.

4.2.2 Siletz River

4.2.2.1 Petrography

The rocks of the Siletz River Volcanics consist predominantly of aphanitic to finely crystalline amygdaloidal basalts (Figure 4.4A). The basalts are hypocrystalline (Figure 4.4B) to holocrystalline and commonly display intersertal textures. Subophitic and intergranular textures are also observed, particularly in coarser grained samples (Figure 4.4C). Minor amounts of porphyritic basalt occur, but in general the samples are equigranular (Figure 4.4D). The primary minerals observed are clinopyroxene and plagioclase, which comprise around 85 % of the basalts, while additional small rounded opaque oxides also occur. The plagioclase

crystals in the groundmass are lath shaped and are moderately compositionally zoned (Figure 4.4D). Ilmenite is the dominant opaque mineral and comprises up to as much as 10 % of the samples. Occasionally altered olivine pseudomorphs are observed in the samples. Additionally partial variolitic textures are observed within the plagioclase crystals (Figure 4.4C).
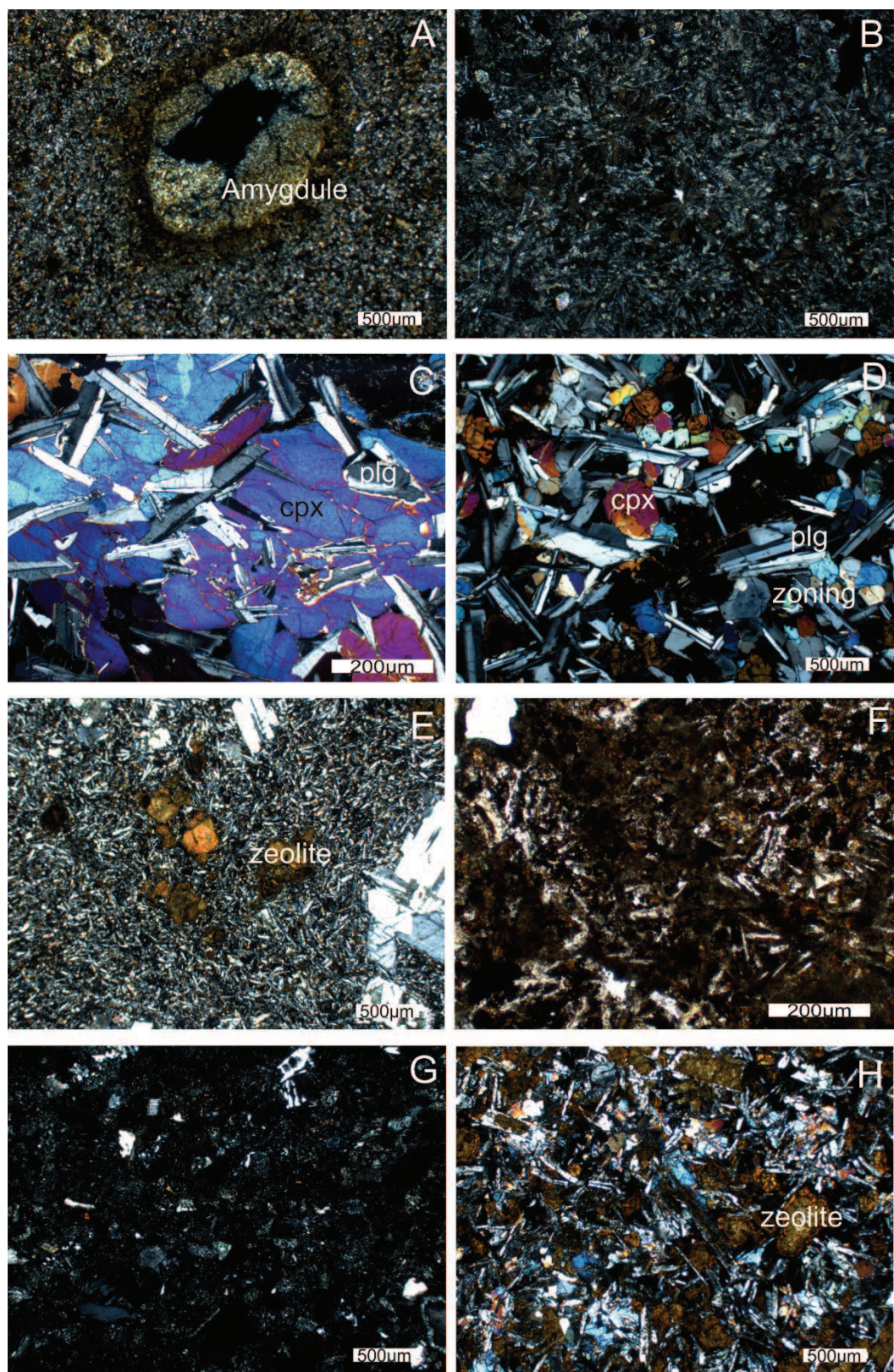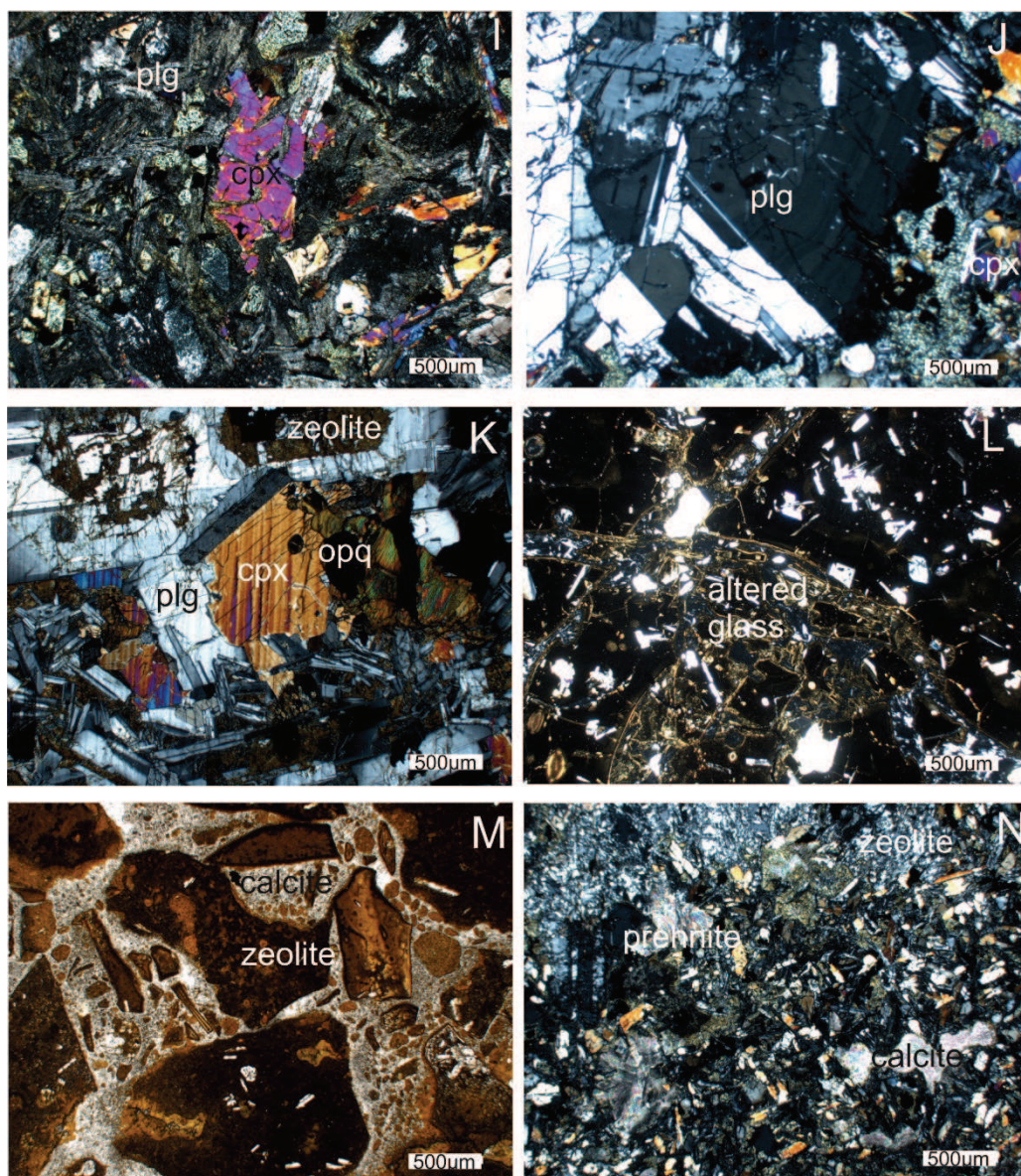
Figure 4.4 Photomicrographs of the Siletz River samples. **A)** XPL view of zeolite infilled amygdales (sample PK002). **B)** XPL view of plagioclase crystals in an altered glass rich groundmass (sample 100SRV) **C)** XPL view of subophitic clinopyroxene and plagioclase (sample CR004). **D)** XPL view of equigranular plagioclase and clinopyroxene crystals (sample CR011). **E)** XPL view zeolite pseudomorphs in a fine grained plagioclase rich groundmass (sample LC009). **F)** PPL view of clay and zeolite altered groundmass (sample LC007). **G)** XPL view of subrounded glass lapilli clasts and plagioclase clasts (sample LC005). **H)** XPL view of typical basalt from the Tillamook area containing plagioclase, clinopyroxene, opaque minerals and zeolite and palagonite alteration (sample 334SRV). **I)** XPL view of clinopyroxene, plagioclase and opaque minerals (sample 181SRV). **J)** XPL view of zoned plagioclase phenocryst (sample TK007). **K)** Clinopyroxene and plagioclase phenocrysts in an intergranular groundmass (sample TK002). **L)** XPL view of brecciated glass with plagioclase and clinopyroxene crystals (sample TK005). **M)** PPL view of angular altered clasts in a calcite rich matrix (sample TK003). **N)** XPL view of zeolite, calcite and prehnite alteration of a basaltic groundmass (sample 185SRV).

Massive feldspar phyric basalts and clinopyroxene phyric pillow basalt flows occur in the Ball Mountain area. The clinopyroxene phenocrysts consist of around 20 % of most samples, and as much as 40 % in some. Altered olivines are also present in these basalts, but have been pseudomorphed by clays and calcite (Figure 4.4E). The groundmass has undergone significant pervasive alteration to clays and zeolites (Figure 4.4F), but originally appears to have consisted of plagioclase, clinopyroxene, olivines and oxides. The plagioclase phyric basalts are comprised of, on average, 15 mm long plagioclase phenocrysts, in intergranular to subophitic textures. Clinopyroxene occurs predominantly in the groundmass (on average 40 %) but additionally occasionally occurs as phenocrysts. Olivine tholeiitic basalts and sills have also been described in this area, which consist of primarily an intergranular groundmass of plagioclase and clinopyroxene crystals with occasional olivine (< 5 %) and opaque minerals (Snavely et al., 1968). Plagioclase and clinopyroxene phenocrysts are observed, and the plagioclase phenocrysts, in particular, exhibit cross cutting relationships, indicating multiple stages of growth. Glomerocrysts of clinopyroxene and plagioclase, and others of entirely plagioclase are also present. Sampled interbedded lapilli tuffs contain abundant fragmented plagioclase crystals and opaque minerals along with calcitic fossiliferous fragments situated in a pervasively altered groundmass, which has been replaced almost completely by zeolite and calcite (Figure 4.4G).

Where the Siletz River Volcanic Formation is exposed in the Tillamook highlands the primary minerals of the aphyric basalts comprise plagioclase (45 %), clinopyroxene (40 %) and rounded and needle opaque oxides (up to 15 %) (which are dominantly ilmenite) (Figure 4.4H; I). Plagioclase phyric basalts are also observed, with tabular and lath shaped crystals exhibiting moderate compositional zoning (Figure 4.4J) and can reach 4 mm in length. Minor plagioclase rich glomerocrysts are also present within these samples. Clinopyroxene phyric basalts occur in minor amounts (Figure 4.4K), although the phenocrysts are generally associated with glomerocrysts. Sub ophitic textures are observed in the basalts and dolerites, although the primary texture is intergranular (Figure 4.4K). Amygdaloidal basalts are abundant with the vesicles having been infilled with clays and zeolites (Figure 4.4H), additionally the basalts locally

display brecciated and fractured textures, with quartz and calcite veins often cross cutting samples. Hyaloclastite breccia are observed (Figure 4.4L) (associated with the pillow lavas) and consists of highly altered fragmented clasts of what was once glass, along with plagioclase and clinopyroxene crystals. Angular clasts are also observed in a now calcite rich matrix, with small plagioclase and clinopyroxene inclusions preserved (Figure 4.4M).

Extensive clay and zeolite alteration has taken place across the majority of these groups of rocks, in particular in the hypocrystalline basalts. While some unaltered glass does persist in vesicles, palagonite, zeolites, calcite and clays have replaced the majority of amygdales. Zeolite, prehnite, pumpellyite and clay alteration is also abundant within the groundmass of the basalts (Figure 4.4N). Many samples have undergone very extensive zeolite and clay alteration and are now composed of mostly altered pseudomorphs, some of which appear to have been olivines. Calcite and quartz veins also cross cut many of the basalts. Plagioclase crystals often exhibit alteration textures at their cores and cross cutting veins of alteration material. Several pillow lava samples are brecciated and are heavily altered to clay and calcite, which is most likely due to hydrothermal alteration on the seafloor.

4.2.2.2 Mineral Compositions

The Tillamook Group clinopyroxenes have a narrow range of Mg# compositions ranging from 66 – 84, while the Corvallis Group clinopyroxenes are highly scattered in Mg# values, varying between 47 – 81 Mg#. CaO and SiO_2 abundances tend to decrease with decreasing Mg# while the TiO_2 content of both groups increases with decreasing Mg# (Figure 4.5). The CaO concentrations of the clinopyroxenes remain relatively constant and clustered with Al_2O_3 wt.%, in particular in the Tillamook Group, before decreasing at lower values. While the Na_2O remains relatively constant, the clinopyroxenes with the highest Mg# also have high Cr_2O_3 wt.% and the Tillamook Group samples in particular display a positive correlation between the two (Figure 4.5).
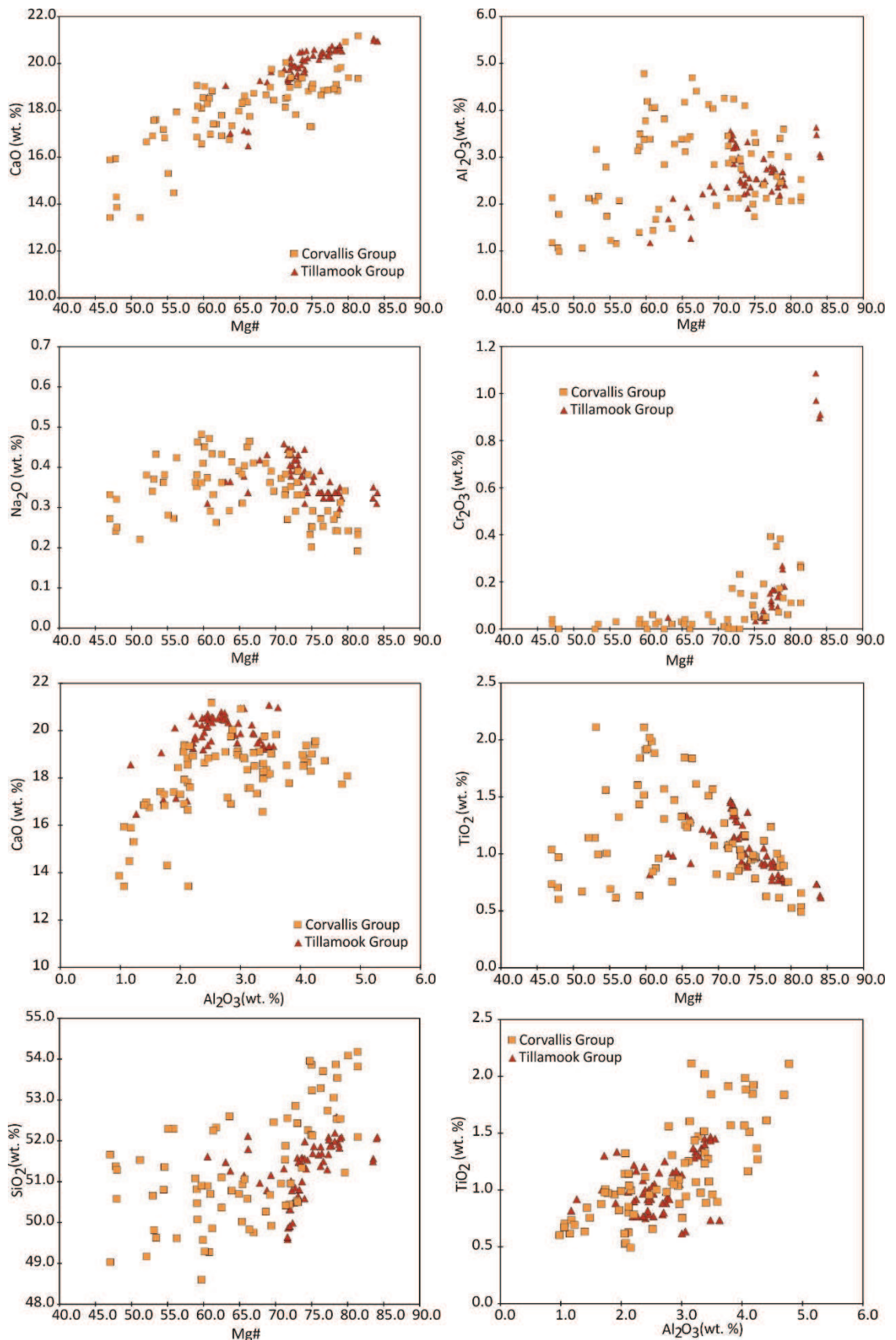
Figure 4.5 Bivariate diagrams of the major element compositions of clinopyroxenes from the Tillamook and Corvallis Groups.

Both the Tillamook Group and Corvallis Group plagioclases display increasing Na_2O and K_2O abundances with increasing SiO_2 wt.%, although K_2O contents are more scattered, especially within the Tillamook Group. The Al_2O_3 contents of the plagioclases however decrease with increasing SiO_2 abundance (Figure 4.6).
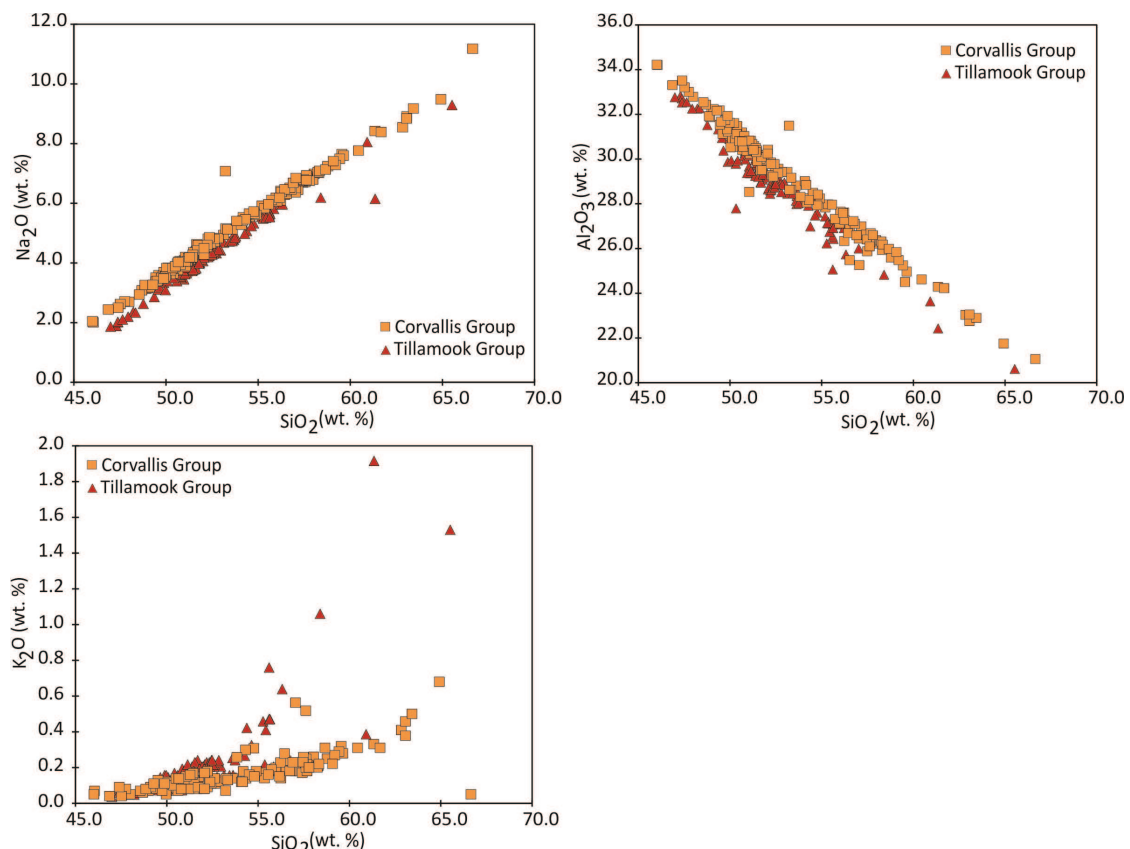
Figure 4.6 Bivariate diagrams of the major element compositions of feldspars from the Tillamook and Corvallis Groups.

4.3 Crescent Formation, Washington

4.3.1 Northern Crescent (Olympic Mountains and Bremerton)

4.3.1.1 Petrography

The basalts of both the lower and upper Crescent Formation unit display a variety of textures including phaneritic, phyric, aphyric, brecciated, variolitic, and sub-ophitic textures (Figure 4.7A). The majority of samples collected contain

abundant lath shaped plagioclase (50 %) along with clinopyroxene (40 %) and opaque minerals (ilmenite) (10 %) (Figure 4.7B). In the samples with hypocrystalline textures the plagioclase crystals are dendritic and display variolitic quench characteristics (Figure 4.7C). Trace amounts to around 20 % of the samples contain tabular plagioclase and alkali feldspar phenocrysts, which range between 2 and 7 mm and occasionally contain inclusions of clinopyroxene crystals. Smaller subhedral clinopyroxene phenocrysts are also observed, and are on average around 0.5 – 1 mm in size. What are presumed to be olivine pseudomorphs are also present, however they have now undergone complete alteration, which is consistent with what is observed elsewhere in the terrane. Vesicles, where present, are infilled with calcite (Figure 4.7C), zeolite or chlorite (Figure 4.7D). The groundmass contains, clinopyroxene, plagioclase and abundant oxides, which are dominantly ilmenite and titanite with additional Fe-Ti oxides.

Coarser textured doleritic samples contain ophitic and sub – ophitic plagioclase, alkali feldspar and clinopyroxene crystals. The feldspar crystals in these samples are pervasively altered and display myrmekitic textures (indicating the replacement of the alkali feldspar with plagioclase feldspar) (Figure 4.7E), while smaller dendritic plagioclases also occur. Opaque metal oxides are abundant and comprise up to 20 % of some samples. Clinopyroxene crystals vary from subrounded to subhedral in shape and also often exhibiting pervasive alteration and uneven margins.

In the Bremerton exposures the massive basalt flows contain on average 45 % plagioclase, 35 % clinopyroxene and 15 % opaque minerals, while the submarine pillow basalts on average comprise 50 % lath shaped plagioclase, 30 % subhedral clinopyroxene and 10 – 20 % opaque minerals (Figure 4.7F). Plagioclase phyric basalts also occur (Figure 4.7F), with the phenocrysts comprising minor amounts of the samples (<1 %). The dolerite dykes at Bremerton are generally amygdaloidal and the plagioclase crystals they contain are moderately compositionally zoned (Figure 4.7G), highly fractured and intergrown with one another. Sub ophitic textures also occur in the clinopyroxene and plagioclase crystals (Figure 4.7H). Abundant chlorite alteration and

recrystallisation has taken place in these samples. Minor amounts (< 1%) of primary orthoclase feldspar occurs within some of the dyke samples.

The leucogabbro sampled at Green Mountain, Bremerton contains 50 % plagioclase 35 % clinopyroxene, 10 % ulvospinel, 4 % K- feldspar and 1 % quartz. The clinopyroxenes are sub angular while the plagioclase crystals are lath shaped. While the Bremerton gabbros are plagioclase and clinopyroxene rich, with ophitic textures commonly occurring (Figure 4.7I; J). Plagioclase crystals exhibit moderate to strong compositional zoning, occasionally displaying cracked textures (Figure 4.7K), additionally feldspar - feldspar intergrowths are observed (Figure 4.7K). Curvilinear crystalline boundaries occur between the some of the plagioclase crystals and the clinopyroxenes, while smaller more needle like plagioclase crystals are also present (and appear to be in equilibrium with the clinopyroxene). Some samples (Figure 4.7L) display two populations of plagioclase crystals, one larger more tabular group which is intergranular with the clinopyroxene and, a second smaller more needle like set that is included within the larger plagioclase and clinopyroxene crystals. While the majority of the clinopyroxene crystals in the gabbroic samples are augitic in composition, a few samples also contain pyroxene of a diopside composition, suggesting that it is derived from a more primitive layer within the melt lens, perhaps at the varitextured and foliated gabbro transition zone. Abundant opaque minerals are present within the gabbroic samples (up to 20 %) and late intersertal oxides are also apparent and are observed clustering around other phases (Figure 4.7M) and smaller recrystallised plagioclase crystals. In addition to ilmenite, spinel and magnetite are also present, and associated with these minerals are baddeleyites and zircons. Occasional sulphide minerals, including pyrite and chalcopyrite, are also found within some of the gabbro samples.

The samples from the lower part of the Crescent Formation in the Olympic Peninsula (Main Crescent and Depleted Crescent) exhibit up to greenschist facies grade alteration, which is thought to be linked to burial (Hirsch and Babcock, 2009; Blakely et al., 2009). These samples consist of predominantly chlorite alteration, and to a lesser extent serpentine. Amygdales and veins are infilled with chlorite, epidote, zeolite, calcite, prehnite (Figure 4.7A; C; D) and pumpellyite.

There appears to be little difference between the alteration styles of the Main Crescent Group and the Depleted Crescent Group. The upper unit of the Crescent Formation in this region however, displays zeolite and prehnite pumpellyite grade alteration, in particular in the groundmass of the samples (Figure 4.7A). Complete replacement of some crystals is also common, and amygdales are infilled with zeolite, calcite, prehnite and pumpellyite. Palagonite alteration also occurs in these groups of rocks, in particular the basaltic samples, and most likely represents altered volcanic glass.

In the Bremerton Group, samples generally display greenschist grade alteration. The most common alteration minerals present are chlorite, prehnite and pumpellyite, which are observed altering the clinopyroxene and plagioclase, indicating an addition of Ca and Al and a stripping of Mg. Some epidote crystals are also present and varying degrees of amphibolisation have taken place across the samples, with clinopyroxenes frequently having being pervasively altered to hornblende and kaersutite amphibole (Figure 4.7L). Phenocrysts are often replaced by chlorite and prehnite and exhibit recrystallization textures (Figure 4.7N), while calcite is also found infilling cross cutting veins. Alteration often appears to be associated with Fe/Ti oxides, which may have been the last phases to crystallise with the water associated with them resulting in the recrystallization of pyroxenes. Secondary chalcopyrite and pyrite are also abundant.
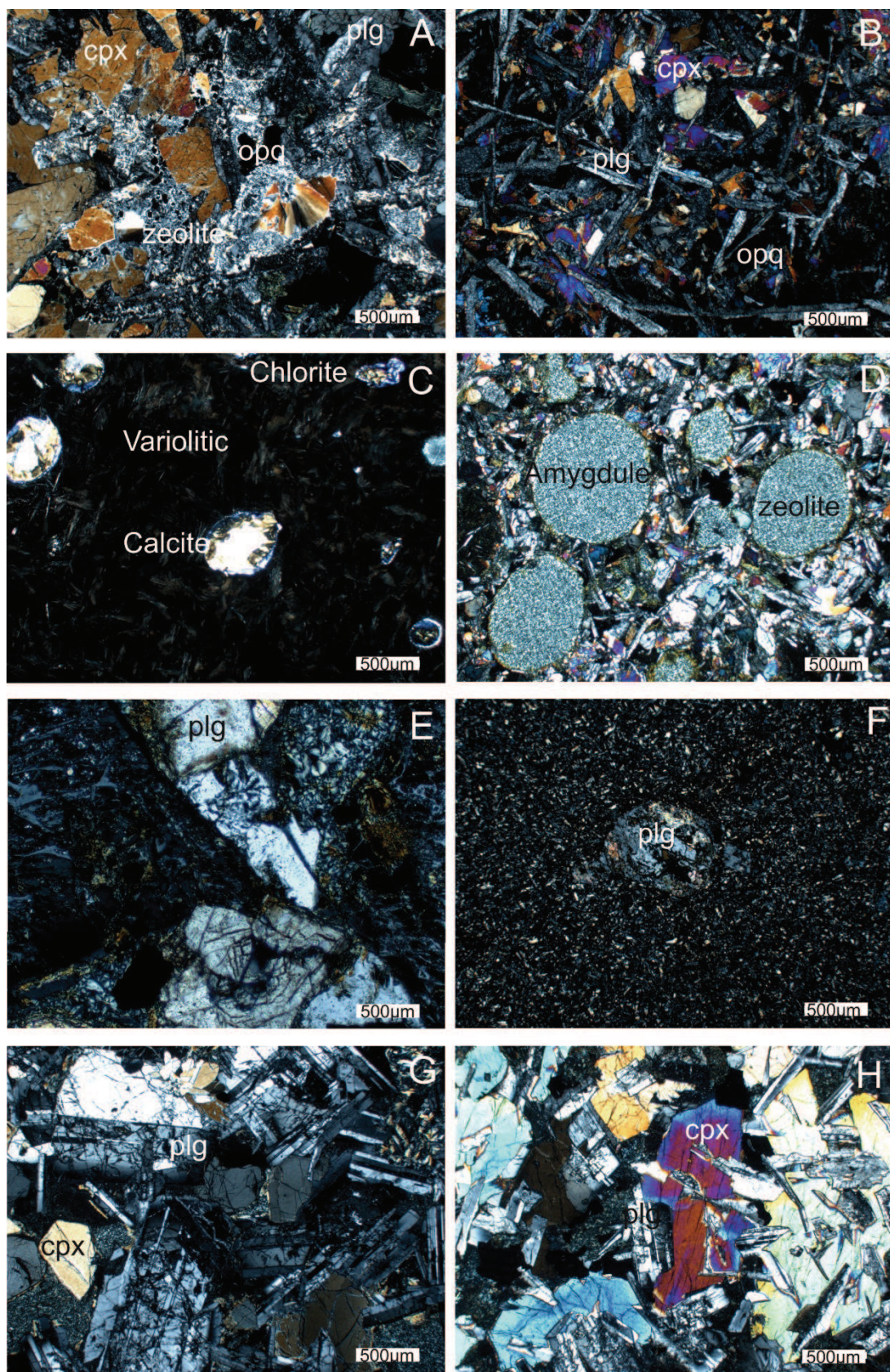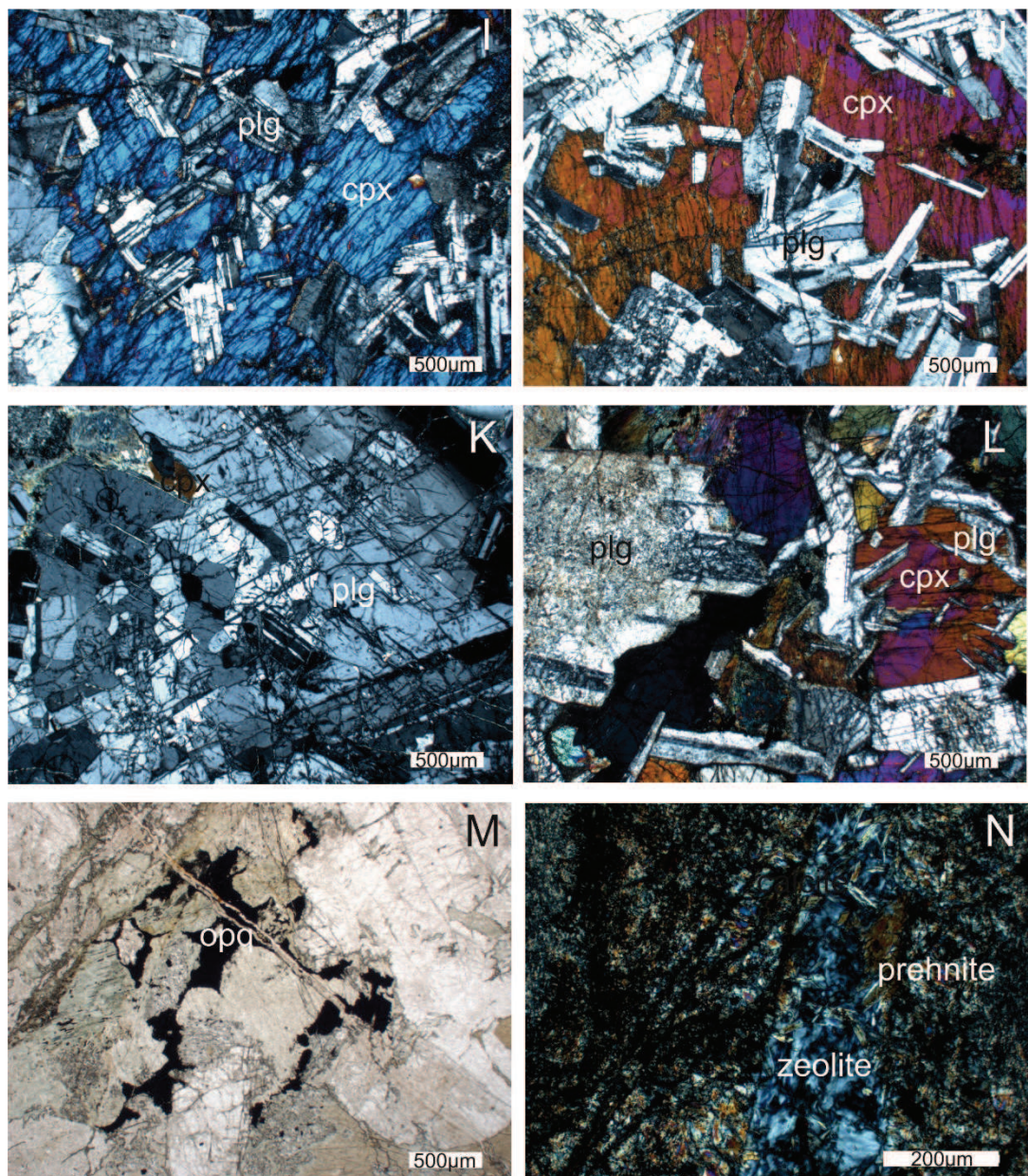
Figure 4.7 Photomicrographs of the Crescent North samples. **A)** XPL view of altered and brecciated basalt, with abundant zeolite and small rounded opaque minerals (sample 267CM). **B)** XPL view of the typical texture of basalts in the Crescent Formation (243CM) **C)** XPL view of calcite and chlorite filled amygdales in groundmass with a variolitic texture (sample 323CM). **D)** XPL view of zeolite infilled amygdales surrounded by a plagioclase and clinopyroxene rich groundmass (sample 317CM). **E)** XPL view of a myrmekitic texture in a plagioclase crystal, along with zeolite alteration (sample 229CM). **F)** XPL view of a plagioclase phenocryst in a fine grained groundmass (sample B013). **G)** XPL view of zoned and intergrown plagioclase crystals (sample B006). **H)** XPL view of subophitic plagioclase and clinopyroxene (sample B007). **I and J)** XPL view of ophitic plagioclases and clinopyroxenes (sample B023). **K)** XPL view of fractured intergrown plagioclase feldspars (sample B018). **L)** XPL view of lager tabular plagioclases which are intergranular with the clinopyroxenes and smaller needle like plagioclase feldspars included within the clinopyroxene crystals (sample B002). **M)** PPL view of insertal opaques oxides crystallised around larger plagioclase crystals (sample B022). **N)** XPL view a plagioclase crystal replaced completely by zeolite along with prehnite alteration within the groundmass (sample B019).

4.3.1.2 Mineral Compositions

The majority of clinopyroxenes analysed from all three groups have Mg# of $61 - 85$, with a group of more evolved Bremerton sample clinopyroxenes displaying a lower range of Mg# values. There is considerable overlap of all groups in the Mg# Al_2O_3 plot with the exception of a group of high Al_2O_3 high Mg# Bremerton clinopyroxenes (Figure 4.8). The Bremerton Gabbros are particularly distinctive in the TiO_2 vs Cr_2O_3 plot (Figure 4.8), with particularly low TiO_2 contents which extend to higher Cr_2O_3 wt.%, indicating a primitive mantle melt origin. The Main Crescent Group CaO wt.% is relatively consistent while both Bremerton Groups display an increasing CaO trend with increasing Al_2O_3. At high Mg# the TiO_2 of the clinopyroxenes from the Bremerton Gabbros and Main Crescent Groups increases with decreasing Mg#, while the Bremerton Group is much more scattered. Generally all three groups show an increasing TiO_2 with Al_2O_3 within the clinopyroxenes analysed, although the Bremerton Gabbros are relatively clustered (Figure 4.8).
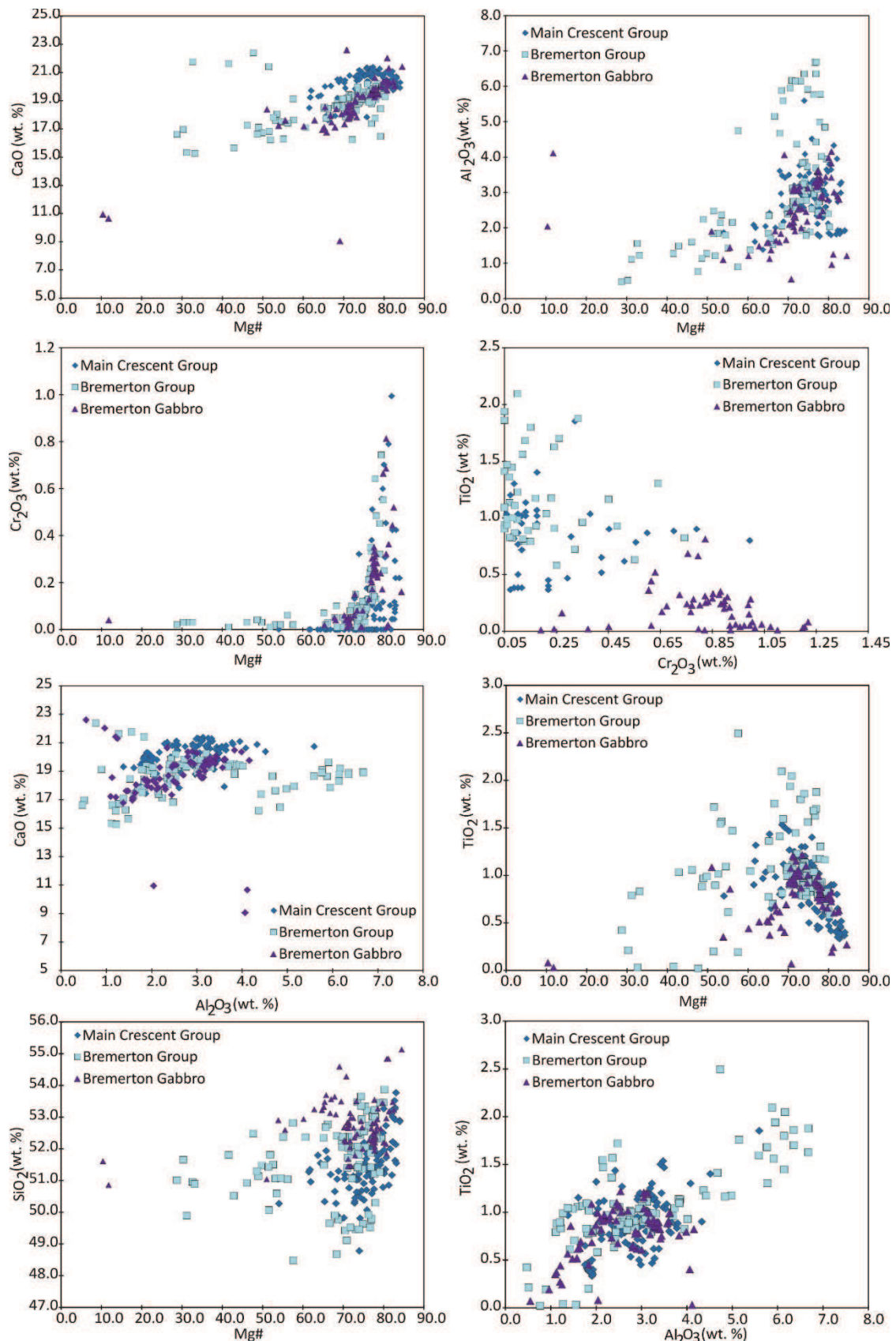
Figure 4.8 Bivariate diagrams of the major element compositions of clinopyroxenes from the Main Crescent Group, the Bremerton Group and the Bremerton Gabbros.

The majority of the feldspars display a positive correlation between Na_2O, K_2O and SiO_2, and a negative correlation between Al_2O_3 and SiO_2. However, a sub set of Bremerton feldspars have low Na_2O and Al_2O_3 and extremely high K_2O values and subsequently plot apart from the main data group (Figure 4.9).
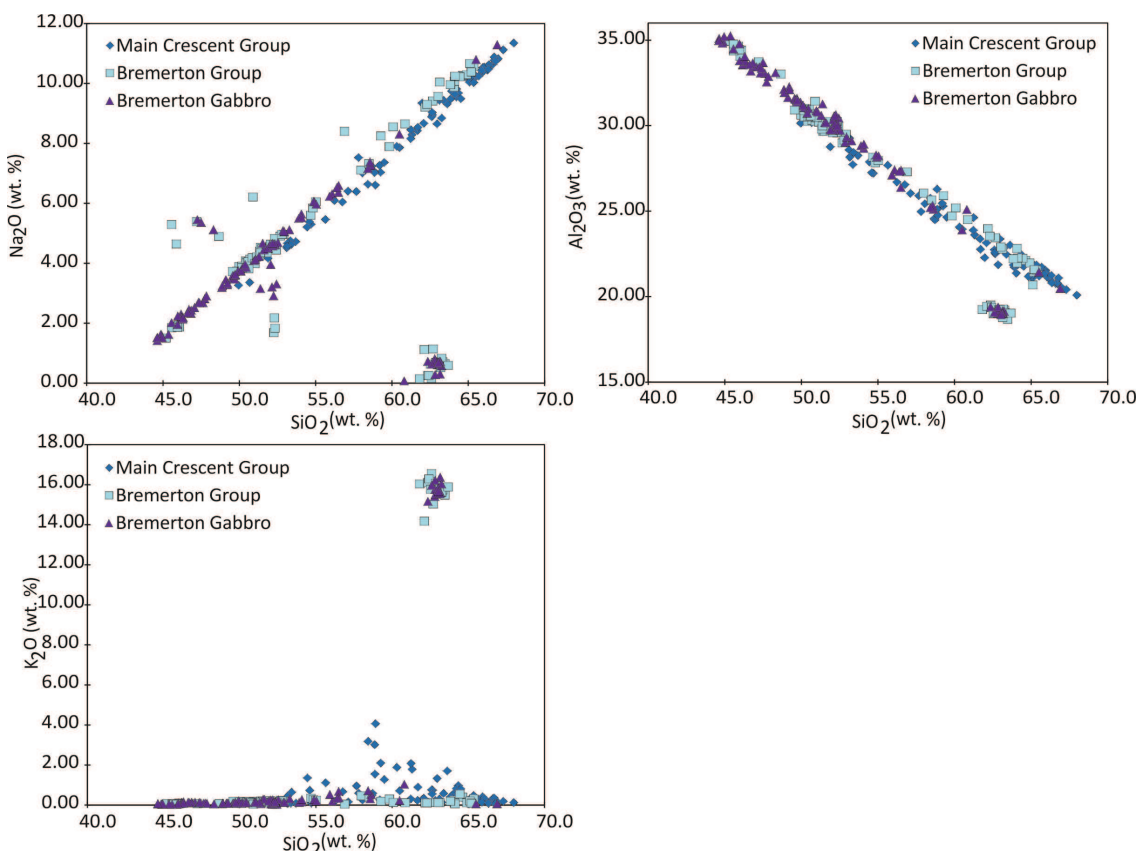
Figure 4.9 Bivariate diagrams of the major element compositions of feldspars from the Main Crescent Group, the Bremerton Group and the Bremerton Gabbros.

4.3.2 Southern Crescent

4.3.2.1 Petrography

The basalts in this region of the Crescent Formation are hypocrystalline to holocrystalline and display both epigranular to glomeroporphyrtic textures (Figure 4.10A). Subophitic textures are also observed within the clinopyroxenes and plagioclases (Figure 4.10A). The groundmass varies from interstitial to intergranular in texture and the primary minerals comprise plagioclase, clinopyroxene, magnetite and ilmenite. Plagioclase crystals consist of between 30

and 47 % of the basalts and occur as epigranular lath-shaped crystals within the groundmass. Tabular to lath shaped subheadral to euhedral plagioclase phenocrysts constitute less than 5 % of the samples, ranging between 0.5 – 2.5 mm. The plagioclase phenocrysts are also moderately to strongly compositionally zoned (Figure 4.10B). Approximately 30 % of the basalt is composed of clinopyroxene, which is predominantly present in the epigranular groundmass (Figure 4.10C). Clinopyroxene phenocrysts are rare (Figure 4.10C), and where present, are 0.5 – 1.5 mm in size and form subophitic textures and glomerocrysts with the plagioclase crystals (Figure 4.10A; D). Rounded amygdales are infilled with zeolite and occur frequently.

The dolerite dyke samples from the Southern Crescent are comprised of primarily subophitic clinopyroxene and plagioclase with abundant opaque minerals (Figure 4.10E). The clinopyroxenes are anhedral to subhedral when present in the groundmass and subhedral to euhedral in phenocrysts. Plagioclase phenocrysts show strong compositional zoning and where present comprise trace amounts to 20 % of samples. Opaque minerals constitute around 15 % of the mineralogy and are often skeletal in structure.

Palagonite alteration is also common in this region of the Crescent Formation. Plagioclase crystals are commonly mildly to moderately sericitised. Pseudomorphs, now altered to zeolites, calcite and clays occur frequently (Figure 4.10E). Rounded amygdales are infilled with zeolites and to a lesser extent chlorite. While abundant zeolite and clay alteration, primarily smectite, occurs in the groundmass (Figure 4.10E). Generally the alteration in the Crescent South samples is consistently composed of prehnite pumpellyite and zeolites, with some calcite veins also apparent.
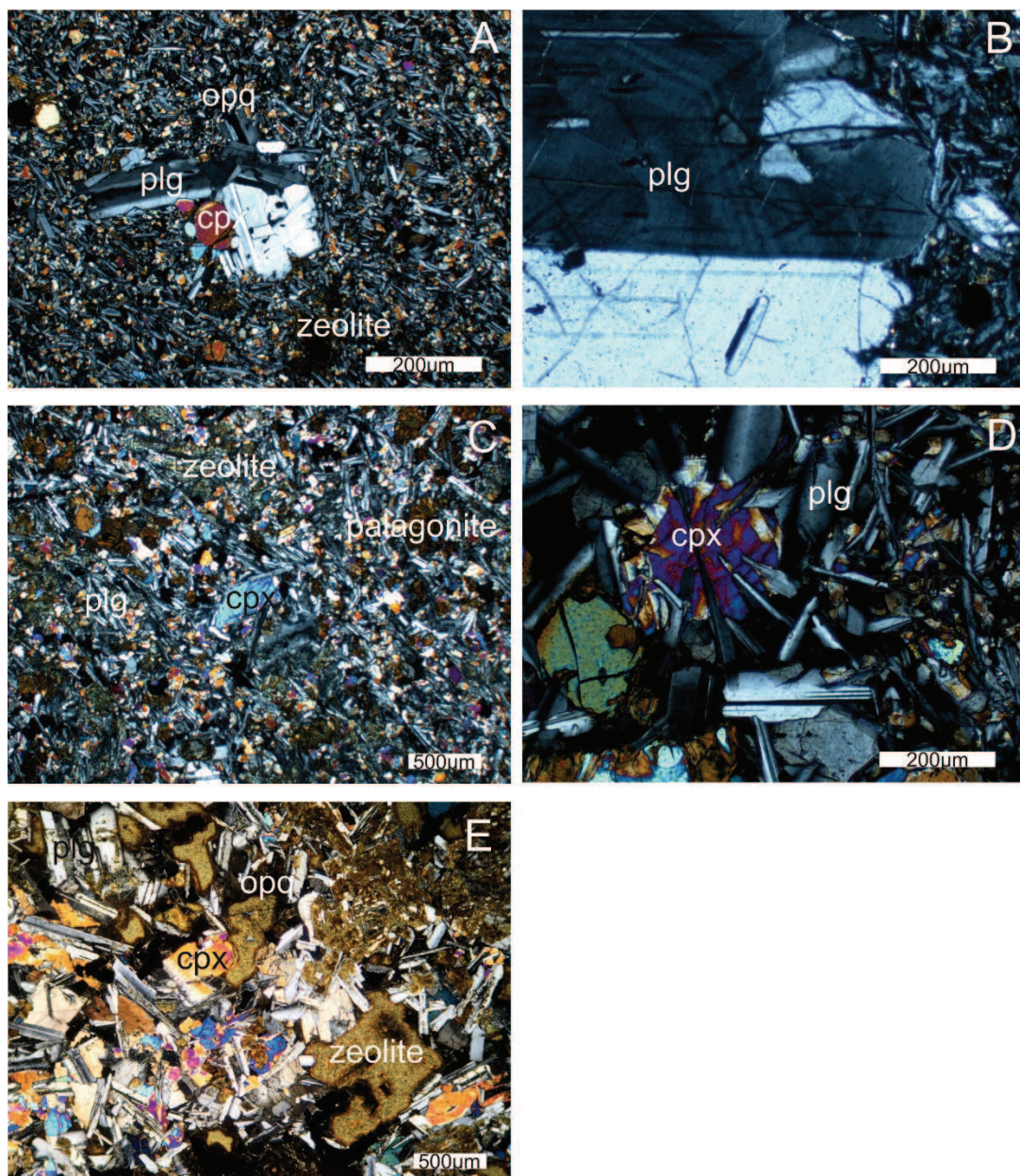
Figure 4.10 Photomicrographs of the Crescent South samples. **A)** XPL view of a clinopyroxene and plagioclase glomerocrysts in a groundmass of similar composition (sample 446CS). **B)** XPL view of a zoned plagioclase phenocryst (392CS) **C)** XPL view of a small clinopyroxene phenocryst in a plagioclase and clinopyroxene rich groundmass, along with palagonite and zeolite alteration (sample 454CS). **D)** XPL view of a subophitic texture in a glomerocrysts (sample 446CS). **E)** XPL view of plagioclase and clinopyroxene crystals which have experienced extensive zeolite and clay alteration (sample 400CS).

4.3.2.2 Mineral Compositions

The Black Hills Group clinopyroxenes have an Mg# range of 59 – 80 while the Willapa Hills Group have a greater range, varying from 45 – 60. The majority of major elements cluster within narrow ranges for the clinopyroxenes in both groups. However, a secondary scattered set of data points are also apparent in Figure 4.11, and is most evident in the Na_2O and TiO_2 vs Mg# plots. Clinopyroxenes from the Black Hills Group with the highest Cr_2O_3 wt. % abundances also display the highest Mg#.
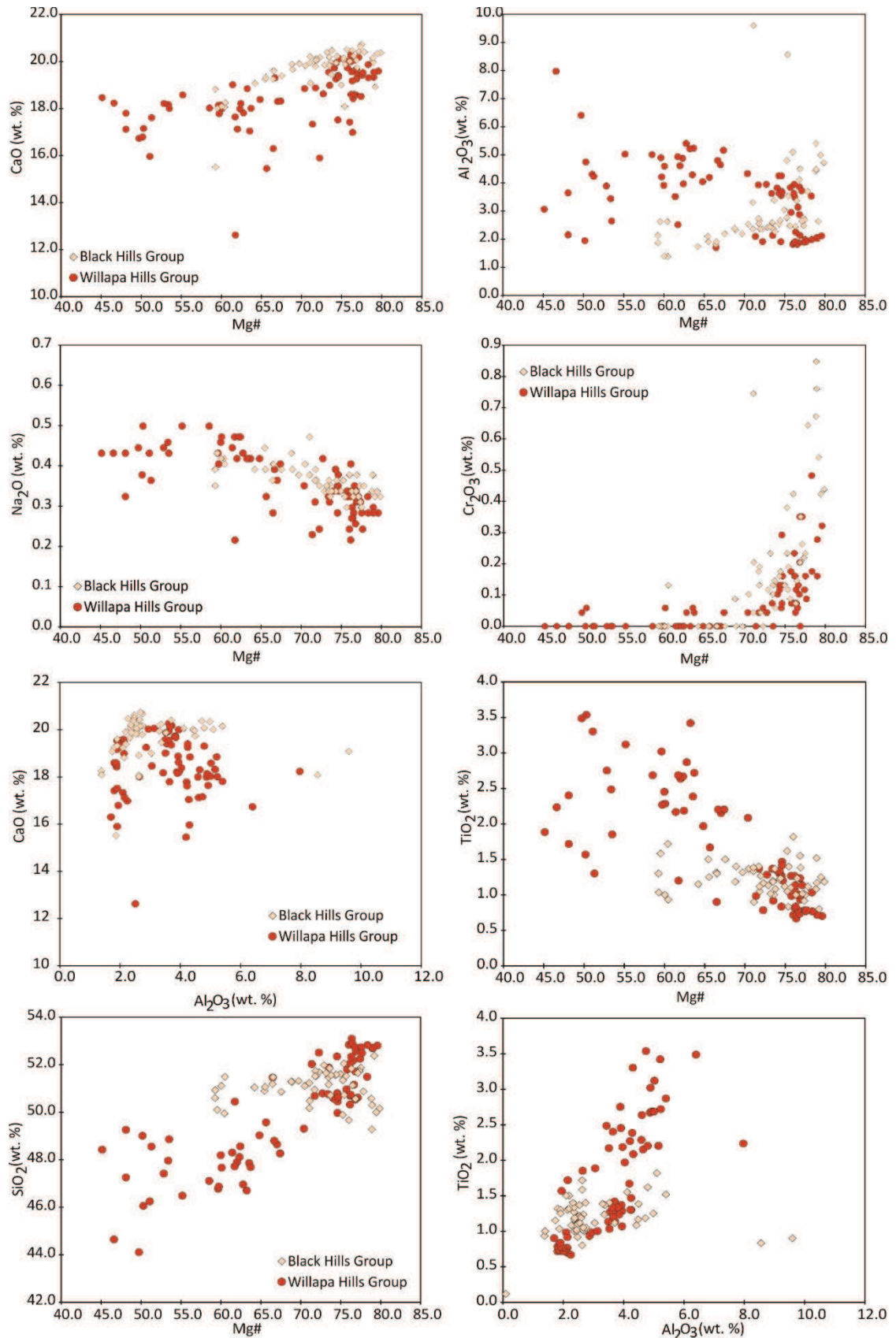
Figure 4.11 Bivariate diagrams of the major element compositions of clinopyroxenes from the Black Hills and Willapa Hills Groups.

In terms of the plagioclase analyses, the Black Hills and Willapa Hills Groups both display increasing Na_2O with increasing SiO_2, however, while the majority of points overlap at 52 – 54 wt.% SiO_2, the Black Hills Group tend to extend to lower SiO_2 contents (Figure 4.12). A positive correlation for both groups is observed in the K_2O vs SiO_2 plot, with the Black Hills Group plagioclases generally exhibiting higher K_2O abundances for any given SiO_2 wt.% in comparison to the Willapa Hills Group. Both groups display decreasing Al_2O_3 concentrations as the plagioclases increase in SiO_2 contents (Figure 4.12).
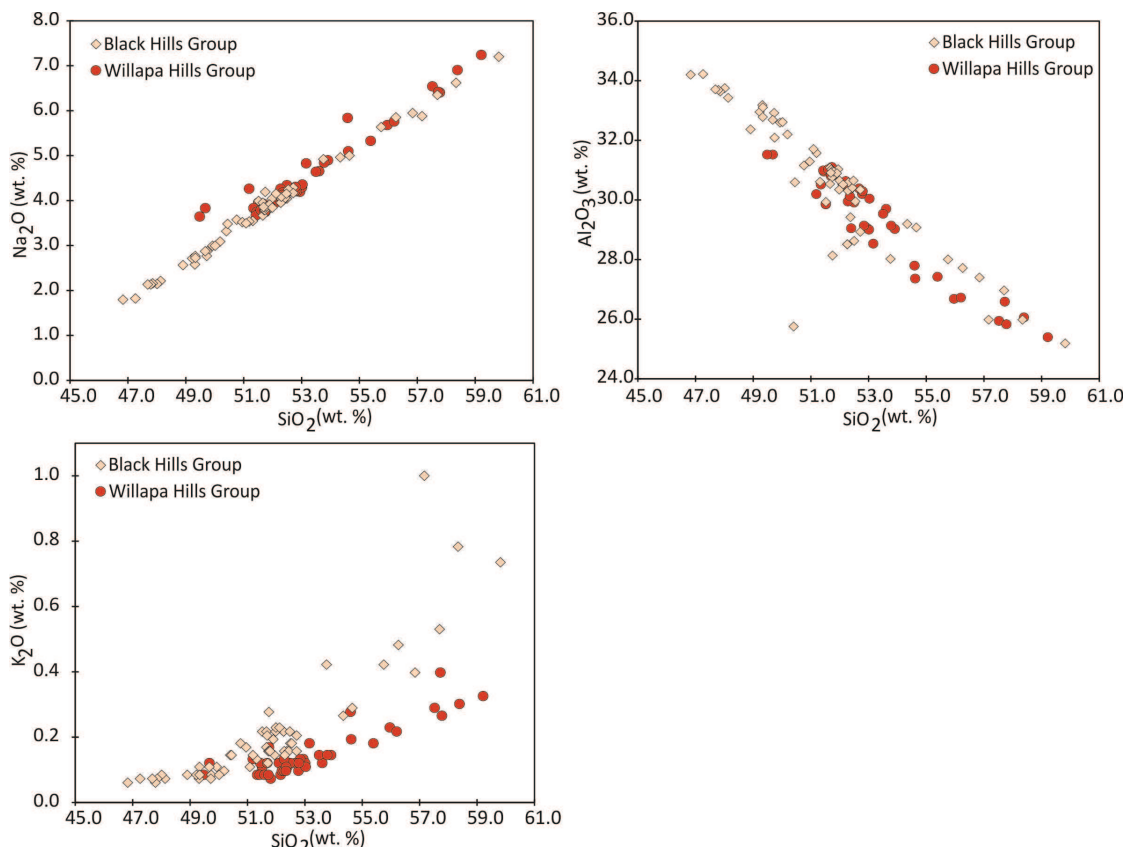
Figure 4.12 Bivariate diagrams of the major element compositions of feldspars from the Black Hills and Willapa Hills Groups.

4.4 Metchosin Igneous Complex, Vancouver Island

4.4.1 Petrography

The basalts of the MIC are generally fine grained, containing less than 5 % replaced glass, however, Hypocrystalline textures are also present and some samples may contain more than 70 % altered glass. The glass in the MIC samples

has been entirely recrystallised to alteration minerals, including chlorite and prehnite (Figure 4.13A), which are not associated with other phases. Samples range from aphyric (Figure 4.13A) to phyric, with up to 20 % phenocrysts. Hypocrystalline samples often exhibit variolitic and spherulitic quench textures along with dendritic plagioclase structures (Figure 4.13B). Both the upper and lower basalts are commonly glomeroporphyritic (Figure 4.13C) and comprise subophitic clinopyroxene surrounding plagioclase crystals. Basalts frequently contain up to ~ 20 % zeolite-filled amygdales and 20 % of the mineralogy is comprised of ilmenite. The groundmass is composed of plagioclase, clinopyroxene and opaque minerals (predominantly ilmenite). The dolerite dykes (Figure 4.13D) predominantly comprise sub-ophitic clinopyroxene and plagioclase crystals, which are often highly fractured. While the gabbros (Figure 4.13E) contain ophitic clinopyroxene and plagioclase in addition to tabular and lath shaped plagioclase crystals. Ilmenite opaque phases comprise of around 5 % of samples, clinopyroxene (both altered and unaltered) 45 % and plagioclase 50 % of the gabbros.

The metamorphic facies grade of the complex is predominantly prehnite/ actinolite to greenschist grade [with some amphibolite grade areas also present in the west of the area (Timpa, 2000)]. While the primary igneous textures are often preserved, especially within the coarser grained samples, the alteration is pervasive throughout the finer basalts. Chlorite is the most common alteration mineral, along with prehnite in samples from the upper volcanic group. The groundmass commonly exhibits chlorite, epidote and albite alteration phases with additional prehnite pumpellyite and amphibole alteration in the upper lavas. Vesicles (Figure 4.13B) and fractures are completely replaced and infilled with, most commonly chlorite and prehnite (in the upper volcanic sequences), although epidote, actinolite, quartz and pumpellyite alteration are also observed. Lower grade zeolites and calcite also infill some of the vesicles and also occur in veins cross cutting the samples. Clinopyroxenes in the gabbros have often undergone alteration to zeolite and kaersutite amphibole, which is not usually identifiable in the thin section (although is through use of a scanning electron microscope and EDS detector), however it is observed as pervasive alteration in streaks within the

clinopyroxene crystals (Figure 4.13F). Plagioclase crystals within glomerocrysts also commonly exhibit sieve textures, indicating that the crystals grew in disequilibrium or have undergone partial reabsorption, and that the glomerocrysts are derived from the gabbros below (Figure 4.1E).
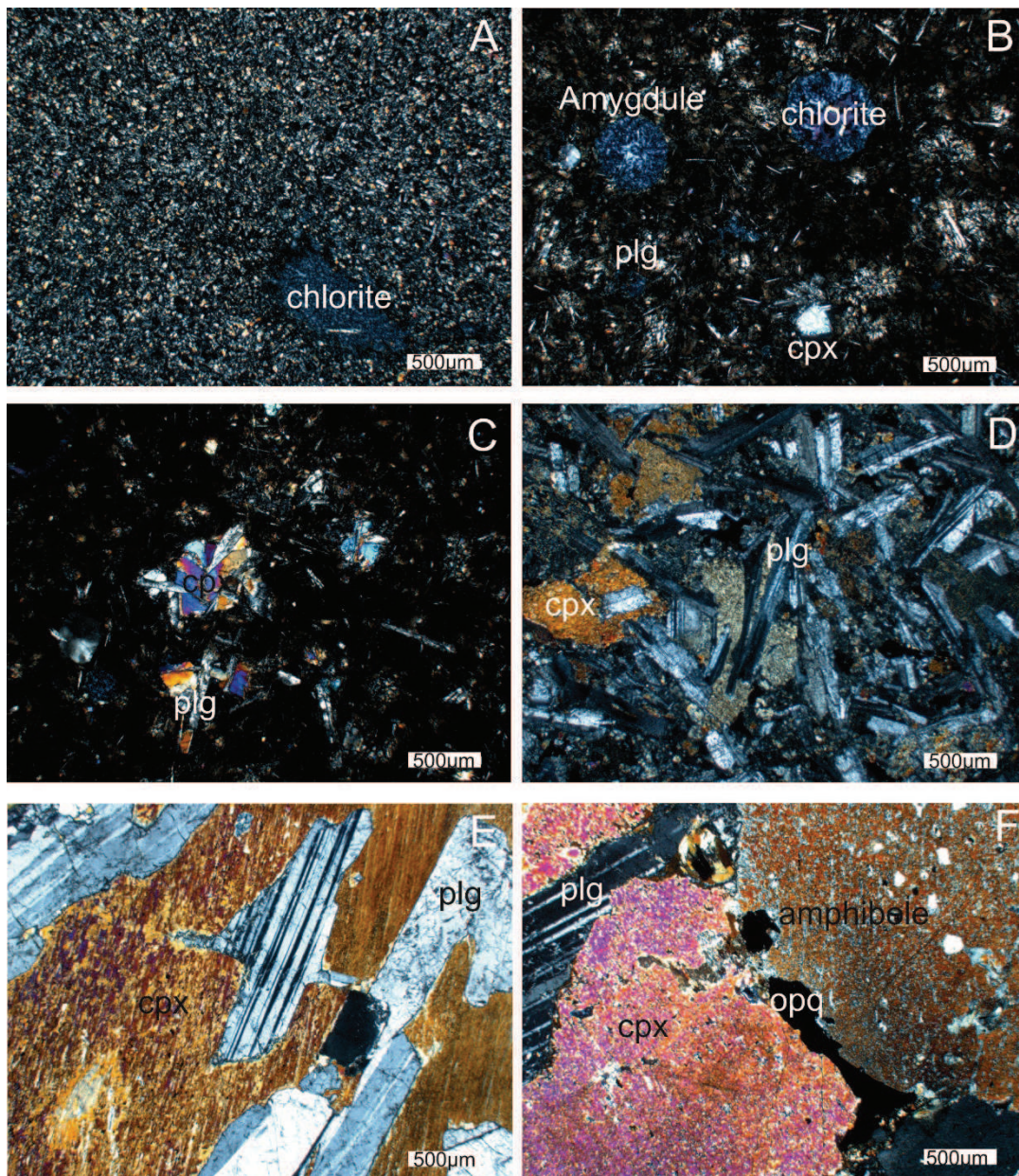
Figure 4.13 Photomicrographs of the Metchosin Igneous Complex samples. **A)** XPL view of a finely crystalline basalt composed of largely plagioclase and clinopyroxene along with a chlorite infilled vesicle (sample 199MET). **B)** XPL view of a chlorite infilled amygdales along with plagioclase and clinopyroxene phenocrysts (210MET) **C)** XPL view of clinopyroxene and plagioclase glomerocrysts (sample 210MET). **D)** XPL view of subophitic plagioclase and clinopyroxene in a dolerite (sample 205MET). **E)** XPL view of ophitc altered plagioclase and clinopyroxene (sample 207MET). **F)** XPL view of amphibole alteration within clinopyroxenes (sample 207MET).

4.4.1. Mineral Compositions

The Metchosin Gabbros clinopyroxenes are particularly distinct in CaO, with one group of elevated abundances (for the majority of clinopyroxenes analysed) and a second scattered low CaO trend. The Upper and Lower basalts have similar CaO abundances, along with an overlap in Mg# number, with the Upper basalts extending to lower Mg# and the Lower basalts extending to higher Mg#. Conversely in the Al_2O_3 vs Mg# plot (Figure 4.14) clinopyroxenes in the Lower basalts are more distinct with higher Al_2O_3 abundances (1.8 – 4.7 wt. %). The majority of the clinopyroxenes from all 3 groups fall between 73 – 86 Mg#. However a subset of low Mg# gabbroic clinopyroxene analyses (at 63 – 68 Mg#) are also present and have particularly high Na_2O abundances, which may be indicative of element mobility during alteration. The Cr_2O_3 content for all groups is relatively low, varying between 0 and 0.3 wt.%, with the gabbros clinopyroxenes displaying the lowest values along with the lowest TiO_2 contents in general. In the CaO vs Al_2O_3 plot (Figure 4.14) a general trend is observed ranging from high CaO low Al_2O_3, through moderate CaO and Al_2O_3 basalts to lower CaO high Al_2O_3 gabbros (up to 10.0 Al_2O_3 wt.%). A similar trend is also observed in the TiO vs Al_2O_3 plot (Figure 4.14). The Upper basalts tend to exhibit the lowest SiO_2 contents (50 – 52 wt.%).
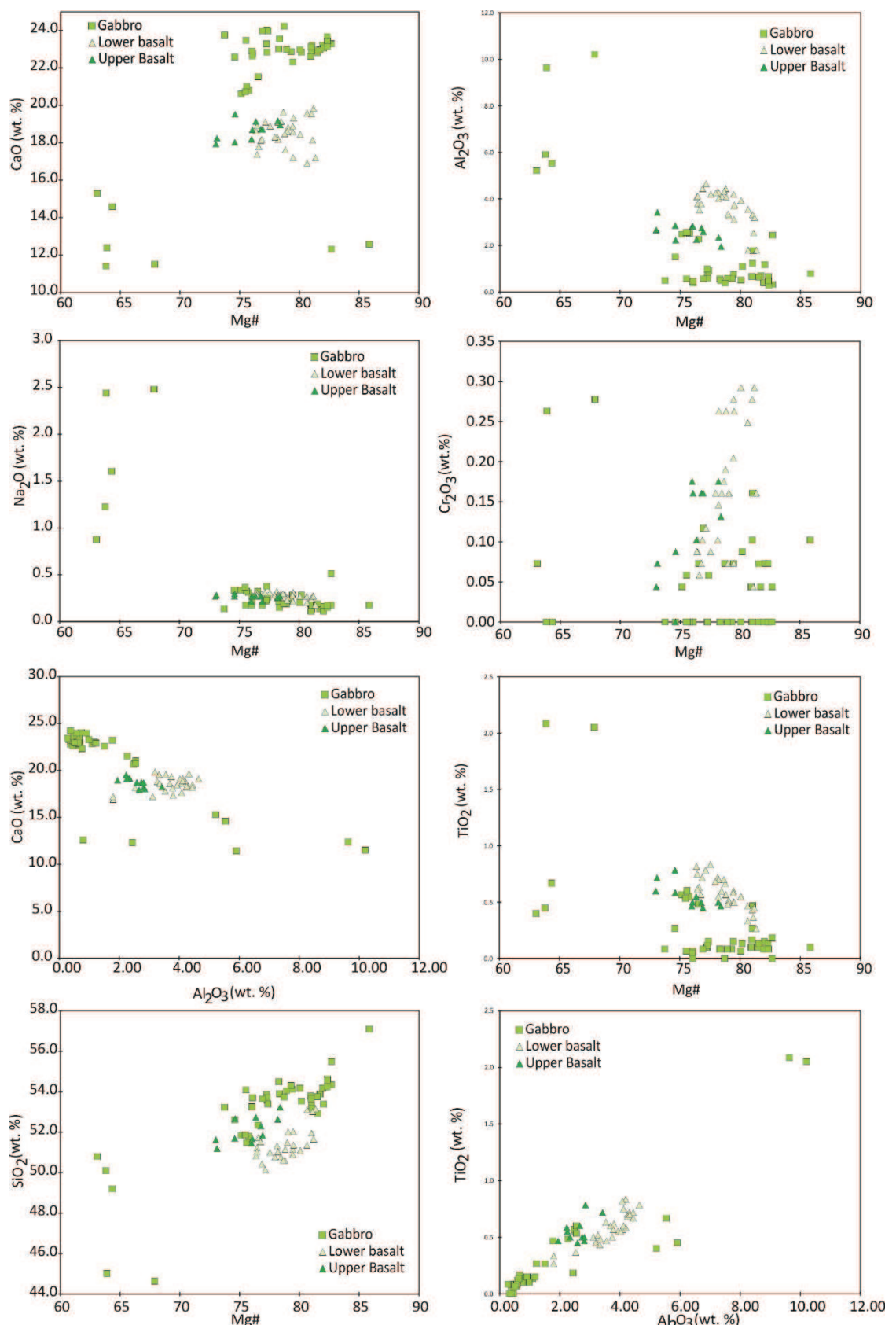
Figure 4.14 Bivariate diagrams of the major element compositions of clinopyroxenes from the Metchosin Igneous Complex, which have been separated into Gabbro, Lower and Upper basalt (Figure 3.12).

The Upper basalt plagioclases have the highest SiO_2 (55.7 – 68 .3 wt.%) and Na_2O contents, along with the lowest overall Al_2O_3 concentrations. While the Lower basalt plagioclases have similar compositions to those from the gabbros, although they extend over a wider range of SiO_2 contents (Figure 4.15).
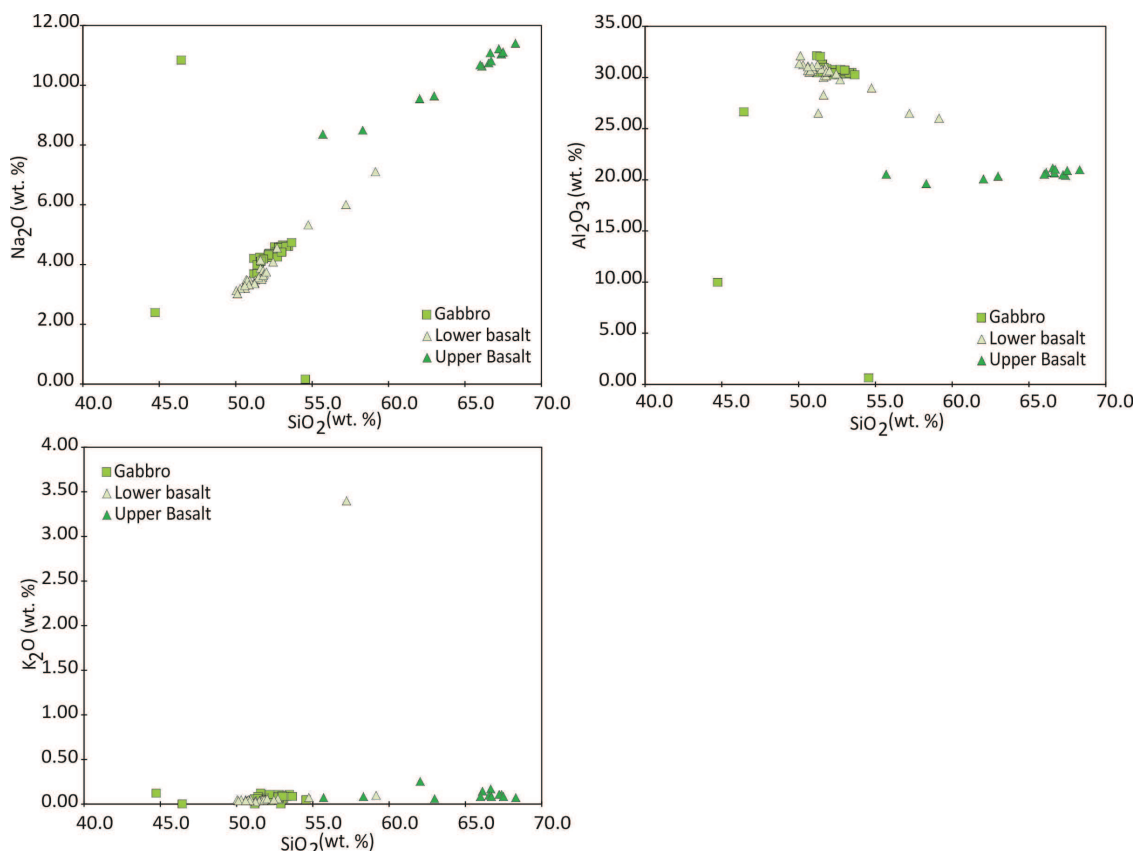
Figure 4.15 Bivariate diagrams of the major element compositions of feldspars from the Metchosin Igneous Complex, which have been separated into Gabbro, Lower and Upper basalt (Figure 3.12).

4.5 Summary

The samples collected from the Siletz River Volcanic Formation, both in Northern Oregon and form the Roseburg area are predominately finely crystalline aphyric amygdaloidal basalts, which comprise plagioclase, clinopyroxene and ilminite, and in some samples a minor amount of olivine. In addition to these fine-grained basalts, more coarsely crystalline basalts and dolerites with intergranular to subophitic textures of similar compositions are also common. Glomerocrysts of clinopyroxene and plagioclase are also frequently observed within the coarser rocks. In terms of their alteration, extensive clay and zeolite (and palagonite in

the Roseburg rocks) replacement occurs in both the groundmass and within the amygdales of the samples.

The Crescent Formation contains a range of vary textured basalts, which include phyric, aphyric, epigranular, variolitic and glomerophyric textures. The basalts comprise clinopyroxene, plagioclase and ilmenite. Dolerite dykes and sills containing subophitic plagioclase and clinopyroxene are also observed in both the Northern and Southern Crescent outcrops. While in the Northern Crescent, gabbros containing ophitic tabular plagioclase and clinopyroxene along with abundant ilmenite and spinel have been sampled. The rocks of the Southern Crescent Formation contain both zeolite and palagonite pseudomorphs and seritisation of plagioclase crystals. In the Northern Crescent Formation, however, the rocks have undergone prehnite-pumpellyite to greenshist grade alteration. Abundant chlorite is observed in the samples along with zeolite, prehnite and pumpellyite infilling amygdales and pervasively alternating the groundmass of samples.

The Metchosin Igneous Complex contains finely crystalline to hypocrystalline basalts with clinopyroxene and plagioclase rich glomerocrysts frequently observed. The dolerite dykes from this formation comprise fractured clinopyroxene and plagioclase, while the gabbros sampled consist of ophitic clinopyroxene and tabular plagioclase. The alteration in the Metchosin Igneous Complex ranges from prehnite to greenschist grade. The groundmass of samples contains abundant chlorite with prehnite also observed in the upper basalts. Additionally epidote, actinilite and pumpellyite are also noted.

Submarine weathering is known to increase the Fe and deplete the Mg content of a given mineral (Pearce, 1996) which may shed light on why certain samples exhibit extremely low and potentially 'false' Mg# (across a consistent SiO_2 wt. %). This exchange suggests that alteration has taken place and that the samples have been sufficiently weathered as to change their chemical compositions.

The diagram in Figure 4.16 summarises the composition of all clinopyroxene grains analysed from across the terrane. The majority of

clinopyroxene point analyses plot at an augite compositions, with some Metchosin sample trending towards diopside like clinopyroxenes and Bremerton samples as hedenbergites. Additionally a number of Roseburg clinopyroxenes (along with one Black Hills clinopyroxene) have no (to very little Ca) and subsequently plot along the enstatite – ferrosilite line. In general most clinopyroxene analysed have a relatively similar composition. There generally appears to be one major clinopyroxene population within the terrane, which as observed in much of the whole rock data (section 5), plots in a cluster with some satellite groups also apparent, although to a lesser extent than observed in the whole rock major and trace element data discussed in the following chapter.
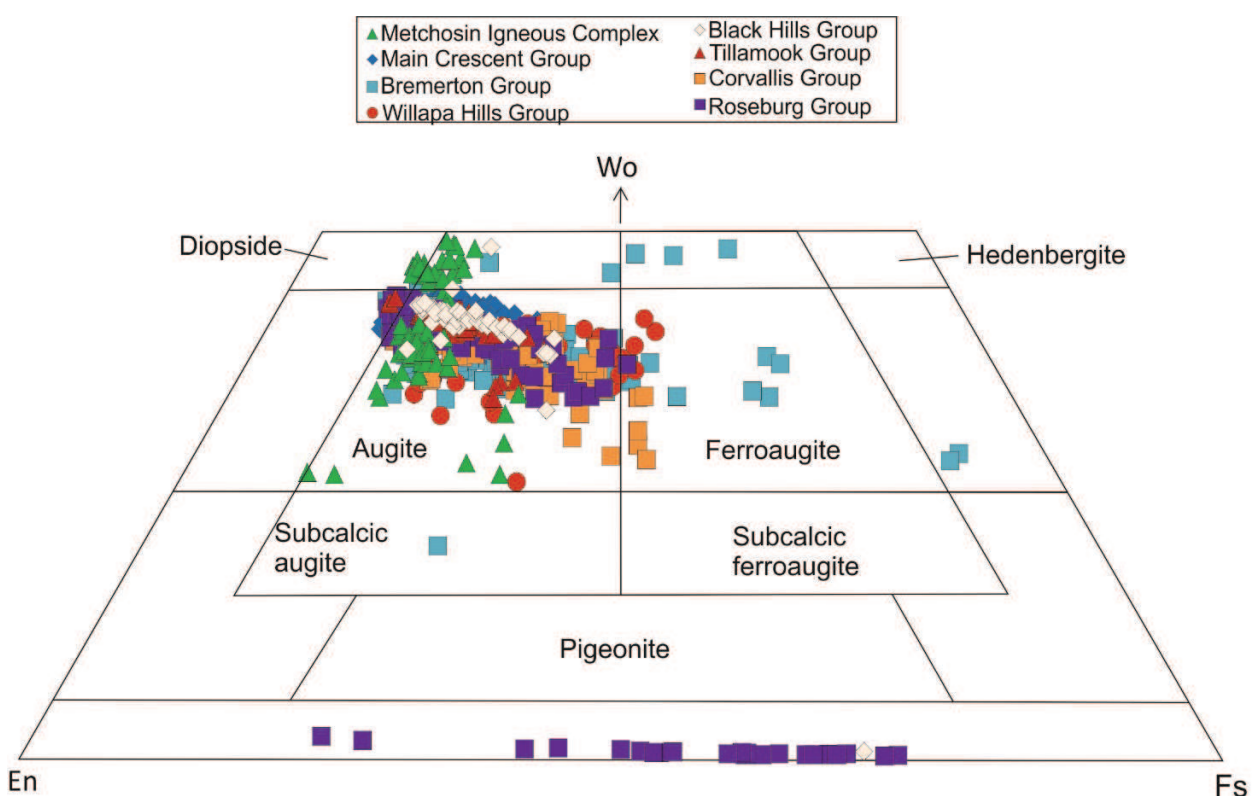
Figure 4.16 Triangular diagram summarising the composition of all clinopyroxene grains analysed from across the terrane.

Figure 4.17 highlights the feldspar compositions of the rocks of the Siletz terrane. The majority of analyses plot along the Albite – Anorthite solid-state solution line, with some Main Crescent samples slightly scattered above this main group of plagioclases. The Bremerton, Corvallis and Main Crescent Groups span

the array of compositions, while the Tillamook, Black Hills, Willapa Hills and the majority of Roseburg Group samples trend towards anorthite compositions or plot at the centre of the array. The Metchosin Igneous Complex plagioclase crystals however, are divided in to an albite like group (the Na rich end member of plagioclase feldspars) and a second more anorthite and Ca rich group. Intriguingly, as demonstrated in figure 4.9 a group of Bremerton feldspars are classified as more orthoclase (K) rich like feldspar (and plot along the solid-state solution line towards albite), indicating a more evolved composition in these samples, which is consistent with the Bremerton sample B017 classification as a leucogabbro. While the samples, which plot along the albite – anorthite solid state array are more typical of mafic suites.
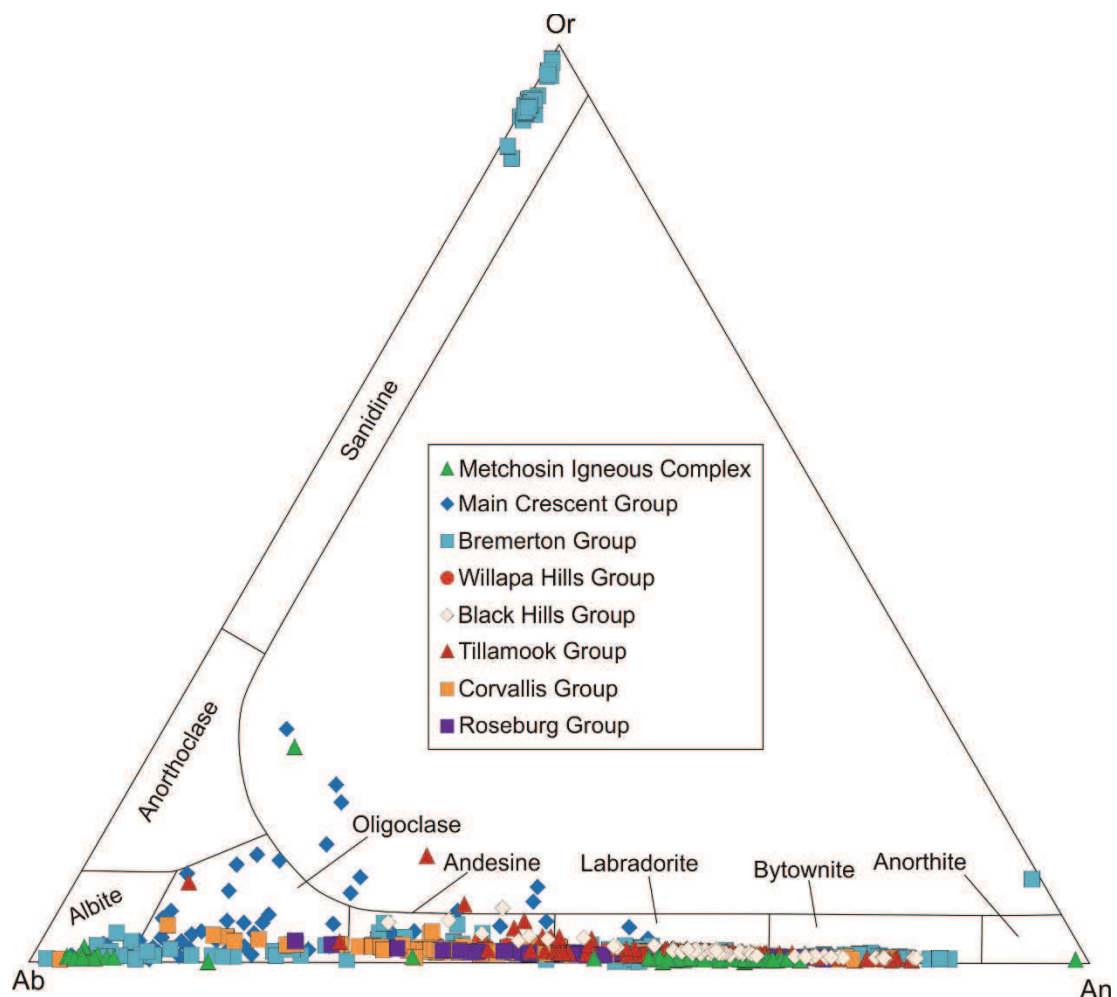
Figure 4.17 Triangular diagram summarising the composition of all plagioclase crystals analysed from across the terrane.

5. GEOCHEMICAL AND GEOCHRONOLOGICAL RESULTS

5.1 Introduction

This section presents the whole rock major and trace element results and radiogenic isotope ratios, along with $^{40}Ar/^{39}Ar$ and palonological geochronological ages from each of the sections of the Siletz terrane. Laboratory methods are described in Appendix A, while data sets can be found in Appendices B and C with further information in Appendices E3, E4, E5 and E6. Total iron is referred to as Fe_2O_3 $^{(T)}$. FeO $^{(EST)}$ and Fe_2O_3 $^{(EST)}$ have been estimated using equation 5.1, while the Mg# for the whole rock results have been calculated using equation 5.2 (Gill, 2011). All of the major element wt.% concentrations have been recalculated on an anhydrous basis.

Equation 5.1 $\qquad FeO\ ^{(T)} = Fe_2O_3\ ^{(T)}\ x\ 0.8998$

$\qquad\qquad\qquad FeO\ ^{(EST)} = 0.9\ x\ FeO\ ^{(T)}$

$\qquad\qquad\qquad Fe_2O_3\ ^{(EST)} = (FeO\ ^{(T)} - FeO\ ^{(EST)})\ x\ 1.11$

Equation 5.2 $\qquad Mg\# = 100\ x\ (MgO/\ MgO + (FeO^{(T)}))$

The effects of secondary alteration and element mobility on the whole rock geochemical results have been assessed by plotting each element against Zr and evaluating the correlation. Any elements which show considerable scatter, which is not the result of petrogenetic processes, are considered to have been remobilised and will not be used in this study. Major and trace elements will be used to classify the rocks according to their rock type and volcanic series. The major, and specifically, trace elements are also plotted with different fractionation indexes, as pairs of ratios, and on chondrite- and primitive mantle-normalised diagrams, to assess the magmatic processes, source composition and tectonic setting of the rocks. The Eu anomaly is calculated using Equation 5.3, and represents an example of how the trace element anomalies (e.g. Nb/Nb* and Ti/ Ti*) are calculated. In addition Pb, Sr, Hf and Nd radiogenic isotope data for 20

samples from across the terrane will also be used to identify the mantle source characteristics, in order to assess the potential role of a mantle plume in the petrogenesis of the Siletz terrane magmas. A limited number of $^{40}Ar/^{39}Ar$ step heating analyses and palynology of interbedded sediments will also be used to help constrain the age of the terrane. Samples have been primarily grouped in conjunction with their geographical location, and then are subsequently further grouped based on their geochemical composition where it is notably distinct.

5.2 Alteration

The rocks of the Siletz terrane have undergone variable amounts of alteration, from zeolite – greenschist grade, with most samples showing at least some signs of alteration, as discussed in the previous section (4.2 – 4.4). The loss on ignition (LOI) values of the samples mostly range between 0.5 and 2 %, but can extend up to ~ 6 %, which, along with the evidence from petrography, reinforces the point that that varying degrees of alteration have affected the rocks of the Siletz terrane. Weathering, metamorphism, hydrothermal fluids and diagenesis can influence the sub solidus element mobility and so the whole rock composition of samples. Therefore, the effects of secondary alteration and element mobility on the major and trace element and isotope data must be assessed before the data can be used to assess petrogenetic processes.

Many elements, in particular the Large-Ion Lithophile Elements (LILE) (i.e., K_2O, Ba, Rb), may become mobile during sub-solidus alteration. This is because the extent of remobilisation is related to an element's charge or ionic potential (e.g., Pearce, 1996; Hastie et al., 2007). Elements with low ionic potential (< 0.03 pm^{-1}) will tend to enter a solution as hydrated cations, while those exhibiting a high ionic potential (> 0.10 pm^{-1}) are more likely to be stripped from a given solution as hydrated oxyanions (e.g., Pearce, 1996; Hastie et al., 2007). For example, all samples show a large variation in Ba/Rb ratio, which is usually constant in unaltered oceanic basalts (Hofmann and White, 1983); this is consistent with Rb depletion during post magmatic alteration.

The most immobile elements generally do not go into solution during alteration. These elements have intermediate ionic potential values (0.03 – 0.10 pm^{-1}; Pearce, 1996) and include elements such as the Rare Earth Elements (REE) (excluding Eu and La), Zr, Hf, Nb, Ta, Ti, (the High Field Strength Elements - HFSE), Y, Cr, Th, Sc and Ga (Arculus, 1987; Hastie et al., 2007). However, while Pearce (1996) suggested that these elements remain immobile until reaching amphibolite – granulite facies conditions, other studies suggest that secondary remobilisation of these elements can occur at lower pressures and temperatures, in particular when exposed to carbonate-, hydrogen sulphide- or halide- bearing fluids (e.g., Giere, 1993; de Hoog and Van Bergen, 2000; Fadda et al., 2012).

In order to assess the degree of sub – solidus element mobility that has occurred in the rocks of the Siletz terrane each element has been plotted against Zr, due to its incompatible behaviour during basalt fractionation and immobile nature at low degrees of metamorphism (Cann, 1970; Pearce, 1996). When elements from a cogenetic suite of rocks (from a uniform mantle source) are plotted against Zr, they should define a linear correlation, assuming that the rocks have not begun fractionating Zr, which is unlikely in a basaltic suite). This method also assumes that the rocks are becoming progressively more evolved and are not all of a uniform composition, where a clustering of the data will occur. Scatter usually occurs in such plots (particularly for the more mobile elements) when secondary alteration has affected the samples. However, scattered trends can also be indicative of other factors and processes affecting the rocks, including; a heterogeneous mantle source region, variable amounts of crustal contamination and partial melting as well as fractionation of Zr.

5.2.1 Siletz River Formation, Oregon

5.2.1.1 Roseburg

There is abundant zeolite and clay alteration within the Roseburg groups and in addition to this the Roseburg samples have LOI values between 0.68 and 9.01 wt.% (with one anomalous sample, which is a tuff, with a LOI value of 24.09

wt.%). Nonetheless, this indicates that variable amounts of alteration have affected these rocks. Five groups have been determined for the Roseburg region, based partially on the stratigraphical position of the samples, which then generally correlates to the geochemical compositions of the rocks. The Roseburg and Sugarloaf groups are predominantly submarine tholeiitic volcanic rocks. The Red Hill and Couquille groups are more transitional in composition and both submarine and subaerial volcanics persist in these outcropping areas. Finally the rocks in the most northern area of the Roseburg region are more alkali in composition (Pyle, 1988). These volcanics are derived from the Drain, Jack Creek, Blue Mountain and Kentucky Slough (see Figure 3.1) areas, however due to constraints on time, expense and exposure, only one sample was collected from the Kentucky Slough region. Of the groups, only 2 have enough samples to be statistically significant; the Roseburg and Coquille groups.

Correlations in this study will be used only for groups containing 10 or more samples in order to accurately reflect any trends in the data and so the amount of secondary remobilisation cannot be determined using this method for these groups. Instead, the petrography is used to correlate the observed mineral assemblage with similar samples for the degree of remobilisation. For the purposes of this study a good correlation reflects an R^2 value of > 0.7, a moderate correlation equates to $0.4 - 0.7$ and poor correlations of < 0.4. The samples in this region have a relatively narrow range of Zr (ppm) and MgO wt.% ($79.2 - 174.5$ (ppm) and $5.1 - 7.8$ wt.% respectively) and so results in a clustering effect on much of the data, which can significantly affect the correlations observed. The Roseburg group volcanics only display good correlations between Zr and Hf and Nb. There are moderate correlations between Zr and TiO_2, Ce, Sm, Gd, Eu, Tb, V, Gd, Co and Ta, (Figure 5.1; Table 1). While the remainder of major and trace elements shown in Table 1 display poor correlations. In general REE display equal amounts of remobilisation (little to none) during metamorphism and so the variations in correlations between the REE and Zr is most likely not a result of alteration but petrogenetic processes. Figure 5.1 also demonstrates that elements such as Rb, Ba and Sr, which are typically mobile during alteration are scattered and have very poor correlations with Zr (less than 0.15), indicating that those

elements with moderate to low correlations likely display these trends as a result of other petrogenetic processes.

R^2 Value with Zr			
Element	Roseburg Main	Element	Roseburg Main
SiO_2	0.08	Ba	0.14
TiO_2	0.07	La	0.33
Al2O3	0.12	Ce	0.44
Fe_2O_3	0.05	Pr	0.38
MnO	0.1	Nd	0.37
MgO	0.34	Sm	0.4
CaO	0.01	Eu	0.46
Na_2O	0.02	Gd	0.51
K_2O	0.27	Tb	0.42
P_2O_5	0.21	Dy	0.31
Sc	0.2	Ho	0.2
V	0.49	Er	0.32
Cr	0.09	Tm	0.31
Co	0.55	Yb	0.12
Ni	0	Lu	0.03
Zn	0.01	Hf	0.9
Ga	0.59	Ta	0.61
Rb	0.07	Pb	0.08
Sr	0.01	Th	0.17
Y	0.38	U	0
Nb	0.79		

Table 1. R^2 value of elements with Zr for the Roseburg Group.
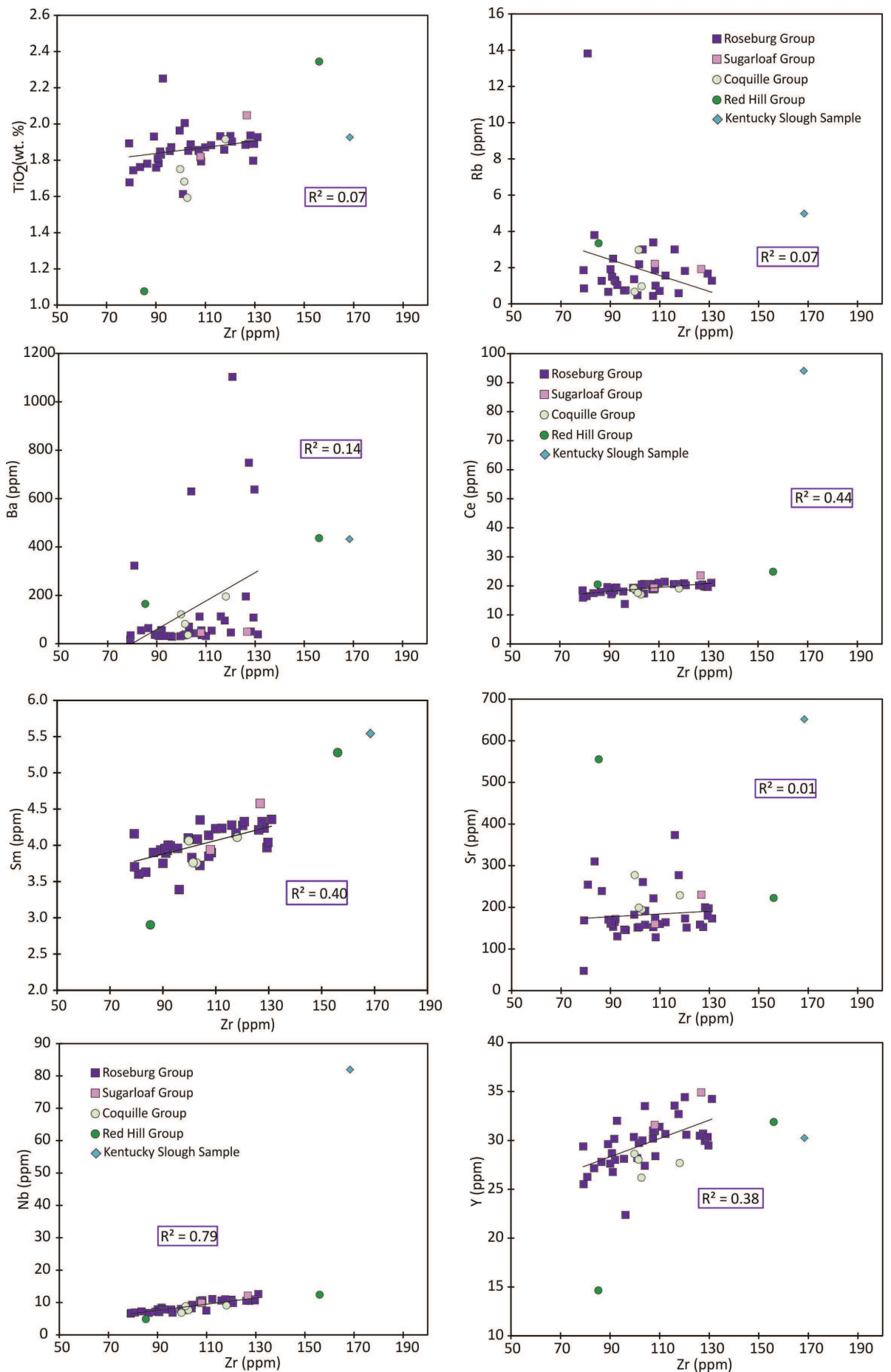
Figure 5.1 Representative bivariate plots of elements vs. Zr for the Roseburg area samples.

5.2.1.2 Siletz River

The rocks of the Siletz River Volcanics in Northern and Central Oregon (Figure 3.4) have extremely variable LOI values of largely between 0.12 and 7 wt.%, but can extend up to 20.33 wt.% (sample LC002). This is consistent with the extensive clay and zeolite alteration, which can be found in many of the samples, additionally calcite and quartz veins are also abundant (as discussed in section 4.2.2.1). Therefore, the likelihood of secondary remobilisation of elements within these samples is high and must be assessed before the geochemistry can be used to interpret the petrogenesis of the rocks.

The rocks of the Siletz River Volcanics region have been divided into several groups. The Corvallis Group comprises volcanics from the southernmost area of the region, and appears to represent a single fractionating suite. The volcanics from the type area of the Siletz River Formation are shown as the Siletz River Group. The Tillamook Group was collected from the northernmost outcropping area of the Siletz River Volcanics Formation. Finally the remainder of samples from the area are more alkaline in composition (discussed in section 5.3.1.2) and are classified as the Alkali Group.

The correlations of the groups described in this area are summarised in Figure 5.2 and Table 2. In the Corvallis Group only Nb and Hf show a very strong correlation with Zr, while TiO_2, P_2O_5, Ga, Y and the REE, show moderately good correlations and the remainder of elements in Table 2 have poor correlations (Figure 5.2). The Siletz River Group has good correlations between Zr and Hf only and moderate correlations between TiO_2, P_2O_5, Ga, Y, Nb, the REE (bar Yb and Lu), Ta, Th and U and displays poor correlations with the other elements (Figure 5.2; Table 2). The Tillamook Group shows a good correlation between Zr and Y, TiO_2, V, the REE, Hf and Ta, and a moderate correlation between Zr and P_2O_5, $Fe_2O_3^{(T)}$, Sc, Ga, Nb, Th and U (Figure 5.2; Table 2). The SRV Alkali Group only has good correlations between Zr and Hf with moderate correlations between Zr and TiO_2, $Fe_2O_3^{(T)}$, Y, Ga, Nb, the LREE and MREE (Figure 5.2; Table 2). The amount of scatter observed for elements, which are known to be highly mobile, for example Rb and to a lesser extent Ba (Figure 5.2) along with

the low R^2 values for these elements, highlights that the moderate to poor correlation for many of the elements may not be a reflection of mobile elements due to alteration.

| Element | R^2 Value with Zr | | | |
	Corvallis	Siletz River	Tillamook	Alkali SRV
SiO_2	0.04	0.38	0.1	0.07
TiO_2	0.59	0.55	0.91	0.65
Al2O3	0.01	0.39	0.03	0.07
Fe_2O_3	0.13	0.18	0.41	0.54
MnO	0.02	0.09	0.11	0.35
MgO	0.38	0.09	0.06	0
CaO	0.03	0.56	0.18	0.07
Na_2O	0.09	0.03	0.17	0.01
K_2O	0.09	0.22	0.07	0.01
P_2O_5	0.5	0.4	0.69	0.39
Sc	0.07	0.25	0.51	0.21
V	0	0.21	0.86	0.1
Cr	0.06	0.05	0	0.21
Co	0.01	0.08	0.09	0.21
Ni	0.16	0	0.22	0
Zn	0.05	0.31	0.12	0.26
Ga	0.59	0.6	0.46	0.57
Rb	0.01	0.39	0.29	0
Sr	0.01	0.09	0.03	0.27
Y	0.58	0.41	0.85	0.39
Nb	0.86	0.62	0.67	0.47
Ba	0.26	0.01	0.01	0.01
La	0.59	0.5	0.79	0.39
Ce	0.57	0.53	0.81	0.4
Pr	0.56	0.6	0.87	0.42
Nd	0.55	0.62	0.89	0.41
Sm	0.54	0.64	0.92	0.5
Eu	0.55	0.67	0.98	0.44
Gd	0.57	0.63	0.93	0.47
Tb	0.54	0.53	0.95	0.45
Dy	0.53	0.45	0.94	0.4
Ho	0.54	0.42	0.92	0.33
Er	0.51	0.35	0.88	0.31
Tm	0.51	0.33	0.85	0.14
Yb	0.47	0.22	0.84	0.08
Lu	0.4	0.18	0.75	0.08
Hf	0.98	0.94	0.99	0.96
Ta	0.52	0.51	0.76	0.46
Pb	0.09	0.08	0.01	0.1
Th	0.04	0.36	0.65	0.32
U	0.5	0.52	0.58	0.29

Table 2. R^2 values for elements with Zr for the Siletz River Groups.
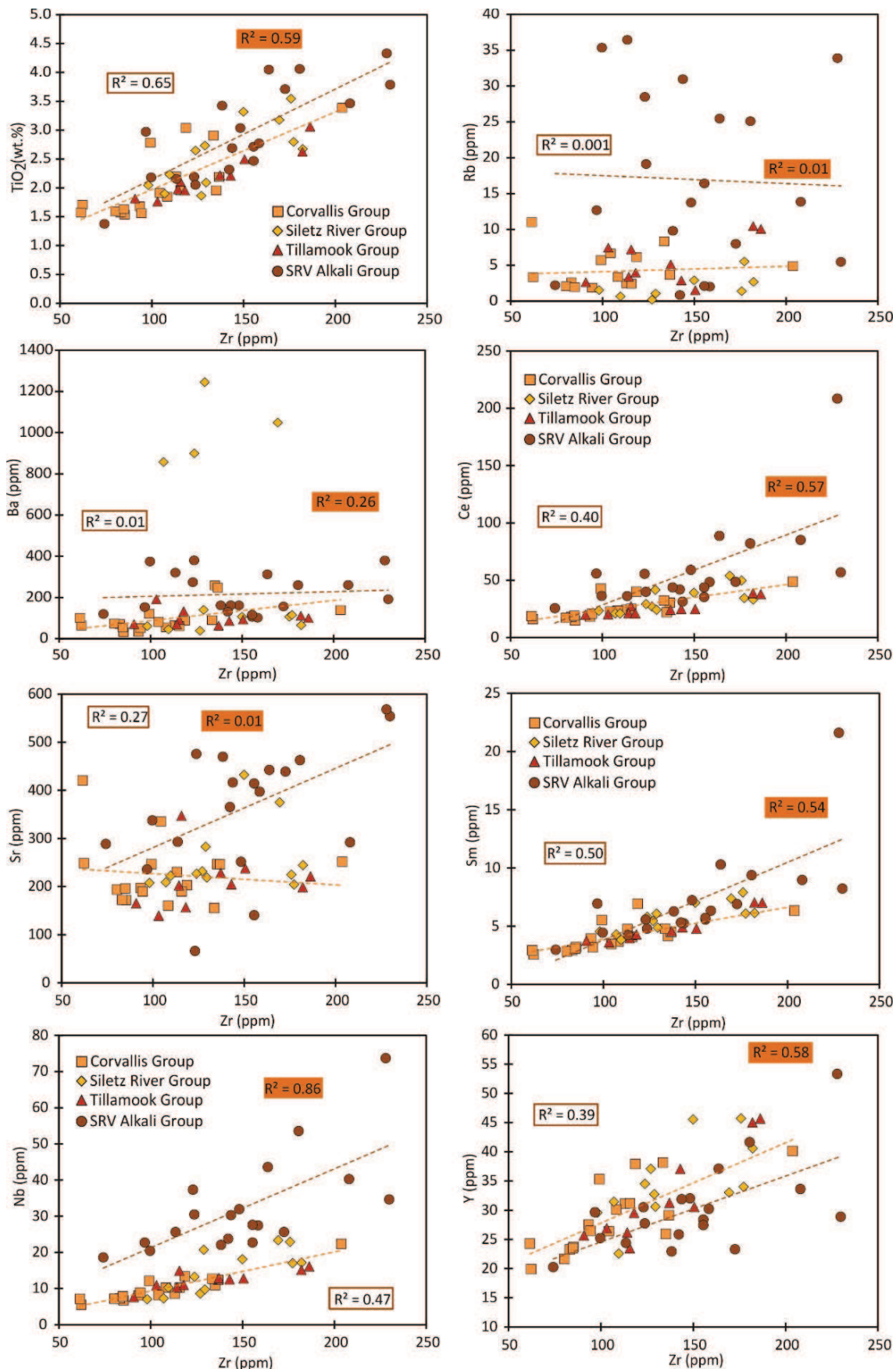
Figure 5.2 Bivariate diagram of elements vs. Zr for the Siletz River area.

5.2.2 Crescent Formation, Washington

5.2.2.1 North Crescent

The Crescent Main Group represents the dominant group of samples from the Northern Crescent Formation in the Olympic Peninsula, while the Depleted Crescent Group, and are distinguished from these samples with consistently lower incompatible element concentrations. The Bremerton Group comprises a sequence of gabbros, sheeted dykes and basaltic lavas that outcrop to the west of the Crescent area (Figure 3.1). There is no discernible geochemical difference between the compositions of the upper and lower units of the Crescent Formation (Figure 5.3), and so for the purposes of this section they are considered as one group (Crescent Main). The samples from the North Crescent region display LOI values between 1.06 and 6.95 wt.%, indicating that variable amounts of alteration have taken place. The Crescent Main and Depleted Crescent Groups contain secondary mineral assemblages of chlorite, epidote, zeolite, calcite, prehnite and pumpellyite, with up to greenschist grade facies alteration having occurred (section 4.3.1.1). The Bremerton Group have also undergone greenschist grade metamorphism, with chlorite, prehnite, pumpellyite, hornblende and kaersutite amphibole as common alteration minerals (section 4.3.1.1).
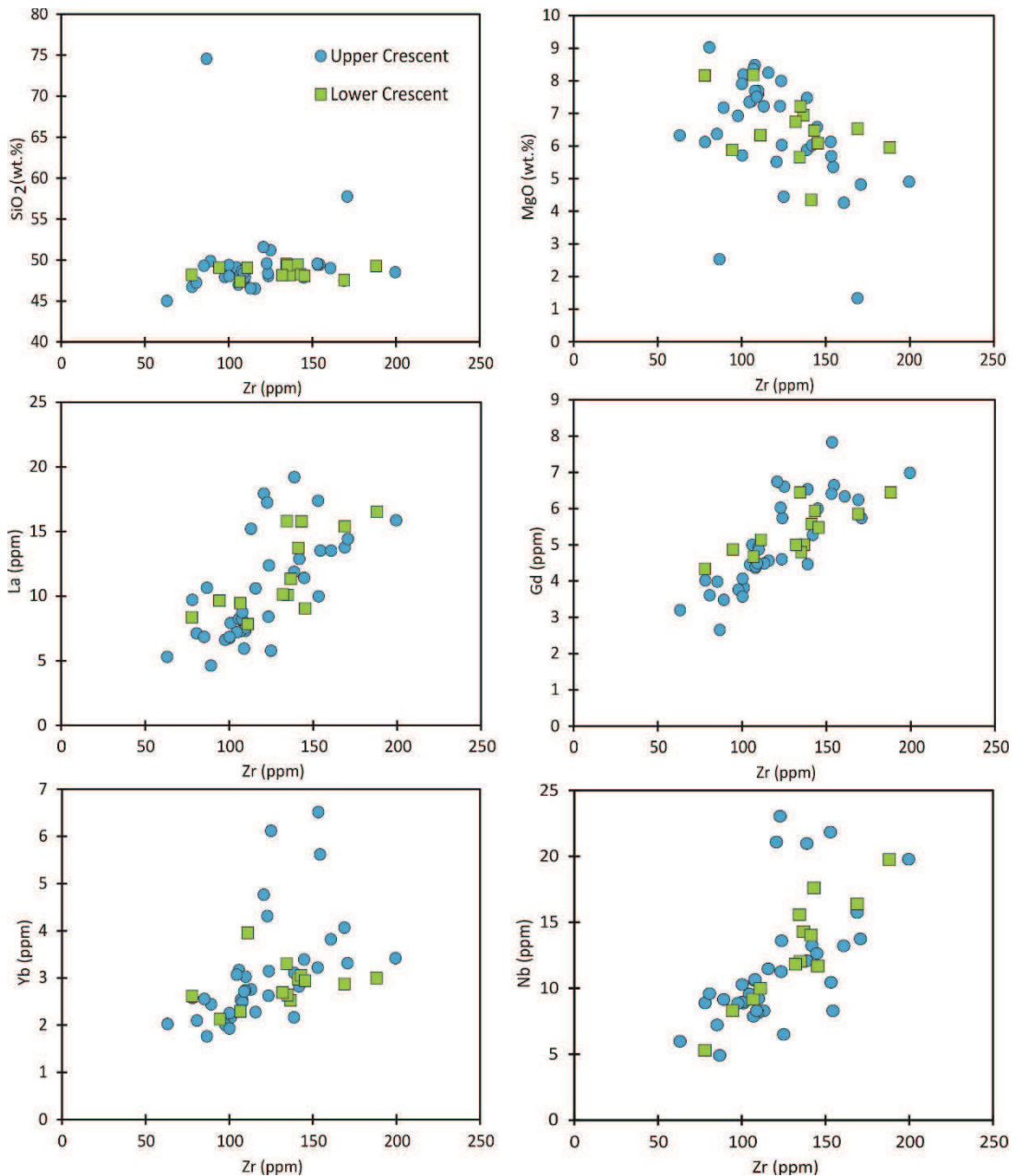
Figure 5.3 Bivariate diagrams highlighting the geochemical similarities between the upper and lower units of the Crescent Formation in the Crescent Main Group.

The Crescent Main Group only displays a good correlation between Zr and Sm, Eu and Hf, while the group have moderate correlations between Zr and TiO_2, Dy, Th, Nb, La, Tb, Ce, Gd, Pr and Nd and the remainder of elements in Table 3 have poor correlations (< 0.4) with Zr (Figure 5.4; Table 3). However, a significant portion of this scatter is the result of a few samples, indicating that they have undergone more alteration than the remainder of the group or different

petrogenetic processes. The Depleted Crescent Group show good correlations between Zr and Gd, Ce, Eu, Sm, Hf, Pr and Nd and moderate correlations between TiO_2, Zn, Nb, Y, Ho, Ta, Dy, Rb, La and Tb (Figure 5.4; Table 3). Finally in the Bremerton group good correlations are observed between CaO, Na_2O, Y, Nb, the REE, Hf, Ta and U and moderate correlations with TiO_2 and Ga (Figure 5.4; Table 3). Again, in all groups there is significantly more scatter in the more traditionally mobile elements, in particular Ba and Sr in comparison to the other elements.

	R2 Value with Zr		
Element	Crescent Main	Bremerton	Crescent Depleted
SiO_2	0.12	0.16	0.01
TiO_2	0.5	0.53	0.67
Al2O3	0.07	0.08	0.07
Fe_2O_3	0.17	0.3	0.06
MnO	0.26	0.21	0.12
MgO	0.32	0.35	0.01
CaO	0.08	0.77	0.06
Na_2O	0.13	0.7	0.04
K_2O	0.03	0.39	0.28
P_2O_5	0.19	0.4	0
Sc	0.02	0.23	0.02
V	0.11	0	0.02
Cr	0.23	0.43	0.04
Co	0.02	0.08	0.19
Ni	0.13	0.26	0.16
Zn	0.01	0.14	0.44
Ga	0.17	0.58	0.28
Rb	0.1	0.35	0.58
Sr	0.02	0.01	0.17
Y	0.32	0.85	0.51
Nb	0.44	0.88	0.49
Ba	0	0.3	0.37
La	0.49	0.8	0.59
Ce	0.57	0.8	0.78
Pr	0.64	0.86	0.9
Nd	0.69	0.85	0.94
Sm	0.74	0.84	0.81
Eu	0.72	0.81	0.79
Gd	0.64	0.84	0.76
Tb	0.52	0.84	0.69
Dy	0.41	0.86	0.58
Ho	0.33	0.86	0.53
Er	0.26	0.83	0.32
Tm	0.2	0.85	0.33
Yb	0.19	0.88	0.26
Lu	0.21	0.87	0.26
Hf	0.95	0.99	0.88
Ta	0.37	0.75	0.55
Pb	0.02	0.02	0.23
Th	0.43	0.11	0.35
U	0.16	0.8	0.11

Table 3. R^2 values for elements with Zr for the North Crescent Groups.
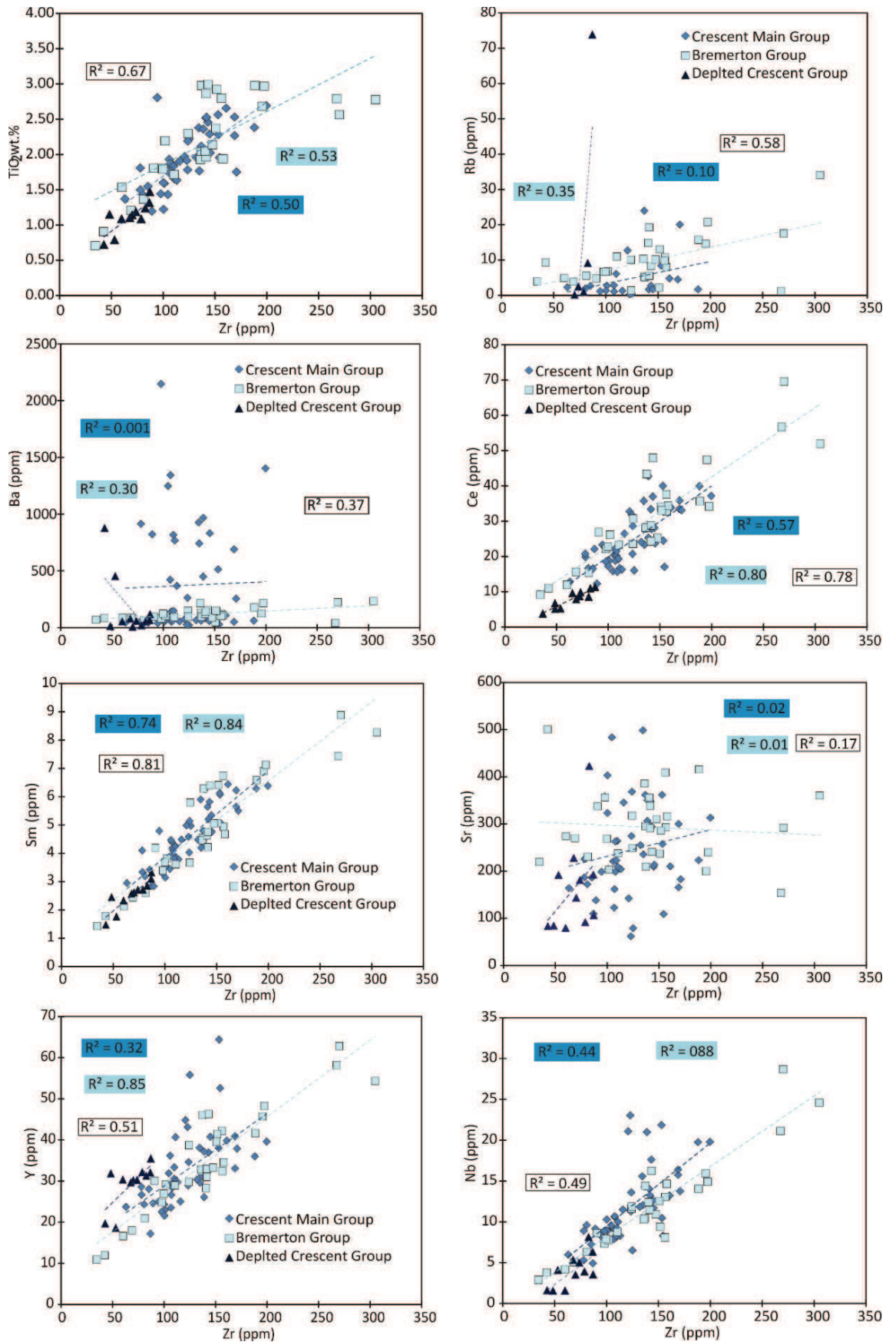
Figure 5.4 Representative elements vs. Zr for the Crescent North samples.

5.2.2.2 South Crescent

The Crescent South rocks display a range of LOI values between -0.02 and 7.03 wt.%, implying that variable amounts of alteration have affected the samples. As discussed in section 4.3.2.1 the different degrees of alteration are also apparent in the mineral assemblages observed, with prehnite, pumpellyite and zeolites frequently appearing along with, more sporadically, chlorite indicating a range of metamorphic conditions.

The Crescent South rocks consist of 4 groups, derived from the geographical location of their outcropping area (Figure 3.10); the Black Hills Group, the Willapa Hills Group, the Doty Hills Group and the Ilwaco Group. The Black Hills group displays a good correlation between Zr and Hf only and a moderate correlation between Zr and Sr, Nb, Ta and the LREE while the remainder of elements in Table 4 have poor correlations with Zr (Figure 5.5; Table 4). While in the Willapa Hills a good correlation is once again only observed between Zr and Hf and a moderate correlation between Zr and TiO_2, Nb, LREE to MREE, Nb and Ta (Figure 5.5; Table 4). Again as noted with the other groups discussed there is considerably more scatter and poorer correlations between Zr and Ba, Rb and Sr in comparison to the other elements.

	R² Value with Zr				
Element	Black Hills	Willapa Hills	Element	Black Hills	Willapa Hills
SiO_2	0	0.06	Ba	0.02	0.01
TiO_2	0.34	0.48	La	0.43	0.53
Al2O3	0.19	0.05	Ce	0.39	0.47
Fe_2O_3	0.1	0.15	Pr	0.4	0.49
MnO	0.36	0.1	Nd	0.37	0.33
MgO	0.34	0.12	Sm	0.43	0.57
CaO	0.02	0.12	Eu	0.46	0.59
Na_2O	0.05	0.02	Gd	0.43	0.62
K_2O	0.13	0.18	Tb	0.33	0.48
P_2O_5	0.39	0.01	Dy	0.36	0.45
Sc	0.28	0.13	Ho	0.25	0.28
V	0.15	0.08	Er	0.24	0.35
Cr	0.27	0.15	Tm	0.15	0.25
Co	0.06	0.1	Yb	0.14	0.16
Ni	0	0.13	Lu	0.1	0.12
Zn	0.04	0.12	Hf	0.86	0.97
Ga	0.27	0.06	Ta	0.42	0.56
Rb	0.07	0.3	Pb	0	0
Sr	0.49	0.21	Th	0.35	0.3
Y	0.3	0.22	U	0.02	0.17
Nb	0.52	0.54			

Table 4. R^2 values for elements with Zr for the South Crescent groups.
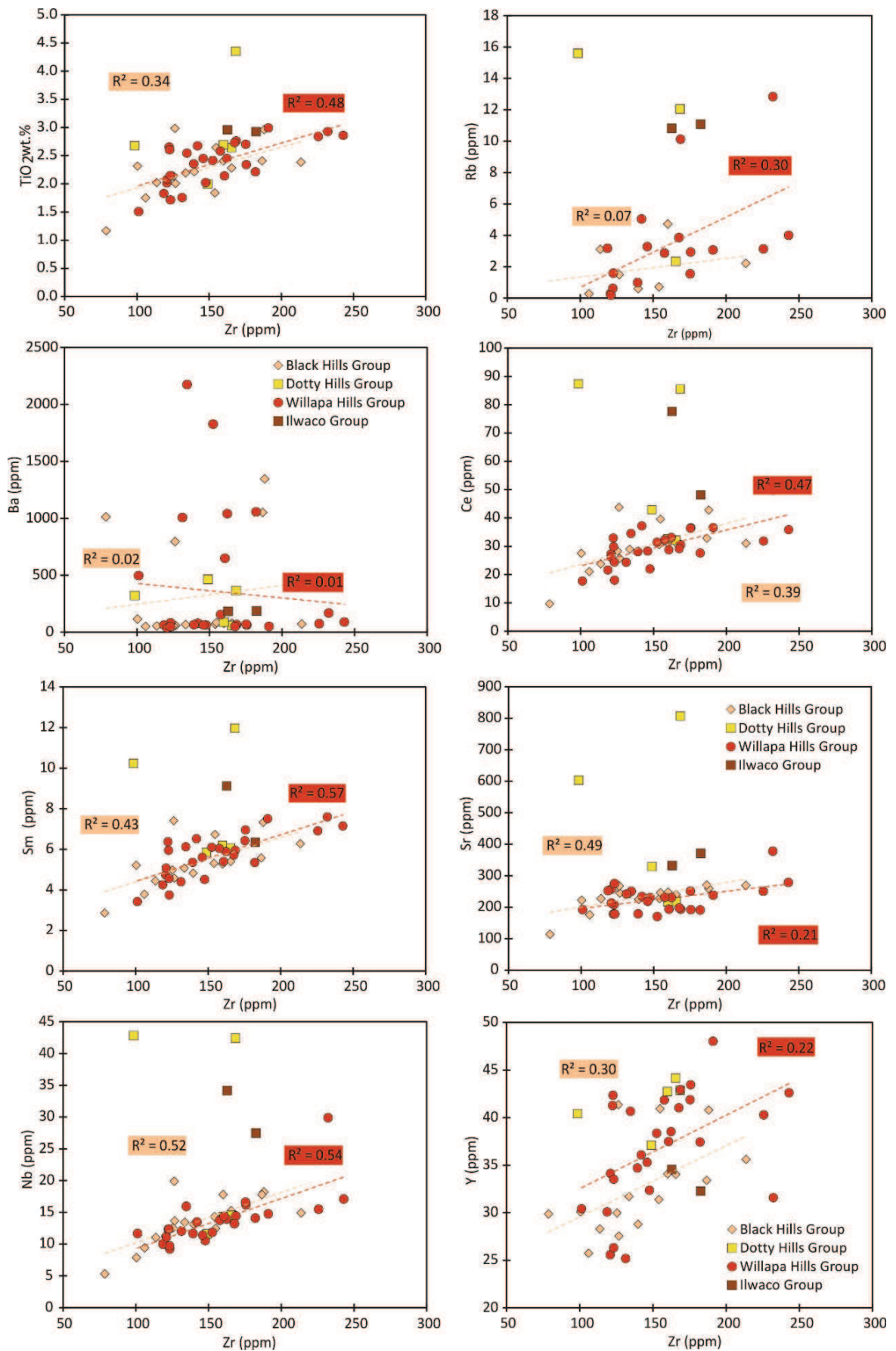
Figure 5.5 Bivariate diagrams of selected elements vs. Zr for the South Crescent samples.

5.2.3 Metchosin Igneous Formation, Vancouver Island

The LOI for the Metchosin Igneous Complex samples ranges from 0.73 – 4.21 wt.% indicating a range in the amount of alteration experienced, as reflected in the petrography of the samples (as discussed above in section 4) the rocks of the Metchosin Igneous Complex have alteration mineral assemblages of chlorite, epidote, albite and prehnite (in the upper volcanic sequences) and therefore all samples collected during this study have undergone greenschist facies grade metamorphism.

Elements and oxides, which show a good correlation include TiO_2, P_2O_5, the REE (bar Dy, Er, Yb and Lu), Nb, Hf and Ta, while those showing a moderate degree of correlation with Zr are SiO_2, Al_2O_3, Fe_2O_3 [T], Dy, Er, Y, Ho, Tm, V and Sr while the remainder of elements in Table 5 have poor correlations with Zr with Ba in particular showing a large amount of scatter (Figure 5.6).

R² Value with Zr			
Element	Metchosin	Element	Metchosin
SiO_2	0.55	Ba	0.27
TiO_2	0.75	La	0.77
Al2O3	0.57	Ce	0.86
Fe_2O_3	0.41	Pr	0.86
MnO	0.25	Nd	0.83
MgO	0.01	Sm	0.85
CaO	0.12	Eu	0.77
Na_2O	0.23	Gd	0.83
K_2O	0.18	Tb	0.78
P_2O_5	0.83	Dy	0.61
Sc	0.02	Ho	0.49
V	0.44	Er	0.55
Cr	0	Tm	0.48
Co	0.32	Yb	0.37
Ni	0.01	Lu	0.31
Zn	0.07	Hf	0.99
Ga	0.4	Ta	0.85
Rb	0.3	Pb	0
Sr	0.51	Th	0.27
Y	0.55	U	0.36
Nb	0.87		

Table 5. R^2 values for elements with Zr for the Metchosin Igneous Complex.
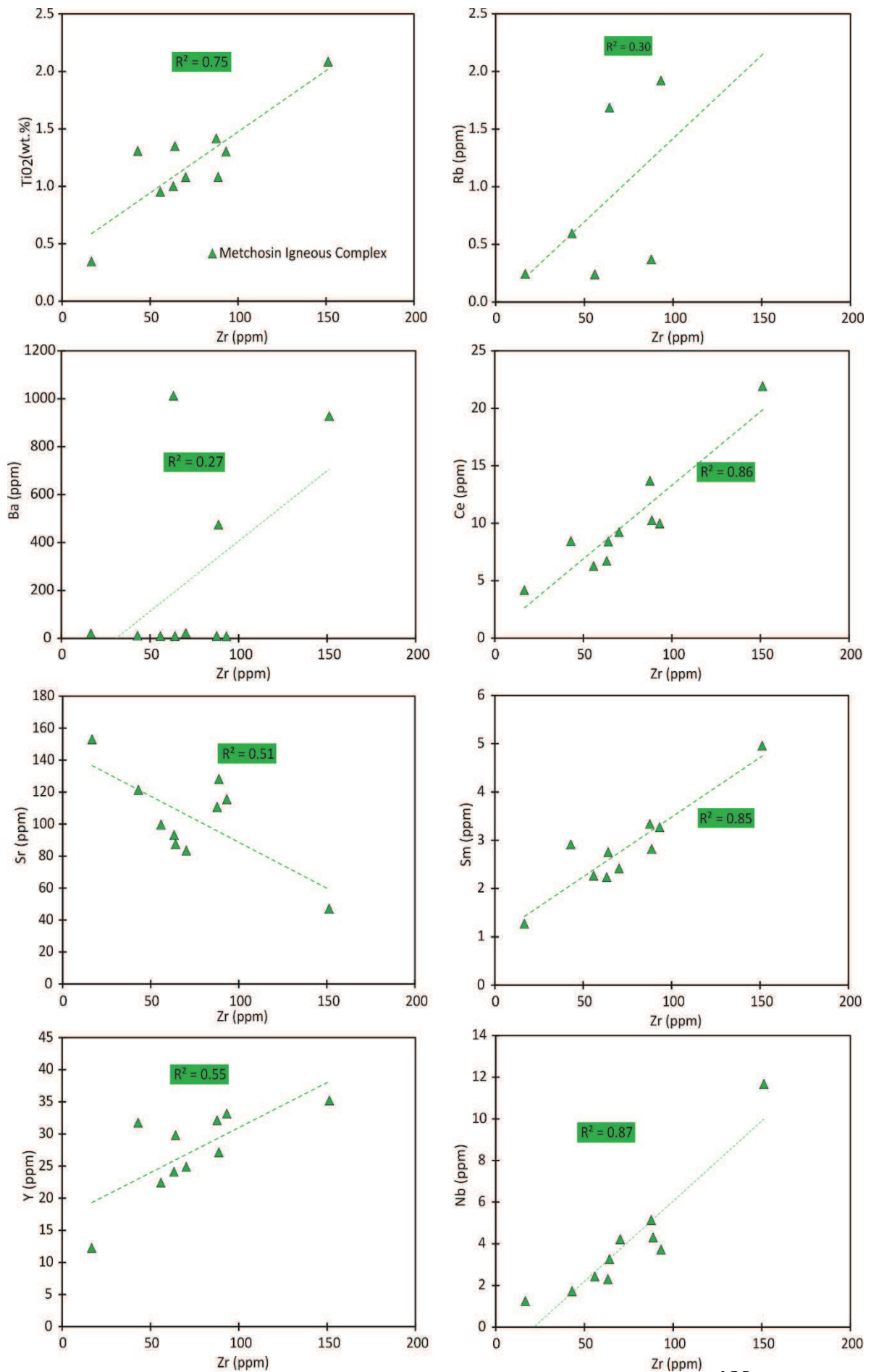
Figure 5.5 Bivariate diagrams of representative elements from the MIC vs. Zr.

5.2.4 Summary

As discussed above, although many of the elements in several of the groups display poor to moderate correlations with Zr only, they show significantly better correlations than elements which are known to be mobile within altered oceanic basalts such as Ba, Rb, and Sr (Hofmann and White, 1983; Hastie et al., 2007). However, despite this several of the major elements appear to have become mobile due to secondary alteration effects, including significantly Na_2O and K_2O. While correlations between elements and Zr can be poor, several factors such as narrow Zr and MgO ranges, slight differences in petrogenetic processes and source compositions along with accumulation and fractionation can lead to this, as discussed below. In addition the petrographic results discussed in section 4 are consistent with varying results of alteration having taken place. It is also worth noting that in some of the groups examined Zr may be beginning to fractionate which can significantly affect the correlations observed and as discussed in Pyle (1989), the groups of rocks within the terrane may not represent fractionating suites (discussed below).

5.3 Classification

In the following section major and trace element diagrams are used to classify the rocks of the Siletz terrane in terms of their rock types and volcanic series. Both the total alkali silica (TAS) diagram and Zr/Ti vs Nb/Yb diagrams are used for each of the groups. However, as discussed above, due to the mobility of the TAS elements within these rocks (in particular Na_2O and K_2O) caution must be practised while using this type of classification. Therefore the Zr/Ti vs Nb/Yb diagram which utilises elements which have shown to be immobile during greenschist facies metamorphism and so is more useful for classifying the rocks in this region is also used.

5.3.1 Siletz River Formation, Oregon

5.3.1.1 Roseburg

On the TAS diagram (Figure 5.6a) samples from the Roseburg Group generally plot within the basalt field however two samples plot above the tholeiitic-alkalic divide (Le Maitre et al., 1989), most likely due to mobility of K_2O. Additionally, sample 060RO, a tuff, plots in the basaltic andesite field. The Coquille Group also plots in the basalt field with one sample plotting near the alkali tholeiitic series boundary line. The Sugarloaf and Red Hill Groups samples plot in the basalt field while the Kentucky Slough sample plots in the alkali basalt field. On the Zr/Ti vs Nb/Yb diagram (Figure 5.6b) the Roseburg, Sugarloaf, Coquille and Red Hill Groups all plot in a tight cluster in the (tholeiitic) basaltic field. This confirms that the TAS diagram has been affected by the mobility of the alkali oxides. The Kentucky Slough sample plots as an alkali basalt, as with the TAS diagram. However, sample 012/2 RO of the Roseburg Group plots as a foidite.
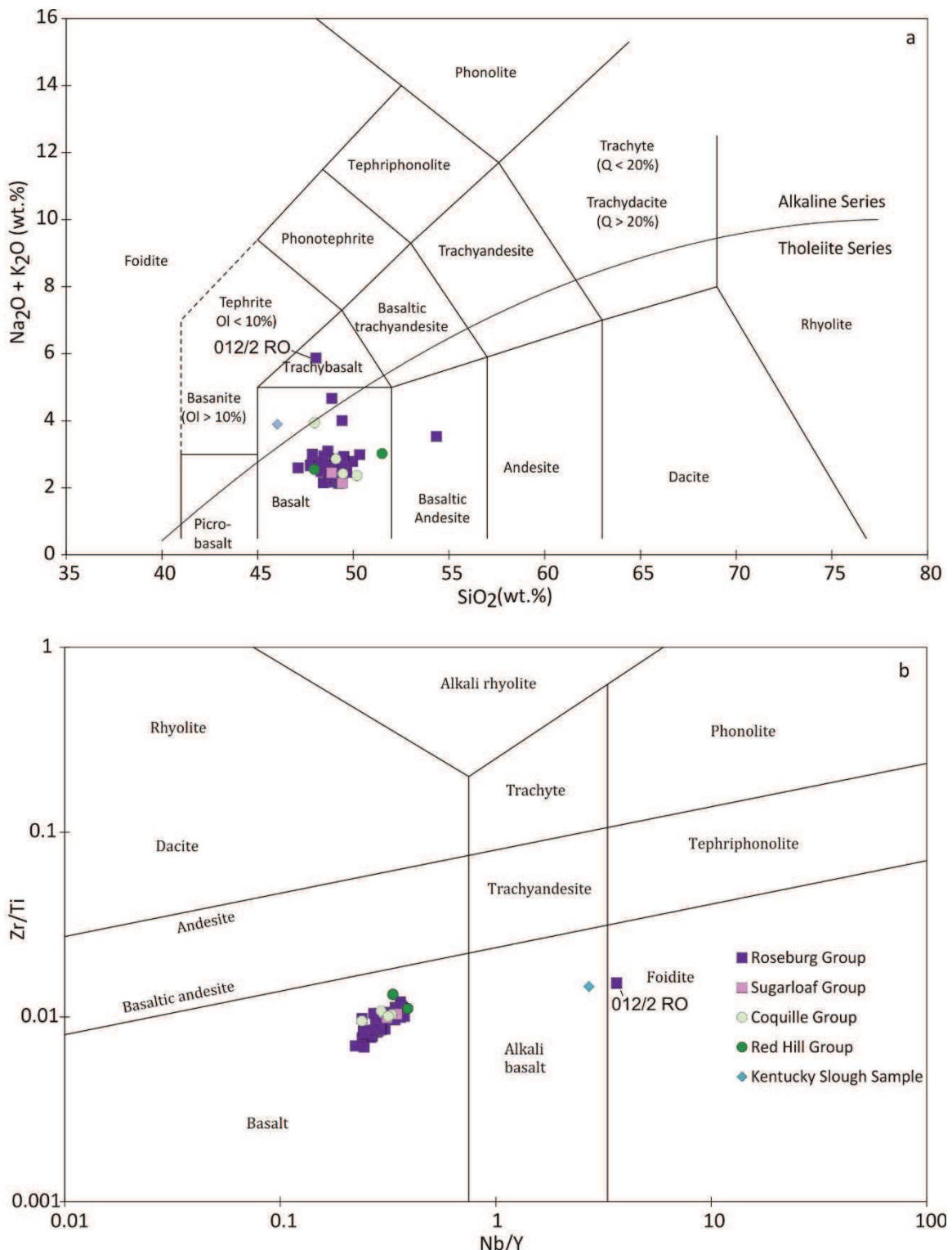
Figure 5.6 a) Total alkali silica classification diagram (Le Bas et al., 1986) and b) Zr/Ti vs. Nb/Y classification diagram (Pearce, 1996) for the Rosebrug area samples

5.3.1.2 Siletz River

On the TAS diagram (Figure 5.7a) the majority of the samples plot within the basalt field while the Alkali Group samples are scattered across several fields at variable alkali contents. There is considerably less scatter observed on the Zr/Ti vs Nb/Yb diagram (Figure 5.7b), and the samples of the Corvallis, Siletz River and Tillamook Groups all plot within a similar area in the (tholeiitic) basalt field with slightly more variation observed across the Siletz River Group. While the SRV Alkali Group all plot within the alkali basalt field with the exception of one sample, which plots in the fodite field (Figure 5.7b).
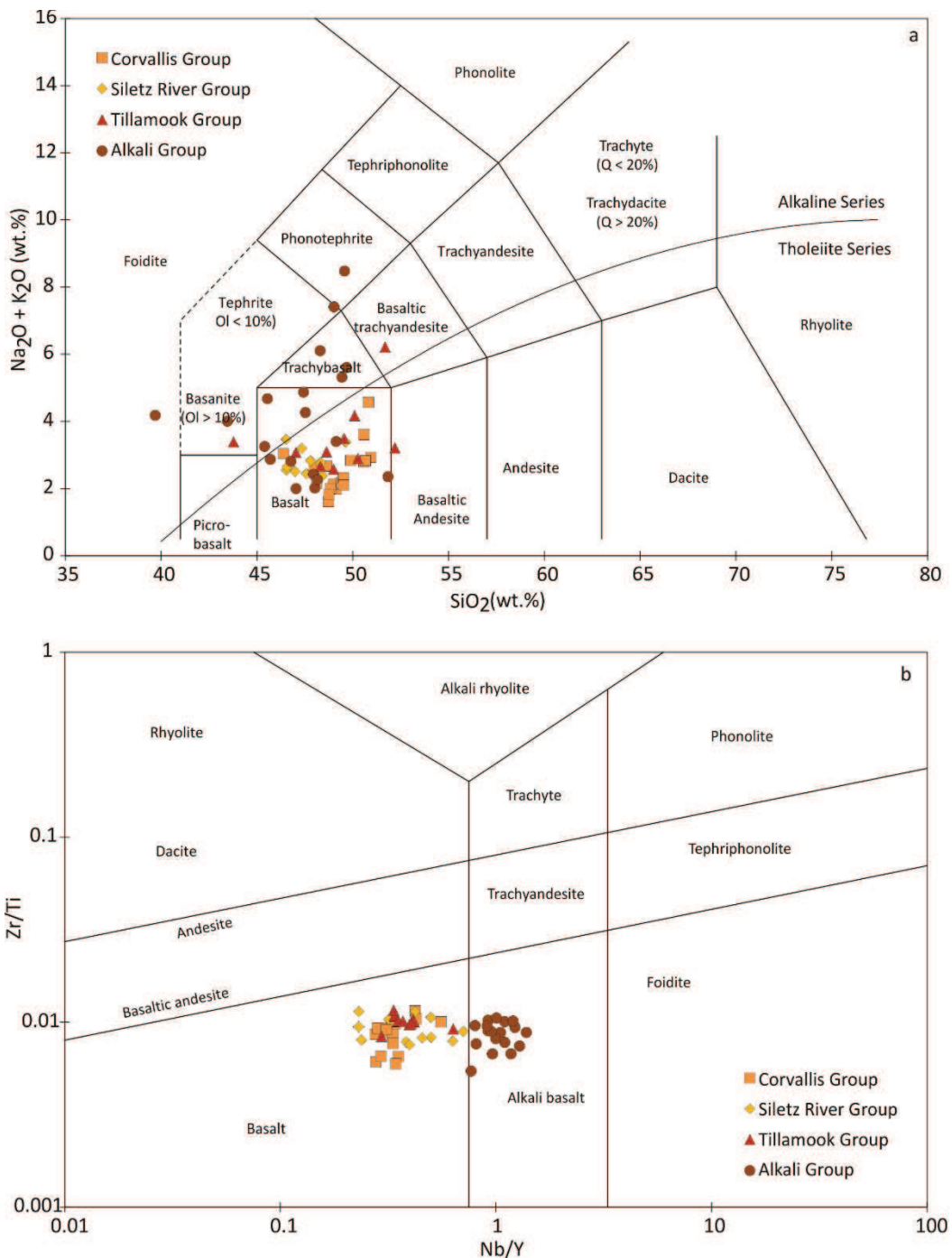
Figure 5.7 a) Total alkali silica classification diagram (Le Bas et al., 1986) and b) Zr/Ti vs. Nb/Y classification diagram (Pearce, 1996) for the for the Siletz River area samples.

5.3.2 Crescent Formation, Washington

5.3.2.1 North Crescent

The North Crescent samples when plotted on the TAS diagram (Figure 5.8a) are scattered across the basalt field and into adjacent fields. The Crescent Main Group and the Bremerton Group both plot in a cluster in the (tholeiitic) basalt field on the Zr/Ti vs Nb/Yb diagram (Figure 5.8b), however some samples do approach the boundary with the basaltic andesite field. The Depleted Crescent Group also plots within the basalt field and this group also displays a relatively linear trend of increasing Nb/Yb across this field.
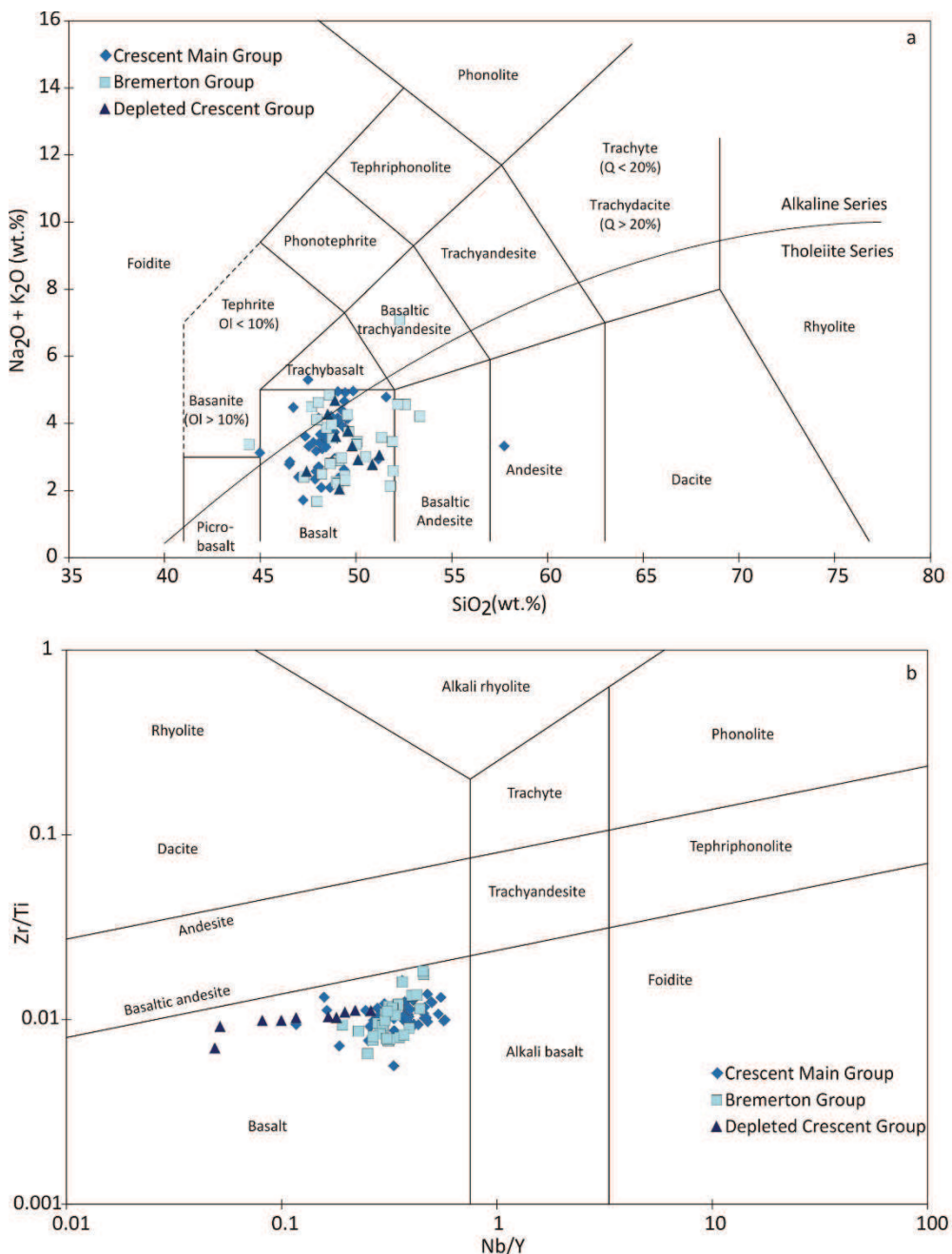
Figure 5.8 a) Total alkali silica classification diagram (Le Bas et al., 1986) and b) Zr/Ti vs. Nb/Y classification diagram (Pearce, 1996) for the Crescent North samples

5.3.2.2 South Crescent

In both the TAS diagram and Zr/Ti vs Nb/Yb diagram (Figure 5.9a; b) the Willapa and Black Hills Groups plot predominantly in the basalt field with one sample from the Willapa Hills Group plotting in the alkali basalt field in Figure 5.9b. The Doty Hills Group samples are variable in both Figure 5.9a and b and

plot in both the basalt (tholeiitic) field and alkali basalt field in Figure 9b. While the Ilwaco samples are both classified as alkali basalts and alkaline series rocks in Figure 9a and b.
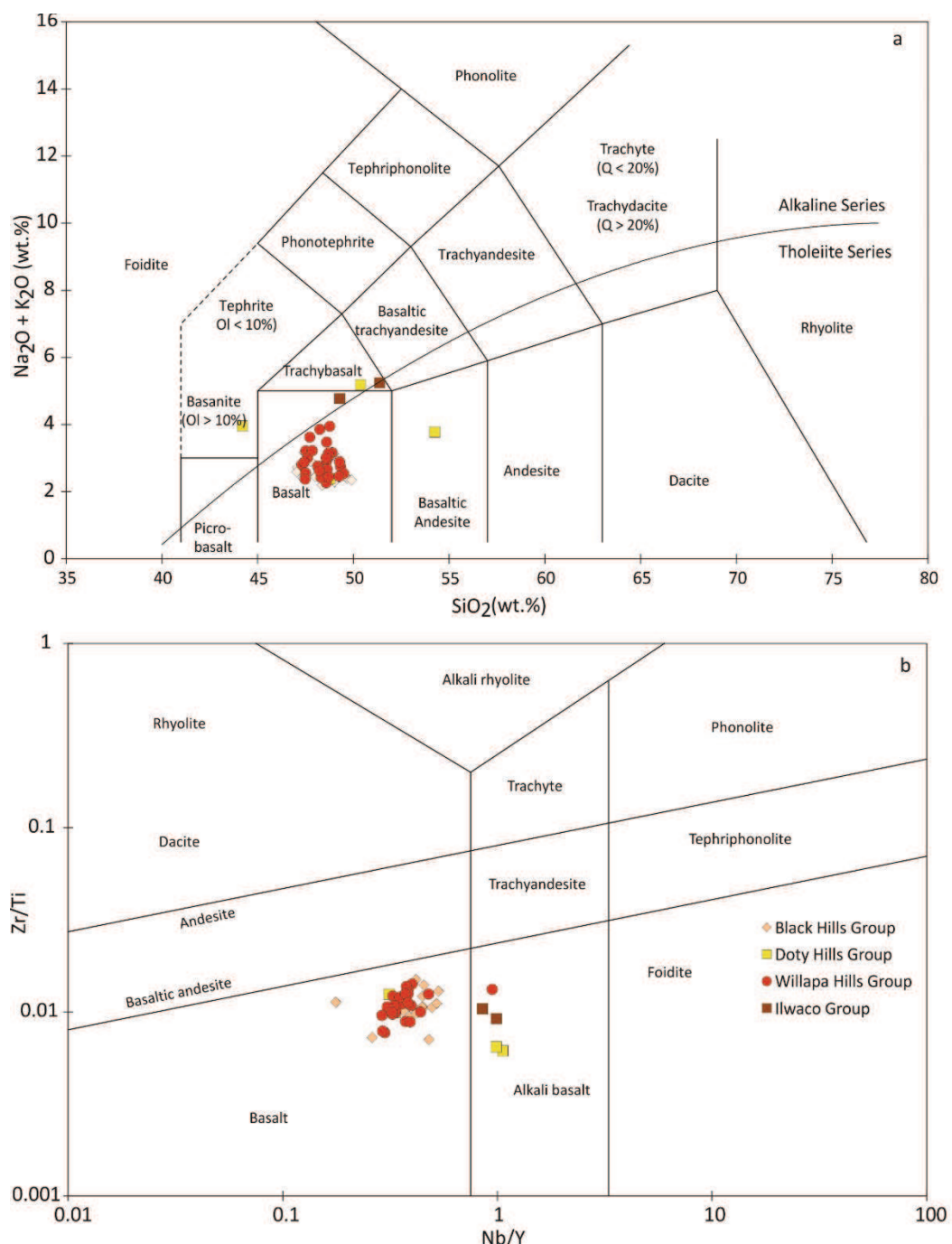
Figure 5.9 a) Total alkali silica classification diagram (Le Bas et al., 1986) and b) Zr/Ti vs. Nb/Y classification diagram (Pearce, 1996) for the Crescent South samples.

5.3.3 Metchosin Igneous Formation, Vancouver Island

On the TAS diagram for the Metchosin Igneous Complex samples generally plot in the basalt field, displaying increasing Total alkali contents (Figure 5.10a). The gabbroic sample plots in the basaltic andesite field. On the Zr/Ti vs Nb/Yb diagram however all samples plot as (tholeiitic) basalts, although the array is relatively variable (Figure 5.10b).
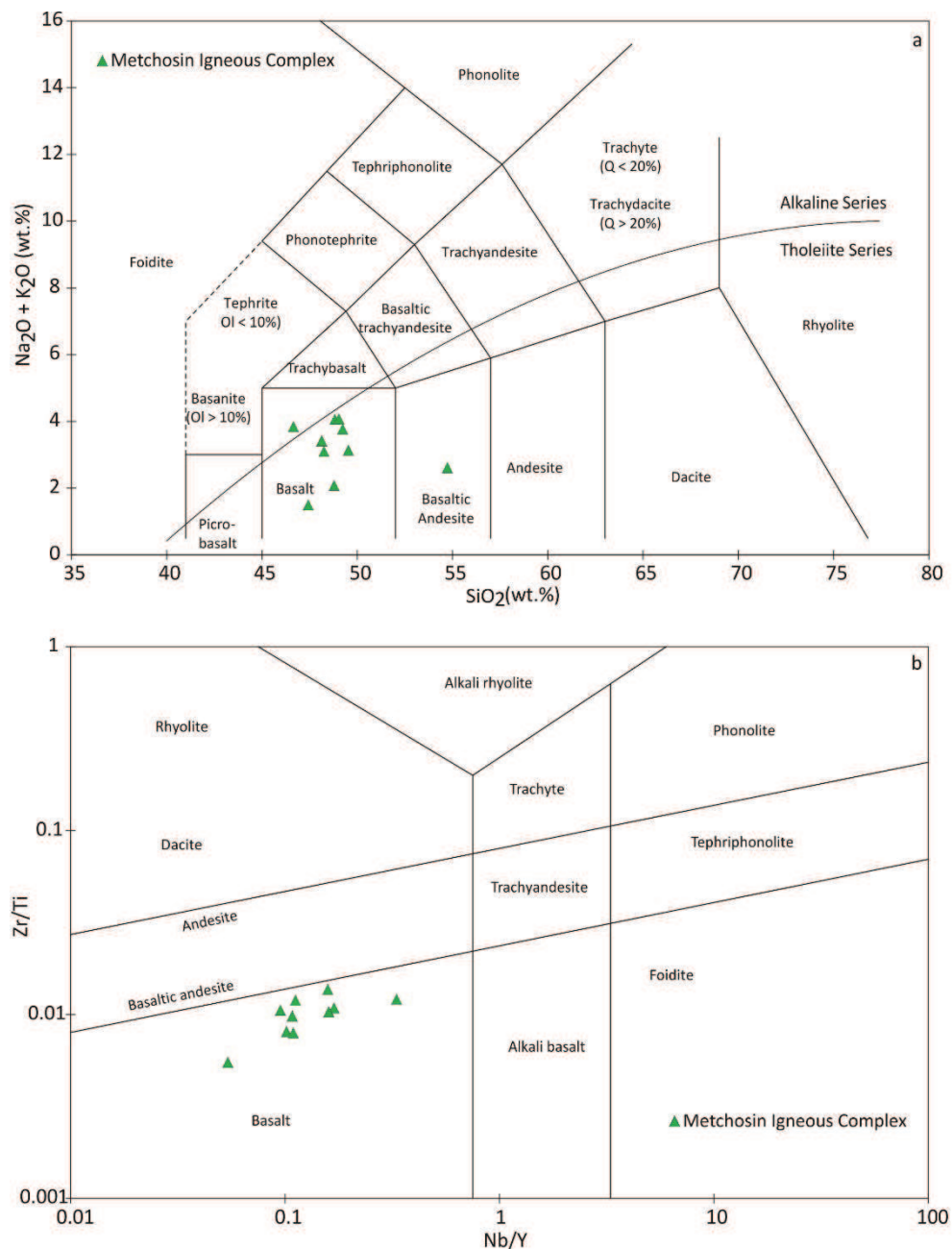
Figure 5.10 a) Total alkali silica classification diagram (Le Bas et al., 1986) and b) Zr/Ti vs. Nb/Y classification diagram (Pearce, 1996) for the Metchosin Igneous Complex samples.

5.4 Major Elements

5.4.1 Siletz River Formation, Oregon

5.4.1.1 Roseburg

The Roseburg Group show a relatively narrow range in most major elements (Figure 5.11), with the exception of MgO, which varies between 5.1 and 7.4 wt.% MgO. The Coquille Group display a similar range to the Roseburg Group in most major elements, with the exception of MgO, which extends to higher values (7.2 – 7.8 wt.%). While the Red Hill Group has narrow range in MgO (6.37 – 6.55 wt.%) the remainder of major oxides have much larger variations (e.g., TiO_2 of 1.08 – 2.34 wt.%.).

Major elements in the Roseburg Group displaying little variation over an increasing MgO wt.% (Figure 5.11). The Coquille Group is relatively removed from the remainder of the groups in the K_2O vs MgO plot (Figure 5.11). The Roseburg and Sugarloaf Groups tend to have higher CaO wt.% contents while the Coquille Group displays an inverse correlation between CaO and MgO. The TiO_2 of the Coquille Group increases with decreasing MgO wt.% while the Roseburg Group TiO_2 remains relatively constant with changing MgO.
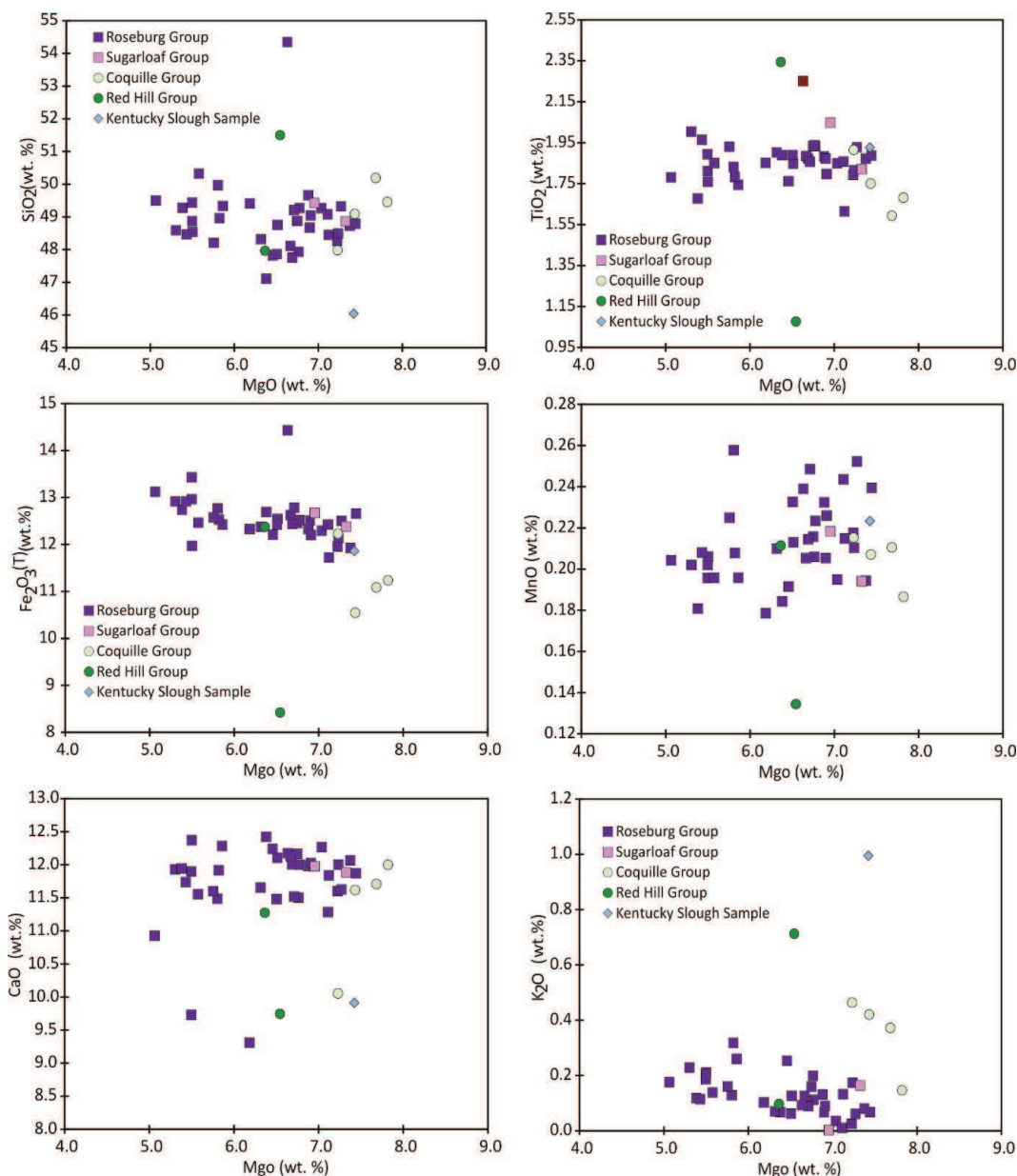
Figure 5.11 Bivariate diagrams of selected major elements vs. MgO for the Roseburg samples.

5.4.1.2 Siletz River

The Corvallis and Tillamook Groups display similar ranges of MgO (2.91 – 9.03 wt.% and 3.69 – 8.72 wt.% respectively) and generally have similar concentrations of most major elements (Figure 5.12). On the TiO₂ vs MgO plot (Figure 5.12) the Corvallis Group displays a curved trend and although the Corvallis Group spans a wide range of MgO contents it shows little variability in

the other major oxides. The Siletz River Group has higher major element abundances than the other groups for most elements for a given MgO wt.% [e.g., MnO, (Figure 5.12)] and displays the narrowest range of MgO concentrations of all groups in this area (5.40 - 7.14 wt.%). The Siletz River Group also tends to plot in clusters on the major element variation diagrams (Figure 5.12). The Alkali Group displays the greatest amount of variation in all major elements except for MgO and MnO (e.g., a TiO_2 range of $1.38 - 4.33$ wt.%).
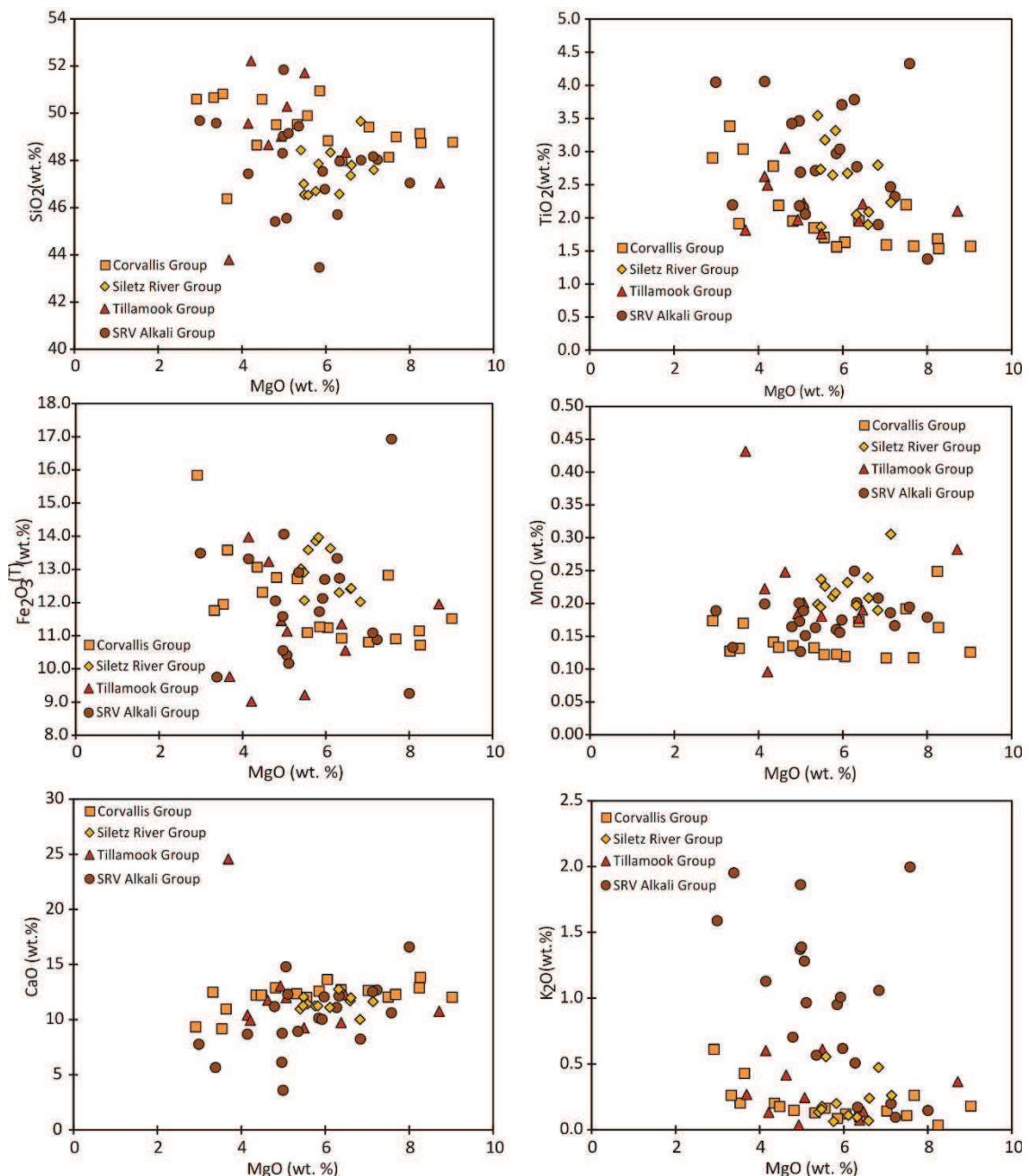
Figure 5.12 Bivariate diagrams of selected major elements vs. MgO for the Siletz River samples.

5.4.2 Crescent Formation, Washington

5.4.2.1 North Crescent

All three North Crescent groups tend to display scattered trends between the major element oxides and MgO (Figure 5.13). While the three groups in this area overlap in MgO the Depleted Crescent Group tends to cluster at highest MgO concentrations (6.45 – 10.27 wt.%), the Crescent Main Group has the largest range in MgO abundances (1.33 – 9.02 wt.%) and the Bremerton Group tends to display lower MgO concentrations overall (1.67 – 7.53 wt.%). On Figure 5.13 CaO wt.% displays a positive correlation with MgO in the Bremerton Group while the remainder of the oxides show scattered trends, with increasing concentrations of SiO_2, TiO_2 and Fe_2O_3 with decreasing MgO wt.% , although a second high TiO_2, low MgO trend is also evident. The Crescent Main Group is relatively compositionally variable (e.g., a TiO_2 of 0.69 – 2.81 wt.% and a SiO_2 of 45.99 – 57.75 wt.%). TiO_2 and Fe_2O_3 tend to increase with decreasing MgO contents, while CaO and Al_2O_3 decrease with falling MgO (Figure 5.13). While the Depleted Crescent Group has consistently narrower ranges in major element abundances, for example, TiO_2 contents of between 0.72 – 1.47 wt.%.
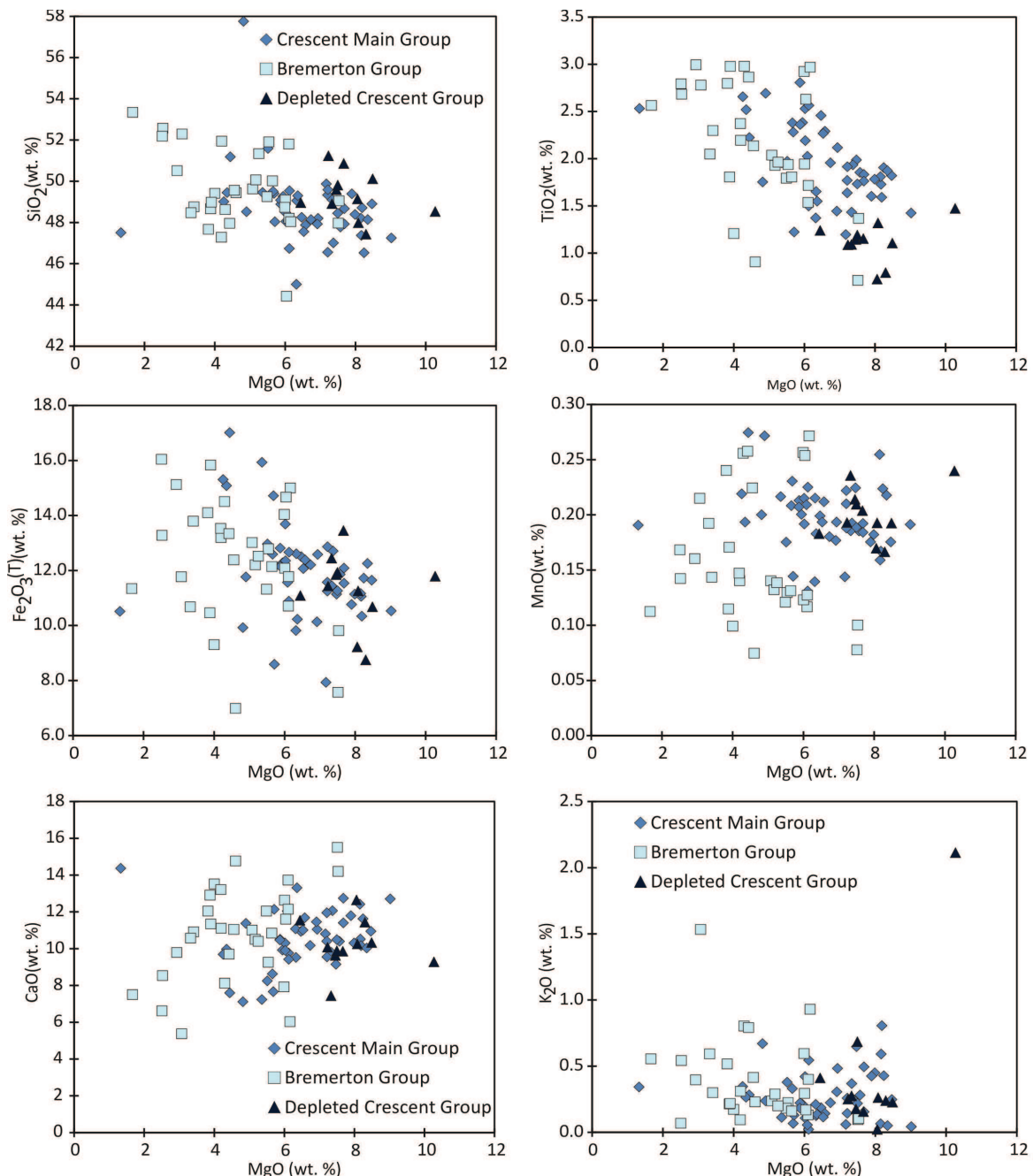
Figure 5.13 Bivariate diagrams of selected major elements vs. MgO for the Crescent North samples.

5.4.2.2 South Crescent

In terms of the South Crescent major element concentrations the Black Hills Group and Willapa Group broadly overlap in abundances (Figure 5.14), with the Black Hills Group extending to higher MgO concentrations (4.9-7.9 wt.% MgO) and the Willapa Hills Group to lower abundances (4.3-7.3 wt.% MgO). The

Black Hills Group and Willapa Hills Group have relatively consistent SiO_2 abundances for a given MgO (47.05 – 49.91 wt.% and 47.31 – 49.50 wt.% respectively), along with increasing TiO_2 concentrations with decreasing MgO (Figure 5.14). All other major elements plot as clusters on Figure 5.14 for the Black Hills and Willapa Hills Groups (e.g., CaO). The Doty Hills Group samples have relatively low MgO contents (3.2 - 5.8 wt.%) but display greater variations in other major elements (e.g., 1.99 – 4.35 wt.% TiO_2). The Doty Hills group generally displays moderate correlations between the major element oxides and MgO in comparison with the low degrees of correlation observed in the other groups. The Ilwaco Group, which only consists of 2 samples, has low MgO contents (4.18 – 4.64 wt.%) and tend to overlap with the extremities of the Black Hills and Willapa Hills Groups major element ranges.
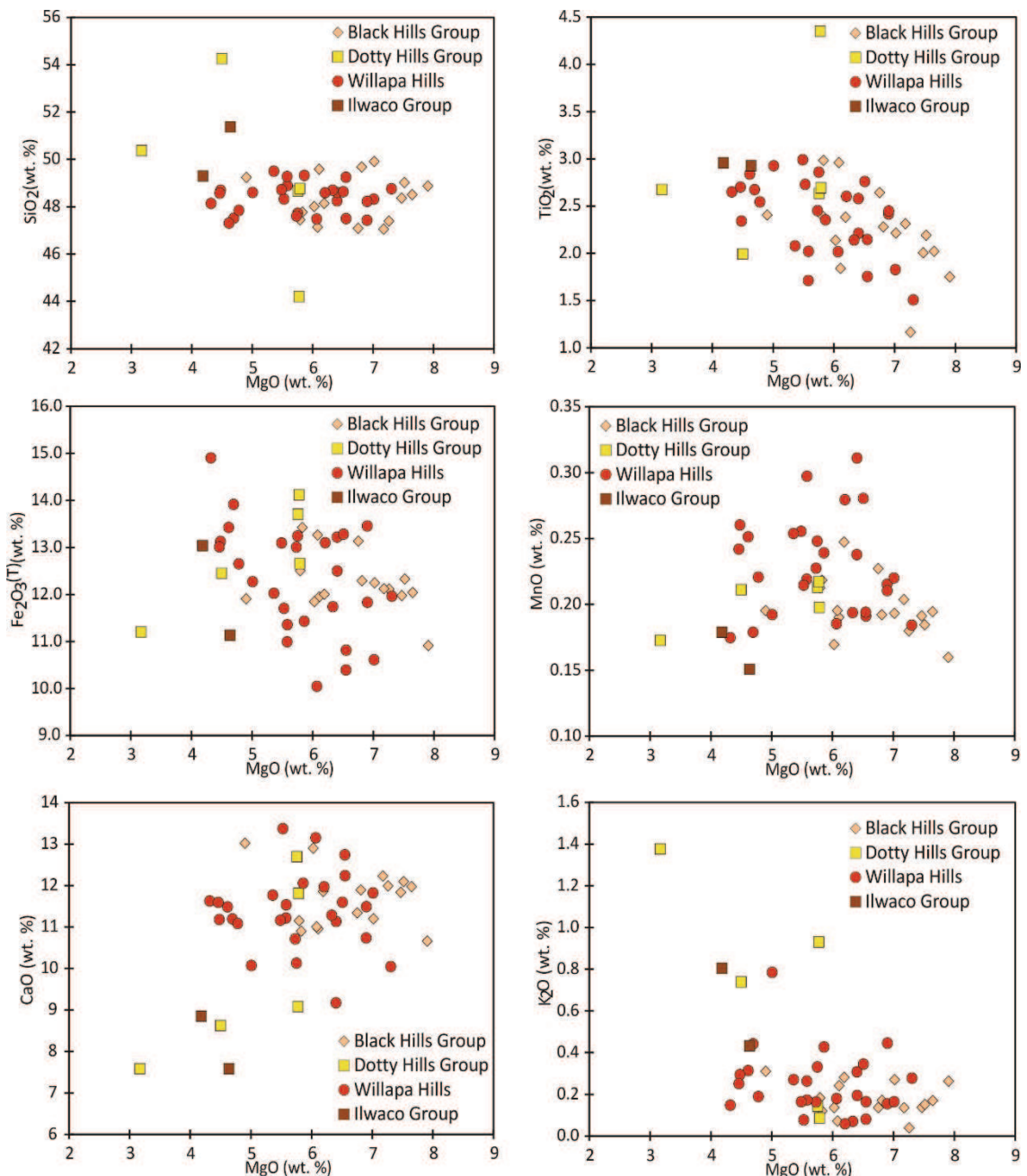
Figure 5.14 Bivariate diagrams of selected major elements vs. MgO for the Crescent South samples.

5.4.3 Metchosin Igneous Complex, Vancouver Island

The rocks of the Metchosin Igneous Complex have a broad range of MgO concentrations (4.82 – 8.78 wt.%) and the upper basalts tend to exhibit the highest

MgO abundances of the rocks (Figure 5.15). While the large variation observed in the SiO_2, TiO_2 and $Fe_2O_3^{(T)}$ concentrations can be attributed to the gabbroic sample (Figure 5.15).
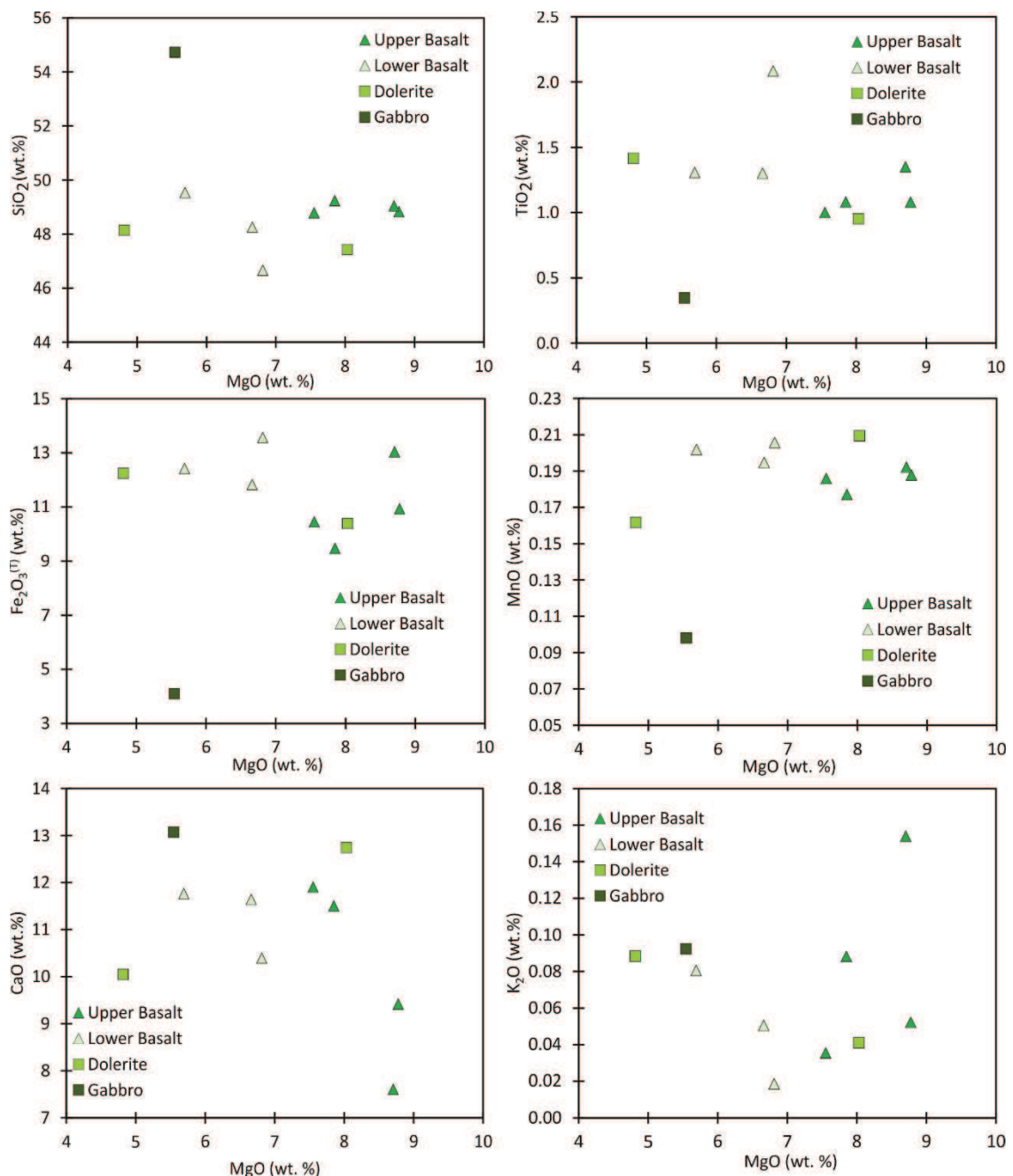
Figure 5.15 Bivariate diagrams of selected major elements vs. MgO for the Metchosin Igneous Complex samples.

5.5 Trace Elements

5.5.1 Siletz River Formation, Oregon

5.5.1.1 Roseburg

In the Roseburg Group the Cr abundance varies from 86 – 203 (ppm) and Ni between 43 – 170 (ppm), while the Coquille Groups Cr varies between 192 – 389 (ppm) and the Ni between 114 – 126 (ppm). The Roseburg Group is generally scattered in the Ni and Cr plots, overlapping with the other groups in this area, except for the Coquille Group which displays higher Ni, Cr and MgO concentrations. The groups for this region display little variation in La and Th with the exception of the Kentucky Slough sample (Figure 5.16). While the Roseburg and Coquille Groups display more variation in the Gd and Yb plots (Figure 5.16) the Red Hill Group shows the greatest amounts of variation in trace element concentration. In addition the Kentucky Slough sample is most enriched in the most incompatible trace elements.
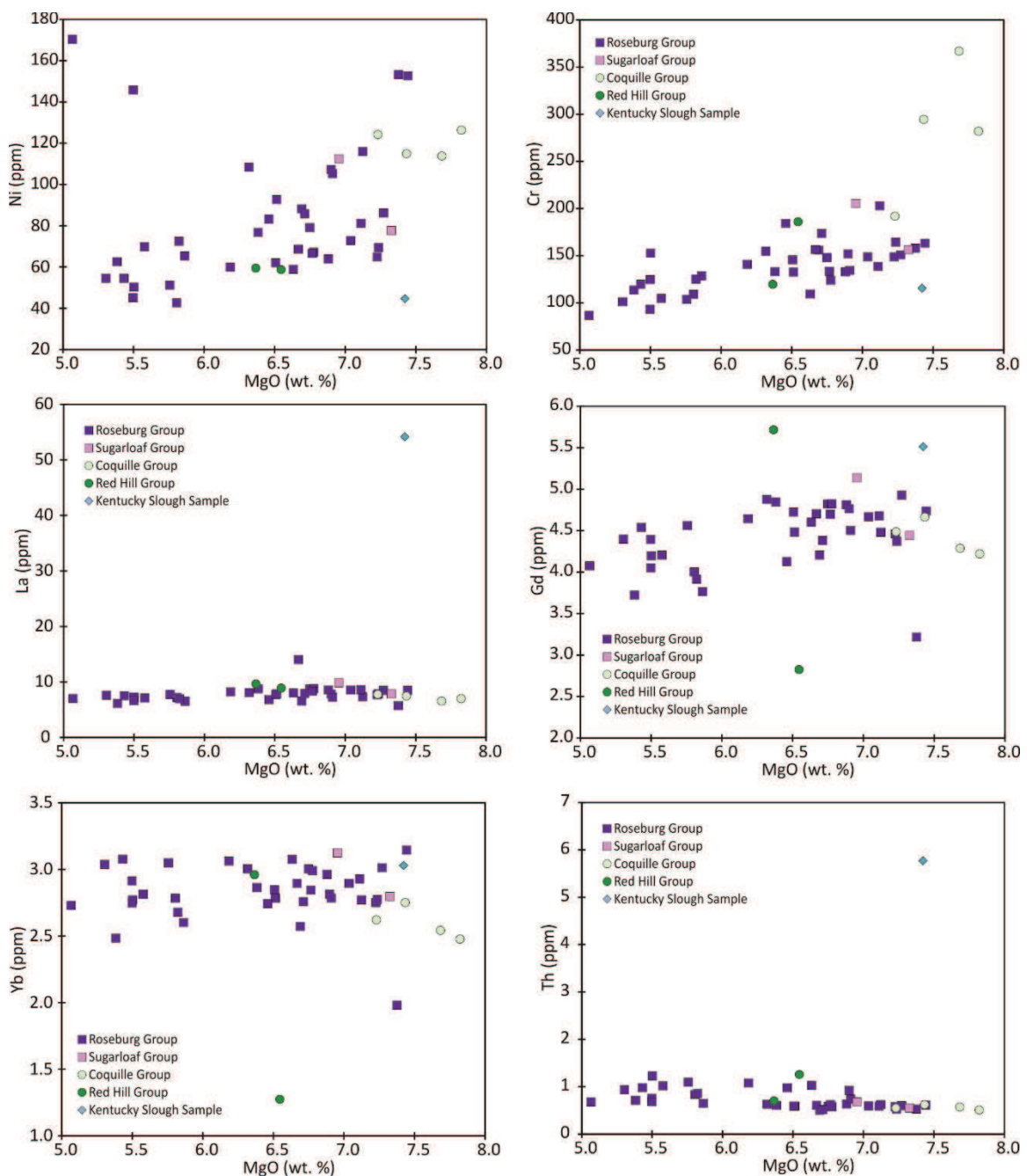
Figure 5.16 Bivariate diagrams of representative trace elements vs. MgO for the Roseburg samples.

The Roseburg Group samples display La/Sm $_{(CN)}$ values between 1.0 – 2.1, along with an additional anomalous sample, 012/2RO, which has a comparatively enriched LREE pattern (La/Sm $_{(CN)}$ = 6.3) (Figure 5.17). When this anomalously high sample (012/2RO) is excluded, the range of La/Sm $_{CN}$ values exhibited by the

Roseburg groups are consistent with what is observed elsewhere in the terrane. The Coquille Group also displays relatively flat patterns, in this group the La/Sm $_{(CN)}$ varies between 1.1 – 1.2, while in the Red Hill Group the La/Sm $_{(CN)}$ ranges from 1.1 – 1.9, the Sugarloaf Group from 1.2 – 1.3 and the Kentucky Slough sample has a value of 6.1. The HREE patterns are generally flat to slightly depleted (Figure 5.17) with the Roseburg Group displaying Gd/Yb $_{(CN)}$ ratios of 1.2 – 2.1, while the Sugarloaf, Coquille, Red Hill and Kentucky Slough samples have Gd/Yb $_{(CN)}$ ratios ranging between 1.3 and 1.8.
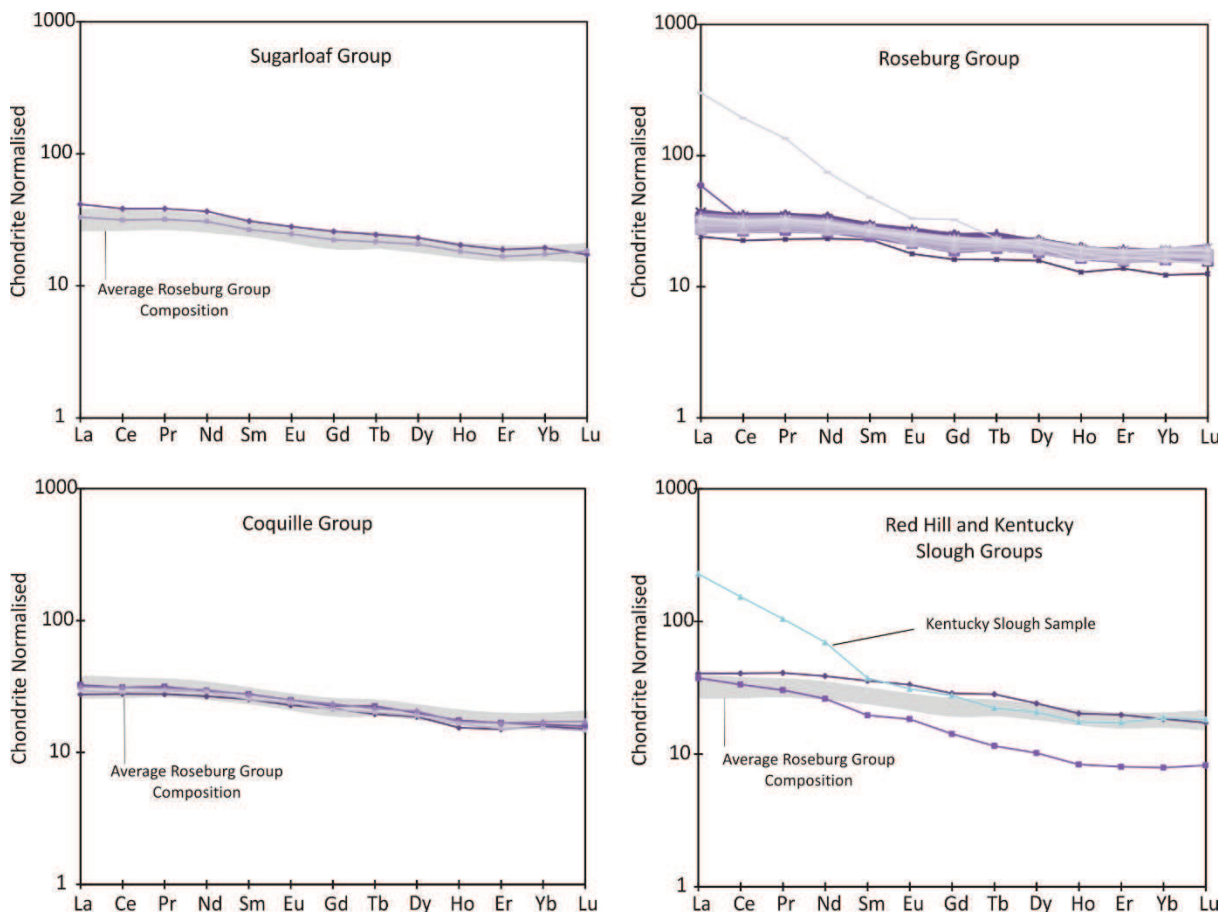
Figure 5.17 Chondrite normalised REE plots for the Roseburg samples.

On a primitive mantle normalised diagram (Figure 5.18) the Roseburg Group, as with the REE plots, are slightly more enriched in the most incompatible elements and display subparallel trends relative to the trace element concentrations in the primitive mantle. . In addition, trace element anomalies, which denote significant enrichments or depletions in normalised trace elements

relative to adjacent elements, are used to assess if a particular petrogenetic process has occurred (Briqueu et al., 1984). Both negative and positive Sr anomalies are observed in all groups in this region. Positive Nb -Ta[1] anomalies are common in this group with Nb/Nb* values of up to 1.8 and Ta/Ta* values of up to 1.6, while small positive Ti anomalies are also observed in the Roseburg Group (Ti/Ti* of up to 1.3). A positive Nb-Ta anomaly is also observed in the other groups of this area, as seen in Figure 5.18. However, sample 095RO of the Red Hill Group exhibits a negative Nb-Ta anomaly (Nb/Nb* = 0.5, Ta/Ta* = 0.5). Negative Th anomalies are also generally observed in samples from this region.

Equation 5.3 $Eu/Eu^* = Eu/\ 0.5 \times (Gd + Sm)$
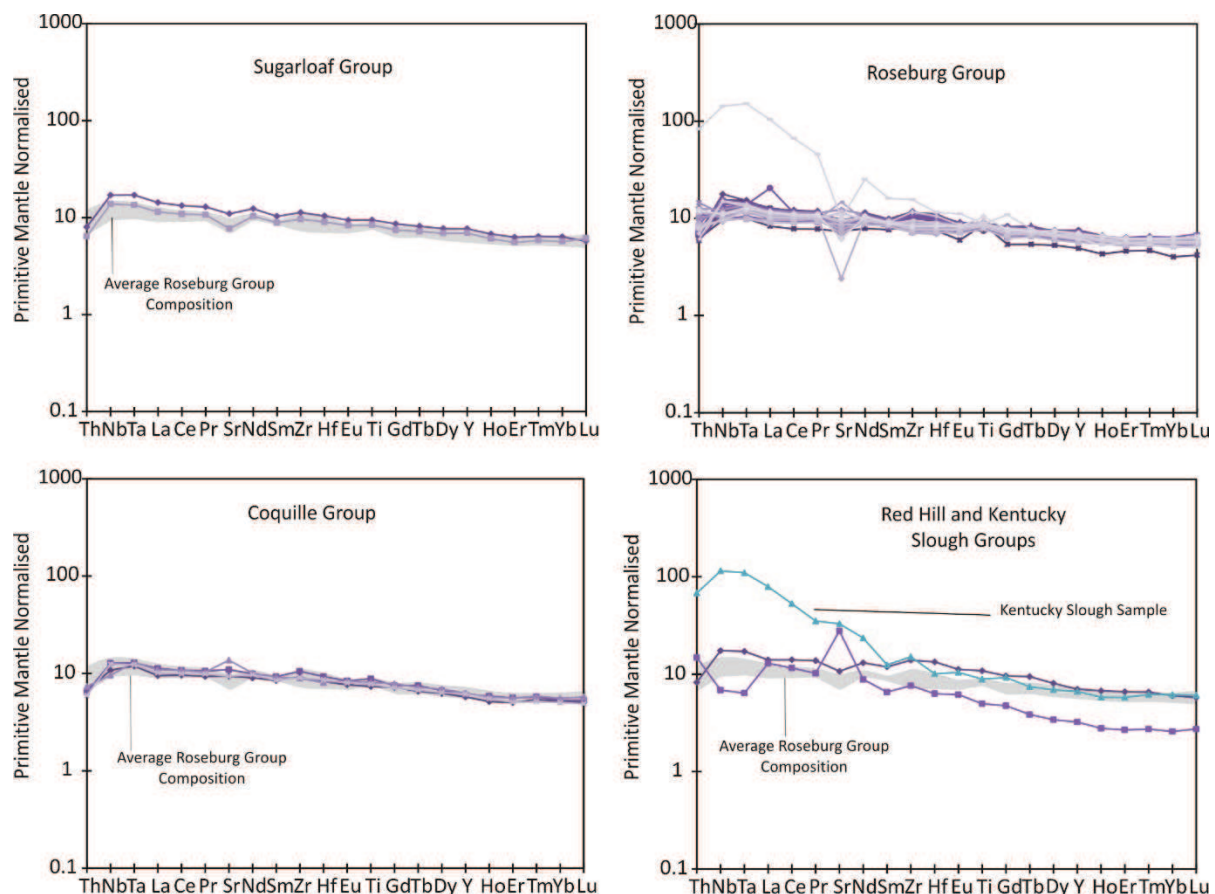
Figure 5.18 Primitive mantle normalised multi-element diagrams for the Roseburg samples.

---

[1] $Na/Nb^* = Nb/0.5 \times (Th + La)$ and $Ta/Ta^* = Ta/\ 0.5 \times (Th + La)$

The diagrams in Figure 5.19 are used to try and constrain the tectonic environment in which the rocks were erupted and emplaced. Generally, the Rosburg samples are clustered in all plots in Figure 5.19, plotting in the MORB/OIB field/ Iceland plume array on all diagrams. However, sample 073RO and 012/2 both plot within the OIB field. In the Nb/Th vs. Zr/Nb plot (Figure 5.19d) all of the Roseburg Groups plot in the Oceanic Plateau Basalt (OPB) field, except the Kentucky Slough sample, which consistently plots in the OIB field. It is worth noting however, that the OPB field overlaps somewhat with the arc field on figure 5.19d and a few of the samples plot in both the arc and OPB fields.
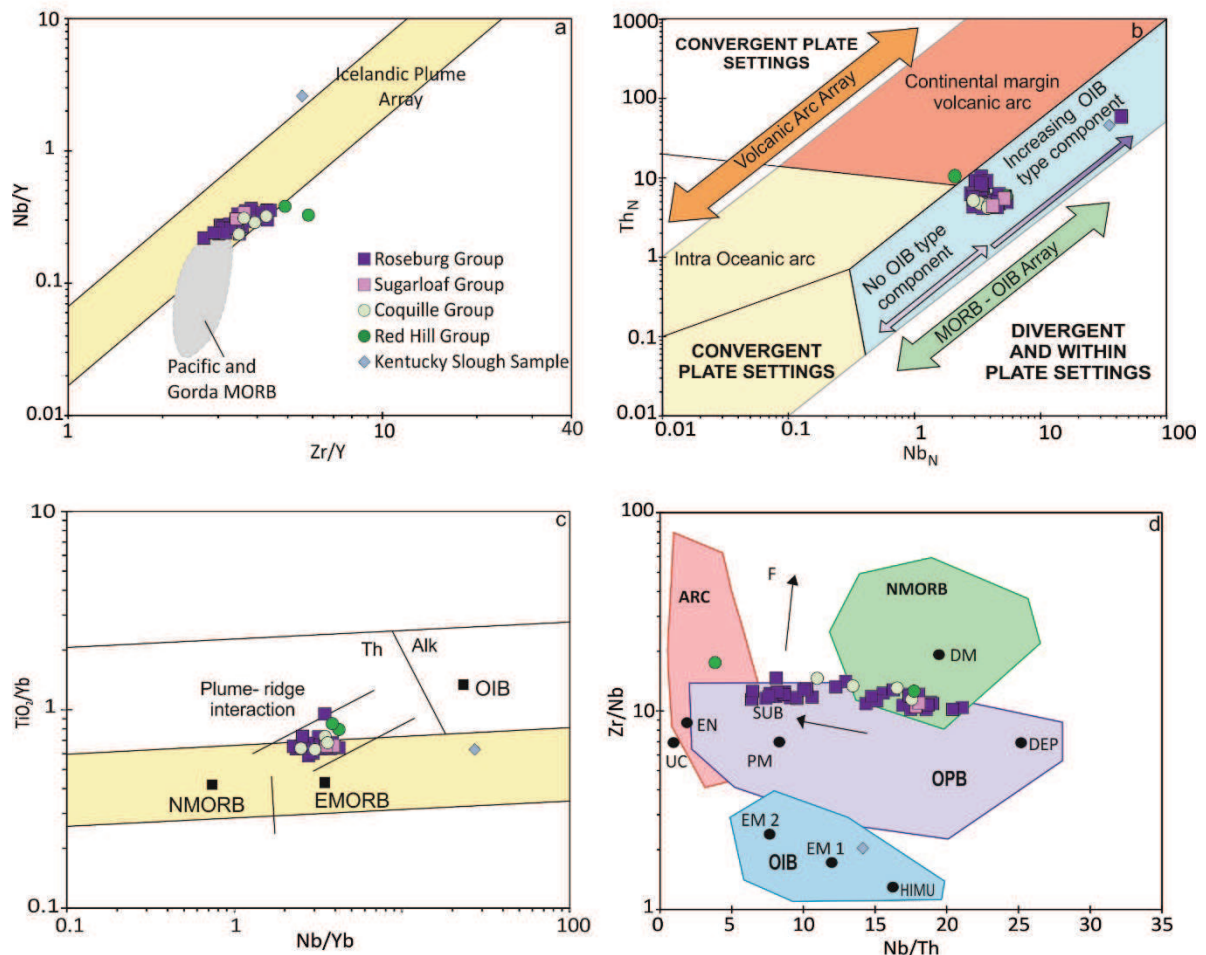
Figure 5.19 For comparison the samples have been plotted on the a) Fitton et al., (1997) Icelandic plume array diagram; b) Ophiolitic basalt tectonic discrimination diagram (Saccani, 2014); c) Proxy for deep melting diagram (Pearce, 2008) and; d) the Zr/Nb vs. Nb/Th discrimination diagram (Condie, 2005). Abbreviations: UC = upper continental crust, PM = Primitive Mantle, DM = shallow depleted mantle, HIMU = high mu (U/Pb) source, EM1 and EM2 = enriched mantle sources, ARC = arc related basalts, NMORB = normal mid-ocean ridge basalt, OPB = oceanic plateau basalt, OIB = oceanic island basalt, DEP = deep depleted mantle, EN = enriched component, F = effects of batch melting and SUB = subduction effect.

5.5.1.2 Siletz River

The Corvallis Group Ni content varies from 26 – 183 (ppm) and the Cr from 62 – 318 (ppm) (Figure 5.20). The Siletz River Group Ni concentration varies from 38 – 143 (ppm), while the Tillamook Group Ni abundances varies from 25 – 169 (ppm) and the Cr from 80 – 267 (ppm) (Figure 5.20). The SRV Alkali Group have Cr contents of 5 - 324 (ppm) and Ni concentrations of 6 – 179 (ppm) (Figure 5.20). Overall for the groups of the Siletz River area the Ni and Cr

148

concentrations decrease with decreasing MgO wt.%, with significant overlap occurring for all groups. The Corvallis Group have consistently lower La, Gd and Yb abundances for any given MgO wt.% (Figure 5.20), while the Alkali Group tend to exhibit higher concentrations of these elements. The Siletz River Group have the lowest amount of variation in the incompatible trace elements.
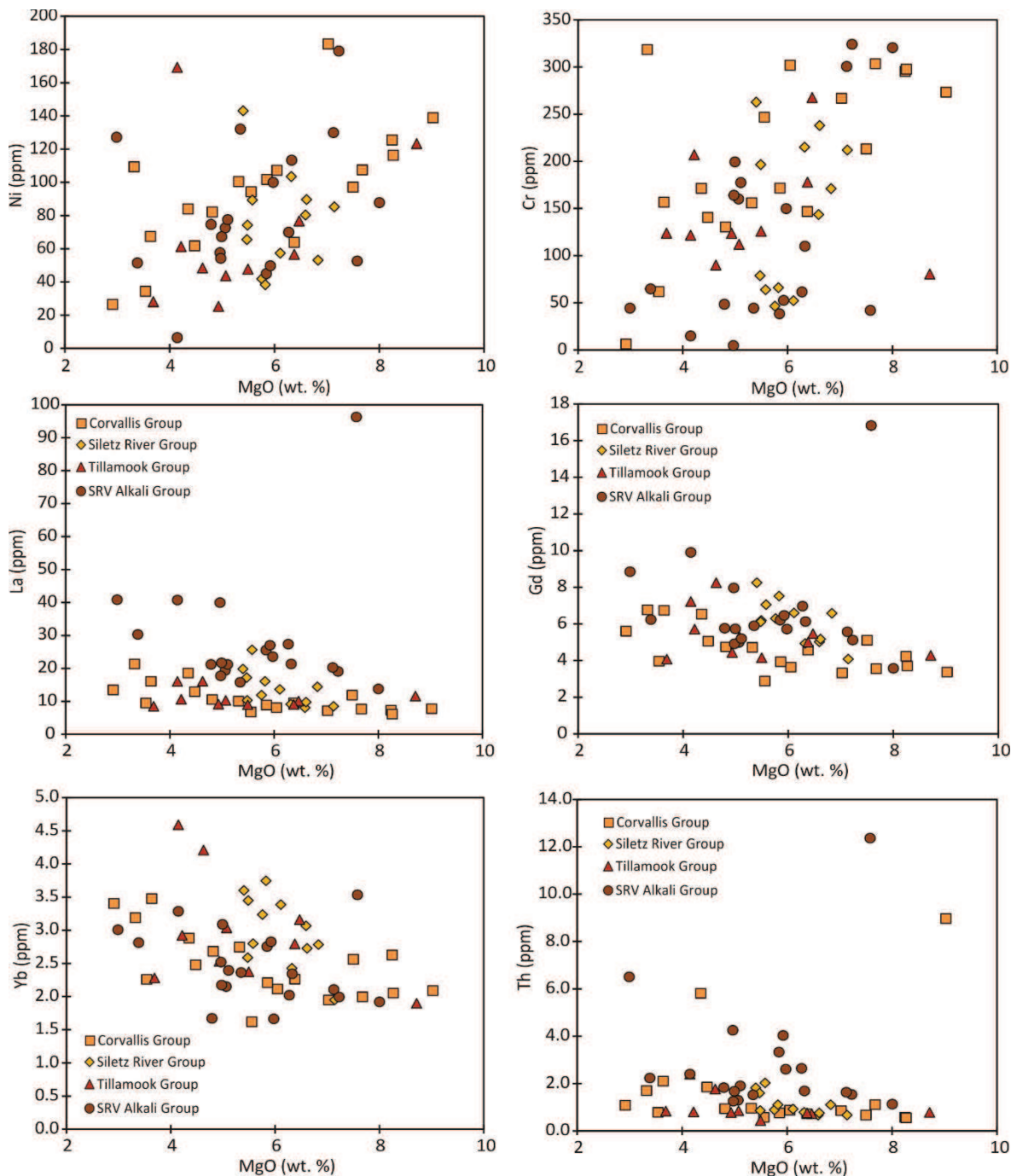
Figure 5.20 Bivariate diagrams of representative trace elements vs. MgO for the Siletz River samples.

The chondrite-normalised REE patterns for the Siletz River, Tillamook and Corvallis Groups are generally LREE-enriched (La/Sm $_{(CN)}$ of 1.2 – 2.2, 1.3 - 1.7 and 1.2 – 2.1 respectively) and slightly HREE-depleted (Gd/Yb $_{(CN)}$ of 1.3 – 2.0, 1.3 – 1.8 and 1.3 – 1.8) (Figure 5.21). The SRV Alkali Group display

markedly more LREE-enriched (La/Sm $_{(CN)}$ of 1.8 – 3.4) and HREE-depleted patterns (Gd/Yb $_{(CN)}$ of 1.5 – 3.6) than the rest of the groups.
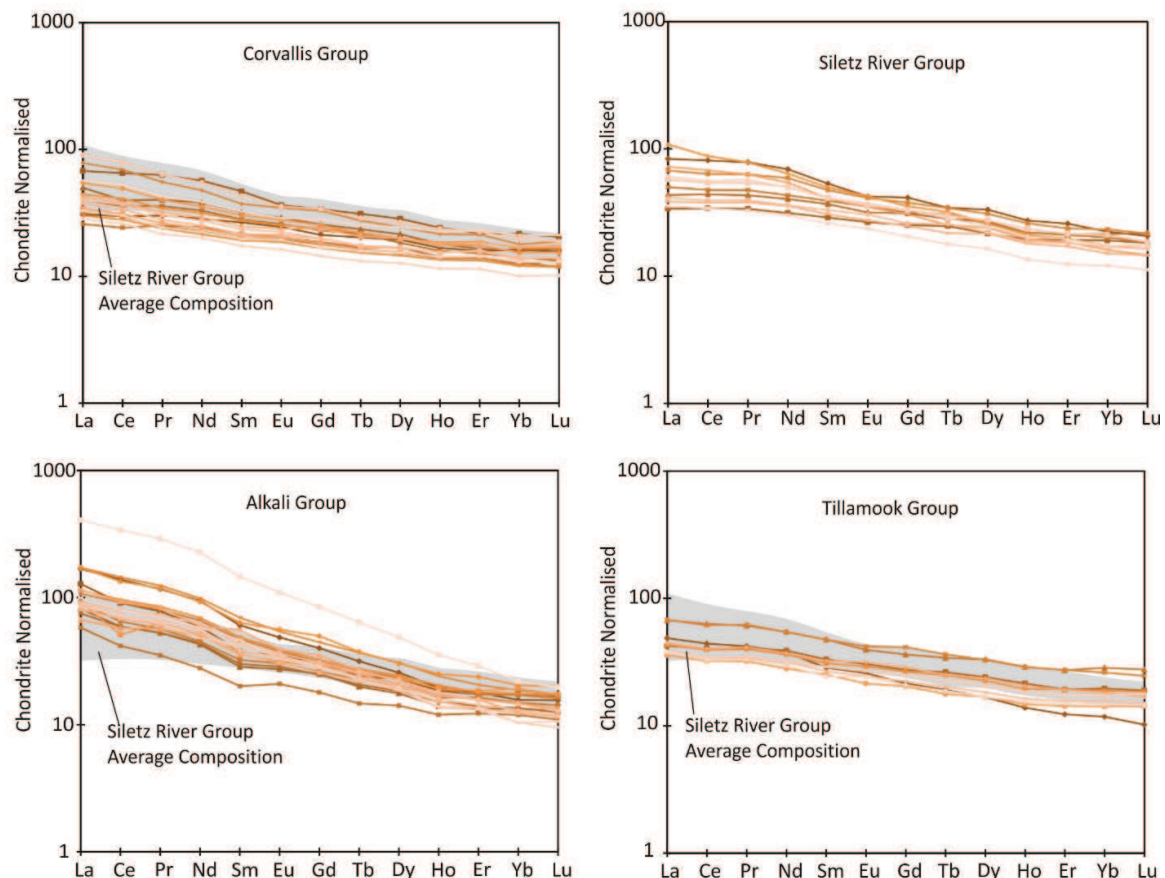
Figure 5.21 Chondrite-normalised REE plots for the Siletz River samples.

The Primitive mantle normalised patterns of all groups are slightly enriched in the most incompatible elements relative to primitive mantle (Figure 5.22). All groups also display positive Nb – Ta anomalies (the overall average Nb/Nb* = 1.2 [ranging up to 1.7] and the average Ta/Ta* = 1.3 [with a highest value of 1.8]). Positive Ti and negative Sr anomalies are also observed frequently in the SRV Alkali Group and are also present to a lesser extent in the other groups.
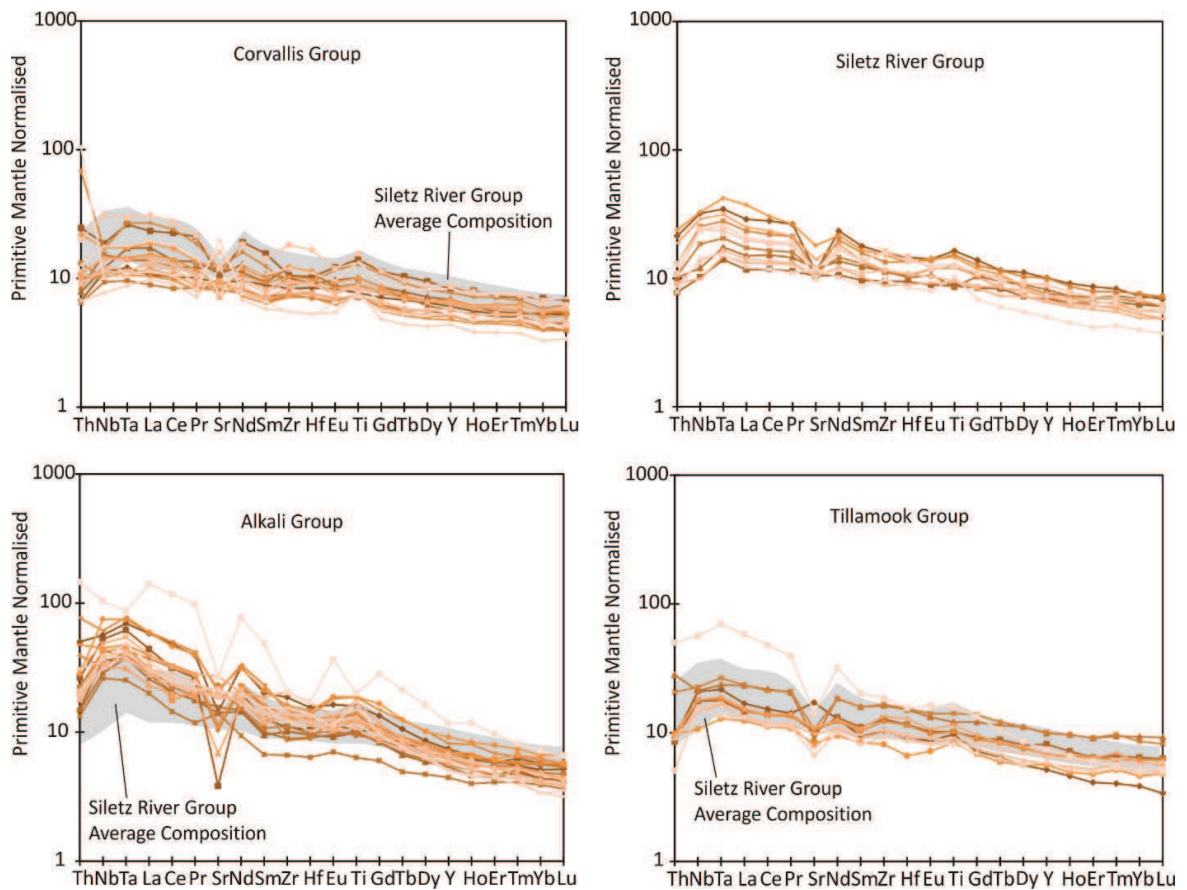
Figure 5.22 Primitive mantle normalised multi-element plots for the Siletz River samples.

On incompatible trace element plots (Figure 5.23) the Tillamook Group and both Siletz River Groups plot in a tight cluster in the Oceanic Plateau field and in the centre of the OIB – MORB arrays. The Corvallis Group also plots in the same region, however, two samples from this group also consistently overlap with the continental arc field. The Alkali Group consistently plot in the OIB/OPB fields.
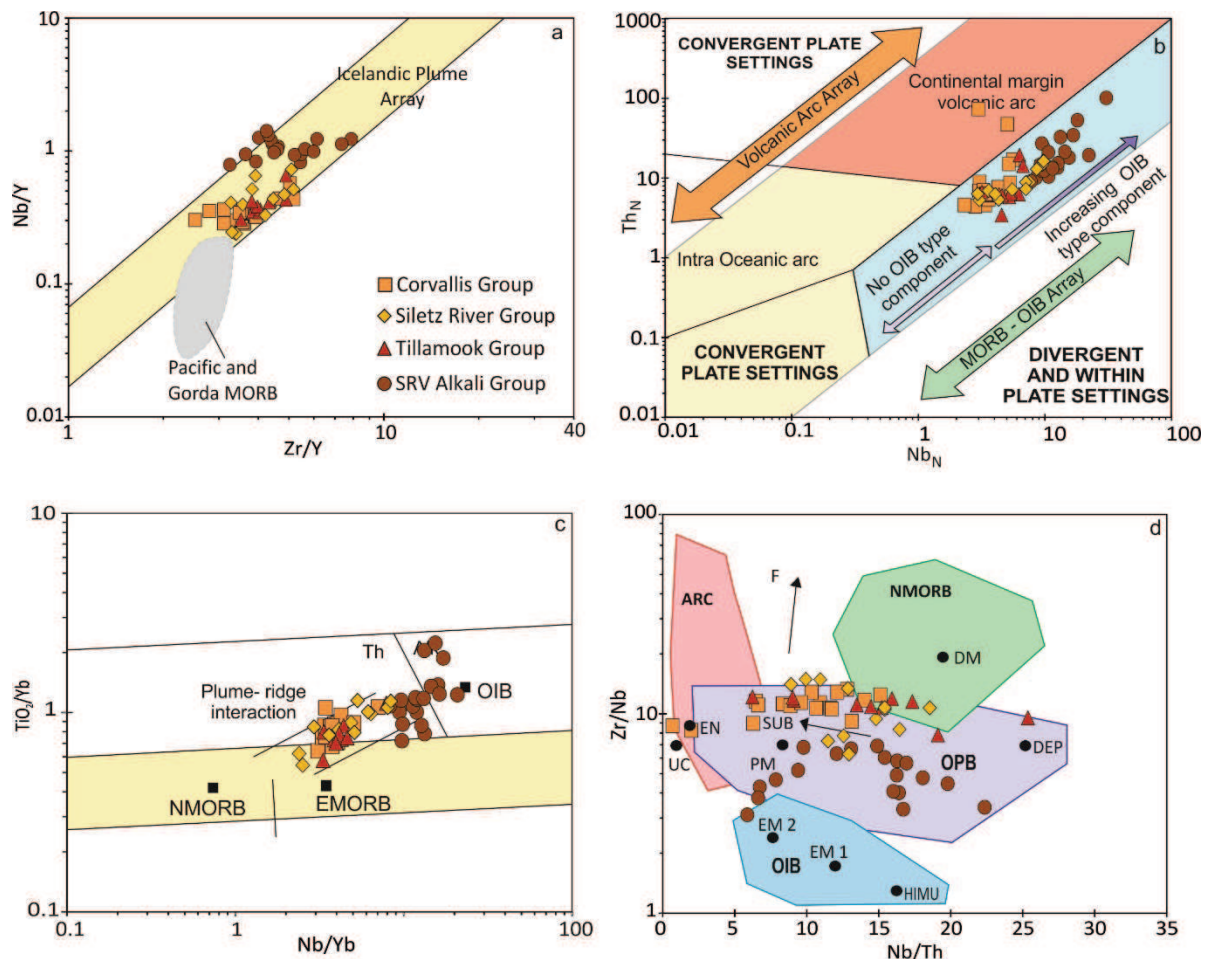
Figure 5.23 For comparison the samples have been plotted on the a) Fitton et al., (1997) Icelandic plume array diagram; b) Ophiolitic basalt tectonic discrimination diagram (Saccani, 2014); c) Proxy for deep melting diagram (Pearce, 2008) and; d) the Zr/Nb vs. Nb/Th discrimination diagram (Condie, 2005). Abbreviations: UC = upper continental crust, PM = Primitive Mantle, DM = shallow depleted mantle, HIMU = high mu (U/Pb) source, EM1 and EM2 = enriched mantle sources, ARC = arc related basalts, NMORB = normal mid-ocean ridge basalt, OPB = oceanic plateau basalt, OIB = oceanic island basalt, DEP = deep depleted mantle, EN = enriched component, F = effects of batch melting and SUB = subduction effect.

5.5.2 Crescent Formation, Washington

5.5.2.1 North Crescent

The Ni and Cr contents of the Crescent Main Group varies from 9 – 279 and 15 – 484 (ppm) respectively. The Bremerton Group has a Ni content ranging from 39 – 185 (excluding the more evolved rocks which have a Ni content of 4.0) and a Cr content of (5.5 for the most evolved) 19 – 599. Finally the Depleted Crescent Group have Ni and Cr contents, which range between 58 – 219 and 94 – 416

respectively. Overall the Cr and Ni concentrations for all groups show a decrease with decreasing MgO wt.%, however, the trends are scattered and relatively inconsistent.
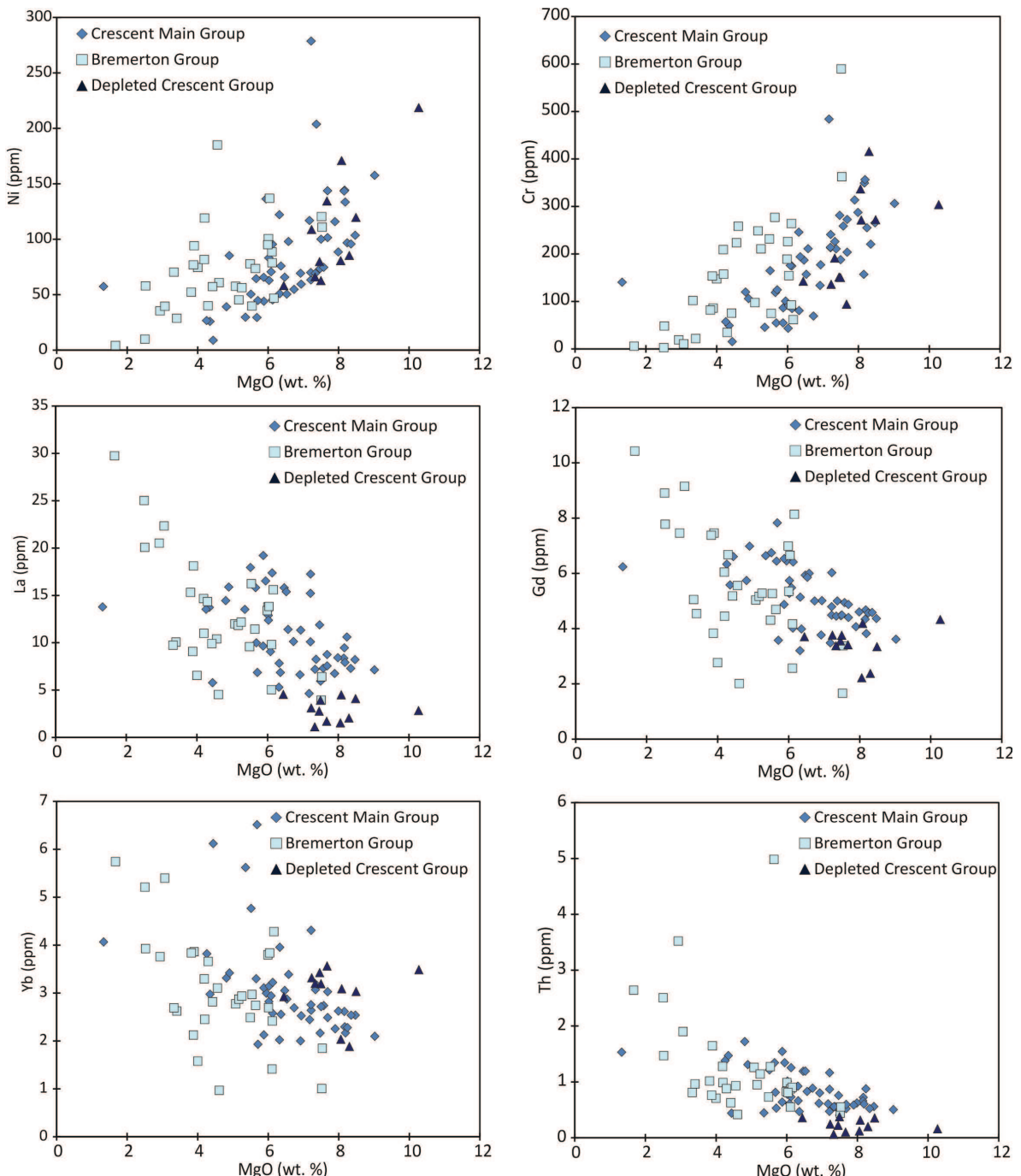
Figure 5.24 Bivariate diagrams of representative trace elements vs. MgO for Crescent North samples.

The Crescent Depleted Group generally have lower incompatible trace element concentrations than the other groups in all plots other than the Yb vs MgO plot (Figure 5.24). The Crescent Main Group plot in a relatively clustered pattern in the Yb and Th plots and have similar incompatible element concentrations at the middle MgO wt.% abundances to the Bremerton Group. The Bremerton Group generally has increasing incompatible trace element concentrations with decreasing MgO wt.% and extend to the highest concentrations of all three groups. There are no consistent differences between different rock types within the Bremerton Group, except for the leucogabbro sample, which, as expected, has low MgO wt.% abundances (Figure 5.25). The Bremerton basalts do however, have consistently higher incompatible trace element concentrations that the majority of dykes and gabbros analysed in this group (Figure 5.25). However, the three Bremerton samples with the highest incompatible trace element abundances are the leucogabbro and other intrusive rocks, which are more evolved (B024 and B020). Despite this, there is considerable overlap between the intrusive and extrusive Bremerton rocks.
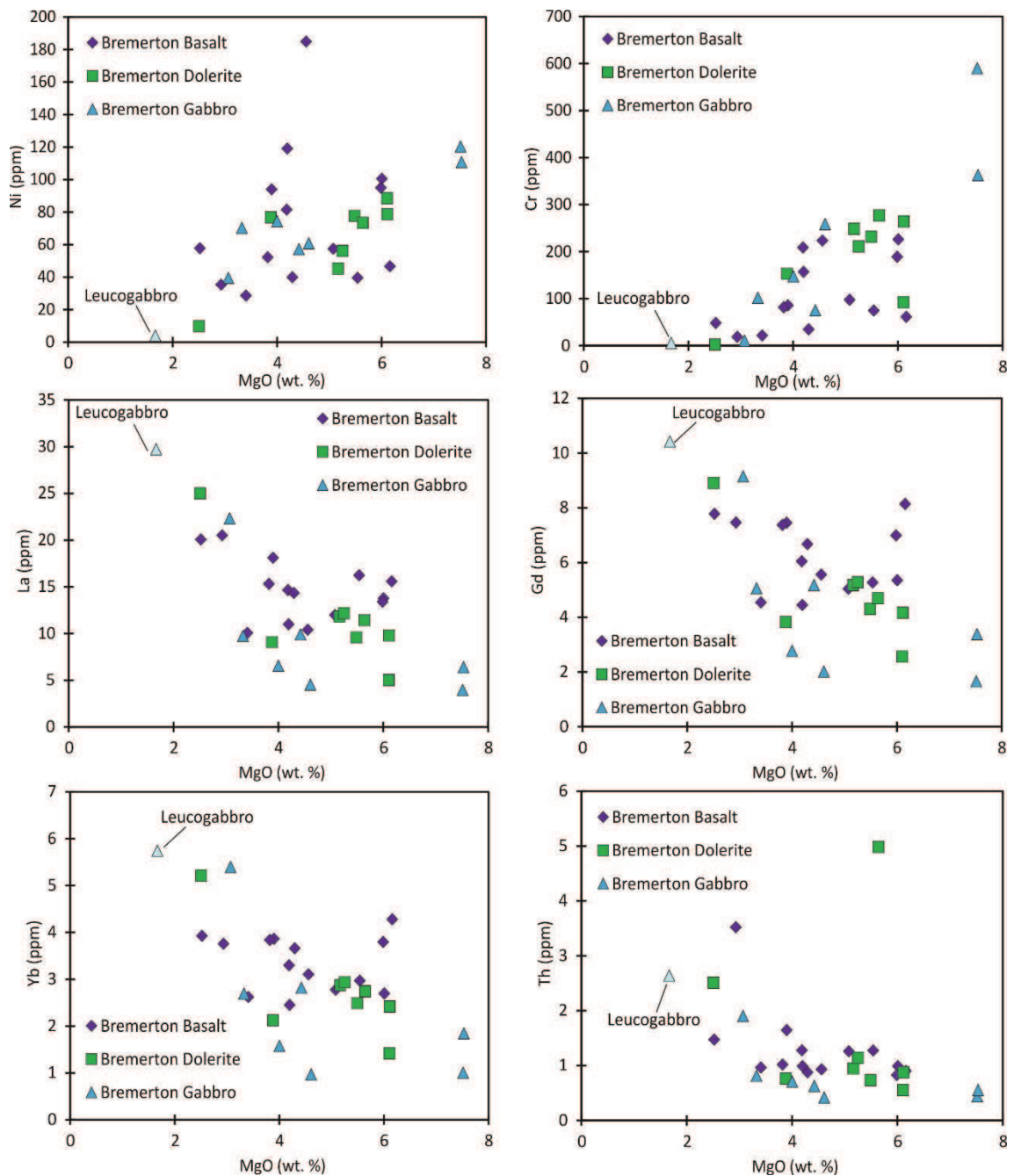
Figure 5.25 Bivariate diagrams of representative trace elements vs. MgO for the Bremerton Group samples.
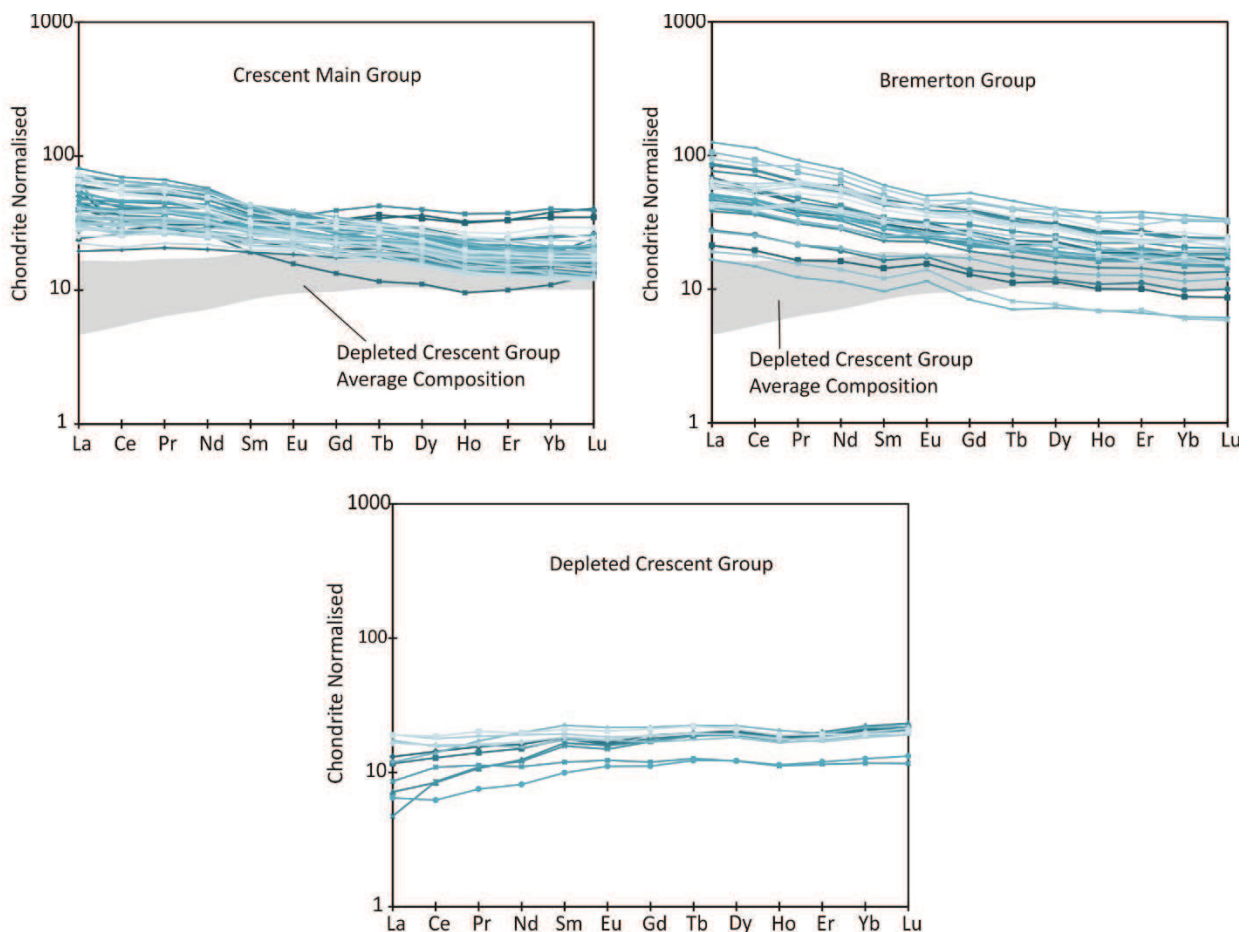
Figure 5.26 Chondrite-normalised REE plots for the Crescent North samples.

Generally the Crescent Main Group displays slightly LREE enriched chondrite-normalised patterns with a sub-set of samples, which have flatter patterns (Figure 5.26) (La/Sm $_{(CN)}$ of 0.7 – 2.5). While the Crescent Main Group has an average Gd/Yb $_{(CN)}$ slope of 1.4 (0.9 – 1.85). Overall the Bremerton Group is more enriched in LREE (La/Sm $_{(CN)}$ of 1.3 – 2.2), which is still within the range displayed by the Crescent Main Group and a flat to slightly depleted HREE pattern (Gd/Yb $_{(CN)}$ of 1.34 – 1.69). There is however, less variability in this group as expected from samples derived from a much smaller area. The Depleted Crescent Group has flat to slightly LREE depleted LREE patterns (La/Sm $_{(CN)}$ ratios of 0.3 -1.0) and also has a relatively flat HREE profile (Figure 5.26), with Gd/Yb $_{(CN)}$ ratios of 0.77 – 1.1.
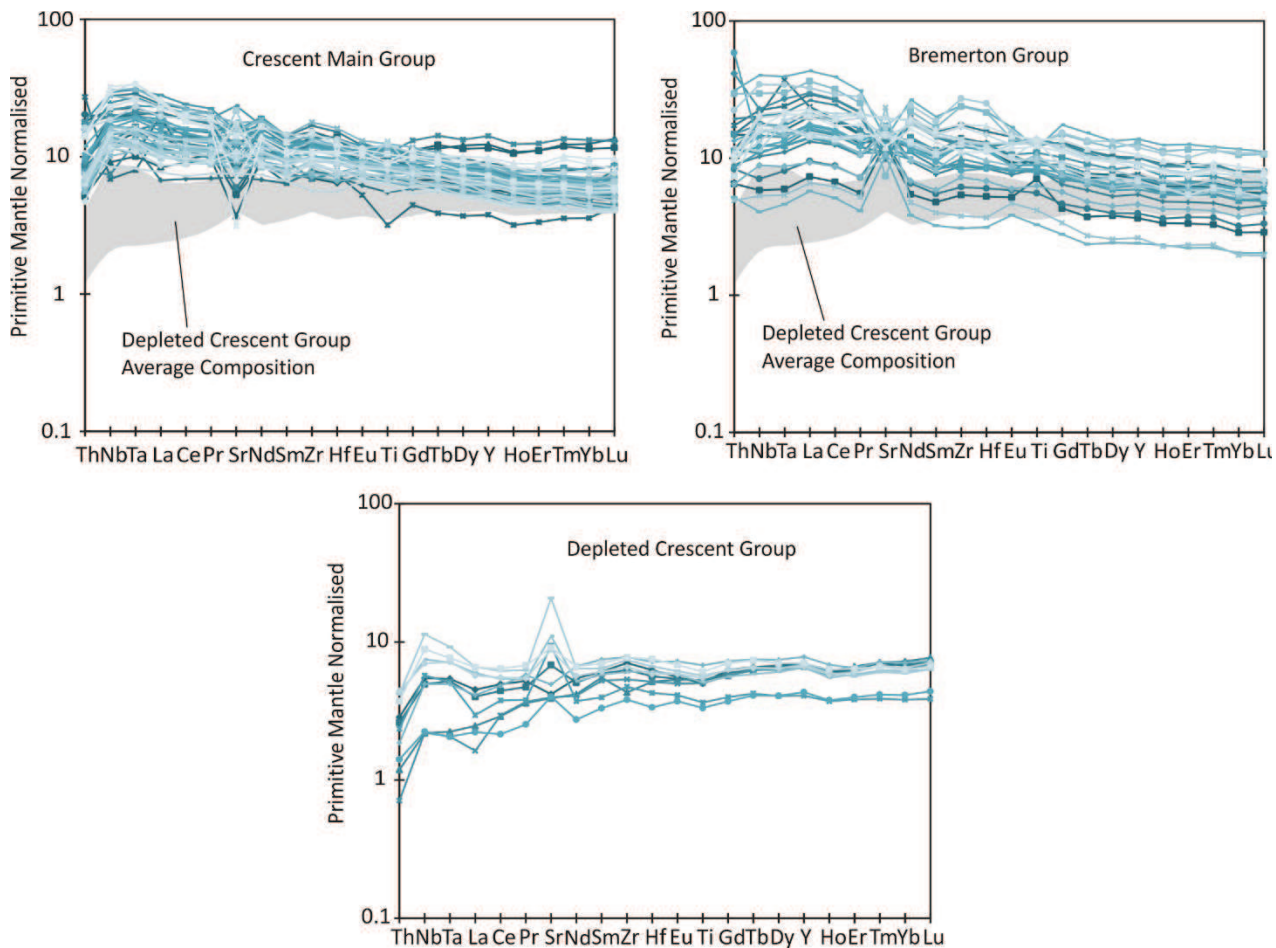
Figure 5.27 Primitive mantle normalised spider diagrams for the Crescent North samples.

The primitive mantle normalised patterns for the Crescent Main Group are generally flat, to slightly more enriched in the most incompatible elements (Figure 5.27). The Crescent Main Group frequently displays positive Nb-Ta anomalies, the largest of which has an Nb/Nb* value of 1.85 and a Ta/Ta* value of 1.7. However in 4 samples a negative Nb-Ta anomaly is also observed (Nb/Nb* < 0.31). The Bremerton Group shows a more variable range in primitive mantle normalised patterns and the samples are again slightly enriched in the most incompatible elements. The Bremerton Group does not possess Nb-Ta anomalies as significant as those observed in the Crescent Main Group and is variably enriched and depleted in Th (Figure 5.27). Positive Zr-Hf anomalies are also observed in the Bremerton Group. The Depleted Crescent Group has lower concentrations of primitive mantle normalised elements that the other two groups

and significantly, this group displays flatter to slightly depleted patterns in the most incompatible elements (Figure 5.27). Positive Nb-Ta anomalies are also observed in this group with Nb/Nb* values ranging between 1.2 and 2.2 and Ta/Ta* between 1.1 and 1.9.

On incompatible trace element ratio diagrams (Figure 5.28) the Bremerton and Crescent Main Groups cluster in the centre of the MORB OIB array/ Oceanic Plateau Basalt field, while the Depleted Group tends to cluster within and towards the MORB field on all discrimination diagrams in Figure 5.28 slightly

overlapping with the Pacific and Gorda MORB field on Figure 5.28a.
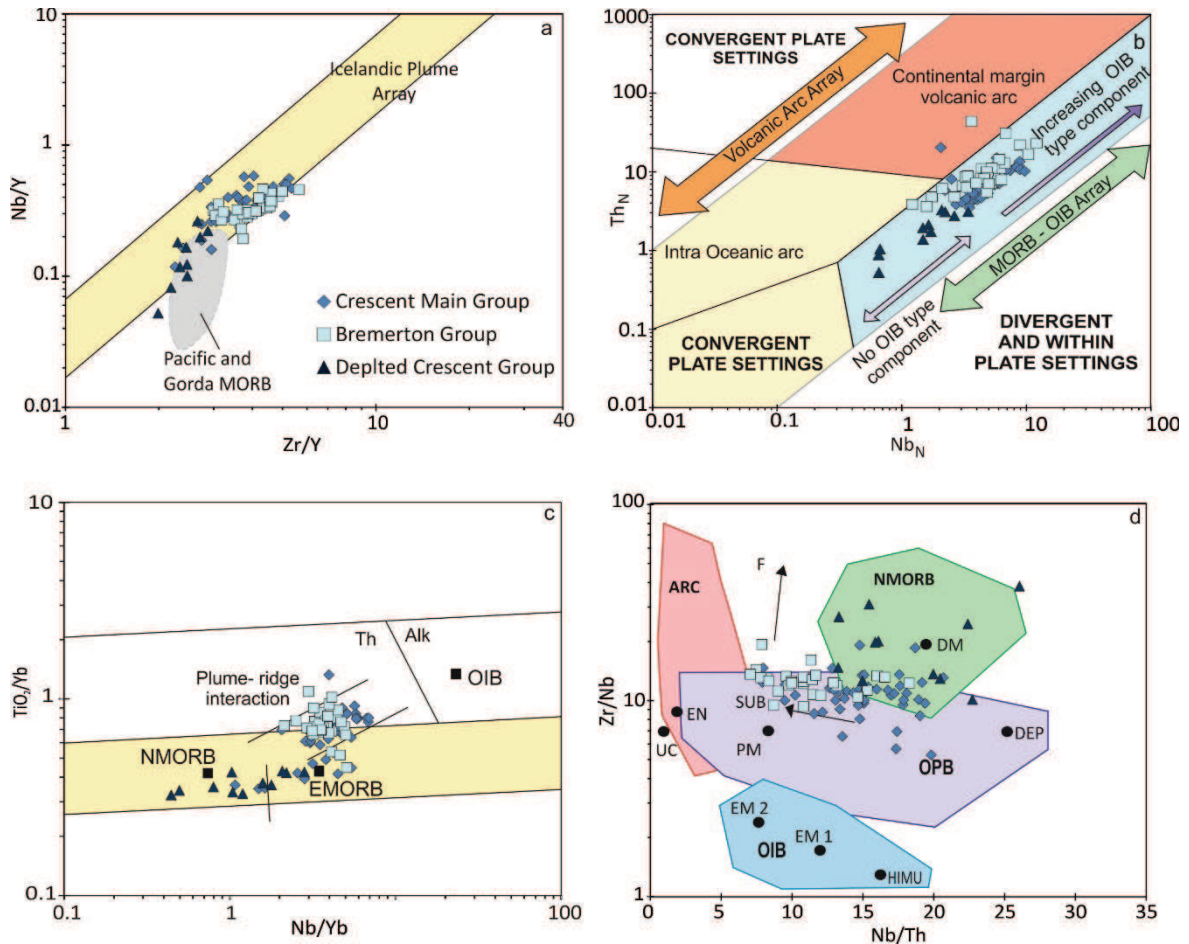
Figure 5.28 For comparison the samples have been plotted on the a) Fitton et al., (1997) Icelandic plume array diagram; b) Ophiolitic basalt tectonic discrimination diagram (Saccani, 2014); c) Proxy for deep melting diagram (Pearce, 2008) and; d) the Zr/Nb vs. Nb/Th discrimination diagram (Condie, 2005). Abbreviations: UC = upper continental crust, PM = Primitive Mantle, DM = shallow depleted mantle, HIMU = high mu (U/Pb) source, EM1 and EM2 = enriched mantle sources, ARC = arc related basalts, NMORB = normal mid-ocean ridge basalt, OPB = oceanic plateau basalt, OIB = oceanic island basalt, DEP = deep depleted mantle, EN = enriched component, F = effects of batch melting and SUB = subduction effect.

5.5.2.2 South Crescent

The Ni and Cr concentrations of the Black Hills Group vary between 56 – 202 and 88 – 373 respectively. The Dotty Hills Group Ni and Cr range between 3 – 619 and 7 – 186 respectively. The Willapa Hills Group Cr and Ni range between 86 – 268 and 48 –267. Both the Black Hills and Willapa Hills Groups have decreasing Ni and Cr with decreasing MgO wt.%. There is also considerable

overlap between the Black Hills and Willapa Hills Groups in all plots in Figure 5.29, with the Black Hills Group extending to higher MgO wt.% and slightly lower incompatible trace element concentrations. The Doty Hills and Ilwaco Groups consists of less samples, however they are more enriched in the majority of the incompatible elements than the other groups.
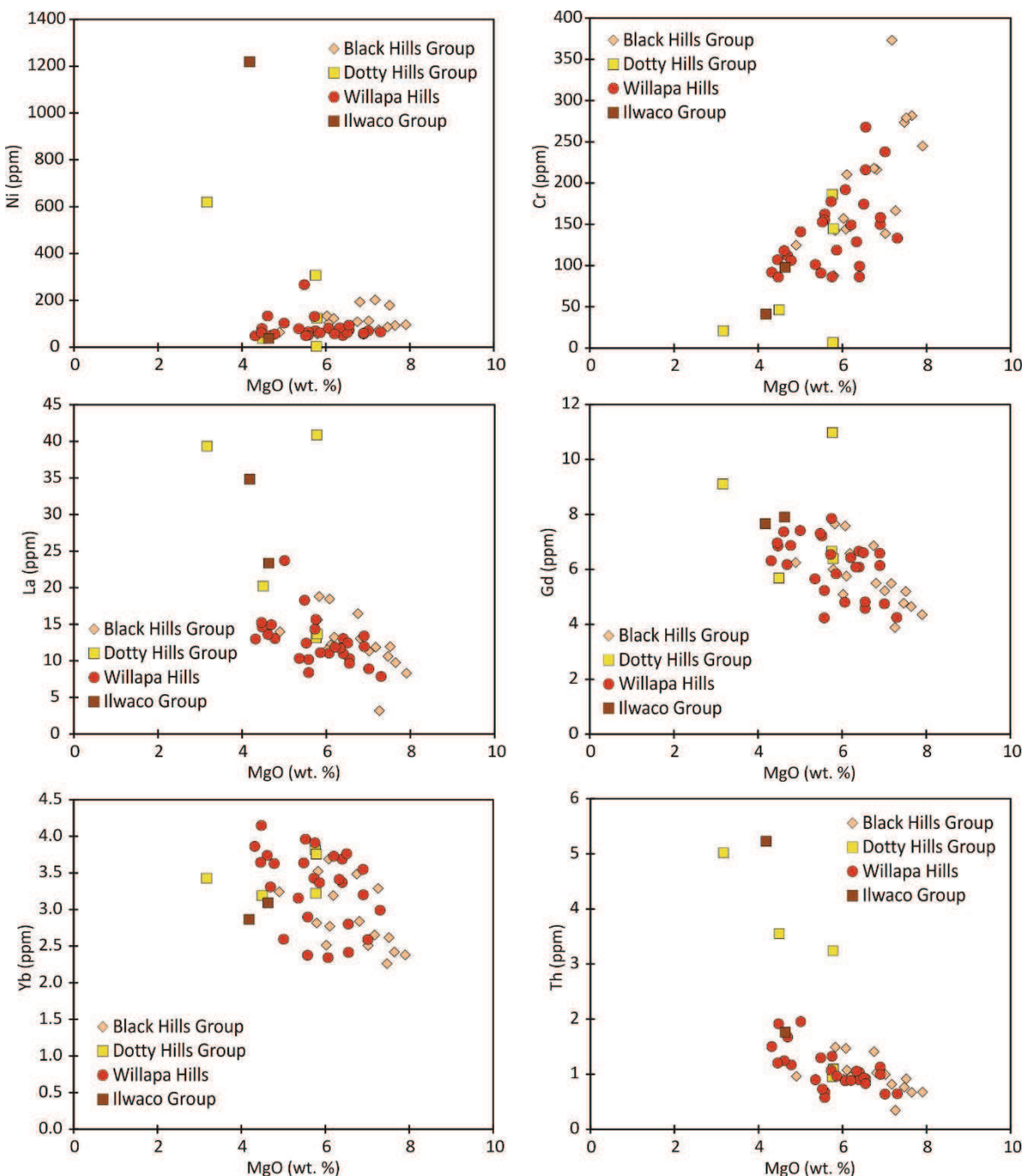
Figure 5.29 Bivariate diagrams of representative trace elements vs. MgO for Crescent South samples.

The Black Hills Group have flat to slightly enriched LREE patterns (La/Sm $_{(CN)}$ ratios of 0.7 – 1.7) and generally flat HREE patterns (Gd/Yb $_{(CN)}$ of 0.95 - 1.76). The Willapa Hills Group has similar REE patterns to the Black Hills Group (Figure 5.30) with La/Sm $_{(CN)}$ ratios of 1.2 – 1.9 and Gd/Yb $_{(CN)}$ ratios of 1.15 - 2.31). A generally greater amount of LREE enrichment is recorded in the Doty Hills and Ilwaco Groups (Figure 5.30), with La/Sm $_{(CN)}$ ratios ranging between 1.4 – 2.4 and 2.3 -2.4 respectively. The Doty Hills Group has a slightly more HREE depleted profile (Figure 5.30), with a Gd/Yb $_{(CN)}$ ratio of 1. 3 – 2.8. The two Ilwaco samples also display a steeper HREE slope (Gd/Yb $_{(CN)}$ of 2.1 - 2.2).
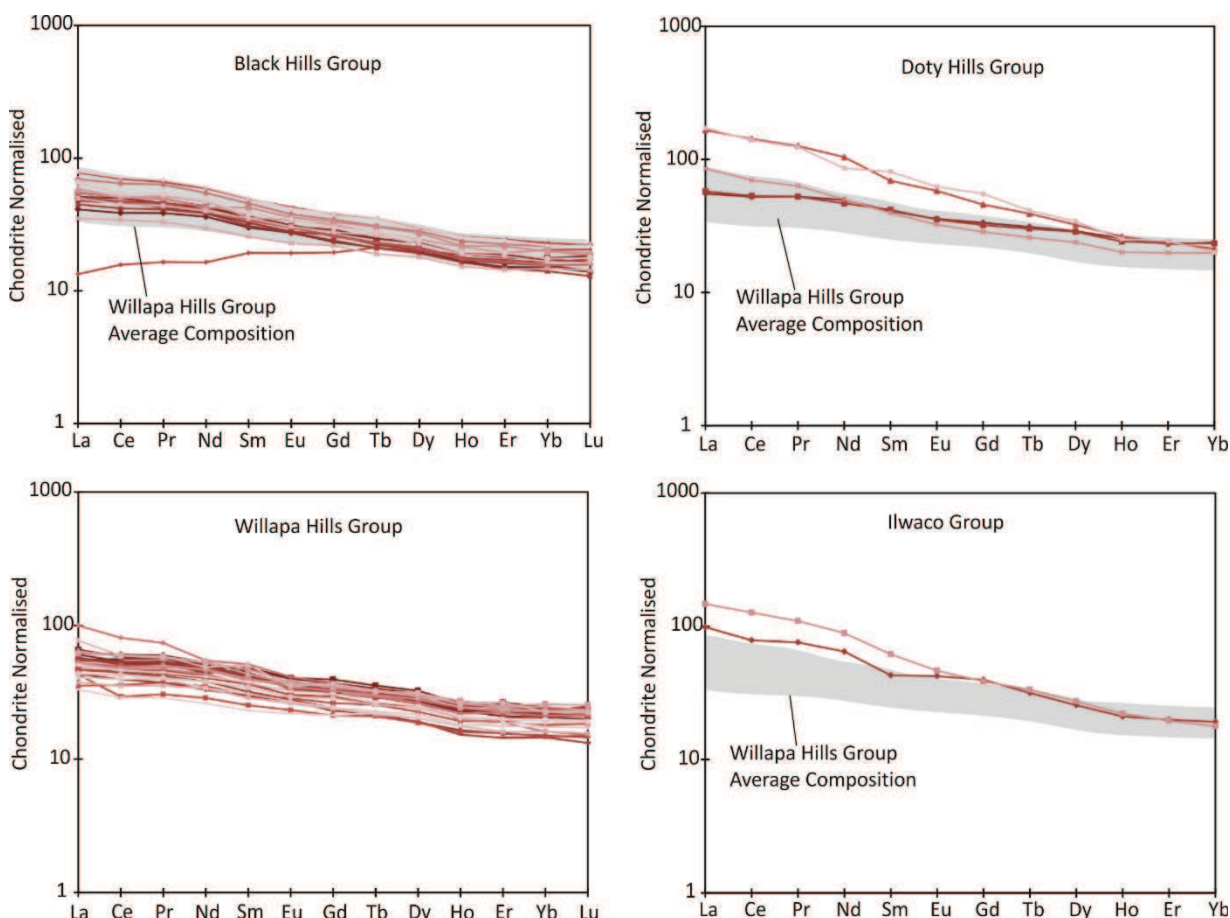
Figure 5.30 Chondrite normalised REE plots for the Crescent South samples.

All groups are more enriched in the most incompatible elements on primitive mantle normalised diagrams (Figure 5.31). All groups also contain prominent negative Sr anomalies (Figure 5.31). The Black Hills Group in

particular has positive Nb-Ta anomalies, the largest of which has both Nb/Nb*
and Ta/Ta* values of 1.7. The Doty Hills Group shows the widest range of
primitive mantle normalised element concentrations with significantly more
variety than the other groups (Figure 5.31).
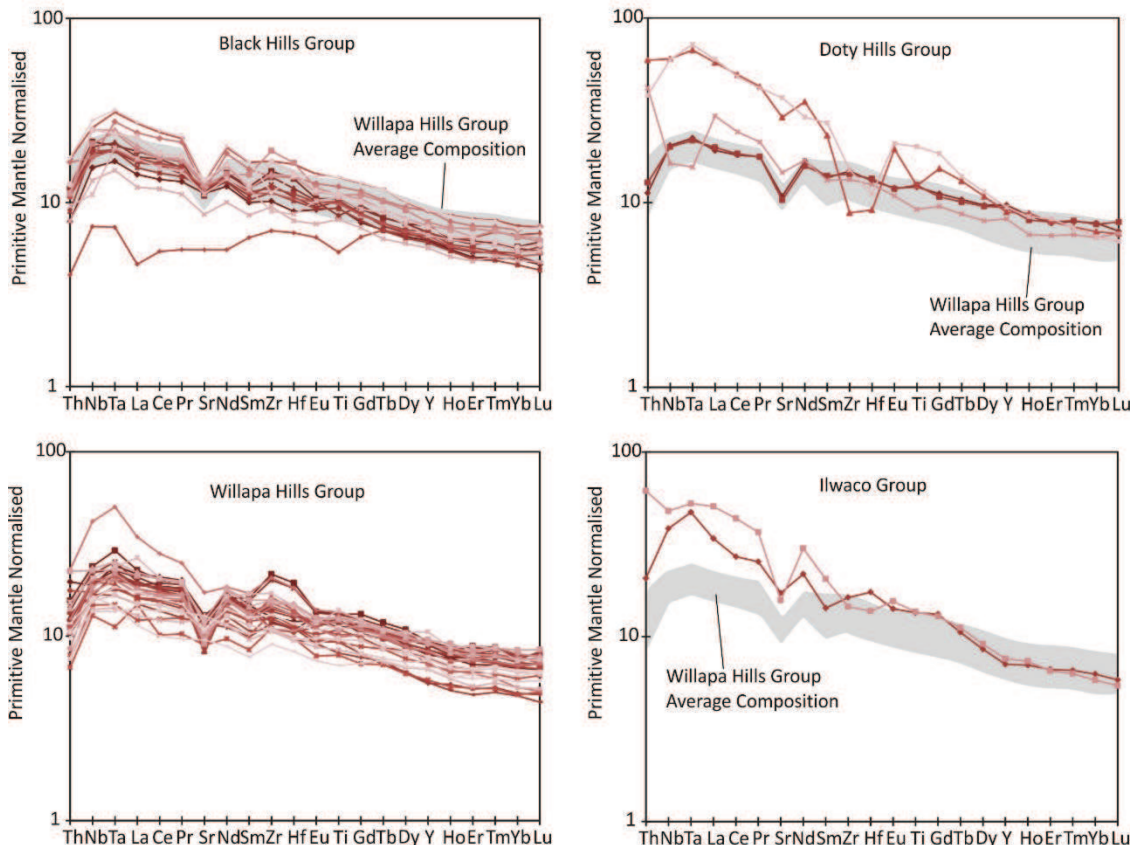
Figure 5.31 Primitive mantle normalised spider diagrams for the Crescent North samples.

On incompatible trace element- ratio plots (Figure 5.32) the Black Hills
and Willapa Hills Groups plot in a tight cluster in the MORB – OIB/ OPB field.
While the Ilwaca Group samples and some of the Doty Hills Group samples trend
towards the OIB area of the diagrams (Figure 5.32).
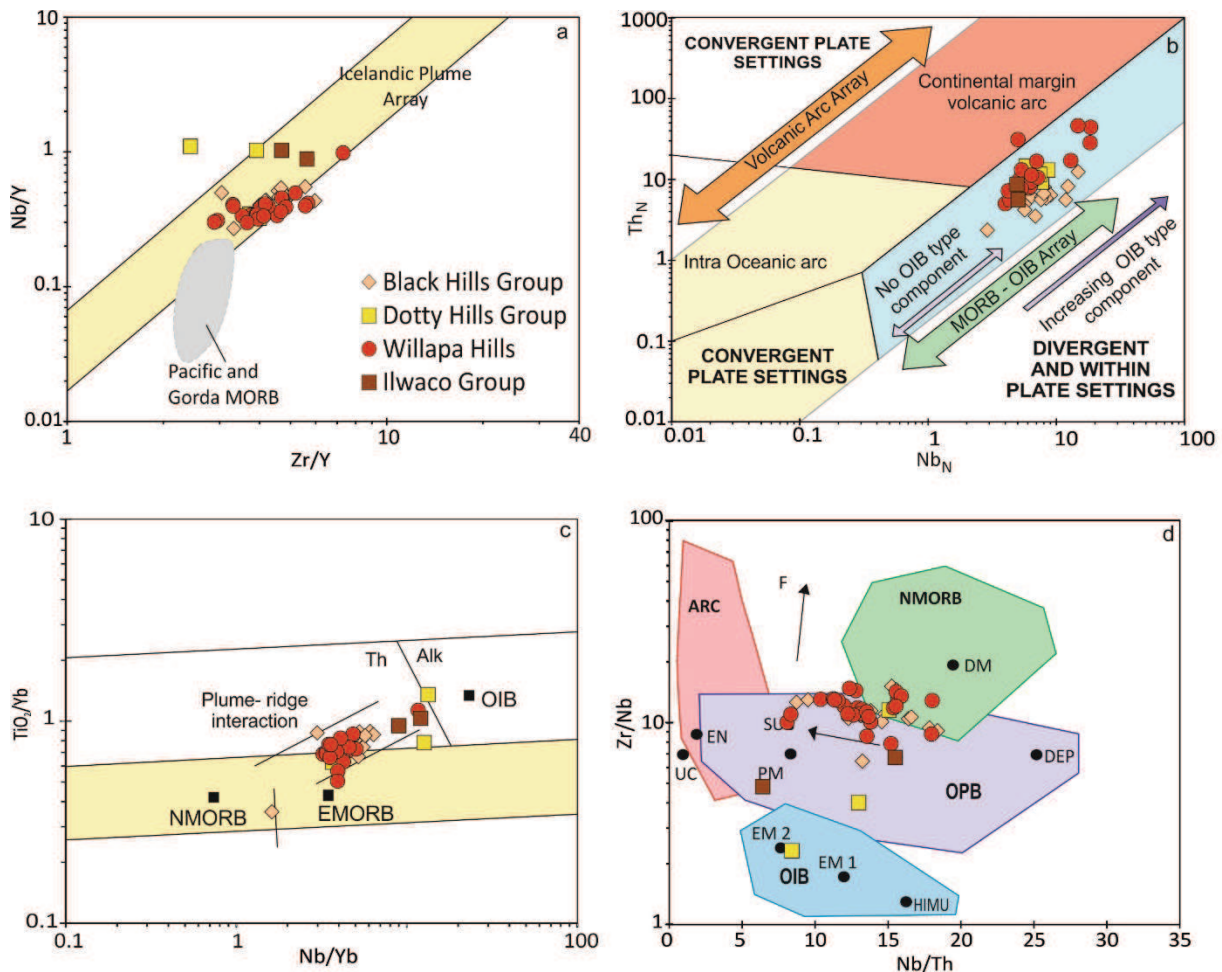
Figure 5.32 For comparison the samples have been plotted on the a) Fitton et al., (1997) Icelandic plume array diagram; b) Ophiolitic basalt tectonic discrimination diagram (Saccani, 2014); c) Proxy for deep melting diagram (Pearce, 2008) and; d) the Zr/Nb vs. Nb/Th discrimination diagram (Condie, 2005). Abbreviations: UC = upper continental crust, PM = Primitive Mantle, DM = shallow depleted mantle, HIMU = high mu (U/Pb) source, EM1 and EM2 = enriched mantle sources, ARC = arc related basalts, NMORB = normal mid-ocean ridge basalt, OPB = oceanic plateau basalt, OIB = oceanic island basalt, DEP = deep depleted mantle, EN = enriched component, F = effects of batch melting and SUB = subduction effect.

5.5.3 Metchosin Igneous Formation, Vancouver Island

There is little difference in the trace element concentrations of the different rock types of the Metchosin Igneous Complex as shown in Figure 5.33, with the exception of the gabbroic sample 207MET, which is consistently more depleted in incompatible elements. The Ni and Cr concentrations in the Metchosin Igneous Complex rocks range between 53 and 1002 ppm and 37 and 321 ppm respectively. The upper basalts have higher concentrations of Cr in comparison to

the other rock types. The concentrations of the remainder of the incompatible
trace elements in Figure 5.33 are relatively consistent across the rock types (again
excluding the gabbroic sample).
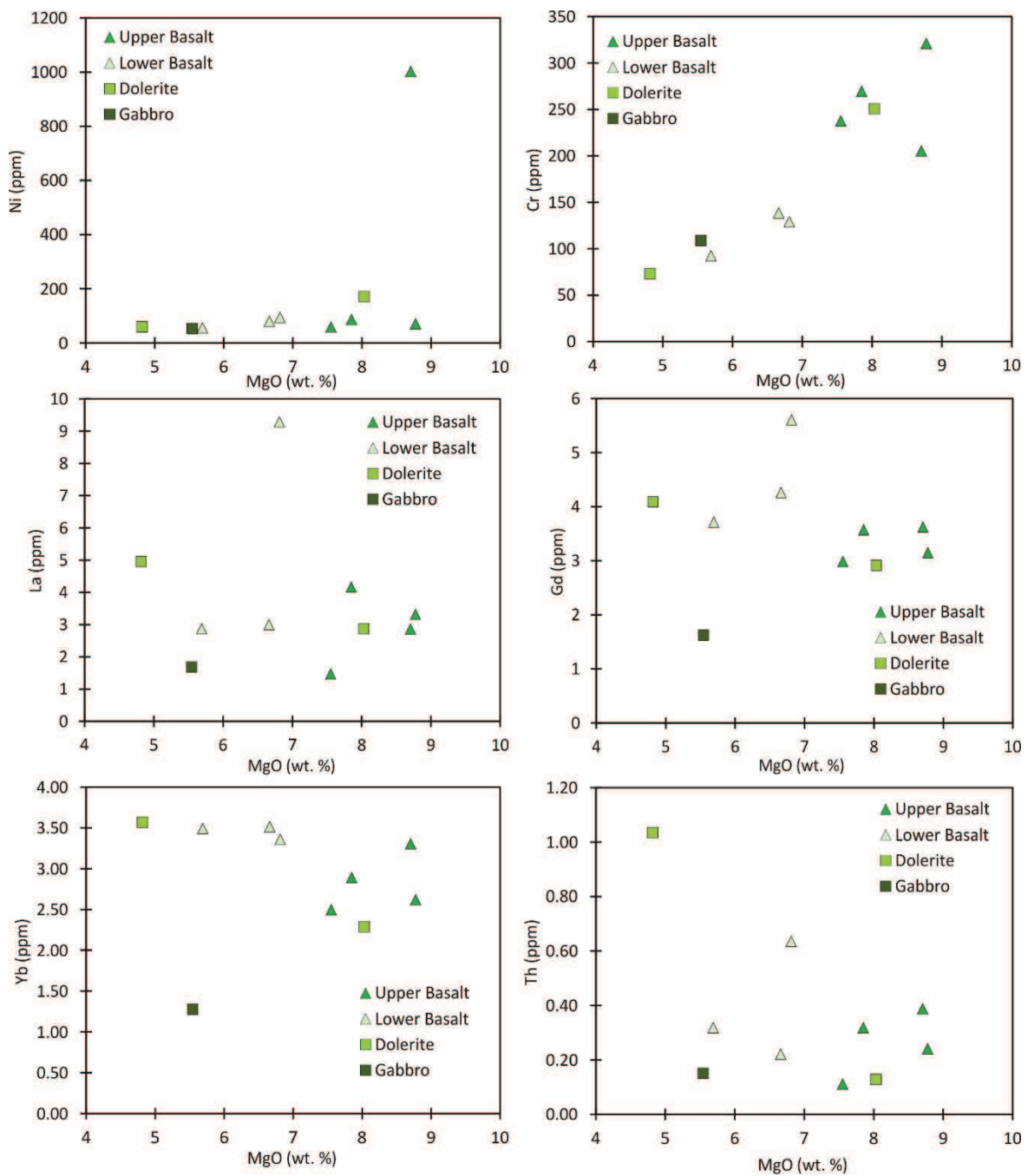
Figure 5.33 Bivariate diagrams of selected trace elements vs. MgO for Metchosin samples.

The Metchosin Igneous Complex samples generally have flat to slightly LREE depleted patterns (Figure 5.34) with La/Sm $_{(CN)}$ ratios between 0.4 – 1.2. The Metchosin Igneous Complex samples have generally flat HREE patterns (Gd/Yb $_{(CN)}$ of 0.86 - 1.35 [Figure 5.34]). The samples from this area are generally only 2-10 times more enriched in incompatible elements than primitive mantle. The patterns are broadly sub-parallel to primitive mantle although significant anomalies are observed in the most incompatible elements (Figure 5.34). Several of the samples show positive Nb-Ta anomalies, have significant Sr spikes and negative Th anomalies. Sample 207MET (the gabbro) has a Eu anomaly of Eu/Eu* = 1.5, significantly greater than observed in any other sample, indicating plagioclase fractionation. A positive Nb-Ta is also observed in sample 201MET although this may be due to the significant La depletion that occurs in this sample (Figure 5.34).
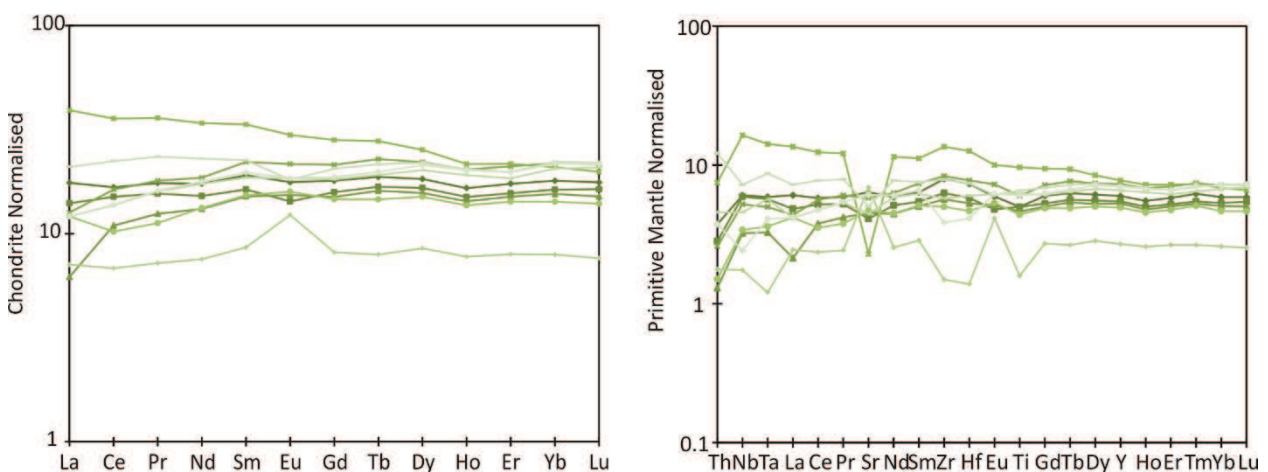
Figure 5.34 Chondrite and primitive mantle normalised spider diagrams for the Metchosin Igneous Complex samples.

The Metchosin Igneous Complex samples plot closer to the MORB field than the Crescent Formation and Siletz River Volcanics Formation in figure 5.35. However, the samples from this formation do not overlap with the MORB field in all diagrams in Figure 5.35 (e.g., Figure 5.35c, d) and show little geochemical variation.
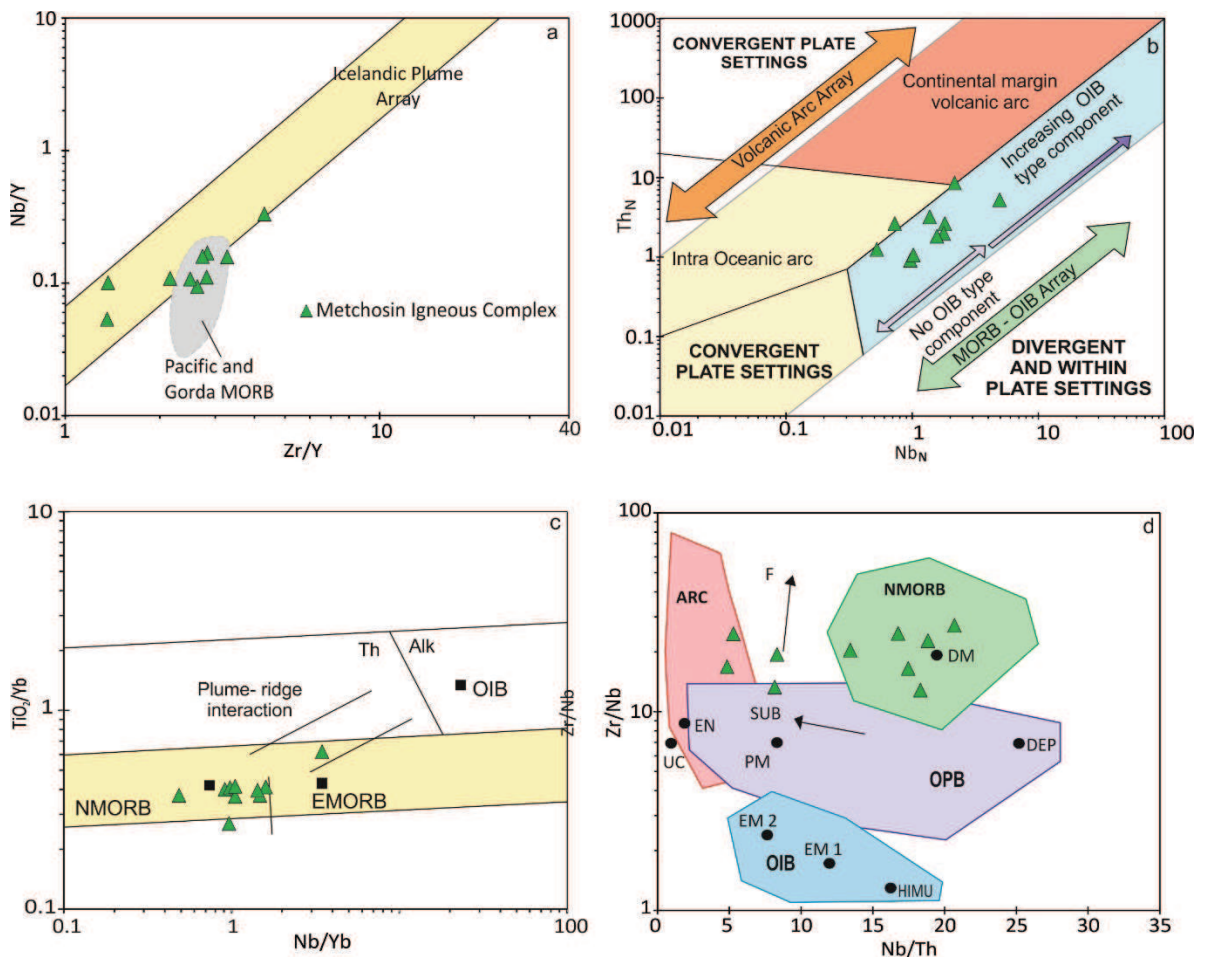
Figure 5.35 For comparison the samples have been plotted on the a) Fitton et al., (1997) Icelandic plume array diagram; b) Ophiolitic basalt tectonic discrimination diagram (Saccani, 2014); c) Proxy for deep melting diagram (Pearce, 2008) and; d) the Zr/Nb vs. Nb/Th discrimination diagram (Condie, 2005). Abbreviations: UC = upper continental crust, PM = Primitive Mantle, DM = shallow depleted mantle, HIMU = high mu (U/Pb) source, EM1 and EM2 = enriched mantle sources, ARC = arc related basalts, NMORB = normal mid-ocean ridge basalt, OPB = oceanic plateau basalt, OIB = oceanic island basalt, DEP = deep depleted mantle, EN = enriched component, F = effects of batch melting and SUB = subduction effect.

5.5.4 Trace Element Summary

Figure 5.36 and 5.37 highlight the compositions of all groups discussed within this section. The majority of the data clusters between $1.0 – 1.5$ La/Sm $_{(CN)}$ and $1.2 – 1.7$ Gd/Yb $_{(CN)}$ (Figure 5.36). A group of more depleted rocks containing largely Depleted Crescent Group and Metchosin Igneous Complex samples, along with samples from the Black Hills and Crescent Main Groups also occurs. Finally a third group of rocks with higher ratios and so steeper chondrite normalised

slopes of predominately alkali samples is also present (Figure 5.36). The Bremerton and Corvallis Groups are also more LREE enriched than the majority of the main cluster of data (Figure 5.36).
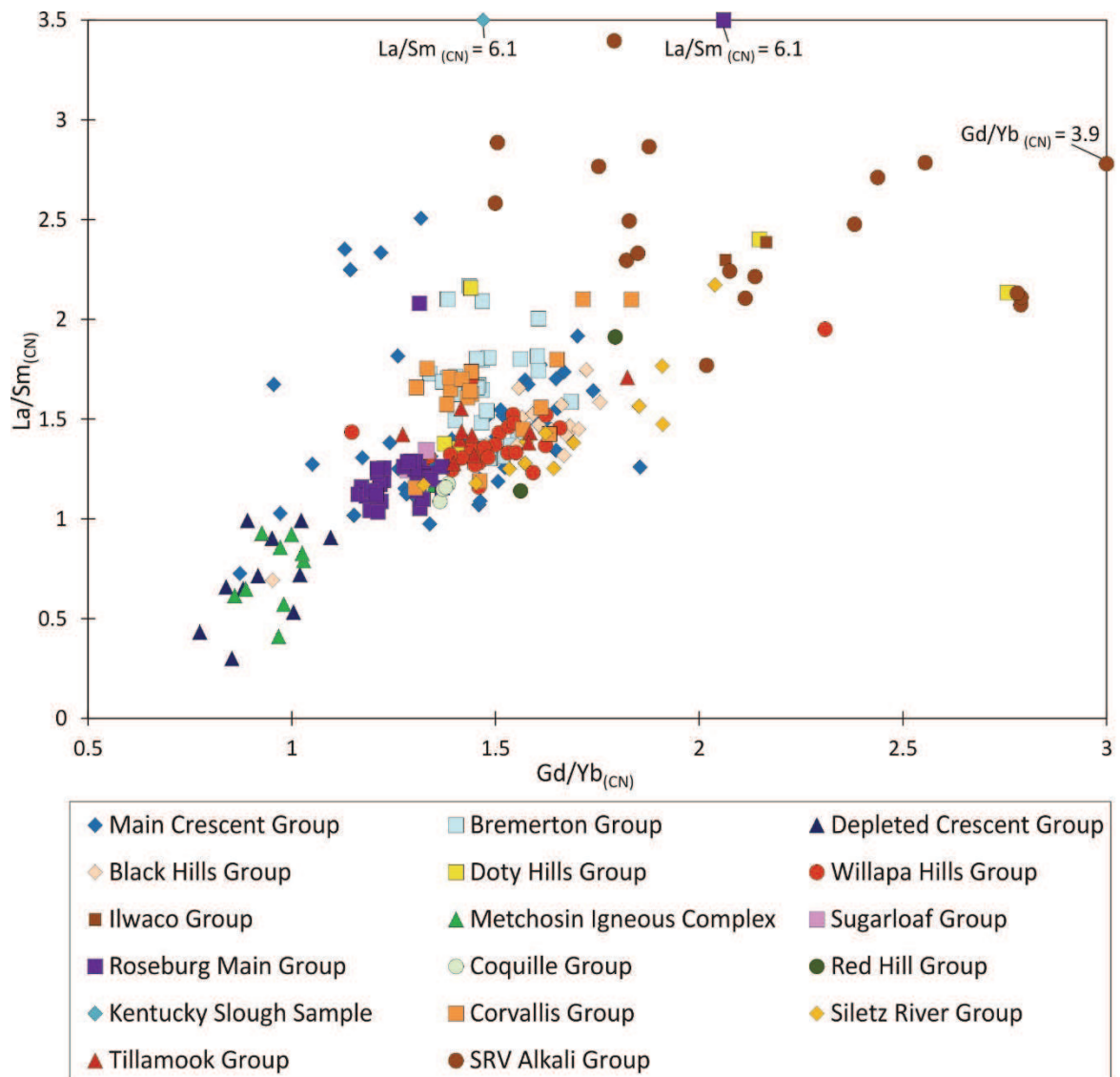
Figure 5.36 La/Sm $_{(CN)}$ vs Gd/Yb $_{(CN)}$ diagram summarising all data discussed in this section.

A similar trend is observed in Figure 5.37 with the majority of data falling into a cluster in the centre of the array with a group of higher Zr/Nb and lower La/Yb $_{(CN)}$ of largely Crescent Depleted and Metchosin Igneous Complex and a group of more alkalic samples at higher La/Yb $_{(CN)}$ and lower Zr/Nb. The Roseburg Group

is also largely more depleted than the remainder of the main data cluster in the centre of the plots (Figures 5.36 and 5.37).
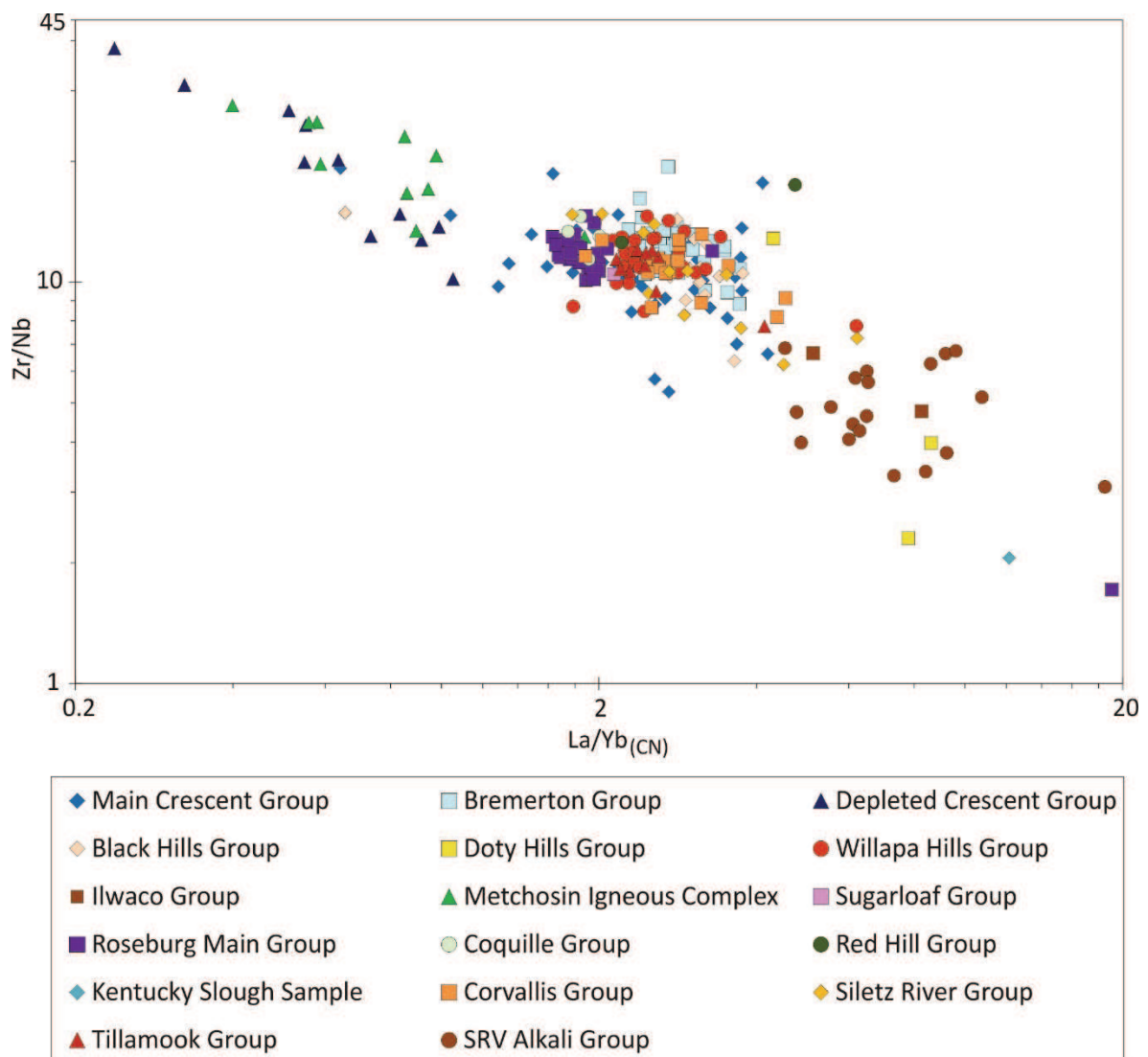
Figure 5.37 Zr/Nb vs La/Yb $_{(CN)}$ diagram summarising all data discussed in this section.

5.6 Radiogenic Isotopes

Twenty representative samples were selected for Sr-Pb-Nd-Hf radiogenic isotope analyses. The samples were chosen based on lack of alteration, geographical spread and geochemical variability for a range of coverage. Three samples were selected from the Metchosin Igneous Formation, 8 from the Crescent Formation of which 4 were from the North Crescent, 1 from Bremerton and 3 from the South Crescent, and 9 samples were selected from the Siletz River Volcanics Formation, with 4 from the Roseburg area and 5 from the Siletz River area. The measured isotope ratios for the samples used in this study have been age corrected for in-situ decay (54.5 – 50.5 Ma, depending on the age of the unit) using the trace element abundances in Appendix E3 and both the measured and initial values are reported in Appendix C (and E4).

It has been demonstrated that the Sm-Nd and Hf-Lu systems are more resistant to metamorphism while the U-Pb and Rb-Sr systems may be affected by alteration (e.g. Gaffney et al., 2011). Leaching was therefore carried out prior to digestion to reduce the effect of post magmatic alteration as most samples show prehnite-pumpellyite to greenschist grade alteration and have LOI values between 0.5 and 2.0 % (the methods are discussed in Appendix A). The aim of obtaining isotope data was to enable a better understanding of the characteristics of the mantle sources from which the magmas of the Siletz terrane were derived.

The initial isotopic ratio of a sample acts as a tracer of the composition of the mantle source region at the time of extraction of the magma, as isotopes are not affected by processes such as partial melting or fractional crystallisation. The initial isotopic ratio can be derived using Equation 5.4, using the Nd isotopic system as an example.

$$\textbf{Equation 5.4} \left(\frac{^{143}Nd}{^{144}Nd}\right)(i) = \left(\frac{^{143}Nd}{^{144}Nd}\right)(m) - \left(\frac{^{147}Sm}{^{144}Nd}\right)(m) \times \left(e^{\lambda t} - 1\right)$$

Additionally, in for example, the $^{143}Nd/^{144}Nd$ system, the differences between ratios tend to be very small due to the long half-life of ^{147}Sm (1.06 x 10^{11} years). Therefore, epsilon values are calculated using the equation of DePaolo and Wasserburg (1976) to represent the data (Equation 5.5).

Equation 5.5 $\varepsilon_{Nd}^{t} \ = \ \left(\dfrac{^{143}Nd/^{144}Nd_{(rock,t)}}{^{143}Nd/^{144}Nd_{(CHUR,t)}} - 1 \right) \times 10^{4}$

The initial isotope ratios for the analysed samples range from $^{206}Pb/^{204}Pb$: 18.751 - 19.668, $^{207}Pb/^{204}Pb$: 15.507 - 15.661, $^{207}Pb/^{204}Pb$: 38.294-39.2128, $^{176}Hf/^{177}Hf$: 0.28300 - 0.28316 (ε_{Hf}: 9.0 - 14.5), $^{143}Nd/^{144}Nd$: 0.51282 - 0.51299 (ε_{Nd}: 5.0 to 8.1) and $^{87}Sr/^{86}Sr$: 0.70302 - 0.70380 (Figure 5.35) (ages used to correct the measured isotopic ratios along with the measured and initial isotopic ratios are detailed in Appendices A and E4).
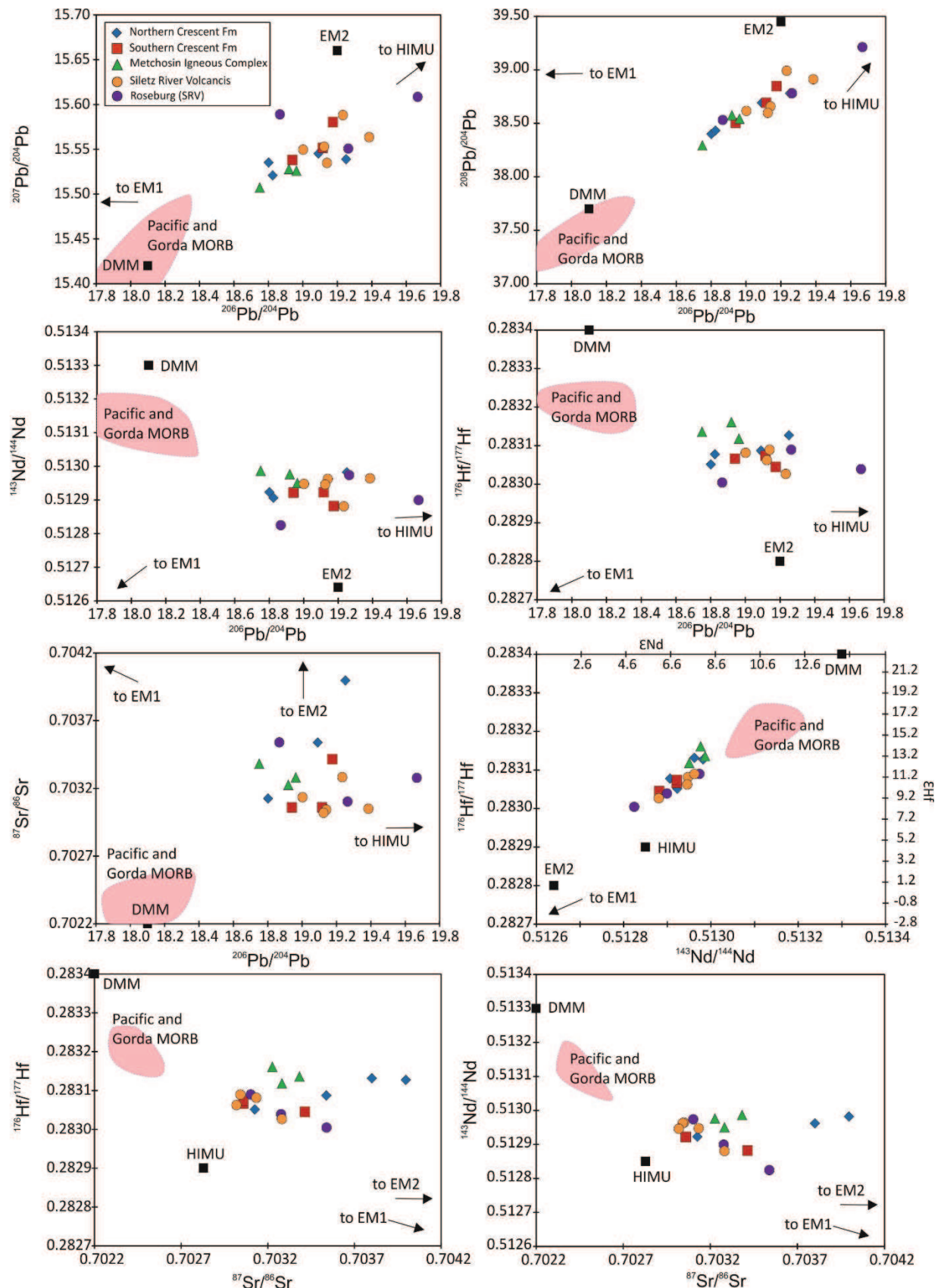
Figure 5.38 Bivariate diagrams of initial isotopic ratios of the Siletz terrane samples. Also displayed are age-corrected (53 Ma) isotope field for the Pacific and Gorda MORB mantle (Chauvel and Blichert-Toft, 2001; Davies et al., 2008; Salters et al., 2011) and the DMM, EM1, EM2 and HIMU mantle components compositions.

Nd and Hf isotope systems in particular are relatively resistant to alteration and so are most likely to represent the primary composition of the rocks (White and Patchett, 1984; Thompson et al., 2008) and the positive ε_{Hf} and ε_{Nd} values of all the samples reflect long-term incompatible element depletion of the source. The Metchosin Igneous Complex samples display the most depleted and restricted isotope ratios of the entire Siletz terrane, which is particularly evident in Hf – Nd isotopic space (Figure 5.38). However, the Metchosin Igneous Complex samples along with the more-depleted Crescent Formation samples are still generally significantly more enriched than Pacific and Gorda MORB compositions and Depleted Mantle MORB (DMM) (Figure 5.38, 5.39). The Crescent Formation samples also show more variation in isotope ratios. Samples CM230 and CM225 from the Northern Crescent, have comparatively elevated $^{87}Sr/^{86}Sr$ values to the other samples, which may be related to seawater alteration as all other isotope values for these samples are not anomalous. The samples from northern Oregon and southern Washington (the Crescent South Group of the Crescent formation, and the Siletz River Volcanics) show a similar amount of isotopic variation to one another, with the majority of samples from this area falling in the main cluster of data (Figure 5.38). The samples from the Roseburg area, in the south of the terrane, show the most isotopic variation (Figure 5.39). For example, Sample 073RB, which has the highest $^{206}Pb/^{204}Pb$ ratio of 19.668 (Figure 5.38) also has the highest La/Sm $_{(CN)}$ ratio of 6.1 (Figure 5.40). The Siletz terrane samples also extend towards the EM2 component in most isotopic spaces while some samples appear to trend towards the HIMU component (Figure 5.38).

There is some correlation between major and trace elements and isotope abundances. In particular the more trace element-depleted samples also have the most depleted isotopic ratios of the terrane (Figures 5.39 and 5.340). Samples with lower Pb and Sr isotopic ratios and higher εHf and εNd values also have the lowest La/Sm $_{(CN)}$ ratios (0.6 – 0.8) and the most-depleted incompatible element abundances (Figure 5.40). Samples from across the terrane tend to display decreasing ε_{Hf} and ε_{Nd} values and increasing Pb ratios with increasing La/Sm $_{(CN)}$ ratios (Figure 5.40).
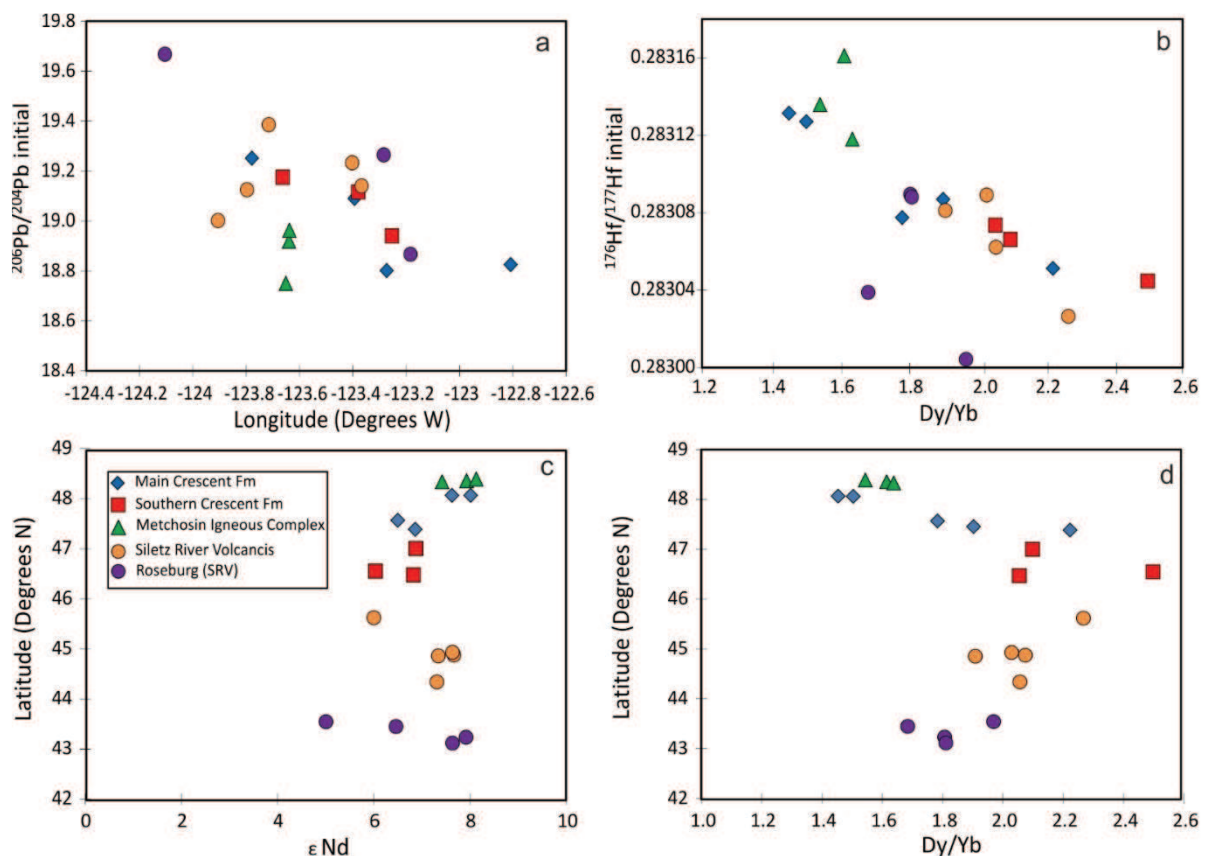
Figure 5.39 a) ^{206}Pb/^{204}Pb (initial) vs. longitude, showing an overall decrease from West to East. b) ^{176}Hf/^{177}Hf (initial) vs. Dy/Yb which displays a noticeable inverse correlation. c) Latitude vs. εNd indicating an overall increase in variability southward across the terrane. d) Latitude vs. Dy/Yb ratio, showing little variation overall with the very lowest values corresponding to the northernmost part of the terrane.

There is also a negative correlation between Dy/Yb and Hf isotopic ratios (Figure 5.39) with the most enriched samples displaying the highest Dy/Yb ratios. As this trend of more trace element – depleted samples also representing the most depleted isotopic signatures distinguishable in both trace elements and radiogenic isotopes it indicates that the differences observed are a reflection of the composition of the source regions rather than varying degrees of partial melting alone. The overall variation in isotopes generally increases southward across the terrane (Figure 5.39). However, there is little variation from east to west in the Dy/Yb ratio or isotopic ratio of the rocks of the Siletz terrane (Figure 5.39). The highest Dy/Yb values are found in the central part of the terrane and the lowest values are seen in the Metchosin Igneous Complex, the northern most samples of

174

the Crescent Terrane and from the Roseburg area in the southernmost part of the terrane. While there is a general decrease in the ^{206}Pb/^{204}Pb ratio of the rocks from West to East, the correlation is not particularly robust (Figure 5.39).
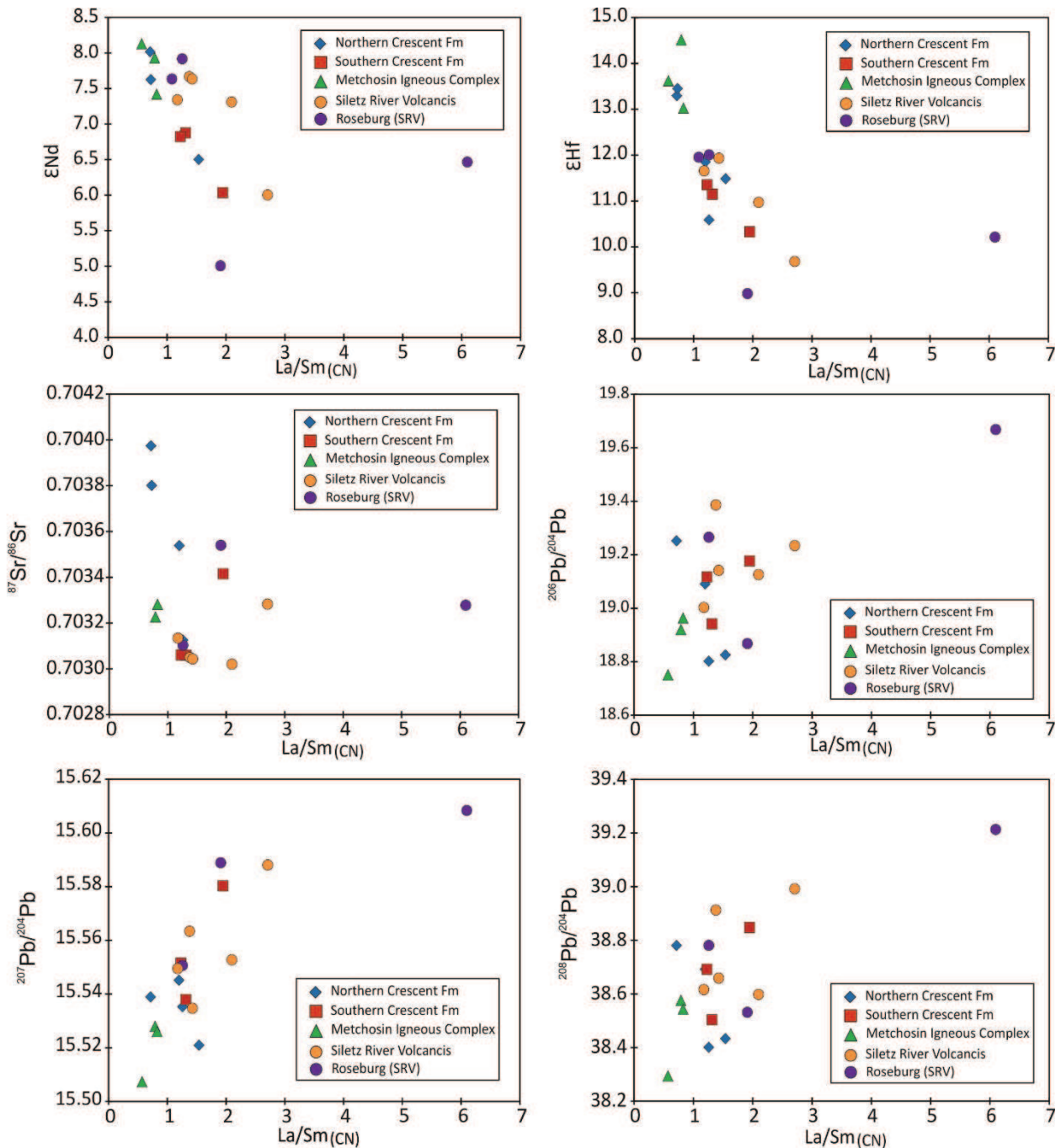
Figure 5.40 Bivariate diagrams of initial isotopic ratios of the Siletz terrane samples with La/Sm.

5.7 Geochronology

5.7.1 ^{40}Ar/ ^{39}Ar step heating dating

Fifteen whole rock samples were dated in 2009 by Fin Stewart and Darren Mark using ^{40}Ar/^{39}Ar techniques to try and constrain the age of certain areas of the Siletz terrane (see Mark et al., 2009 for methods). Sample preparation and analyses was undertaken at the Scottish Universities Environmental Research Centre (SUERC) (a summary of the data can be found in Appendix E5). The ^{40}Ar/^{39}Ar method of dating involves the step heating of whole rock samples or mineral separates at increasing temperatures before subsequently using the ^{40}Ar/^{39}Ar ratios of the gas released at each step to determine a spectrum of dates. If the sample has not been exposed to Ar and K since the initial cooling event, then both the ^{40}Ar/^{39}Ar ratios and the dates produced will be constant. Alternatively any addition or subtraction of Ar from certain minerals but not others will result in a spectrum of dates being produced as the ^{40}Ar/^{39}Ar ratios released at different temperatures may vary. Excess ^{40}Ar can be added to minerals during crystallisation or during metamorphism (Maluski et al., 1990).

The ^{40}Ar/^{39}Ar and ^{39}Ar/^{36}Ar ratios of the gas released at increasing temperatures define a straight line, the slope of which represents the ^{40}Ar/^{39}Ar ratio of the specimen and the intercept is the ^{40}Ar/^{36}Ar ratio of the atmosphere and/ or the contaminant Ar. Of the 15 samples analysed, 6 recorded excess Ar and so were unsuitable for age determinations. The results of the remaining 9 samples are also not always consistent with previously published data, highlighting the problems with ^{40}Ar/^{39}Ar dating for rocks, which have undergone metamorphism.

Sample 407 CS from the Black Hills Group in southern Washington has been determined to have an Ar-Ar plateau age of 58.29 ± 1.13 Ma (Figure 5.41). While there are few published ages for this region, they range between 56-51 Ma, using K-Ar dating (Duncan, 1982). The plateau contains approximately 55 % ^{39}Ar and so does not fit the criteria that at least 60 % ^{39}Ar is required within at least 3 continuous steps (Mark et al., 2009), for the age to be reliable. The spectrum shows that there are two different mineral phases degassing, a low temperature high – K, high – Ca phase followed by a higher temperature low – K, low – Ca

phase. The sample shows no signs of excess Ar but the inverse isochron for the younger steps also has an atmospheric signature, which is represents the degassing of a second mineral phase. The plateau is also distinctly different to the others from the terrane (Figures 5.41 – 5.48), as there is no pattern of a low temperature plateau rising to small excess Ar component in the highest temperature steps, indicating that the second phase has been reset. Significantly, the sample contains abundant xenocrysts, which may explain this older age.
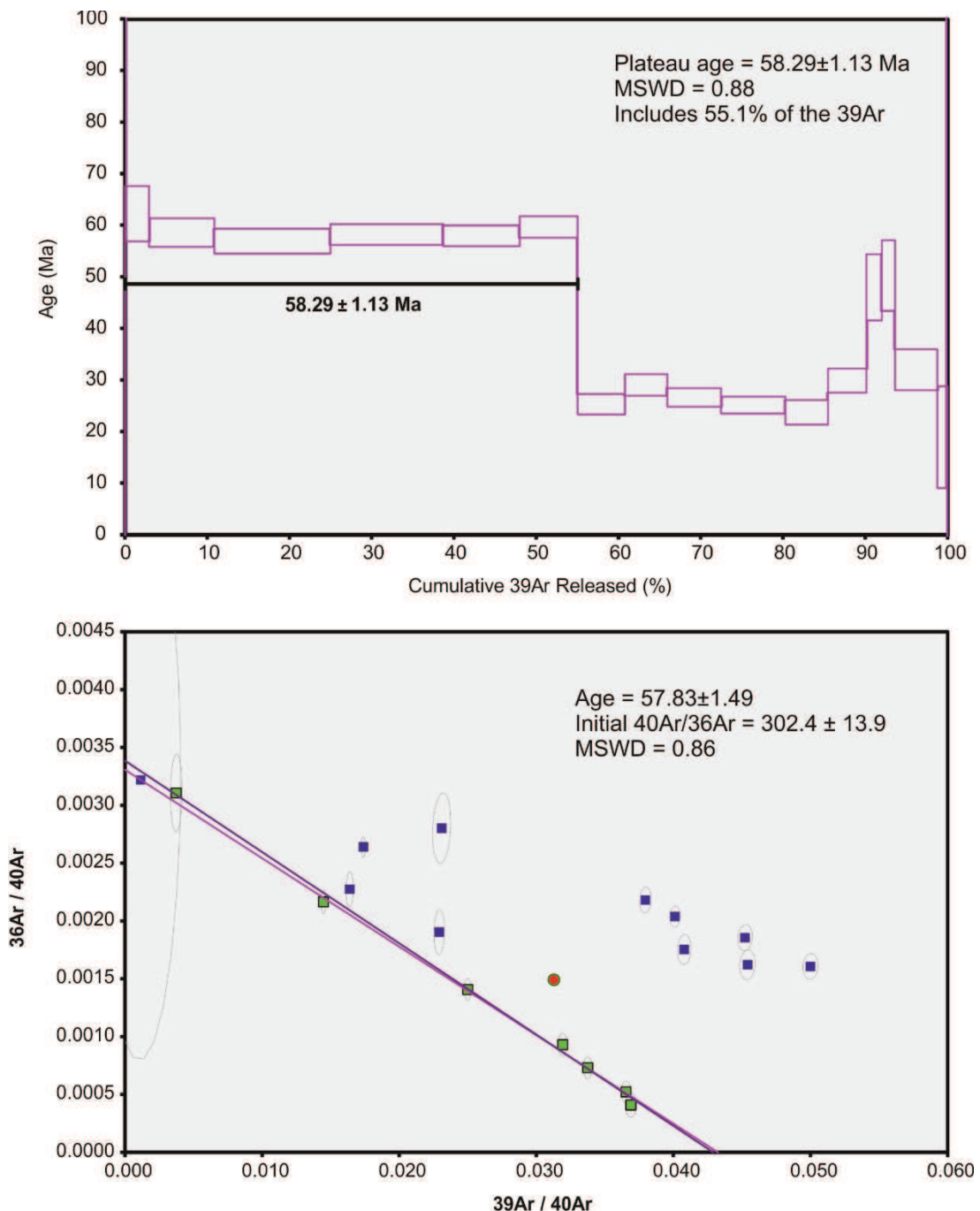
Figure 5.41 Ar-Ar step heating plateau and inverse isochron plots for sample 407CS.
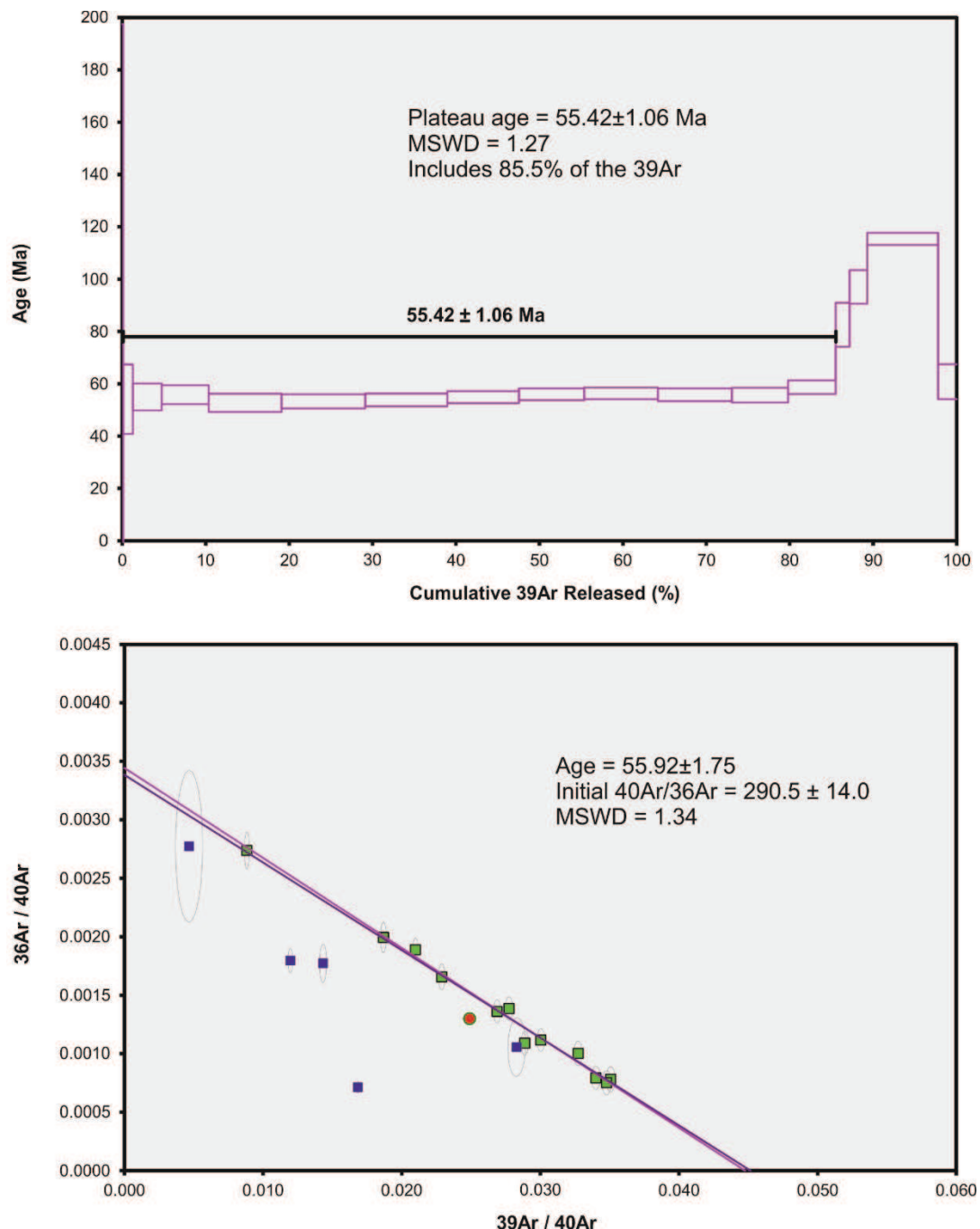
Figure 5.41 Ar-Ar step heating plateau and inverse isochron plots for sample 441CM.

Sample 441 CM is from near the base of the upper Crescent Formation in the south of the Main Crescent sequence and has been determined to have an age of 55.42 ± 1.06 Ma (Figure 5.41). However, this age is older than published whole rock $^{40}Ar/^{39}Ar$ ages for the basalts at the base of this subaerial sequence, 51 ± 4.7 Ma to 50.5 ± 1.06 Ma (Babcock and Hirsch, 2006; Hirsch and Babcock, 2009).

Calcareous nanoplankton ages of 53.5 – 49 Ma have also been determined for interbedded marine mudstones (Bukry and Snavely, 1988). Ages for this area of the Siletz terrane have not always been consistent, however, as the Blue Mountain Formation sediments found at the base of the lower Crescent Formation have a younger peak age of 49 Ma (U-Pb detrital zircon) (Wells et al., 2014). Although the age of sample 441CM is older than the published ages, it does fall within the reported error of 51 ± 4.7 Ma, and so may be a consequence of poorly constrained ages for this part of the terrane. Sample 450CS, also from the Black Hills Group, yielded an Ar-Ar plateau age of 34.16 ± 0.52 Ma (Figure 5.42) which greatly contrasts with the 56 – 51 Ma K-Ar and Ar-Ar ages reported by Duncan (1982). The sample is geochemically identical to sample 441 and is not alkaline in nature and so does not appear to represent a late stage seamount. Isotopically this sample is also very typical of the terrane (Figure 5.38) and generally plots in the main cluster of data in all isotopic space. Therefore the sample may have been thermally reset during alteration, which while consistent with the zeolite and epidote alteration minerals observed in the sample, these alteration products are also prevalent in most samples analysed.

Plateau age = 34.16±0.52 Ma
MSWD = 1.57
Includes 87.3% of the 39Ar

34.16±0.52 Ma

Age = 33.90±0.62
Initial 40Ar/36Ar = 300.4 ± 6.8
MSWD = 1.39
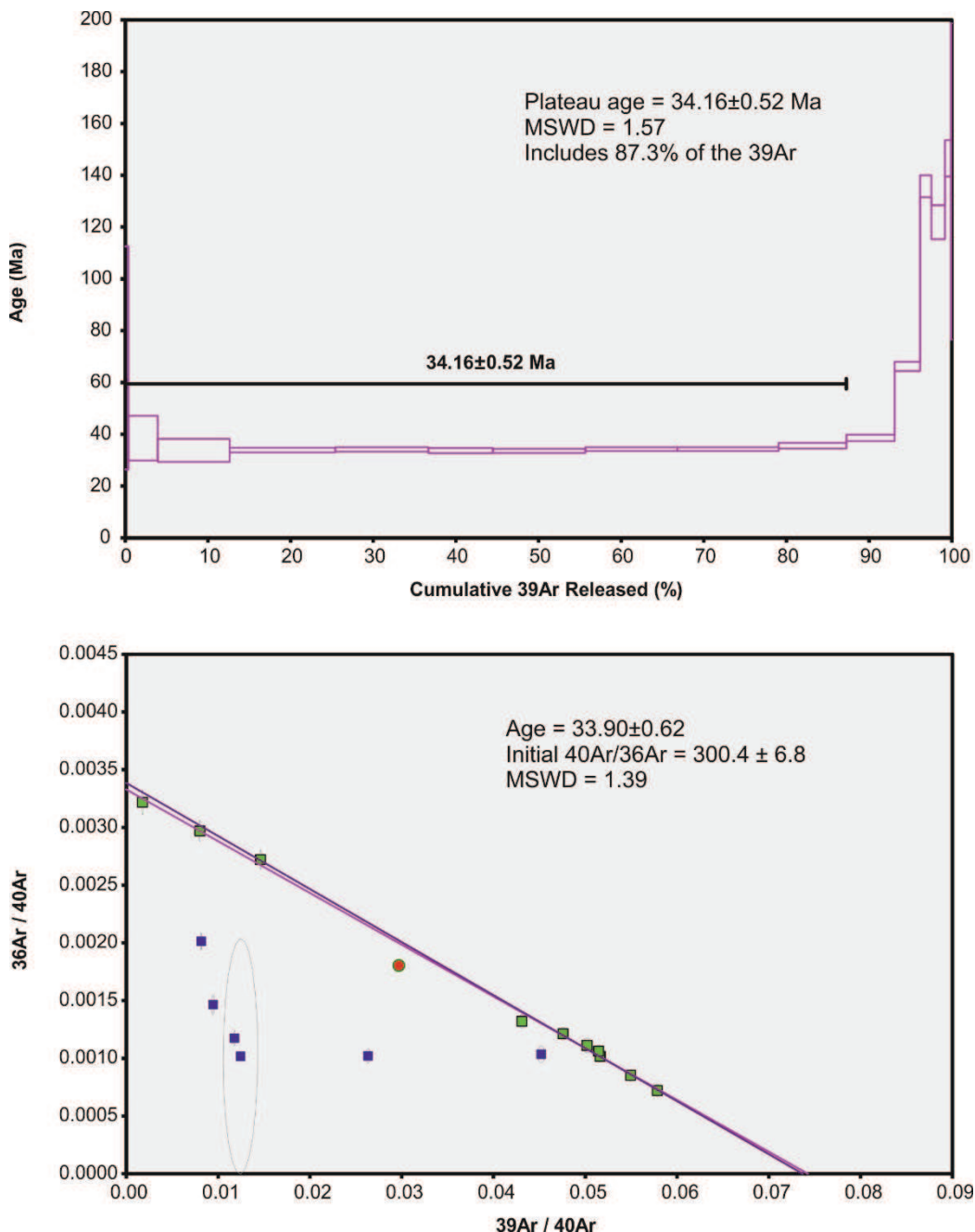
Figure 5.42 Ar-Ar step heating plateau and inverse isochron plots for sample 450CS.

Samples 390CS (Figure 5.43) and 389CS (Figure 5.44) are from the Doty Hills Group in southern Washington. While there are no published ages for this particular region of the Crescent Formation, the Willapa Hills area ~ 15 km to the south have ^{40}Ar/^{39}Ar ages ranging from 53.6 ± 2 Ma (at the base of the sequence) to 48.7 ± 0.5 Ma (at the top of the sequence) (Duncan, 1982; Moothart, 1993; Wells et al., 2014). The average age of sample 390CS from the step heating is

47.17 ± 0.54 Ma, while sample 389CS has been calculated to have an age of 49.01 ± 0.63 Ma, which are relatively consistent with the youngest published ages.
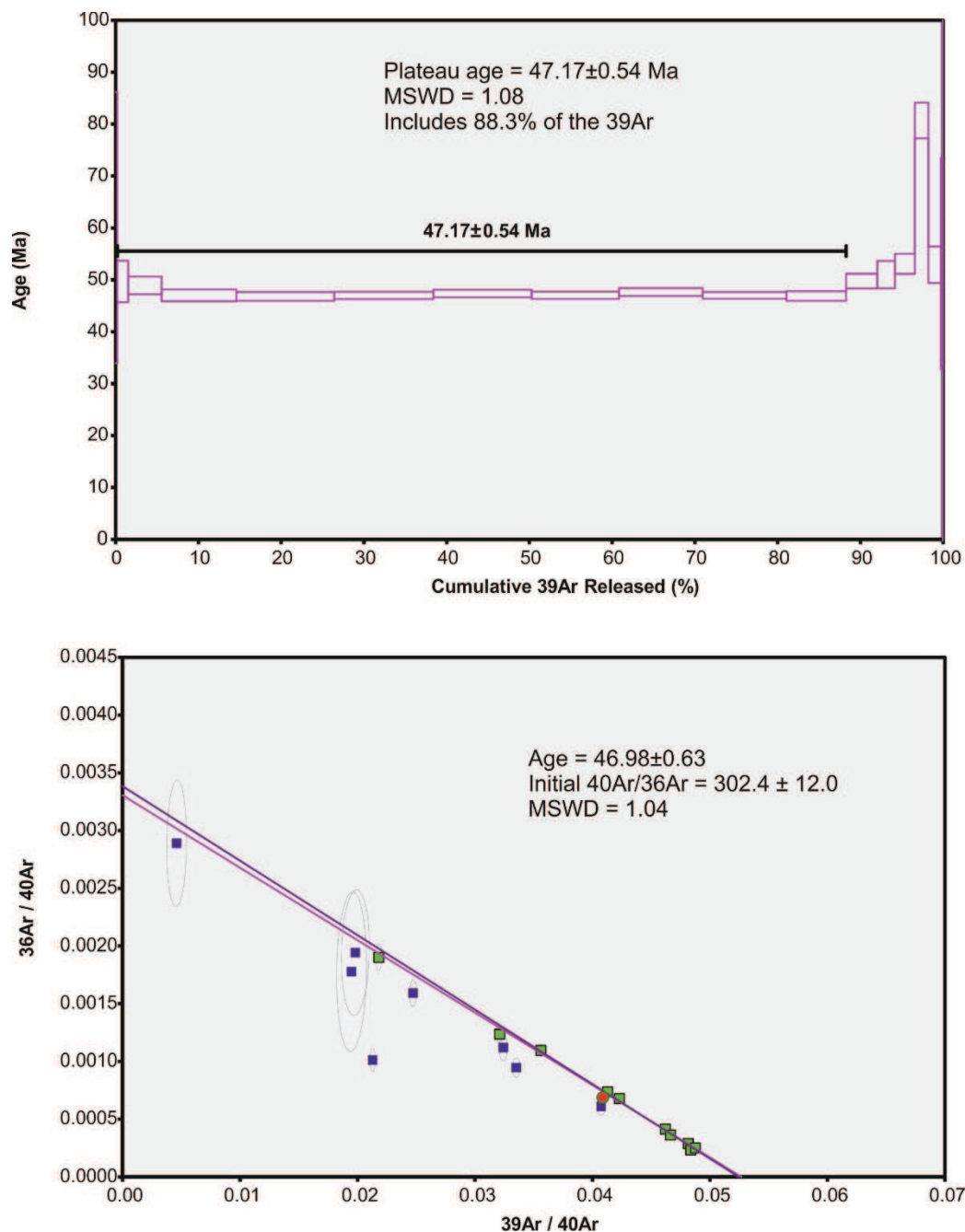
Figure 5.43 Ar-Ar step heating plateau and inverse isochron plots for sample 390CS.
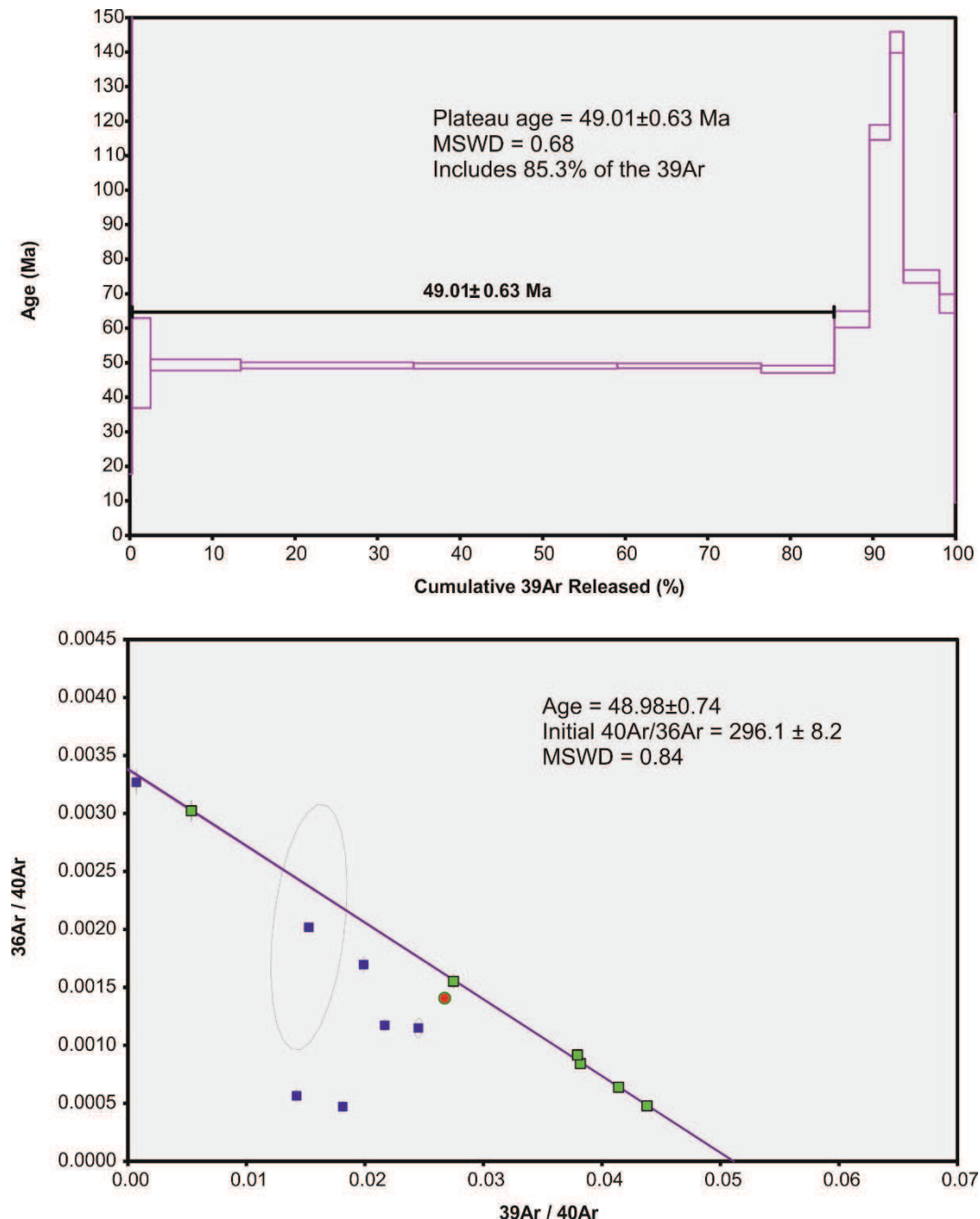
Figure 5.44 Ar-Ar step heating plateau and inverse isochron plots for sample 389CS.

Sample 162SRV is from the Siletz River Formation type area in Oregon (Figure 5.45). This sample has yielded an Ar-Ar age of 58.27 ± 5.21 Ma which is significantly older than published ages of $53.5 - 49$ Ma (coccolith zones CP10 and CP11) (Burky and Snavely, 1988) and $53.3 - 49.5$ Ma (^{40}Ar/^{39}Ar step heating ages) (Pyle et al., 2009). The error of 5.21 Ma however, does make this older age easier to reconcile with the younger published ages and that of sample 116 SRV.

Sample 116SRV (Figure 4.46), also from the Siletz River type area, has an $^{40}Ar/^{39}Ar$ age of 52.84 ± 0.57 Ma which is more consistent with the other published ages for the rocks of the area.
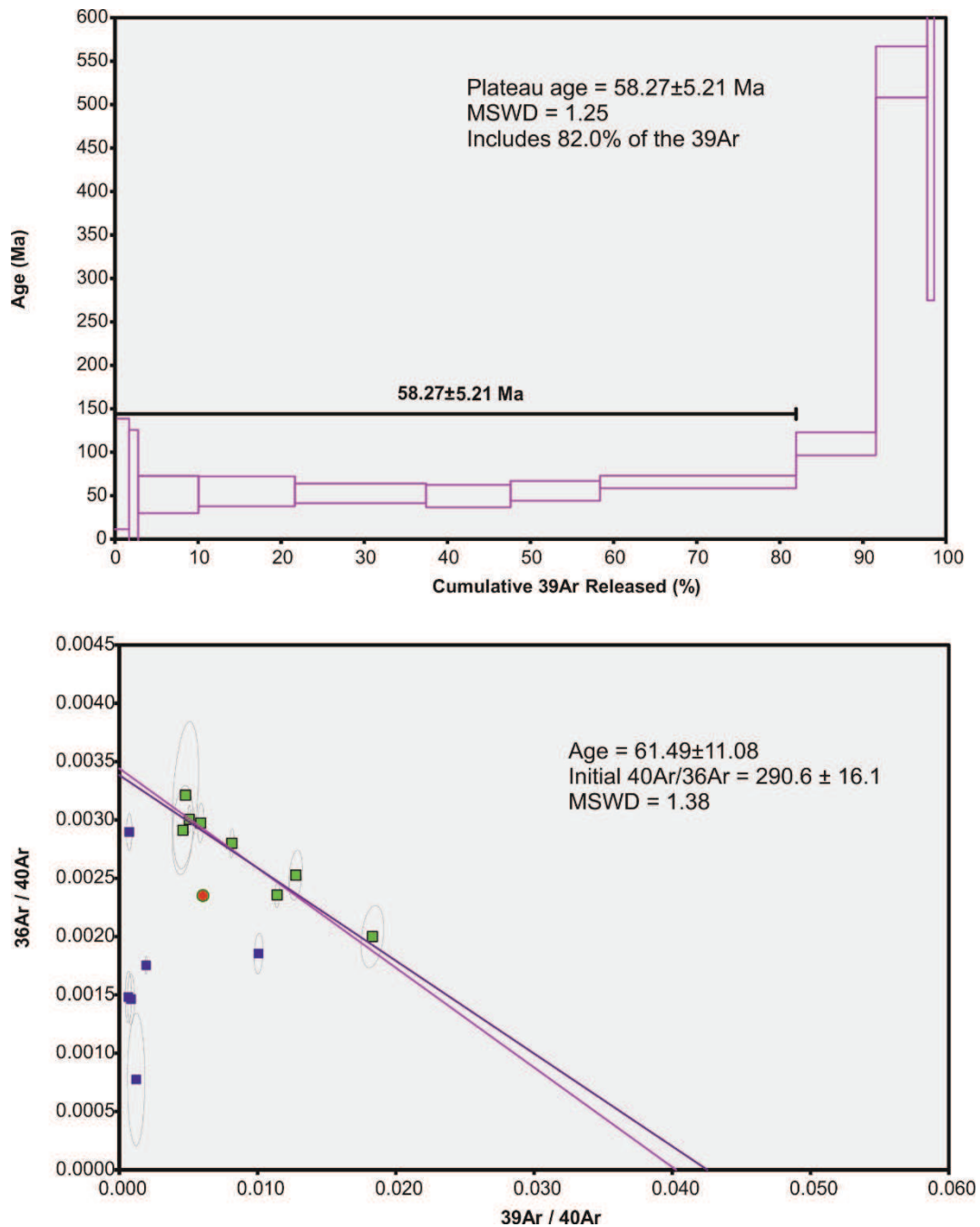
Figure 5.45 Ar-Ar step heating plateau and inverse isochron plots for sample 162SRV.
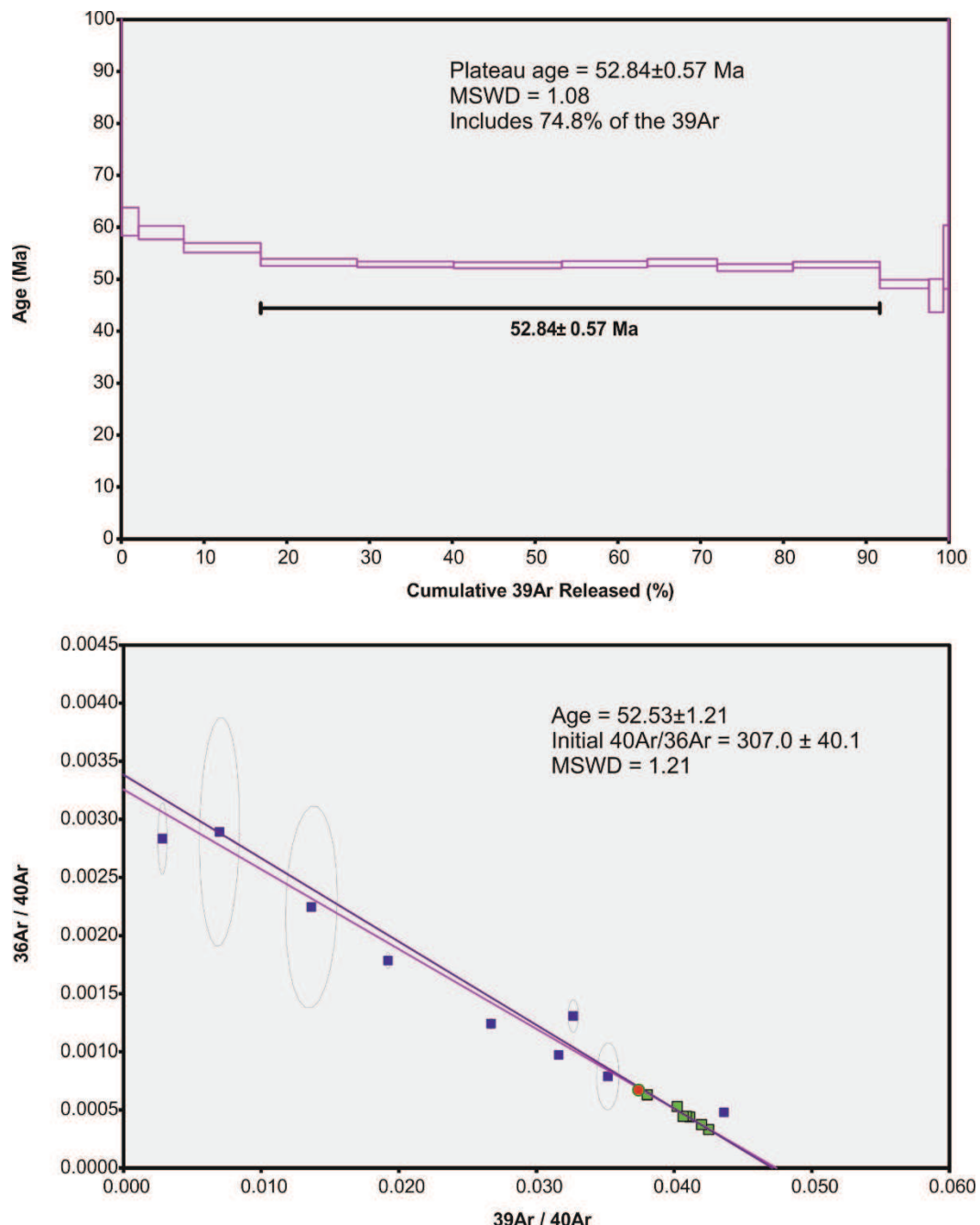
Figure 5.46 Ar-Ar step heating plateau and inverse isochron plots for sample 116SRV.

Sample 103 SRV, from the Corvallis area, Oregon is part of the Siletz River Volcanic Formation. While there are no specific ages available for the Corvallis area, the ages can be assumed to be similar to those discussed above for the Siletz River region. The ^{40}Ar/^{39}Ar step heating age determined for this sample

is 50.98 ± 0.71 Ma, which is again consistent with the published ages (Figure 5.47).
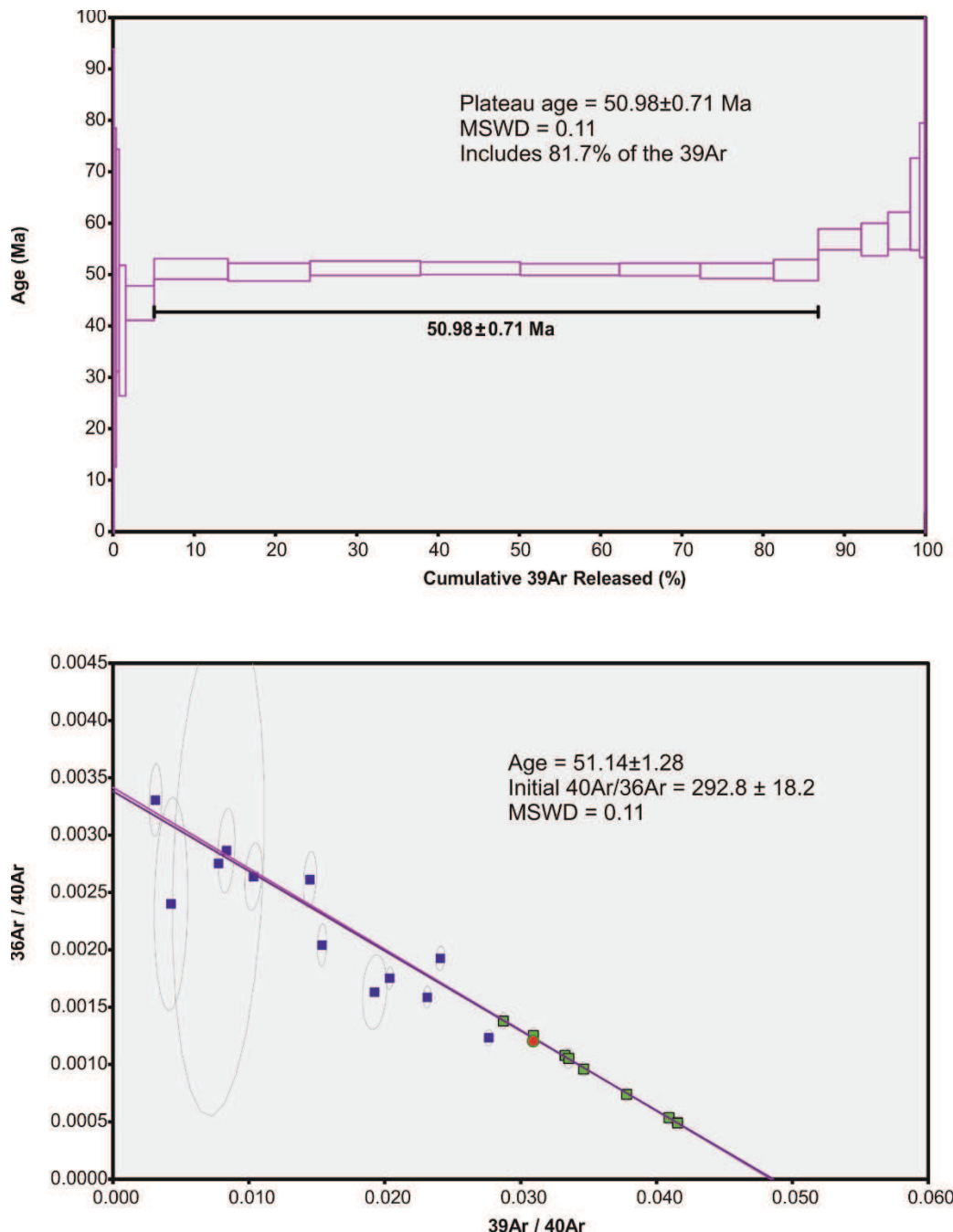
Figure 5.47 Ar-Ar step heating plateau and inverse isochron plots for sample 103SRV.

Finally, sample 073RO is a phyric basalt from the Kentucky Slough Group in southern Oregon, and is classified as part of the Roseburg area of the Siletz River Formation in this study. While there are no specific ages published for the

Kentucky Slough Group the rocks in the Roseburg Group have been dated to be between 56 – 53.3 Ma (^{40}Ar/^{39}Ar and calcareous nanoplankton) (Pyle et al., 2009). The ^{40}Ar/^{39}Ar for this sample has been determined to be 48.08 ± 0.55 Ma, which is significantly younger than the ages published for the Roseburg basalts (Figure 5.48). This may be a result of significant zeolite and prehnite pumpellyite alteration undergone by the sample. Alternatively the more alkalic nature of the sample, with higher LREE concentrations (Figure 5.17) and its stratigraphic position high in the section (discussed in section 3), may indicate a later stage ocean island/seamount phase of volcanism.
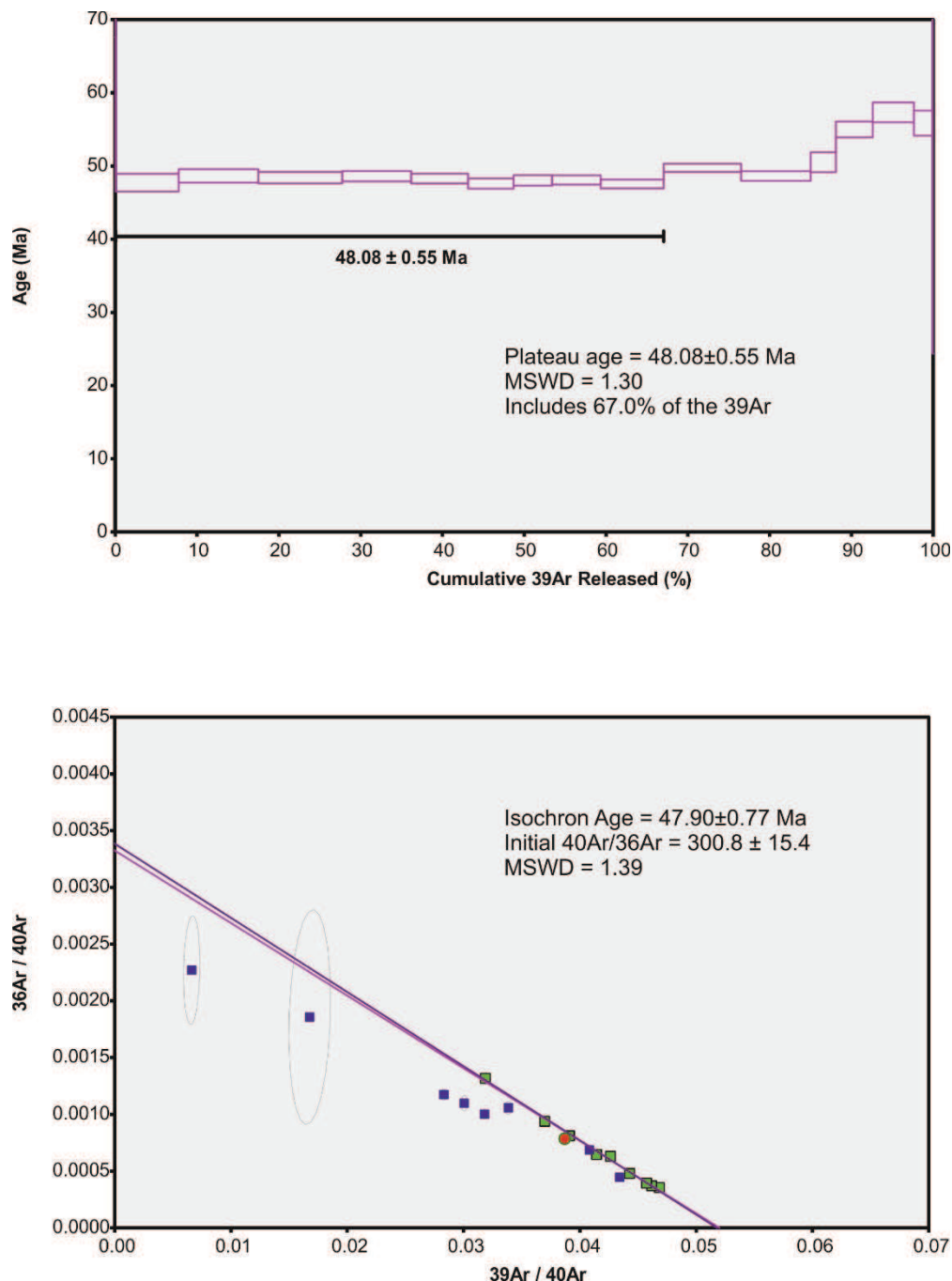
Figure 5.48 Ar-Ar step heating plateau inverse and isochron plots for sample 073RO.

Of the samples in this study, which did not produce a reliable ^{40}Ar/^{39}Ar age due to the presence of excess Ar, the samples with anomalously young ages, 095RO and 431CM (37.31 ± 62 Ma and 45.35 ± 11.35 Ma, respectively) most likely accumulated this excess Ar during metamorphism. Both show abundant zeolite, clay and prehnite pumpellyite alteration. Samples 442CS, 385CS and

362CS on the other hand also contain excess Ar and show anomalously old ages of 107.63 ± 32.98 Ma, 128.19 ± 43.51 Ma and 115.20 ± 23.59 Ma respectively, this appears to be related to large, mostly plagioclase xenocrysts in the samples or alternatively it may also be a consequence of alteration.

5.7.2 Palynology of sediments and ash layers

Nine samples inter-lava ash and sediment samples have been investigated for the composition of their pollen and nanoplankton to try and ascertain information on the timing and depth of eruption of the associated volcanics by Dave Jolley at The University of Aberdeen (data table and interpretations in Appendix E6). The results generally indicate a relatively shallow eruption depth, with a substantial terrestrial plume from a fluvial source, however the structure and composition of the pollen is not entirely consistent with this assessment, as the percentage of conifer pollen is lower than expected (as it has good taphonic transport potential) and the percentage of heavy spores is relatively high. A shallow water depth of between $50 - 1000$ m is suggested by the results expected and it is therefore proposed that the inter-lava sediments may reflect changes in relative sea level. The age of the samples appear to be early Eocene but do not extend to the Palaeocene Eocene Thermal Maximum.

In the Siletz River samples, which are predominantly ash layers found between basalt flows, there is more disruption of the pollen in the samples from the Siletz River area than those from the Tillmook area, which are generally around 2 Ma younger than the Siletz River rocks. The overall age constraints place the samples between 56 Ma (*c veripites* and *p platycaryoides* do not appear in the US record before this time) (Condon et al., 1992; Jolley and Widdowson, 2005) and 46 Ma (the Lower Middle Eocene or *Dipheys Colligem*). The palynofloras recovered from the Roseburg samples, however, are more poorly preserved than those in the Siletz River and Tillmook samples, and consist of mudstones and fine grained interlava sediments. The pollen flora from these samples are generally Early Eocene in age, no older than 56 Ma, but most likely range between $53 - 49$ Ma. The microplankton flora are very restricted, but also

appear to agree with the proposed pollen ages. These results are in agreement with other published data for the cocoliths in sedimentary interbeds in basalt flows along the limbs of the Roseburg anticlorium, which are of early Eocene age (53.5 – 50.5 Ma) and are seen to interfinger with the Umpqua Group (Wells et al., 2000).

There are no palynological derived ages for the Crescent and Metchosin areas to provide a comparison with the 58 – 47 Ma Ar – Ar derived age range discussed above. However, the Siletz River and Roseburg areas have produced comparable results. While the Ar-Ar age from the Roseburg area is younger than the suggested age range from the palonology, this is consistent with the stratigraphical position of the samples used. Sample 073RO, from which an ^{40}Ar/^{39}Ar age of 48.08 Ma was produced, is from the top of the Roseburg section, and has an alkali composition, which suggests a late stage seamount origin for this sample. The Ar – Ar ages of the Siletz terrane varies between 58.27 – 52.84 Ma for the Siletz River area and 50.98 Ma for the Corvallis area, and are generally comparable with the 56 – 49 Ma age range of the palanological results. However, the ages which are older than 56 Ma are not consistent with the range produced by the pollen and the presence of *c.vripites* (Condon et al., 1992; Jolley and Widdowson, 2005). The large error (of ~ 5 Ma) of these samples may explain this disparity however.

5.8 Summary

The rocks of the Siletz terrane display consistently low MgO wt.%, with the majority of samples containing MgO wt.% contents of less than 8 wt.%. The silica content of the analysed samples varies between 40 – 58 wt.% with the majority of samples having <50 wt.% SiO_2, while the Mg# varies between 18.5 and 70.8. The Cr abundance varies between 4 and 576 ppm and the Ni ranges between 3 and 1244 ppm. The LOIs of the samples are mostly between 0.5 and 2 % but extend up to ~6 %, which, along with the petrography, indicates that varying degrees of alteration have affected the rocks of the Siletz terrane. Under such conditions many elements, in particular the large-ion lithophile elements

(i.e., K_2O, Ba, Rb), have become mobile (e.g., Pearce, 1996; Hastie et al., 2007).

The majority of samples in this study are tholeiitic basalts while a small number of samples, largely from the Siletz River Volcanics, trend towards alkaline compositions (Figure 5.7a, b). This immobile element-based classification is generally in broad agreement with the major element data, with the majority of samples falling in a range of 44 - 52 SiO_2 wt.%, although there is more variability in the alkali oxides ($K_2O + Na_2O$) (Figure 5.7a), than reflected in Figures 5.6 – 5.10.

The more immobile elements such as Nb, Th and La generally show a positive correlations with Zr, and so are a more robust representation of the original magmatic variations among the rocks. The scatter observed on the bivariate diagrams discussed is therefore unlikely to be related to alteration but due to variation in magmatic composition such as an enriched source or degree of partial melting. Other, more mobile, trace elements such as Sr display a positive correlation in most of the samples but much more scatter is evident. The LREE patters for the terrane vary from flat to slightly enriched, along with a smaller subset of samples with very enriched LREE patterns. While the HREE patterns are generally slightly depleted, with samples from the Metchosin Igneous Complex and the Depleted Crescent Group displaying flattest HREE patterns.

On primitive mantle normalised diagrams, samples from the Siletz River Volcanics and Crescent South and some samples from Roseburg show enrichment in the most incompatible elements relative to the less incompatible elements, while the remainder of samples show generally flat patterns. All samples show a large variation in Ba/Rb ratio, which is usually constant in unaltered oceanic basalts (Hofmann and White, 1983); this is consistent with Rb depletion during post magmatic alteration.

Samples generally plot within a tight cluster in the centre of MORB - OIB arrays on tectonic discrimination diagrams, although, some trend more towards MORB and others to OIB ends, and additionally, a few samples tend to plot in the more arc like fields.   In terms of the radiogenic isotope data, the Roseburg samples show the most amount of variation in all isotopic space, while the

Metchosin samples display the least variation and are, additionally the least radiogenic in Pb isotopes and have the highest eps Hf and eps Nd.

Nine samples yielded statistically acceptable ^{40}Ar/^{39}Ar ages, which vary between around 58 – 47 Ma, along with a substantially younger age of 34 Ma for one sample. The pollen ages produce a similar range of 56 – 48 Ma and a shallow depositional depth.

6. DISCUSSION

The following chapter will discuss and evaluate the geochemical data presented in the previous two sections and its implication for the origin and evolution of the Siletz terrane. The discussion will begin by examining the processes, which have affected the chemistry of the rocks, primarily whether fractional crystallisation has occurred within and across the various groups of the rocks of the Siletz terrane. This will be achieved through utilising both the whole rock major and trace element data and the mineral chemistry major element data and abundances. Fractional crystallisation models of different conditions, produced partially through the use of the MELTS program (Asimow and Ghiorso 1998; Ghiorso et al., 2002) program, will be used to constrain the under what conditions and how the evolution of the Siletz terrane magmas occurred within the crust.

The melting conditions, which produced the primary Siletz magmas will be determined using the PRIMELTS3 programme of Herzberg and Asimov (2015) and the programme of Lee et al., (2009). These models will try and constrain the temperature, pressure and composition of the primary magmas of the terrane. The composition of the mantle source of the Siletz terrane will then be investigated through trace element melting models of different mantle reservoirs, mixing models of both trace element and isotopic ratios and comparison with other provinces with well-characterised isotopic signatures. The results of the mantle source investigations and modelling will then be used to constrain the tectonic setting within which the magmas formed and primarily whether or not the source conditions and compositions can be reconciled with the involvement of a mantle plume in the formation of the Siletz terrane. Finally, the conclusions of the larger tectonic environment of the Siletz terrane will be evaluated within the greater context of Cordilleran evolution, and the development of the region and resulting later magmatism.

6.1 Fractional Crystallisation

The following section examines the nature of fractional crystallisation during the evolution of the magmas and resulting trends observed within the groups of the Siletz terrane. Fractional crystallisation has been modelled using the MELTS computer software programme of Ghiorso et al (2002). The MELTS software, based on the original work of Ghiorso and Sack (1995) and Asimow and Ghiorso (1998), allows users to model various phase relations within igneous systems over a range of pressures (0-2 GPa) and temperatures (500 – 2000 °C). MELTS can model fractional crystallisation paths in both hydrous and anhydrous mafic magmatic systems. The resulting models help to assess and constrain the conditions and extent of fractional crystallisation observed in the Siletz terrane suites.

Fractional crystallisation models for each group were carried out using the most primitive sample of that group, i.e., the sample with the highest MgO and lowest incompatible element concentrations. However, the most primitive sample for any given group is unlikely to represent a true primary magma composition, particularly given the relatively low MgO concentrations of the Siletz terrane samples (section 5.4). Despite this, the most primitive sample is assumed to represent the closest estimate of the primary magma for the group. In addition, for comparison, best fit major element models for each group with a primary East Pacific Rise (EPR) MORB parent magma composition (derived from an average of the most primitive 10 % EPR compositions - based on Zr - from the GEOROC database) have also been calculated. For each starting composition the MELTS programme was used to model major element geochemical models at 5 different fractional crystallisation schemes: *Model 1*: fractional crystallisation at 0.5 kbar (anhydrous); *Model 2*: fractional crystallisation at 1 kbar (anhydrous); *Model 3*: fractional crystallisation at 3 kbar (anhydrous); *Model 4*: fractional crystallisation at 7 kbar (anhydrous); and *Model 6*: fractional crystallisation at 1 kbar (1 % H_2O wt.%). All models calculate the liquid composition of the magma at 10 % crystallisation intervals using a quartz - fayalite - magnetite (QFM) oxygen buffer.

The models which produce the closest prediction of the Siletz terrane

groups' whole rock major element trends are then compared with the major element data for each group of the Siletz terrane. Additionally using the mineral composition data produced in the models, the Mg# of clinopyroxenes and An number of plagioclases which were in equilibrium in the MELTS models (crystallising at the same time) are compared with actual plagioclase and clinopyroxene phenocryst compositions from the Siletz terrane.

The fractional crystallisation model which best predicts the major element trends of the group of rocks is then used to determine the evolution of the trace element chemistry of the starting parent melt composition. The trace element crystallisation trends are derived using the mineral assemblages predicted to crystallise by MELTS for a given model. The mineral/melt partition coefficients given in Table 6.1 and the fractional crystallisation equation shown in Equation 6.1.

Equation 6.1 $$C_{liq}^i = C_0^i f^{D^i - 1}$$

Where C_{liq}^i = concentration of element i in the evolving liquid, C_o^i = concentration of element i in the parent magma, f = the residual parent liquid fraction, D^i = the bulk partition coefficient for element i.

The mineral/ melt partition coefficients were derived from the data set presented in Bedèard (2001). These partition coefficients were selected as they represent mineral/ melt behaviour for a basaltic magma, which is fractionating olivine, plagioclase and clinopyroxene, which is also assumed to be the crystallising assemblage for the Siletz terrane parental magmas. The partition coefficients were based on anhydrous systems and were derived using experimental data. The choice of partition coefficients does however somewhat limit the robustness of the fractional crystallisation trace element modelling as partition coefficients need to be suitable for a given process and so can be difficult to select when investigating what process and what setting a particular process is taking place in (Bedèard, 2001). There is no universally agreed collection of partition coefficients for a given magmatic system and therefore trace element

modelling can only produce a semi quantitative measure of petrological processes. However, the use of partition coefficients derived from one source means that any errors will be systematic across all partition coefficients used. Small changes in partition coefficients can also manifest as measurable changes in the equivalent calculations in crystals and residue melts (Bedèard, 2001). In addition the use of anhydrous partition coefficients also introduces a source of error into the hydrous fractional crystallisation models, limiting their robustness. Therefore, while the trace element fractional crystallisation modelling undertaken in this study can when used in conjunction with other models and data, give an indication of the processes taking place they are by no means conclusive models.

	Olivine	Orthopyroxene	Clinopyroxene	Spinel	Plagioclase	Magnetite
Th	0.0000001	0.0004	0.014	0.013	0.3435	0.1
Nb	0.0001	0.002825	0.00605	0.01	0.09725	0.7
Ta	0.0001	0.002825	0.00605	0.01	0.0795	0.23
La	0.000007	0.0000535	0.05025	0.0006	0.0631	0.015
Ce	0.00001	0.0026	0.089	0.0006	0.0457	0.016
Pr	0.00004	0.0065	0.1335	0.0006	0.1375	0.02
Nd	0.00007	0.010267	0.178	0.0006	0.0478	0.026
Zr	0.0005	0.01775	0.1975	0.07	0.0094	0.71
Hf	0.0038	0.027225	0.2115	0.003	0.082	0.16
Sm	0.0007	0.018	0.3775	0.0006	0.06575	0.024
Eu	0.00095	0.0215	0.458	0.0006	0.3254	0.025
Ti	0.015	0.082	0.3955	0.15	0.0473	16.5
Gd	0.002	0.028	0.487	0.0009	0.07175	0.018
Tb	0.003	0.035	0.516	0.0012	0.084	0.019
Dy	0.004	0.041	0.5455	0.0015	0.057167	0.018
Y	0.007365	0.0935	0.412	0.002	0.00989	0.0039
Ho	0.0065	0.05	0.603	0.00225	0.0592	0.017
Er	0.009	0.063917	0.66	0.003	0.07633	0.017
Tm	0.015	0.078	0.66	0.00375	0.072	0.017
Yb	0.023	0.093917	0.5165	0.0045	0.0903	0.018
Lu	0.03	0.1	0.536	0.00525	0.1175	0.023

Table 6.1 Mineral/ melt partition coefficients for basaltic and basaltic andesite liquids. Compiled from the dataset listed by Bèdard (2001). See reference for data sources.

The CIPW normative mineralogy of each investigated group has also been calculated in order to test the validity of the MELTS fractional crystallisation models. The modal abundances have been plotted onto an expanded basalt tetrahedron, which highlights various experimentally determined primary mantle melt compositions and fractionation paths (Thompson, 1982; Brueseke and Hart, 2008). The resulting fractionation pressures obtained from the diagram are then compared and contrasted with those of the MELTS modelling results.

6.1.1 Siletz River Formation, Oregon

6.1.1.1 Roseburg Groups

Sample 071RO from the Corvallis Group has been selected as an estimate for the parent magma for all Roseburg groups due to the relatively low number of samples from the majority of groups from this region. While this sample has the highest MgO wt.% content of any sample from Roseburg (7.8 wt.%) its Zr (and REE) content is more moderate at 101.5 ppm. However, samples from the Roseburg Group displaying the lowest Zr abundances (79.1 – 80.8 ppm) also have relatively low MgO wt.%.
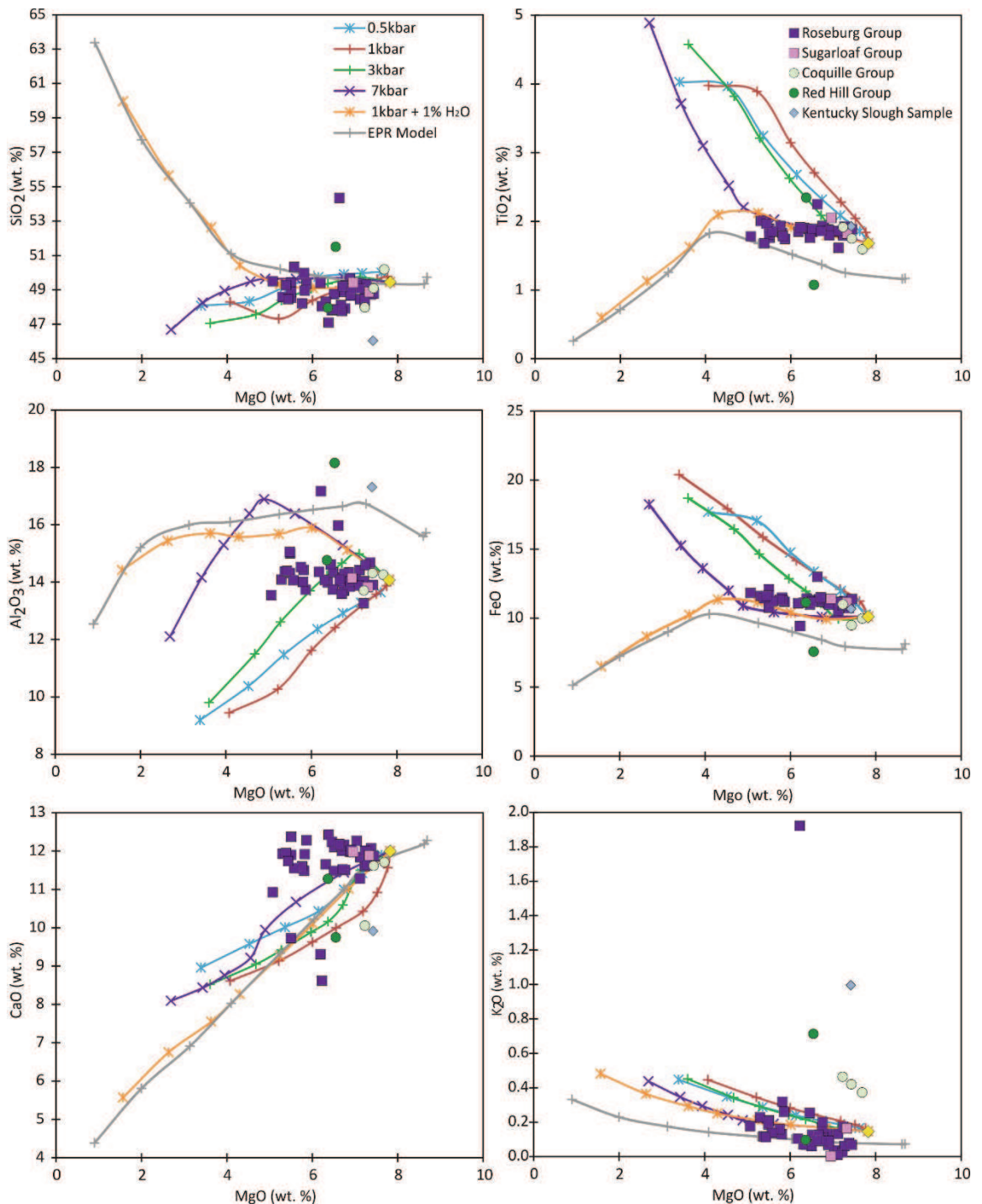
Figure 6.1 Bivariate diagrams of representative major elements vs MgO for the Roseburg rocks along with the predicted fractional crystallisation models from a parent magma with the composition of sample 071RO. Markers indicate intervals of 10 % crystallisation.

The major element fractional crystallisation model, which best predicts the trend observed in the Roseburg data appears to be the 071RO 7 kbar. While in

comparison the EPR derived model, discussed above, which best approximates the major element data is the 1kbar + 1% H_2O wt.% model (Figure 6.1). The 071RO 7kbar model generally reflects the SiO_2, TiO_2 FeO, K_2O abundances well, while none of the models can account for the trends seen in the Al_2O_3 and CaO contents (Figure 6.1). However, several other models can also predict the SiO_2 compositions along with some of the data's TiO_2 and FeO concentrations, indicating that perhaps no one model can approximate the major element abundances of the Roseburg data. Nevertheless, the 7 kbar model predicts that crystallisation will begin at 1302 °C with clinopyroxene being the first mineral to crystallise, feldspar then joins the assemblage at 1250 °C and ~ 28 % crystallisation. Spinel then crystallises at 1170 °C after ~ 72 % crystallisation of the parent magma (Figure 6.2). This assemblage then continues to crystallise. However, the model predicts that the magma will reach the lowest recorded MgO content in the Roseburg samples (5.1 wt.%) at ~ 25 % crystallisation, before plagioclase joins the assemblage, which is not entirely consistent with the plagioclase phenocrysts observed in some of the Roseburg samples.
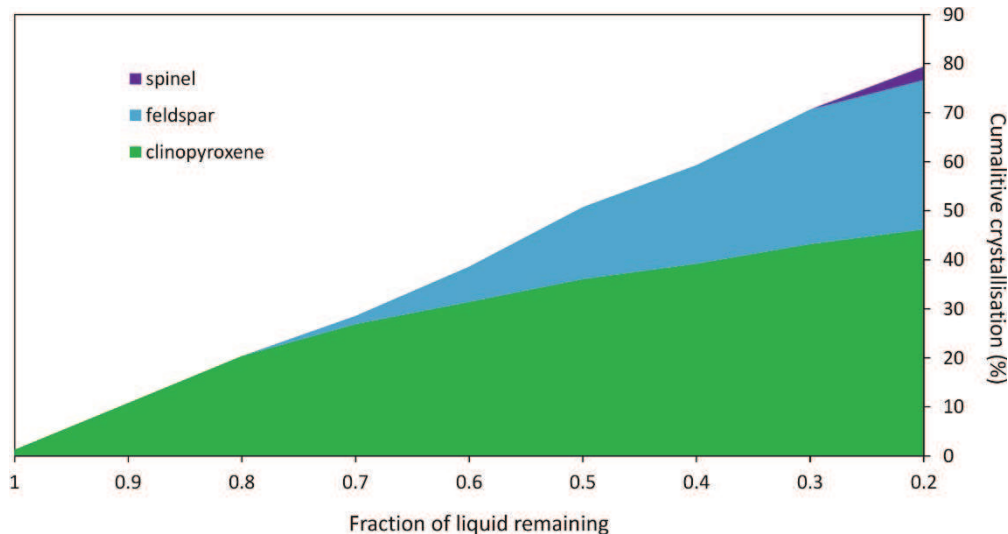
Figure 6.2 A diagram of the cumulative proportions of crystals formed during fractional crystallisation of the Roseburg parent magma at 10 % intervals of crystallisation.

Trace element modelling of factional crystallisation trends using the parameters and mineral abundances produced by the 071RO 7kbar model are shown in Figure 6.3. This model can replicate the trends of the samples with

greater abundances of incompatible trace elements relatively well, however, as a result of its moderate REE contents, sample 071RO cannot be used to model the samples with lower trace element abundances. Also apparent are samples with negative Ti anomalies (indicative of Fe-Ti oxide fractionation), which are not modelled by the trace element fractionation models. However, this group of data, with negative Ti anomies, is not distinguishable in the major elements, and so is difficult to model with the MELTS programme. Despite this the general trace element compositions of the Roseburg group can be replicated by low degrees of fractionation of a parent magma with sample 071RO composition, at high pressures.
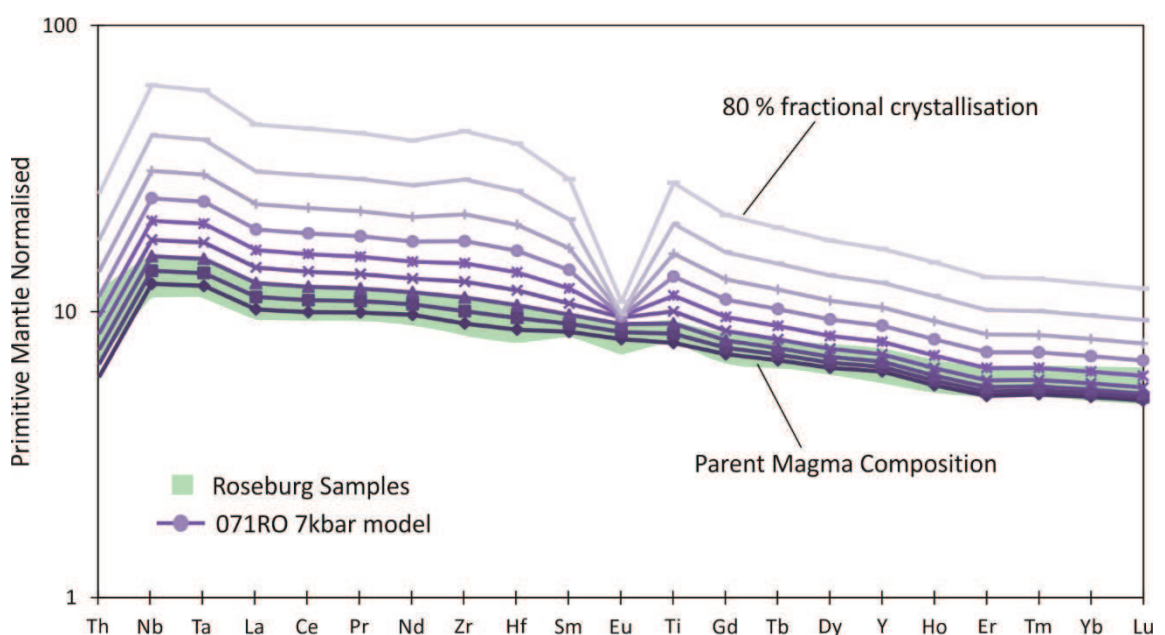
Figure 6.3 Primitive mantle normalised spider diagram of the Roseburg rocks along with the best fit predicted fractional crystallisation model from a parent magma with the composition of sample 071RO. Model compositional lines indicate intervals of 10 % crystallisation.

The equilibrium feldspar and clinopyroxene compositions predicted by the 7 kbar model have also been compared to the An and Mg# of the Roseburg feldspar and clinopyroxene phenocrysts (Figure 6.4). The 071RO 7 kbar model shows little similarity to the plagioclase and clinopyroxenes of the samples, with the majority of phenocrysts analysed displaying higher Mg# and An. One reason for this may be that the analysed clinopyroxenes and feldspars are not in true equilibrium with one another and did not crystallise at similar times. Additionally several of the

clinopyroxenes analysed display compositions which suggest crystallisation from relatively primitive parent magma, with Mg# of >84 (Figure 6.4 and 4.2), along high Cr_2O_3 and low TiO_2 abundances (see Figure 4.2). A model, which incorporates fractionation under relatively high pressures, cannot therefore provide a mechanism that produces the majority of mineral assemblages observed in the Roseburg rocks.
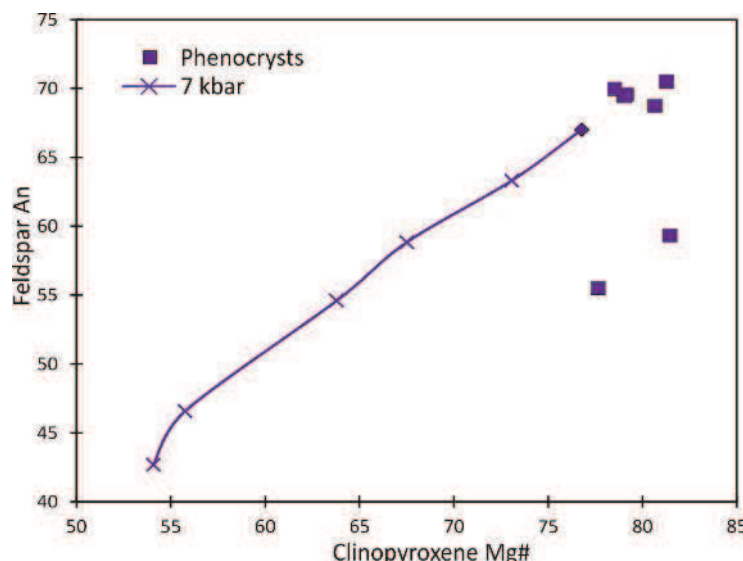
Figure 6.4 Diagram showing the feldspar An number and clinopyroxene Mg# of analysed crystals compared with that of the predicted fractional crystallisation model of the 071RO parent, at 10 % intervals of crystallisation.

The CIPW normative mineral abundances, when plotted on the diagram in Figure 6.5, appear to indicate fractionation along a low-pressure crystallisation path. Therefore, fractional crystallisation of a parent magma with a composition which is more primitive at more moderate pressures may provide an explanation for some of the trends observed in the Roseburg Group. Although, the relatively homogeneous major and trace element compositions of the Roseburg Group does suggest, that in reality, little fractionation has taken place within the group itself.
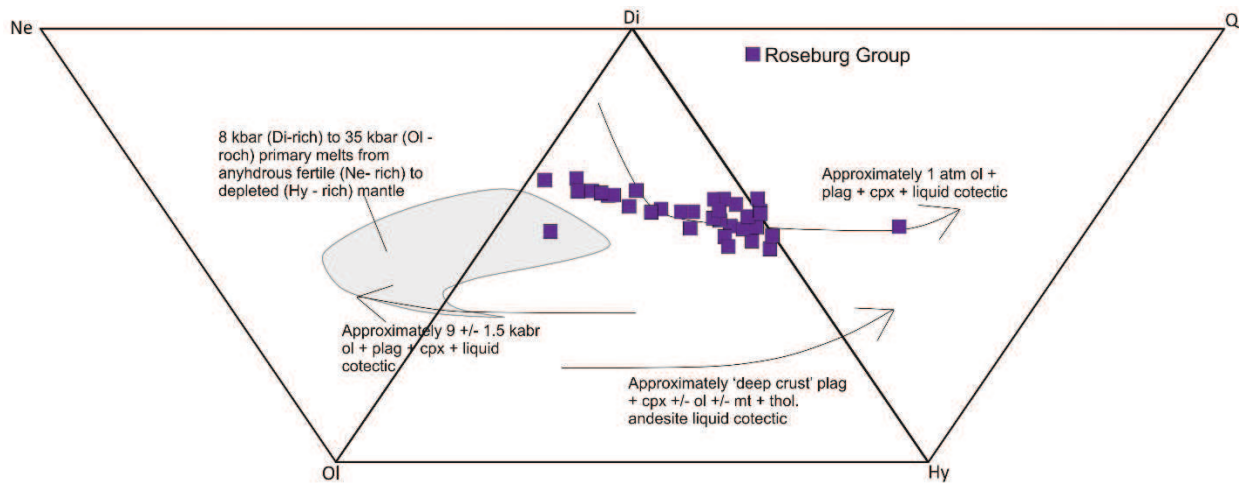
Figure 6.5 Expanded basalt tetrahedron with experimentally derived fractional crystallisation trends and the compositions of primary mantle melts along with the composition of the Roseburg Group samples (Thompson, 1982; Brueseke and Hart, 2008).

6.1.1.2 Corvallis Group

The composition for the estimate parent magma for the Corvallis Group has been derived from sample CR014, which has the highest MgO content (9.03 wt.%) of the group along with the lowest Zr abundance (61.4 ppm) and low REE concentrations. The Corvallis model, which best predicts the composition of the group is the 7 kbar model. Also shown in figure 6.6 is the EPR model which best approximates the data, the 1kbar + 1% H_2O wt.% model (only one EPR parent magma derived fractionation curve is shown for clarity). The CR014 7 kbar model predicts the lower to more moderate SiO_2 wt. % samples compositions, along with the TiO_2, FeO abundances and the general CaO and K_2O trends (Figures 6.6). The CR014 7 kbar model predicts that crystallisation begins at 1315 °C with clinopyroxene before being joined by plagioclase at 1255 °C (~31% crystallisation) (Figure 6.7). Spinel then joins the crystallising assemblage at 1167 °C after 76 % fractionation. The lowest MgO in this group is 2.9 wt.% which corresponds with around 70 % crystallisation.
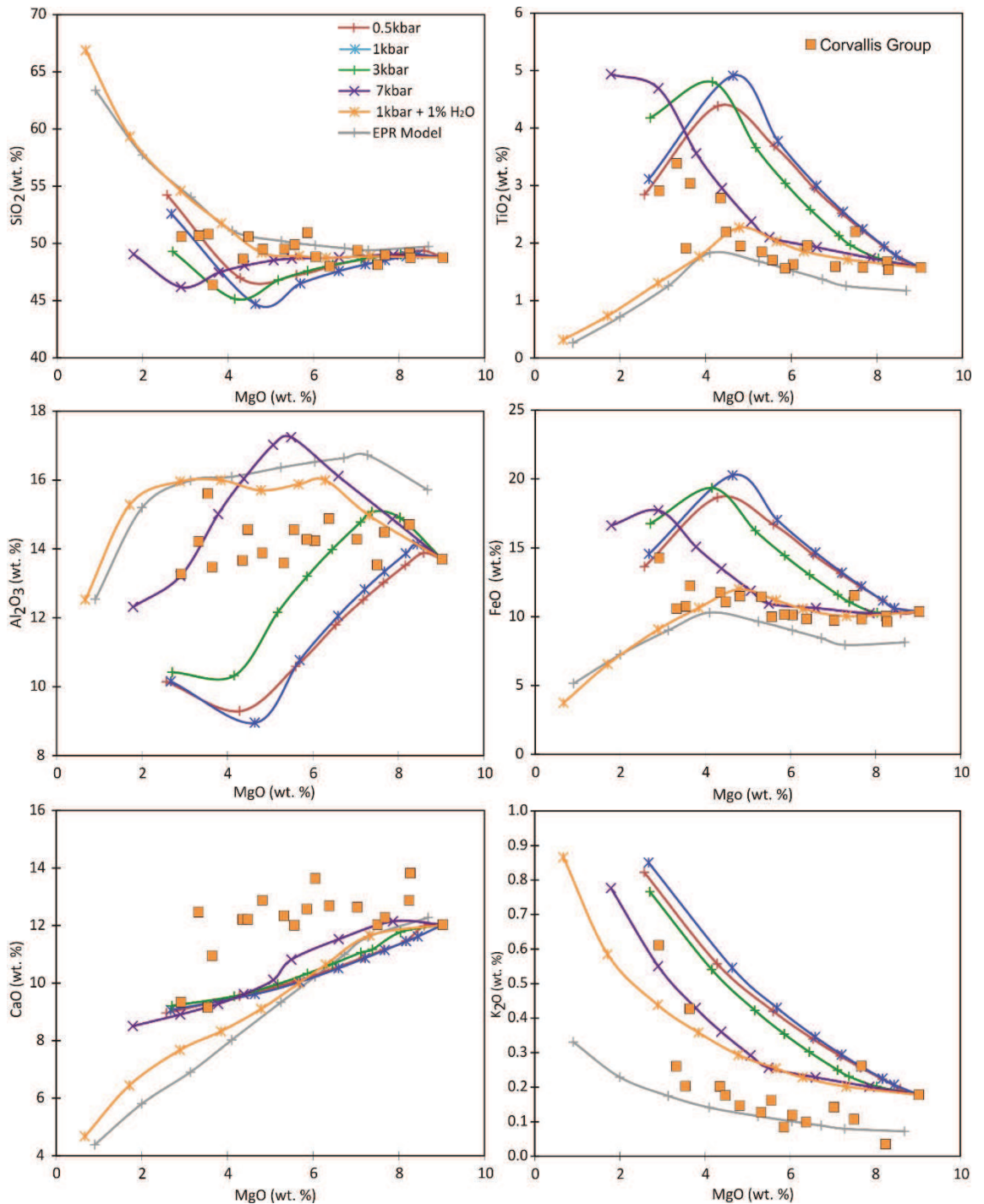
Figure 6.6 Bivariate diagrams of representative major elements vs MgO for the Corvallis Group along with the predicted fractional crystallisation models from a parent magma with the composition of sample CR014. Markers indicate intervals of 10 % crystallisation.
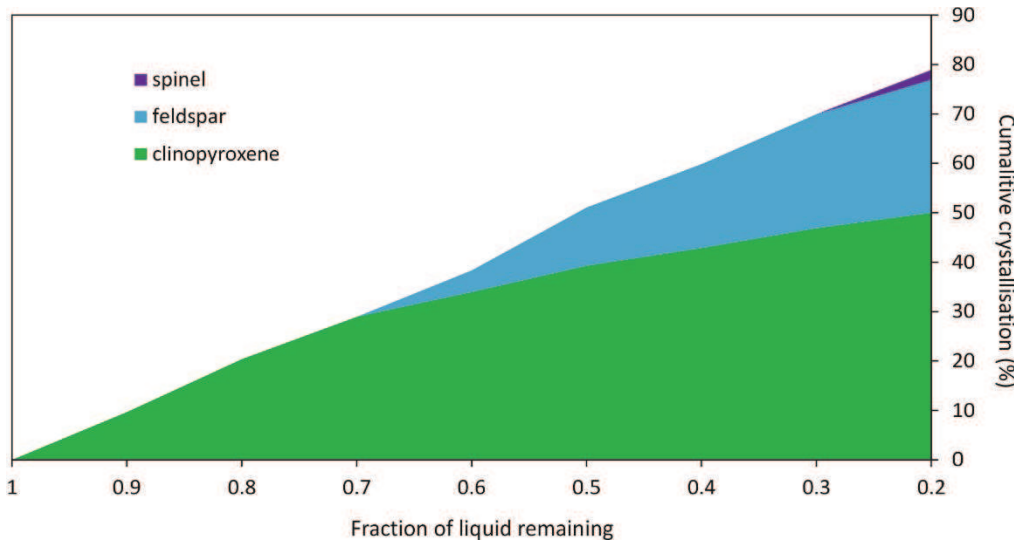
Figure 6.7 A diagram of the cumulative proportions of crystals formed during fractional crystallisation of the Corvallis Group parent magma at 10 % intervals of crystallisation.

The CR014 7 kbar trace element models in figure 6.8 can generally model the incompatible trace elements, with the exception of Th. The 7 kbar model does however predict a steeper La/Sm than is observed in the Corvallis Group data. However, while the 7 kbar model from a parent composition similar to sample CR014 can reasonably explain the major elements and some of the incompatible trace element compositions recorded in the Corvallis Group it is not reconciled with the approximated fractionation pressure suggested by figure 6.9. The Corvallis Group generally has an affinity towards lower pressure cotectics and appears to have undergone significant differentiation in an upper crustal magma chamber. This however, may be a result of the relatively high SiO_2 contents for a given MgO wt.% observed in this group, which results in a greater normative abundance of quartz than occurs in the samples in reality (Chapter 4).
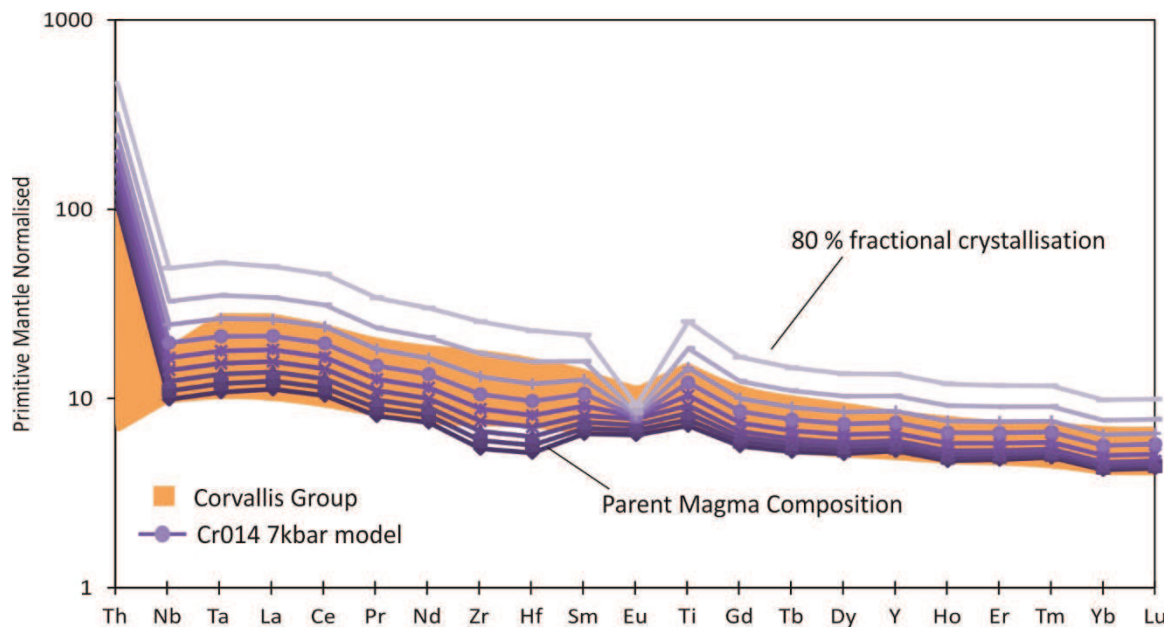
Figure 6.8 Primitive mantle normalised spider diagram of the Corvallis Group along with the best fit predicted fractional crystallisation model from a parent magma with the composition of sample CR014. Model compositional lines indicate intervals of 10 % crystallisation.
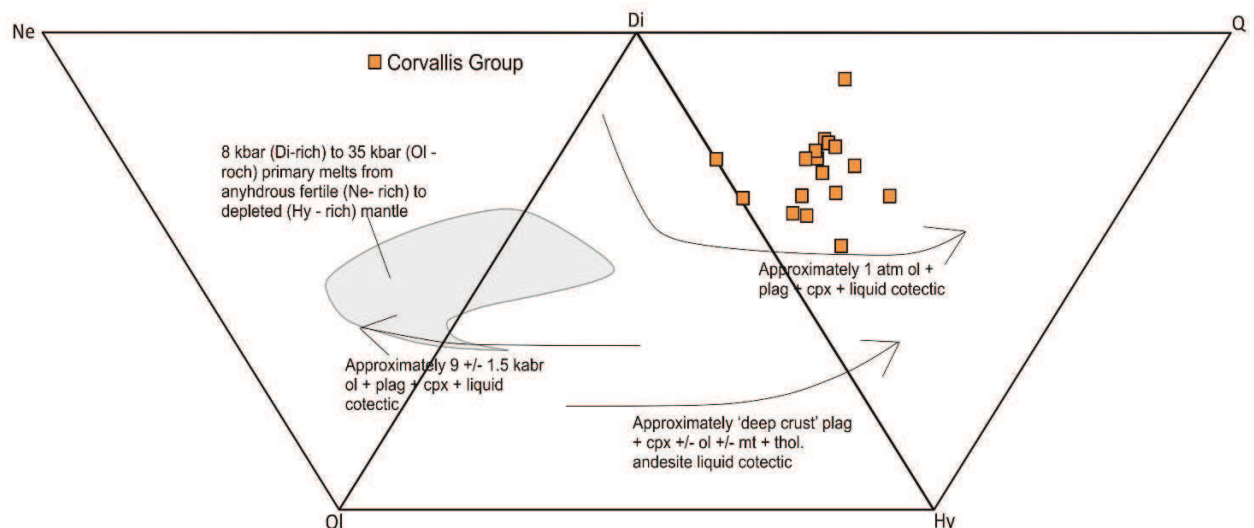
Figure 6.9 Expanded basalt tetrahedron with experimentally derived fractional crystallisation trends and the compositions of primary mantle melts along with the composition of the Corvallis Group samples (Thompson, 1982; Brueseke and Hart, 2008).

6.1.1.3 Siletz River Group

The sample selected as an estimate for the parent magma composition of the

Siletz River Group is sample 116SRV, which has a MgO of 7.12 wt.% and a Zr of 109.7 ppm, the highest MgO and third lowest Zr of the Siletz River Group. The major element fractional crystallisation models which best predicts the major element trends of the group are, for the 116SRV parent a 7 kbar model and for the EPR parent estimate the 3 kbar model (with the other EPR fractionation models excluded for clarity) (Figure 6.10). However, the 116SRV 7 kbar model can only replicate the composition of some of the sample's SiO_2, FeO and CaO contents and, to a lesser extent, the TiO_2 abundances while it cannot reproduce any of the Al_2O_3 and K_2O trends of the Siletz River Group (Figure 6.10). The EPR 3kbar model is also able to approximate the SiO_2 evolution of the group along with the general TiO_2, Al_2O_3 and K_2O trends of the data (Figure 6.10).
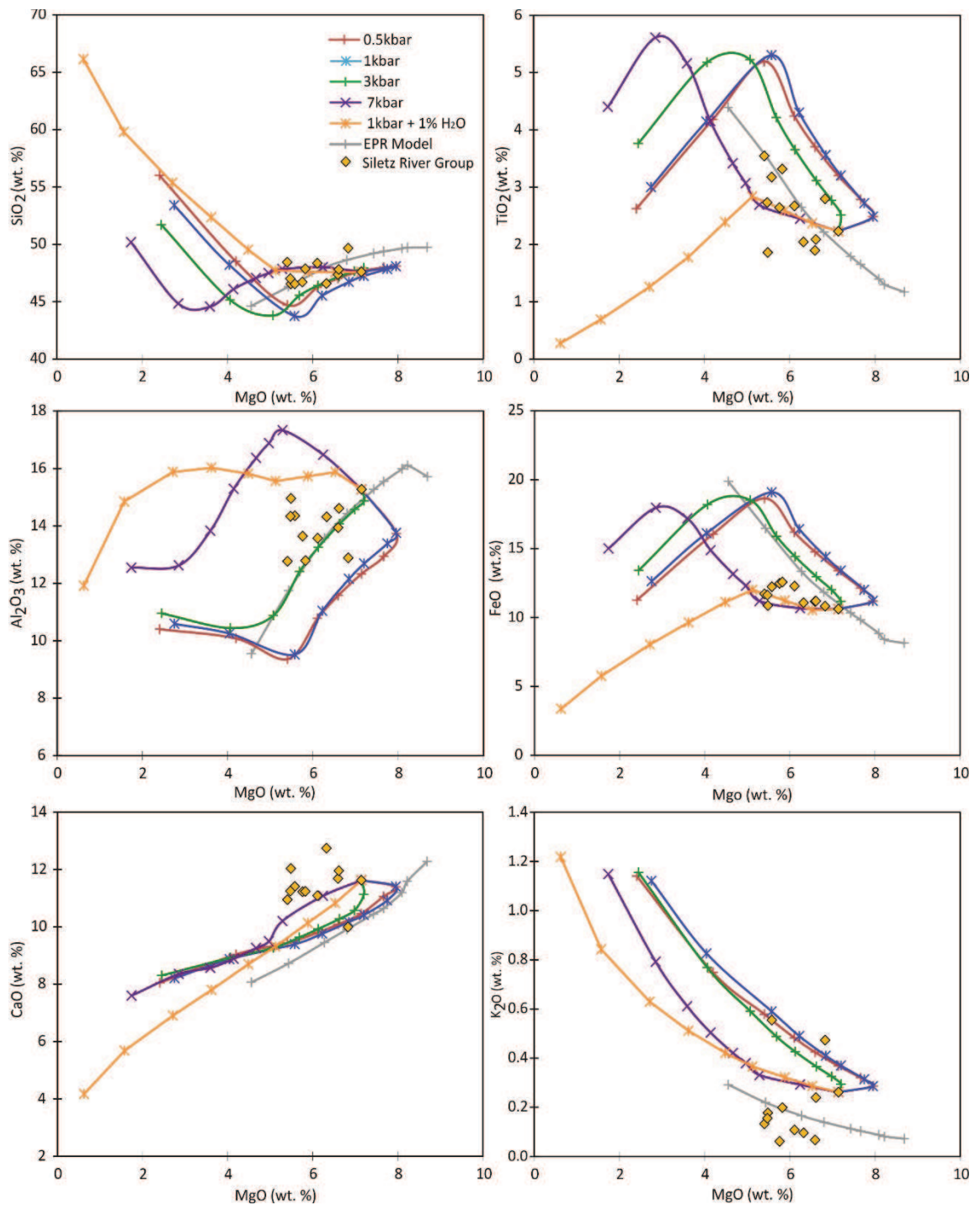
Figure 6.10 Bivariate diagrams of representative major elements vs MgO for the Siletz River Group along with the predicted fractional crystallisation models from a parent magma with the composition of sample 116SRV. Markers indicate intervals of 10 % crystallisation.

The 116SRV 7 kbar model predicts that crystallisation begins with clinopyroxene at 1281 °C, plagioclase then begins to crystallise at 1249 °C when

20 % crystallisation has taken place. The next phase to crystallise, at 1177 °C, is spinel at 68 % crystallisation along with other oxides at 1173 °C and 70 % crystallisation (Figure 6.11). This assemblage is relatively consistent with what is observed in the Siletz River Group samples (see section 4.2.2.1).
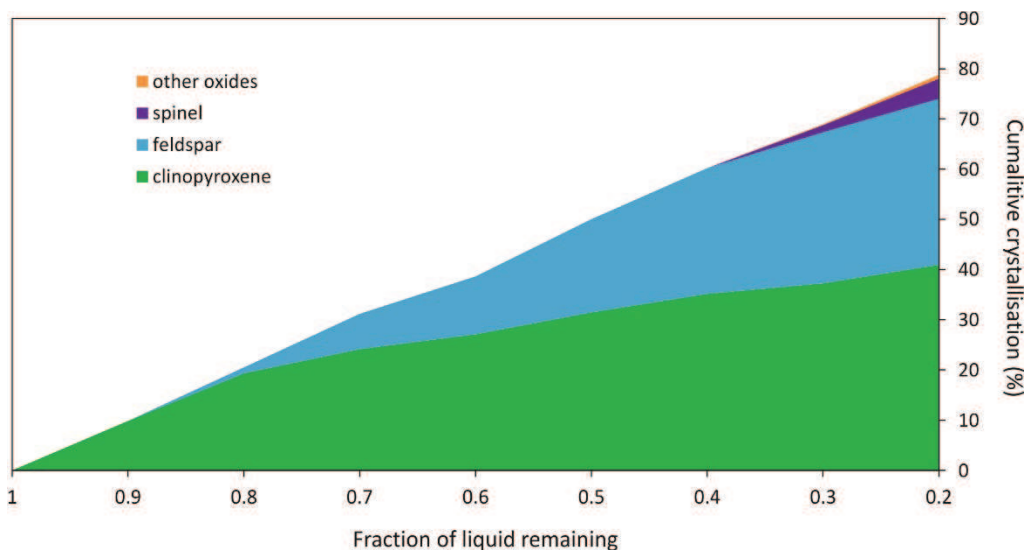
Figure 6.11 A diagram of the cumulative proportions of crystals formed during fractional crystallisation of the Siletz River Group parent magma at 10 % intervals of crystallisation.

Models using incompatible trace elements to model fractional crystallisation using the parameters and mineral assemblages predicted to form during fractionation are shown in figure 6.12. The model predicts some of the incompatible trace element trends, although the abundances for Y for example, are too low for the majority of the data. The 7 kbar model does however predict the La/Sm and Gd/Yb trends relatively well.
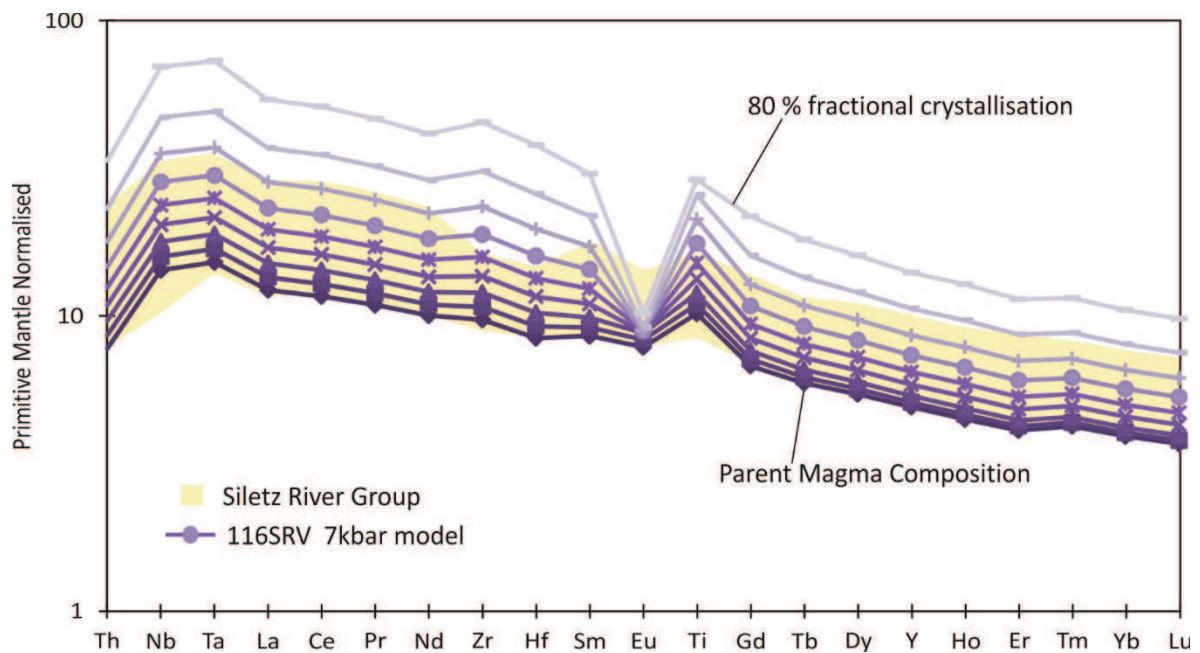
Figure 6.12 Primitive mantle normalised spider diagram of the Siletz River Group along with the best fit predicted fractional crystallisation model from a parent magma with the composition of sample 116SRV. Model compositional lines indicate intervals of 10 % crystallisation.

However, in somewhat of a contradiction to the MELTS modelling, the CIPW normative mineral abundances, when plotted on the expanded basalt tetrahedron appear to trend towards low - pressure fractional crystallisation (Figure 6.13). Clinopyroxene and plagioclase rich glomerocrysts observed in this group also indicate that open system processes took place within the magma chamber(s) from which the Siletz River Group are derived from. Overall, heterogeneities in the geochemistry of this group cannot be modelled by any one fractionation trend, indicating, fractionation over different pressures from numerous magma chambers, each with slight differences in source composition may have occurred.
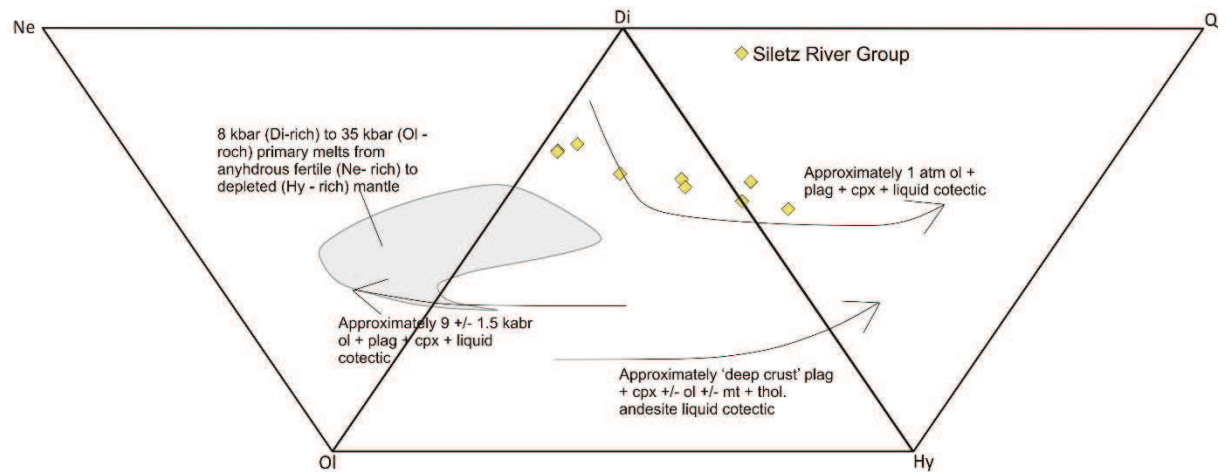
Figure 6.13 Expanded basalt tetrahedron with experimentally derived fractional crystallisation trends and the compositions of primary mantle melts along with the composition of the Siletz River Group samples (Thompson, 1982; Brueseke and Hart, 2008).

6.1.1.4 Tillamook Group

Sample 171SRV has been chosen as an estimate for the parent magma for the Tillamook Group, due to its high MgO content (8.7 wt.%) and relatively low Zr (115 ppm) and REE values. The major element models are shown in figure 6.8. The model which best approximates the trends observed within the Tillamook Group is the 7 kbar model, however in reality none of the 171SRV derived models reproduce an accurate model of the data (Figure 6.14). The 7 kbar EPR model can predict the general trends observed in SiO_2, TiO_2, CaO, FeO and K_2O, but it is also far from conclusive.
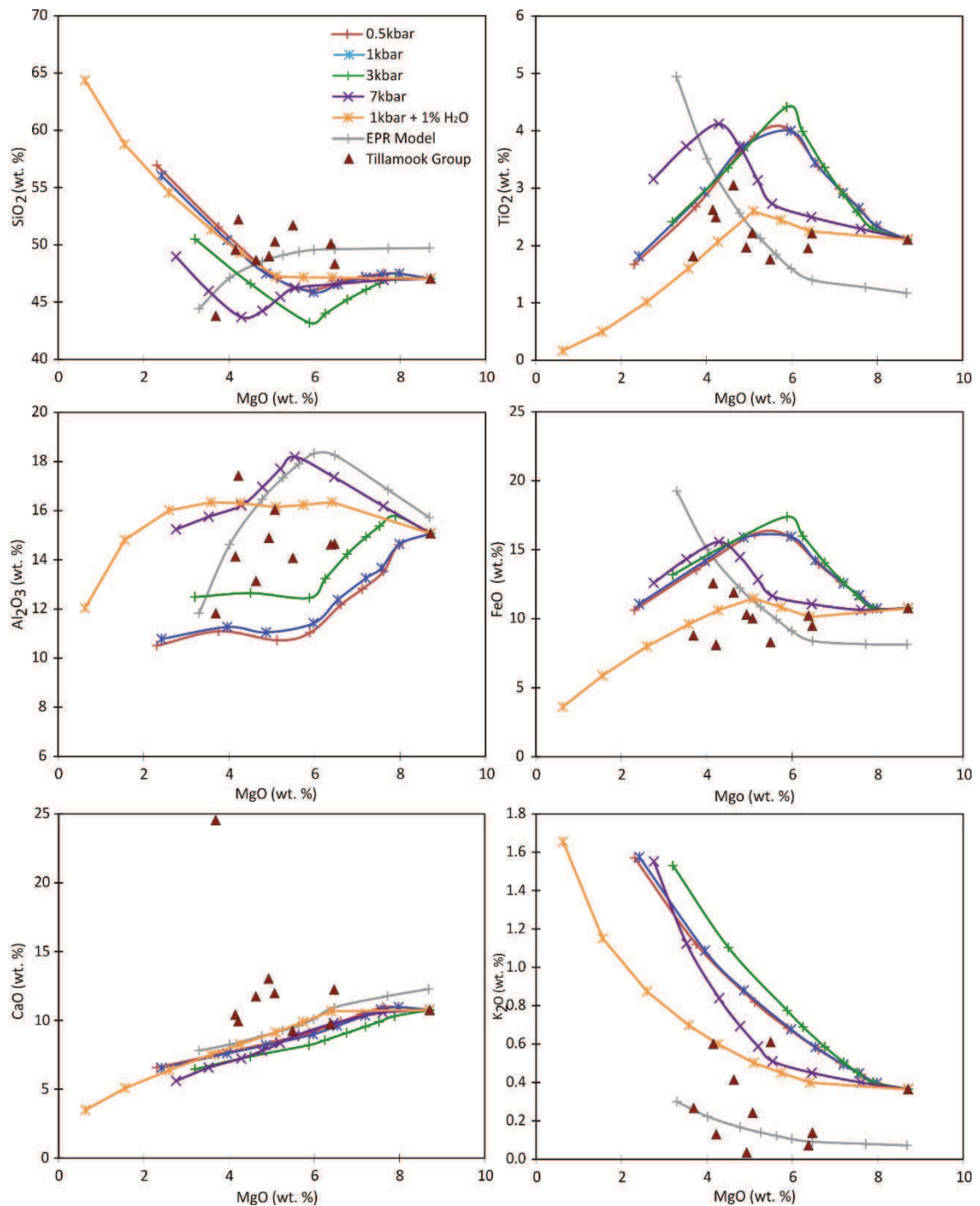
Figure 6.14 Bivariate diagrams of representative major elements vs MgO for the Tillamook Group along with the predicted fractional crystallisation models from a parent magma with the composition of sample 171SRV. Markers indicate intervals of 10 % crystallisation.

The 171SRV 7 kbar model predicts that the parent magma begins crystallising at 1295 °C with clinopyroxene being the first mineral to crystallise.

Plagioclase then joins the assemblage at ~29 % crystallisation at 1239 °C before shortly being joined by orthopyroxene at 1235 °C and ~36 % crystallisation, Finally, at 1195 °C, spinel joins the assemblage at 60 % fractional crystallisation (Figure 6.15). However, it is worth noting that no orthopyroxene has been observed within the Tillamook Group samples. This lack of orthopyroxene is however, consistent with an anhydrous model. In addition the MgO of the liquid at 60 % fractional crystallisation is ~ 5.4 wt.%, which is higher than the MgO of the Tillamook samples. These two factors indicate, along with the lack of overlap in figure 6.14, that the Tillamook samples did not originate from a magma with a similar composition to sample 171SRV.
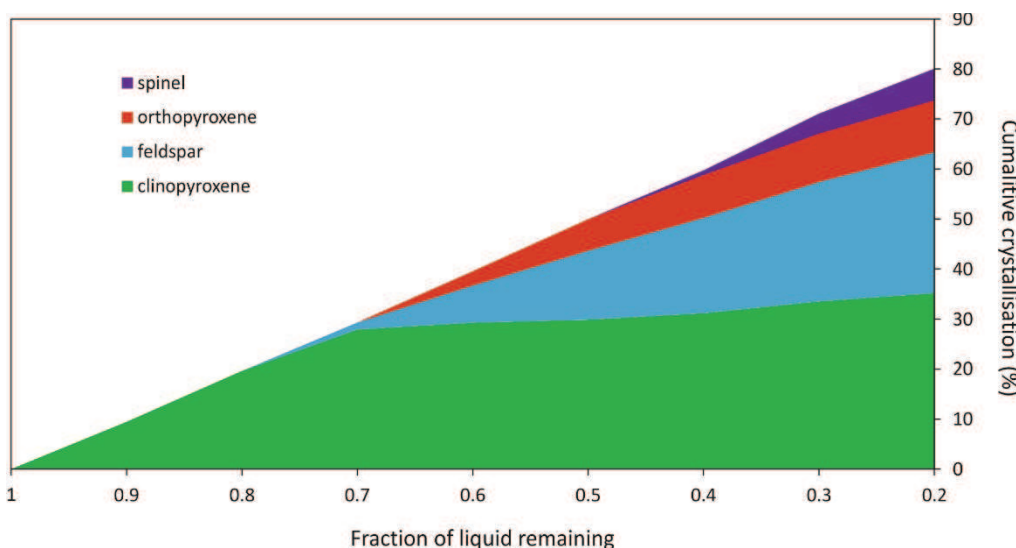
Figure 6.15 A diagram of the cumulative proportions of crystals formed during fractional crystallisation of the Tillamook Group parent magma at 10 % intervals of crystallisation.

The 7 kbar EPR parent model begins crystallising clinopyroxene at 1305 °C before crystallising spinel at 1289 °C after ~14 % crystallisation. Plagioclase then joins the assemblage at ~27 % crystallisation at 1269 °C. The model reaches the lowest MgO of the Tillamook samples at ~ 46 % crystallisation. This model, therefore, with its lack of orthopyroxene crystallisation may represent a more adequate starting estimate parent composition for the Tillamook Group.

Modelling using incompatible trace elements for the Tillamook lavas is shown in Figure 6.16. The 7 kbar parent model cannot successfully reproduce the incompatible trace element abundances and trends shown by the Tillamook

Group, with the Tillamook data frequently having lower incompatible trace element concentrations (Figure 6.16).
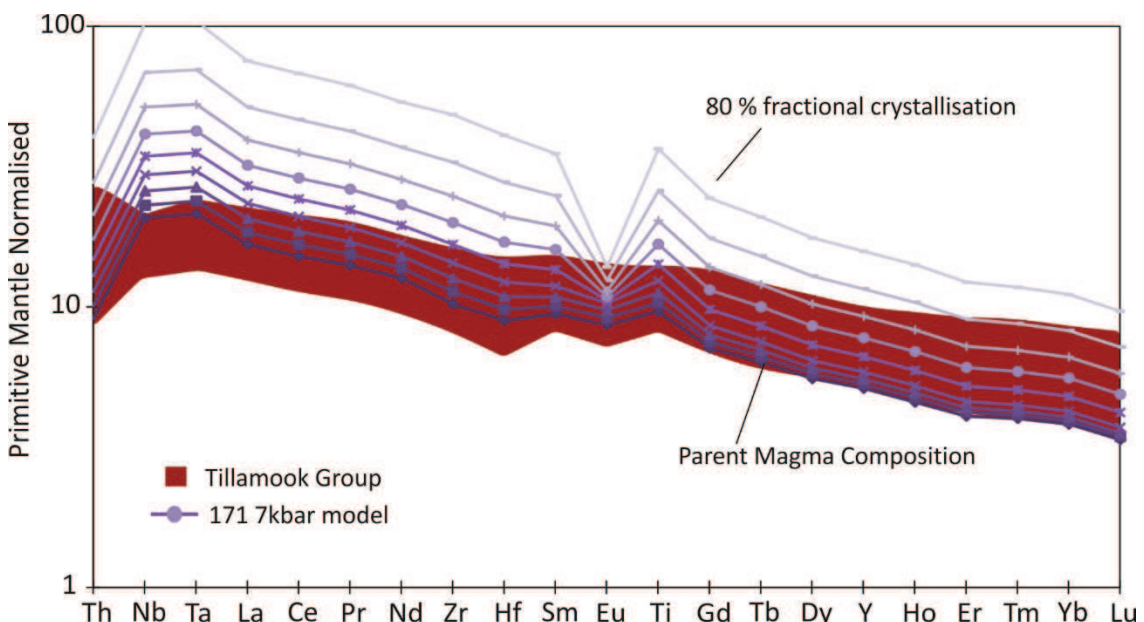
Figure 6.16 Primitive mantle normalised spider diagram of the Tillamook Group along with the best fit predicted fractional crystallisation model from a parent magma with the composition of sample 171SRV. Model compositional lines indicate intervals of 10 % crystallisation.

Figure 6.17 shows the An and Mg# values of the equilibrium feldspar and clinopyroxene produced by the 171SRV 7 kbar model, compared with that of the Tillamook Group. In general the model cannot be readily reconciled with the Tillamook data, with the glomerocrysts from the Tillamook Group containing higher values than observed in the models. In addition the high Mg# high Cr_2O_3 low TiO_2 clinopyroxenes shown in Figure 4.5, suggest a primitive parental magma composition for this group, the composition of which is most likely more primitive than that of sample 171SRV (Ross and Elthon, 1997). However, the 171SRV 7 kbar model is able approximate the trend if not the composition of the phenocrysts analysed.
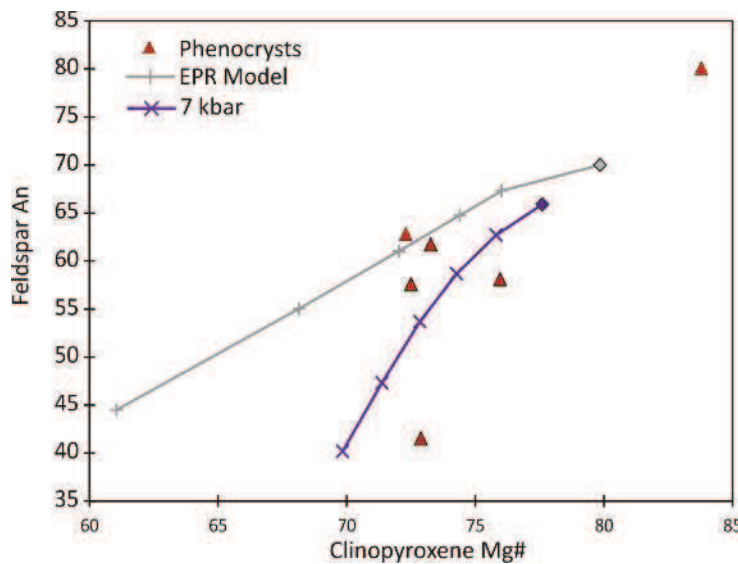
Figure 6.17 Diagram showing the feldspar An number and clinopyroxene Mg# of analysed crystals compared with that of the predicted fractional crystallisation model of the 171SRV parent, at 10 % intervals of crystallisation.

As discussed above, due to the relatively heterogeneous nature of the rocks, fractional crystallisation trends for the Tillamook Group are difficult to model. This is also reflected in figure 6.18, which generally illustrates that Tillamook Group has an affinity towards lower pressure fractional crystallisation, of predominantly olivine, clinopyroxene and plagioclase. However, there is also significant scatter across the tetrahedrons within the group, highlighting most likely a relatively heterogeneous source composition or fractionating conditions.
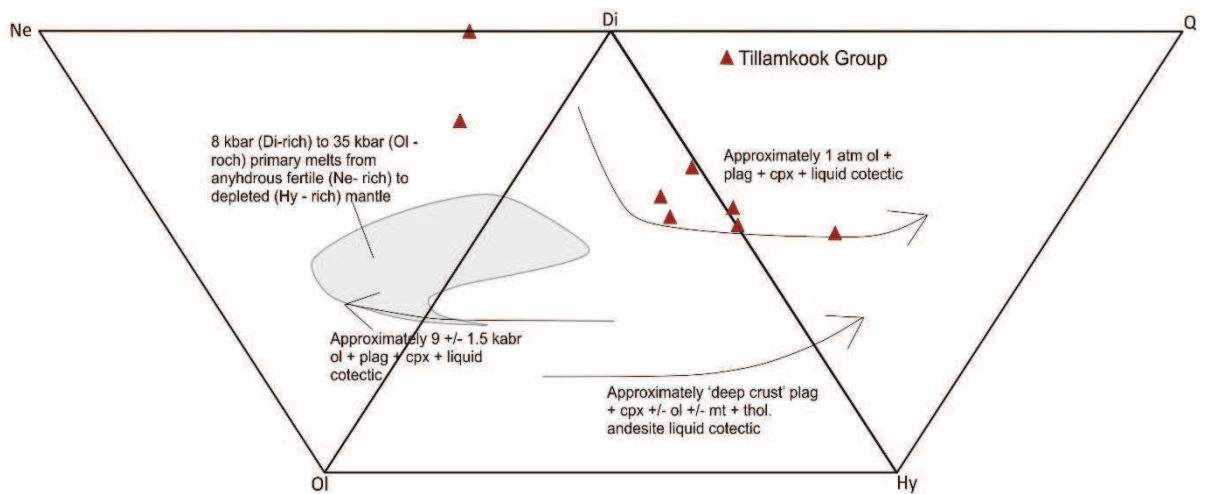

Figure 6.18 Expanded basalt tetrahedron with experimentally derived fractional crystallisation trends and the compositions of primary mantle melts along with the composition of the Tillamook Group samples (Thompson, 1982; Brueseke and Hart, 2008).

6.1.1.5 Alkali Group

Sample LC008 has been selected as an estimate for the parent magma for this group as it has the highest MgO (8.0 wt.%) and lowest Zr (74.2 ppm) of the group. As observed in figure 6.14 it is not apparent which model best approximates the major element abundances in this group. Of the EPR models, the 3 kbar model best predicts the spread of the data, although relatively poorly. The Alkali Group samples plot between the LC008 7 kbar and 3 kbar models, although several samples are not in this range with both higher and lower major element abundances observed (Figure 6.19). Overall, the 7 kbar model appears to best represent the data. The 7 kbar model predicts that crystallisation begins at 1319 °C with clinopyroxene. The next mineral to crystallise, at 1287 °C, is plagioclase after ~31 % crystallisation before being joined by spinel at 1191 °C after ~76 % crystallisation (Figure 6.20).
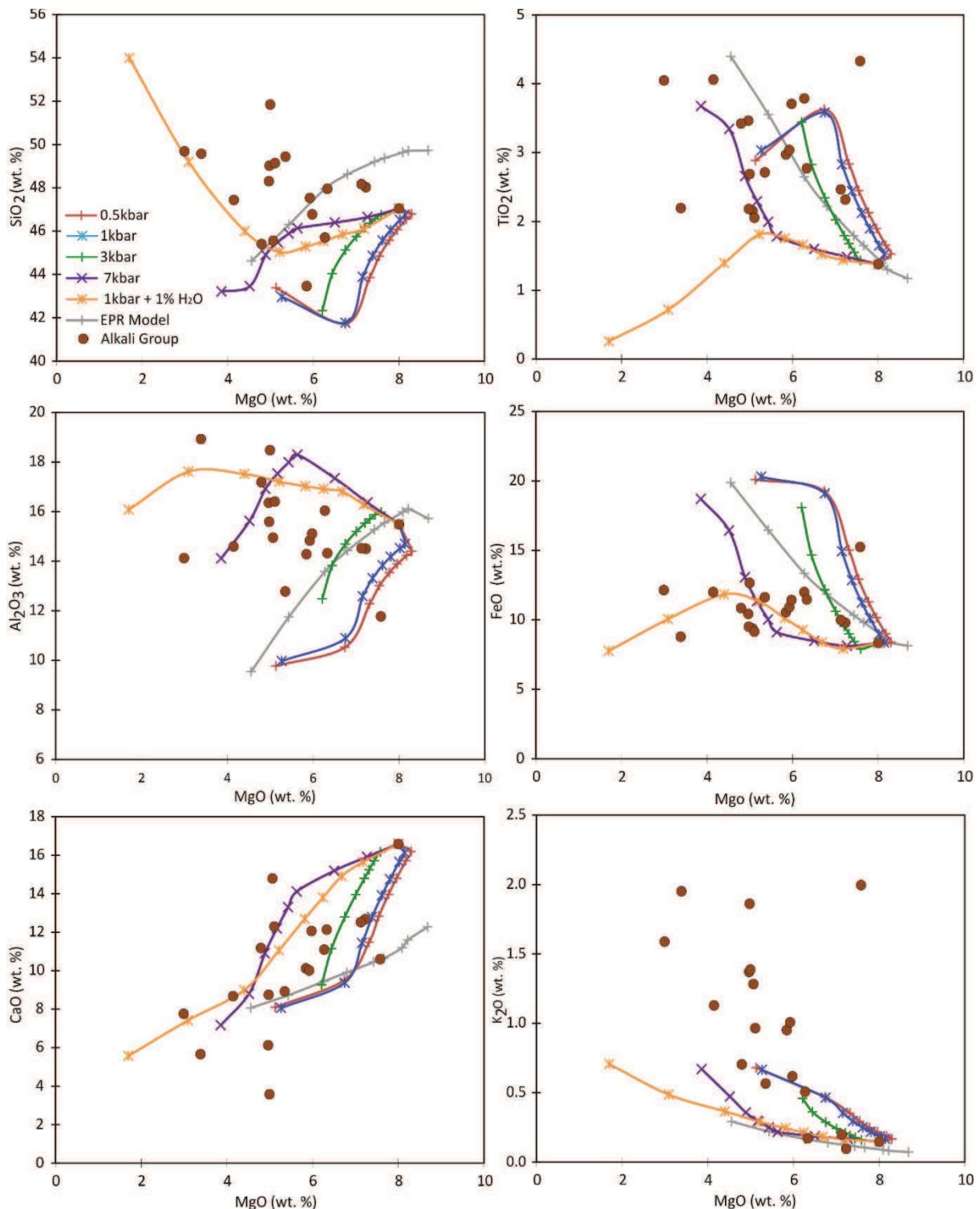
Figure 6.19 Bivariate diagrams of representative major elements vs MgO for the Alkali Group along with the predicted fractional crystallisation models from a parent magma with the composition of sampleLC008. Markers indicate intervals of 10 % crystallisation.
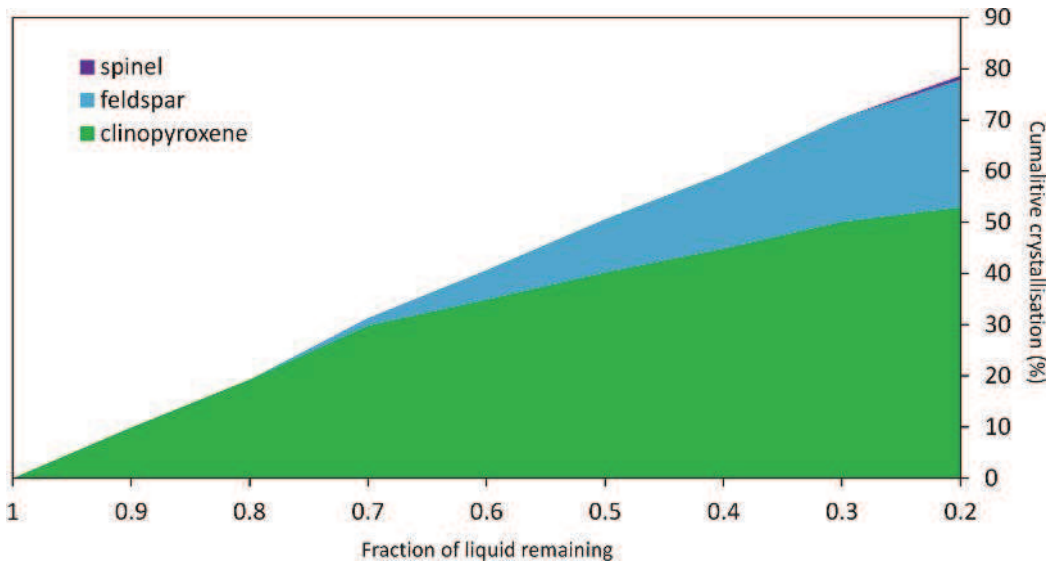
Figure 6.20 A diagram of the cumulative proportions of crystals formed during fractional crystallisation of the Alkali Group parent magma at 10 % intervals of crystallisation.

The incompatible trace elements of the Alkali Group, although scattered, are broadly reproduced by the LC008 7 kbar model, using the conditions and minerals produced (Figure 6.21. In addition, the model fails to reproduce the Gd/Yb and La/Sm ratios of the data and can only predict the magnitude of some of the anomalies in the data (Figure 6.16). The variations observed in the incompatible trace elements, in particular the Gd/Yb ratios are most likely a result in variations in the source composition and as discussed previously, the alkali basalts of the Siletz River area are generally located towards the top of the sequence and form a thin veneer across much of the terrane where exposed here (Chapter 3 and 4). Figure 6.22 also illustrates this considerable heterogeneity, highlighting an array of normative mineral compositions and potential fractionation paths. Therefore, the Alkali Group rocks are most likely derived from several small individual magma chambers and conduits in the later stages of eruption, as opposed to evolving as one composite group.
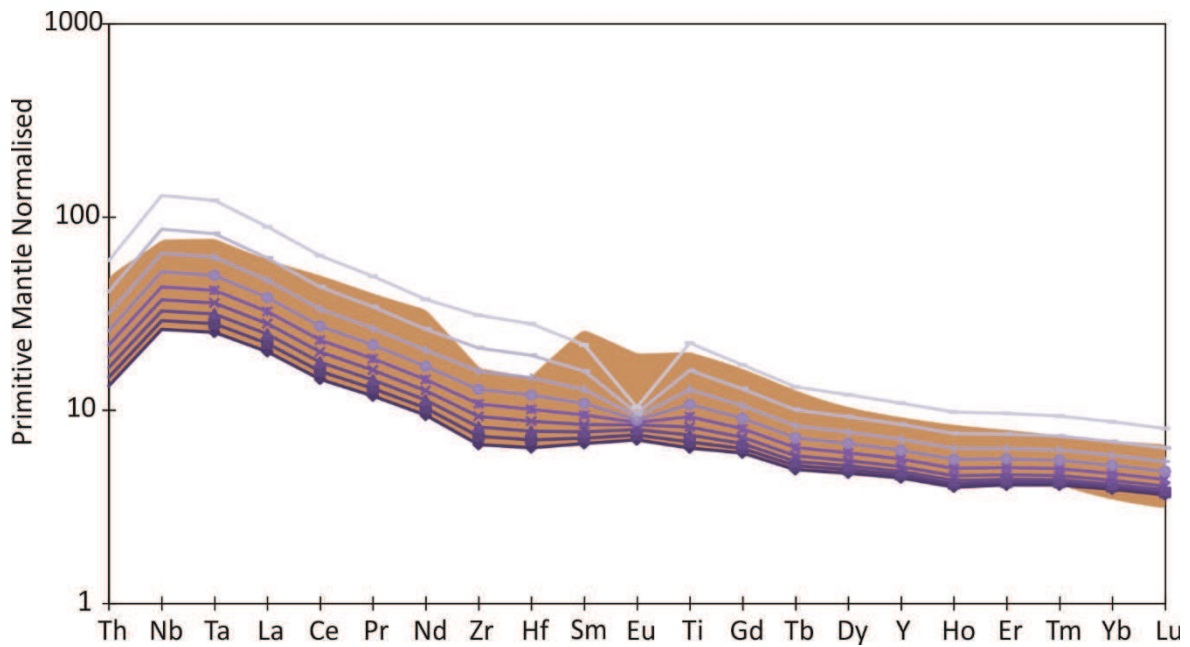
Figure 6.21 Primitive mantle normalised spider diagram of the Alkali Group along with the best-fit predicted fractional crystallisation model from a parent magma with the composition of sample LC008. Model compositional lines indicate intervals of 10 % crystallisation.
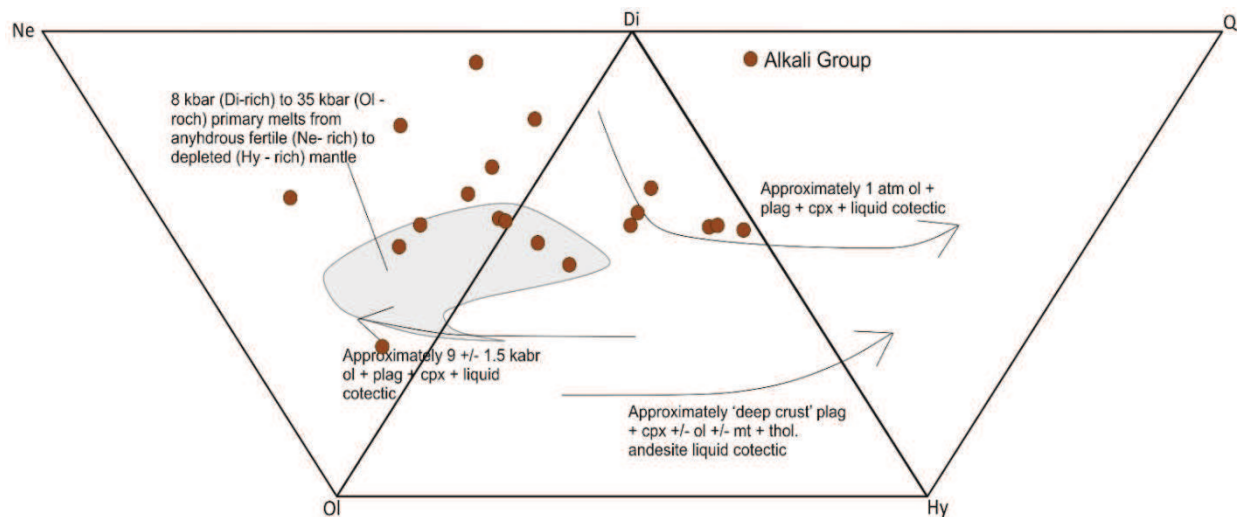

Figure 6.22 Expanded basalt tetrahedron with experimentally derived fractional crystallisation trends and the compositions of primary mantle melts along with the composition of the Alkali Group samples (Thompson, 1982; Brueseke and Hart, 2008).

6.1.2 Crescent Formation, Washington

6.1.2.1 Crescent Main Group

Sample 270CM has been selected as an estimate for the parent magma of the Crescent Main Group. Sample 270CM contains relatively high MgO concentrations (8.16 wt.%) and one of the lowest abundances Zr (78.0 ppm) and REE concentrations. While sample 316CM has the highest MgO content of the group (9.0 wt.%) it also has comparatively high SiO_2 and Al_2O_3 abundances, which promote the early fractionation of high SiO_2 plagioclase in the MELTS models. The result of this is significant depletions in the SiO_2 content, which is not observed within the Crescent Main Group major element data and thus sample 270CM has been selected as a representative parent magma composition in its place.

It is apparent that no one major element model of fractionation from a parent magma with sample 270CM's composition (Figure 6.23) can approximate the abundances observed within the data, with the majority of the data overlapping with models of several different pressures, indicating fractionation may have been polybaric, across several magma chambers within the crust. However, of the trends, the overall the 7 kbar model is most representative of the abundances observed in SiO_2, TiO_2, and the majority of the CaO concentrations (Figure 6.23). The scatter observed in the K_2O of the Crescent Main Group is not reproduced by any of the models and is most likely a result of alteration (discussed in Chapters 4 and 5) (Figure 6.23). The 7 kbar model predicts that crystallisation begins at 1299 °C with clinopyroxene. Plagioclase then join the assemblage at 1263 °C at around ~ 24 % crystallisation, before finally being joined by orthopyroxene at 40 % crystallisation at 1247 °C (Figure 6.24). Of the EPR composition parent magma models, the 3 kbar model best approximates the trends of the data, with the model predicting the TiO_2 trends of the data, along with the general major element compositions of several of the samples with greater MgO abundances in the group.
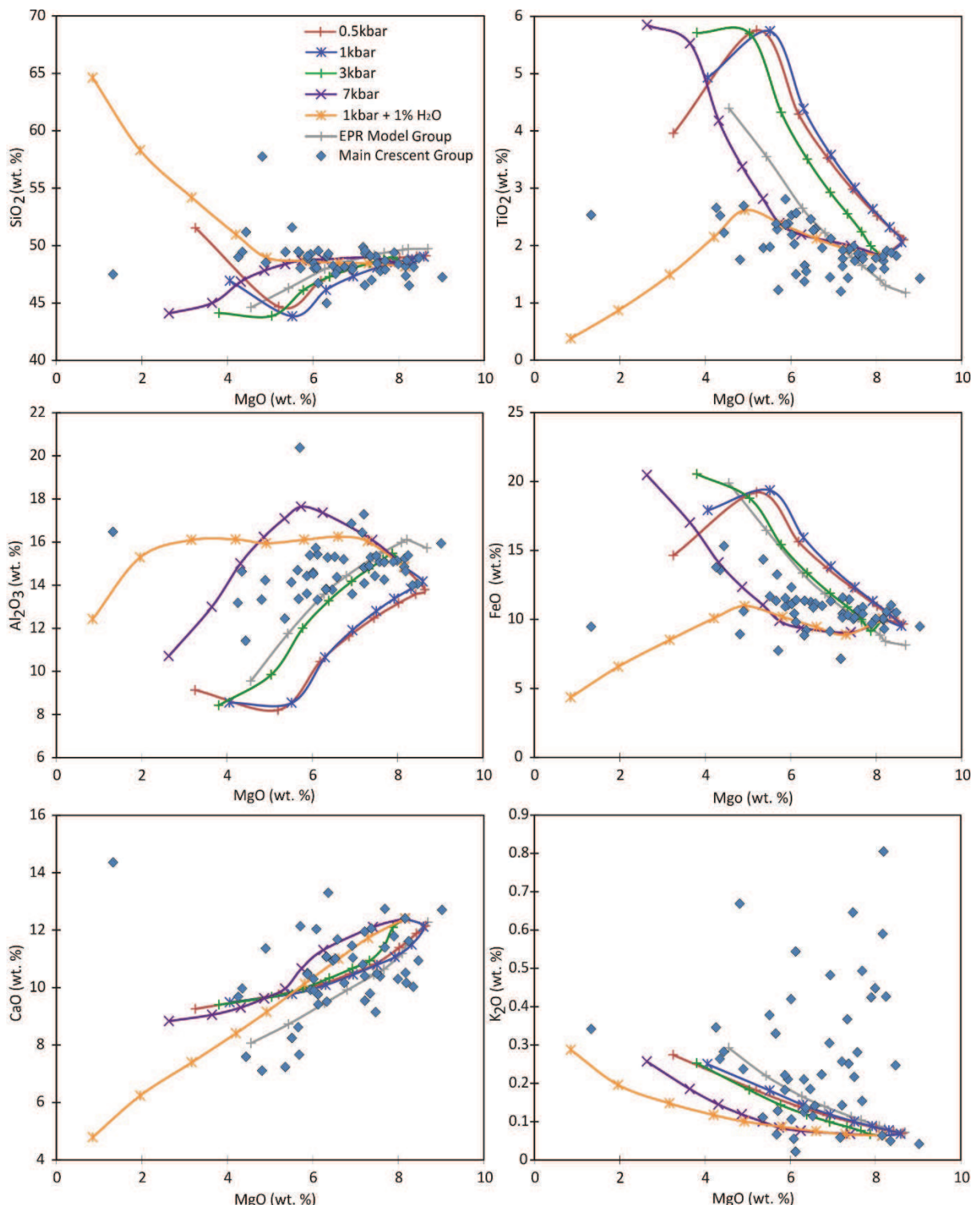
Figure 6.23 Bivariate diagrams of representative major elements vs MgO for the Crescent Main Group along with the predicted fractional crystallisation models from a parent magma with the composition of sample 316CM. Markers indicate intervals of 10 % crystallisation.
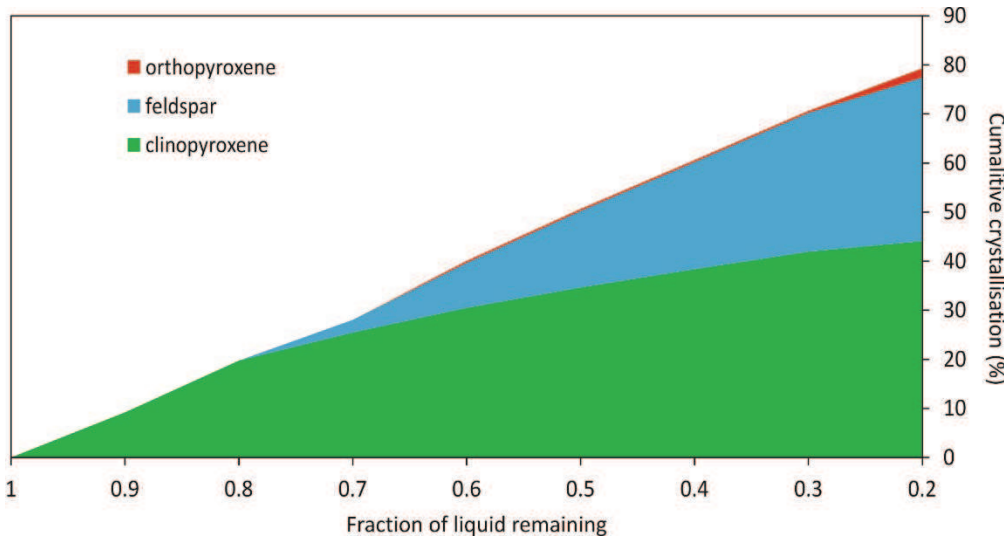
Figure 6.24 A diagram of the cumulative proportions of crystals formed during fractional crystallisation of the Crescent Main Group parent magma at 10 % intervals of crystallisation.

The models that use incompatible trace elements, calculated using the parameters of the 7 kbar model, can recreate the general trends observed in the Crescent Main data (Figure 6.25). However, due to the heterogeneity of the Crescent Main Group, the 7 kbar fractionation model cannot predict several of the samples HREE patterns or the extent of the Nb anomalies (Figure 6.25). While the model can replicate some of the incompatible trace element concentrations, several samples have lower abundances than the modelled primary magma composition (Figure 6.25). Overall therefore, it appears that no one model can explain the fractionation trends of this varied group.
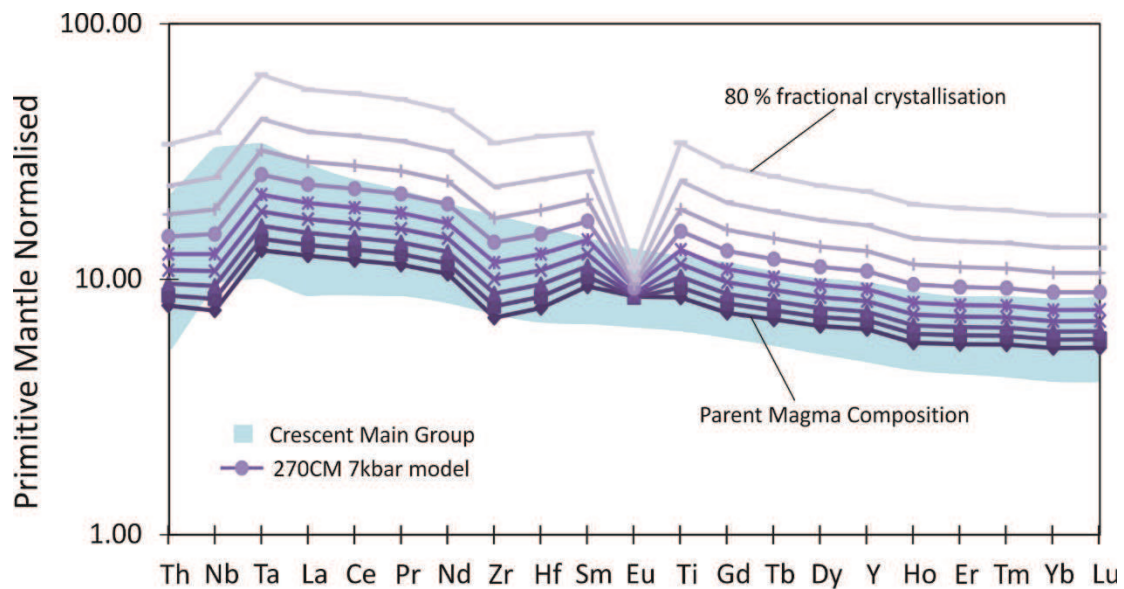
Figure 6.25 Primitive mantle normalised spider diagram of the Crescent Main Group along with the best-fit predicted fractional crystallisation model from a parent magma with the composition of sample 270CM. Model compositional lines indicate intervals of 10 % crystallisation.

The composition of the equilibrium clinopyroxene and feldspar calculated by the model does not approximate that of the data (Figure 6.26). The Crescent Main feldspars generally have much lower An numbers than the model in the phenocrysts. Some of the clinopyroxenes analysed from this group display high Mg#, high Cr_2O_3 and low TiO_2 indicative of a primitive parent magma composition (e.g., Ross and Elthom, 1997), however, the overall composition is relatively varied (with the Mg# for the majority of samples ranging from 70 – 80) (Figure 4.8).
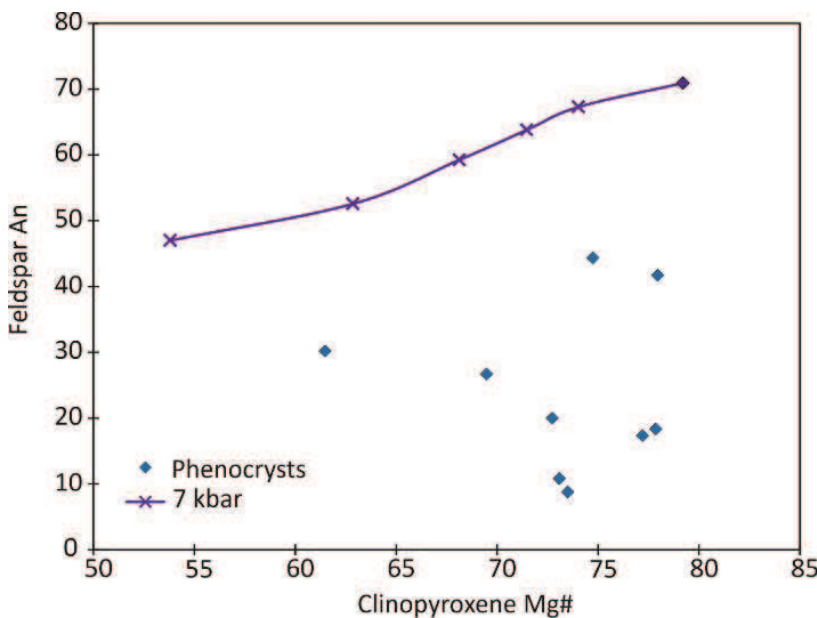
Figure 6.26 Diagram showing the feldspar An number and clinopyroxene Mg# of analysed crystals compared with that of the predicted fractional crystallisation model of the 270CM parent, at 10 % intervals of crystallisation.

Therefore, as discussed above, while a parent magma with sample 270CMs composition or a more primitive composition may explain the trends observed in some of the data, they are by no means conclusive. The majority of samples from this group are most likely not related by fractionation crystallisation in one discrete magma chamber, but may represent multiple magmatic bodies, which have experienced slightly different conditions and compositions. The lack of relationship via fractional crystallisation is further supported by the results presented in Figure 6.27, which indicate that several fractionation paths, over different pressures have occurred to produce the rocks of the Crescent Main Group. In addition, glomerocrysts and xenocrysts noted within the group (Chapter 4) are indicative of a relatively open magmatic system, which may also explain the heterogeneity observed.
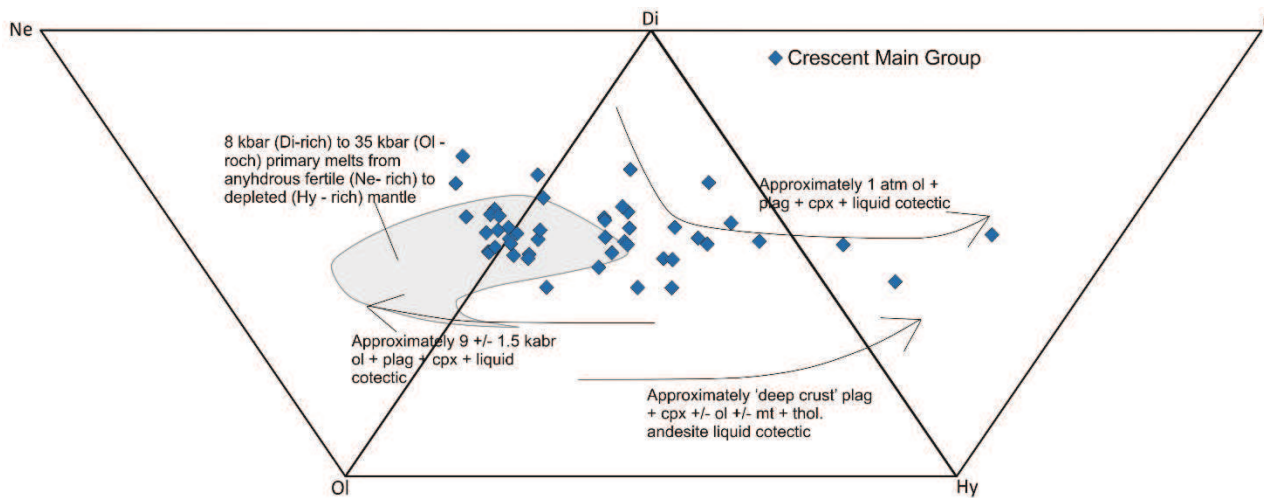
Figure 6.27 Expanded basalt tetrahedron with experimentally derived fractional crystallisation trends and the compositions of primary mantle melts along with the composition of the Crescent Main Group samples (Thompson, 1982; Brueseke and Hart, 2008).

6.1.2.2 Depleted Crescent Group

Sample 237CM has been selected to represent an estimate of the parent magma composition, as this sample has one of the highest MgO (8.30 wt.%) contents and one of the lowest Zr (53.1 ppm) and REE abundances. The major element models produced are shown in figure 6.28. Both the EPR and 237CM models, which best approximate the major element trends in the data, are the 1 kbar models. The 1 kbar 237CM can predict some of the SiO_2, Al_2O_3 and FeO abundances of the Depleted Crescent Group, while none of the models produced can reproduce the trends observed in the other major elements (Figure 6.28).
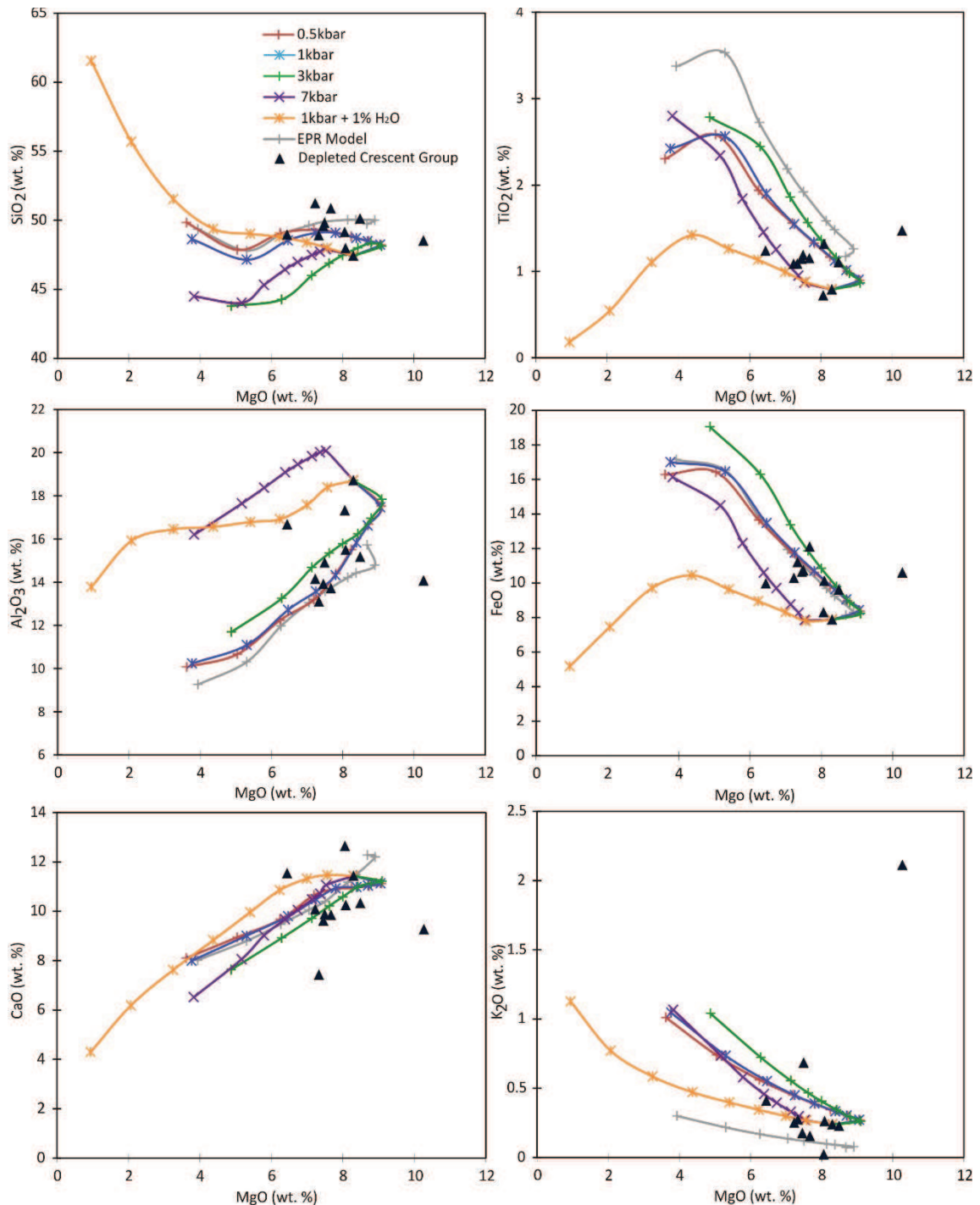
Figure 6.28 Bivariate diagrams of representative major elements vs MgO for the Depleted Crescent Group along with the predicted fractional crystallisation models from a parent magma with the composition of sample 237CM. Markers indicate intervals of 10 % crystallisation.

This model predicts that the parent magma begins to crystallise at 1242 °C with feldspar (Figure 6.29). Olivine then begins to crystallise at 1226 °C (~ 12 %

fractionation) before clinopyroxene joins the assemblage at 1186 °C and ~ 46 % crystallisation. Orthopyroxene then begins to crystallise at ~55 % fractionation at 1174 °C and the model reaches the lowest MgO of the group at around 59 % crystallisation.
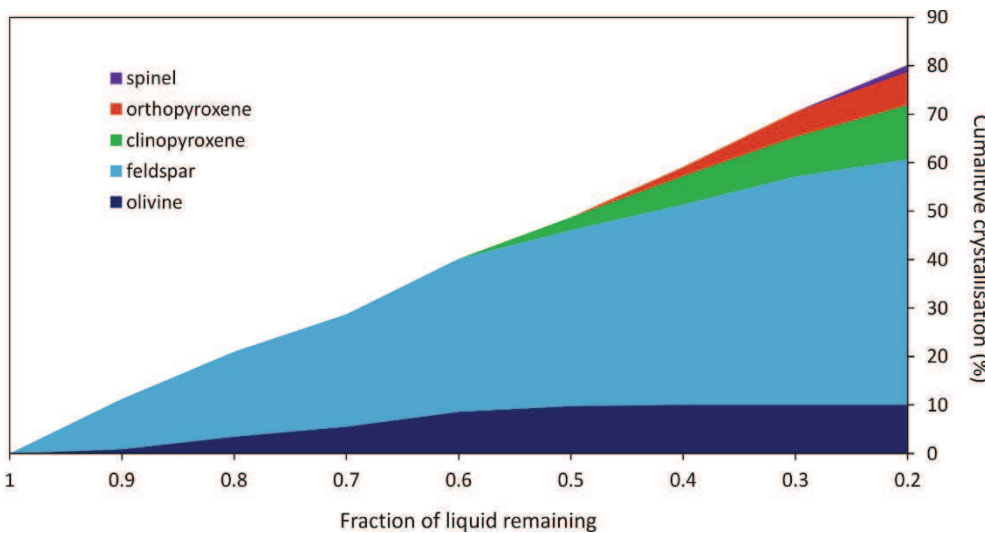
Figure 6.29 A diagram of the cumulative proportions of crystals formed during fractional crystallisation of the Depleted Crescent Group parent magma at 10 % intervals of crystallisation.

The incompatible trace element models, which are calculated using the conditions and mineral compositions produced by the 237CM 1 kbar model are shown in figure 6.30. The trace element abundances and ratios are generally not well reproduced in the fractionating modes, however, the HREE elements are modelled reasonably well (Figure 6.30).
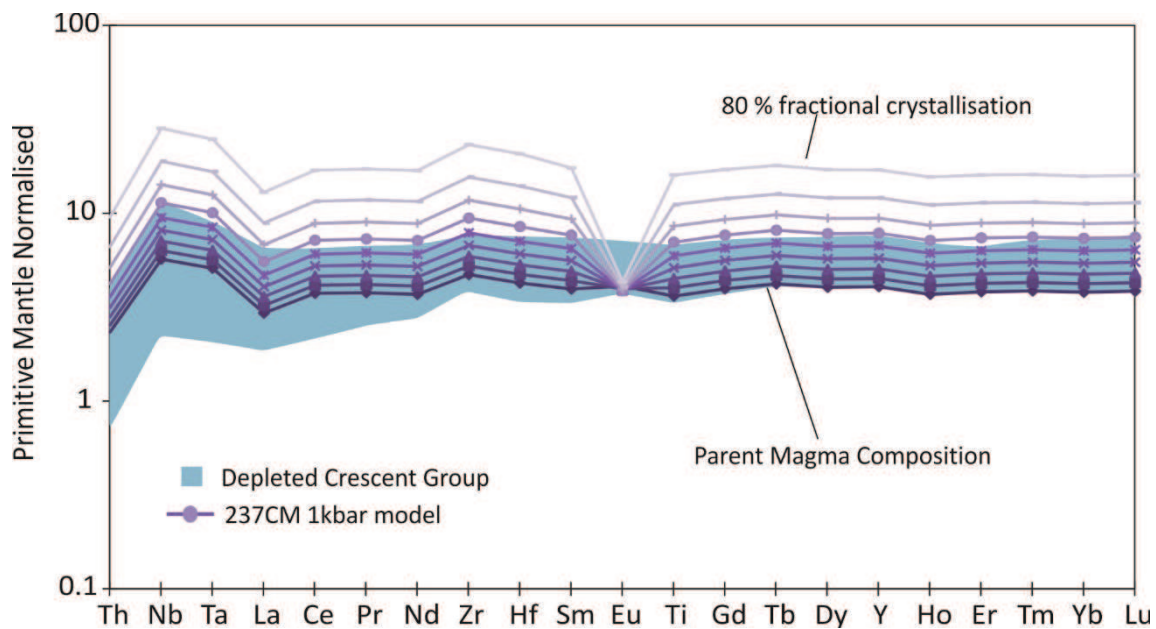
Figure 6.30 Primitive mantle normalised spider diagram of the Depleted Crescent Group along with the best-fit predicted fractional crystallisation model from a parent magma with the composition of sample 237CM. Model compositional lines indicate intervals of 10 % crystallisation.

In general there appears to have been little fractional crystallisation within this group, as reflected by its homogeneous and relatively depleted composition, which may explain why the models do not fit the trends observed in the data. The normative mineral results (Figure 6.31) do appear to illustrate that where is has occurred, fractional crystallisation of a parent magma at low pressures, is the most likely model for the Depleted Crescent Group.
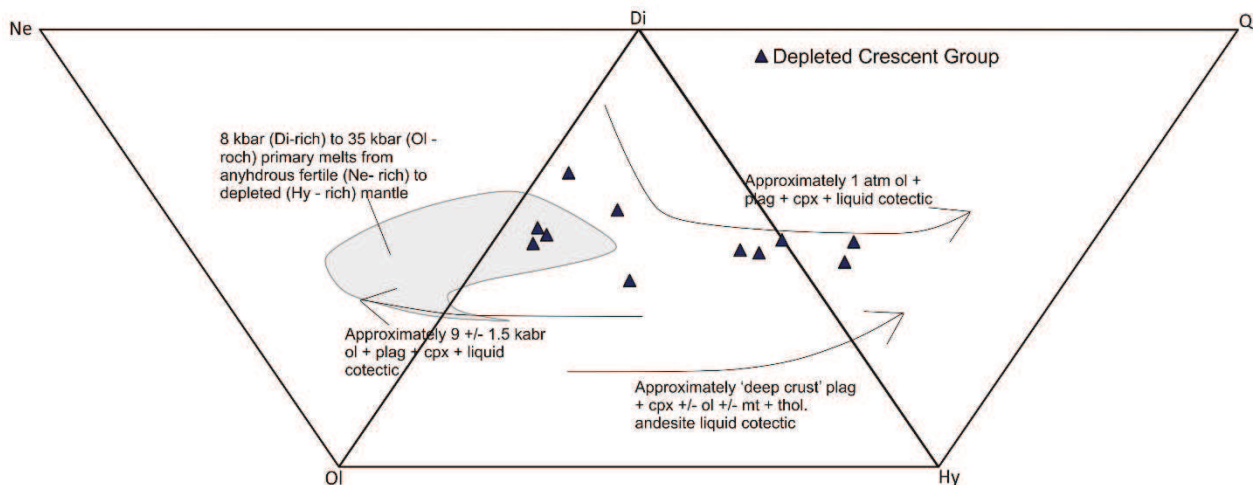
Figure 6.31 Expanded basalt tetrahedron with experimentally derived fractional crystallisation trends and the compositions of primary mantle melts along with the composition of the Depleted Crescent Group samples (Thompson, 1982; Brueseke and Hart, 2008).

6.1.2.3 Bremerton Group

Sample B018 has been chosen as an estimate of the parent magma composition for the Bremerton Group. The sample has the highest MgO abundance (7.5 wt.%) and the lowest Zr and REE abundances of the group. Of the major element models produced (figure 6.32) the 7 kbar model is best able to approximate the abundances of the data. While the EPR parent composition 1 kbar + 1 % H_2O wt.% model best reflects the abundances of the Bremerton major elements. The B018 7 kbar model can replicate some of the SiO_2, TiO_2, CaO and K_2O abundances whereas the flatter pattern of the EPR model can recreate the trends observed in the Al_2O_3 and FeO abundances (Figure 6.32). However, this group displays considerable variation, in particular its MgO (wt.%), which is difficult to reconcile with the models produced by fractionation of a parent magma with a composition of sample B018.
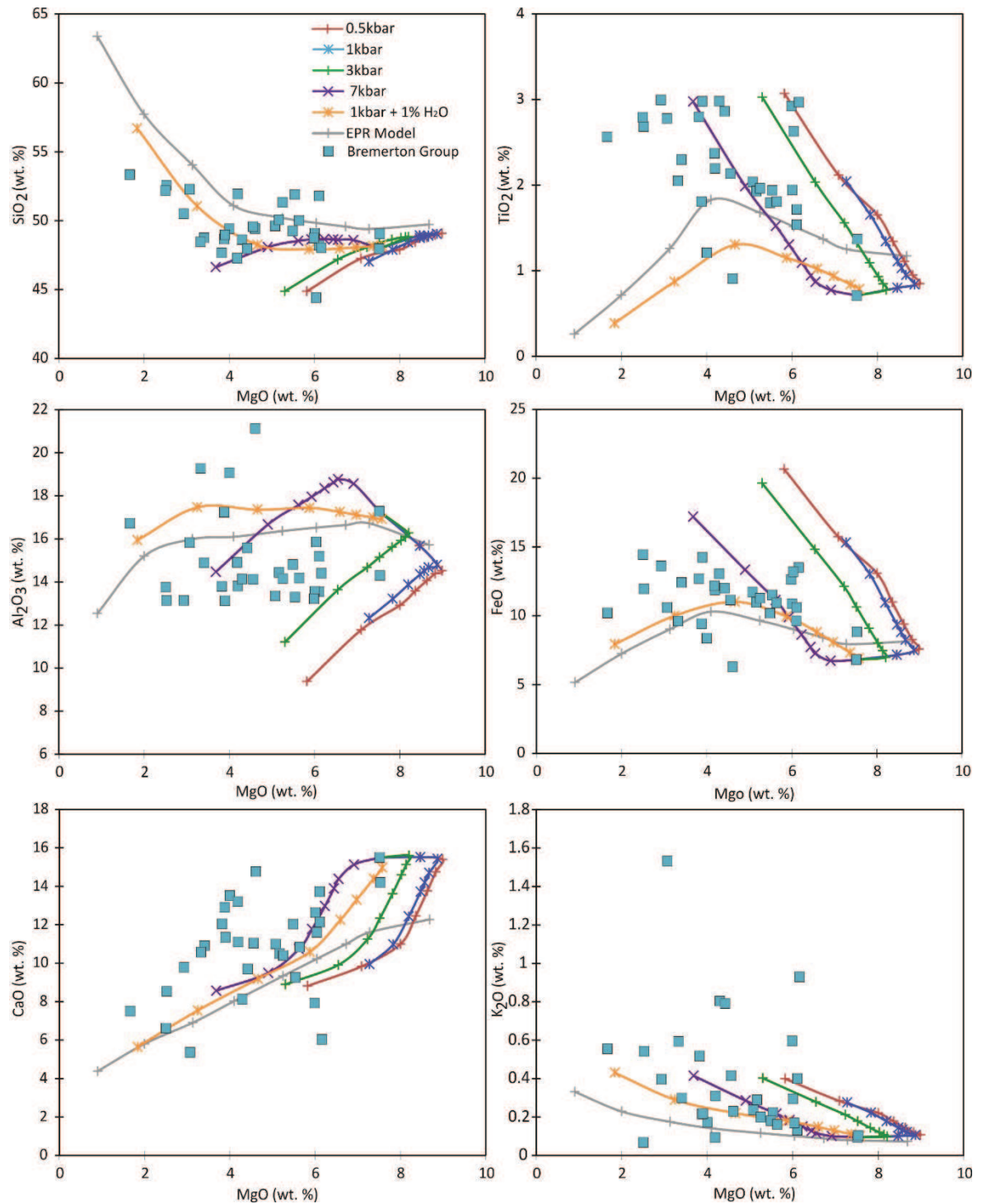
Figure 6.32 Bivariate diagrams of representative major elements vs MgO for the Bremerton Group along with the predicted fractional crystallisation models from a parent magma with the composition of sample B018. Markers indicate intervals of 10 % crystallisation.

The 7 kbar B018 model predicts that fractionation begins at 1312 °C with clinopyroxene followed by plagioclase at 1304 °C and ~12 % crystallisation

(Figure 6.33). This assemblage is consistent with what is observed in the majority of samples from the Bremerton Group, however, as discussed, some samples from the group have more a evolved composition and mineralogy (Chapter 4).
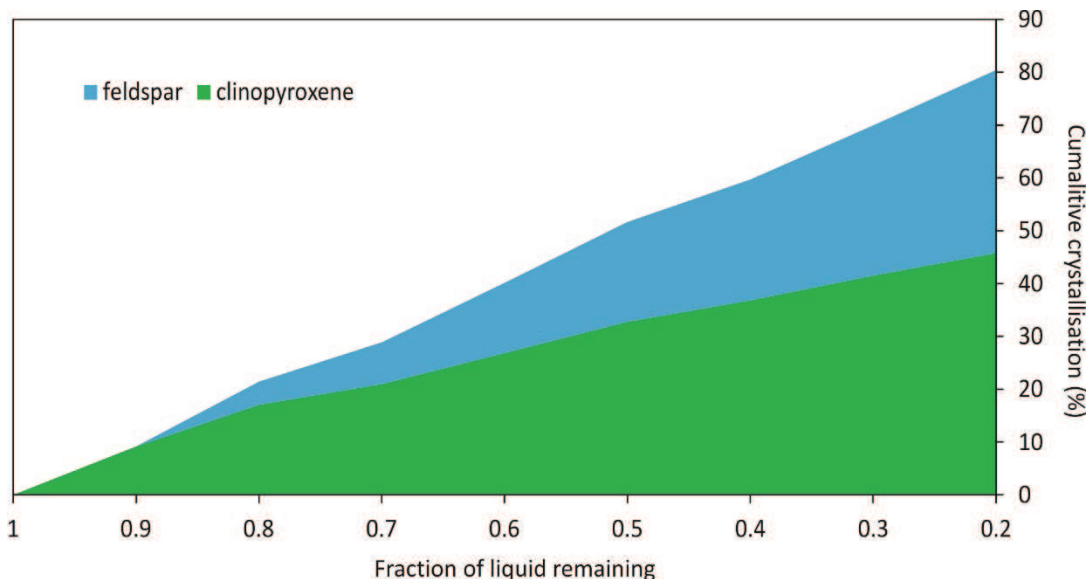
Figure 6.33 A diagram of the cumulative proportions of crystals formed during fractional crystallisation of the Bremerton Group parent magma at 10 % intervals of crystallisation.

Incompatible trace element models have been produced using the parameters and mineral abundances produced by the model have also been compared to the Bremerton data (Figure 6.34). The model can predict the incompatible trace element abundances in the majority of samples, however some samples are also more evolved than the most fractionated composition produced by the model (Figure 6.34). Additionally, the model overestimates the Th composition of almost all samples in the Bremerton Group. The model frequently overestimates the magnitude of the Ti anomalies and underestimates the Eu and Nb anomalies in the data, which is a result of the range of compositions observed in this group. However, the 7 kbar B018 model can replicate the general trend and values of the Gd/Yb ratios, although it frequently overestimates the La/Sm ratios (Figure 6.34).
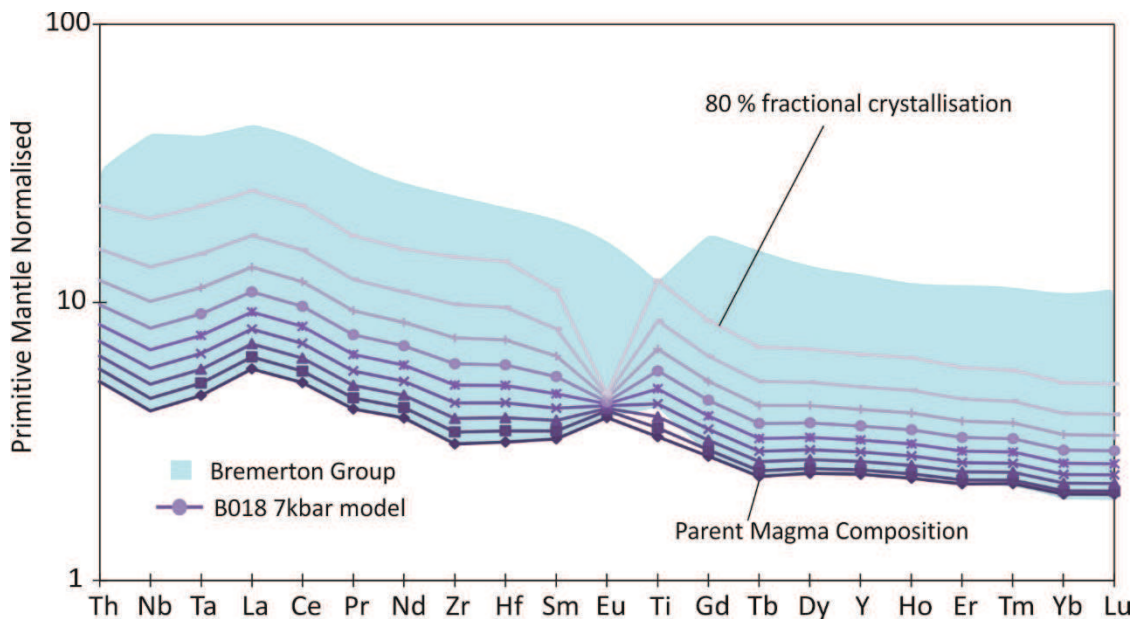
Figure 6.34 Primitive mantle normalised spider diagram of the Bremerton Group along with the best-fit predicted fractional crystallisation model from a parent magma with the composition of sample B018. Model compositional lines indicate intervals of 10 % crystallisation.

The equilibrium feldspar and clinopyroxene compositions produced by the model are also compared with that of the Bremerton Group. The model can reproduce some of the trends observed in the phenocrysts and gabbroic samples analysed (Figure 6.35). The majority of the clinopyroxenes of the Bremerton Gabbros display high Mg# values, high Cr_2O_3 and low TiO_2 concentrations, consistent with a composition more primitive than typical MORB (Ross and Eltholm, 1997) (Figure 4.8). Abundant ophitic textures are also observed in the Bremerton gabbros (Figure 4.7), which suggest crystallisation at lower pressures than the suggested 7 kbar, as cumulate textures are more typical of crystallisation at higher pressures (Ross and Eltholm, 1997). Therefore, these two factors suggest that crystallisation of a parent magma with a composition more primitive than sample B018 at lower pressures than the 7 kbar may represent a better model for the fractional crystallisation conditions of the more mafic Bremerton samples.
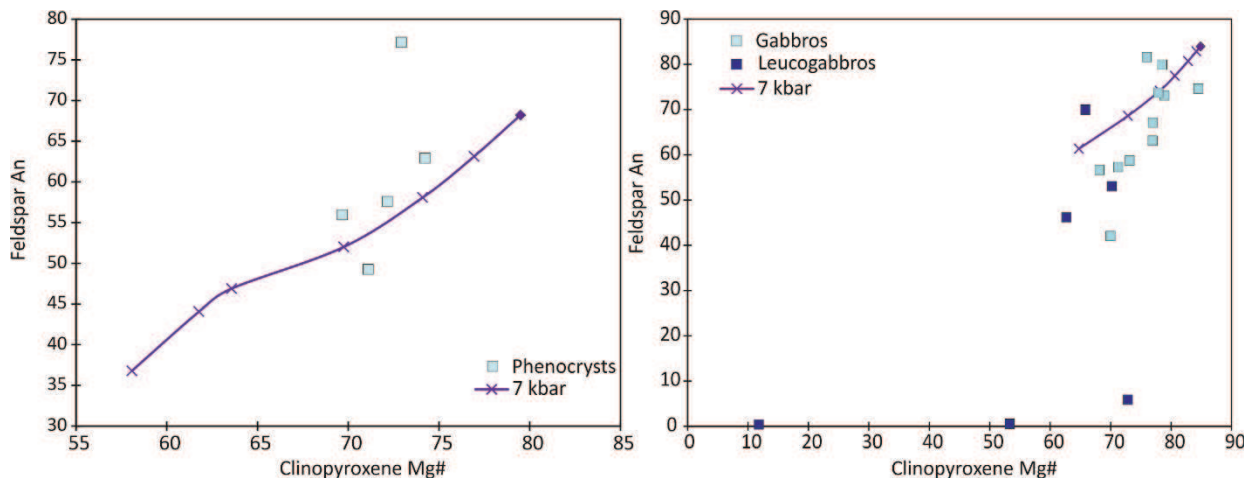
Figure 6.36 Diagram showing the feldspar An number and clinopyroxene Mg# of analysed crystals compared with that of the predicted fractional crystallisation model of the B018 parent, at 10 % intervals of crystallisation.

As discussed above, some of the samples in the Bremerton Group are more evolved than the fractional crystallisation models with the most primitive sample parent composition can account for. In addition, as shown in figure 6.36, a second group of the plutonic samples also have lower An values, as they represent orthoclase feldspars of sample B017, a leucogabbro. This sample also contains clinopyroxenes with low Mg# and Cr_2O_3 wt.% values (Figure 4.8). Therefore, a second set of fractionation models using a lower MgO estimate parent magma composition have been produced. The sample selected to represent this estimate is sample B003, which has a MgO content of 6.0 wt.% and moderate Zr and REE abundances.

The major element fractional crystallisation models produced using B003 as a starting composition are shown in figure 6.37. The majority of the Bremerton Group data lies between the 3 kbar and 7 kbar models, with the 3 kbar model approximating the SiO of the group especially well (Figure 6.37). The TiO_2 however, is better approximated by the 7 kbar model while the Al_2O_3, FeO and CaO are intermediate between the two (Figure 6.37). The 3 kbar model predicts that crystallisation begins at 1222 °C with clinopyroxene, before plagioclase begins to fractionate at 1218 °C after ~5 % crystallisation (Figure 6.38). Orthopyroxene joins the assemblage at 1154 °C and 50 % crystallisation before spinel begins to crystallise at 1134 °C after 61 % crystallisation (Figure 6.38).
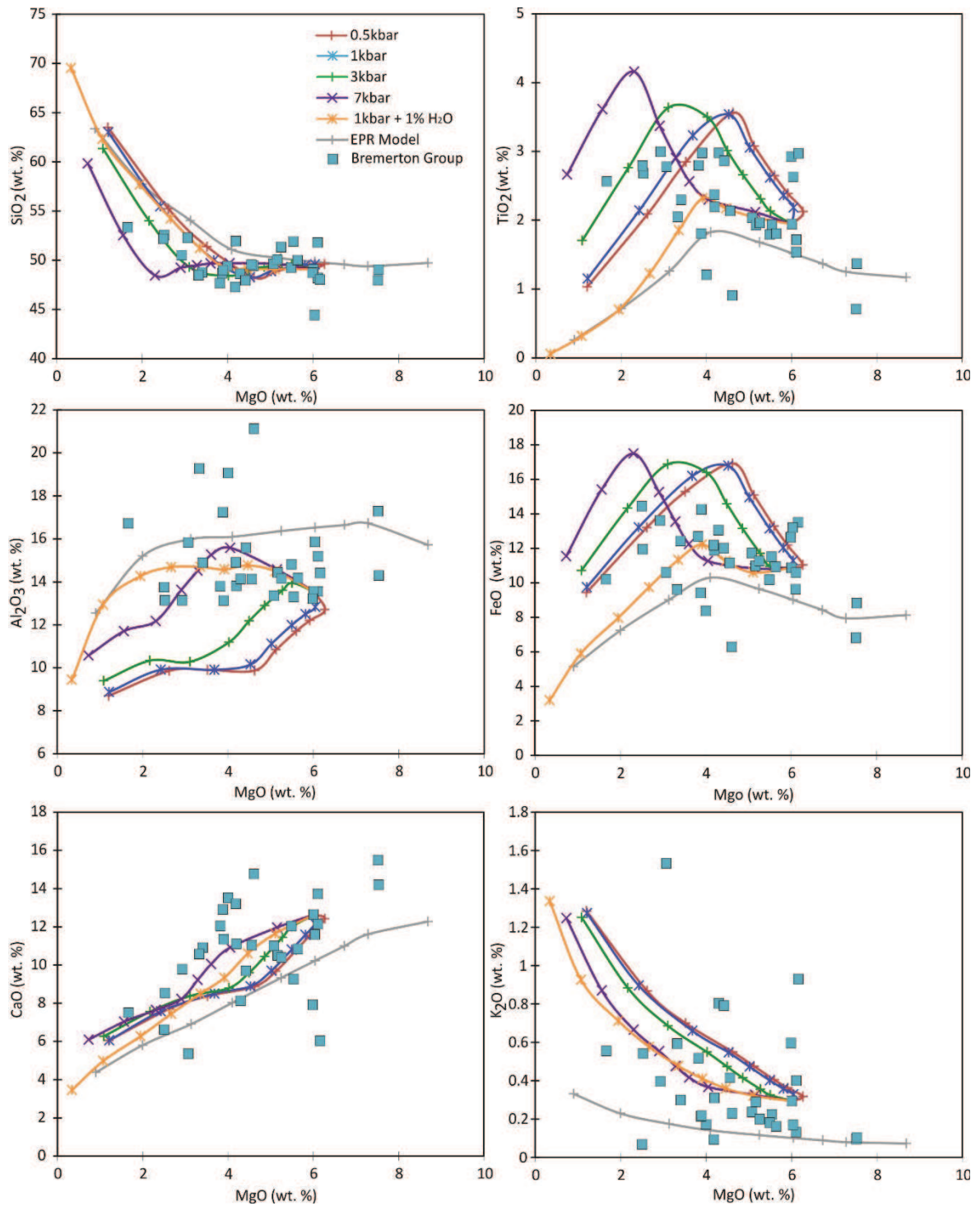
Figure 6.37 Bivariate diagrams of representative major elements vs MgO for the Bremerton Group along with the predicted fractional crystallisation models from a parent magma with the composition of sample B003. Markers indicate intervals of 10 % crystallisation.
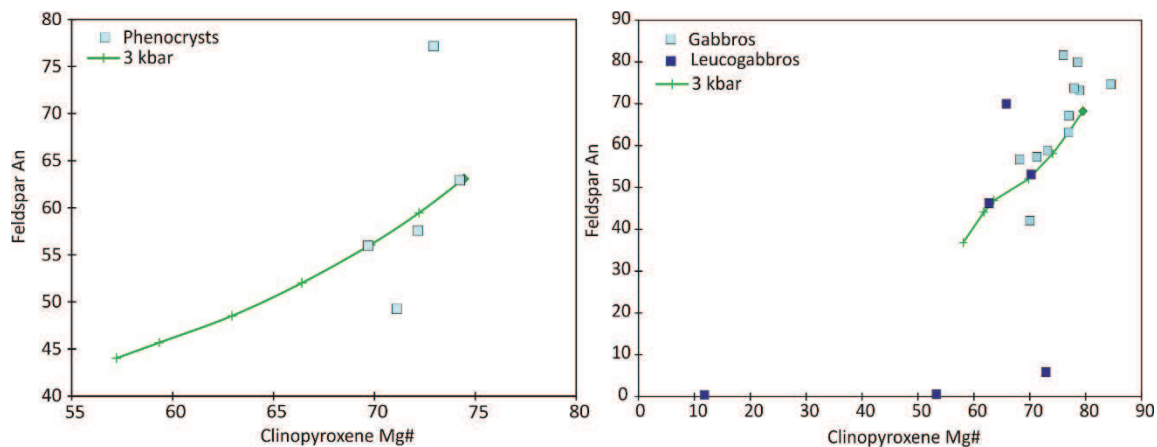
Figure 6.38 A diagram of the cumulative proportions of crystals formed during fractional crystallisation of the second Bremerton Group parent magma at 10 % intervals of crystallisation.

The trace element models produced using the parameters and mineral assemblages derived the 3 kbar model can reasonably estimate the incompatible trace element compositions of the more evolved samples (Figure 6.39). The model generally overestimates the Gd/Yb ratios, however, it can broadly replicate the higher La/Sm ratios. Additionally the model cannot reproduce the extent of most of the more evolved samples anomalies, in particular the negative Ti anomalies of the data, and so it is by no means conclusive (Figure 6.39).
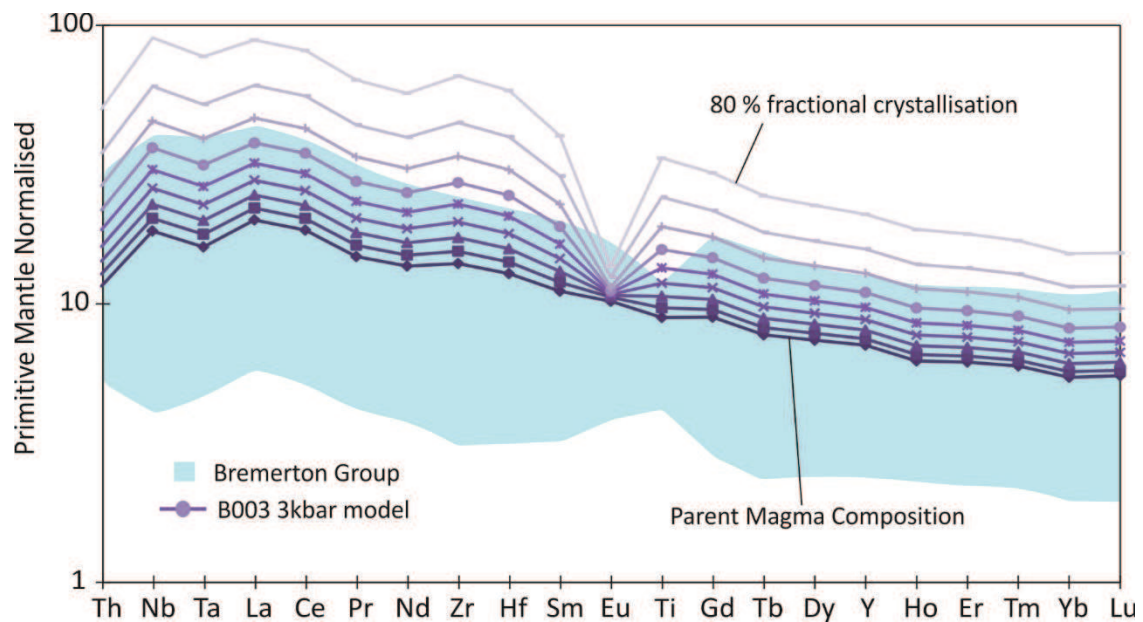
Figure 6.39 Primitive mantle normalised spider diagram of the Bremerton Group along with the best-fit predicted fractional crystallisation model from a parent magma with the composition of sample B003. Model compositional lines indicate intervals of 10 % crystallisation.

A comparison of the equilibrium An of plagioclase and Mg# of clinopyroxene calculated by the model with that of the Bremerton samples is shown in figure 6.40. The results of the model can broadly replicate the equilibrium clinopyroxene and feldspar compositions of the gabbros and leucogabbros and to a certain extent the phenocrysts.

The mineral data, along with the major and trace element models, therefore indicates that 3 kbar fractionation of a parent magma with the composition of B003 may represent a viable explanation for the fractionation path of many of the more evolved Bremerton Group samples. While as discussed above, fractionation of a parent magma with a composition more primitive than that of sample B018, at lower pressures than the 7 kbar model discussed, appears to represent a more viable model for the more mafic Bremerton samples. Low-pressure fractional crystallisation paths also appear most applicable to the samples when plotted on the extended basalt tetrahedron in figure 6.41. Although, some variations in pressure can be applied to the group, sample B030, for instance is better represented by deep crustal fractionation, which appears at odds with the

remainder of the group.
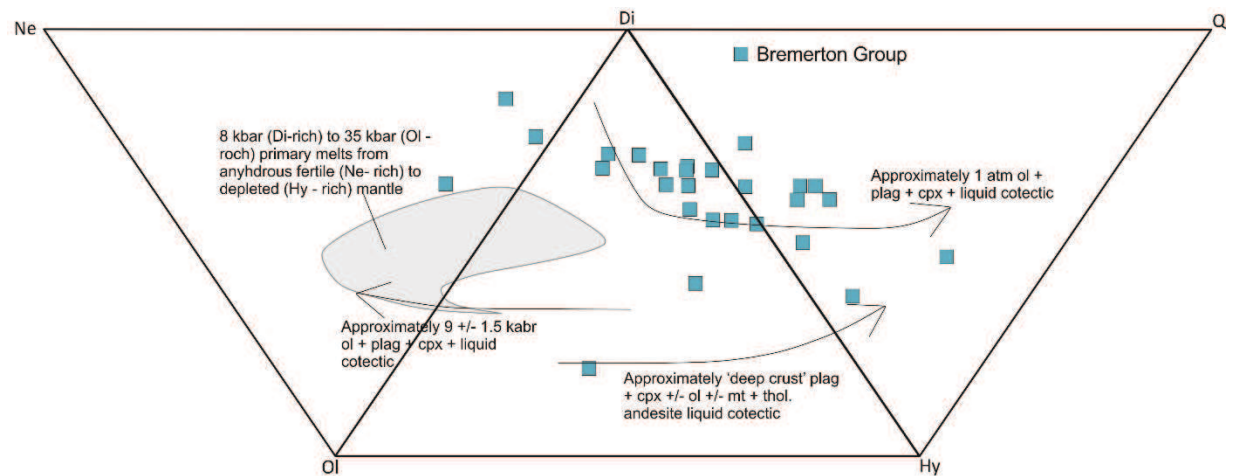
Figure 6.41 Expanded basalt tetrahedron with experimentally derived fractional crystallisation trends and the compositions of primary mantle melts along with the composition of the Bremerton Group samples (Thompson, 1982; Brueseke and Hart, 2008).

6.1.2.4 Black Hills Group

The estimated parent magma for the Black Hills Group has the composition of sample 451CS, as this sample has the highest MgO of the group (7.9 wt.%) along with low Zr and REE abundances. The fractional crystallisation models produced using this starting composition are shown in figure 6.42. Of the models, the 1 kbar – 3 kbar models are best able to approximate the composition of the Black Hills samples along with the 3 kbar EPR starting composition model. Both models can generally reproduce the trends observed in the SiO_2 abundances, while the EPR 3 kbar can better estimate the K_2O trend of the samples. In terms of the other major elements (CaO, FeO and Al_2O_3) shown in figure 6.42, no one model can explain the abundances of these elements within the Black Hills Group. The 451CS 1 kbar model predicts that crystallisation begins at 1196 °C with olivine and feldspar (Figure 6.43). Clinopyroxene joins the assemblage at 1188 °C and ~13 % crystallisation before orthopyroxene begins to crystallise at 1176 °C (~27 % fractionation). Finally, at 1124 °C and ~ 64 % fractionation spinel joins the fractionating assemblage (Figure 6.43). The basalts of the Black Hills Group frequently contain clinopyroxene and feldspar phenocrysts and so are generally

consistent with the mineral abundances predicted by the model, and while no olivine phenocrysts are observed within this group, the alteration products of olivine are noted (Chapter 4).
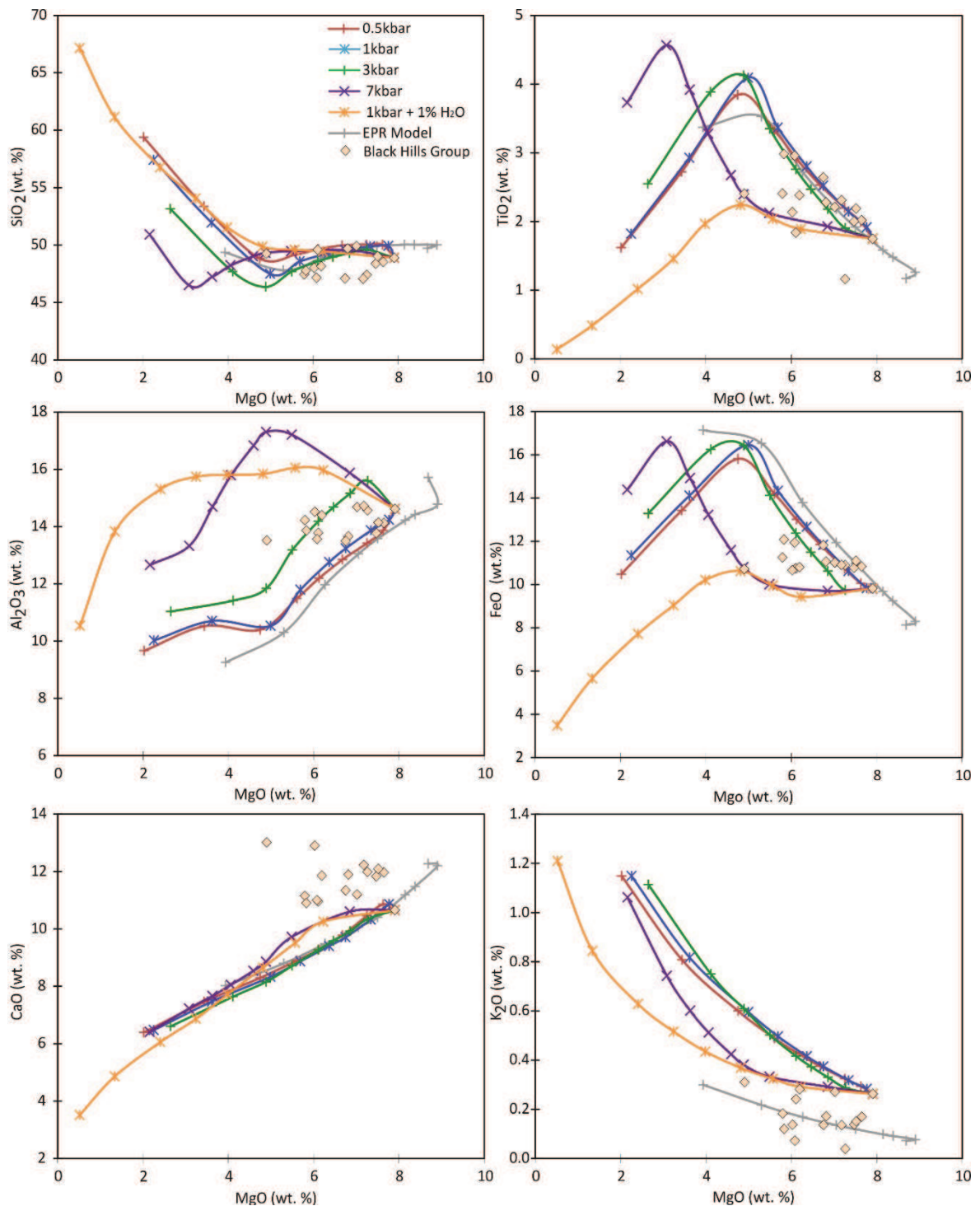
Figure 6.42 Bivariate diagrams of representative major elements vs MgO for the Black Hills Group along with the predicted fractional crystallisation models from a parent magma with the composition of sample 451CS. Markers indicate intervals of 10 % crystallisation.
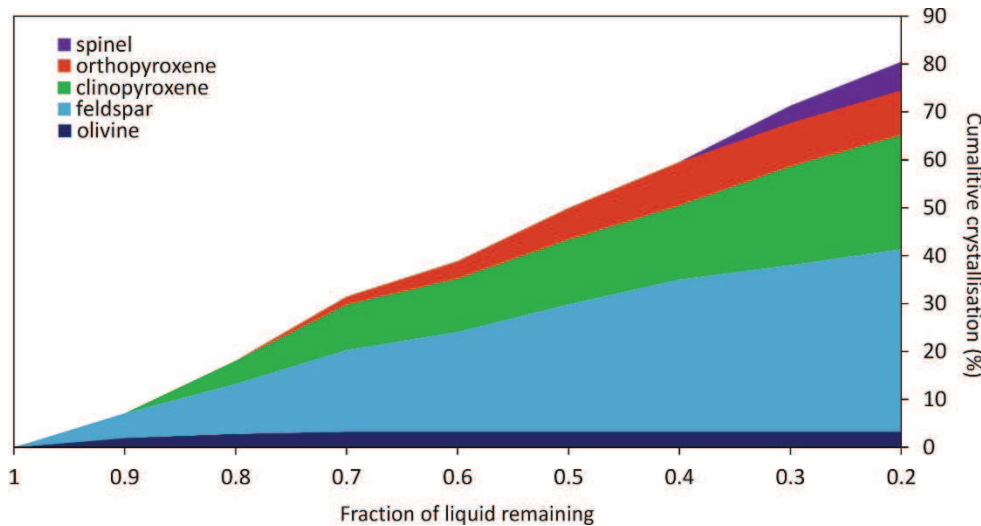
Figure 6.43 A diagram of the cumulative proportions of crystals formed during fractional crystallisation of the Black Hills Group parent magma at 10 % intervals of crystallisation.

The trace element models produced using the conditions and mineral compositions predicted by the 1 kbar 451CS fractional crystallisation models are shown in figure 6.44. The models produced by fractionation of a parent magma with sample 451 CS composition can reproduce the majority of incompatible trace element trends of the samples (Figure 6.44). The model does however underestimate both the Gd/Yb and La/Sm ratios and the magnitude of the Eu anomalies of the Black Hills Group (Figure 6.44).
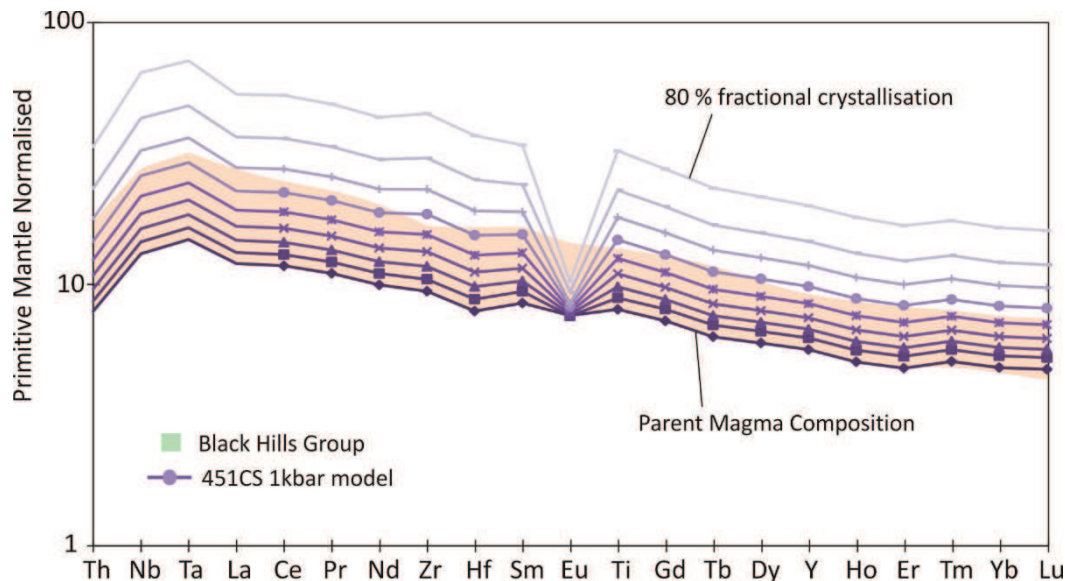
Figure 6.44 Primitive mantle normalised spider diagram of the Black Hills Group along with the best-fit predicted fractional crystallisation model from a parent magma with the composition of sample 451CS. Model compositional lines indicate intervals of 10 % crystallisation.

In general low pressure fractional crystallisation appears to best approximate the major and trace element abundances, and this generally consistent with what is observed in figure 6.41, whereby a low pressure fractional crystallisation path can be applied to the majority of the group. However, a parent magma with a greater concentration of the incompatible trace elements may better predict those observed in the Black Hills Group data.
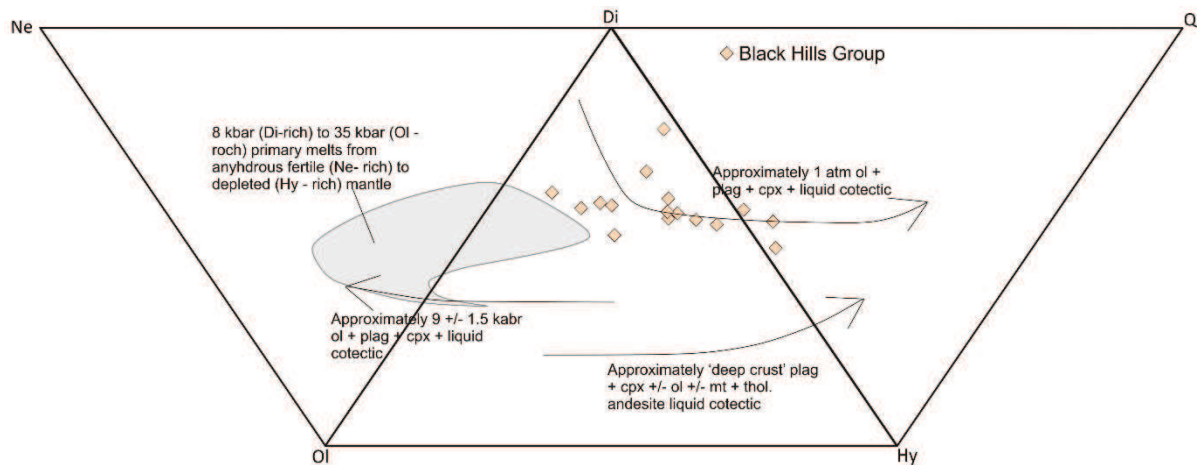
Figure 6.41 Expanded basalt tetrahedron with experimentally derived fractional crystallisation trends and the compositions of primary mantle melts along with the composition of the Black Hills Group samples (Thompson, 1982; Brueseke and Hart, 2008).

6.1.2.5 Willapa Hills Group

Sample 342/2CS has been selected as an estimate of the parent magma composition as it displays the highest MgO concentration (7.3 wt.%) and relatively low Zr and REE abundances. No one model replicates all of the major element abundances of the data, with the 342/2 CS 1 and 3 kbar models reproducing the SiO_2 and TiO_2 concentrations and the 7 kbar model approximating the FeO trend of the data (Figure 6.42). Of the EPR parent magma compositions, the 1 kbar model appears to best predict the trends observed within the Willapa Hills Group major element data (Figure 6.42). Overall, the 342/2 CS 1 kbar model appears to best reproduce the trends observed within the Willapa Hills Group major element data, although this is far from conclusive. A parent magma with a similar composition to sample 342/2CS but with higher abundances of Al_2O_3 and CaO, may better reproduce the trends of the Willapa Hills Group.
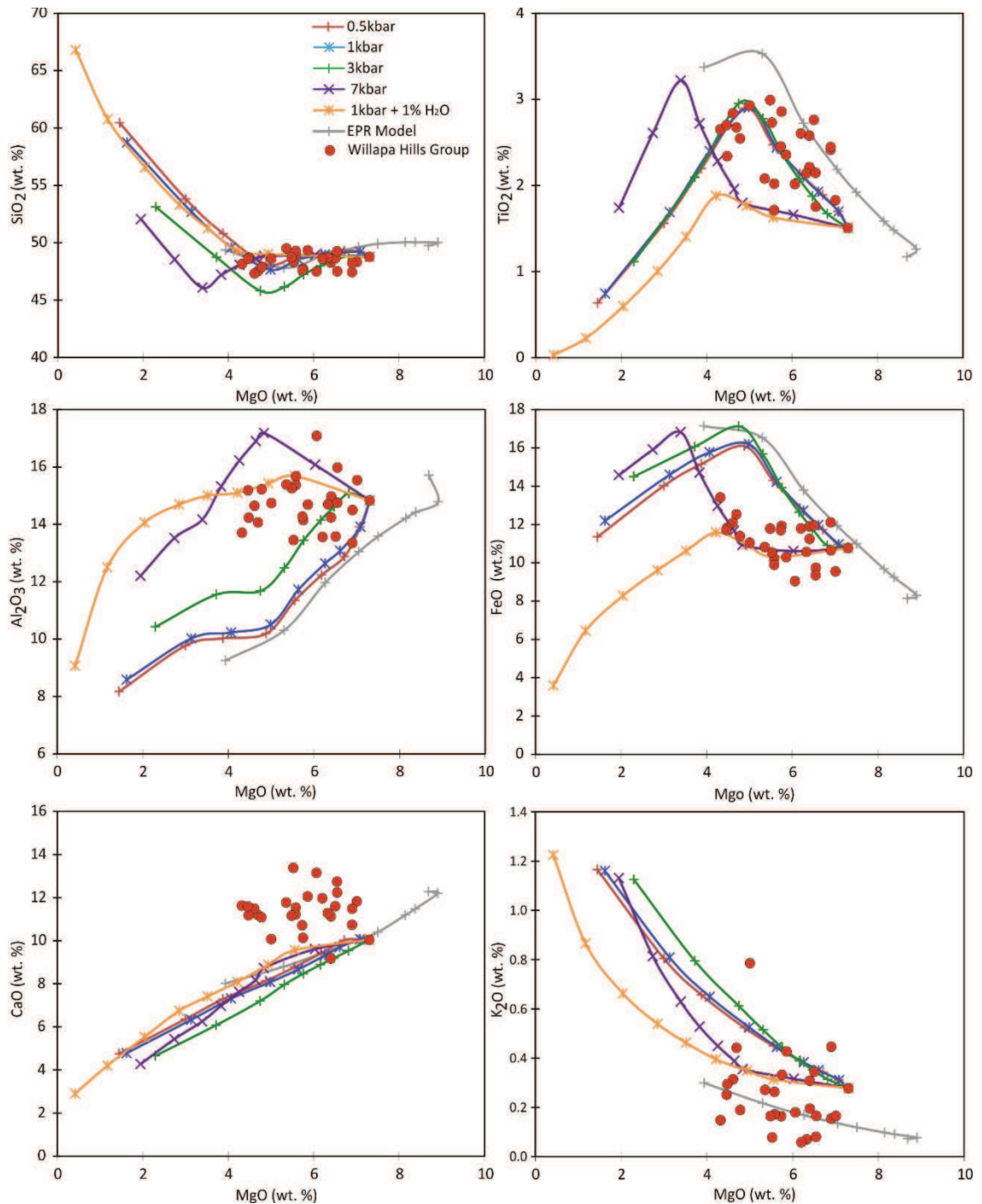
Figure 6.42 Bivariate diagrams of representative major elements vs MgO for the Willapa Hills Group along with the predicted fractional crystallisation models from a parent magma with the composition of sample 342/2 CS. Markers indicate intervals of 10 % crystallisation.

The 342/2 CS 1 kbar model predicts that the parent magma will begin to crystallise at 1192 °C with olivine and feldspar (Figure 6.43). This is followed by

clinopyroxene at 1176 °C and ~18 % crystallisation before orthopyroxene crystallises at 1136 °C after ~47 % of the magma has fractionated. Finally spinel joins the crystallising assemblage at 1120 °C and ~54 % crystallisation (Figure 6.43). The crystallising magma reaches the lowest MgO recorded within the Willapa Hills Group at ~ 55 % crystallisation. Again, however, as with many of the models discussed in this section, no orthopyroxene has been observed within the Willapa Hills Group. Additionally, no olivine is observed either, however, it has most likely been completely altered (Chapter 4).
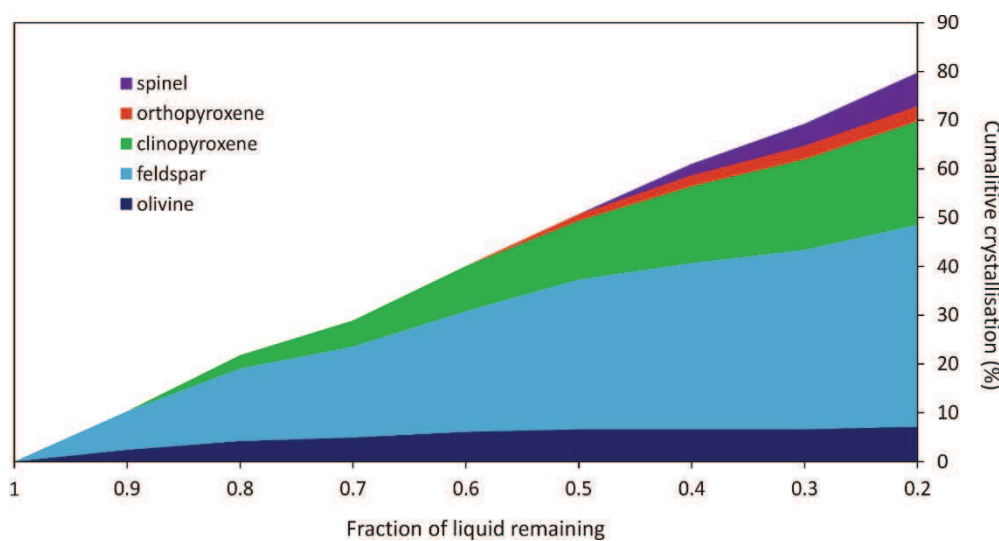
Figure 6.43 A diagram of the cumulative proportions of crystals formed during fractional crystallisation of the Willapa Hills Group parent magma at 10 % intervals of crystallisation.

Trace element models have been calculated using the parameters and estimated mineral compositions of the 342/2 CS 1 kbar model. The Th composition of the Willapa Hills Group is generally well estimated by the model; however, the model often overestimates many of the other incompatible trace elements, such as Nb (Figure 6.44). While the model generally reproduces the La/Sm ratio of the group it consistently underestimates Gd/Yb ratios, producing a flatter pattern than that which is observed in the data (Figure 6.44). The fractional crystallisation model also predicts a larger Eu anomaly than is noted for the Willapa Hills Group (Figure 6.44).
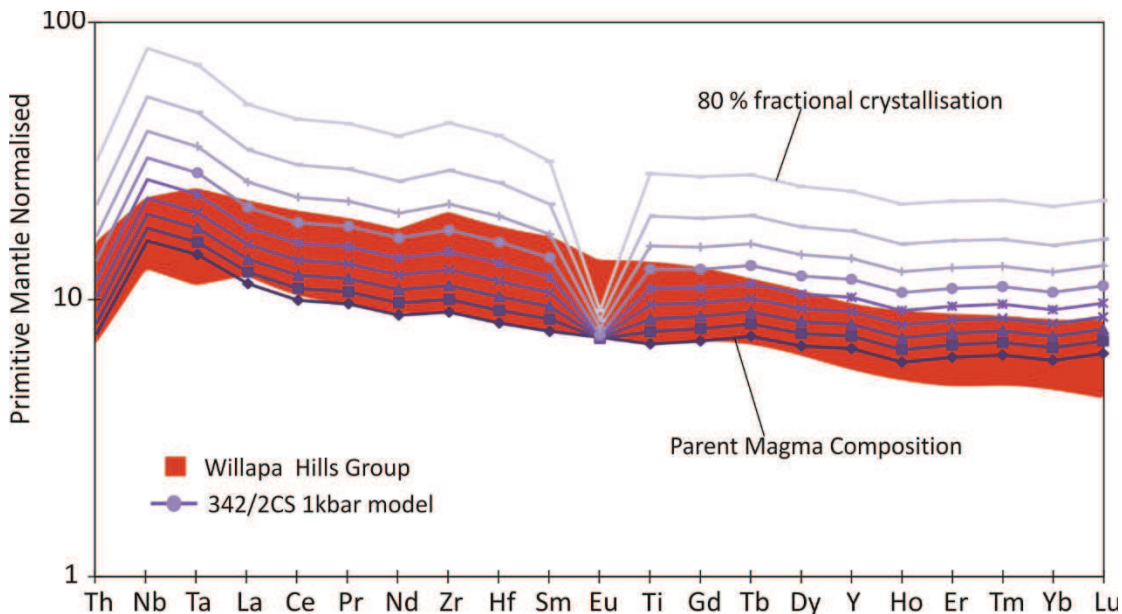
Figure 6.44 Primitive mantle normalised spider diagram of the Willapa Hills Group along with the best-fit predicted fractional crystallisation model from a parent magma with the composition of sample 342/2CS. Model compositional lines indicate intervals of 10 % crystallisation.

Figure 6.45 illustrates that in general low-pressure fractional crystallisation best approximates the normative mineral abundances, however, there is still significant variations in the compositions of the group. Therefore, while a relatively low-pressure fractional crystallisation model can explain some of the trends in the data, a parent magma with a more primitive composition was most likely present in reality. Additionally the variety of compositions observed in this group indicates that the rocks may have been derived from several magma chambers with slight variations in major and trace element abundances.
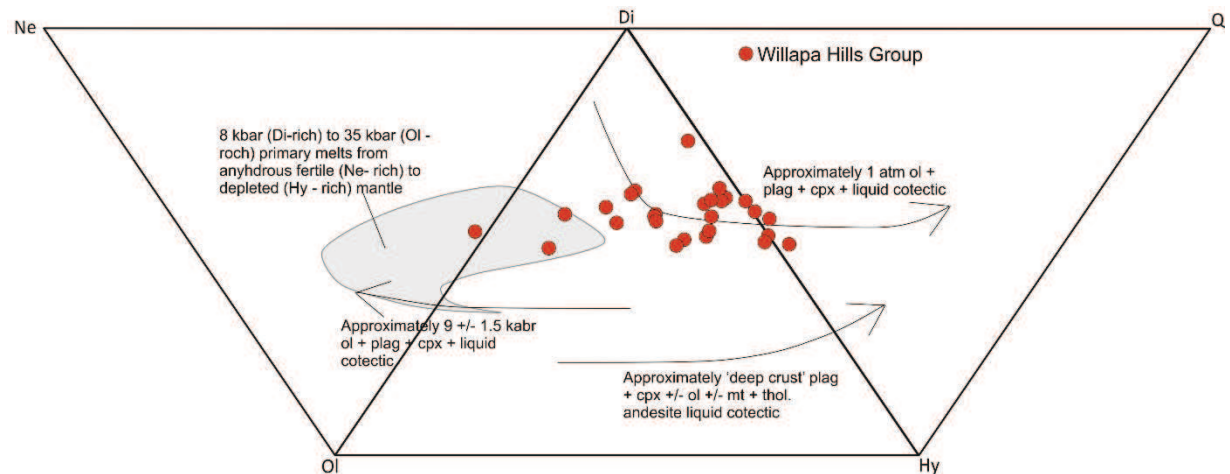
Figure 6.45 Expanded basalt tetrahedron with experimentally derived fractional crystallisation trends and the compositions of primary mantle melts along with the composition of the Willapa Hills Group samples (Thompson, 1982; Brueseke and Hart, 2008).

6.1.3 Metchosin Igneous Complex, Vancouver Island

Sample 200MET from the upper basalts of the Metchosin Igneous Complex has been selected as an estimate parent magma for the Metchosin Igneous Complex. Sample 200MET has the highest MgO concentration of the complex's samples (9.8 wt.%) and a moderate Zr (70.3 ppm) and REE content. The major element models shown in figure 6.46 demonstrate that no one model can predict the trends observed in the data. However, the 200MET 1 kbar + 1 % H_2O wt.% model yields the best approximation of the major element abundances of the Metchosin Igneous Complex. Fractional crystallisation using the 200MET 1 kbar + 1 % H_2O wt.% model can explain the trends observed in the TiO_2, FeO and K_2O vs MgO diagrams, however, no one model can reproduce the SiO_2 trends of the data.
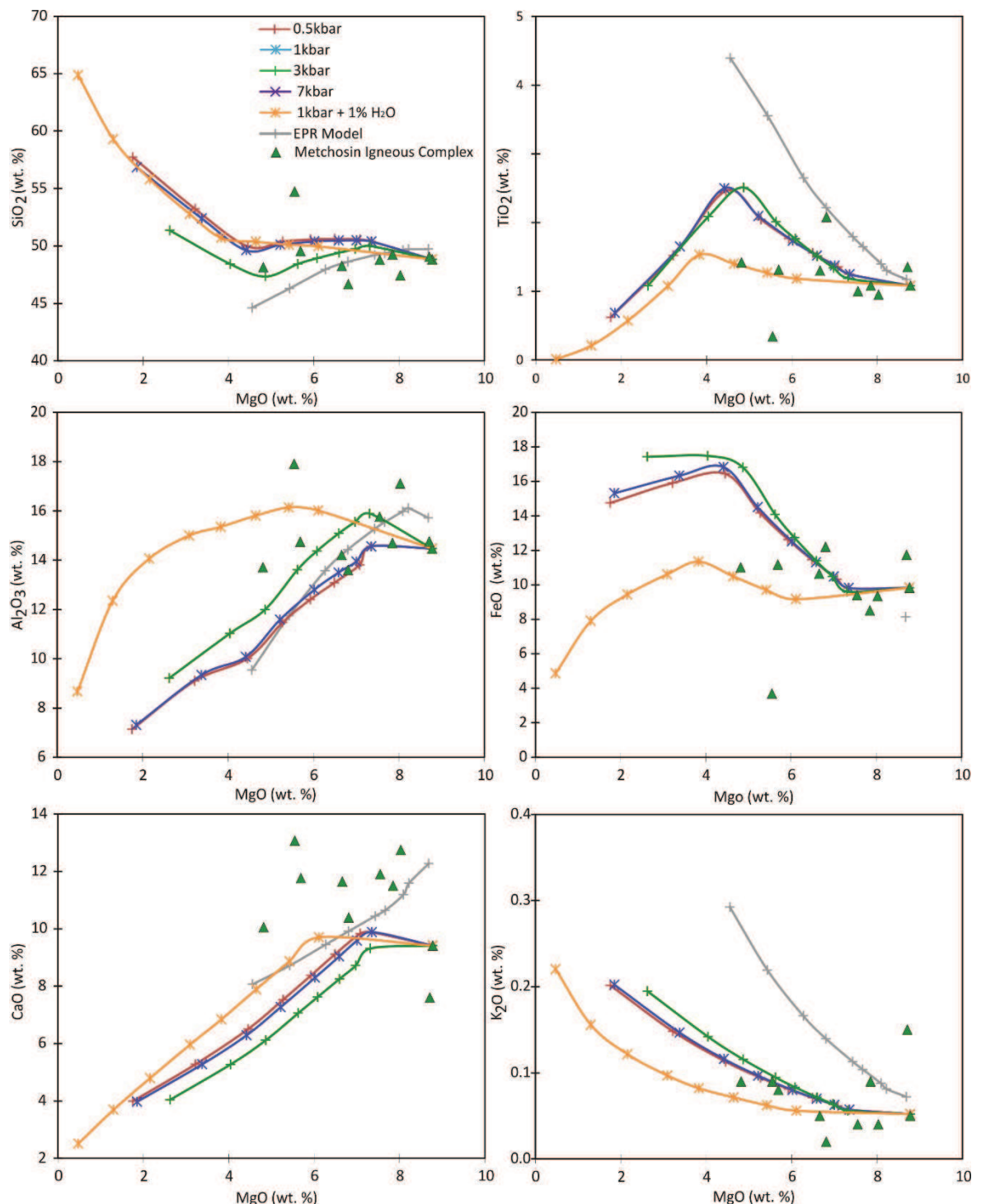
Figure 6.46 Bivariate diagrams of representative major elements vs MgO for the Metchosin Igneous Complex along with the predicted fractional crystallisation models from a parent magma with the composition of sample 200MET. Markers indicate intervals of 10 % crystallisation.

The 1 kbar + 1 % H_2O wt.% model predicts that fractional crystallisation

begins at 1227 °C with olivine fractionation, followed by clinopyroxene at ~6 %

crystallisation and 1155 °C (Figure 6.47). The next mineral phase to crystallise is plagioclase at 1139 °C (~ 14 % crystallisation) before finally being joined by spinel at 1083 °C and ~42 % crystallisation. The fractionating liquid reaches the lowest MgO of the Metchosin Igneous Complex at ~ 28 % fractional crystallisation, before spinel is predicted to join the assemblage which is consistent with what is observed in the samples.
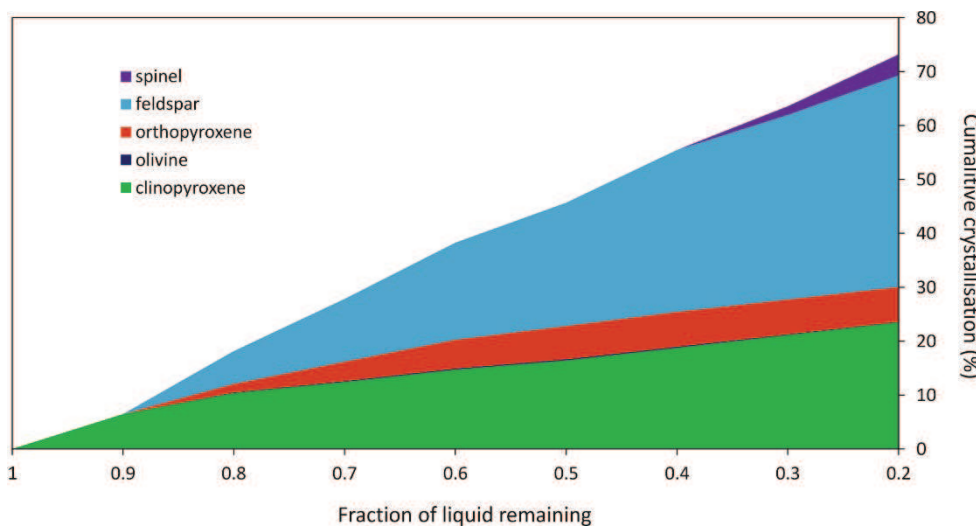
Figure 6.49 A diagram of the cumulative proportions of crystals formed during fractional crystallisation of the Metchosin Igneous Complex parent magma at 10 % intervals of crystallisation.

Fractional crystallisation models using the parameters and compositions calculated by the 200MET 1 kbar + 1 % H_2O wt.% model predict the trend some of the incompatible trace element concentrations reasonably well in the rocks, however, it often overestimates the abundances (Figure 6.50). The 200MET 1 kbar + 1 % H_2O wt.% model can replicate the Gd/Yb ratios of some of the samples, however, the scatter in the La/Sm ratios is not reflected in the models. Additionally, while the model can predict the extent of the Ti and Eu anomalies it does not reproduce the range of Nb anomalies observed in the of the Metchosin Igneous Complex samples (Figure 6.50).
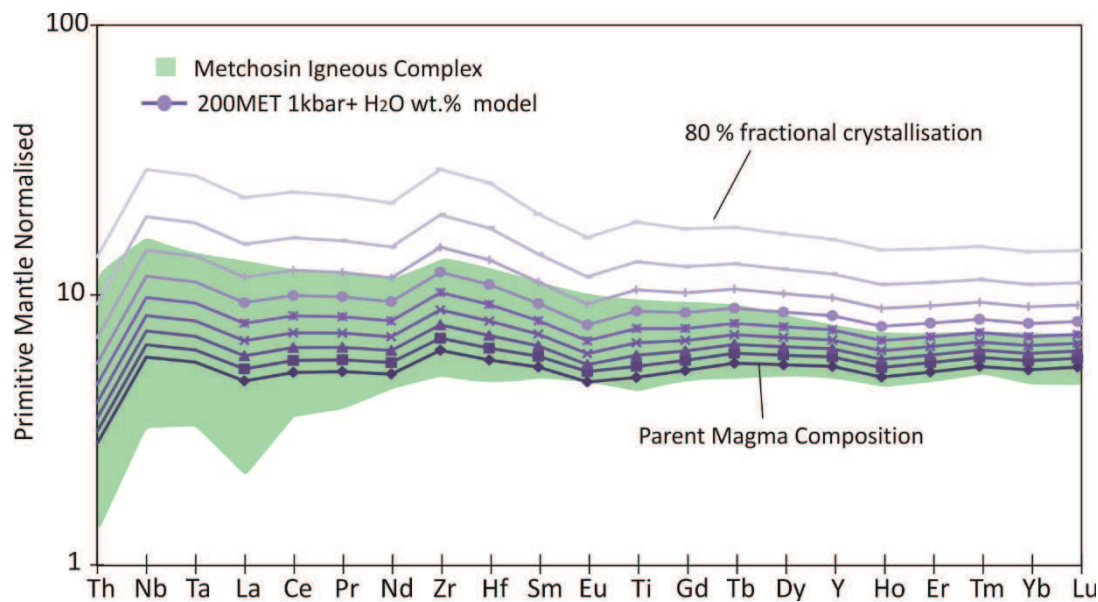
Figure 6.50 Primitive mantle normalised spider diagram of the Metchosin Igneous Complex along with the best-fit predicted fractional crystallisation model from a parent magma with the composition of sample 200MET. Model compositional lines indicate intervals of 10 % crystallisation.

The compositions of clinopyroxene and feldspars that the 200MET 1 kbar + 1 % H_2O wt.% fractional crystallisation model predicts will crystallise simultaneously is compared with the composition of clinopyroxene and feldspars from the Metchosin Igneous Complex, which are also thought to be in equilibrium. The results of this comparison are shown in figure 6.51. The 1 kbar + 1 % H_2O wt.% model can explain the An and Mg# equilibrium of the glomerocrysts analysed can be approximated by the model. However, while there is some similarity between the model and the mineral compositions observed in the gabbros, the general trend cannot be explained by the model (Figure 6.51).
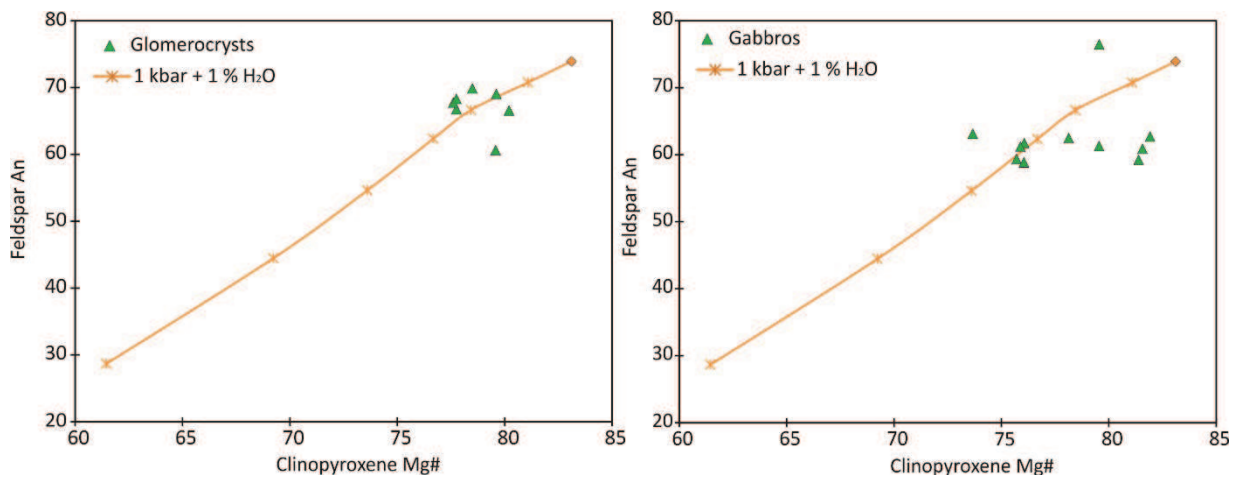
Figure 6.51 Diagram showing the feldspar An number and clinopyroxene Mg# of analysed crystals compared with that of the predicted fractional crystallisation model of the 200MET parent, at 10 % intervals of crystallisation.

Due to the previous models relatively moderate Zr and REE concentrations a second set of models for the Metchosin Igneous Complex have been produced, based on a parent magma whose composition is that of sample 205MET, a dolerite dyke. This sample has one of the highest MgO (8.0 wt.%) and lowest Zr (55.9 ppm) concentrations, although not the extreme values of either. The major element model which best estimates this suite of rocks compositions is the 1 kbar + 1 % H_2O wt.% model, which reflects the some of the samples compositions in SiO_2, TiO_2, FeO and K_2O while also predicting the general trend of the data observed in CaO and Al_2O_3 abundances (Figure 6.52).
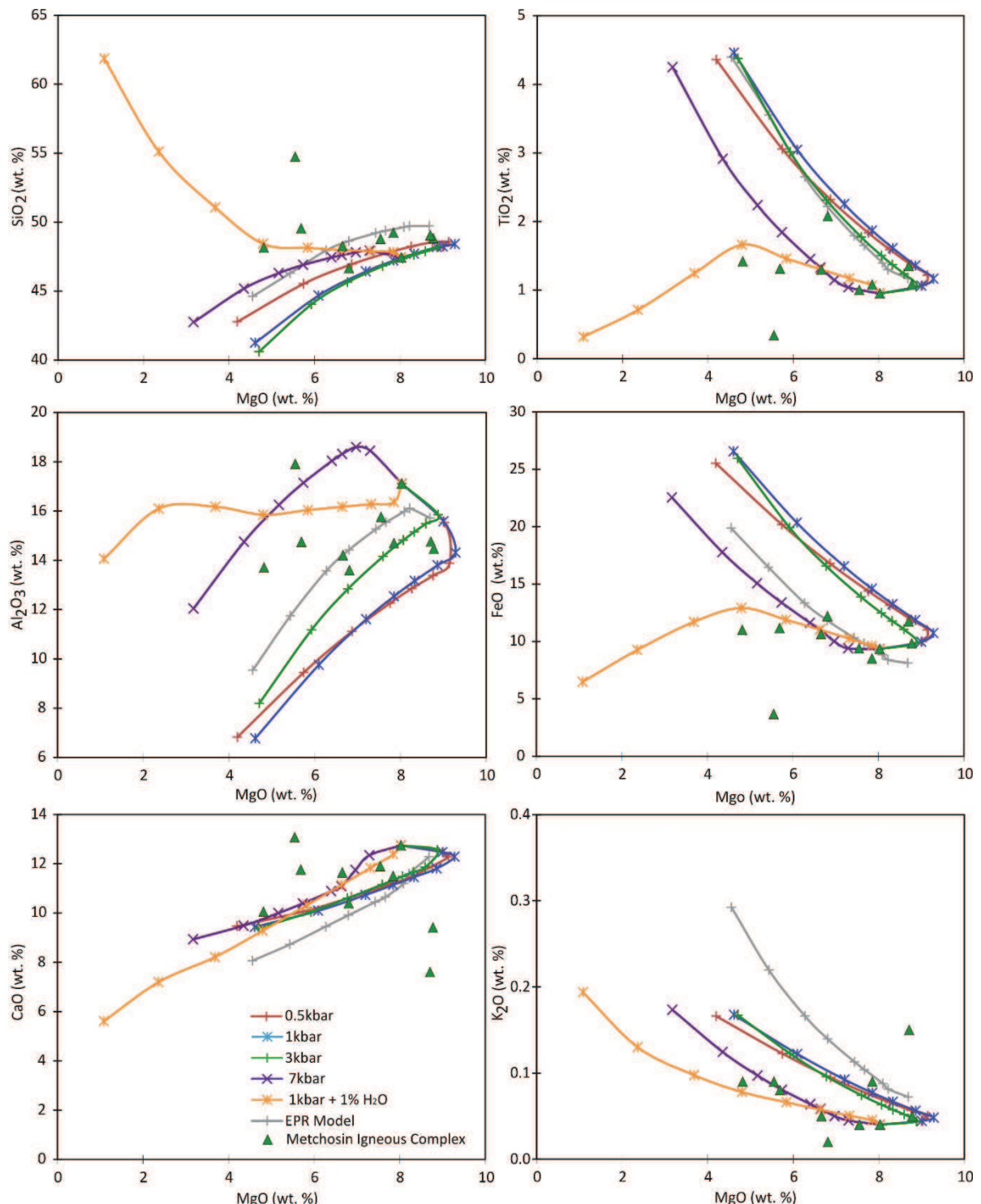
Figure 6.52 Bivariate diagrams of representative major elements vs MgO for the Metchosin Igneous Complex along with the predicted fractional crystallisation models from a parent magma with the composition of sample 205MET. Markers indicate intervals of 10 % crystallisation.

The 1 kbar + 1 % H_2O wt.% model predicts that the magma begins to

crystallise feldspar at 1173 °C, olivine then joins the assemblage at 1165 °C and ~5 % crystallisation followed closely by clinopyroxene at 1161 °C and ~8 % crystallisation (Figure 6.53). The next mineral predicted to crystallise is then spinel at 64 % crystallisation at which point the MgO of the liquid magma is lower than that of any of the samples. The fractionating magma reaches a MgO of 4.8 wt.% (that of the most evolved sample in the Metchosin Igneous Complex calculated) at ~50 % crystallisation (Figure 6.53). This assemblage is also generally consistent with the observed mineralogy of the samples.
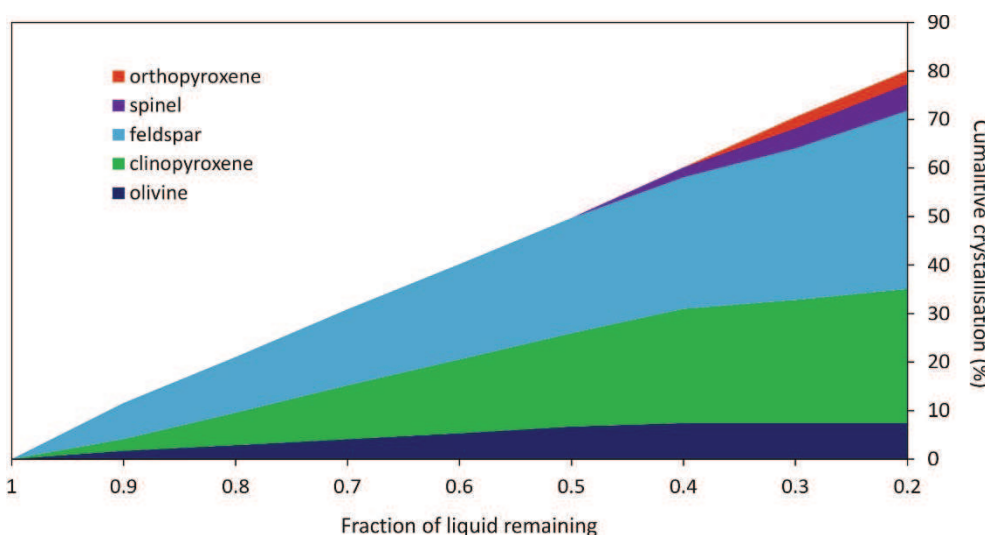
Figure 6.53 A diagram of the cumulative proportions of crystals formed during fractional crystallisation of the second Metchosin Igneous Complex parent magma at 10 % intervals of crystallisation.

Trace element fractionation models based on the assemblages predicted to form during fractionation at 1 kbar + 1 % H_2O wt.% are presented in Figure 6.54. The model predicts the incompatible trace element abundances of the Metchosin Igneous Complex although the model does yield lower Th than is observed in the data (Figure 6.54). The La/Sm ratios of the group are varied, and so are not modelled well, while the model produces Gd/Yb ratios, which are higher than those of the samples (Figure 6.54). The model does however predict some of the Eu and Ti anomalies observed within the data.
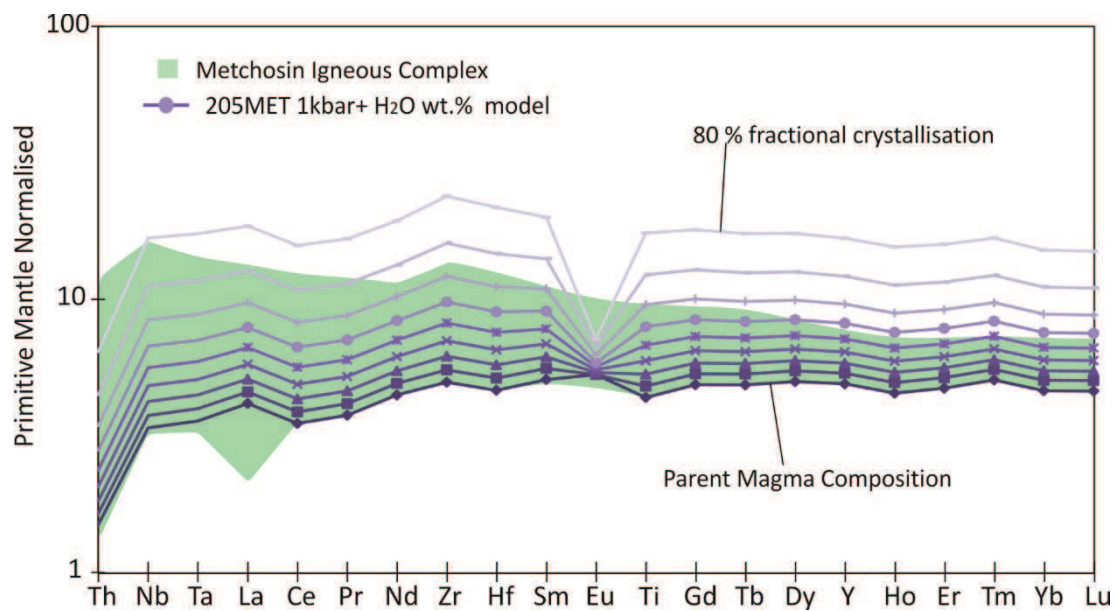
Figure 6.54 Primitive mantle normalised spider diagram of the Metchosin Igneous Complex along with the best-fit predicted fractional crystallisation model from a parent magma with the composition of sample 205MET. Model compositional lines indicate intervals of 10 % crystallisation.

The mineral composition models shown in Figure 6.49, for the 1 kbar + 1 % H$_2$O wt.% models compare the equilibrium feldspar and clinopyroxene compositions calculated at different degrees of fractionation, with those from the Metchosin Igneous Complex samples. There is little similarity between the two, with the model consistently significantly overestimating the An and Mg# values (Figure 6.55).
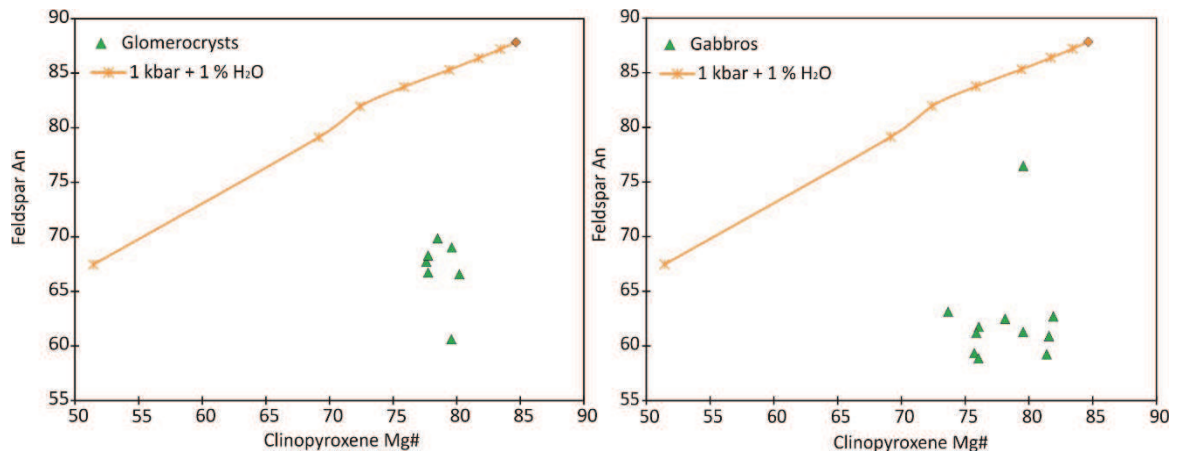
Figure 6.55 Diagram showing the feldspar An number and clinopyroxene Mg# of analysed crystals compared with that of the predicted fractional crystallisation model of the 205MET parent, at 10 % intervals of crystallisation.

Figure 6.56 highlights, that while some of the samples trend towards a low-pressure fractionation path, others are more compatible with higher-pressure settings. However, despite discrepancies observed in the modelling, generally, the low-pressure setting is consistent with the proposed ridge adjacent tectonic environment suggested for the Metchosin Igneous Complex, based on its major, trace and isotope compositions. This is also consistent with the composition of the most of the most primitive clinopyroxenes analysed from the Metchosin Igneous Complex which have a Mg# of > 84 (bar one sample; Figure 4.14), which indicates that crystallisation from a MORB like parent magma at low pressures may explain the evolution of the rocks in this group (Langmuir et al., 1992; Ross and Eltholm, 1997).
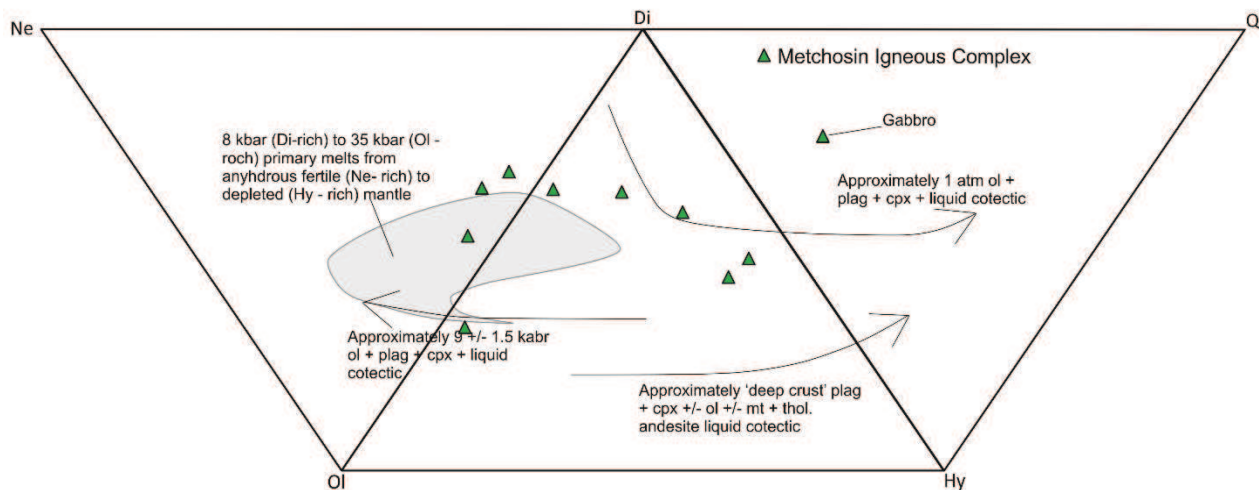
Figure 6.56 Expanded basalt tetrahedron with experimentally derived fractional crystallisation trends and the compositions of primary mantle melts along with the composition of the Metchosin Igneous Complex samples (Thompson, 1982; Brueseke and Hart, 2008).

6.1.4 Summary

As shown in this section, modelling the fractional crystallisation trends of the rocks of the Siletz terrane has not produced consistent results. This appears to most likely be a reflection of compositional heterogeneities in the mantle source and subsequently across several magma chambers from which the lavas and intrusive rocks of the terrane were derived. In addition while there is clearly a large amount of geochemical variation within the mafic rocks of the terrane, relatively few examples of more evolved and more primitive rocks have been observed, meaning that significant amounts of fractionation and complete fractionation trends are difficult to model.

Many of the basalts of the Siletz terrane are aphyric; however, as discussed in Chapter 4, plagioclase phenocrysts, clinopyroxene phenocrysts and what appear to be the remnants of olivine phenocrysts are observed across the terrane, which suggests the fractionation of these minerals has occurred. However, models consistently overestimate the extent of plagioclase fractionation across the groups, as illustrated by the large negative Eu anomalies of most models in comparison to those of the data. Negative Ti anomalies are observed in the most evolved basalts

suggesting that they have also begun to crystallise Fe-Ti oxides and this is generally reflected in the fractional crystallisation models. In addition figure 6.57 demonstrates that, while in general, the Siletz terrane has undergone clinopyroxene fractionation (decreasing Sc/Y with decreasing MgO wt. % indicating an increasing degree of clinopyroxene fractionation), within groups its relative importance is variable. For example clinopyroxene fractionation appears to have played an important role in the evolution of the Bremerton Group, while this is much less evident in the Roseburg Group, which displays a narrow range of both CaO/Al_2O_3 and Sc/Y values.
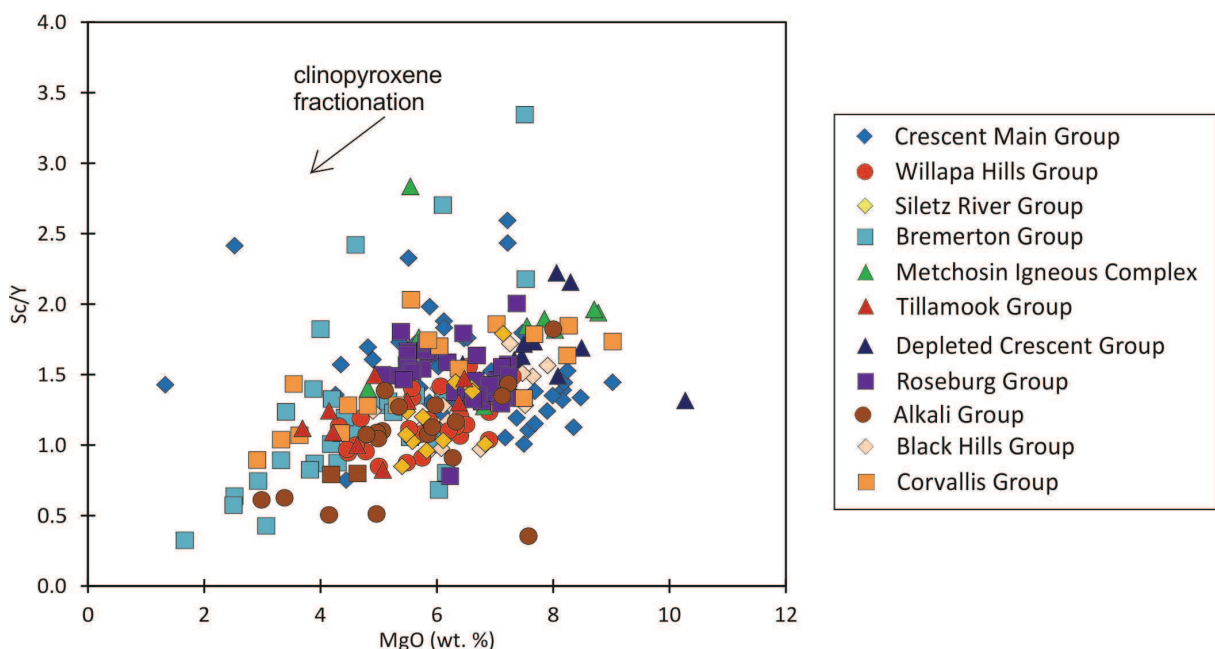
Figure 6.57 Sc/Y vs MgO (wt. %) for the Siletz terrane group, highlighting the extent of clinopyroxene fractionation that has taken place.

Figures 6.57 and 6.58 highlight that fractionation of a parent magma with slightly different compositions at a variety of pressures, produces models which can be applied across the spread of compositions observed in the Siletz terrane rocks. The evolution of the Roseburg Group appears to be best modelled by low degrees of fractional crystallisation of a parent magma or several parent magmas, the composition of which is more primitive than sample 071RO. However, the pressure under which the Roseburg Group samples have fractionated is difficult to constrain. In general it appears as though little differentiation has taken place

within this group, as highlighted in figure 5.58 and 5.59, which illustrate the relatively homogeneous compositions of the group in comparison to the of the remainder of the terrane. The Corvallis Group trends are best modelled by higher-pressure fractionation of parent magma with samples CR014 composition; however, the CIPW normative compositions of this group appear to indicate lower pressure crystallisation. One fractional crystallisation model for the Siletz River Group is also difficult to reconcile with the geochemistry of the group. In terms of major elements, no one model can explain the trends observed in all of the data, while the 7 kbar model predicts the trace element trends reasonably well and the CIPW norms compositions suggest that the samples have undergone low pressure crystallisation. This last model may in fact represent the most viable model for the group, with lower pressure crystallisation from a more primitive sample able to model some of the compositions of the group reasonably well, as highlighted in figures 6.58 and 6.59. The proposed models cannot adequately model the composition of samples from the Tillamook Group, nor those of the Alkali Group, as in both these cases they most likely did not originate from one single magma chamber.
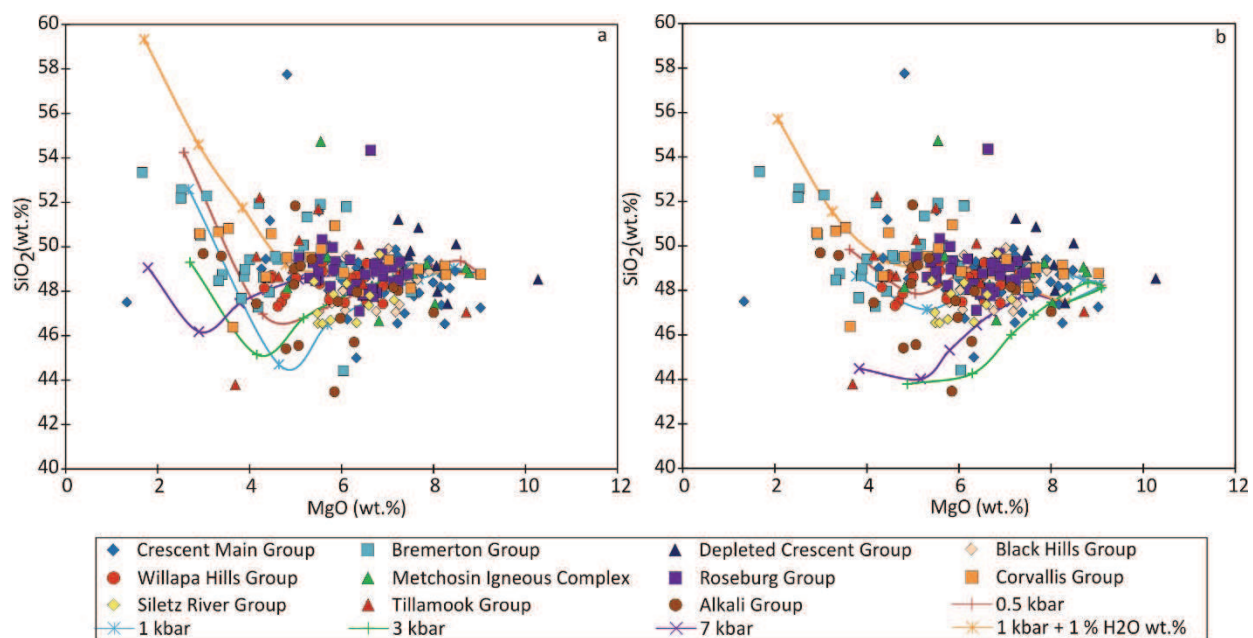
Figure 6.58 MgO (wt.%) vs SiO$_2$ (wt.%) composition of fractional crystallisation models of a parent magma with a composition of a) sample CR014 and b) sample 237CM with those of the Siletz terrane groups investigated in this section.

The Crescent Main Group samples appear to have undergone fractionation over a range of pressures, most likely from parent magmas with varying compositions (as highlighted in Figure 6.58). Fractionation of a parent magma with a composition more primitive than sample B018 at moderate to low pressures may represent the best model for the evolution of the more mafic Bremerton rocks. While the composition of the more evolved samples of the Bremerton Group are best modelled by fractional crystallisation at 3 kbar of a parent magma with similar composition to sample B003. The Depleted Crescent Group samples show a narrow range of compositions and therefore do not appear to be related to one another by fractional crystallisation. The compositions of the Southern Crescent rocks (the Black Hills and Willapa Hills Groups) are best modelled by lower pressure crystallisation models. In terms of the Vancouver Island rocks, the compositions of the Metchosin Igneous Complex rocks are best approximated by hydrous fractionation at low pressures of a parent magma with a composition between that of sample 205 and 200 MET.

Overall, lower pressure models appear to best approximate the trends in groups where fractional crystallisation has taken place. However, this is not applicable to all groups, some of which are better modelled by higher-pressure crystallisation. While deeper fractional crystallisation would be plausible in the thickened crust of the terrane (e.g., Trehu et al., 1994) as opposed to normal thin oceanic crust, a large low-pressure magma chamber is more consistent with large amounts of partial melting expected from melting of a mantle plume head, discussed below (e.g., Fitton and Goddard, 2004).
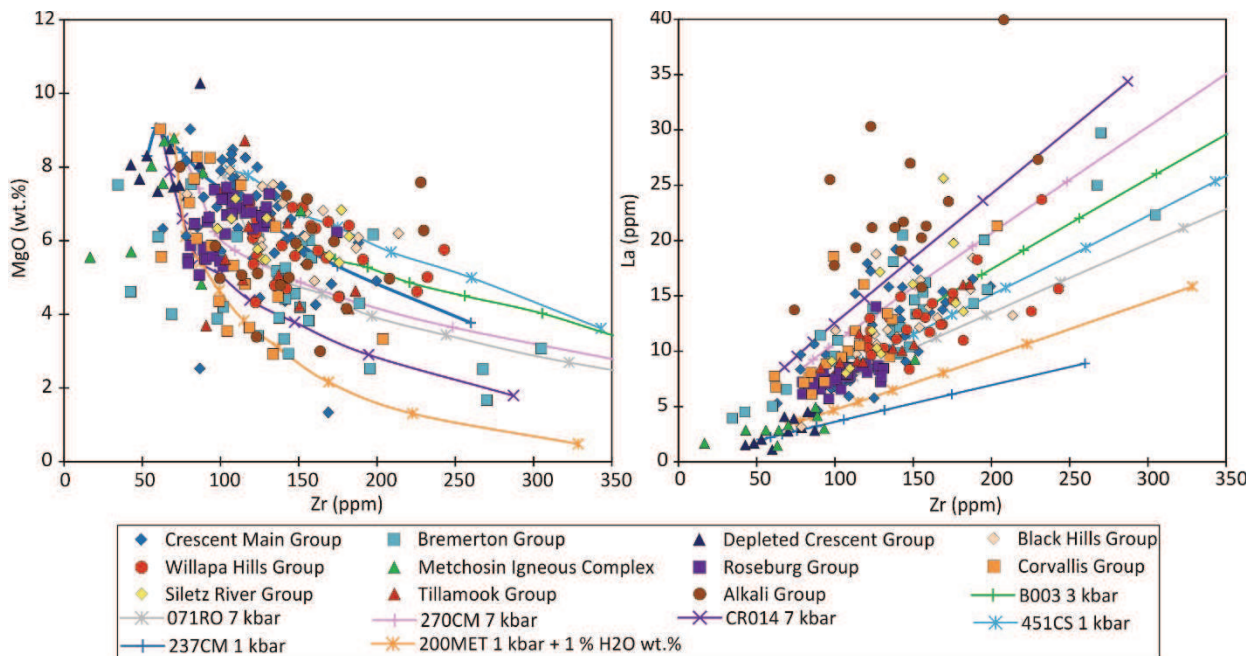
Figure 6.59 Best-fit fractional crystallisation models for a range of groups from this section with the MgO (wt.%) vs Zr (ppm) and La (ppm) vs Zr (ppm) compositions of the Siletz terrane samples.

There are several caveats with applying the fractional crystallisation models to the Siletz terrane data. Major elements may have mobilised during alteration, limiting the robustness of the initial MELTS modelling. Additionally there is a lack of primary or near primary magma compositions available in the data to model. It is also apparent that models which may model the data when applied to either the major elements, trace elements or mineral compositional data do not always work consistently across all three types of analyses. Nor are the pressure results of the CPIW normative mineralogies when plotted on the extended basalt tetrahedron always consistent with those of the MELTS models.

The spread of the data, observed across the majority of groups is also indicative of heterogeneities in the mantle source composition itself, which is to be expected across such a large terrane. Multiple magma chambers, which may exist over different pressures, each with slight to significant compositions, most likely explain the origin of the rocks, and therefore why one parent fractionation models are not generally applicable to the Siletz terrane data. Therefore polybaric crystallisation, occurring in different magma chambers, appears to be a likely

petrogenetic process affecting the rocks. Variations in the magmatic source composition are highlighted in figure 6.60. The majority of the data fall into a cluster of relatively similar Nb/Zr and Ce/Yb ratios, with the exception of the more depleted Metchosin Igneous Complex and Depleted Crescent Group, and the high Nb, high Ce Alkali Group (Figure 6.60). However, within the main cluster of data most groups display systematic variations in their Nb/Zr and Ce/Yb ratios, indicating that they may not be related by fractional crystallisation processes, and instead are the result of slight variations in the source composition (Figure 6.60). This will be further discussed in the following sections. Additionally, the magmatic systems in which the magmas evolved appear to be open systems as evidenced by abundant glomerocrysts in the samples and to a lesser extent, the presence of xenocrysts and zoned and reabsorbed plagioclases, indicating that simple fractionation is not an adequate model.
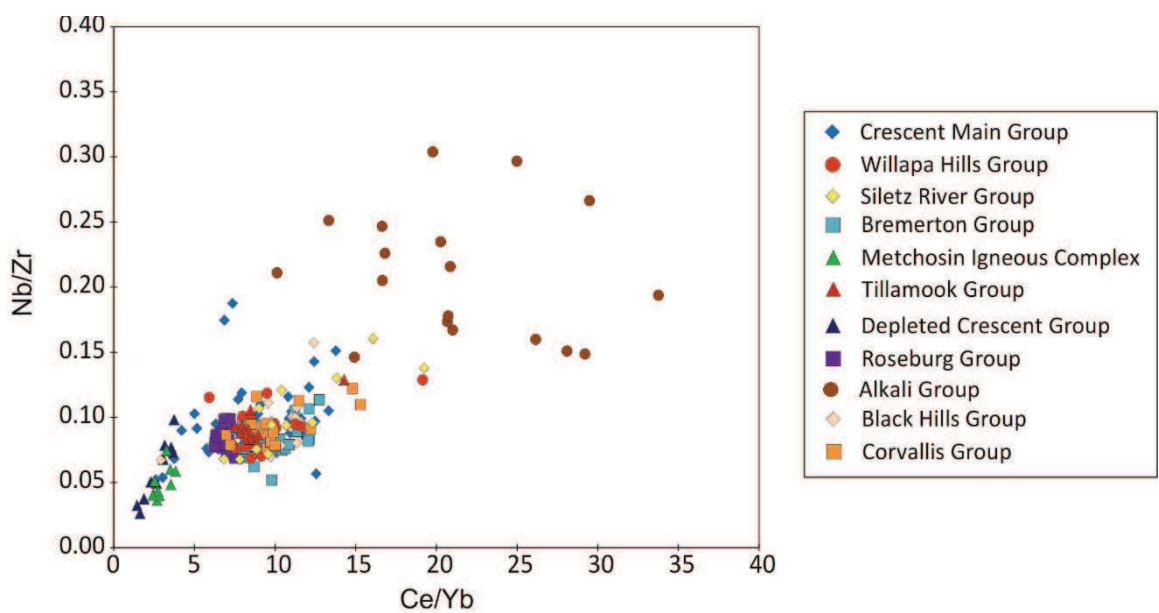
Figure 6.60 Nb/Zr vs Ce/Yb diagram for the Siletz terrane data, highlighting variations in source compositions within the terrane.

6.2 Primary Magmas and Melting Conditions

6.2.1 Introduction

In this section the likely melting conditions required to produce the calculated primary magmas of the Siletz terrane, will be determined. Primary magmas are defined as undifferentiated magmas, which formed as a result of direct melting of the upper mantle (e.g., O'Hara, 1965) and thus may provide insights into the petrogenesis of the Siletz terrane. The PRIMELT3 software of Herzberg and Asimow (2015) and the Lee et al., (2009) spreadsheet will be used to calculate the primary magma compositions of the basaltic rocks, along with the pressures and temperatures under which they were formed.

PRIMELT3 calculates melt fractions using both batch and accumulated fractional melting of fertile peridotite. The program also produces the major element abundances of the predicted primary magmas through both forward and reverse modelling. The inverse modelling produces estimated compositions of possible primary magmas from a primitive lava composition through sequential incremental addition and subtraction of equilibrium olivine. Results are produced for magmas for which the PRIMELTS algorithm has determined that only olivine fractionation has taken place (Herzberg and Asimow, 2015). The forward model uses mass balance solutions to determine the composition and the amount of melting required to form magmas from a peridotite source composition over a variety of temperatures and pressures, and melting types (i.e., batch and fractional). The methods of Lee et al., (2009), which are based on Si and Mg contents of the magma involve a silica activity thermobarometer that assumes that the melt is derived from an olivine and orthopyroxene-bearing source. The program also utilises fractionation correction through incrementally adding olivine to the samples composition, and therefore best approximates the parent magma when applied to samples, which have undergone only olivine fractionation (i.e., no plagioclase or clinopyroxene fractionation) (Lee et al., 2009).

Using the samples for which both the PRIMELT3 and Lee et al., (2009) programs are able to calculate primary magma compositions and conditions, melt modelling of a variety of mantle sources was used to try and replicate the major

and trace element compositions of the calculated primary magmas. Issues and potential problems with the melting models and primary magma models are then discussed.

6.2.2 Primary Magmas

6.2.2.1 Composition of the Primary Magmas

As discussed above, the composition of the primary magmas have been derived from the calculations of the PRIMELT3 and Lee et al., (2009) programmes. In accordance with modern analyses of oceanic plateaus the $Fe^{2+}/\Sigma Fe$ has been set at 0.9 and the composition of the fertile mantle peridotite from which the partial melts are derived is that of KR-4003 [discussed in Walter, (1998)] (Hastie et al., 2016). However, basalts in general and, more specifically, oceanic plateau lavas commonly fractionate olivine, clinopyroxene and plagioclase, meaning it is often difficult to obtain primitive lavas which have exclusively fractionated olivine (e.g., Kerr et al., 1996; Korenaga and Kelemen, 2000; Fitton and Godard, 2004; Hastie and Kerr, 2010; Loewen et al., 2013). Therefore, due to the relatively low magnesium contents (MgO values of up 10.27 wt.%) and abundant clinopyroxene fractionation (Chapters 4; 5 and section 6.1), few of the samples are suitable for the calculations.

The methods outlined in Lee et al. (2009), resulted in only 8 samples producing primary magma compositions, while the PRIMELT3 modelling software of Herzberg and Asimow (2015) produced results for 30 samples, 7 of which are the same those which also worked using the Lee et al., (2009) modelling. It is also worth noting that while in general the compositions produced are relatively similar, the Lee et al., (2009) programme consistently calculates MgO values that are ~ 3 wt.% lower than those of calculated by PRIMETLT3.

The PRIMELT3 programme also calculates the percentage of melting of fertile mantle peridotite required to produce the primary magma along with the calculated subsequent olivine fractionation (Table 6.2). The average amount of melting predicted to have occurred in the PRIMELT3 models is 28 %, indicating a

significant amount of melting has occurred (Table 6.2) (Fitton and Godard, 2004; Herzberg and Gazel, 2009). The PRIMELT3 modelling results also require an olivine addition of, on average 39 %, which indicates that subsequent to melting of the source, the magmas underwent significant fractionation in a crustal magma chambers to generate the observed compositions (Table 6.2).

PRIMELTS3.xsl AFM (Herzberg and Asimow, 2015)		
Sample #	% Melting of peridotite	% Olivine addition
270CM	27.71	35.51
305CM	19.30	45.63
313CM	10.56	33.89
316CM	20.18	25.51
423CM	29.69	34.66
430CM	30.95	41.47
B019	22.37	27.65
306CM	24.64	21.96
404CS	30.13	44.73
407CS	33.03	47.06
409CS	31.18	47.36
443CS	25.41	46.08
455CS	17.98	42.55
201MET	29.86	34.95
205MET	25.04	30.25
67RO	31.80	49.62
68RO	32.33	39.42
71RO	31.15	39.08
4RO	34.07	51.49
25RO	32.03	46.10
42RO	27.46	46.41
50RO	30.84	50.23
101SRV	29.31	35.28
103/1SRV	29.67	50.73
99/2SRV	26.59	31.56
CR001	30.69	37.65
CR003	31.06	40.27
CR014	31.58	36.24
168SRV	28.92	38.62
170SRV	27.85	39.80

Table 6.2 Calculated percentage of accumulated fractional melting and olivine addition for the samples for which PRIMELTS3 was able to produce results.

The Lee et al., (2009) programme was unable to calculate any primary magma compositions for the samples collected from the Roseburg area. While

PRIMELT3 was able to calculate primary magma compositions of 5 samples using batch melting and 7 samples using accumulated fractional melting (Table 6.3). The MgO wt.% of the primary magmas for the Roseburg Main Group range between 22.2 – 23.2 wt.% (for accumulated fractional melting) (Table 6.3) while the percentage of melting for this group varies from 27.5 – 34.1 % (Table 6.2).

	Sugarloaf Group		Coquille Group			Roseburg Main Group				
Sample:	67RO		68RO	71RO	4RO	25RO		42RO		50RO
(wt. %)	BM	AFM	AFM	AFM	AFM	BM	AFM	BM	AFM	AFM
SiO$_2$	45.53	45.82	47.22	46.82	45.84	45.51	45.86	45.50	45.81	45.62
TiO$_2$	1.07	1.14	1.10	1.16	1.13	1.12	1.21	1.10	1.17	1.17
Al$_2$O$_3$	8.06	8.58	9.74	9.67	8.56	8.71	9.40	8.41	8.99	8.53
FeO	11.12	11.39	10.47	10.55	11.34	10.77	11.06	11.03	11.30	11.52
MnO	0.18	0.18	0.20	0.18	0.18	0.18	0.18	0.19	0.20	0.22
MgO	24.74	23.00	20.67	20.71	23.24	24.35	22.18	24.03	22.12	23.19
CaO	6.97	7.42	8.04	8.29	7.49	7.21	7.78	7.24	7.74	7.34
Na$_2$O	1.32	1.41	1.36	1.56	1.26	1.23	1.33	1.49	1.59	1.40
K$_2$O	0.09	0.10	0.25	0.10	0.02	0.05	0.05	0.10	0.11	0.04
Fe$_2$O$_3$	0.80	0.85	0.84	0.85	0.82	0.78	0.84	0.80	0.86	0.86
Fo	93.1	92.4	92.1	92.1	92.5	93.2	92.3	93.0	92.2	92.4

Table 6.3 Primary magma compositions calculated for the Roseburg area samples, where BM – PRIMELTS Batch melting results and AFM – PRIMELTS Accumulated fractional melting results

In terms of the Siletz River area samples, PRIMELT3 was successful in calculating the primary magma composition for 6 samples from the Corvallis Group (using accumulated fractional melting) and for 2 samples from the Alkali Group (through both batch and accumulated fractional melting) (Table 6.4). While the Lee et al., (2009) programme was able to produce primary compositions for 3 samples from the Corvallis Group (Table 6.4). The Alkali Group calculated primary magma MgO wt.% varies from 20.37 – 22.27 wt.%. The primary magma MgO wt.% for the Corvallis Group ranges from 18.94 – 23.37 wt. % for the PRIMELT3 models and 16.19 – 17.58 wt.% for the Lee et al., (2009) models (Table 6.4). The amount of melting which is predicted to have occurred varies from 26.59 – 31.58 % for the Corvallis Group and 27.85 - 28.91 % for the Alkali Group (Table 6.2).

Primary magma compositions for 9 of the Northern Crescent Formation samples were able to be calculated (Table 6.5). Seven of these samples are from the Crescent Main Group, with the PRIMELT3 programme calculating both accumulated fractional melting and batch melting for all 7 samples, and the Lee et al., (2009) programme calculating primary magma compositions for 3 samples (Table 6.5). PRIMELT3 also able to successfully calculate the primary magma composition of one sample from the Bremerton Group and one sample from the Depleted Crescent Group (using both batch and accumulated fractional melting models), while the Lee et al., (2009) programme also yielded a primary magma composition for the Depleted Crescent Group sample (Table 6.5).

Sample:	101SRV		103/1SRV	99/2SRV		CR001	CR003	CR014		168SRV		170SRV	
						Corvallis Group					Alkali Group		
(wt. %)	AFM	Lee et al	AFM	AFM	Lee et al	AFM	AFM	AFM	Lee et al	BM	AFM	BM	AFM
SiO_2	46.45	47.17	45.35	46.56	47.18	46.83	46.96	46.65	47.43	45.83	46.18	45.70	46.01
TiO_2	1.19	1.31	1.36	1.13	1.23	1.11	1.10	1.12	1.24	1.52	1.63	1.60	1.70
Al_2O_3	10.36	11.48	8.32	10.80	11.76	10.16	9.77	9.71	10.81	9.42	10.10	9.33	9.94
FeO	10.33	11.04	11.66	10.05	10.68	10.39	10.45	10.61	11.40	10.24	10.45	10.39	10.58
MnO	0.24	0.19	0.18	0.16	0.13	0.11	0.11	0.12	0.10	0.16	0.16	0.18	0.18
MgO	19.93	16.72	23.37	18.94	16.19	20.26	20.46	20.92	17.58	22.29	20.18	22.27	20.37
CaO	9.13	10.05	7.44	10.20	11.06	8.66	8.70	8.57	9.50	8.29	8.88	8.10	8.63
Na_2O	1.37	1.52	1.25	1.18	1.29	1.31	1.39	1.16	1.30	1.24	1.33	1.32	1.41
K_2O	0.02	0.03	0.07	0.00	0.00	0.18	0.10	0.13	0.14	0.06	0.07	0.13	0.13
Fe_2O_3	0.87	0.48	0.87	0.87	0.48	0.85	0.82	0.90	0.51	0.78	0.84	0.79	0.84
Fo	92.0	90.0	92.4	91.8	90.0	92.0	92.0	92.1	90.0	92.9	92.0	92.9	92.0

Table 6.4 Primary magma compositions calculated for the Siletz River area samples, where BM – PRIMELTS Batch melting results; AFM – PRIMELTS Accumulated fractional melting results and Lee et al – The primary magma compositions calculated by the Lee et al., (2009) programme.

| (wt. %) | Crescent Main Group | | | | | | | | | | | | | | | Bremerton Group | | Depleted Crescent Group | | |
| | 270CM | | | 305CM | | 313CM | | 316CM | | | 299CM | 423CM | | 430CM | | B019 | | 306CM | | |
	BM	AFM	Lee et al	BM	AFM	BM	AFM	BM	AFM	Lee et al	Lee et al	BM	AFM	BM	AFM	BM	AFM	BM	AFM	Lee et al
SiO_2	45.85	46.15	46.82	44.59	44.76	44.85	44.91	45.88	46.10	46.49	45.55	46.44	46.91	45.79	46.12	47.10	47.42	47.22	47.55	48.12
TiO_2	1.22	1.30	1.42	1.20	1.25	1.17	1.19	1.08	1.12	1.18	1.46	1.06	1.15	1.11	1.19	1.01	1.06	0.56	0.59	0.62
Al_2O_3	9.92	10.55	11.63	9.40	9.84	12.25	12.44	11.98	12.52	13.21	11.79	9.91	10.77	8.93	9.55	10.49	11.02	13.29	13.99	14.84
FeO	10.26	10.43	11.16	11.50	11.68	10.65	10.68	9.77	9.86	10.48	11.69	9.94	10.16	10.53	10.76	9.44	9.51	8.80	8.84	9.28
MnO	0.24	0.25	0.20	0.18	0.18	0.21	0.21	0.19	0.19	0.16	0.17	0.17	0.17	0.17	0.18	0.10	0.10	0.17	0.17	0.15
MgO	21.86	19.99	16.95	23.22	21.92	19.14	18.66	19.25	17.84	16.04	17.81	22.11	19.55	23.22	21.23	18.86	17.25	17.65	15.90	14.00
CaO	8.34	8.87	9.72	7.47	7.81	8.52	8.64	9.60	10.02	10.54	8.90	7.79	8.46	8.04	8.59	10.47	10.99	9.74	10.25	10.83
Na_2O	1.34	1.43	1.58	1.31	1.37	1.84	1.86	1.25	1.31	1.38	1.80	1.44	1.56	1.20	1.29	1.54	1.62	1.54	1.63	1.73
K_2O	0.04	0.05	0.05	0.15	0.16	0.18	0.18	0.03	0.03	0.03	0.33	0.28	0.30	0.10	0.10	0.08	0.08	0.02	0.02	0.02
Fe_2O_3	0.82	0.88	0.49	0.86	0.90	0.88	0.90	0.88	0.92	0.49	0.50	0.78	0.85	0.80	0.86	0.80	0.84	0.78	0.83	0.44
Fo	92.8	92.0	90.0	92.6	92.0	91.6	91.4	92.2	91.5	90.0	90.0	93.0	91.9	93.0	92.2	92.2	91.5	92.2	91.3	90.0

Table 6.5 Primary magma compositions calculated for the Northern Crescent Formation samples, where BM – PRIMELTS Batch melting results; AFM – PRIMELTS Accumulated fractional melting results and Lee et al – The primary magma compositions calculated by the Lee et al., (2009) programme.

The MgO wt.% for the Crescent Main Group calculated primary magmas ranges from 17.8 – 21.9 wt. % for PRIMELT3 accumulated fractional melting and from 16.0 – 17.8 wt.% (Table 6.5). While the amount of melting predicted for the Crescent Main Group primary magmas formation has been calculated to vary from 10.6 – 31.0 % (Table 6.2). This degree of variation in melting is also reflected in the variety of compositions observed in the major and trace elements of the group.

PRIMELT3 was able to successfully calculate the primary magma compositions for 5 of the Black Hills Group samples (from the Southern Crescent Formation) through both batch and accumulated fractional melting models (Table 6.6). The MgO wt.% of the calculated primary magmas varies from 21.0 – 22.6 wt.% (for the accumulated fractional melting models) (Table 6.6). The percentage of melting of the fertile peridotite source required to produce the primary magma compositions range from 18.0 – 33.0 % (Table 6.2).

	Black Hills Group									
Sample:	404CS		407CS		409CS		443CS		455CS	
(wt. %)	BM	AFM	BM	AFM	BM	AFM	BM	AFM	BM	AFM
SiO_2	45.50	45.83	45.54	45.95	45.35	45.73	45.35	45.63	44.94	45.10
TiO_2	1.23	1.32	1.19	1.30	1.28	1.39	0.72	0.77	1.50	1.55
Al_2O_3	8.53	9.18	8.10	8.84	8.16	8.87	8.95	9.52	9.44	9.81
FeO	10.83	11.11	10.80	11.15	10.90	11.25	11.17	11.41	11.23	11.37
MnO	0.18	0.18	0.17	0.18	0.17	0.17	0.17	0.17	0.19	0.20
MgO	24.11	22.02	25.00	22.56	24.90	22.54	23.90	22.12	22.18	21.03
CaO	7.28	7.83	7.01	7.64	7.03	7.64	7.41	7.89	7.89	8.20
Na_2O	1.31	1.41	1.20	1.31	1.23	1.34	1.44	1.53	1.56	1.62
K_2O	0.10	0.11	0.08	0.09	0.09	0.09	0.02	0.03	0.09	0.09
Fe_2O_3	0.80	0.86	0.78	0.85	0.78	0.85	0.82	0.87	0.86	0.89
Fo	93.1	92.3	93.4	92.4	93.3	92.4	92.9	92.1	92.4	91.8

Table 6.6 Primary magma compositions calculated for the Black Hills Group samples, where BM – PRIMELTS Batch melting results and AFM – PRIMELTS Accumulated fractional melting results.

PRIMELT3 was successful in obtaining primary magma compositions for only 2 of the Metchosin Igneous Complex samples (through the accumulated fractional melting model only), one of which the Lee et al., (2009) programme was also able to calculate a primary magma composition for (Table 6.7). The

MgO wt.% of the primary magma ranges from 18.4 – 19.4 wt.% for the PRIMELT3 derived compositions while the Lee et al., (2009) calculated composition is 15.8 wt.%. The amount of melting of fertile mantle peridotite required to produce the estimated primary magma ranges from 30.3 – 35.0 % (Table 6.2).

Metchosin Igneous Complex			
Sample:	201MET	205MET	
(wt. %)	AFM	AFM	Lee et al
SiO_2	47.07	46.12	46.66
TiO_2	0.73	0.72	0.78
Al_2O_3	11.42	12.89	13.97
FeO	10.11	9.91	10.51
MnO	0.18	0.21	0.17
MgO	19.44	18.44	15.83
CaO	8.67	9.64	10.40
Na_2O	1.47	1.09	1.18
K_2O	0.03	0.03	0.03
Fe_2O_3	0.84	0.87	0.47
Fo	91.9	91.7	90.0

Table 6.6 Primary magma compositions calculated for the Black Hills Group samples, where BM – PRIMELTS Batch melting results and AFM – PRIMELTS Accumulated fractional melting results.

6.2.2.2 Pressure and Temperature

The PRIMELT3 and Lee et al., (2009) models (Table 6.7) have also determined estimates of the pressures and temperatures under which the primary magmas of the Siletz terrane formed. As discussed above, both types of models are able to calculate the primary magma compositions and melting conditions of 7 samples. The results for these 7 samples, were relatively consistent across the two techniques, producing a range of initial mantle potential temperatures (Tp) between ~ 1400 - 1500 °C and pressures between 1.5 GPa and 2.4 GPa (i.e., melting at less than 100 km). Mid-ocean ridge basalts generally display Tp ranges between ~1280 and 1400 °C, while intra-plate magmas are produced at Tp above >1400 °C (Herzberg et al., 2007; Lee et al., 2009). The Tp conditions estimated for the Siletz terrane data therefore appear to support a mantle plume related intra-plate origin for the Siletz terrane.

| Sample # | Lee et al., 2009 | | Herzberg and Asimow, 2015 |
	Temperature °C	Pressure GPa	Temperature °C
270CM	1499	2.39	1436
299CM	1537	3.12	
305CM			1475
313CM			1424
316CM	1474	2.19	1394
423CM			1431
430CM			1457
B019			1384
306CM	1401	1.53	1360
404CS			1473
407CS			1480
409CS			1481
443CS			1478
455CS			1460
201MET			1426
205MET	1465	2.05	1403
67RO			1490
68RO			1448
71RO			1450
4RO			1491
25RO			1474
42RO			1478
50RO			1493
101SRV	1490	2.23	1433
103/1SRV			1495
99/2SRV	1476	2.04	1411
CR001			1440
CR003			1443
CR014	1512	2.33	1449
168SRV			1437
170SRV			1442

Table 6.7 Calculated pressure and temperatures for the primary magmas of the Siletz terrane from the Lee et al., (2009) and PRIMELTS3 programmes.

There appears to be little correlation between the calculated mantle temperature and the geographical position of the samples within the terrane (Figure 6.61). While there is an overall increasing temperature (using both Herzberg and Asimow, 2015 and Lee et al., 2009 calculated initial temperatures) southwards, the trend is not very statistically significant ($R^2 = 0.2$). The lowest calculated source temperatures generally cluster in the north of the terrane and are

associated with the more 'depleted' samples, with sample 306CM from the Depleted Crescent Group exhibiting the lowest calculated temperature (1401 °C or 1360 °C, for Lee et al., (2009) and PRIMELT3 respectively) (and a pressure of 1.53 GPa). In terms of the pressures predicted by the Lee et al., (2009) models, there is no observable N-S trend in the data, however from W-E (excepting the low pressure sample 306CM) there is a significant trend ($R^2 = 0.73$) of increasing calculated pressures (Figure 6.61). However, this is only over a small range of pressures and in addition there is a cluster of samples in the South Crescent Formation with relatively high, calculated source temperatures, while the Roseburg area samples also display consistently high temperatures. The source temperatures increase with pressure as expected, but despite this there is little correlation overall. Sample 205MET and 306CM however have lower predicted initial pressures and temperatures along with more comparatively depleted compositions (discussed in Chapter 5).
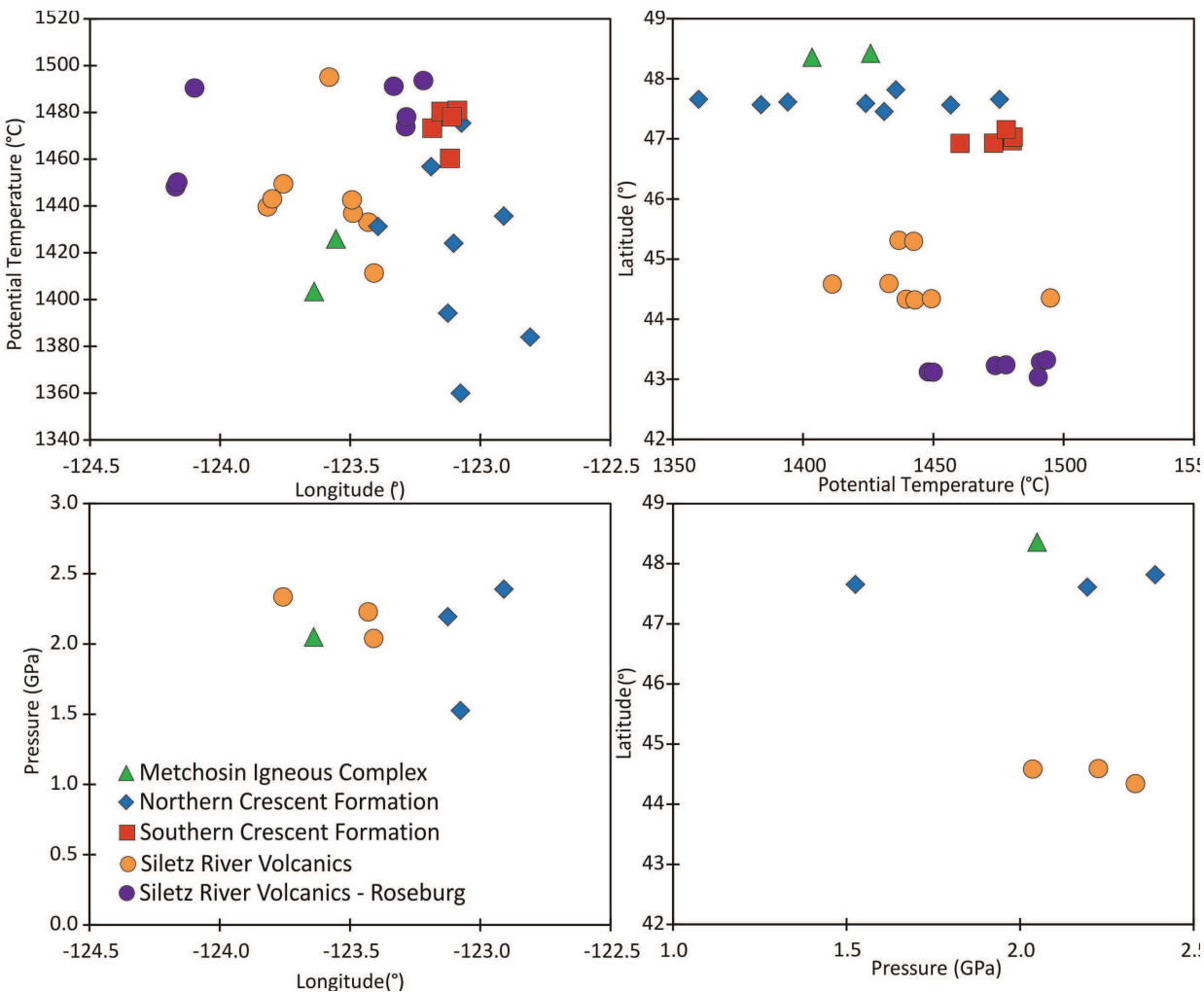
Figure 6.61 Calculated pressure and temperature for the primary magmas of the Siletz terrane with the latitude and longitude of the input sample.

6.2.2.3 Tectonic Implications

As discussed above, the suggested temperatures and pressures for the primary magmas appear to indicate a hotter than ambient source for the primary magmas of the Siletz terrane (Table 6.7). Figure 6.62 shows a comparison between the Siletz data Lee et al., (2009) modelling results and those of MORBs and the Hawaiian hotspot, which span a range of source pressure and temperatures. The Tp conditions of the Siletz terrane primary magmas generally overlap with the Hawaiian (predominantly shield phase) Tp space, although one Crescent Main sample (sample 306CM, from the Depleted Crescent Group)

overlaps with the MORB field (Figure 6.62). Overall, the data points lie between 20 and 30 % melt fractions, excluding the sample which lies at hotter and deeper melting (sample 299CM) which exhibits < 20 % melting, however, PRIMELT3 was unable to calculate primary magma conditions for this sample, which may limit its robustness. The samples largely plot in the garnet- spinel transition zone and above, which is generally reflected in the trace element patters, i.e the Gd/Yb $_{PM}$ ratios of the data are usually less than 1.4. The samples also all plot above the dry lherzolite solidus and the melting amount seems consistent with that produced by the PRIMELT3 programme (Table 6.2). Overall Figure 6.62 suggests that the pressure and temperature conditions predicted by the Lee et al., (2009) programme appear to be consistent with at least some degree of plume ridge interaction.
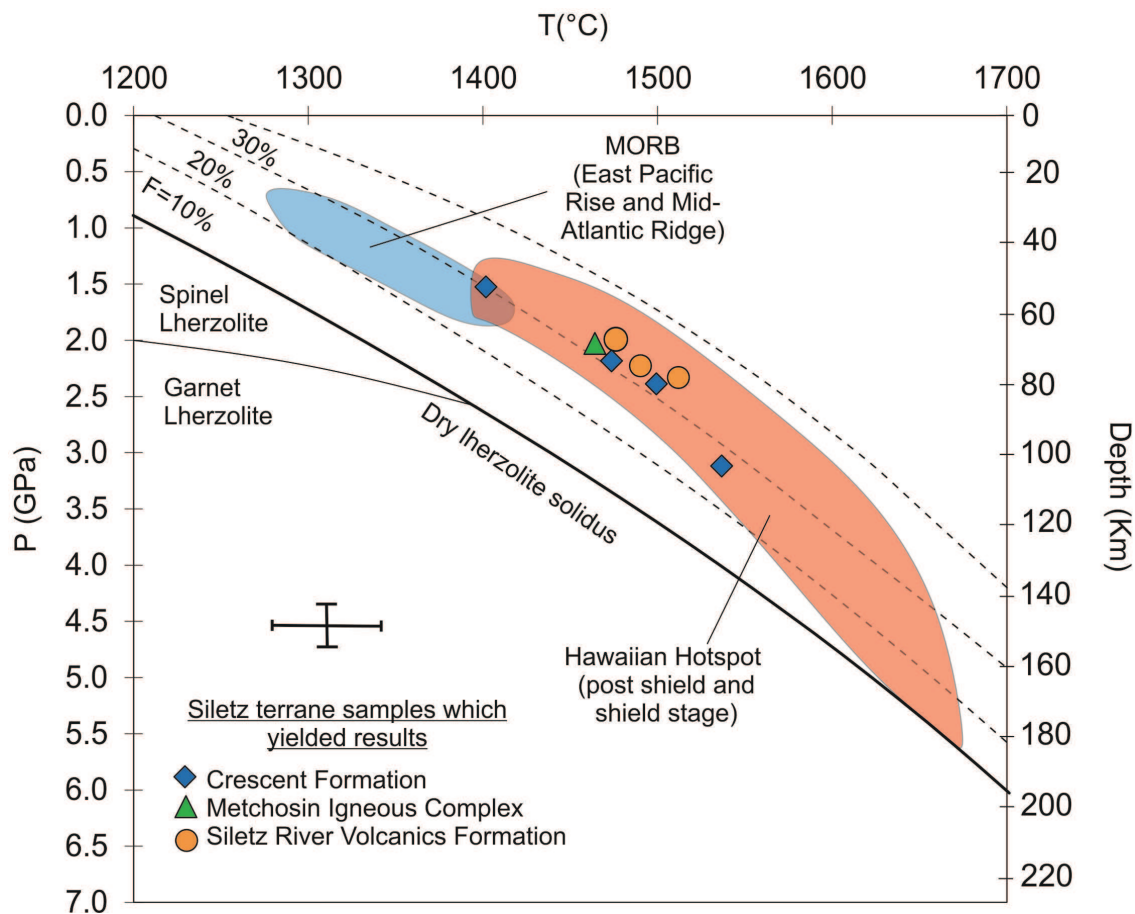
Figure 6.62 Comparison of calculated primary magma pressures and temperatures of the Siletz terrane [Lee et al., (2009) programme] with those of MORBS (East Pacific Rise and Mid Atlantic Ridge) and the Hawaiian hotspot source regions. The curved dotted lines represent melting adiabats. Adapted from Lee et al., (2009). The garnet and spinel lherzolite fields are derived from O'Hara et al., (1971).

The results of this modelling indicate that the melts forming the Siletz terrane were derived from a mantle source with an elevated temperature. In addition, the volume of magmatism produced [~2.6 x 10^6 km^3 (Trehu et al., 1994)] is consistent with extensive melting of a mantle plume head (Fitton and Godard, 2004; Herzberg and Gazel, 2009). While the range in calculated pressures may indicate inaccuracies in the models they may also point to melting over a significant range of depths, which may represent the interaction of a plume with depleted upper mantle (discussed further in section 6.3). The amount of melting modelled in PRIMELT3 is also indicative of a hotter-than-ambient mantle source with melting percentages of ~ 28 % (with the majority of samples producing results between 25 – 33 %) (Table 6.2), which are comparable to the extent of

melting calculated for the Ontong Java Plateau and the Caribbean Plateau (~30 % melting) (Fitton and Godard, 2004; Herzberg and Gazel, 2009).

6.2.3 Melting Conditions and Modelling Mantle Reservoirs

The amount of melting and fractionation calculated by the PRIMELT3 program can be used to try and determine whether the primary magmas of the Siletz terrane were produced via partial melting or mixing of the partial melts of one or more sources, or via another mechanism entirely. The whole rock geochemical results, discussed in Chapter 5, indicate that the Siletz terrane rocks generally have E-MORB to OIB like characteristics, which are generally typical of oceanic plateaus (Kerr et al., 2014). The following sections will therefore attempt to use both major and trace element mantle melting models to determine if melting or mixing of various mantle reservoirs and sources using the conditions outlined by the PRIMELT3 programme can explain the trends observed in the Siletz terrane data. Due to uncertainties in the modelling discussed below, only samples for which both the PRIMELT3 and Lee et al., (2009) models can produce results will be used in the following melting models.

6.2.3.1 Major Element Models

The following major element melting models were produced using the MELTS programme (Ghiorso et al., 2002) under isenthalpic adiabatic melting conditions. Therefore the models assume local equilibrium between solid and liquid phases and that no transfer of heat has taken place between the rising mantle diaper and the surrounding mantle during the ascent (Ghiorso et al., 2002). Melting was modelled at a range of starting temperatures, rising through decreasing pressures. The mantle reservoirs modelled for the major element partial melt modelling include KR-4003, a sub continental xenolith from West Kettle River Basin, British Columbia (Walker, 1998). This xenolith has been selected as a proxy for the mantle plume source region of the Caribbean and Ontong Java Plateaus (Hastie et al., 2016) and so as a potential analogue for a

plume source composition for the Siletz terrane. Mantle melting of a reservoir with a Depleted MORB Mantle (DMM) composition was also carried out. This DMM composition represents a primitive mantle composition which been depleted by 2-3 % melt extraction (Workman and Hart, 2005). Also for comparison, melting of a reservoir with a Primitive Upper Mantle composition (PUM) and PUM which has undergone 3% depletion through melting (PUM – 3 %) have also been modelled. The starting composition of the modelled mantle sources are shown in Table 6.8.

Sample	Source	SiO_2	TiO_2	Al_2O_3	FeO	MnO	MgO	CaO	Na_2O	K_2O	P_2O_5
KR-4003	Walker, 1998	44.9	0.16	4.26	8.02	0.13	37.3	3.45	0.22	0.09	–
Bulk DMM	Workman and Hart, 2005	44.71	0.13	0.57	8.18	0.13	38.73	0.24	0.13	0.006	0.019
PUM	Workman and Hart, 2005	44.9	0.2	0.38	8.03	0.13	37.71	0.25	0.36	0.029	0.021
PUM - 3% N-MORB	Workman and Hart, 2005	44.87	0.18	0.39	8.05	0.13	38.68	–	0.3	0.028	0.019

Table 6.8 Major element concentrations of the mantle sources used in the major element melting modelling.

The modelling results were then compared with the predicted primary magma compositions calculated by PRIMELT3, to determine if they represent a viable model of formation. All discussed major melting models begin at pressures of 2.5 GPa and run through to 0.1 GPa. The best - fit model for each sample's primary magma composition, at the degree of melting predicted by the PRIMELT3 models, are shown in Table 6.9. The best fit models were determined through comparison of the difference between the sample and each model composition, with the model that produced the smallest total difference taken as the best fit.

	SiO$_2$	TiO$_2$	Al$_2$O$_3$	Fe$_2$O$_3$	FeO	MnO	MgO	CaO	Na$_2$O	K$_2$O	P$_2$O$_5$	Melting Fraction %
					Major Element (wt.%)							
306CM	47.22	0.56	13.29	0.78	8.80	0.17	17.65	9.74	1.54	0.02	0.23	24.6
KR-4003 at 1300 °C	46.86	0.53	12.19	1.34	8.81	0.02	18.36	10.61	0.82	0.34	-	26.5
270CM	45.85	1.22	9.92	0.82	10.26	0.24	21.86	8.34	1.34	0.04	0.11	27.0
DMM at 1400 °C	45.23	0.41	10.47	1.41	10.09	0.03	22.17	9.47	0.47	0.02	0.07	27.0
316CM	45.88	1.08	11.98	0.88	9.77	0.19	19.25	9.60	1.25	0.03	0.09	21.5
KR-4003 at 1400 °C	43.74	0.60	11.91	1.51	10.03	0.03	19.42	11.22	1.01	0.44	-	25.3
205MET	45.83	0.68	12.15	0.82	9.79	0.20	20.32	9.10	1.03	0.03	0.06	25.0
KR-4003 at 1400 °C	44.70	0.53	11.51	1.44	9.71	0.03	20.11	10.65	0.85	0.36	-	25.3
101SRV	46.08	1.11	9.67	0.81	10.13	0.23	22.05	8.52	1.27	0.02	0.10	29.3
DMM at 1400 °C	45.87	0.39	10.21	1.36	9.89	0.03	22.62	8.93	0.43	0.02	0.06	29.5
99/2SRV	46.21	1.06	10.11	0.81	9.89	0.16	21.00	9.56	1.10	0.00	0.10	26.6
KR-4003 at 1400 °C	45.23	0.41	10.47	1.41	10.09	0.03	22.17	9.47	0.47	0.02	0.07	27.0
CR014	46.07	1.01	8.71	0.81	10.24	0.11	24.09	7.69	1.04	0.11	0.11	31.6
DMM at 1450 °C	45.47	0.37	9.62	1.36	10.07	0.04	24.00	8.40	0.40	0.02	0.06	31.7

Table 6.9 Major element compositions of the calculated primary magmas of the Siletz terrane with the most applicable major element isenthalpic adiabatic melting model from the MELTS modelling software (Ghiorso et al., 2002).

The temperature ranges of the melting models are generally consistent with the PRIMELT3 predicted temperature of the primary magmas source, although they are generally around 50 °C cooler than those calculated by the Lee et al., (2009) programme. Additionally the primary magma composition of sample 306CM is best reconciled with melting at a lower temperature than the other samples, which is consistent with the modelling results discussed above (Figure 6.62; Table 6.2; Table 6.9). While the primary magma of sample CR014 appears to be more closely represented by melting of a hotter mantle source (~1450 °C) which also corresponds with the calculated PRIMELT3 temperature (Figure 6.62; Table 6.2; Table 6.9). The compositions of the source of the modelled primary magmas either correspond to DMM or KR-4003. Furthermore, the geographical location of the samples appears to have no correlation to the modelled source compositions. However, the composition of these sources are relatively similar in major element compositions, with the greatest differences observed in the Al$_2$O$_3$ and CaO concentrations (Table 6.8). Allègre et al. (1995) and McDonough (2001) suggest that the composition of the mantle is relatively homogeneous in terms of its major element concentrations, which limits the suitability of the major element

melting models. Therefore, despite DMM representing a primary magma source more typical of mid ocean ridge settings (Workman and Hart, 2005) and a fertile peridotite KR-4003 representing an analogue for a mantle plume source (Walker, 1998; Hastie and Kerr., 2010; Hastie et al., 2016) there are clear overlaps in the major element modelling. The major element melting modelling does however, reaffirm the hotter than ambient temperature of the mantle source for the majority of the calculated primary magmas.

6.2.3.2 Trace Element Models

Due to the difficulties of unravelling the source compositions in the major element modelling, trace element melting modelling has been undertaken. In addition, the range of trace elements observed in possible mantle source compositions is more extensive than that observed in the major elements, resulting in modelling that is better able to resolve discrete mantle source compositions. The mantle reservoirs modelled include: Depleted MORB Mantle (DMM), Enriched Mantle 2 (EM2), High - μ Mantle (HIMU), Primitive Mantle (PM), Inamha Mantle Source (IM), Gorda MORB Mantle (GMM), Caribbean Mantle Source (CAB) and Ontong Java Mantle Source (OJP) (Appendix E7) (Figure 6.63). The DMM composition of Workman and Hart (2005) is derived from the depletion trends of abyssal peridotites. The EM2 and HIMU reservoir compositions were obtained from Willbold and Stracke (2006), where it was determined using inverse modelling of the basalt compositions of the Tristan da Cuhna, Gough, Samoan and Society islands, that EM2 is best modelled by a mixture of 90 % DMM, 9.8 % oceanic crust and 0.2 % upper continental crust (Rudnick and Gao, 2003). The HIMU source trace element compositions were also derived using inverse non-modal fractional melting modelling of the basalts composition of the St Helena and islands of the Cook-Austral chains (Willbold and Stracke, 2006). The PM composition has been obtained from McDonough and Sun (1995) from studies on chondritic meteorites and mantle peridotites. The IM source is thought to represent the mantle plume source of the Columbia River Flood Basalts (CRFB) and the Snake–Yellowstone volcanics (Wolff et al., 2008).

While the GMM is used as a representation of a possible regional depleted mantle component (Davis et al., 2008; Salters et al., 2011). Trace element compositions for Gorda MORB are an average obtained from Davis et al., (2008) and Salters et al., (2011), while trace element abundances for the Imnaha component are an average of Wolff et al., (2008) data. Finally, the Caribbean Mantle Source and Ontong Java Mantle Source trace element compositions were derived from the work of Hastie et al., (2016) and are both thought to represent the mantle source composition of the mantle plumes, which produced the Caribbean Plateau and Ontong Java Plateau respectively. In addition, mixtures of melts from the discussed mantle reservoirs, to varying degrees, were also modelled.
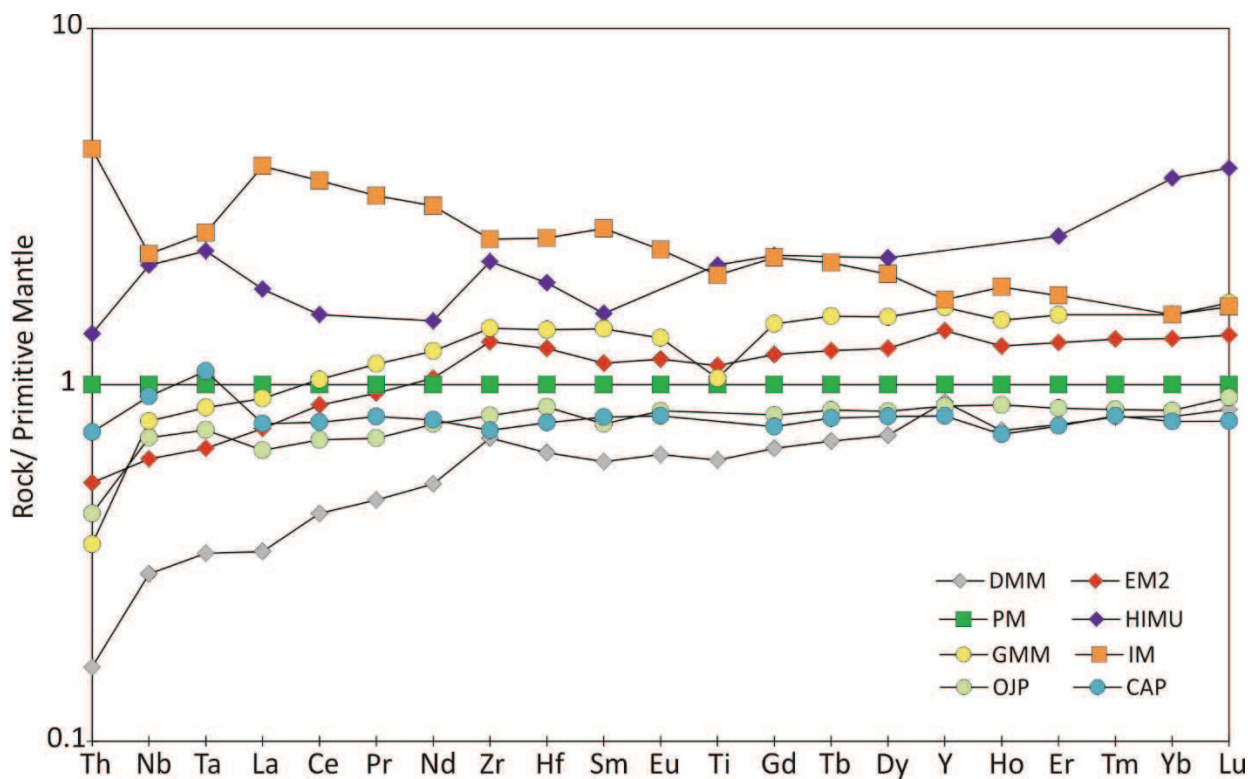
Figure 6.63 Primitive mantle normalised primitive mantle-normalised plot of the composition of the mantle reservoirs used in the modelling in Section 6.2.3.2. See text for data sources.

Partial melting was modelled for the Siletz Terrane suites using samples which both PRIMELT3 and Lee et al., (2009) successfully produced a solution for their primary magma compositions. The non – modal batch melting equation (Equation 6.2) after Shaw (1970), using the degree of partial melting calculated by

PRIMELT3 for spinel lherzolites for the different mantle reservoirs described above, is used to calculate the composition of the melts. The mineral modes for spinel lherzolite and garnet lherzolite and the derived partial melts for both were obtained from Johnson et al., (1990). The batch melting equation was in part chosen as the high amounts of melting predicted in the PRIMELT3 models mean that the results of the models are basically indistinguishable from those produced by accumulated fractional melting models for incompatible elements (e.g. Rollinson, 1993; Fitton and Goddard, 20004; Hastie and Kerr, 2010).

$$\text{Equation 6.2} \qquad C^i_{liq} = C^i_o f^{D^{i-1}}$$

Where C^i_{liq} = concentration of element i in the evolving liquid; C^i_o = concentration of element i in the parent magma, f = the residual parent liquid fraction; D^i = the bulk partition coefficient for element i.

Spinel lherzolite sources were chosen for the majority of models, as the Siletz terrane basalts which produced results, generally have relatively flat HREE patterns with the primitive mantle normalized ratios of middle to heavy REE of <1.4, with the exception of sample 99/2SRV, which has a Gd/Yb $_{PM}$ of 1.5. Subsequent to melting, the calculated composition is then required to have undergone a certain degree of olivine fractionation as predicted by the PRIMELT3 modelling in order to reproduce the Siletz Terrane sample composition, using Equation 6.1. For clarity only four representative models which approximate each sample composition will be displayed.

Figure 6.64 shows the chondrite normalised trace element compositions of sample 270CM from the Main Crescent Group, along with the composition of magmas formed via melting and subsequent olivine fractionation, derived from spinel lherzolite melting for 4 of the reservoirs and mixtures of the reservoirs described above. Of all the melting models, melting of a mixture of 70 % PM and 30 % IM with subsequent olivine fractionation required by the PRIMELT model for this sample.
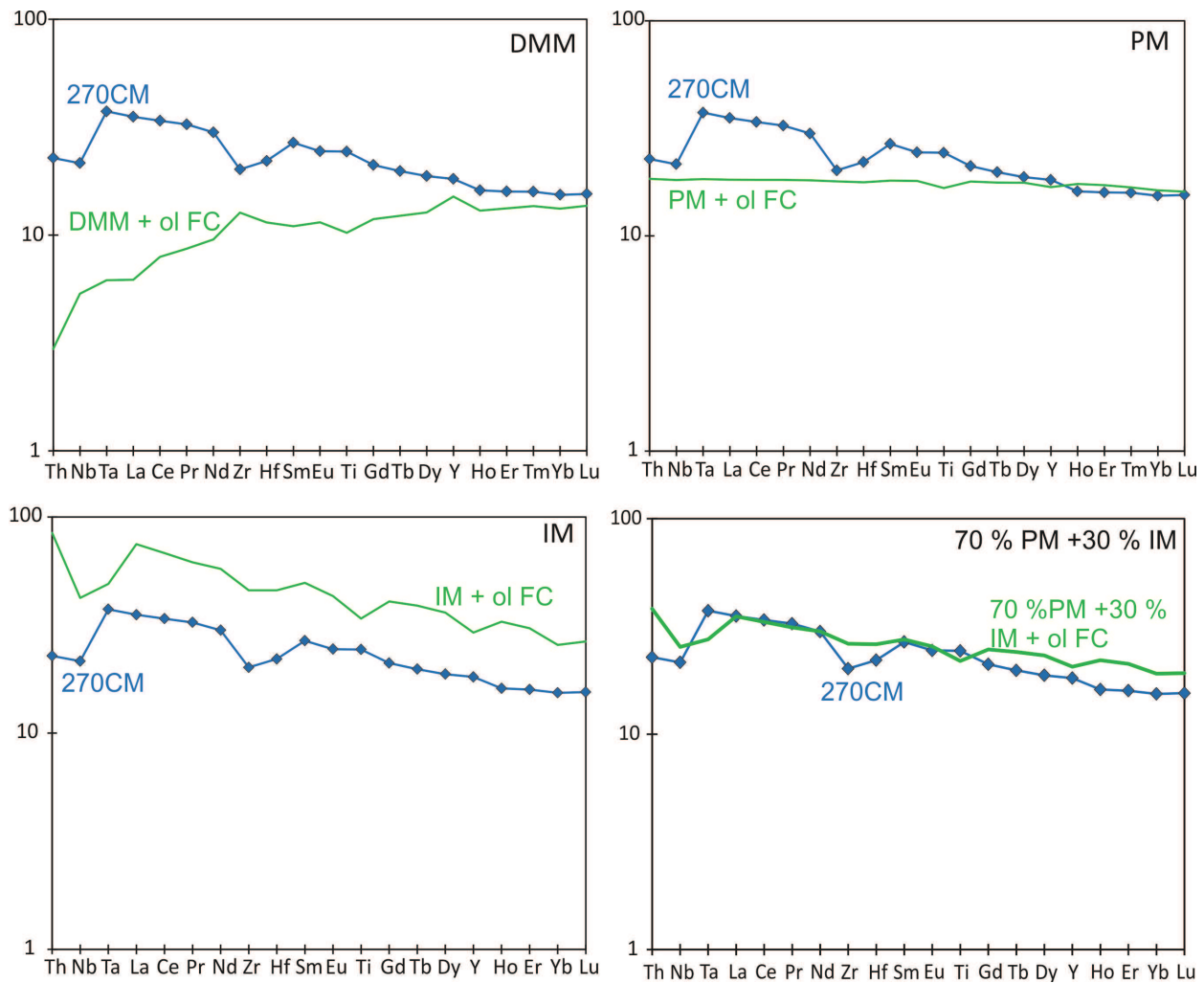
Figure 6.64 Chondrite normalised batch melting models with subsequent olivine fractionation in comparison the composition of sample 270CM. The degree of melting and fractionation have been determined by the PRIMELTS3 modelling discussed above (Table 6.2).

Sample 316CM, also from the Main Crescent Group, composition is best modelled by melting of the IM source, however this model does significantly overestimate all of the trace element abundances (Figure 6.65). In addition, even this model does not reproduce the positive Nb-Ta anomaly of the sample, most likely due to the continental nature of the Imnaha magmas, which have negative Na – Ta anomalies. As discussed, the IM is thought to represent the source composition of the Columbia River Flood Basalts and Snake River basalts, and so has likely been contaminated by continental material (Wolff et al., 2008) or alternatively may represent melting of subducted sediment (Carlson, 1984). In addition this model does not reproduce the exact trace element compositions of

the sample, nor does melting of any of the other mantle sources and melt mixtures.
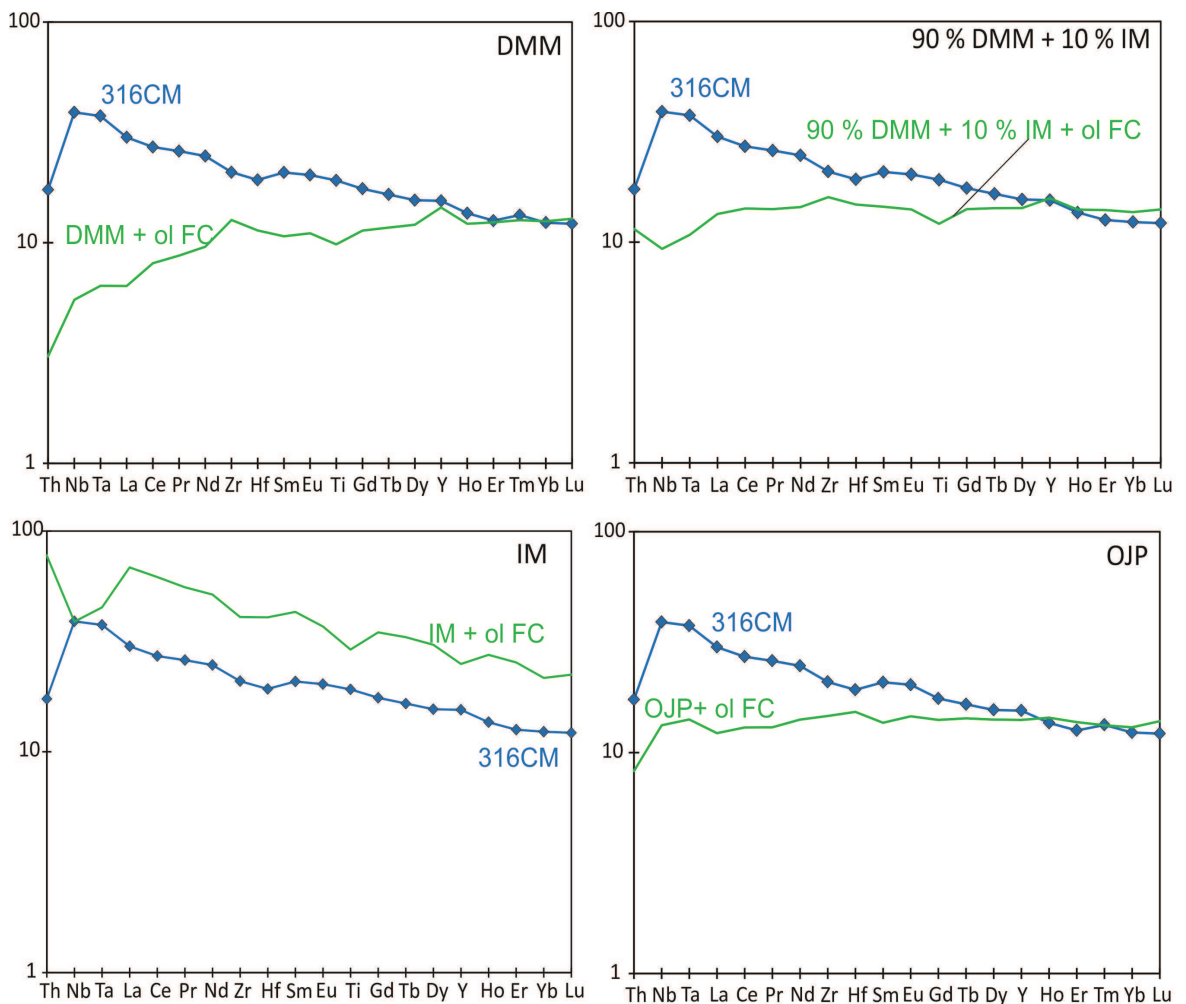
Figure 6.65 Chondrite normalised batch melting models with subsequent olivine fractionation in comparison the composition of sample 316CM. The degree of melting and fractionation have been determined by the PRIMELTS3 modelling discussed above (Table 6.2).

Figure 6.66 shows that sample 306CM, from the Depleted Crescent Group, is best modelled by melting and subsequent olivine fractionation of DMM. Other models which also predict the trace element compositions of the sample include 60 % DMM + 40 % EM2, and to a lesser extent 80 % DMM + 20 % HIMU. This illustrates that while different mixtures of depleted and enriched compositions can reproduce the trends observed in sample 306CM, a depleted component is needed to model the trace element signature of this sample. In

addition it is clear that an enriched mantle component is required to produce the
Th-Nb-Ta concentrations of sample 306CM.
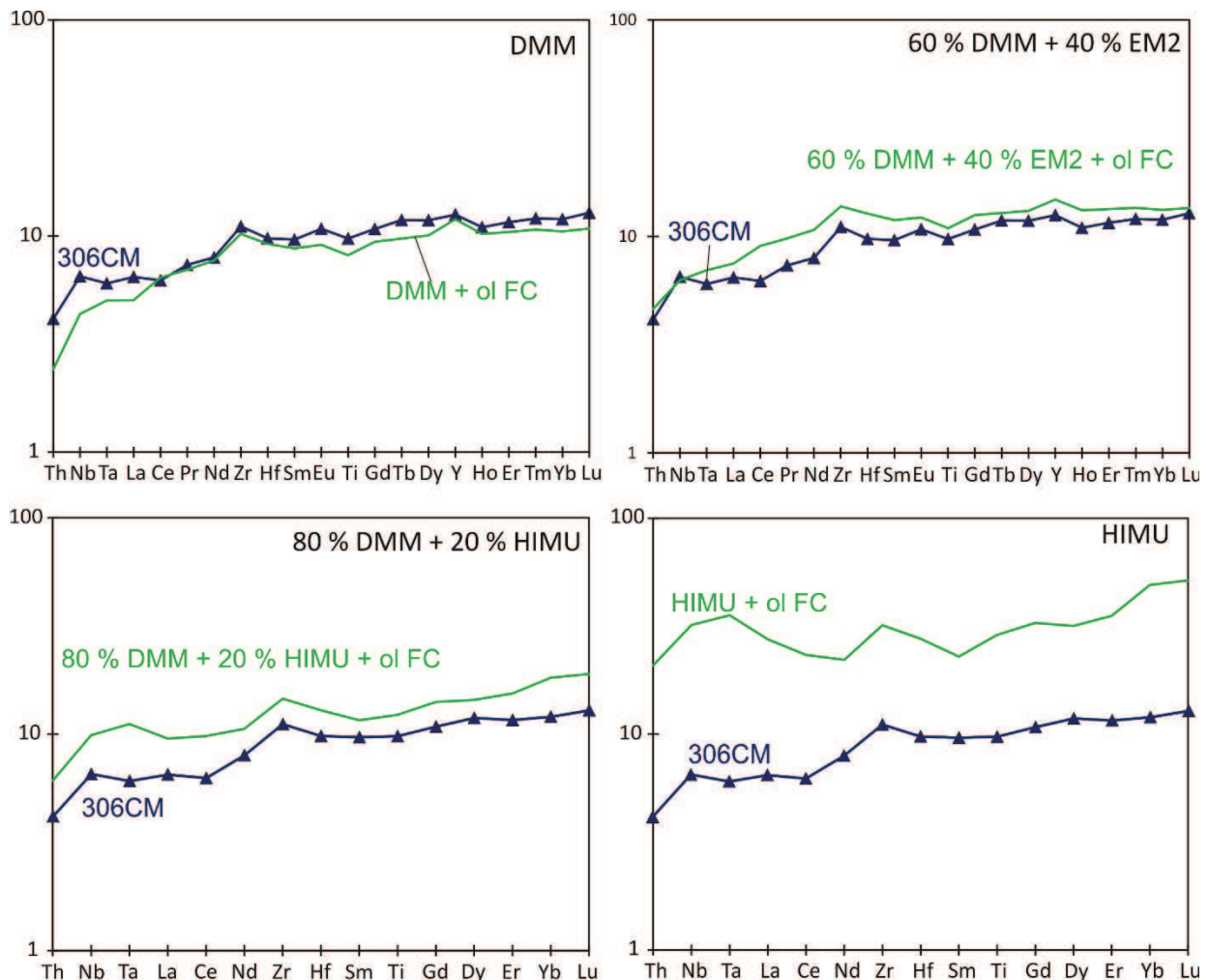
Figure 6.66 Chondrite normalised batch melting models with subsequent olivine fractionation in comparison the composition of sample 306CM. The degree of melting and fractionation have been determined by the PRIMELTS3 modelling discussed above (Table 6.2).

The composition of sample 205MET is best replicated by melting of spinel lherzolite source with a 90 % DMM and 10 % IM source with subsequent olivine fractionation. This model generally approximates the trace element composition of sample 205MET, with the exception of the sample's Th content (Figure 6.67).
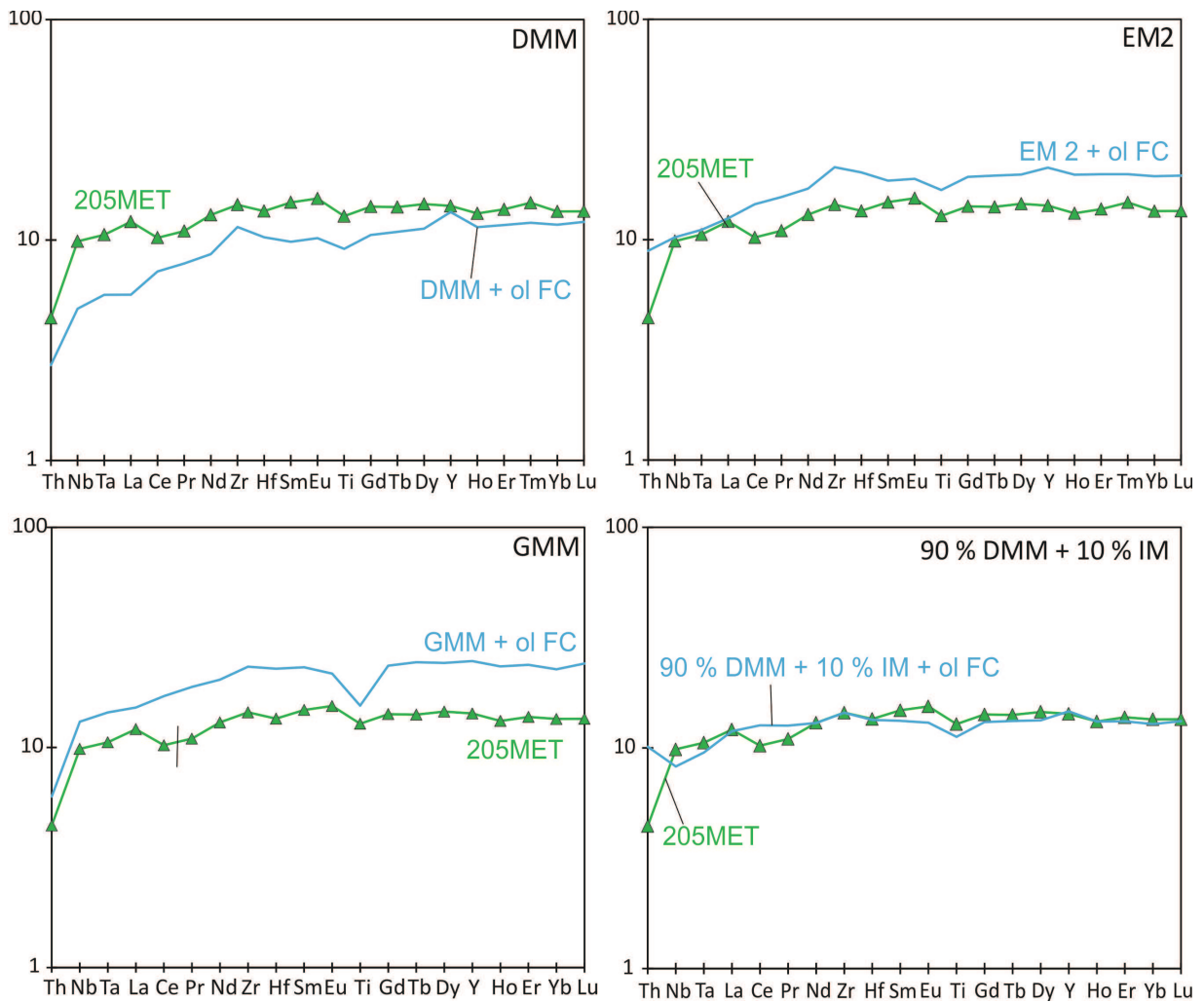
Figure 6.67 Chondrite normalised batch melting models with subsequent olivine fractionation in comparison the composition of sample 205MET. The degree of melting and fractionation have been determined by the PRIMELTS3 modelling discussed above (Table 6.2).

Melting of a mantle source with a 70 % PM and 30 % IM composition is the model which can best approximate the trace element abundances of sample 101SRV (Figure 6.68) However, this model cannot replicate the observed Nb-Ta anomaly. Conversely, melting of a mantle source with a HIMU type composition can reproduce the degree of the Nb-Ta anomaly, but cannot replicate the remainder of the incompatible trace elements of sample 101SRV (Figure 6.68).
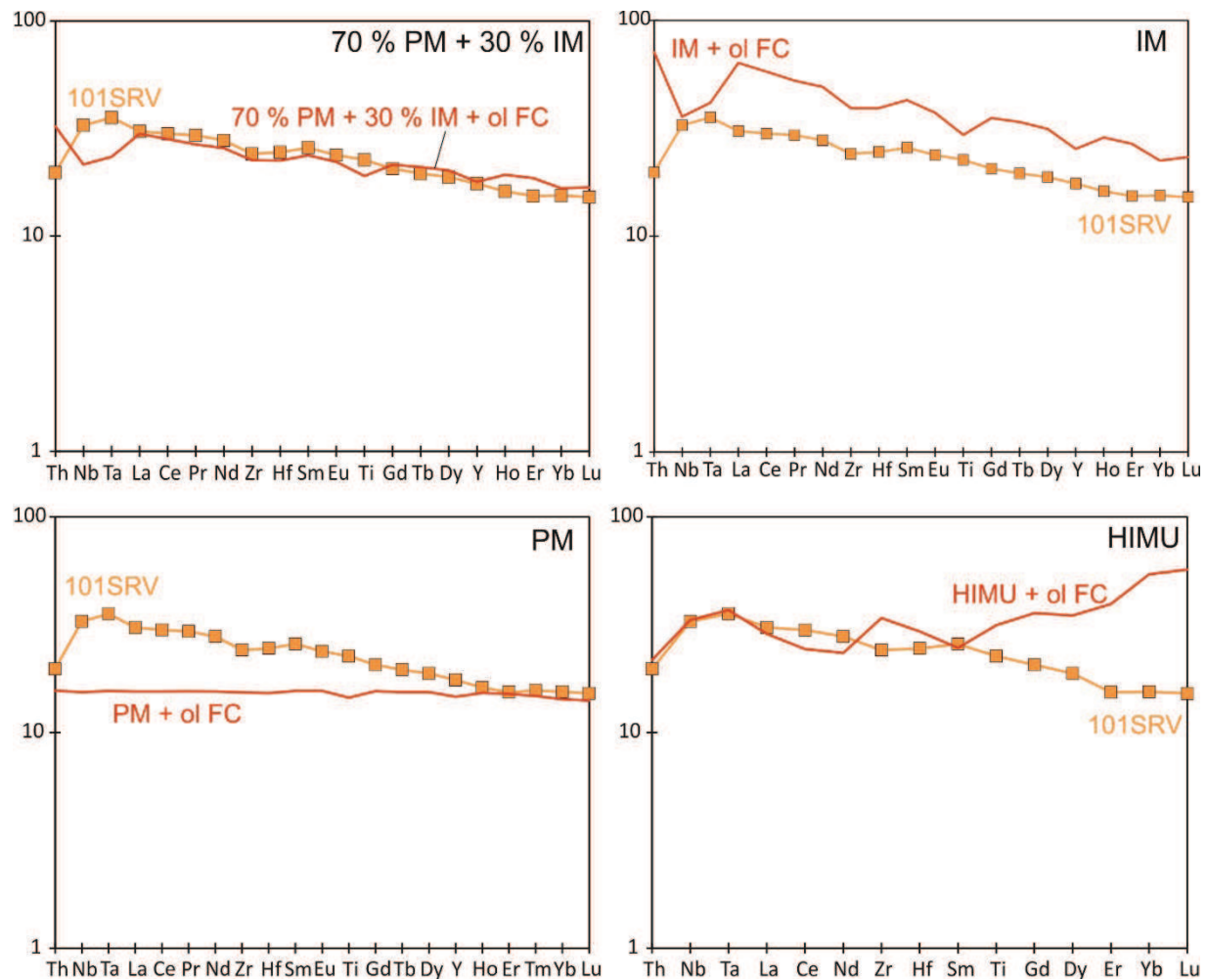
Figure 6.68 Chondrite normalised batch melting models with subsequent olivine fractionation in comparison the composition of sample 101SRV. The degree of melting and fractionation have been determined by the PRIMELTS3 modelling discussed above (Table 6.2).

Figure 6.69 illustrates that melting of none of the reservoirs or mixtures modelled can recreate the incompatible trace elements of sample CR014. However, melting of a PM mantle source can explain the trends observed in the less incompatible elements of sample CR014 (Figure 6.69). In addition melting of a source with comprising 70 % PM + 30 % IM can replicate the general trend and abundances of sample CR014, with the notable excpetion of Th.
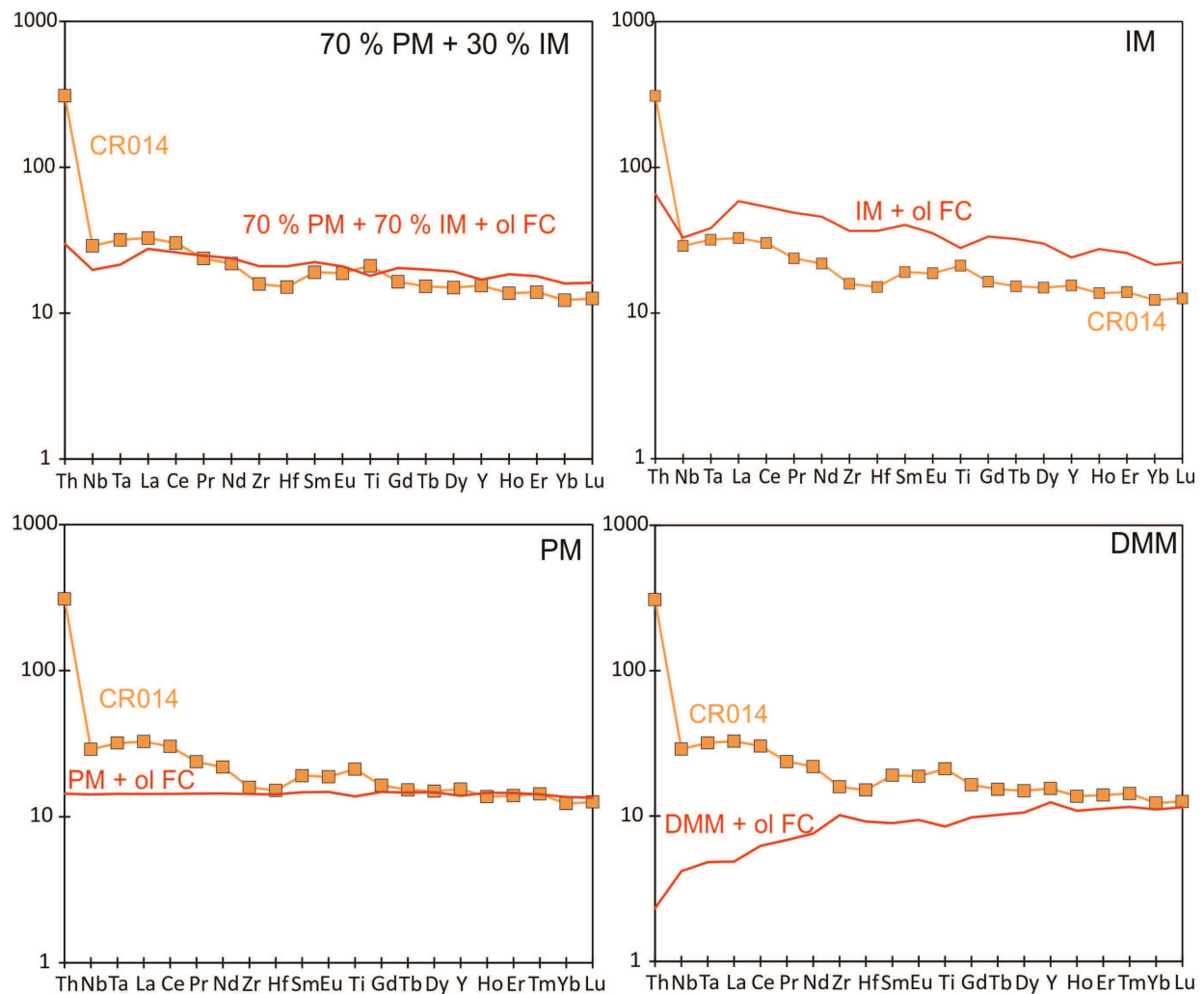
Figure 6.69 Chondrite normalised batch melting models with subsequent olivine fractionation in comparison the composition of sample CR014. The degree of melting and fractionation have been determined by the PRIMELTS3 modelling discussed above (Table 6.2).

Finally none of the models can model the trace element compositions of sample 99/2SRV (Figure 6.70). This appears to be due to its relatively depleted HREE pattern and enrichment of the most incompatible elements in this sample. With the exception of the IM melting models, sample 99/2SRV consistently has greater abundances of the most incompatible elements.
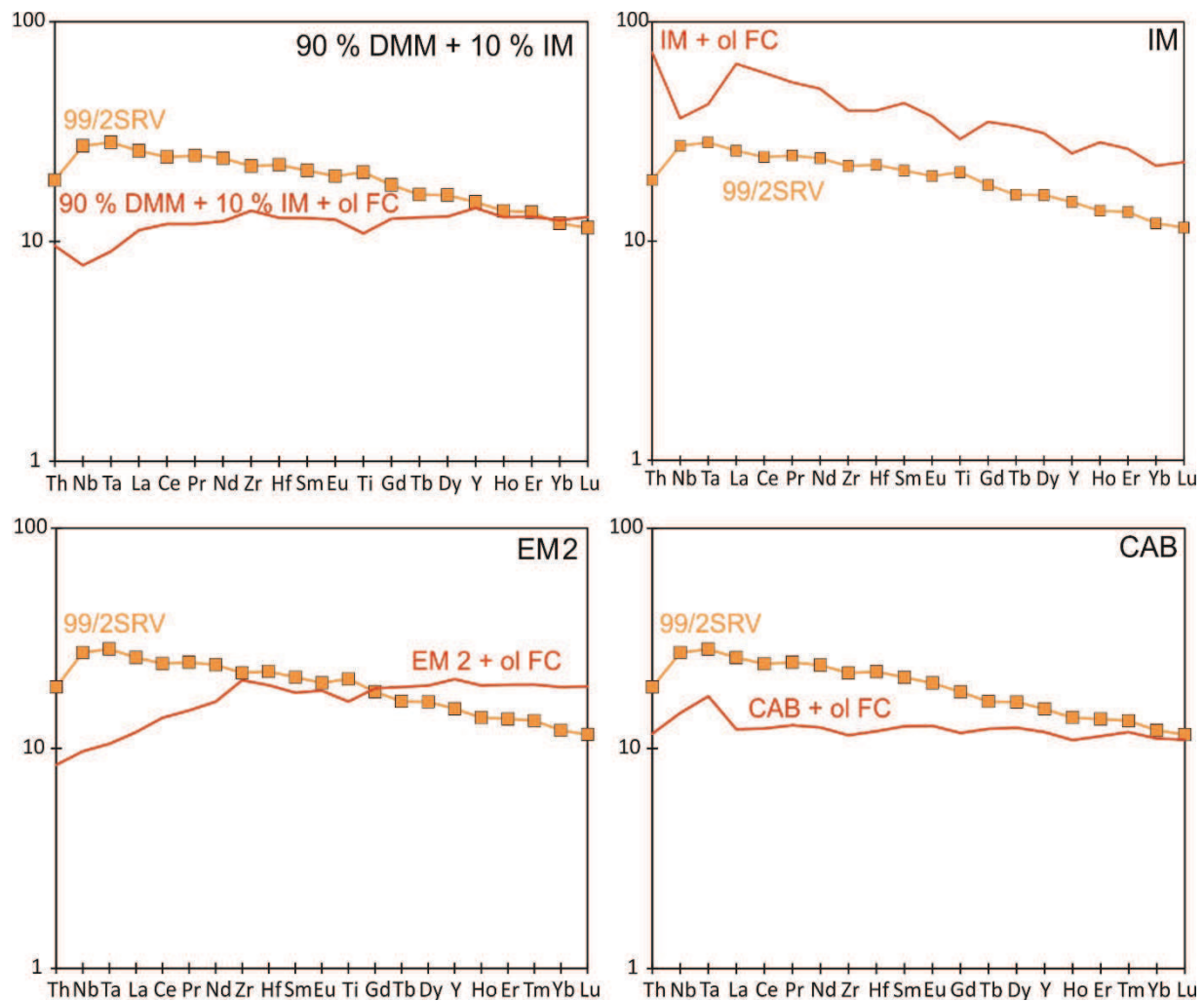
Figure 6.70 Chondrite normalised batch melting models of a spinel lherzolite source with subsequent olivine fractionation in comparison the composition of sample 99/2SRV. The degree of melting and fractionation have been determined by the PRIMELTS3 modelling discussed above (Table 6.2).

The results of the spinel lherzolite modelling discussed above, along with sample 99/2SRV's Gd/Yb $_{PM}$ ratio of 1.5, suggest that this sample may be derived from a deeper garnet bearing lherzolite source. PRIMELTS3 predicts that 26.6 % melting can produce the composition of sample 99/2SRV, which, using the source mineral abundances of Johnston et al., (1990) results in HREE enriched trends. However, when the proportion of garnet in the source is increased from 0.10 to 0.15 and that of olivine is reduced from 0.55 to 0.50, more depleted HREE abundances can be modelled. A starting model composition which utilises an increased abundance of garnet in the source than is proposed by Johnston et al.,

(1990) may indicate that previous melting of the source has taken place, which would also suggest a depleted mantle composition for the source. Using these proportions, the incompatible trace element patters shown in Figure 6.71 are produced. As highlighted in Figure 6.71 however, the melting model which can most closely model the composition of sample 99/2 SRV (with subsequent olivine fractionation) is the 70 % PM + 30 % IM mixed melting model, which is not consistent with a depleted mantle source.
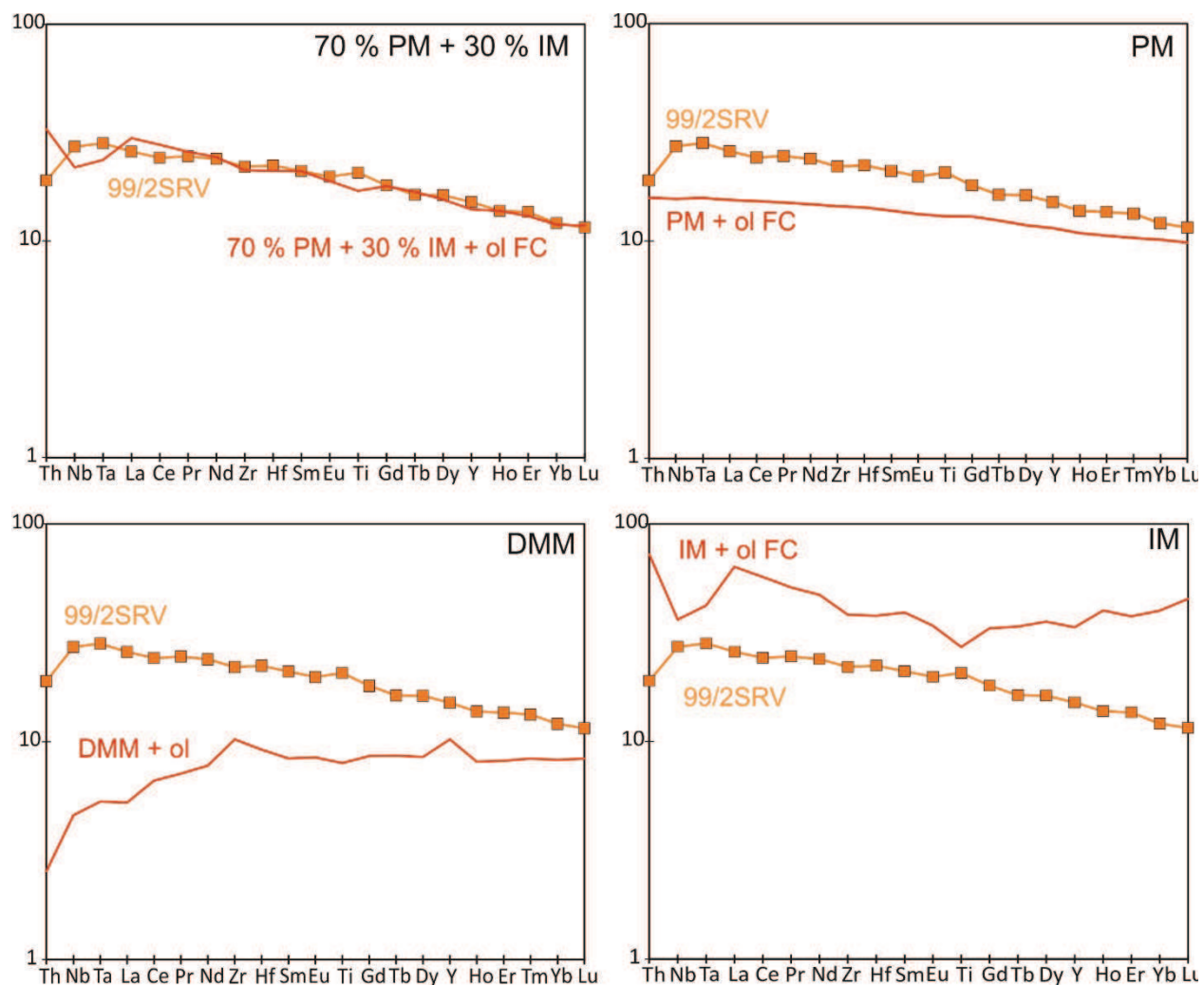
Figure 6.71 Chondrite normalised batch melting models of a garnet lherzolite source with subsequent olivine fractionation in comparison the composition of sample 99/2SRV. The degree of melting and fractionation have been determined by the PRIMELTS3 modelling discussed above (Table 6.2).

In general while the degree of melting that is suggested to have taken place is relatively similar, the modelled source compositions of the 7 samples discussed are variable in composition. Samples from both the Crescent and Siletz River Formation require some input of an Imnaha like composition in their source, while this is not apparent in the sample from the Metchosin Igneous Complex. A depleted mantle MORB is also required in some of the melting models to reproduce the compositions of several of the samples. Despite these similarities, few samples can be modelled by melting by the same reservoir or melt mixtures. However, it is clear that not all sample's incompatible trace element abundances can be produced by the melting and olivine fractionation percentages outlined by the PRIMELT3 modelling, which may indicate a flaw in the modelling.

The melting and mixing models often underestimate the LREE composition of the Siletz terrane basalts, which stems from the fact that (on average) ~27% partial melting is predicted to have occurred by PRIMELT3 programme. This results in, for almost all sources modelled, lower abundances of the LREE than recorded in the Siletz terrane samples. In order to reproduce the LREE abundances, generally much lower degrees of partial melting are required. This suggests that either the mantle source had much higher original abundances of LREE, or that the amount of melting is less than predicted by the PRIMELT3 modelling or that the samples which produce a solution have undergone fractionation of minerals other than olivine (discussed in section 6.1). In addition, the PRIMELT3 programme uses FeO, CaO and MgO concentrations in the samples to determine the predicted amount of partial melting and therefore, one potential source of error in the calculations may be the sub solidus remobilisation of these elements during alteration (discussed in Chapters 4 and 5).

6.2.4 Summary

The results of the PRIMELT3 and Lee et al., (2009) modelling indicate that on average a large degree of melting (~28 %) has taken place to produce the rocks of the Siletz terrane. Subsequent to this samples have undergone significant

amounts of fractionation, to reach their observed compositions. Melting has been modelled to have taken place at hotter than ambient temperatures (1400 – 1500 °C) at pressures of between 1.5 – 2.4 GPa. These results are generally consistent with the input of a mantle plume, which produces above average degrees of melting at above average temperatures for the mantle. Major element melt models in general concur with temperatures at around 1400 °C of a source with either a DMM or KR-4003 composition, which are associated with mid-oceanic ridges and oceanic plateaus respectively. Trace element mantle melting and mixing models indicate a heterogeneous source, with a variety of reservoirs and mixtures of melts from reservoirs being able to reproduce the composition of the samples investigated. The best fit modelled sources include, melting of DMM, 90 % DMM + 10 % IM, 70 % PM + 30 % IM, 60 % DMM + 40 % EM2 and PM compositions. Although some samples cannot be reproduced by melting of any of the mantle compositions investigated, some issues with the modelling may arise from its initial emphasis on major elements along with the fact that all of the samples of the Siletz terrane appear to have undergone fractionation of minerals other than olivine. Despite this 7 samples are consistent across both modelling platforms, indicating some consistency.

6.3 Nature of the Mantle Source

6.3.1 Introduction

As discussed in both section 6.1 and section 6.2, the Siletz terrane appears to have been derived from a relatively heterogeneous mantle, which appears to consist of both depleted and more enriched mantle reservoirs. The results of the PRIMELT3 and Lee et al., (2009) modelling also indicate that the mantle source region was hotter than that of ambient mantle, and that the primary magmas of the terrane were derived through high degrees of melting (on average around 28 %), indicating the presence of an additional heat source, which may represent a mantle plume (Fitton and Godard, 2004; Herzberg et al., 2007; Herzberg and Gazel, 2009). The following section will use trace elements and, radiogenic isotope

ratios, to characterise the mantle reservoirs in the source of the Siletz terrane (also discussed in Phillips et al., 2017 in Appendix E8). Comparisons will also be made with other well-characterised magmatic.

6.3.2 Trace Element Considerations

The results discussed in Chapter 5 highlight, through the use of incompatible trace element ratio diagrams, that the composition of groups from the terrane range from N-MORB to OIB, i.e., along a MORB – OIB array, with samples clustering in areas of the diagrams which correspond to E-MORB and plume ridge interaction (see Figures 5.19; 5.23; 5.28; 5.32; 5.35). The majority of groups from the Siletz River Formation (in both northern and southern Oregon) and Crescent Formation (in both northern and southern Washington), plot in the centre of the MORB-OIB array (at ~ E-MORB) and in the oceanic plateau basalts or plume ridge interaction region of the diagrams (e.g., Figure 6.72 and Figure 6.73, also see Figures 5.19; 5.23; 5.28; 5.32). Included in these discrimination diagrams is the Nb/Y – Zr/Y diagram, developed by Fitton et al., (1997), which can be used to distinguish between shallow upper mantle MORB like rocks and those derived from a mantle plume source. The Nb/Y – Zr/Y diagram has been successfully applied to many Phanerozoic igneous provinces, with rocks originating from plume derived melts plotting between the tramlines (e.g., Fitton et al., 1997; Greene et al., 2009ab; Kerr et al., 2009). As observed in the Nb/Y – Zr/Y diagrams, most of the samples from the Siletz River and Crescent Formations plot between the tramlines, showing little overlap with the Pacific and Gorda MORB field, which supports the involvement of a mantle plume in the source of these rocks (e.g., Figure 6.72 and Figure 6.73, also see Figures 5.19; 5.23; 5.28; 5.32) (Fitton et al., 1997).
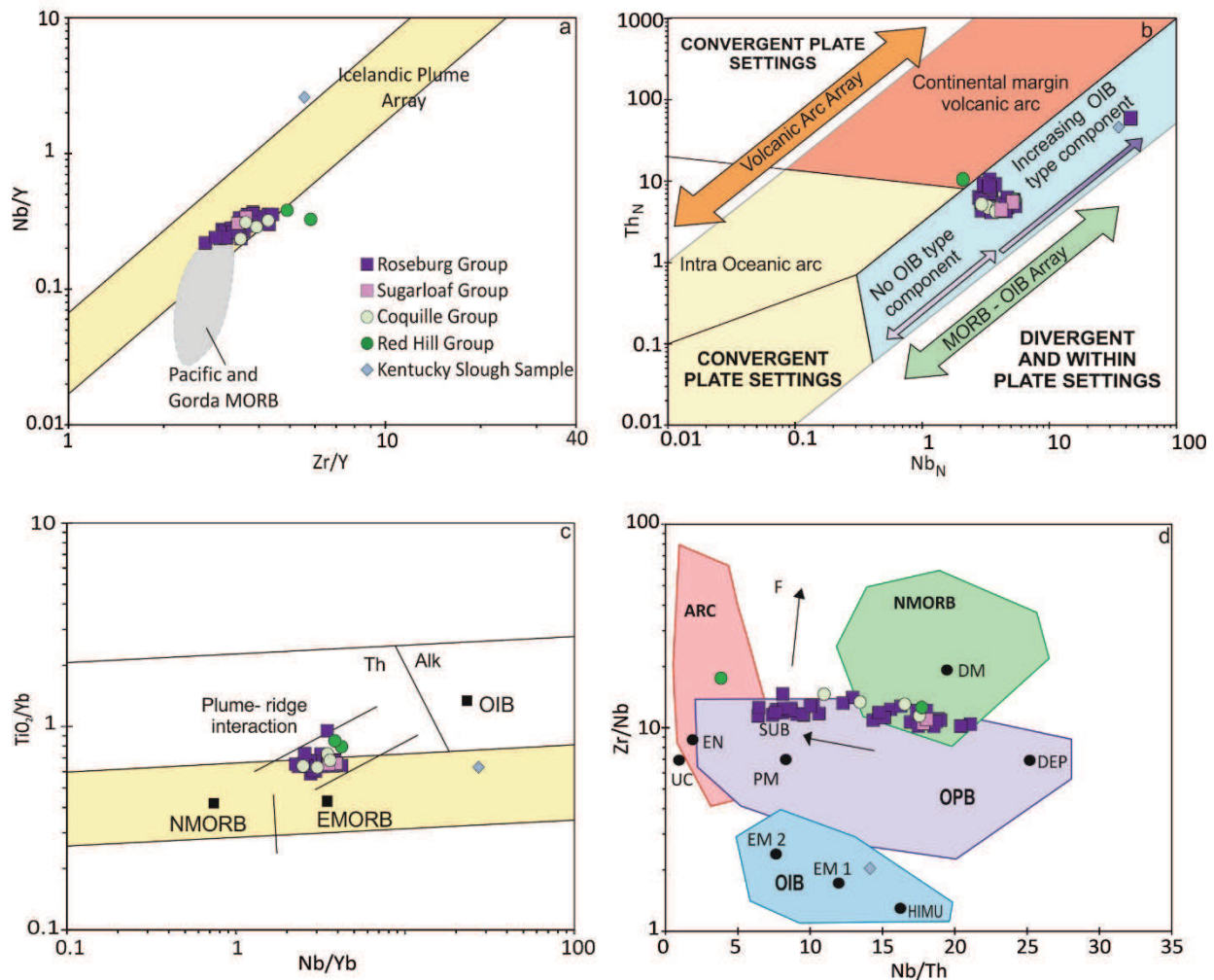
Figure 6.72 The Rosbeurg area samples have been plotted on the a) Fitton et al., (1997) Icelandic plume array diagram; b) Ophiolitic basalt tectonic discrimination diagram (Saccani, 2014); c) Proxy for deep melting diagram (Pearce, 2008) and; d) the Zr/Nb vs. Nb/Th discrimination diagram (Condie, 2005). Abbreviations: UC = upper continental crust, PM = Primitive Mantle, DM = shallow depleted mantle, HIMU = high mu (U/Pb) source, EM1 and EM2 = enriched mantle sources, ARC = arc related basalts, NMORB = normal mid-ocean ridge basalt, OPB = oceanic plateau basalt, OIB = oceanic island basalt, DEP = deep depleted mantle, EN = enriched component, F = effects of batch melting and SUB = subduction effect.

The exception to this are the Depleted Crescent Group, which plots closer to the N-MORB compositional fields. Also distinct to the majority of samples are the Alkali and Ilwaco Groups and the Kentucky Slough sample, which consistently plot closer to the OIB field (e.g., Figure 6.72 and Figure 673, also see Figures 5.19; 5.23; 5.28; 5.32). The samples of the Metchosin Igneous Complex (Figure 5.35) frequently plot in the N-MORB compositional region of the discrimination diagrams in figure 5.35. Therefore, while in general the high field strength

element ratios suggest that the majority of groups from the Siletz terrane are derived from a source which has been influenced by a mantle plume (Fitton et al., 1997; Condie, 2003; 2005), there are a subset of groups (from the north of the terrane) which do not display such a strong plume signature.
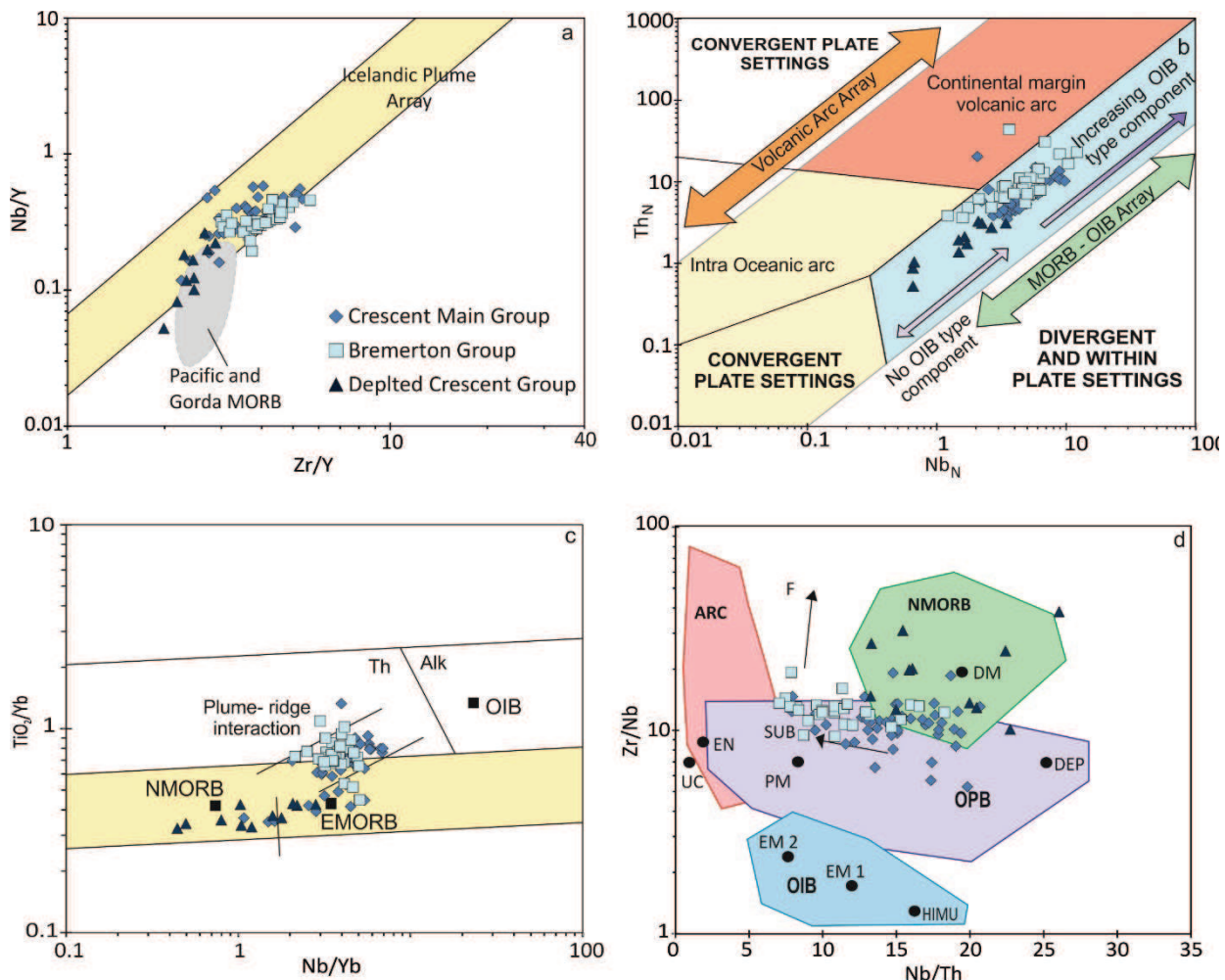
Figure 6.73 The Crescent North samples have been plotted on the a) Fitton et al., (1997) Icelandic plume array diagram; b) Ophiolitic basalt tectonic discrimination diagram (Saccani, 2014); c) Proxy for deep melting diagram (Pearce, 2008) and; d) the Zr/Nb vs. Nb/Th discrimination diagram (Condie, 2005). See figure 6.dd for abreviations.

Figure 6.74, which also utilises incompatible trace element ratios, that are largely not modified by petrogenetic processes such as partial melting (with the exception of Dy/Yb, which can indicate depth of melting) or fractional crystallisation, further illustrates the variety of mantle source compositions in the Siletz rocks. While the data falls into a spectrum of compositions, three general

groups are observed in figure 6.74a; 1) a low Nb/Zr low Ce/Yb group of mostly Metchosin Igneous Complex and Depleted Crescent Group samples, 2) a cluster at more moderate ratios which contains the majority of samples analysed and 3) a high Nb/Zr high Ce/Yb scattered group of predominantly Alkali Group samples. These groups are less apparent in figure 6.74b, with the data as a whole displaying a relatively narrow range of Nb/La ratios. However, variations in the Dy/Yb $_{(PM)}$ abundances, do reflect the groups identified in figure 6.74a to a greater extent. In addition the three groups represented here, are consistent with those in the discrimination diagrams discussed above and in Chapter 5 (Figures 5.19; 5.23; 5.28; 5.32; 5.35), indicating that the rocks of the terrane are derived from a mantle source which has experienced differing degrees of input from a mantle plume, with samples ranging from compositions slightly more enriched than N-MORB, to E-MORB and OIB. However, the Nb/La ratio variation of 0.45 to 2.01 are indicative of the presence of recycled oceanic crust in the source that has been derived from a deep-rooted mantle plume (Fitton et al., 1997).
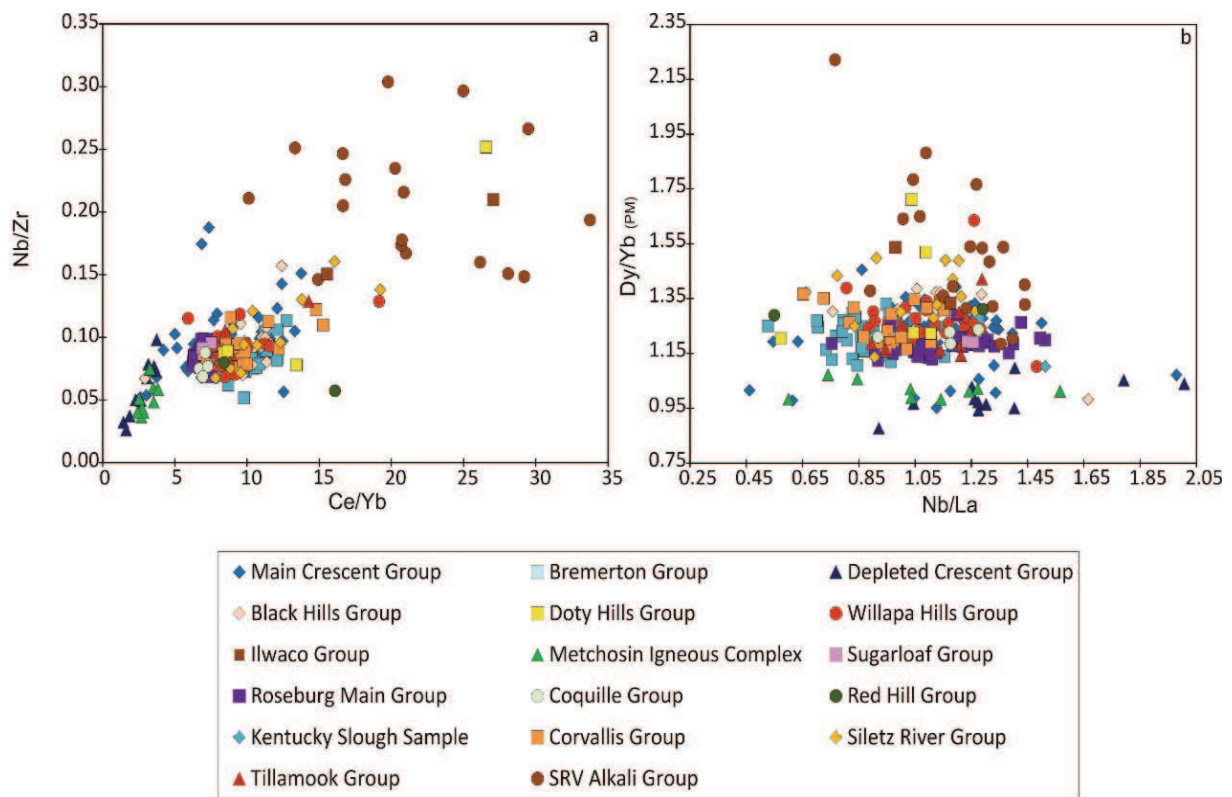
Figure 6.74 Ratio ratio diagrams for the rocks of the Siletz terrane, displaying the heterogeneity of the mantle source. a) Ce/Yb vs Nb/Zr and b) Nb/La vs Dy/Yb (PM).

6.3.3 Radiogenic Isotopes

Although the samples analysed in this study span a range of compositions from basalts to more evolved rocks there is no correlation between the degree of fractionation undergone by each sample and the radiogenic isotope ratios. This indicates that the samples are unlikely to have been contaminated with lithospheric material during fractionation and are therefore likely to record the isotopic signature of the mantle source. Although, no evidence for crustal contamination has been observed, some LREE enrichments are noted, which are most likely related to enriched components in the source or subsequent differentiation. In radiogenic isotope ratio diagrams (Figure 6.75), the Siletz terrane data frequently show similarity with the trends observed in the Karmutsen flood basalts, the remnants of an Triassic accreted oceanic plateau in Vancouver island (Greene et al., 2009b), and so comparable in geographic and tectonic setting to the Siletz Terrane.
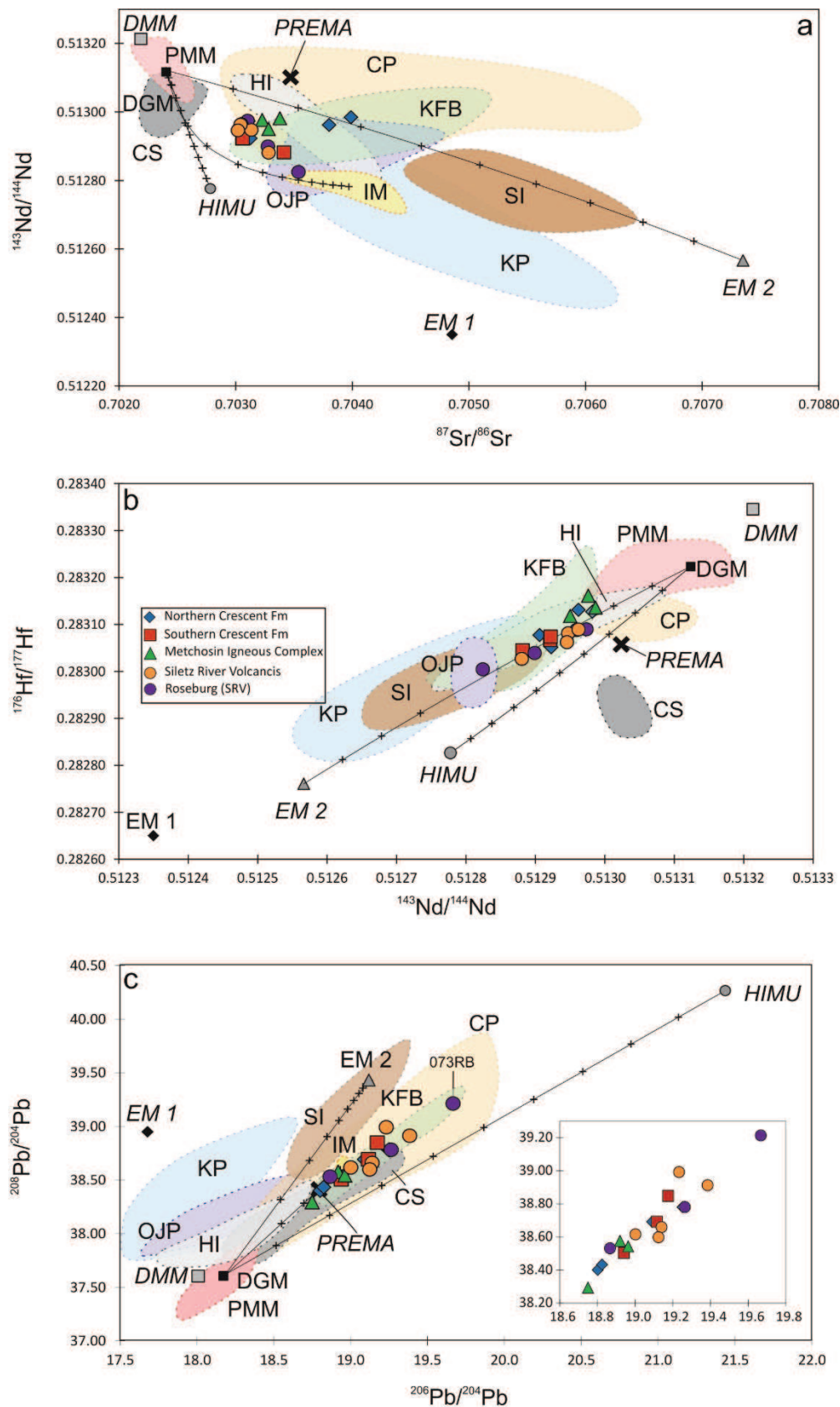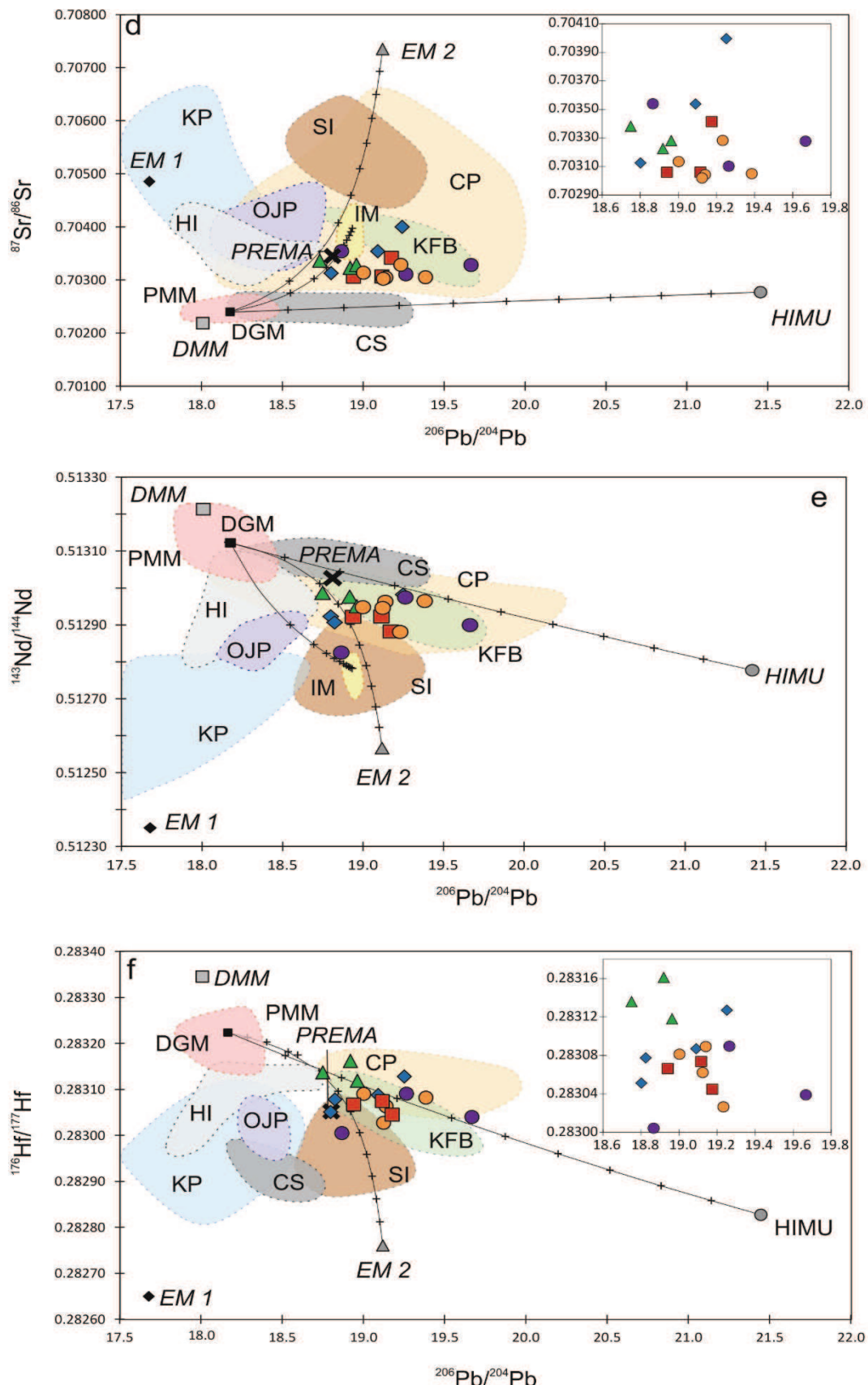
Figure 6.75 Initial isotope ratios of the Siletz terrane samples. Also plotted are age-corrected (53 Ma) isotope ratios for mantle components (Supplementary Material 7), PMM - Pacific MORB mantle (Chauvel and Blichert-Toft, 2001), DGM - Depleted Gorda MORB mantle (Davis et al., 2008; Salters et al., 2011), IM - Imnaha mantle component (source of the primary Columbia River Flood basalts and thought to represent the Yellowstone hotspot; (Wolff et al., 2008), CS - Cobb seamount chain (a series of seamounts located near the East Pacific Rise; (Chadwick et al., 2014), and KFB - Karmutsen flood basalts of the Wrangellia terrane, Vancouver Island (Greene et al., 2009b). Also shown are compositional fields of the Ontong Java Plateau (OJP) (Mahoney et al., 1993a; 1993b; Tejada et al., 2002; Tejada et al., 2004), Caribbean Plateau (CP) (Kerr et al., 1997; Hauff et al., 2000; Kerr et al., 2002b; Thompson et al., 2004; Hastie et al., 2008), Kerguelen Plateau (KP) (Weis et al., 2002; Weis and Frey, 2002), the Hawaiian Islands (HI) (Tanaka et al., 2002; Garcia et al., 2010; Weis et al., 2011 and the Samoan Islands (SI) (Workman et al., 2004; Salters et al., 2011). Error bars for the Siletz terrane data are smaller than the symbols. Binary mixing curves between DGM and the Imnaha mantle component, EM2 and HIMU mantle components are also

Binary mixing curves between MORB-source mantle and the Imnaha mantle component (the source of the primary Columbia River Flood basalts and thought to represent the Yellowstone hotspot [Wolff et al., 2008]), EM2, and HIMU mantle components are shown in Figure 6.75, with 10% increments marked. Trace element abundances used for the mantle components are discussed in Appendix E7. Depleted Gorda MORB mantle (DGM) (age-corrected to 53 Ma) (Davis et al., 2008; Salters et al., 2011) was used as the end-member to represent a possible depleted MORB mantle component.

The positive ε_{Hf} and ε_{Nd} values of all the Siletz samples reflect long-term incompatible element depletion of the source. In Pb-Pb, Pb-Nd and Pb-Hf isotopic space the Siletz data lies mostly between the DGM – HIMU and DGM – EM2 mixing curves (Figure 6.75), while a more distinct EM2 and-member is required in the other diagrams, especially for three samples, B019, 424CM and 095RB (and to a lesser extent 202MET). The Imnaha component also lies adjacent to the DGM-EM2 mixing curve, which indicates that the 3 samples with a significant EM2 component share similar isotopic signatures to the Columbia River Flood Basalts and the Snake River – Yellowstone hotspot (Wolff et al., 2008). Carlson (1984) also recognised that the Imnaha component (described as C2) was present in the source of the CRFB, but proposed that it represented subducted sediment rather than a mantle plume component. However, the trace element data rule out the possibility of subducted sediment in the analysed samples as there is no 'arc

signature' present in the mantle-normalised diagrams (i.e., no marked negative Nb-Ta anomaly or Th spike) (Chapter 5). Therefore, except for the 3 samples discussed above, the Siletz isotope data are generally quite different from that of the Imnaha component and require different source compositions or at least variations to the source composition than that of the Columbia River Flood Basalts and Snake River - Yellowstone hotspot track.

The significant EM2 signature observed in the majority of the data, indicates the presence of a deep mantle derived component (Weaver, 1991; Workman et al., 2004); this EM2 component however, is not as significant as in other Pacific OIBs, such as the Samoan Islands (Figure 6.75). The most enriched samples display higher Gd/Yb $_{(PM)}$ values (above 1.4), indicating that these samples have undergone smaller amounts of melting of a deeper source relative to the more depleted samples from largely the Metchosin Igneous Complex and Northern Crescent Formation (Figure 6.76). The distinctive isotopic ratios of some of the samples with higher Gd/Yb $_{PM}$ ratios may indicate that the lower melt fractions are preferentially sampling isotopically distinct enriched pods or plums (Cousens, 1996) or streaks within a mantle plume (cf. Kerr et al., 1995).
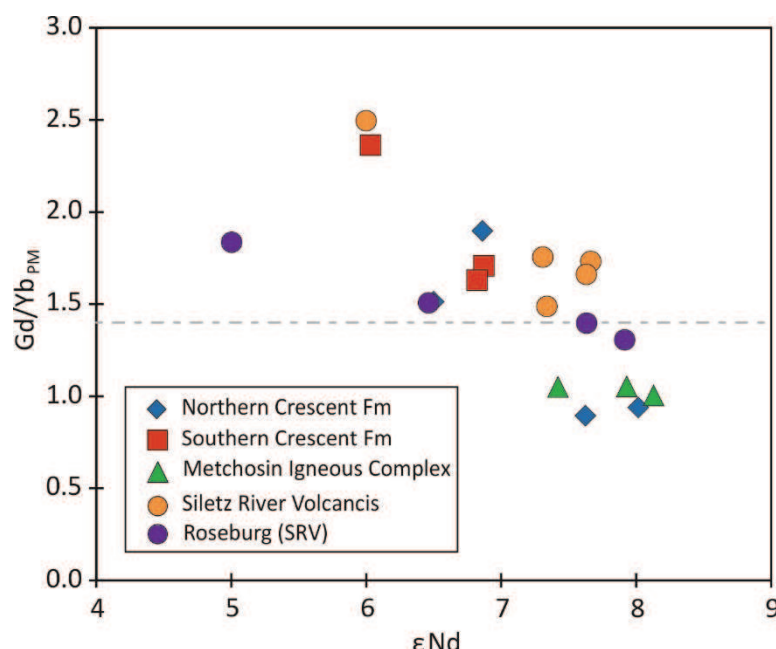
Figure 6.76 Primitive mantle normalised Gd/Yb with ε_{Nd} value for the Siletz terrane samples. The dashed grey line represents a Gd/Yb $_{PM}$ ratio of 1.4. Samples with less radiogenic ε_{Nd} contents display higher Gd/Yb $_{PM}$ ratios.

As noted above, the data also extend partially towards the HIMU component in Pb-Pb, Pb-Nd and Pb-Hf, isotopic space (Figure 6.75), indicating

that this component may be present in the source of the Siletz basalts (especially in sample 073RB and to a lesser extent sample TK009). The involvement of a HIMU like signature is consistent with observations in other NE Pacific locations, such as the Cobb Seamounts (Chadwick et al., 2014), Explorer MORB (Cousens et al., in review), the Triassic Karmutsen flood basalt province (Greene et al., 2009a; 2009b) and the Garibaldi belt (Mullen and Weis, 2013). The samples which plot closest to HIMU have a more alkaline signature (highlighted in Figure 6.75c) which suggests a relationship between the HIMU component and less extensive (deeper) melting, in particular sample TK009, which has a Gd/Yb $_{PM}$ of 2.5, as is also observed at the Cobb Seamounts (Chadwick et al., 2014).

The PREMA component (Figure 6.75) represents a common deep mantle component [or FOZO or C (Hanan and Graham, 1996; Stracke, 2012)]. It is also thought to be the Kea component in Hawaii and was interpreted to represent the average deep Pacific mantle composition (Nobre Silva et al., 2013). Some of the samples analysed from the Crescent Formation and Metchosin Igneous Complex lie adjacent to, or at the PREMA component composition in the Pb-Pb, Pb-Hf and Pb-Sr isotopic diagrams (Figure 6.75c, d, e, f). However, while Siletz samples do appear to trend towards PREMA in some isotope diagrams (Pb-Pb), the majority of the Siletz terrane data, for most isotopic ratios, do not overlap with this component (Figure 6.75). Although it has been debated whether this signature actually exists as a discrete physical component, PREMA does appear to be a relatively common source composition for other well-characterized Pacific oceanic lavas, including the Hawaiian basalts (Figure 6.75) (e.g., Nobre Silva et al., 2013), as well as those related to the Iceland and Yellowstone plumes (Hanan and Graham, 1996). While the Siletz terrane isotopic data demonstrates some similarity to the trends observed in, for example, the Hawaiian Islands, most notably in Hf – Nd isotopic space, the Siletz terrane samples have distinctly more radiogenic Pb isotopic ratios together with lower $^{87}Sr/^{86}Sr$ (Figure 6.75).

Multiple components are therefore most likely required to explain the trends observed in the isotopic data (Figure 6.75) i.e., a depleted component isotopically similar to DGM, along with an enriched signature that straddles

between EM2 and HIMU. The enriched signature, although prevalent throughout the terrane, is less apparent in the samples from the north-east, i.e., the Metchosin Igneous Complex and some Crescent Formation samples (Figure 6.75).

6.3.4 Pyroxenite Source?

The mantle melting and mantle source composition models utilised in this study, along with many in other investigations, are based on the assumption that the primary melt has formed in a source which is in equilibrium with olivine, as the upper mantle consists largely of peridotite which has >50 % mineral olivine (McDonough and Sun, 1995; Sobolev, 2005). However, some oceanic basalts, such as the Hawaiian basalts have been suggested to not have been derived from a source in equilibrium with olivine, due to enrichments in their relatively incompatible elements (e.g Ba, Nb, Ti and LREE) and SiO_2 (even at high MgO concentrations) and depletions in elements compatible with garnet (HREE) (Sobolev, 2005). Therefore, it has been suggested that some OIBs and other plume derived oceanic basalts are melted from a source which contains a pyroxenite component, for example as a plume containing eclogite bodies entrained within it (Sobolev, 2005). This source composition therefore, may provide a viable alternative explanation for why the melting models at high degrees of melting cannot always reproduce the enriched LREE/ incompatible element signatures recorded within the Siletz terrane samples, and so should also be considered. However, the trace element composition of pyroxenite in the mantle is likely extremely variable, being dependant on both the composition of the subducted oceanic crust and any associated sediments (Petermann and Hirshmann, 2003) thus making successful modelling of the source regions composition, difficult.

A reaction has been proposed to occur between entrained eclogite bodies, which melt at greater depths than the surrounding peridotite, and the peridotite would produce pyroxenite in a solid state (Korzhiski, 1970). This pyroxenite along with the peridotite are then thought to proceed to melt, resulting in a mixed source region (Sobolev, 2005; 2007). The eclogite in question is believed to be

derived from recycled oceanic crust (Hofmann and White, 1982; Sobolev, 2005; 2007). The resulting melts of the pyroxenite peridotite source are more enriched in Ni and SiO_2 and depleted in Mn, Ca and Mg than those melts which are derived from a solely peridotite source (Sobolev, 2007).

Hybrid melts have been suggested to occur elsewhere in the NE Pacific Ocean region, such as in the basalts of the Explorer Mid Oceanic Ridge (Petermann and Hirshmann, 2003; Cousins et al., in review). Tejeda et al. (2002) have also proposed that a pyroxenite/ eclogite bearing source can also explain the geochemical compositional trends observed in the Ontong Java Plateau. Cousins et al (in review) have suggested that a mixture of 2% pyroxenite and 98% peridotite yields $^{87}Sr/^{86}Sr$ values of 0.725 and $^{206}Pb/^{204}Pb$ of 18.5, while a 5 % pyroxenite and 95 % peridotite mixture results in $^{87}Sr/^{86}Sr$ ratios of 0.7029 and $^{206}Pb/^{204}Pb$ values of 19.1 (Figure 6.77). The peridotite composition of $^{87}Sr/^{86}Sr$ = 0.7022, $^{206}Pb/^{204}Pb$ = 18, Sr = 10 ppm, Pb = 0.018 ppm was derived from Cousins et al. (1995) and the pyroxenite composition of $^{87}Sr/^{86}Sr$ = 0.7050, $^{206}Pb/^{204}Pb$ =22, Sr = 66 ppm, Pb = 0.013 ppm from Petermann and Hirshmann (2003). When this mixing model is compared with the Siletz terrane data it appears to suggest that the isotopic composition of some of the Siletz terrane samples, in particular those from the Siletz River Volcanics Formation (the Siletz River Volcanics and Roseburg samples) can be approximated by mixing between the pyroxenite and peridotite mantle components (where here peridotite and DMM are indistinguishable) (Figure 6.77). The majority of samples however, trend towards the EM and PREMA mantle components. Therefore, while figure 6.77 demonstrates that, in terms of their isotopic compositions at least, some samples can be modelled by a peridotite pyroxenite hybrid source, this is not consistent for all samples in the terrane, nor in the groups that these individual samples are derived from.
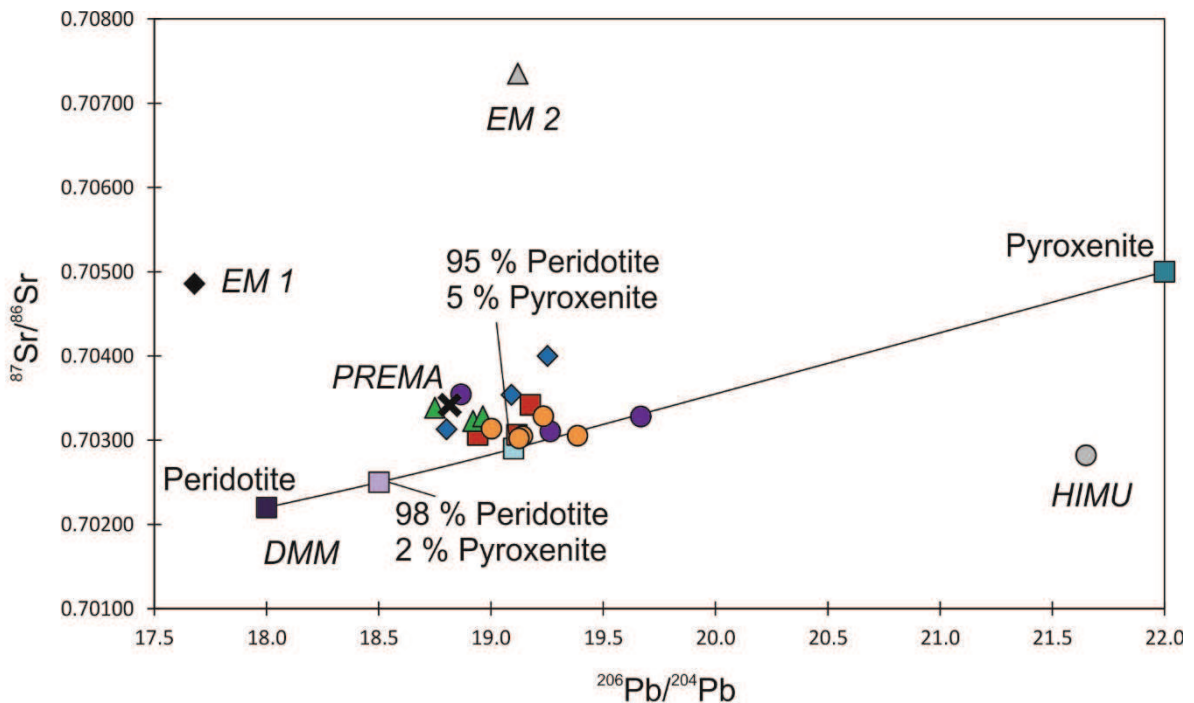
Figure 6.77 Initial Sr and Pb isotope ratios of the Siletz terrane samples along with peridotite – pyroxenite mixing model. See text for detailed sources.

6.3.5 Summary

The mafic rocks of the Siletz terrane have been derived from a heterogeneous and partially enriched mantle source with an above ambient temperature. As discussed in the previous section (section 6.2) the estimated initial mantle potential temperatures of 1400 - 1500 °C and the amount of partial melting undergone (~ 25 – 33 %), is similar to other mantle plume derived provinces such as the Ontong Java Plateau and the Caribbean plateau (Fitton and Godard, 2004; Herzberg and Gazel, 2009). The source composition appears to comprise a somewhat depleted signature along with EM2- and HIMU-like enrichments. The enriched components may therefore represent melting of a heterogeneous mantle plume, possibly the Yellowstone Hotspot, which likely interacted with a mid-oceanic ridge, the Kula – Farallon (or Farallon – Resurrection) ridge. The results of the isotope comparisons and mixing models appear to generally be consistent with their trace element compositions, whereby the plume like signature is prevalent throughout the terrane, but is less apparent in the rocks derived from the north-east. However it is worth noting that the isotopic

variations observed in the reservoirs from which OIBs and LIPs are derived either indicate that there are either distinct enriched components which are then mixed in unique ways to produce OIBs and oceanic plateaus or that each one is derived from a source with an individual composition (Stracke et al., 2003). This therefore highlights the problem encountered when attempting to model a source composition using the described components.

6.4 Tectonic Setting

There have been many tectonic models proposed to explain the origin of the Siletz terrane and its resulting geochemical and physical characteristics. One model which may explain the characteristics of the Siletz terrane is its formation in a marginal basin setting (Wells et al., 1984; Brandon, 2014). Suggested rifted margin models involve the oblique rifting of the continental margin between the Kula and North American plates, with additional input from a coeval Yellowstone hotspot in some models (Wells et al., 1984; Clowes et al., 1987; Snavely 1987; Babcock et al., 1992; Brandon, 2014). The marginal basin rifting model is consistent with the geometry of the terrane, which lies parallel to the continental margin along with the observed sedimentary interbeds, including the continentally derived Blue Mountain Formation, situated at the base of the Crescent Formation. However, this model does not adequately explain the proposed configuration of the plates at the time of eruption (Wells et al., 2014), the enriched isotopic signatures discussed in section 6.3.3, nor the lack of arc signatures in the samples of the Siletz terrane (Chapter 5). In addition, most other tectonic models (discussed in detail in Chapter 2) along with the paleontological evidence in Chapter 5, indicate that the Siletz terrane formed adjacent to the coast, and this also explains the deposition of continentally derived sediments.

Another suggested model of formation for the Siletz terrane proposes subduction initiation along a transform fault (Stern, 2004; Denny, 2012). The general model, first suggested by Stern and Bloomer (1992), involves a density variation across the transform fault. This then drives a transform collapse, where by the denser plate sinks below the other, before propagating along pre-existing

crustal weaknesses (Stern and Bloomer, 1992),. In this model a transform fault parallel to the North American margin between the Farallon and the partially subducted Kula/Resurrection plate represents a zone of weakness along which subduction can propagate (Babcock et al., 1992; Wells et al., 1998; Haeussler et al., 2003; Stern, 2004; Denny, 2012). This model can explain both the linear geometry of the terrane and its suggested volume (Stern, 2004). However, the composition of the Siletz basalts does not support an early-arc tectonic setting resulting from subduction initiation as the primary mechanism of formation of the Siletz terrane (Reagan et al., 2010). Isotopically, the Siletz basalts are much more enriched than those related to subduction initiation e.g., in the basalts of the Izu Bonin and Mariana areas, with the Siletz terrane basalts consistently displaying lower ε_{Nd} and ε_{Hf} values (Figure 6.78) (Stern, 2004; Reagan et al., 2010; Arculus et al., 2015).
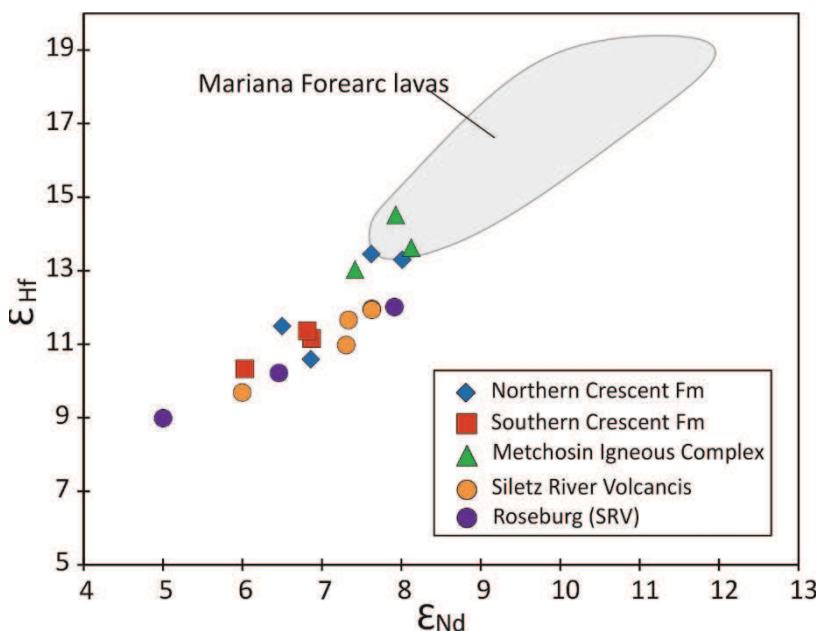
Figure 6.78 Comparison of the Siletz terrane composition and that of the Mariana forearc lavas. The data for the Mariana forearc field is derived from Reagen et al., (2010).

An alternative slab window model (Babcock et al., 1992) consists of mantle upwelling through a slab gap or via slab fragmentation initiated by the arrival of the Yellowstone hotspot or another plume head (Babcock et al., 1992). This model is not supported by the initial temperatures calculated for the mantle source of the Siletz terrane, as the temperature of primary magmas derived from slab windows are thought to be comparable to mid ocean ridges (1300-1400 °C) (Hastie and Kerr, 2010), compared to 1400-1500 °C calculated for the Siletz

terrane. Typically however, slab window mafic volcanism observed elsewhere is volumetrically much smaller than the suggested volume for the Siletz terrane (e.g., Hole, 1991; Hastie et al., 2010). The suggested characteristics of the mantle source of the Siletz terrane are also more enriched than the DMM-like mantle that is thought to produce slab window related magmatism (Herzberg et al., 2007; Hastie and Kerr, 2010). Finally, the trace elements of Siletz rocks do not generally display typical subduction-related characteristics, such as Nb-Ta depletion or significant Th enrichment (Chapter 5) which would be expected, even with the presence and geochemical input of a mantle plume head in the setting (Pearce, 2008; Hastie et al., 2010).

The lack of consistent resemblance to the Imnaha component in the majority of Siletz samples appears to rule out the Yellowstone hotspot mantle plume head as a source region (Pyle et al., 2009). However, the composition of the plume source is unlikely to have been consistent over time, or may be heterogeneous, and therefore variation in the amount of melting for example may result in the sampling of parts of the plume with markedly different compositions (e.g., Kerr et al., 1995; Escuder-Viruete et al., 2007). In addition to this, several plate reconstructions propose that the Yellowstone hotspot was present in this area at the time of the formation of the Siletz terrane (Muller et al., 1993; O'Neill et al., 2005; Doubrovine et al., 2012).

Although volcanic ash layers/ tuffs are typically unusual in oceanic plateaus (Kerr, 2014), abundant volcanoclastic horizons occur throughout the Siletz terrane, especially between the upper subaerial flows. This can be explained by progressive shallowing throughout the sequence from deep to shallow water to subaerial environments. This indicates continual dynamic uplift by the plume (as well as accumulation of the lava pile) while also explaining the abundance of ash and volcanoclastic material. This has also been observed at other well-characterised mantle plume-related oceanic plateaus, such as in the Western Cordillera of Colombia, in the Caribbean Plateau (Kerr, 2014) and also in limited occurrences in the Ontong Java Plateau where tuff layers and sedimentary reworking occur (Mahoney et al., 2001).

The Siletz basalts are most depleted in the north and north east, becoming more enriched in the central and southern areas and towards the west. The basalts comprise a range of moderately enriched compositions (E-MORB-like) with even the most depleted samples being more enriched than typical N-MORB. The depth of melting also appears to increase towards the centre of the terrane. Sample 073RB is the westernmost sample and additionally has the largest HIMU component.

Overall, the mantle characteristics of the Siletz terrane best represent mixing of depleted mantle with an additional enriched input from a mantle plume. The temperature of the primary magmas has been calculated at 1400 – 1500 °C, which is hotter than ambient mid ocean-ridge source mantle. The enriched component and mantle plume source has been proposed to represent the Yellowstone hotspot (Figure 6.79) (cf. Duncan, 1982; McCrory and Wilson, 2013; Wells et al., 2014). The depleted mantle source component, recorded in the relatively depleted samples from the NE (the Metchosin Igneous Complex and Crescent Formation) is compositionally similar to mid ocean ridge source mantle (more extensive melting) and most likely indicate off-axis interaction between the Farallon – Kula/ Resurrection ridge, and a hotter enriched mantle source region (Figure 6.79). Alternatively, the depleted component may be sampling a depleted relatively refractory portion of the mantle plume (cf. Kerr et al., 1995; Kempton et al., 2000).
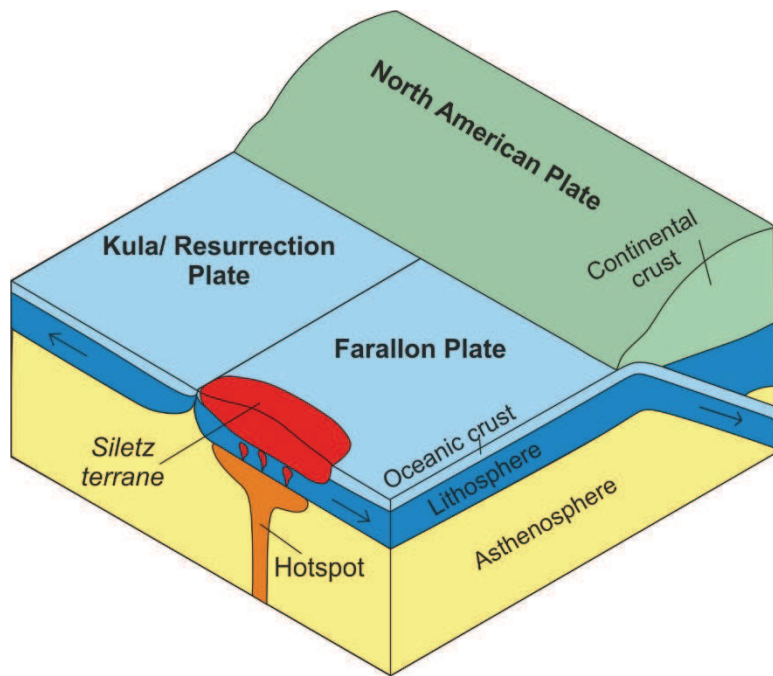
Figure 6.79 Schematic diagram of the tectonic setting in which the rocks of the Siletz terrane were formed.

The Siletz terrane comprises part of the greater North American Cordillera, which extends from Alaska to Mexico and consists of primarily rocks related to the Cretaceous – Tertiary Cordilleran orogeny (Birchfiel and Davies, 1972; 175; Hildebrand, 2009). Formation and subsequent accretion of the Siletz terrane has therefore had a notable impact on the evolution of the Cordillera. Most significantly, in addition to plate configurations, a long lived Yellowstone hotspot appears to have contributed to magmatism in the region since at least the initial eruption of the Siletz terrane at ~ 56 Ma. Previous studies (e.g., McCrory and Wilson, 2013), along with the palynology results discussed in section 5.7.2 indicate that the Siletz terrane formed near the continental margin (within 300 – 100 km), which helps constrain the location of the plume to this region. In addition, accretion of the Siletz terrane at around 49 Ma, has been suggested to initiate the rollback of the subducting Farallon slab and so the formation of a slab window, which then lead to a southward shift in the magmatism in the region (Humphreys, 2011; Gao et al., 2011). Finally, a remnant of the Siletz terrane is suggested to persist beneath the basement rocks of the southern Columbia Plateau

in eastern Washington (Schmandt and Humphreys, 2011). Although, Bedrosian and Feucht (2014) suggest that the extent of the terrane is restricted to the present day regional forearc. Schmidt et al (2008) has suggested that the basalts of the Cascade arc with minimal arc signatures and low $^{87}Sr/^{86}Sr$ (the Mt Adams basalts, Washington), which overlap with some of the proposed margins of the Siletz terrane, were derived from accreted mantle associated with the Siletz terrane. However, the Siletz terrane generally displays slightly higher $^{87}Sr/^{86}Sr$ ratios than those recorded from the Mt Adams basalts (i.e minimal arc signature Cascades arc basalts) (e.g. Mullen et al., 2017). Additionally, Mullen et al., (2017) conclude that these rocks are derived from sub – slab mantle which has subsequently flowed through a slab window gap and undergone decompression melting. Despite this, the Siletz terrane appears to have had a significant impact on the development of the Cordilleran region.

6.4.1 Youngest Oceanic Plateau?

Oceanic plateaus represent vast areas of over-thickened predominantly basaltic oceanic crust ($>5 \times 10^5$ km^3) the majority of which erupted over a few million years (Kerr, 2014). Elevated topography and greater crustal thickness in comparison with 'normal' oceanic crust leads to oceanic plateaus being more buoyant. Therefore, notably for plateaus that collide with subduction zones shortly after formation (< 5 Ma), the probability of partial accretion to the adjacent upper continental plate margin and so preservation within the geologic record is greatly increased (Cloos, 1993). Accreted oceanic plateaus have had a significant role in the growth of the continental crust, throughout Earth history (Condie, 1998; Stern and Scholl, 2010) however, secondary processes such as deformation and burial, lead to difficulties in the recognition of their characteristics once accreted (Kerr et al., 2000). Despite this, many examples of crustal growth through oceanic plateau accretion have been recognised in the geological record, including sections of the Wrangellia, Cache Creek and Angayucham terranes (Pallister et al., 1989; Tardy et al., 2001; Lapierre et al., 2003; Greene et al., 2009a; b), which along with the

Siletz terrane highlights the role of oceanic plateaus in the growth and evolution of the western margin of North America.

Several well-characterised oceanic plateaus have similar heterogeneous trace element compositions to the Siletz terrane, e.g., the Cretaceous Caribbean plateau (Kerr and Mahoney, 2007) and the Late Triassic (ca. 225-231 Ma) Karmusten flood basalts of Vancouver Island and Alaska (Greene et al., 2009a;b). In contrast, the largest oceanic plateau, the Cretaceous Ontong Java Plateau, is more depleted and anomalously homogeneous in composition (Fitton and Godard, 2004) (e.g., Figure 6.75). While geochemistry alone cannot be used to distinguish oceanic plateaus in the geological record, their Nb/La ratio is often ~1 (Kerr, 2014), and this is generally reflected in the Siletz terrane data, which clusters between ratios of 1 and 1.5 (Chapter 5).

Features of the terrane which support an oceanic plateau origin include; moderately enriched isotopic compositions, flat to slightly enriched REE patterns and the vast size and magmatic volume of the terrane (estimated to be 2.6 x $10^6 \, km^3$; Trehu et al., 1994), the bulk of which erupted within 5 – 7 Ma . In addition to this, mantle melt modelling for the Siletz terrane (as discussed in section 6.2) indicates elevated mantle source potential temperatures, and similar amounts of partial melting and subsequent fractionation to the Caribbean and Ontong Java Plateaus. The terrane however, thins to 10 km at Vancouver Island and 6 km offshore, which is more typical of normal oceanic crust, compared to the average ~ 20 km thickness estimated for the remainder of the terrane (Hyndman et al., 1990; Trehu et al., 1994; Parsons et al., 1999). Sheeted dykes present at Bremerton (Crescent Formation) and on Vancouver Island (Metchosin Igneous Complex), which while unknown in other oceanic plateaus are consistent with plume – ridge interaction (Kerr, 2014). Finally, as discussed above, there are relatively depleted signatures present in some sequences from the north of the terrane, compositionally similar to mid oceanic ridge environments. Overall, the evidence appears to support the conclusion that the Siletz terrane is an accreted oceanic plateau, and hence represents the youngest oceanic plateau preserved in the geological record.

6.5 Future Work

While this project presents the most complete available geochemical synthesis of the rocks of the Siletz terrane to date, constraints on time and expense prevented the collection of samples from certain locations within the terrane. In particular, further sampling of the Metchosin Igneous Complex on Vancouver Island would be beneficial to the overall understanding of the Siletz terrane. In addition, a small outcrop of picrites have been described in southern Oregon, and sampling of this material would allow the composition and temperature of primary magmas of the terrane to be better constrained. Sampling and geochemical comparison of the Wheatfield Fork terrane, California and the Yakutat terrane, Alaska with the results of the Siletz terrane would also be beneficial.

A primary aim of any future work should also be to produce a number of high precision U/Pb ages for units from across the terrane. Several baddeleyites and some zircons were identified during the microanalyses of the mineral composition using an EDS analyser. This would not only constrain the timing of eruption to a greater extent but may also provide greater understanding of the temporal evolution of the composition and depth of melting of the rocks of the terrane. In addition, more precise and comprehensive dating could potentially provide clear evidence for any temporal overlap between the eruption of the Siletz terrane and the onset of the Palaeocene Eocene Thermal Maximum (PETM) and so potential causation.

Although the Pb, Sr, Nd and Hf isotopic ratios of the analysed samples are relatively homogeneous, a larger number of analyses would also provide greater resolution of mantle source heterogeneity. Additionally, Os isotopes may prove useful for characterising whether the source contains any recycled oceanic lithosphere and so should be considered in any further work on the Siletz terrane.

7. CONCLUSIONS

The Siletz accreted mafic terrane has a large magmatic volume (2.6 x 10^6 km^3) (Trehu et al., 1994) which represents a sequence of rocks that progressively shallow from marine to more terrestrial environments and erupted over a relatively short time period (56 – 49 Ma). The terrane consists of a series of basaltic pillow lavas, massive flows, intrusive sheets, occasional dolerite dykes and gabbros. Brecciated lapilli tuffs, laminated tuffs, volcaniclastic sediments, marine and continentally derived sediments are interbedded with the lava flows. Basalts and dolerites range from aphyric to phyric, may be intergranular or subophitic and are frequently containing glomerocrysts. The mafic rocks largely comprise clinopyroxene, plagioclase and ilmenite with occasional olivine. Clinopyroxenes are mostly augitic, although other compositions are found while feldspars tend to range from albite to anorthite compositions.

Eruption and intrusion of the Siletz terrane magmas is thought to have taken place from ~56-49 Ma (Duncan, 1982; Massey, 1986; Haeussler et al., 2000; Hirsch and Babcock, 2009; Wells et al., 2014). However, nine samples from this study yielded statistically acceptable ^{40}Ar/^{39}Ar ages, which vary between around 58 – 47 Ma, along with a substantially younger age of 34 Ma for one sample. In addition, the pollen ages, derived from inter-lava ash and sediments in the Siletz River Volcanic Formation, have produced a similar range of 56 – 48 Ma. The palynological studies of samples collected during this study also suggest a shallow depositional and so eruption depth, which is consistent with a near (> 300 km) continetal margin source for the terrane suggested in previous studies (e.g., McCrory and Wilson, 2013).

The igneous rocks of the Siletz terrane have undergone variable degrees of alteration since their formation. The alteration mineral assemblages preserved in the rocks of the terrane suggest that the metamorphic facies largely represent zeolite and prehnite – pumpellyite alteration. However, some samples, in particular those from the upper basalts of the Metchosin Igneous Complex, have experienced alteration up to greenschist facies. This alteration has subsequently affected the geochemistry of the suites, resulting in remobilisation of several of

the more mobile elements, meaning that they are not suitable for assessing the petrogenesis of the Siletz terrane. For example all samples show a large variation in Ba/Rb ratio, consistent with Rb depletion during post magmatic alteration (Hofmann and White, 1983).

The majority of samples in this study are tholeiitic basalts while a small number of samples, largely from the Siletz River Volcanics, trend towards alkaline compositions. In general, the rocks of the Siletz terrane have a similar trace element geochemistry, frequently characterised by positive Nb-Ta anomalies. Samples from across the terrane show flat to enriched LREE and flat to slightly depleted HREE primitive mantle normalised patterns. Using trace elements, geochemically three primary groups are recognized for the terrane as a whole. The first of these includes a group of primarily Metchosin Igneous Complex and Depleted Crescent Group samples, along with some samples from the Black Hills Group, which are slightly more enriched than N-MORB, and are the most depleted basalts in the terrane. A second group of samples are more enriched, especially in incompatible trace elements and LREE, and consist of predominantly alkali rocks, largely from the Alkali Group (of the Siletz River Formation) but also include samples from the Kentucky Slough Group, Roseburg Group and Ilwaco Group. The third and final group contains the majority of samples analysed in this study and geochemically its composition is intermediate between the two other groups. Within this main cluster of data, the Roseburg Group and some samples from the Main Crescent Group, are the most depleted in incompatible trace elements.

Fractional crystallisation appears to be best modelled by crystallisation of a parent magma more primitive than any of the samples analysed at low pressures under anhydrous conditions. However, fractional crystallisation trends were generally difficult to model due to heterogeneities in source compositions, variations in magma chamber conditions (e.g., pressure) and the open nature of the systems in which the rocks were fractionating.

The estimated initial mantle potential temperatures of the Siletz terrane range from 1400 - 1500 °C while the amount of partial melting undergone

generally varies between ~ 25 – 33 % over an estimated pressure range of 1.5 – 2.4 GPa. These results are similar to other mantle plume-derived provinces such as the Ontong Java Plateau and the Caribbean plateau (Fitton and Godard, 2004; Herzberg and Gazel, 2009). Trace element melt modelling requires a heterogeneous source to reproduce the compositions found in samples of the Siletz terrane, with modelled potential sources including a range of reservoirs and mixtures of reservoirs, representing variably depleted and enriched mantle sources.

The mafic rocks of the Siletz terrane appear to have been derived from a heterogeneous and partially enriched mantle source with an above ambient temperature. This source composition comprises a relatively depleted signature along with EM2- and HIMU-like enrichments. A mantle plume-like signature is prevalent throughout the terrane, but is far less apparent in the rocks derived from the north – east, specifically those from the Metchosin Igneous Complex, and to a lesser extent the Crescent Formation. In addition, the most enriched samples (those with the largest EM2 signatures) appear have undergone smaller amounts of melting of a deeper source relative to the more depleted samples from largely the Metchosin Igneous Complex and Northern Crescent Formation (Figure 6.76). This is also consistent with shallower melting depths and more depleted trace element signatures recorded in the north – eastern samples.

The rocks of the terrane are geochemically similar, both in trace element (generally flat to LREE enriched REE patterns) and radiogenic isotope composition to several well characterised oceanic plateaus, for example the Karmutsen Flood Basalts on Vancouver Island. The enriched components recorded in the Siletz terrane rocks represent melting of a heterogeneous mantle plume, (hotter than ambient mantle) and may possibly represent the Yellowstone Hotspot. The depleted mantle source components which are recorded in the relatively depleted samples from the NE (the Metchosin Igneous Complex and Crescent Formation) may indicate the presence of mid oceanic ridge type mantle. Overall, the geochemistry of the terrane suggests off-axis interaction between the Farallon – Kula/ Resurrection ridge and a hotter enriched mantle source region.

Alternatively, the depleted component recorded in the terrane may be sampling a depleted relatively refractory portion of a mantle plume (cf. Kerr et al., 1995; Kempton et al., 2000). Therefore, although individually, the geochemical signatures and physical characteristics of the Siletz terrane can be interpreted differently, when taken together, the evidence for the Siletz terrane representing an accreted oceanic plateau linked to a mantle plume is compelling. The Late Palaeocene – Early Eocene Siletz terrane therefore represents the youngest oceanic plateau thus far characterised.

REFERENCES

Abbott, D., and Mooney, W., 1995. The structural and geochemical evolution of the continental crust: support for the oceanic plateau model of continental growth: Revs. Geophy., 33 (Supplement), p. 231-242.

Allegre, C. J., and Lewin, E., 1995. Isotopic systems and stirring times of the earth's mantle: Earth and Planetary Science Letters, 136, no. 3-4, p. 629-646.

Anderson, D. L., 2013. The persistent mantle plume myth: Australian Journal of Earth Sciences, 60, no. 6-7, p. 657-673.

Anderson, D. L., and Natland, J. H., 2007. Evidence for mantle plumes?: Nature, 450, no. 7169, p. E15-E15.

Arculus, R. J., Ishizuka, O., Bogus, K. A., Gurnis, M., Hickey-Vargas, R., Aljahdali, M. H., Bandini-Maeder, A. N., Barth, A. P., Brandl, P. A., and Drab, L., 2015. A record of spontaneous subduction initiation in the Izu-Bonin-Mariana arc: Nature Geoscience, 8, no. 9, p. 728-733.

Arculus, R. J., and Powell, R., 1986. Source component mixing in the regions of arc magma generation: Journal of Geophysical Research: Solid Earth., 91, p. 5913-5926.

Arthur, M. A., Schlanger, S. O., and Jenkyns, H. C., 1987. The Cenomanian-Turonian Oceanic Anoxic Event, II: Paleoceanographic controls on organic-matter production and preservation, *in* Brooks, J., and Fleet, A. J., eds., Marine Petroleum Source Rocks, Volume 26, Geological Society, London, Special Publication, p. 401-420.

Asimow, P. D., and Ghiorso, M. S., 1998. Algorithmic modifications extending MELTS to calculate subsolidus phase relations: American Mineralogist, 83, no. 9-10, p. 1127-1132.

Atwater, T., 1989. Plate tectonic history of the northeast Pacific and western North America: The eastern Pacific Ocean and Hawaii: Boulder, Colorado, Geological Society of America, Geology of North America, p. 21-72.

Babcock, R. S., Burmester, R. F., Engebretson, D. C., Warnock, A., and Clark, K. P., 1992. A rifted margin origin for the crescent basalts and related rocks

in the Northern Coast Range Volcanic Province, Washington and British-Columbia: Journal of Geophysical Research: Solid Earth, 97, no. B5, p. 6799-6821.

Baldwin, E. M., 1974. Eocene stratigraphy of southwestern Oregon, State of Oregon, Department of Geology and Mineral Industries.

Barclay, R. S., McElwain, J. C., and Sageman, B. B., 2010. Carbon sequestration activated by a volcanic CO2 pulse during Ocean Anoxic Event 2: Nature Geoscience, 3, no. 3, p. 205-208.

Beck, C. M., Girard, D., and DeWeber, P., 1984. "Volcano-sédimentaire du Rio Guare": Un élément de la nappe ophiolitique de Lomo de Hierro, chaone Caraôbe Vénézuélienne: Comptes Rendus de Seances (D), 299, p. 337-342.

Bedrosian, P. A., and Feucht, D. W., 2014. Structure and tectonics of the northwestern United States from EarthScope USArray magnetotelluric data: Earth and Planetary Science Letters, 402, p. 275-289.

Ben-Avraham, Z., Nur, A., Jones, D., and Cox, A., 1981. Continental accretion: from oceanic plateaus to allochthonous terranes: Science, 213, p. 47-54.

Bercovici, D., and Mahoney, J., 1994. Double flood basalts and plume head seperation at the 660-km discontinuity: Science, 266, p. 1367-1369.

Blakely, R. J., Sherrod, B. L., Hughes, J. F., Anderson, M. L., Wells, R. E., and Weaver, C. S., 2009. Saddle Mountain fault deformation zone, Olympic Peninsula, Washington: Western boundary of the Seattle uplift: Geosphere, 5, no. 2, p. 105-125.

Bond, D. P., and Wignall, P. B., 2014. Large igneous provinces and mass extinctions: An update: Geological Society of America Special Papers, 505, p. SPE505-502.

Bowen, G. J., Maibauer, B. J., Kraus, M. J., Röhl, U., Westerhold, T., Steimke, A., Gingerich, P. D., Wing, S. L., and Clyde, W. C., 2015. Two massive, rapid releases of carbon during the onset of the Palaeocene-Eocene thermal maximum: Nature Geoscience, 8, no. 1, p. 44-47.

Bowen, G. J., and Steimke, A., 2014. Hydroclimatic modulation of continental carbon burial through the PETM, *in* Proceedings 2014 GSA Annual Meeting in Vancouver, British Columbia 2014.

Bradley, D., Haeussler, P., Nelson, S., Kusky, T., Donley, D., and Goldfarb, R., 1995. Geologic effects of Paleogene ridge subduction, Kenai Peninsula [abs.], *in* Proceedings Geological Society of America, Abstracts with Programs 1995, Volume 27, p. 7.

Brandon, M. T., 2014. New evidence for Backarc Basin interpretation for Eocene Coast -Range Terrane *in* Proceedings 2014 GSA Annual Meeting in Vancouver, British Columbia 2014.

Breitsprecher, K., Thorkelson, D., Groome, W., and Dostal, J., 2003. Geochemical confirmation of the Kula-Farallon slab window beneath the Pacific Northwest in Eocene time: Geology, 31, no. 4, p. 351-354.

Brueseke, M. E., and Hart, W. K., 2008. Intermediate composition magma production in an intracontinental setting: Unusual andesites and dacites of the mid-Miocene Santa Rosa–Calico volcanic field, Northern Nevada: Journal of Volcanology and Geothermal Research, 188, no. 1, p. 197-213.

Bryan, S. E., and Ferrari, L., 2013. Large igneous provinces and silicic large igneous provinces: Progress in our understanding over the last 25 years: Bulletin of the Geological Society of America, 125, no. 7-8, p. 1053-1078.

Bucher, K., and Frey, M., 1994. Petrogenesis of Metamorphic Rocks. Springer, Berlin.

Bukry, D., and Snavely, P. D., 1988. Coccolith zonation for Paleogene strata in the Oregon Coast Range.

Cady, W., 1975. Tectonic setting of the Tertiary volcanic rocks of the Olympic Peninsula, Washington: Journal of Research of the U. S. Geological Survey, 3, no. 5, p. 573-582.

Camp, E., 1995. Mid-miocene propagation of the Yellowstone mantle plume head beneath the Columbia River basalt source region: Geology, 23, no. 5, p. 435-438.

Camp, E., and Ross, M. E., 2004. Mantle dynamics and genesis of mafic magmatism in the intermontane Pacific Northwest - art. no. B08204: Journal of Geophysical Research: Solid Earth, 109, no. B8, p. 8204.

Campbell, I. H., 2007. Testing the plume theory: Chemical Geology, 241, p. 153-176.

Campbell, I. H., and Griffiths, R. W., 1990. Implications of mantle plume structure for the evolution of flood basalts: Earth and Planetary Science Letters., 99, p. 79-93.

Cann, J. R., 1970. Rb, Sr,Y, Zr and Nb in some ocean floor basaltic rocks: Earth and Planetary Science Letters., 10, p. 7-11.

Carlson, R. W., 1984. Isotopic constraints on Columbia River flood basalt genesis and the nature of the subcontinental mantle: Geochim. Cosmochim. Acta, 48, p. 2357-2372.

Carlson, R. W., and Hart, W. K., 1988. Flood basalt volcanism in the northwestern United States, *in* Macdougall, J. D., ed., Continental Flood Basalts: Dordrecht, Netherlands, Kluwer Academic Publishers, p. 35-62.

Chadwick, J., Keller, R., Kamenov, G., Yogodzinski, G., and Lupton, J., 2014. The Cobb hot spot: HIMU-DMM mixing and melting controlled by a progressively thinning lithospheric lid: Geochemistry, Geophysics, Geosystems, 15, no. 8, p. 3107-3122.

Chambers, L. M., Pringle, M. S., and Fitton, J. G., 2004. Phreatomagmatic eruptions on the Ontong Java Plateau: an Aptian 40Ar/39Ar age for volcaniclastic rocks at ODP Site 1184, *in* Fitton, J. G., Mahoney, J. J., Wallace, P. J., and Saunders, A. D., eds., Origin and evolution of the Ontong Java Plateau, Geological Society of London, Special Publication, 229, 325–331.

Chen, L., Sun, Y., Pei, X., Gao, M., Feng, T., Zhang, Z., and Chen, W., 2001. Northernmost paleo-tethyan oceanic basin in Tibet: Geochronological evidence from40Ar/39Ar age dating of Dur'ngoi ophiolite: Chinese Science Bulletin, 46, no. 14, p. 1203-1205.

Christiansen, R. L., Foulger, G. R., and Evans, J. R., 2002. Upper-mantle origin of the Yellowstone hotspot: Geological Society of America Bulletin, 114, no. 10, p. 1245-1256.

Clark, K. P., 1989. Comparative stratigraphy, petrology, and geochemistry of the Crescent Formation and related exposures near Bremerton and Port Townsend, Washington: MS Thesis, 171 pp., West. Wash. Uni, Bellingham.

Cloos, M., 1993. Lithospheric buoyancy and collisional orogenesis: Subduction of oceanic plateaus, continental margins, island arcs, spreading ridges, and seamounts: Geological Society of America Bulletin, 105, no. 6, p. 715-737.

Clowes, R., Brandon, M., Green, A., Yorath, C., Brown, A. S., Kanasewich, E., and Spencer, C., 1987. Lithoprobe -southern Vancouver Island: Cenozoic subduction complex imaged by deep seismic reflections: Canadian Journal of Earth Sciences, 24, no. 1, p. 31-51.

Coble, M. A., and Mahood, G. A., 2008. New geologic evidence for additional 16.5–15.5 Ma silicic calderas in northwest Nevada related to initial impingement of the Yellowstone hot spot, *in* Proceedings IOP Conference Series: Earth and Environmental Science 2008, Volume 3, IOP Publishing, p. 012002.

Coffin, M. F., and Eldholm, O., 1992. Volcanism and continental break-up: a global compilation of large igneous provinces, *in* Storey, B. C., Alabaster, T., and Pankhurst, R. J., eds., Magmatism and the Causes of Continental Breakup, Volume 68: London, Geological Society of London, p. 17-30.

Coffin, M. F., and Eldholm, O., 1994. Large igneous provinces: crustal structure, dimentions, and external consequences: Reviews of Geophysics, 32, p. 1-36.

Coffin, M. F., Pringle, M. S., Duncan, R. A., Gladczenko, T. P., Storey, M., Muller, R. D., and Gahagan, L. A., 2002. Kerguelen hotspot magma output since 130 Ma: Journal of Petrology, 43, no. 7, p. 1121-1139.

Cole, J. W., 1990. Structural control and origin of volcanism in the Taupo volcanic zone, New Zealand: Bulletin of Volcanology., 52, p. 445-459.

Condie, K. C., 1998. Episodic continental growth and supercontinents: a mantle avalanche connection?: Earth and Planetary Science Letters. 163, no. 1-4, p. 97-108.

Condie, K. C., 2003. Incompatible element ratios in oceanic basalts and komatiites: Tracking deep mantle sources and continental growth rates with time - art. no. 1005: Geochemistry, Geophysics, Geosystems, 4, p. 1005.

Condie, K. C., 2005. High field strength element ratios in Archean basalts: a window to evolving sources of mantle plumes?: Lithos, 79, no. 3-4, p. 491-504.

Condon, P., Jolley, D., and Morton, A., 1992. Eocene succession on the east Shetland platform, North Sea: Marine and petroleum geology, 9, no. 6, p. 633-647.

Courtney, R. C., and White, R. S., 1986. Anomalous heat flow and geoid across the Cape Verde Rise: evidence for dynamic support from a thermal plume in the mantle: Geophysical Journal International, 87, no. 3, p. 815-867.

Cousens, B. L., 1996. Depleted and enriched upper mantle sources for basaltic rocks from diverse tectonic environments in the northeast Pacific Ocean: The generation of oceanic alkaline vs. tholeiitic basalts: Earth Processes: Reading the Isotopic Code, p. 207-231.

Cousens, B.,Weis, D., Constantin, M., Scott, S., 2017. Radiogenic isotopes in enriched mid ocean ridge basalts from Explorer Ridge, Northeast Pacific Ocean: The HIMU Connection: Geochimica et Cosmochimica Acta (in review).

Darold, A., and Humphreys, E., 2013. Upper mantle seismic structure beneath the Pacific Northwest: A plume-triggered delamination origin for the Columbia River flood basalt eruptions: Earth and Planetary Science Letters, 365, p. 232-242.

Davaille, A., Girard, F., and Le Bars, M., 2002. How to anchor hotspots in a convecting mantle?: Earth and Planetary Science Letters, 203, no. 2, p. 621-634.

Davaille, A., and Vatteville, J., 2005. On the transient nature of mantle plumes: Geophysical research letters, 32, no. 14.

Davis, A., Clague, D., Cousens, B., Keaten, R., and Paduan, J., 2008. Geochemistry of basalt from the North Gorda segment of the Gorda Ridge: Evolution toward ultraslow spreading ridge lavas due to decreasing magma supply: Geochemistry, Geophysics, Geosystems, 9, no. 4.

Davis, A. S., and Plafker, G., 1986. Eocene basalts from the Yakutat terrane: Evidence for the origin of an accreting terrane in southern Alaska: Geology, 14, no. 11, p. 963-966.

de Hoog, J. C., and van Bergen, M. J., 2000. Volatile-induced transport of HFSE, REE, Th and U in arc magmas: evidence from zirconolite-bearing vesicles in potassic lavas of Lewotolo volcano (Indonesia): Contributions to Mineralogy and Petrology, 139, no. 4, p. 485-502.

DeConto, R. M., Galeotti, S., Pagani, M., Tracy, D., Schaefer, K., Zhang, T., Pollard, D., and Beerling, D. J., 2012. Past extreme warming events linked to massive carbon release from thawing permafrost: Nature, 484, no. 7392, p. 87-91.

Denny, A. C., 2012. Geochemistry of the Lower Crescent Formation, Washington, and Re evaluation of Proposed Formation Hypotheses.

DePaolo, D. J., and Wasserburg, G. J., 1976. Inferences about magma sources and mantle structure from variations of $^{143}Nd/^{144}Nd$: Geophys. Res. Lett., 3, p. 743-746.

Dickens, G. R., Castillo, M. M., and Walker, J. C. G., 1997. A blast of gas in the latest Paleocene: Simulating first-order effects of massive dissociation of oceanic methane hydrate: Geology, 25, no. 3, p. 259-262.

Dickinson, W. R., 1997. Overview: Tectonic implications of Cenozoic volcanism in coastal California: Geological Society of America Bulletin, 109, no. 8, p. 936-954.

Dickinson, W. R., and Snyder, W. S., 1979. Geometry of subducted slabs related to San Andreas transform: The Journal of Geology., 87, p. 609-627.

Doubrovine, P. , Steinberger, B., and Torsvik, T. H., 2012. Absolute plate motions in a reference frame defined by moving hot spots in the Pacific, Atlantic,

and Indian oceans: Journal of Geophysical Research: Solid Earth, 117, no. B9.

Duncan, R. A., 1982. A captured island chain in the coast range of Oregon and Washington: Journal of Geophysical Research., 87, p. 10827-10837.

Duncan, R. A., 2002. A time frame for construction of the Kerguelen Plateau and Broken Ridge: Journal of Petrology, 43, no. 7, p. 1109-1119.

Eddy, M. P., Bowring, S. A., Umhoefer, P. J., Miller, R. B., McLean, N. M., and Donaghy, E. E., 2016. High-resolution temporal and stratigraphic record of Siletzia's accretion and triple junction migration from nonmarine sedimentary basins in central and western Washington: Geological Society of America Bulletin, 128, no. 3-4, p. 425-441.

Eddy, M. P., Clark, K. P., and Polenz, M., 2017. Age and volcanic stratigraphy of the Eocene Siletzia oceanic plateau in Washington and on Vancouver Island: Lithosphere, 9, no. 3

Engebretson, D. C., 1985. Relative motions between oceanic and continental plates in the Pacific basin, Geological society of America.

England, P., and Wells, R. E., 1991. Neogene rotations and quasicontinuous deformation of the Pacific Northwest continental margin: Geology, 19, no. 10, p. 978-981.

Ernst, R., Srivastava, R., Bleeker, W., and Hamilton, M., 2010. Precambrian Large Igneous Provinces (LIPs) and their dyke swarms: New insights from high-precision geochronology integrated with paleomagnetism and geochemistry: Precambrian Research., 183, no. 3, p. vii-xi.

Escuder-Viruete, J., Perez-Estaun, A., Contreras, F., Joubert, M., Weis, D., Ullrich, T. D., and Spadea, P., 2007. Plume mantle source heterogeneity through time: Insights from the Duarte Complex, Hispaniola, northeastern Caribbean: Journal of Geophysical Research: Solid Earth, 112, no. B4.

Fadda, S., Fiori, M., Grillo, S. M., and Prochaska, W., 2012. REE Mobilization in Complex Hydrothermal–Metasomatic Systems: Fluid Chemistry Evidence of Albitite And Chlorite-Talc Mineralisations in Central Sardinia, Italy, *in* Proceedings Proceedings of the 10th International Congress for Applied Mineralogy (ICAM) 2012, Springer, p. 171-178.

Falloon, T. J., Green, D. H., and Danyushevsky, L., 2007. Crystallization temperatures of tholeiite parental liquids: Implications for the existence of thermally driven mantle plumes: Special Papers - Geological Society of America, 430, p. 235.

Farnetani, C. G., Richards, M. A., and Ghiorso, M. S., 1996. Petrological models of magma evolution and deep crustal structure beneath hotspots and flood basalt provinces: Earth and Planetary Science Letters, 143, no. 1, p. 81-94.

Farnetani, C. G., and Samuel, H., 2005. Beyond the thermal plume paradigm: Geophysical Research Letters, 32, L07311, doi:10.1029/2005GL022360.

Farnetani, D. G., and Richards, M. A., 1995. Thermal entrainment and melting in mantle plumes: Earth and Planetary Science Letters, 136, no. 3-4, p. 251-267.

Fitton, J. G., and Godard, M., 2004. Origin and evolution of magmas on the Ontong Java Plateau, *in* Fitton, J. G., Mahoney, J. J., Wallace, P. J., and Saunders, A. D., eds., Origin and evolution of the Ontong Java Plateau, Geological Society of London, Special Publication, 229, 151-178.

Fitton, J. G., Saunders, A. D., Norry, M. J., Hardarson, B. S., and Taylor, R. N., 1997. Thermal and chemical structure of the Iceland plume: Earth and Planetary Science Letters., 153, p. 197-208.

Fleming, S. W., and Tréhu, A. M., 1999. Crustal structure beneath the central Oregon convergent margin from potential-field modeling: Evidence for a buried basement ridge in local contact with a seaward dipping backstop: Journal of Geophysical Research, 104, no. B9, p. 20431-20420,20447.

Forsythe, R., and Nelson, E., 1985. Geological manifestations of ridge collision: Evidence from the Golfo de Penas-Taitao Basin, southern Chile: Tectonics, 4, no. 5, p. 477-495.

Forsythe, R., and Prior, D., 1992. Cenozoic continental geology of South America and its relations to the evolution of the Chile triple junction, *in* Proceedings Proceedings of the Ocean Drilling Program, Initial Reports 1992, Volume 141, p. 23-31.

Fouch, M. J., 2012. The Yellowstone Hotspot: Plume or Not?: Geology, 40, no. 5, p. 479-480.

Foulger, G. R., and Jurdy, D. M., 2007. Plates, plumes, and planetary processes, Geological Society of America.

Gaffney, A. M., Borg, L. E., Asmerom, Y., Shearer, C. K., and Burger, P. , 2011. Disturbance of isotope systematics during experimental shock and thermal metamorphism of a lunar basalt with implications for Martian meteorite chronology: Meteoritics & Planetary Science, 46, no. 1, p. 35-52.

Gao, H., Humphreys, E. D., Yao, H., and van der Hilst, R. D., 2011. Crust and lithosphere structure of the northwestern US with ambient noise tomography: Terrane accretion and Cascade arc development: Earth and Planetary Science Letters, 304, no. 1, p. 202-211.

Geist, D., and Richards, M., 1993. Origin of the Columbia Plateau and Snake River plain: deflection of the Yellowstone plume: Geology, 21, p. 789-792.

Ghiorso, M. S., Hirschmann, M. M., Reiners, P. W., and Kress, C., 2002. The pMELTS: A revision of MELTS for improved calculation of phase relations and major element partitioning related to partial melting of the mantle to 3 GPa: Geochemistry, Geophysics, Geosystems, 3, no. 5, p. 1-35.

Ghiorso, M. S., and Sack, R. O., 1995. Chemical mass transfer in magmatic processes .4. A revised and internally consistent thermodynamic model for the interpolation and extrapolation of liquid solid equilibria in magmatic systems at elevated temperatures and pressures: Contributions to Mineralogy and Petrology, 119, no. 2-3, p. 197-212.

Gieré, R., 1993. Transport and deposition of REE in H2S-rich fluids: evidence from accessory mineral assemblages: Chemical Geology, 110, no. 1-3, p. 251-268.

Gill, J. B., 1981. Orogenic Andesites and Plate Tectonics, Berlin, Springer Verlag, 389 p.:

Gill, R., 2011. Igneous rocks and processes: a practical guide. John Wiley & Sons.

Ginibre, C., Wörner, G., and Kronz, A., 2007. Crystal zoning as an archive for magma evolution: Elements, 3, no. 4, p. 261-266.

Glassley, W., 1974. Geochemistry and tectonics of crescent volcanic-rocks, Olympic Peninsula, Washington: Geological Society of America Bulletin, 85, no. 5, p. 785-794.

Greene, A. R., Scoates, J. S., Weis, D., and Israel, S., 2009a. Geochemistry of Triassic flood basalts from the Yukon (Canada) segment of the accreted Wrangellia oceanic plateau: Lithos, 110, no. 1-4, p. 1-19.

Greene, A. R., Scoates, J. S., Weis, D., Nixon, G. T., and Kieffer, B., 2009b. Melting history and magmatic evolution of Basalts and picrites from the accreted Wrangellia Oceanic Plateau, Vancouver Island, Canada: Journal of Petrology, 50, no. 3, p. 467-505.

Groome, W. G., Thorkelson, D. J., Friedman, R. M., Mortensen, J. K., Massey, N. W., Marshall, D. D., and Layer, P. W., 2003. Magmatic and tectonic history of the Leech River Complex, Vancouver Island, British Columbia: Evidence for ridge-trench intersection and accretion of the Crescent Terrane: Special Papers-Geological Society of America, p. 327-354.

Gurnis, M., Turner, M., Zahirovic, S., DiCaprio, L., Spasojevic, S., Müller, R. D., Boyden, J., Seton, M., Manea, C., and Bower, D. J., 2012. Plate tectonic reconstructions with continuously closing plates: Computers & Geosciences, 38, no. 1, p. 35-42.

Haeussler, P., Clark, J., and Kenneth, P., 2000. Geologic map of the Wildcat Lake 7.5' Quadrangle Kitsap and Mason counties, Washington.

Haeussler, P. J., Bradley, D. C., Wells, R. E., and Miller, M. L., 2003. Life and death of the Resurrection plate: Evidence for its existence and subduction in the northeastern Pacific in Paleocene-Eocene time: Geological Society of America Bulletin, 115, no. 7, p. 867-880.

Hales, T. C., Abt, D. L., Humphreys, E. D., and Roering, J. J., 2005. A lithospheric instability origin for Columbia River flood basalts and Wallowa Mountains uplift in northeast Oregon: Nature, 438, p. 842-845.

Hanan, B. B., and Graham, D. W., 1996. Lead and helium isotope evidence from oceanic basalts for a common deep source of mantle plumes: Science, 272, no. 5268, p. 1573.

Hansen, D. M., Cartwright, J. A., and Thomas, D., 2004. The development of intersecting igneous sills from 3D seismic, *in* Davies, R. J., Cartwright, J. A., Stewart, S. A., Lappin, M., and Underhill, J. R., eds., 3D Seismic Technology: Application to the Exploration of Sedimentary Basins, Geological Society, London, Memoir, 29, 301-316.

Hastie, A. R., Fitton, J. G., Kerr, A. C., McDonald, I., Schwindrofska, A., and Hoernle, K., 2016. The composition of mantle plumes and the deep Earth: Earth and Planetary Science Letters, 444, p.13-25.

Hastie, A. R., and Kerr, A. C., 2010. Mantle plume or slab window?: Physical and geochemical constraints on the origin of the Caribbean oceanic plateau: Earth-Science Reviews, 98, no. 3-4, p. 283-293.

Hastie, A. R., Kerr, A. C., Pearce, J. A., and Mitchell, S., 2007. Classification of altered volcanic island arc rocks using immobile trace elements: development of the Th–Co discrimination diagram: Journal of Petrology, 48, no. 12, p. 2341-2357.

Heller, P. L., and Ryberg, P. T., 198. Sedimentary record of subduction to forearc transition in the rotated Eocene basin of western Oregon: Geology, 11, no. 7, p. 380-383.

Herzberg, C., 2004. Partial melting below the Ontong Java Plateau, *in* Fitton, J. G., Mahoney, J. J., Wallace, P. J., and Saunders, A. D., eds., Origin and evolution of the Ontong Java Plateau, Geological Society of London, Special Publication, 229, 179-184.

Herzberg, C., and Asimow, P., 2015. PRIMELT3 MEGA. XLSM software for primary magma calculation: Peridotite primary magma MgO contents from the liquidus to the solidus: Geochemistry, Geophysics, Geosystems, 16, no. 2, p. 563-578.

Herzberg, C., Asimow, P. D., Arndt, N., Niu, Y., Lesher, C. M., Fitton, J. G., Cheadle, M. J., and Saunders, A. D., 2007. Temperatures in ambient mantle and plumes: Constraints from basalts, picrites, and komatiites: Geochemistry, Geophysics, Geosystems, 8, p. 2006GC001390.

Herzberg, C., and Gazel, E., 2009. Petrological evidence for secular cooling in mantle plumes: Nature, 458, no. 7238, p. 619-622.

Hibbard, J. P., and Karig, D. E., 1990. Structural and magmatic responses to spreading ridge subduction: an example from southwest Japan: Tectonics, 9, no. 2, p. 207-230.

Higgins, J. A., and Schrag, D. P., 2006, Beyond methane: towards a theory for the Paleocene–Eocene thermal maximum: Earth and Planetary Science Letters, 245, no. 3, p. 523-537.

Hildreth, W., 2007. Quaternary magmatism in the Cascades: Geologic perspectives, US Geological Survey, 1744.

Hirsch, D. M., and Babcock, R. S., 2009. Spatially heterogeneous burial and high-P/T metamorphism in the Crescent Formation, Olympic Peninsula, Washington: American Mineralogist, 94, no. 8-9, p. 1103-1110.

Hofmann, A. W., and White, W. M., 1983. Ba, Rb and Cs in the Earth's mantle: Zeitschrift für Naturforschung A, 38, no. 2, p. 256-266.

Hole, M. J., and Larter, R. D., 1993. Trench-proximal volcanism following ridge crest-trench collision along the Antarctic Peninsula: Tectonics, 12, no. 4, p. 897-910.

Hole, M. J., Rogers, G., Saunders, A. D., and Storey, M., 1991. Relation between alkalic volcanism and slab-window formation: Geology, 19, p. 657-660.

Hooper, P. R., 1997. The Columbia River Flood Basalt Province: Current status, *in* Mahoney, J. J., and Coffin, M. F., eds., Large Igneous Provinces: Continental, Oceanic, and Planetary Flood Volcanism, Volume 100: Washington, D.C., American Geophysical Union, p. 1-27.

Hoover, L., 1963. Geology of the Anlauf and Drain quadrangles, Douglas and Lane counties, Oregon, US Government Printing Office, 1122.

Humphreys, E., and Darold, A., 2015. A plume-triggered delamination origin for the Columbia River flood basalt eruptions, *in* Proceedings AGU Fall Meeting Abstracts 2015.

Humphreys, E., and Schmandt, B., 2011. Looking for mantle plumes: Physics today, 64, no. 8, p. 34-39.

Hyndman, R., Yorath, C., Clowes, R., and Davis, E., 1990. The northern Cascadia subduction zone at Vancouver Island: Seismic structure and tectonic history: Canadian Journal of Earth Sciences, 27, no. 3, p. 313-329.

Ichiyama, Y., Ishiwatari, A., Kimura, J.-I., Senda, R., and Miyamoto, T., 2014. Jurassic plume-origin ophiolites in Japan: accreted fragments of oceanic plateaus: Contributions to Mineralogy and Petrology, 168, no. 1, p. 1-24.

Ingle, S., and Coffin, M. F., 2004. Impact origin for the greater Ontong Java Plateau?: Earth and Planetary Science Letters, 218, no. 1-2, p. 123-134.

Irving, E., 1979. Paleopoles and paleolatitudes of North America and speculations about displaced terrains: Canadian Journal of Earth Sciences, 16, no. 3, p. 669-694.

Ito, G. T., and Clift, P. D., 1998. Subsidence and growth of Pacific Cretaceous plateaus: Earth and Planetary Science Letters, 161, p. 85-100.

Ivany, L. C., and Sessa, J. A., 2010. Effects of ocean warming and acidification during the Paleocene-Eocene Thermal Maximum on deep and shallow marine communities: Ecol. Soc. Am. Annu. Meet., Pittsburgh, PA.

James, D. E., Fouch, M. J., Carlson, R. W., and Roth, J. B., 2011. Slab fragmentation, edge flow and the origin of the Yellowstone hotspot track: Earth and Planetary Science Letters, 311, no. 1, p. 124-135.

Jaramillo, C., Ochoa, D., Contreras, L., Pagani, M., Carvajal-Ortiz, H., Pratt, L. M., Krishnan, S., Cardona, A., Romero, M., and Quiroz, L., 2010. Effects of rapid global warming at the Paleocene-Eocene boundary on Neotropical vegetation: Science, 330, no. 6006, p. 957-961.

Johnson, K. T. M., Dick, H. J. B., and Shimizu, N., 1990. Melting in the Oceanic Upper Mantle - an Ion Microprobe Study of Diopsides in Abyssal Peridotites: Journal of Geophysical Research: Solid Earth and Planets, 95, no. B3, p. 2661-2678.

Johnson, S. Y., Potter, C. J., and Armentrout, J. M., 1994. Origin and evolution of the Seattle fault and Seattle basin, Washington: Geology, 22, no. 1, p. 71-74.

Johnston, S. T., and Acton, S., 2003. The Eocene Southern Vancouver Island Orocline—a response to seamount accretion and the cause of fold-and-thrust belt and extensional basin formation: Tectonophysics, 365, no. 1, p. 165-183.

Johnston, S. T., and Thorkelson, D. J., 2000. Continental flood basalts: episodic magmatism above long-lived hotspots: Earth and Planetary Science Letters, 175, no. 3, p. 247-256.

Johnston, S. T., Wynne, P. J., Francis, D., Hart, C. J. R., and Engebretson, D. C., 1996. Yellowstone in Yukon: The late Cretaceous Carmacks group: Geology, 24, no. 11, p. 997-1000.

Jolley, D. W., and Widdowson, M., 2005. Did Paleogene North Atlantic rift-related eruptions drive early Eocene climate cooling?: Lithos, 79, no. 3-4, p. 355-366.

Kempton, P. D., Fitton, J. G., Saunders, A. D., Nowell, G. M., Taylor, R. N., Hardarson, B. S., and Pearson, G., 2000. The Iceland plume in space and time: a Sr-Nd-Pb-Hf study of the North Atlantic rifted margin: Earth and Planetary Science Letters, 177, no. 3-4, p. 255-271.

Kerr, A. C., 1995. The melting processes and composition of the North Atlantic (Iceland) plume: Geochemical evidence from the early tertiary basalts: Journal of the Geological Society, 152, no. Part 6, p. 975-978.

Kerr, A. C., Marriner, G. F., Arndt, N. T., Tarney, J., Nivia, A., Saunders, A. D., and Duncan, R. A., 1996. The petrogenesis of Gorgona komatiites, picrites and basalts: New field, petrographic and geochemical constraints: Lithos, 37, no. 2-3, p. 245-260.

Kerr, A.C., Marriner, G., Tarney, J., Nivia, A., Saunders, A., Thirlwall, M., and Sinton, C., 1997a. Cretaceous Basaltic Terranes in western Columbia: elemental, chronological and Sr–Nd isotopic constraints on petrogenesis: Journal of Petrology, 38, no. 6, p. 677-702.

Kerr, A. C., Tarney, J., Marriner, G. F., Nivia, A., and Saunders, A. D., 1997b. The Caribbean-Colombian Cretaceous Igneous Province: The Internal Anatomy of an Oceanic Plateau: Large Igneous Provinces: Continental, Oceanic, and Planetary Flood Volcanism, p. 123-144.

Kerr, A. C., 1998. Oceanic plateau formation: a cause of mass extinction and black shale deposition around the Cenomanian–Turonian boundary?: Journal of the Geological Society, 155, no. 4, p. 619-626.

Kerr, A. C., White, R. , and Saunders, A. D., 2000. LIP reading: Recognizing oceanic plateaux in the geological record: Journal of Petrology, 41, no. 7, p. 1041-1056.

Kerr, A. C., Aspden, J. A., Tarney, J., and Pilatasig, L. F., 2002. The nature and provenance of accreted oceanic terranes in western Ecuador: geochemical and tectonic constraints: Journal of the Geological Society, 159, p. 577-594.

Kerr, A. C., White, R. , Thompson, P. M., Tarney, J., and Saunders, A. D., 2003. No oceanic plateau—No Caribbean plate? The seminal role of an oceanic plateau in Caribbean plate evolution: The circum-Gulf of Mexico and the Caribbean, p. 126-168.

Kerr, A. C., 2005. Oceanic LIPs: The kiss of death: Elements, 1, p. 289-292.

Kerr, A. C., and Mahoney, J. J., 2007. Oceanic plateaus: Problematic plumes, potential paradigms: Chemical Geology, 241, no. 3-4, p. 332-353.

Kerr, A. C., Pearson, D. G., and Nowell, G. M., 2009. Magma source evolution beneath the Caribbean oceanic plateau: new insights from elemental and Sr-Nd-Pb-Hf isotopic studies of ODP Leg 165 Site 1001 basalts, *in* James, K. H., Lorente, M. A., and Pindell, J. L., eds., The Origin and Evolution of the Caribbean Plate, Volume 328, Geological Society, London, Special Publication, p. 809-827.

Kerr, A. C., 2014. Oceanic plateaus. In: Holland, H.C. & Turekian K. (series eds.). Treatise on Geochemistry 2nd Edition, Volume 4, Rudnick, R. (ed.) The Crust. Chapter 18, pp. 631-667. Elsevier.

Kimura, G., and Ludden, J., 1995. Peeling oceanic crust in subduction zones: Geology, 23, p. 217-220.

Kimura, G., Sakakibara, M., and Okamura, M., 1994. Plumes in central Panthalassa? Deductions from accreted oceanic fragments in Japan: Tectonics, 13, no. 4, p. 905-916.

Kokelaar, P., 1986. Magma-water interactions in subaqueous and emergent basaltic: Bulletin of Volcanology, 48, no. 5, p. 275-289.

Korenaga, J., and Kelemen, P. B., 2000. Major element heterogeneity in the mantle source of the North Atlantic igneous province: Earth and Planetary Science Letters, 184, no. 1, p. 251-268.

Kroenke, L. W., 1974. Origin of continents through development and coalescence of oceanic flood basalt plateaus: EOS, 55, p. 443.

Kuroda, J., Ogawa, N. O., Tanimizu, M., Coffin, M. F., Tokuyama, H., Kitazato, H., and Ohkouchi, N., 2007a. Contemporaneous massive subaerial volcanism and late cretaceous Oceanic Anoxic Event 2: Earth and Planetary Science Letters, 256, no. 1, p. 211-223.

Kuroda, J., Ogawa, N. O., Tanimizu, M., Coffin, M. F., Tokuyama, H., Kitazato, H., and Ohkouchi, N., 2007b. Contemporaneous massive subaerial volcanism and late cretaceous Oceanic Anoxic Event 2: Earth and Planetary Science Letters, 256, no. 1-2, p. 211-223.

Kusky, T. M., Chow, J. S., and Bowring, S. A., 1997. Age and origin of the Boil Mountain ophiolite and Chain Lakes massif, Maine: Implications for the Penobscottian orogeny: Canadian Journal of Earth Sciences, 34, no. 5, p. 646-654.

Kvenvolden, K. A., 1993. Gas hydrates—geological perspective and global change: Reviews of Geophysics, 31, no. 2, p. 173-187.

Lapierre, H., Bosch, D., Tardy, M., and Struik, L. C., 2003. Late Paleozoic and Triassic plume-derived magmas in the Canadian Cordillera played a key role in continental crust growth: Chemical Geology, 201, no. 1-2, p. 55-89.

Lee, C. T. A., Luffi, P., Plank, T., Dalton, H., and Leeman, W. P., 2009. Constraints on the depths and temperatures of basaltic magma generation on Earth and other terrestrial planets using new thermobarometers for mafic magmas: Earth and Planetery Science Letters, 279, no. 1-2, p. 20-33.

Lin, S. C., and van Keken, P. E., 2006a. Dynamics of thermochemical plumes: 1. Plume formation and entrainment of a dense layer: Geochemistry, Geophysics, Geosystems, 7, no. 2.

Lin, S. C., and van Keken, P. E., 2006b, Dynamics of thermochemical plumes: 2. Complexity of plume structures and its implications for mapping mantle plumes: Geochemistry, Geophysics, Geosystems, 7, no. 3.

Loewen, M. W., Duncan, R. A., Kent, A. J., and Krawl, K., 2013. Prolonged plume volcanism in the Caribbean Large Igneous Province: new insights from Curaçao and Haiti: Geochemistry, Geophysics, Geosystems, 14, no. 10, p. 4241-4259.

Lytwyn, J., Casey, J., Gilbert, S., and Kusky, T., 1997. Arc-like mid-ocean ridge basalt formed seaward of a trench-forearc system just prior to ridge subduction: An example from subaccreted ophiolites in southern Alaska: Journal of Geophysical Research: Solid Earth, 102, no. B5, p. 10225-10243.

Madsen, J. K., Thorkelson, D. J., Friedman, R. M., and Marshall, D. D., 2006. Cenozoic to Recent plate configurations in the Pacific Basin: Ridge subduction and slab window magmatism in western North America: Geosphere, 2, no. 1, p. 11-34.

Mahoney, J. J., 1987. An isotopic survey of Pacific oceanic plateaus: Implications for their nature and origin, Volume 43, p. 207-220.

Mahoney, J. J., Fitton, J. G., Wallace, P. J., and al., e., 2001. Proceedings of the Ocean Drilling Program, Initial Reports, College Station, Texas, Ocean Drilling Program, 75.

Mahoney, J. J., Storey, M., Duncan, R. A., Spencer, K. J., and Pringle, M., 1993a. Geochemistry and age of the Ontong Java Plateau, *in* Pringle, M. S., ed., The Mesozoic Pacific: Geology, Tectonics and Volcanism, Volume Geophysical Monograph 77, American Geophysical Union, p. 233-261.

Mahoney, J. J., Storey, M., Duncan, R. A., Spencer, K. J., and Pringle, M., 1993b. Geochemistry and geochronology of Leg 130 basement lavas: nature and origin of the Ontong Java Plateau, *in* Berger, W. H., Kroenke, L. W., and Mayer, L. A., eds., Proceedings of the Ocean Drilling Program, Scientific Results, Volume 130: College Station, TX, Ocean Drilling Program, Texas A&M University, p. 3-22.

Maluski, H., Coulon, C., Popoff, M., and Baudin, P., 1995. Ar-40/Ar-39 chronology, petrology and geodynamic setting of Mesozoic to early Cenozoic magmatism from the Benue Trough, Nigeria: Journal of the Geological Society, 152, no. Part 2, p. 311-326.

Maluski, H., Monié, P., Kienast, J., and Rahmani, A., 1990. Location of extraneous argon in granulitic-facies minerals: A paired microprobe-laser probe 40Ar39Ar analysis: Chemical Geology: Isotope Geoscience section, 80, no. 3, p. 193-217.

Mark, D., Barfod, D., Stuart, F., and Imlach, J., 2009. The ARGUS multicollector noble gas mass spectrometer: Performance for 40Ar/39Ar geochronology: Geochemistry, Geophysics, Geosystems, 10, no. 10.

Massey, N. W. D., 1986. Metchosin Igneous Complex, southern Vancouver Island - ophiolite stratigraphy developed in an emergent island setting: Geology, 14, no. 7, p. 602-605.

McCrory, P. A., and Wilson, D. S., 2013. A kinematic model for the formation of the Siletz-Crescent forearc terrane by capture of coherent fragments of the Farallon and Resurrection plates: Tectonics, 32, no. 3, p. 718-736.

McDonough, W. F., 2001. The composition of the Earth: International Geophysics, 76, p. 3-23.

McDonough, W. F., and Sun, S.-s., 1995. The composition of the earth: Chem. Geol., 120, p. 223-253.

McInerney, F. A., and Wing, S. L., 2011. The Paleocene-Eocene thermal maximum: a perturbation of carbon cycle, climate, and biosphere with implications for the future: Annual Review of Earth and Planetary Sciences, 39, p. 489-516.

McLaughlin, R. J., 2009. The Wheatfield Fork terrane: A remnant of Siletzia in Franciscan Complex Coastal Belt of northern California, *in* Proceedings 2009 Portland GSA Annual Meeting 2009.

Miura, S., Suyehiro, K., Shinohara, M., Takahashi, N., Araki, E., and Taira, A., 2004. Seismological structure and implications of collision between the Ontong Java Plateau and Solomon Island Arc from ocean bottom seismometer-airgun data: Tectonophysics, 389, no. 3-4, p. 191-220.

Moghadam, H. S., Stern, R. J., and Rahgoshay, M., 2010. The Dehshir ophiolite (central Iran): Geochemical constraints on the origin and evolution of the Inner Zagros ophiolite belt: Geological Society of America Bulletin, p. B30066. 30061.

Moothart, S. R., 1992. Geology of the middle and upper Eocene McIntosh Formation and adjacent volcanic and sedimentary rock units, Willapa Hills, Pacific County, southwest Washington.

Morsi, A.-M. M., Speijer, R. P., Stassen, P., and Steurbaut, E., 2011. Shallow marine ostracode turnover in response to environmental change during the Paleocene–Eocene thermal maximum in northwest Tunisia: Journal of African Earth Sciences, 59, no. 2, p. 243-268.

Mullen, E. K, Weis, D., Marsh, N., and Martindale, M., 2017. Primitive arc magma diversity: New geochemical insights in the Cascade Arc: Chemical Geology, 448, p. 43-70.

Mullen, E. K., and Weis, D., 2013. Sr-Nd-Hf-Pb isotope and trace element evidence for the origin of alkalic basalts in the Garibaldi Belt, northern Cascade arc: Geochemistry, Geophysics, Geosystems, 14, no. 8, p. 3126-3155.

Mullen, E. K., and McCallum, I. S., 2014. Origin of basalts in a hot subduction setting: petrological and geochemical insights from Mt. Baker, Northern Cascade Arc: Journal of Petrology, 55, no. 2, p. 241-281.

Muller, J., 1980. Chemistry and origin of the Eocene Metchosin Volcanics, Vancouver Island, British Columbia: Canadian Journal of Earth Sciences, 17, no. 2, p. 199-209.

Müller, R. D., Royer, J. Y., and Lawver, L. A., 1993. Revised plate motions relative to the hotspots from combined Atlantic and Indian Ocean hotspot tracks: Geology, 16, p. 275-278.

Murphy, J. B., Hynes, A. J., Johnston, S. T., and Keppie, J. D., 2003. Reconstructing the ancestral Yellowstone plume from accreted seamounts and its relationship to flat-slab subduction: Tectonophysics, 365, no. 1-4, p. 185-194.

Newbury, D. E., and Ritchie, N. W. M., 2012. Is Scanning Electron Microscopy/Energy Dispersive X-ray Spectrometry (SEM/EDS) Quantitative?: Scanning, 35, no.3, p. 141-168.

Nobre Silva, I. G., Weis, D., and Scoates, J. S., 2013. Isotopic systematics of the early Mauna Kea shield phase and insight into the deep mantle beneath the Pacific Ocean: Geochemistry, Geophysics, Geosystems, 14, no. 3, p. 659-676.

O'Hara, M. J., 1965. Primary magmas and the origin of basalts: Scottish Journal of Geology., 1, no. 1, p. 19-40.

O'Neill, C., Muller, D., and Steinberger, B., 2005. On the uncertainties in hot spot reconstructions and the significance of moving hot spot reference frames - art. no. Q04003: Geochem Geophys Geosyst, 6, p. 4003.

Obrebski, M., Allen, R. M., Xue, M., and Hung, S. H., 2010. Slab-plume interaction beneath the Pacific Northwest: Geophysical Research Letters, 37, no. 14.

Pagani, M., Caldeira, K., Archer, D., and Zachos, J. C., 2006. An ancient carbon mystery: Science, 314, no. 5805, p. 1556.

Pallister, J. S., Budahn, J. R., and Murchey, B. L., 1989. Pillow Basalts of the Angayucham Terrane - Oceanic Plateau and Island Crust Accreted to the Brooks Range: Journal of Geophysical Research: Solid Earth and Planets, 94, no. B11, p. 15901-15923.

Parsons, T., Wells, R. E., Fisher, M. A., Flueh, E., and ten Brink, U. S., 1999. Three-dimensional velocity structure of Siletzia and other accreted terranes in the Cascadia forearc of Washington: Journal of Geophysical Research: Solid Earth, 104, no. B8, p. 18015-18039.

Pearce, J. A., 1996. A user's guide to basalt discrimination diagrams, *in* Wyman, D. A., ed., Trace Element Geochemistry of Volcanic Rocks: Applications for Massive Sulphide Exploration, Volume Geological Association of Canada, Short Course Notes, 12, p. 79-113.

Pearce, J. A., 2008. Geochemical fingerprinting of oceanic basalts with applications to ophiolite classification and the search for Archean oceanic crust: Lithos, 100, no. 1, p. 14-48.

Pearce, J. A., Ernewein, M., Bloomer, S. H., Parson, L. M., Murton, B. J., and Johnson, L. E., 1994. Geochemistry of Lau Basin volcanic rocks: influence of ridge segmentation and arc proximity: Geological Society, London, Special Publications, 81, no. 1, p. 53-75.

Perry, S., Garver, J., and Ridgway, K., 2009. Transport of the Yakutat terrane, southern Alaska: Evidence from sediment petrology and detrital zircon fission-track and U/Pb double dating: The Journal of Geology, 117, no. 2, p. 156-173.

Pertermann, M., and Hirschmann, M. M., 2003. Partial melting experiments on a MORB-like pyroxenite between 2 and 3 GPa: Constraints on the presence of pyroxenite in basalt source regions from solidus location and melting rate - art. no. 2125: Journal of Geophysical Research: Solid Earth, 108, no. B2, p. 2125.

Petterson, M. G., 2004. The geology of north and central Malaita, Solomon Islands: the thickest and most accessible part of the world's largest (Ontong Java) ocean plateau, *in* Fitton, J. G., Mahoney, J. J., Wallace, P. J., and Saunders, A. D., eds., Origin and evolution of the Ontong Java Plateau, Geological Society of London, Special Publication, 229, 63-81.

Petterson, M. G., Neal, C. R., Mahoney, J. J., Kroenke, L. W., Saunders, A. D., Babbs, T. L., Duncan, R. A., Tolia, D., and McGrail, B., 1997. Structure and deformation of north and central Malaita, Solomon Islands: tectonic implications for the Ontong Java Plateau Solomon arc collision, and for the fate of oceanic plateaus: Tectonophysics, 283, no. 1-4, p. 1-33.

Phillips, W., Walsh, T., and Mumford, D., 1989. Relationship between the Grays River Volcanics of southwest Washington and the Tillamook Volcanics of northwest Oregon: Eos, Transations of the American Geophysical Union, 70, p. 137.

Pierce, K. L., and Morgan, L. A., 1992. Chapter 1: The track of the Yellowstone hot spot: Volcanism, faulting, and uplift, Volume 179, p. 1-53.

Pierce, K. L., and Morgan, L. A., 2009. Is the track of the Yellowstone hotspot driven by a deep mantle plume? — Review of volcanism, faulting, and

uplift in light of new data: Journal of Volcanology and Geothermal Research, 188, no. 1–3, p. 1-25.

Pierce, K. L., Morgan, L. A., and Saltus, R. W., 2000. Yellowstone plume head: Postulated tectonic relations to the Vancouver slab, continental boundaries, and climate, Citeseer.

Presnall, D. C., Dixon, J. R., O'Donnell, T. H., and Dixon, S. A., 1979. Generation of mid-ocean ridge tholeiites: Journal of Petrology., 20, no. 1, p. 3-35.

Putirka, K., 2008. Excess temperatures at ocean islands: Implications for mantle layering and convection: Geology, 36, no. 4, p. 283-286.

Pyle, D., Duncan, R., Wells, R., Graham, D., Hanan, B., Harrison, B., and Haileab, B., 2015. Longevity of Yellowstone hotspot volcanism: Isotopic evidence linking the Siletzia LIP (56 Ma) and early Columbia River Basalt Group (17 Ma) mantle sources, *in* Proceedings AGU Fall Meeting Abstracts 2015.

Pyle, D. G., 1988. Geochemical evolution of the Roseburg formation basaltic rocks, southern Oregon coast range.

Pyle, D. G., Duncan, R. A., Wells, R. E., Graham, D. W., Harrison, B., and Hanan, B., 2009. Siletzia: An oceanic large igneous province in the Pacific Northwest, *in* Proceedings of Portland GSA Annual Meeting 2009.

Ramp, L., 1972. Geology & Mineral Resources of Douglas County, Oregon, State of Oregon, Dept. of Geology and Mineral Industries.

Rau, W. W., 1981. Pacific Northwest Tertiary benthic foraminiferal biostratigraphic framework—An overview: Geological Society of America Special Papers, 184, p. 67-84.

Reagan, M. K., Ishizuka, O., Stern, R. J., Kelley, K. A., Ohara, Y., Blichert-Toft, J., Bloomer, S. H., Cash, J., Fryer, P., and Hanan, B. B., 2010. Fore-arc basalts and subduction initiation in the Izu-Bonin-Mariana system: Geochemistry, Geophysics, Geosystems, 11, no. 3.

Rivers, T., and Corrigan, D., 2000. Convergent margin on southeastern Laurentia during the Mesoproterozoic: tectonic implications: Canadian Journal of Earth Sciences, 37, no. 2-3, p. 359-383.

Rogers, G. C., 1982. Oceanic plateaus as meteorite impact signatures: Nature, 299, p. 341-342.

Rollinson, H., 1993. Using geochemical data, Longman, London, p. 352.

Roth, J. B., Fouch, M. J., James, D. E., and Carlson, R. W., 2008. Three-dimensional seismic velocity structure of the northwestern United States: Geophysical Research Letters, 35, no. 15.

Rudnick, R., and Gao, S., 2003. Composition of the continental crust: Treatise on geochemistry, 3, p. 1-64.

Ryu, I. C., Niem, A. R., and Niem, W. A., 1992. Schematic fence diagram of the southern Tyee basin, Oregon Coast Range, showing stratigraphic relationships of exploration wells to surface measured sections, State of Oregon, Department of Geology and Mineral Industries.

Sager, W. W., Kim, J., Klaus, A., Nakanishi, M., and Khankishieva, L. M., 1999. Bathymetry of Shatsky Rise, northwest Pacific Ocean: Implications for ocean plateau development at a triple junction: Journal of Geophysical Research Solid Earth, 104, no. B4, p. 7557-7576.

Salters, J., Mallick, S., Hart, S. R., Langmuir, C. E., and Stracke, A., 2011. Domains of depleted mantle: New evidence from hafnium and neodymium isotopes: Geochemistry, Geophysics, Geosystems, 12, no. 8.

Schmandt, B., and Humphreys, E., 2011. Seismically imaged relict slab from the 55 Ma Siletzia accretion to the northwest United States: Geology, 39, no. 2, p. 175-178.

Schmidt, M. E., Grunder, A. L., and Rowe, M. C., 2008. Segmentation of the Cascade Arc as indicated by Sr and Nd isotopic variation among diverse primitive basalts: Earth and Planetary Science Letters, 266, no. 1, p. 166-181.

Schutt, D. L., Dueker, K., and Yuan, H., 2008. Crust and upper mantle velocity structure of the Yellowstone hot spot and surroundings: Journal of Geophysical Research: Solid Earth, 113, no. B3.

Seligman, A. N., Bindeman, I. N., McClaughry, J., Stern, R. A., and Fisher, C., 2014. The earliest low and high $\delta18O$ caldera-forming eruptions of the Yellowstone plume: implications for the 30–40 Ma Oregon calderas and

speculations on plume-triggered delaminations: Frontiers in Earth Science, 2, p. 34.

Sepkoski, J. J., 1996. Patterns of Phanerozoic extinction: a perspective from global data bases, Global events and event stratigraphy in the Phanerozoic, Springer, p. 35-51.

Seton, M., Müller, R. D., Zahirovic, S., Gaina, C., Torsvik, T., Shephard, G., Talsma, A., Gurnis, M., Turner, M., Maus, S., and Chandler, M., 2012. Global continental and ocean basin reconstructions since 200 Ma: Earth-Science Reviews, 113, no. 3-4, p. 212-270.

Shaw, D. M., 1970. Trace element fractionation during anatexis: Geochimica et Cosmochimica Acta, 34, no. 2, p. 237-243.

Sheth, H. C., 2007. Large Igneous Provinces (LIPs): Definition, recommended terminology, and a hierarchical classification: Earth Science Reviews, 85, no. 3-4, p. 117-124.

Simpson, R. W., and Cox, A., 1977. Paleomagnetic evidence for tectonic rotation of the Oregon Coast Range: Geology, 5, no. 10, p. 585-589.

Sinton, C. W., and Duncan, R. A., 1997. Potential links beween ocean plateau volcanism and global ocean anoxia at the Cenomanian-Turonian boundary: Economic Geology, 92, p. 836-842.

Sinton, J., 1997. The Manus Spreading Center near 3 degrees 22'S and the Worm Garden hydrothermal site: results of Mir2 submersible dive 15: Mar Geology, 142, no. 1-4, p. 207-209.

Snavely, P., 1987. Tertiary geologic framework, neotectonics, and petroleum potential of the Oregon-Washington continental margin.

Snavely, P. D., MacLeod, N. S., and Wagner, H. C., 1968. Tholeiitic and alkalic basalts of the Eocene Siletz River volcanics, Oregon coast range: American Journal of Science, 266, no. 6, p. 454-481.

Snavely, P. D., Wagner, H. C., and Lander, D. L., 1980. Interpretation of the Cenozoic geologic history, central Oregon continental margin: Cross-section summary: Geological Society of America Bulletin, 91, no. 3, p. 143-146.

Sobolev, A. , Hofmann, A. W., Kuzmin, D. , Yaxley, G. M., Arndt, N. T., Chung, S.-L., Danyushevsky, L. , Elliott, T., Frey, F. A., and Garcia, M. O., 2007. The amount of recycled crust in sources of mantle-derived melts: Science, 316, no. 5823, p. 412-417.

Sobolev, A. , Hofmann, A. W., Sobolev, S. , and Nikogosian, I. K., 2005. An olivine-free mantle source of Hawaiian shield basalts: Nature, 434, no. 7033, p. 590-597.

Spencer, P. K., 1984. Lower tertiary biostratigraphy and paleoecology of the Quilcene-Discovery Bay area, northeast Olympic Peninsula, Washington.

Squires, R. L., Goedert, J. L., and Kaler, K. L., 1992. Paleontology and stratigraphy of Eocene rocks at Pulali Point, Jefferson County, eastern Olympic Peninsula, Washington, Washington State Department of Natural Resources, Division of Geology and Earth Resources.

Stern, R. J., 2004. Subduction initiation: spontaneous and induced: Earth and Planetary Science Letters, 226, no. 3-4, p. 275-292.

Stern, R. J., and Bloomer, S. H., 1992. Subduction Zone Infancy - Examples from the Eocene Izu-Bonin-Mariana and Jurassic California Arcs: Geological Society of America Bulletin, 104, no. 12, p. 1621-1636.

Stern, R. J., and Scholl, D. W., 2010. Yin and yang of continental crust creation and destruction by plate tectonic processes: International Geology Review, 52, no. 1, p. 1-31.

Stracke, A., 2012. Earth's heterogeneous mantle: A product of convection-driven interaction between crust and mantle: Chemical Geology, 330, p. 274-299.

Swanson, D. A., Cameron, K. A., Evarts, R. C., Pringle, P. T., and Vance, J. A., 1989. Cenozoic volcanism in the Cascade Range and Columbia Plateau, southern Washington and northernmost Oregon: New Mexico Bureau of Mines and Mineral Resources Memoir, 47, p. 50.

Tabor, R. W., and Cady, W. M., 1978. The structure of the Olympic Mountains, Washington: Analysis of a subduction zone, US Govt. Print. Off.

Tabor, R. W., Haugerud, R. A., Haeussler, P. J., and Clark, K. P., 2011. Lidar-revised Geologic Map of the Wildcat Lake 7.5' Quadrangle, Kitsap and

Mason Counties, Washington, US Department of the Interior, US Geological Survey.

Tardy, M., Lapierre, H., Struik, L. C., Bosch, D., and Brunet, P., 2001. The influence of mantle plume in the genesis of the Cache Creek oceanic igneous rocks: implications for the geodynamic evolution of the inner accreted terranes of the Canadian Cordillera: Canadian Journal of Earth Sciences, 38, no. 4, p. 515-534.

Tejada, M. L. G., Mahoney, J. J., Duncan, R. A., and Hawkins, M. P., 1996. Age and geochemistry of basement and alkalic rocks of Maliata and Santa Isabel, Solomon Islands, southern margin of Ontong Java Plateau: Journal of Petrology, 37, p. 361-394.

Tejada, M. L. G., Mahoney, J. J., Neal, C. R., Duncan, R. A., and Petterson, M. G., 2002. Basement geochemistry and geochronology of central Malaita, Solomon islands, with implications for the origin and evolution of the Ontong Java Plateau: Journal of Petrology, 43, no. 3, p. 449-484.

Ten Brink, U., Molzer, P., Fisher, M., Blakely, R., Bucknam, R., Parsons, T., Crosson, R., and Creager, K., 2002. Subsurface geometry and evolution of the Seattle fault zone and the Seattle basin, Washington: Bulletin of the Seismological Society of America, 92, no. 5, p. 1737-1753.

Tetreault, J., and Buiter, S., 2014. Future accreted terranes: a compilation of island arcs, oceanic plateaus, submarine ridges, seamounts, and continental fragments: Journal of Geophysical Research: Solid Earth, 5, no. 2, p. 1243.

Thomas, D. J., Bralower, T. J., and Jones, C. E., 2003. Neodymium isotopic reconstruction of late Paleocene–early Eocene thermohaline circulation: Earth and Planetary Science Letters, 209, no. 3–4, p. 309-322.

Thomas, E., 2007. Cenozoic mass extinctions in the deep sea: What perturbs the largest habitat on Earth?: Special Papers-Geological Society of America, 424, p. 1.

Thompson, P. M., Kempton, P. D., and Kerr, A. C., 2008. Evaluation of the effects of alteration and leaching on Sm–Nd and Lu–Hf systematics in submarine mafic rocks: Lithos, 104, no. 1, p. 164-176.

Thompson, R., 1982. Magmatism of the British Tertiary volcanic province: Scottish Journal of Geology, 18, no. 1, p. 49-107.

Thorkelson, D. J., 1996. Subduction of diverging plates and the principles of slab window formation: Tectonophysics, 255, no. 1-2, p. 47-63.

Thorkelson, D. J., Mortensen, J. K., Marsden, H., and Taylor, R. R., 1995. Age and tectonic setting of Early Jurassic episodic volcanism along the northeastern margin of the Hazelton Trough, northern British Columbia: Geological Society of America Special Papers, 299, p. 83-94.

Thorkelson, D. J., and Taylor, R. P., 1989. Cordilleran slab windows: Geology, 17, p. 833-836.

Timm, C., Hoernle, K., Werner, R., Hauff, F., den Bogaard, P. , Michael, P., Coffin, M. F., and Koppers, A., 2011. Age and geochemistry of the oceanic Manihiki Plateau, SW Pacific: New evidence for a plume origin: Earth and Planetary Science Letters, 304, no. 1-2, p. 135-146.

Timpa, S., 2000. The geological history of the Metchosin Igneous Complex: University of Victoria.

Trehu, A. M., Asudeh, I., Brocher, T. M., Luetgert, J. H., Mooney, W. D., Nabelek, J. L., and Nakamura, Y., 1994. Crustal Architecture of the Cascadia Forearc: Science, 266, no. 5183, p. 237-243.

Vogt, K., and Gerya, T. , 2014. From oceanic plateaus to allochthonous terranes: Numerical Modelling: Gondwana Research 25, p. 494-508.

Vogt, P. R., 1989. Volcaniogenic upwelling of anoxic, nutrient-rich water: A possible factor in carbonate-bank /reef demise and benthic faunal extinctions: Geological Society of America Bulletin., 101, p. 1225-1245.

Waite, G. P., Schutt, D. L., and Smith, R. B., 2005. Models of lithosphere and asthenosphere anisotropic structure of the Yellowstone hot spot from shear wave splitting - art. no. B11304: Journal of Geophysical Research: Solid Earth, 110, no. B11, p. 11304.

Walter, M. J., 1998. Melting of garnet peridotite and the origin of komatiite and depleted lithosphere: Journal of Petrology, 39, no. 1, p. 29-60.

Weaver, C. E., 1937. Tertiary stratigraphy of western Washington and northwestern Oregon, University of Washington, 1.

Weaver, B.L., 1991. The origin of ocean island basalt end-member compositions: trace element and isotopic constraints: Earth and Planetary Science Letters 104, 381–397.

Wells, R., Bukry, D., Friedman, R., Pyle, D., Duncan, R., Haeussler, P., and Wooden, J., 2014. Geologic history of Siletzia, a large igneous province in the Oregon and Washington Coast Range: Correlation to the geomagnetic polarity time scale and implications for a long-lived Yellowstone hotspot: Geosphere, 10, no. 4, p. 692-719.

Wells, R., Engebretson, D., Snavely, P., and Coe, R., 1984. Cenozoic plate motions and the volcano-tectonic evolution of western Oregon and Washington: Tectonics, 3, no. 2, p. 275-294.

Wells, R. E., 1981. Geologic map of the eastern Willapa Hills, Cowlitz, Lewis, Pacific, and Wahkiakum counties, Washington, 2331-1258.

Wells, R. E., 1994, Geologic Map of the Tillamook Highlands, Northwest Oregon Coast Range (Tillamook, Nehalem, Enright, Timber, Fairdale, and Blaine 15 Minute Quadrangles), US Geological Survey.

Wells, R. E., Jayko, A. S., Niem, A., Black, G. L., Wiley, T. J., Baldwin, E., Molenaar, K., Wheeler, K., DuRoss, C., and Givler, R., 2000. Geologic map and database of the Roseburg 30 x 60 quadrangle, Douglas and Coos counties, Oregon, US Department of the Interior, US Geological Survey.

Wells, R. E., and Sawlan, M. G., 2014. Preliminary geologic map of the eastern Willapa Hills, Cowlitz, Lewis, and Wahkiakum Counties, Washington: US Geological Survey, 2331-1258.

Wells, R. E., Weaver, C. S., and Blakely, R. J., 1998. Fore-arc migration in Cascadia and its neotectonic significance: Geology, 26, no. 8, p. 759-762.

Weis, D., Frey, F.A., 2002. Submarine basalts of the northern Kerguelen Plateau: Interaction between the Kerguelen Plume and the Southeast Indian Ridge revealed at ODP Site 1140. Journal of Petrology 43 (7), 1287–1309.

Weis, D., Frey, F.A., Schlich, R., Schaming, M., Montigny, R., Damasceno, D., Mattielli, N.,

Nicolaysen, K.E., Scoates, J.S., 2002. Trace of the Kerguelen mantle plume: evidence from seamounts between the Kerguelen Archipelago and Heard Island, Indian Ocean. Geochemistry, Geophysics, Geosystems, 3, 6. http://dx.doi.org/10.1029/ 2001GC000251.

Weis, D., Garcia, M.O., Rhodes, J.M., Jellinek, M., Scoates, J.S., 2011. Role of the deep mantle in generating the compositional asymmetry of the Hawaiian mantle plume. Nature Geoscience 4 (12), 831–838.

Westerhold, T., Röhl, U., and Laskar, J., 2012. Time scale controversy: Accurate orbital calibration of the early Paleogene: Geochemistry, Geophysics, Geosystems, 13, no. 6.

Westerhold, T., Röhl, U., McCarren, H. K., and Zachos, J. C., 2009. Latest on the absolute age of the Paleocene–Eocene Thermal Maximum (PETM): new insights from exact stratigraphic position of key ash layers+ 19 and− 17: Earth and Planetary Science Letters, 287, no. 3, p. 412-419.

Whattam, S. A., and Stern, R. J., 2011. The 'subduction initiation rule': a key for linking ophiolites, intra-oceanic forearcs, and subduction initiation: Contributions to Mineralogy and Petrology, 162, no. 5, p. 1031-1045.

White, W. M., and Patchett, P. J., 1984. Hf-Nd-Sr isotopes and incompatible element abundances in island arcs: Implications for magma origins and crust-mantle evolution: Earth and Planetary Science Letters., 7, p. 167-185.

Willbold, M., and Stracke, A., 2006. Trace element composition of mantle end-members: Implications for recycling of oceanic and upper and lower continental crust: Geochemistry Geophysics Geosystems, 7.

Williams, H., and McBirney, A. R., 1979. Volcanology, San Francisco, California, Freeman, Cooper and Co.

Winterer, E., 1976. Anomalies in the tectonic evolution of the Pacific, *in* Sutton, G., Manghnani, M., and Moberly, R., eds., The Geophysics of the Pacific Ocean Basin and its Margins: Washington, D.C., AGU, p. 269-278.

Winterer, E., Lonsdale, P., Matthews, J., and Rosendahl, B., 1974. Structure and acoustic stratigraphy of the Manihiki Plateau: Deep-Sea Res., 21, p. 793-814.

Wolff, J., Ramos, F., Hart, G., Patterson, J., and Brandon, A., 2008. Columbia River flood basalts from a centralized crustal magmatic system: Nature geoscience, 1, no. 3, p. 177-180.

Workman, R. K., and Hart, S. R., 2005. Major and trace element composition of the depleted MORB mantle (DMM): Earth and Planetary Science Letters, 231, no. 1-2, p. 53-72.

Worthington, L. L., Van Avendonk, H. J., Gulick, S. P., Christeson, G. L., and Pavlis, T. L., 2012. Crustal structure of the Yakutat terrane and the evolution of subduction and collision in southern Alaska: Journal of Geophysical Research: Solid Earth (1978–2012), 117, no. B1.

Xue, M., and Allen, R. M., 2007. The fate of the Juan de Fuca plate: Implications for a Yellowstone plume head: Earth and Planetary Science Letters, 264, no. 1, p. 266-276.

Yorath, C. J., Sutherland Brown, A., and Massey, N. W. D., 1999. Lithoprobe, southern Vancouver Island, British Columbia: geology; With contributions by TDJ England, RM Bustin, Ottawa.

Zachos, J., Pagani, M., Sloan, L., Thomas, E., and Billups, K., 2001. Trends, rhythms, and aberrations in global climate 65 Ma to present: Science, 292, no. 5517, p. 686-693.

APPENDIX A – WHOLE ROCK LABORATORY METHODS USED IN THIS STUDY

A.1 Major and Trace element analysis

A.1.1 Preparation of rock samples into powder

Rock samples were prepared into powder using the rock preparation facilities at Cardiff University. Weathered surfaces, veins and alteration patches were removed from the rock samples using a diamond-bladed rock saw. Samples were then crushed to a coarse grit by a steel jaw crusher. Approximately 80 ml of each sample was reduced to a fine powder in an agate ball mill. Afterwards, approximately 2 g of each powdered sample was ignited for two hours in a furnace at 900°C to drive off volatile substances and determine loss on ignition (LOI) values. The LOI of a sample was calculated using the following equation (Equation A.1):

Equation A1 $\quad LOI\ (wt.\%) =$

$$\frac{Mass\ of\ wet\ powder - Mass\ of\ ignited\ powder}{Mass\ of\ wet\ powder}\ x100$$

A.2 Preparation of solutions for ICP-OES and ICP-MS

Samples in this study were prepared for ICP analysis using the lithium metaborate fusion method. To prepare the samples, 0.1 ± 0.001 g of each ignited sample was mixed with 0.6 ± 0.004 g of lithium metaborate flux in a platinum crucible. A few drops of lithium iodide wetting agent were added to each mixture which was then fused using the Claisse Fluxy automated fusion system. After the mixture was then dissolved in a 50 ml solution of 20 ml of 10% HNO3 and 30 ml of 18.2 Ω deionised water obtained using a Milli-Q purification system. After the mixture had fully dissolved, 1 ml of 100 ppm Rh spike was added to the solution

which was then made up to 100 ml with 18.2 Ω deionised water. Approximately 20 ml of each solution was run on ICP-OES to obtain major element and some trace element abundances. An aliquot of 1 ml of each solution was added to 1 ml of In and Tl and 8 ml of 2% HNO3 and run on the ICP-MS to obtain trace element abundances. The instruments at Cardiff University used to analyse elemental abundances are a Jobin Yvon Horiba Ultima 2 ICP-OES and a Thermo Elemental X7 series ICP-MS. The samples were run on the mass spectrometers by Dr. Iain McDonald.

A.1.3 Evaluation of the accuracy and precision of the geochemical data

A.1.3.1 Standards

In order to assess the accuracy and precision of the whole rock elemental data obtained by ICP-OES and ICP-MS, external and internal standards were analysed. The external standards used were JB1-A and MRG1. JB1-A is a basalt issued by the Geological Survey of Japan with certified element values published in Imai et al. (1995). MRG1 is a gabbro standard issued by the Canadian Certified Reference Materials Project of CANMET's Mining and Mineral Sciences Laboratories with values reported in Abbey (1981). These three standards were run in every batch of samples analysed mainly to assess the accuracy of the results but also to help determine the precision of the results. Three internal standards were also run in every sample batch. JB1-A was run with every batch of samples and were used to assess the accuracy and precision of the elemental data.

A.1.3.2 Accuracy

All of the results from the different runs of standards are given in tables B1 & 2 along with percentage errors of the measured values compared to certified values. The % errors for all elements in the standards are given in Appendix E3. The percentage error for each element was calculated using the following equation (Equation A2):

$$\%error = \frac{Difference\ between\ measured\ and\ certified\ concentrations\ of\ element}{Certified\ concentration\ of\ element}\ x100$$

 Equation A.2

A.1.3.3 Precision

The precision of the elemental data can be determined by examining the multiple analyses of the external and internal standards. The precision of a standard sample with respect to each element is represented by the relative

standard deviation (RSD). The RSD is a percentage value and is calculated for each element using equations A3 through A5 below.

The RSD for all the elements in the standards are given in Appendix E3.

Equation A3
$$x_\alpha = \frac{\sum x}{n}$$

Where x_α is the average element concentration, x is the element concentration and n is the number of measurements.

Equation A4
$$s = \frac{\sqrt{\sum(x-x_\alpha)^2}}{n-1}$$

Where s is the standard deviation.

Equation A5
$$RSD\ (\%) = \frac{100s}{x_\alpha}$$

A.2 Sr-Nd-Pb-Hf isotopic analysis

A.2.1. Sample selection and initial preparation

Care was taken in sample selection to choose the least altered samples that were representative of all of the Siletz terrane. This was achieved by examining polished thin sections the major and trace element chemistry of all the rocks samples. Samples were initially cut using a diamond-bladed mechanical rock saw to remove any weathered surfaces. The samples were then crushed to a coarse grit

using a steel jaw crusher and ground into a fine powder using an agate planetary ball mill. The initial preparation steps were conducted at Cardiff University.

A.2.2 Preparation for Sr-Nd-Pb isotopic analyses

A.2.2.1 Leaching

Chemical separations and mass spectrometric analysis were conducted in Class 100 laminar flow hoods in the Class 1,000 clean laboratories at the Pacific Centre for Isotope and Geochemical Research at the University of British Columbia. Leaching was carried out prior to digestion as most samples show prehnite-pumpellyite to greenschist grade alteration and have LOI values between 0.5 and 2.0 %. The leaching procedures are described in detail in Nobre Silva et al. (2009). For each sample around 250 mg of rock powder was weighed out and then leached. Leaching the sample acts to remove secondary phases from slightly altered rocks and was achieved by adding ~ 5ml of 6N HCL to each sample before ultrasonicating for 20 minutes. After each ultrasonication, the acid leachate was removed and discarded and ~ 5ml of new HCL was added to the sample. This was repeated until the liquid was transparent, ~ 10 cycles for each sample, with an additional final two cycles where H_2O was added in place of the HCL. The samples were then placed on a hotplate at around 110 °C for 30 minutes to dry down. The remaining powder was then weighed.

A.2.2.2 Digestion

For each sample around 100 mg of rock powder was digested in sub-boiled HF and HNO_3 in 15 ml savillex beakers on a hotplate for around 48 hours at 130 °C. The samples were subsequently dried down, 6N HCl added and fluxed for 24 hours, as outlined in Weis et al. (2006).

A.2.2.3 Chemical separation

Pb, Sr, Hf and Nd were separated from single powder dissolutions by sequential ion exchange column chemistry, having passed through the Pb columns twice to ensure purity. Full details on the procedures are given in (Weis et al. (2007); 2006). For the chemical separation of Pb all acids used are sub-boiled, while quartz distilled acids are used for other elements where stipulated. Initially 1.8 ml of 0.5N HBr was added to each sample, before being fluxed on a hotplate for 30 minutes and subsequently ultrasonicated for 30 minutes. Samples were then centrifuged for 6 minutes at 500 rpm. Then following the procedures of Weis et al., (2006; 2007) Pb were separated first on columns of Biorad AG1-X8 resin with two sequential passes to ensure purification of Pb. Sr was then separated from the REE and HFSE by cation exchange using Bio- rad AG50-X8 resin. Nd was then separated from the other REE using HDEHP-coated Teflon resin. Hf separations were conducted using Todga resin following a method modified after Connelly et al. (2006). 30 microliters of concentrated sub boiled HNO_3 was added to the cuts before analyses.

A.2.2.4 Mass spectrometric analysis

Pb, Hf, and Nd isotopic ratios were measured on a Nu Plasma MC-ICP-MS 1700 or Nu Plasma II MC-ICP-MS instrument and Sr isotopic ratios were measured on a Triton TIMS instrument following procedures described by Weis et al. (2006). Along with the 20 samples selected an in house standard, Kil-93 also underwent leaching, column chemical separation and analysis. The results of this along with duplicates and replicates analysed can be found in Appendix E4. Repeat analysis of the in-house Kil-93 reference materials gave RSD values of < 5% and mean concentrations within 10% of accepted values.

External reproducibilities were determined by repeat standard analyses and are reported as 2σ, where σ is the standard deviation calculated on the mean of individual analyses. Re- ported Sr isotope ratios were corrected for mass fractionation using $^{86}Sr/^{88}Sr = 0.1194$ and data were normalized to $^{87}Sr/^{86}Sr = 0.710248$ for the SRM987 standard (Weis et al., 2006) using wheel averages. The

2σ external reproducibility of SRM987 ranged from 13 to 33 ppm on a per-wheel basis. Reported Nd isotope ratios were corrected for mass fractionation using $^{146}Nd/^{144}Nd = 0.7219$ and normalized to $^{143}Nd/^{144}Nd = 0.511973$ for the Rennes standard (Chauvel and Blichert-Toft, 2001) by sample-standard bracketing. The 2σ external reproducibility of the Rennes standard (analyzed every two samples) ranged from 18 to 25 ppm on a daily basis. Reported Pb isotope ratios were corrected for mass fractionation using the Tl doping method and normalized to SRM981 standard values of $^{208}Pb/^{204}Pb = 36.7219$, $^{207}Pb/^{204}Pb = 15.4963$, $^{206}Pb/^{204}Pb = 16.9405$ (Galer and Abouchami, 1998) by sample-standard bracketing. On a daily basis, the 2σ external reproducibility of SRM981 (analyzed every two samples) ranged from 84 to 166 ppm, 82 to 139 ppm, and 57 to 134 ppm for $^{208}Pb/^{204}Pb$, $^{207}Pb/^{204}Pb$, and $^{206}Pb/^{204}Pb$, respectively. Reported Hf isotope ratios are corrected for mass fractionation using $^{179}Hf/^{177}Hf = 0.7325$ (Patchett and Tatsumoto, 1981) and normalized to $^{176}Hf/^{177}Hf = 0.282160$ for the JMC 475 standard (Vervoort and BlichertToft, 1999) by sample-standard bracketing. On a daily basis, the 2σ external reproducibility of the ULB-JMC standard (analyzed every two samples) ranged from 19 to 35 ppm. Values of 2SE (twice the standard errors calculated from counting statistics) on individual isotopic analyses (the internal errors) are smaller than external reproducibilities. Full procedural blanks gave Sr, Nd, Hf and Pb concentrations of: Pb: 23.4 pg; Hf: 4-5 pg; Sr: 0.2-0.6 pg and Nd: 53 - 495 pg, which are negligible relative to sample concentrations.

A.2.2.5 Age correction of measured isotopic ratios

The measured isotopic ratios of the Siletz terrane have been age corrected in accordance with dates derived from the literature. The samples from the Metchosin Igneous complex were corrected to 53 Ma as an average of U –Pb zircon dates determined for the formation; 52 and 54 Ma (Yorath et al., 1999). A U-Pb zircon date of 50.5 Ma (Haeussler et al., 2000) has been determined for the Bremerton area of the Crescent formation and therefore sample B019 has been age corrected to this age. The remainder of the Crescent Main group, samples

225CM, 230CM, 423CM and 424CM, have been age corrected to 52 Ma, an average of available dates for this part of the formation (Babcock, 2006; Hirsch and Babcock, 2009; Gradstein et al., 2012). The Crescent South samples, 374 CS, 362 CS and 392 CS have been corrected to an average age of 51 Ma for the Willapa Hills region of Washington (Duncan, 1982; Moothart, 1992; Wells et al., 2014). Sample 450 CS from the Black Hills, Washington has been corrected to an age of 53.5 Ma (Duncan, 1982). Samples from the Newport and Corvallis regions in Oregon, 116SRV, 144SRV, 150SRV and CR011 have been corrected to an average age of 52 Ma for the area (Duncan, 1982; Pyle et al., 2009; Wells et al., 2014) and sample TK009 from the Tillmook area in northern Oregon to an age of 50.5 Ma (Wells et al., 2014). Finally the samples from the south of Oregon, the Roseburg portion of the Siletz River Volcancis, 042RB, 073RB, 095RB and 068RB have been corrected to an average age of 54.5 Ma (Duncan, 1982; Wells et al., 1984). Due to the higher RSD % values obtained for the Pb trace element values, alternative Pb (and for consistency Th and U) values were calculated using the Nd calculated approach of Arevalo Jr and McDonough (2010) whereby Pb = 0.0536 x Nd, Th = 0.0061 x Nd and U = 0.0158 x Nd (Buchs et al., 2016). However, the difference in the calculated Pb and measured calculated Pb on the initial isotope ratio was smaller than the symbols used and so negligible.

A.3 References

Abbey, S., 1981, The Search for "Best Values"-A Study Of Three Canadian Rocks: Geostandards Newsletter, v. 5, no. 1, p. 13-26.

Arevalo Jr, R., and McDonough, W. F., 2010, Chemical variations and regional diversity observed in MORB: Chemical Geology, v. 271, no. 1-2, p. 70-85.

Babcock, S., Geochemistry and petrology of a thick sequence of Crescent Basalt in the Dosewallips River Valley, Olympic Peninsula, Washington State, *in* Proceedings 102nd Annual Meeting of the Cordilleran Section, GSA, 81st Annual Meeting of the Pacific Section, AAPG, and the Western Regional Meeting of the Alaska Section, SPE2006.

Buchs, D. M., Hoernle, K., Hauff, F., and Baumgartner, P. O., 2016, Evidence from accreted seamounts for a depleted component in the early Galapagos plume: Geology, v. 44, no. 5, p. 383-386.

Chauvel, C., and Blichert-Toft, J., 2001, A hafnium isotope and trace element perspective on melting of the depleted mantle: Earth and Planetary Science Letters, v. 190, no. 3-4, p. 137-151.

Connelly, J. N., Ulfbeck, D. G., Thrane, K., Bizzarro, M., and Housh, T., 2006, A method for purifying Lu and Hf for analyses by MC-ICP-MS using TODGA resin: Chemical Geology, v. 233, no. 1, p. 126-136.

Duncan, R. A., 1982, A captured island chain in the coast range of Oregon and Washington: J Geophy. Res., v. 87, p. 10827-10837.

Galer, S., and Abouchami, W., 1998, Practical application of lead triple spiking for correction of instrumental mass discrimination: Mineral. Mag. A, v. 62, p. 491-492.

Gradstein, F. M., Ogg, J. G., Schmitz, M., and Ogg, G., 2012, The geologic time scale 2012 2-volume set, elsevier.

Haeussler, P., Clark, J., and Kenneth, P., 2000, Geologic map of the Wildcat Lake 7.5'Quadrangle Kitsap and Mason counties, Washington.

Hirsch, D. M., and Babcock, R. S., 2009, Spatially heterogeneous burial and high-P/T metamorphism in the Crescent Formation, Olympic Peninsula, Washington: American Mineralogist, v. 94, no. 8-9, p. 1103-1110.

Imai, N., Terashima, S., Itoh, S., and Ando, A., 1995, 1994 compilation values for GSJ reference samples," Igneous rock series": Geochemical Journal, v. 29, no. 1, p. 91-95.

Moothart, S. R., 1992, Geology of the middle and upper Eocene McIntosh Formation and adjacent volcanic and sedimentary rock units, Willapa Hills, Pacific County, southwest Washington.

Nobre Silva, I. G., Weis, D., Barling, J., and Scoates, J. S., 2009, Leaching systematics and matrix elimination for the determination of high-precision Pb isotope compositions of ocean island basalts: Geochemistry, Geophysics, Geosystems, v. 10, no. 8.

Patchett, P., and Tatsumoto, M., 1981, A routine high-precision method for Lu-Hf isotope geochemistry and chronology: Contributions to Mineralogy and Petrology, v. 75, no. 3, p. 263-267.

Pyle, D. G., Duncan, R. A., Wells, R. E., Graham, D. W., Harrison, B., and Hanan, B., Siletzia: An oceanic large igneous province in the Pacific Northwest, *in* Proceedings 2009 Portland GSA Annual Meeting2009.

Vervoort, J. D., and BlichertToft, J., 1999, Evolution of the depleted mantle: Hf isotope evidence from juvenile rocks through time: Geochim Cosmochim Acta, v. 63, no. 3-4, p. 533-556.

Weis, D., Kieffer, B., Hanano, D., Nobre Silva, I., Barling, J., Pretorius, W., Maerschalk, C., and Mattielli, N., 2007, Hf isotope compositions of US Geological Survey reference materials: Geochemistry, Geophysics, Geosystems, v. 8, no. 6.

Weis, D., Kieffer, B., Maerschalk, C., Barling, J., de Jong, J., Williams, G. A., Hanano, D., Pretorius, W., Mattielli, N., and Scoates, J. S., 2006, High-precision isotopic characterization of USGS reference materials by TIMS and MC-ICP-MS: Geochemistry, Geophysics, Geosystems, v. 7, no. 8.

Wells, R., Bukry, D., Friedman, R., Pyle, D., Duncan, R., Haeussler, P., and Wooden, J., 2014, Geologic history of Siletzia, a large igneous province in the Oregon and Washington Coast Range: Correlation to the geomagnetic polarity time scale and implications for a long-lived Yellowstone hotspot: Geosphere, v. 10, no. 4, p. 692-719.

Yorath, C. J., Sutherland Brown, A., and Massey, N. W. D., 1999, Lithoprobe, southern Vancouver Island, British Columbia: geology; With contributions by TDJ England, RM Bustin, Ottawa.

APPENDIX B – REPRESENTATIVE MAJOR AND TRACE ELEMENT RESULTS

The following table (Table B1) contains the major and trace element results for a representative selection of samples. Full results can be found in Appendix E3.

Table B1. Representative major and trace element data

Sample #	225CM	423CM	B019	450CS	374CS	205MET	202MET	073RB	116SRV
SiO_2	51.31	49.06	49.14	48.37	47.71	47.61	48.94	45.92	47.64
TiO_2	1.09	1.59	1.37	2.39	2.86	0.96	1.32	1.92	2.23
Al_2O_3	14.17	14.98	14.32	14.46	14.77	17.17	14.41	17.26	15.29
FeO*	12.73	11.88	10.92	13.40	15.05	11.58	13.32	13.15	13.12
MnO	0.19	0.17	0.10	0.25	0.25	0.21	0.20	0.22	0.31
MgO	7.25	7.85	7.55	6.22	4.65	8.06	6.76	7.40	7.15
CaO	10.09	11.71	14.23	11.91	11.58	12.79	11.81	9.88	11.64
Na_2O	2.82	2.18	2.11	2.43	2.51	1.46	3.09	2.90	2.18
K_2O	0.25	0.42	0.10	0.28	0.32	0.04	0.05	0.99	0.26
P_2O_5	0.10	0.16	0.16	0.26	0.27	0.09	0.11	0.34	0.19
LOI	1.29	1.11	1.90	1.01	1.54	1.11	1.68	0.95	1.39
Total	99.83	100.67	99.80	99.53	99.15	99.63	98.60	100.25	99.89
(ppm)									
Sc	47	46	46	42	40	41	47	25	40
V	375	308	nda	350	403	262	334	227	313
Cr	136	313	363	147	118	250	138	116	212
Co	46	45	51	61	41	43	47	49	51
Ni	109	116	111	122	133	171	80	45	85
Cu	106	63	153	158	177	108	118	53	98
Zn	102	107	70	114	144	96	57	83	118
Rb	0.94	1.34	5.52	2.22	3.14	0.24	1.29	4.98	0.68
Sr	91	323	231	269	250	100	116	652	222
Y	32.2	24.3	20.9	35.6	40.3	22.4	33.1	30.2	22.6
Zr	79	100	81	214	226	56	93	168	110
Nb	3.91	8.95	6.31	14.89	15.47	2.42	3.72	81.93	10.29
Ba	19	62	65	71	74	10	8	432	45
La	3.10	6.74	6.40	13.24	13.61	2.87	2.99	54.14	8.48
Ce	8.77	17.21	15.39	30.98	31.80	6.26	9.97	94.02	20.87
Pr	1.44	2.55	2.00	4.64	4.84	1.04	1.67	9.69	3.04
Nd	7.38	11.83	9.24	19.29	20.10	6.07	8.49	31.84	13.71
Sm	2.71	3.51	2.60	6.28	6.91	2.27	3.27	5.54	3.83
Eu	0.93	1.21	1.01	2.02	2.24	0.90	1.22	1.75	1.33
Gd	3.76	4.07	3.37	6.58	7.36	2.91	4.26	5.51	4.07
Tb	0.71	0.66	0.52	1.09	1.22	0.53	0.82	0.80	0.65
Dy	4.99	4.29	3.29	6.69	7.68	3.70	5.43	5.10	4.04
Ho	1.00	0.80	0.70	1.19	1.38	0.75	1.11	0.95	0.74
Er	3.01	2.23	2.03	3.46	4.16	2.28	3.37	2.77	1.99
Tm	0.52	0.36	0.31	0.52	0.63	0.38	0.55	0.46	0.32
Yb	3.32	2.25	1.85	3.19	3.74	2.29	3.51	3.03	1.95
Lu	0.53	0.32	0.29	0.46	0.55	0.34	0.53	0.45	0.28
Hf	1.93	2.40	2.10	5.07	5.62	1.44	2.39	3.13	2.62
Ta	0.22	0.48	0.36	0.99	1.04	0.15	0.20	4.51	0.63
Pb	5.21	3.08	2.16	0.66	2.96	0.17	1.03	4.02	7.41
Th	0.24	0.59	0.55	0.95	1.24	0.13	0.22	5.77	0.67
U	0.09	0.52	0.14	0.31	0.33	0.06	0.07	1.37	0.22

* Denotes total Iron. ** Total recalculated to an anhydrous basis

APPENDIX C – RADIOGENIC ISOTOPE RESULTS

The following table (Table C1) contains the radiogenic isotope results produced in this study. The table includes both measured and initial values, along with the 2σ standard errors. ε_{Hf} and ε_{Nd} are also displayed.

Table C1. Radiogenic Isotope Results

Sample #	225CM	230CM	423CM	424CM	B019	450CS	374 CS	362 CS	205MET	207MET	202MET	073RB
^{208}Pb/^{204}Pb	38.7887		38.7246	38.6958	38.4750	38.7580	38.7620	39.1266	38.7082	38.5715	38.3307	39.4752
2SE	0.0029		0.0022	0.0047	0.0022	0.0023	0.0015	0.0019	0.0020	0.0018	0.0019	0.0031
^{207}Pb/^{204}Pb	15.5393		15.5493	15.5495	15.5224	15.5498	15.5541	15.5927	15.5362	15.5273	15.5091	15.6173
2SE	0.0011		0.0009	0.0016	0.0009	0.0009	0.0006	0.0008	0.0009	0.0007	0.0007	0.0009
^{206}Pb/^{204}Pb	19.2607		19.1790	19.1042	18.8581	19.1943	19.1743	19.4409	19.0965	18.9909	18.7884	19.8567
2SE	0.0013		0.0009	0.0023	0.0010	0.0011	0.0007	0.0009	0.0011	0.0008	0.0007	0.0011
^{208}Pb/^{204}Pb i	38.781		38.691	38.332	38.431	38.724	38.737	39.085	38.626	38.551	38.294	39.220
^{207}Pb/^{204}Pb i	15.539		15.545	15.533	15.521	15.548	15.553	15.591	15.533	15.527	15.507	15.609
^{206}Pb/^{204}Pb i	19.252		19.089	18.763	18.823	19.163	19.151	19.403	19.028	18.975	18.750	19.673
^{176}Hf/^{177}Hf	0.283166	0.283175	0.283106	0.283070	0.283097	0.283079	0.283087	0.283054	0.283196	0.283182	0.283168	0.283060
2SE	0.000005	0.000006	0.000006	0.000005	0.000005	0.000006	0.000006	0.000007	0.000007	0.000004	0.000005	0.000005
^{176}Hf/^{177}Hf i	0.28313	0.28313	0.28309	0.28306	0.28308	0.28306	0.28307	0.28304	0.28317	0.28315	0.28315	0.28304
εHf	13.3	13.4	11.9	10.8	11.5	10.9	11.3	10.3	14.8	14.2	14.0	10.2
^{143}Nd/^{144}Nd	0.513058	0.513038		0.512985	0.512962	0.512990	0.512991	0.512943	0.513055	0.513028	0.513067	0.512937
2SE	0.000006	0.000005		0.000006	0.000007	0.000007	0.000008	0.000006	0.000007	0.000005	0.000007	0.000007
^{143}Nd/^{144}Nd i	0.51298	0.51296		0.51292	0.51290	0.51293	0.51293	0.51289	0.51297	0.51295	0.51299	0.51290
εNd	8.0	7.6		6.9	6.5	7.1	7.0	6.3	7.9	7.5	8.1	6.4
^{87}Sr/^{86}Sr		0.703813	0.703547	0.703137		0.703077	0.703086	0.703486	0.703232	0.703285	0.703407	0.703294
2SE		0.000009	0.000009	0.000008		0.000010	0.000009	0.000009	0.000012	0.000010	0.000010	0.000009
^{87}Sr/^{86}Sr i		0.70380	0.70353	0.70300		0.70297	0.70307	0.70348	0.70316	0.70323		0.70328

Table C1 continued. Radiogenic Isotope Results

Sample #	042 RB	095 RB	068RB	116SRV	144SRV	150SRV	CR011	TK009
$^{208}Pb/^{204}Pb$	38.7880	38.5914		38.9278	38.6587	38.6768	38.9113	39.1397
2SE	0.0030	0.0023		0.0025	0.0028	0.0030	0.0030	0.0025
$^{207}Pb/^{204}Pb$	15.5510	15.5918		15.5641	15.5516	15.5356	15.5650	15.5974
2SE	0.0012	0.0007		0.0010	0.0009	0.0011	0.0010	0.0008
$^{206}Pb/^{204}Pb$	19.2733	18.9291		19.4013	19.0478	19.1604	19.3876	19.4326
2SE	0.0013	0.0009		0.0010	0.0011	0.0013	0.0015	0.0011
$^{208}Pb/^{204}Pb$ i	38.781	38.532		38.912	38.615	38.658	38.592	38.984
$^{207}Pb/^{204}Pb$ i	15.551	15.589		15.563	15.549	15.535	15.552	15.588
$^{206}Pb/^{204}Pb$ i	19.265	18.869		19.385	19.001	19.140	19.120	19.224
$^{176}Hf/^{177}Hf$	0.283111	0.283020	0.283110		0.283106	0.283107	0.283075	0.283042
2SE	0.000005	0.000006	0.000005		0.000006	0.000008	0.000004	0.000004
$^{176}Hf/^{177}Hf$ i	0.28309	0.28301	0.28308		0.28308	0.28309	0.28306	0.28303
εHf	12.0	9.0	11.6		11.7	11.9	9.7	11.0
$^{143}Nd/^{144}Nd$	0.513035	0.512877	0.513025	0.513022	0.513008	0.513016	0.512998	0.512925
2SE	0.000005	0.000006	0.000008	0.000004	0.000006	0.000008	0.000007	0.000008
$^{143}Nd/^{144}Nd$ i	0.51298	0.51283	0.51296	0.51296	0.51295	0.51296	0.51294	0.51288
εNd	7.9	5.0	7.6	7.7	7.3	7.6	7.3	6.0
$^{87}Sr/^{86}Sr$	0.703126	0.703553		0.703056	0.703136	0.703057	0.703061	0.703395
2SE	0.000009	0.000007		0.000008	0.000008	0.000007	0.000010	0.000009
$^{87}Sr/^{86}Sr$ i	0.70310	0.70354		0.70305	0.70313	0.70304	0.70304	0.70311

SUMMARY OF ELECTRONIC APPENDICES

APPENDIX E1 – Contains an excel workbook with the sample locations and descriptions.

APPENDIX E2 – An excel file containing all SEM data and standards for this study.

APPENDIX E3 – Contains an excel file with the entirety of the Siletz terrane whole rock data, for both ICP_MS and ICP-OES data. Also included in this file are analytical tables for whole rock precision and accuracy.

APPENDIX E4 – An excel file with all radiogenic isotope results including the results for all standards, duplicates and replicates analysed.

APPENDIX E5 – An excel file containing data tables with the $^{40}Ar/^{39}Ar$ analytical results.

APPENDIX E6 – Is a PDF file summarising the palynological results of Dave Jolley for samples from this study.

APPENDIX E7 – Is an excel file which presents the mantle end members used to constrain the petrogenetic modelling and isotope mixing curves used in this study.

APPENDIX E8 – Contains a PDF presenting the work of Phillips et al., 2017, regarding the Siletz terrane.